Characterisation of a gain-of-function mutant of *CYSTEINE-RICH RECEPTOR-LIKE KINASE 10* (*CRK10*) in *Arabidopsis thaliana*

Submitted by

Maiara Piovesana

to the University of Exeter as a thesis for the degree of Doctor of Philosophy in Biological Sciences, September 2021

I certify that all material in this thesis which is not my own work has been identified and that no material has previously been submitted and approved for the award of a degree by this or any other University.

Signature: ……..

Abstract

Receptor-like kinases (RLKs) comprise a large superfamily of proteins in plant genomes, and play essential roles in plant growth, development and response to biotic and abiotic stresses. The CYSTEINE-RICH RECEPTOR-LIKE KINASES (CRKs) comprise one of the largest subfamilies of RLKs with over 40 members in *Arabidopsis thaliana*, and although a few members of the family have been initially characterised, their precise biological functions remain largely unknown. This thesis reports the characterisation of a novel gain-of-function allele of *CYSTEINE-RICH RECEPTOR-LIKE KINASE 10* (*CRK10*) in *A. thaliana* which was isolated from a chemical mutagenesis screen. This mutation causes the substitution of alanine 397 with a threonine residue in subdomain III / αC-helix of the kinase domain of CRK10, and this novel allele has been accordingly registered as *crk10-A397T* with the Arabidopsis community database. The *crk10-A397T* mutant is a dwarf, and anatomical characterisation unveiled severely collapsed xylem vessels in the root and hypocotyl of the plant. Reporter lines suggested *CRK10* is expressed in close association to vascular tissues, and a translational fusion with the fluorescent protein mCherry indicates that CRK10 is a plasma membrane-bound protein. Analysis of the recombinant WT and *crk10-A397T* versions of the cytoplasmic kinase domain of CRK10 demonstrated their auto-phosphorylation activity, and liquid chromatography tandem mass spectrometry (LC-MS/MS) analysis concluded that Thr397 acts as an additional auto-phosphorylation site *in situ*. Furthermore, an RNA-seq experiment revealed the constitutive induction of defence-related genes in the transcriptome of *crk10-A397T* mutant hypocotyls, including genes involved in the signalling pathways of the stress hormones salicylic acid (SA) and abscisic acid (ABA). Analysis of the composition of cell walls in the *crk10-A397T* mutant hypocotyls revealed extensive differences compared to the WT, an indication of cell wall remodelling mechanisms that are likely associated with the collapse of xylem vessels in this organ. Bioassays with the soil-borne vascular pathogen *Fusarium oxysporum* revealed that *crk10-A397T* mutant has a greater probability of survival to infection compared to WT plants. Analysis of genetic crosses demonstrated that key components of SA signalling pathways are required for the disease resistance phenotype of the *crk10-A397T* mutant.

Acknowledgements

I would like to express my profound gratitude to my PhD supervisors, who have offered me unwavering support whilst guiding me throughout these years. To Dr Michaela Matthes, Dr Smita Kurup and Prof Johnathan Napier, thank you very much. You have and will continue to inspire me as a scientist, and I consider myself lucky to have had the opportunity to work with you. Thank you for your patience and kindness, and for always making sure I had the best possible experience during my PhD studies. I can only hope I am worthy of following in your footsteps. To Dr Vinod Kumar and Prof Nicholas Talbot, my sincere gratitude for sharing your knowledge and always being willing to help. Special thanks to the University of Exeter for funding the PhD studentship which has allowed me to complete my studies, and all my gratitude to Rothamsted Research for welcoming me for the past four years.

To the collaborators who have so kindly shared their time and expertise with me, thank you. To Hannah Walpole, Kirstie Halsey and Dr Eudri Venter, thank you for helping me in my pursuit to explore the microscopic wonders of plant life. To Prof Colin Turnbull and Dr Nikolaus Wellner, thank you for welcoming me in your lab and for sharing your technical expertise. To Dr Ana Karla Machado Wood and Dr Ondrej Kosik, my sincere gratitude for sharing your time and knowledge; your mentoring support and scientific advice were vital for the completion of this work. To Dr Jason Rudd and Prof Kim Hammond-Kosack, thank you for the insightful scientific discussions and for your invaluable advice. To Dr Kirsty Hassall, thank you for the crucial help with the analysis of my experiments.

To the friends who have made these four years some of the happiest of my life, thank you. I cannot imagine what this journey would have been like without your support and friendship. In special, to my amazing friends and housemates Emily, Tania and Hannah, I will be forever grateful for having met you and shared these years with you. We have made some of my happiest memories together, and I am looking forward to what the future holds for Dr Masters-Clark, Dr Chancellor and Dr McGrath.

To Jean Marc Roberti, who has been the most supportive partner I could have asked for throughout this PhD, thank you for your words of encouragement and for always being so thoughtful and caring. Your unwavering support has

propelled me every step of the way, and I am ever so grateful for having such a wonderful, loving husband to share my life with. You once told me to trust the journey, and here I am. Thank you for inspiring me and holding my hand before, during and as I arrive at the end of this cycle.

Finally, my deepest gratitude goes to the ones who have followed this process from far away. To my grandparents, thank you for the endless love and support that you have always given me, I have thought of you every single day of these past four years. Mum and Dad, since I was a child you have instilled in me the desire to learn, to always strive to be the best version of myself and to pursue my dreams with all my heart. You have shown me what hard work looks like, and you have taught me the values and principles which I live by to this day. You were understanding when following my dreams meant moving to the other side of the Atlantic, and you have supported me every day from afar, as if you were right here by my side. Thank you for being a constant source of inspiration in my life, and for dreaming my dreams with me. I dedicate this achievement to you.

Table of Contents

List of Figures and Tables

Abbreviations

µg	microgram
µl	microlitre
µM	micromolar
µm	micrometre
ABA	Abscisic acid
ATP	Adenosine triphosphate
bp	base pairs
C	Celsius
cDNA	complementary DNA
cm	centimeter
CRK	Cysteine-rich receptor-like kinase
Col-0	Columbia-0
DAMP	Damage-associated molecular pattern
DNA	Deoxyribonucleic acid
DPI	Days post inoculation
EMS	Ethyl methanesulfonate
ET	ethylene
ETI	Effector-triggered immunity
FTIR	Fourier-transform infrared spectroscopy
h	hours
HR	Hypersensitive response
kb	kilobase
kd	Kinase domain
LC	Liquid chromatography
LRR	Leucine-rich repeat
JA	Jasmonic acid
mL	mililiter
mm	milimitre
mM	milimolar
M	molar
MS	Mass spectrometry / Murashige and Skooge
OD	Optical density

p	p value
PAMP	Pathogen-associated molecular pattern
PCR	Polymerase chain reaction
PDB	Potato dextrose broth
PRR	Pattern-recognition receptor
PTI	Pattern-triggered immunity
qPCR	Real time quantitative PCR
RNA	Ribonucleic acid
RNA-Seq	RNA sequencing
RLK	Receptor-like kinase
ROS	Reactive oxygen species
RT	Reverse transcription
SA	Salicylic acid
Taq	*Thermus aquaticus* polymerase
TEM	Transmission electron microscopy
TF	Transcription factor
WAS	Weeks after sowing
YT	Yeast extract, triptone

Chapter 1. Introduction

1.1 Signal transduction in eukaryotes

Signal perception and transduction are ubiquitous processes in eukaryotic organisms, which allow them to perceive environmental and endogenous cues and subsequently activate appropriate cellular responses. While all living beings rely on signal transduction to respond to environmental changes, including single-cell organisms, the development of signalling mechanisms between cells was a defining event for the emergence of multicellular life (Miller, 2012). The divergence of plants, animals and fungi occurred at least a billion years ago (Doolittle et al., 1996), and although each group has evolved its own mechanisms of perception and signalling, a few characteristics are still widely shared by all eukaryotes. An example is the generic structure of a signalling cascade comprised of a (1) receptor molecule, which often localises at the cell surface; (2) second messengers, which amplify the initial signal; (3) a cascade of phosphorylation and dephosphorylation of proteins in the cytosol; and (4) a cellular response as the final outcome of the signal transduction pathway (Tuteja and Mahajan, 2007).

A comparison between signal transduction cascades in animals and plants, for example, reveals the presence of several analogous components such as transmembrane receptors, GTP-binding proteins (G proteins), reactive oxygen species (ROS) and mitogen-activated protein kinases (MAPK) (Yang et al., 1997). Examples of structural and functional homology among signalling components observed between kingdoms include the well-known homeotic genes, which are important players in both flower development and animal segmentation (McCarty and Chory, 2000). Another example is the similarity between the octadecanoid and nitric oxide pathways, regulators of responses to wounding and pathogen attack in plants that are functionally related to animal pathways (Bergey et al., 1996; Durner et al., 1999). As sessile, photosynthetic organisms, the ability of plants to sense environmental stimuli is essential for their growth, development and survival, and it is as equally important as intercellular signalling processes. Light, gravity, temperature and pathogen elicitors are some of the exogenous cues which modulate a series of biological processes upon perception by the plant cells (McCarty and Chory, 2000). For instance, the recognition of a pathogen-derived elicitor triggers a series of intracellular

signalling events, including the phosphorylation and dephosphorylation of proteins, generation of ion fluxes and ROS, and the recruitment of transcription factors which modulate the expression of genes such as redox homeostasis regulators, detoxifying enzymes and pathogenesis-related (PR) genes (Zhu et al., 1996; Hammond-Kosack and Jones, 1996; Yang et al., 1997).

To further explore the mechanism of signal transduction in eukaryotes, a brief overview of some of the main signalling components in these organisms are described below.

1.1.1 Cell surface receptors

Lefkowitz and Michel (1983) defined a receptor as a macromolecule which localises within or on the surface of cells and regulates physiological processes by perceiving specific ligands. Cell surface receptors, which are anchored at the plasma membrane by a transmembrane domain, are specialized in the recognition of signals in the extracellular environment. In animals, receptors recognise a wide range of molecules, such as hormones, peptides, antigens, pathogen-derived compounds, glycoproteins, among others (Lefkowitz and Michel, 1983). Although the total number of receptors exposed at the cell surface at any given time is elusive, it is known to be continuously regulated as a mechanism to fine tune signal sensitivity. The removal of receptors from the cell surface is achieved, for example, by sequestration into the intracellular environment via endocytosis, which is followed by degradation, processing or recycling (Goldstein et al., 1979). The three largest classes of eukaryotic transmembrane receptors are ion channel-linked receptors, G-protein-coupled receptors (GPCRs), and enzyme-linked receptors (Alberts, 2002; Figure 1.1), which are explored in more detail in the following sections.

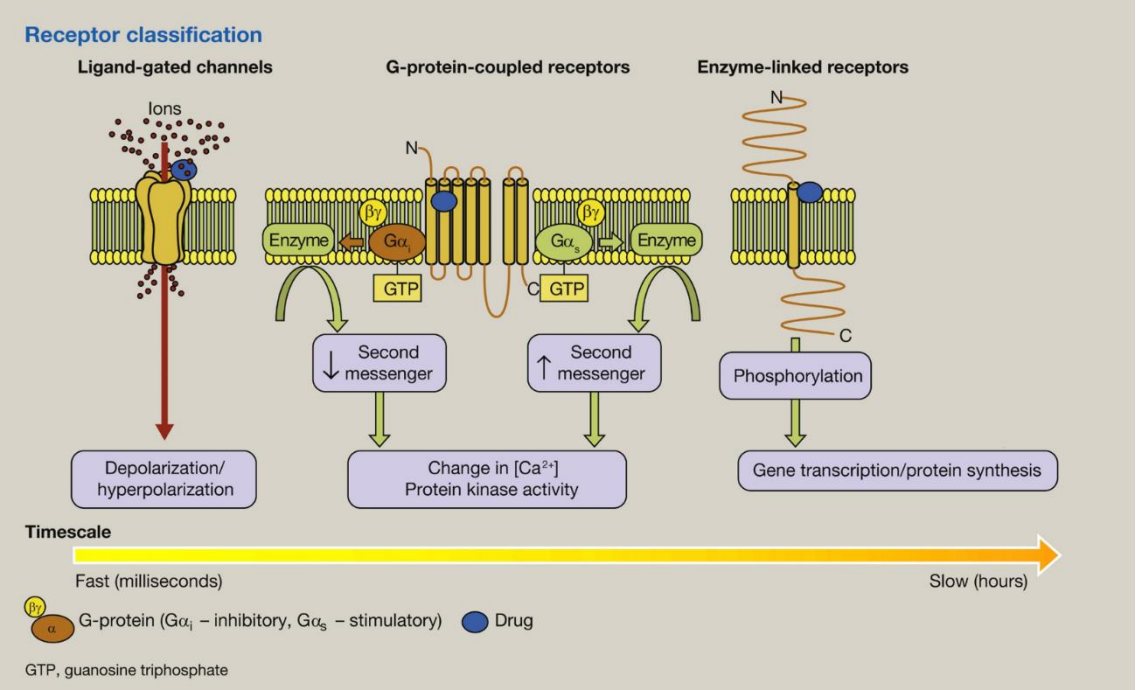

Figure 1.1 Classes of cell surface receptors in eukaryotic organisms.
The scheme depicts the three general classes of cell surface receptors found in eukaryotic organisms: ligand-gated channels (also known as ion channel-linked receptors), G-protein-coupled receptors (GPCRs) and enzyme-linked receptors. The scheme also shows the timescale of the downstream events which are usually triggered upon activation of each class of receptors. Adapted from Weir, 2019 (https://doi.org/10.1016/j.mpaic.2019.10.022); copyright notice in Appendix 1.1.

1.1.1.1 Ion-channel receptors

The movement of charged particles across lipid membranes is crucial for signalling between and within eukaryotic cells (Weir, 2019). One of the mechanisms through which this is accomplished is via ion-channel receptors, which are membrane-bound pores that selectively transport ions upon stimulation. Various stimuli can cause the activation (or gating) of ion channels in eukaryotic systems, such as chemical compounds, mechanical pressure, temperature and changes in H^+ ion concentration (Weir, 2019). The nature of the stimulus which induces the opening of the ion channel is used as the basis for their classification. For example, channels which are stimulated by ligands are known as ligand-gated ion channels, whereas changes in membrane potential induce the opening of voltage-gated channels. Upon opening of the channel, the movement of ions such as Na^+, K^+ and Ca^{+2} occurs in a passive manner

according to the electrochemical gradient across membranes. Up to 100 million ions can pass through an open ion channel per second, a much greater rate of transport compared to other carrier proteins (Alberts, 2002). The influx of positive ions (cations) and the efflux of negative ions (anions) causes what is known as the depolarization of the cell, whereas the opposite scenario (influx of anions and efflux of cations) causes hyperpolarization (Weir, 2019).

In animals, a classic example of ligand-gated ion channels are the ones activated by neurotransmitters during neuronal communication, such as the nicotinic acetylcholine receptors (nAChRs), γ-aminobutyric acid (GABA) receptors, glutamate receptors and ATP receptors (Li et al., 2014). These channels are oligomeric protein complexes which are involved in brain processes such as learning and memory (Ashcroft, 2006). In the case of the pentameric $GABA_A$ receptor, for example, N- and C- terminal domains containing the ligand binding sites are exposed in the extracellular environment (Li et al., 2014). The receptor is anchored at the plasma membrane by four transmembrane domains which encompass the ion channel wall. An intracellular loop between transmembrane domains 3 and 4 harbours regulatory motifs, binding and phosphorylation sites that mediate protein interaction, stability and function (Maksay et al., 2009). Upon binding to the neurotransmitter, the ion channel undergoes a conformational change which promotes the opening of the pore and consequent flux of ions.

Ion-channel receptors also play important physiological roles in plants (Dietrich et al., 2010). Voltage-gated ion channels known as *Shaker*-type K^+ channels, for instance, are essential for the maintenance of the K^+ ion homeostasis in higher plants (Gambale and Uozomi, 2006). These receptors, named after the animal *Shaker* channels due to their high sequence homology, are comprised of four transmembrane voltage sensor subunits, each one composed of six segments (Latorre et al., 2013). Based on their voltage-dependence, plants *Shaker*-type K^+ channels have been divided into three groups: (1) inward-rectifying channels, which are activated by hyperpolarization and promote K^+ influx; (2) outward-rectifying channels, which are activated by depolarization and allow K^+ efflux; and (3) weakly-rectifying channels, which can mediate both the uptake and the release of K^+ ions (Gambale and Uozomi, 2006).

Ligand-gated ion channels are also present in plants, such as the cyclic nucleotide-gated ion channels (CNGCs) family. The structure of CNGCs is

comprised of four subunits, each containing six transmembrane domains (Dietrich et al., 2010). With 20 members in *Arabidopsis thaliana* (herein referred to as Arabidopsis), CNGCs bind cyclic nucleotides such as cyclic nucleotide monophosphates (cNMPs) to induce the gating of the channel and movement of ions across membranes. The signalling pathways mediated by cNMPs via CNGCs are involved in developmental processes such as pollen tube growth and photomorphogenesis, and responses to abiotic and biotic stresses (Kaplan et al., 2007).

1.1.1.2 G-protein-coupled receptors

Both animal and plant cells rely on G proteins as a component of their signal transduction cascades (Tuteja, 2009). In animals, G protein-mediated signalling requires a plasma membrane-bound GPCR or an equivalent protein with guanine nucleotide exchange factor (GEF) function (Gilman, 1987). The heterotrimeric G protein and GPCRs were reported as the “signal transducer” and the “discriminator” molecules predicted by Rodbell in the 1970s as part of the signalling cascade initiated by the hormone glucagon (Gilman, 1987). The impact of this work for the understanding of eukaryotic signal transduction was so significant that the scientists behind these discoveries were later awarded the Nobel Prize (Rodbell, 1995; Gilman, 1995). Since then, the large superfamily of seven-pass transmembrane GPCRs in animals has been shown to regulate processes such as cell communication, sensory perception and chemotaxis. These receptors bind a variety of ligands in the extracellular environment and are reportedly the targets of 50-60% of all existing medicines (Tuteja et al., 2009). Binding between the GPCR and its cognate ligand in the extracellular environment is crucial for the activation of G protein-mediated signalling in animals. In the absence of the ligand, subunits Gα, Gβ and Gγ associate to form the inactive heterotrimeric complex, which is bound to a guanosine diphosphate (GDP) molecule via the Gα subunit (Figure 1.2 A). The binding of GPCR to a ligand activates the GEF function of the receptor, which promotes the dissociation of the Gα-GDP interaction. The Gα-subunit rapidly interacts with a guanosine triphosphate (GTP) molecule, which triggers a conformational change and the consequent activation of Gα. This event disrupts the interaction between the GTP-bound Gα and the Gβγ-subunits, releasing Gα to interact with and regulate the activity of effectors in the cytoplasm. The hydrolysis of the GTP molecule by

Gα and GTPase-accelerating proteins (GAP) such as regulators of G protein signalling (RGS), causes the inactivation of the Gα subunit and the reassembly of the heterotrimer (Tuteja et al., 2009; Urano et al., 2013).

Despite sharing structural similarities with their animal counterparts, plant G proteins have been shown to utilise distinct mechanisms and effector molecules to regulate aspects of plant growth and adaptation to stresses (Urano and Jones, 2013). The early 1990s saw the cloning of the first α-subunit of G protein in Arabidopsis, which was followed by multiple studies in other plant species investigating the roles of G proteins in defence to pathogens, oxidative stress and developmental processes (Urano et al., 2013). During the next decade, some of the distinctive features of G protein-mediated signalling in plants were discovered. Johnston et al. demonstrated that the α-subunit of the G protein of Arabidopsis can spontaneously dissociate from GDP and bind GTP *in vitro*, which suggested plant G proteins were capable of self-activation without the requirement of a GPCR. (Johnston et al., 2007; Urano et al., 2013; Figure 1.2 B). In agreement with this observation, no genes encoding canonical GPCR proteins were found in plant genomes. Furthermore, a class of chimeric proteins comprised of a seven-transmembrane (7TM) domain reminiscent of animal GPCRs and a cytosolic RGS domain was identified in plants, surprising the G protein community with its hybrid architecture (Chen et al., 2003; Johnston et al., 2007). The GAP activity of these 7TM-RGS proteins plays an important role in the regulation of G protein-mediated signalling in plants by hydrolysing the GTP nucleotide bound to the Gα-subunit (Johnston et al., 2007; Figure 1.2 B). The binding of a ligand to the 7TM-RGS protein promotes the release of the Gα-GTP dimer, which allows the self-activated α-subunit to interact with cytoplasmic effectors (Urano and Jones, 2013). Therefore, although signalling via G proteins is also ubiquitous in plants, the regulation of the plant G protein cycle differs significantly to that of animals.

Some of the roles played by G proteins in plants have been elucidated by the analysis of mutant lines. For instance, the phenotypes of loss-of-function mutants of Gα (AtGPA1) and Gβ (AGB1) revealed that G proteins participate in the regulation of several developmental processes in Arabidopsis, including leaf, flower and fruit development (Lease et al., 2001) and seed germination (Ullah et al., 2002). The dwarf phenotype of a Gα-subunit mutant of rice (*Oryza sativa*), named *dwarf1* (*d1*), showed that G proteins are also involved in the regulation of

plant morphology and hormone perception, as the mutant was isolated in a screen for gibberellin (GA)-insensitive mutants (Ashikari et al., 1999). Moreover, the rice *d1* and the Arabidopsis *agb1* mutants display increased susceptibility to fungal pathogens (Suharsono et al., 2002; Trusov et al., 2006), highlighting the importance of G proteins in mediating responses to biotic stress.

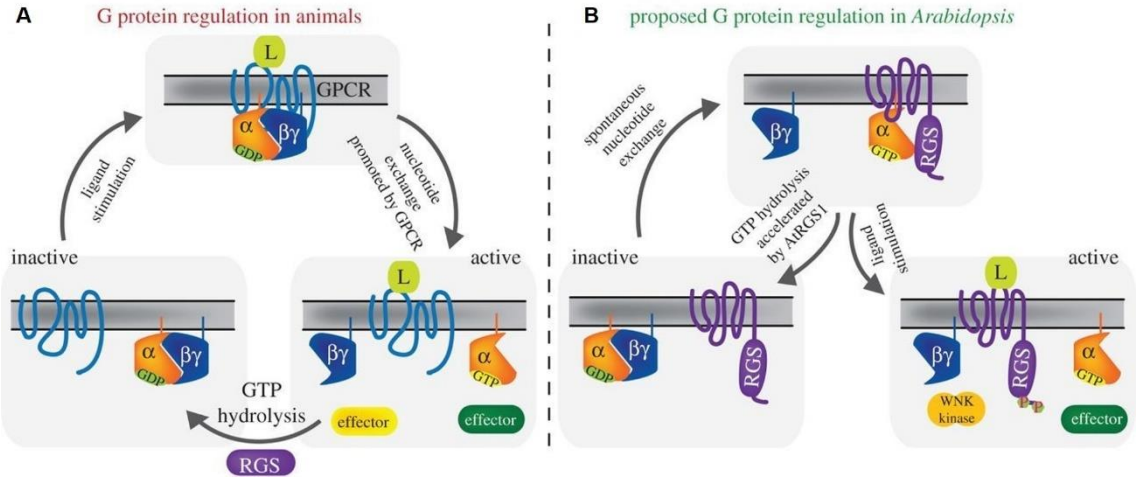

Figure 1.2 The regulation of G proteins in animals and plants.
Animal and plant cells possess different components which act in the regulation of G protein activity. (A) In animals, the heterotrimeric G protein is inactive in the absence of the ligand which is recognised by the GPCR (bottom left). Upon ligand-receptor binding, the GPCR promotes the dissociation of the G protein and the GDP molecule, which is exchanged by GTP (top). GTP-Gα is then released from the heterotrimer and activated G subunits interact with effectors in the cytoplasm (bottom right). The hydrolysis of the GTP molecule by Gα and regulator of G protein signalling (RGS) proteins causes the inactivation of Gα and promotes the reassembly of the inactive heterotrimeric complex.
(B) In plants, the inactive heterotrimeric G protein is also bound to GDP (bottom left). However, the Gα subunit can self-activate by spontaneously releasing the GDP molecule and exchanging it for GTP. The activity of GTP-bound Gα is regulated by its interaction with hybrid 7TM-RGS proteins, which accelerate the hydrolysis of the GTP molecule (top). Ligands such as d-glucose interact with the 7TM-RGS to promote the release of the Gα-GTP complex, allowing the active Gα to interact with effectors in the cytoplasm. Reproduced from Urano et al., 2013 (https://doi.org/10.1098/rsob.120186) under the terms of the Creative Commons Attribution License.

1.1.1.3 Enzyme-linked receptors

Enzyme-linked receptors are single-pass transmembrane proteins that have a ligand-binding extracellular domain and an intracellular domain which has enzymatic activity or associates with an enzyme (Alberts, 2002). One of the largest groups of enzyme-linked receptors in animals is the receptor tyrosine kinase (RTK) family. These receptors control essential cellular processes, such as cell cycle, migration, proliferation and differentiation (Schlessinger, 2000; Schlessinger, 2014). Their extracellular domain recognises a wide range of hormones and growth factors, such as the epidermal growth factor (EGF), fibroblast growth factors (FGFs) and insulin (Alberts, 2002). Their cytoplasmic kinase domain has tyrosine kinase activity, and it is subject to regulation via auto- and trans-phosphorylation events on regulatory motifs (see section 1.2.2 for details on the regulation of eukaryotic protein kinases).

It has long been known that the mechanism of activation of these receptors relies on the ligand binding event in the extracellular environment, which generally promotes receptor dimerization and phosphorylation of the kinase domain (Schlessinger, 1988). Certain ligands are bivalent and bind simultaneously to two receptor molecules, as it is the case of the growth hormone (GH) cytokine recognised by the growth hormone receptor (GHR; Jiang and Hunter, 1999; Schlessinger, 2000). Other growth factors require accessory molecules to activate their cognate receptors; this is the case of the interaction between FGFs and FGF receptors (FGFRs), which is stabilised by heparin-like molecules (Yayon et al., 1991). Upon ligand-binding and receptor oligomerisation, tyrosine residues in the activation loop of the kinase domain of RTKs are usually the first to be phosphorylated to promote kinase activation (Lemmon and Schlessinger, 2010). Secondary phosphorylation events create phosphotyrosine docking sites for interaction with downstream signalling molecules, which is followed by another set of auto-phosphorylation events to enhance kinase activity (Furdui et al., 2006).

In plants, receptor-like kinases (RLKs) are transmembrane enzyme-linked receptors which share structural and functional homology with animal RTKs (Walker, 1994; Shiu and Bleecker, 2001). Despite being initially regarded as serine/threonine kinases, tyrosine kinase activity of plant RLKs has been increasingly reported as an important aspect of the signalling cascades mediated by these receptors (Oh et al., 2009; Lin et al., 2014). Given that an RLK of

Arabidopsis is the object of study of this project, plant RLKs are reviewed in further detail in section 1.2.

1.1.2 Second messengers

An important feature of eukaryotic signalling pathways is the prompt production of second messengers upon signal perception by cell surface receptors (Newton et al., 2016). These compounds are capable of rapidly diffusing within the cell, which enables them to quickly amplify and relay the initial signal to intracellular components of the transduction cascade. To illustrate their importance and function as signalling molecules in eukaryotic systems, two classes of second messengers are explored in the sections below: calcium ion (Ca^{+2}) and ROS.

1.1.2.1 Calcium ions

Ca^{+2} ions are an important class of second messenger molecules in eukaryotic organisms, participating in every aspect of a cell's life and death (Clapham, 2007). Binding to calcium ions can affect a protein's subcellular localisation and function by altering its structure and charge and, therefore, intracellular calcium levels must be tightly regulated. However, it is this capacity to modify electrostatic fields and protein structure that renders Ca^{+2} ions as invaluable signalling agents. Strategies employed by eukaryotic cells to regulate cytosolic levels of Ca^{+2} include compartmentalization, chelation and extrusion. For instance, plant cells store calcium in several compartments, including the vacuoles, mitochondria, and the cell wall. Whilst the intracellular concentration of Ca^{+2} is kept in the nanomolar range, the extracellular environment holds millimolar amounts of this cation (Clapham, 2007). In animals, the efflux of calcium is performed by P type Ca^{+2}-ATPase, Na^{+}/Ca^{+2} and Na^{+}/Ca^{+2}-K^{+} transporters (Strehler and Treiman, 2004), while the influx is regulated by voltage-gated Ca^{+2}-selective channels. The latter are the fastest calcium signalling proteins, with the ability to conduct approximately a million Ca^{+2} ions per second (Clapham, 2007). In plant cells, the active extrusion of Ca^{+2} ions from the cytosol is also performed by P-type Ca^{+2}-ATPases, as well as by H^{+}/Ca^{+2} transporters (Axelsen and Palmgren, 2001; Hirschi, 2001). Interestingly, several plant Ca^{+2}-ATPases are exclusively expressed under stress conditions, which indicates their

role in maintaining low levels of cytosolic Ca^{+2} levels to avoid exaggerated responses.

As a second messenger, increased Ca^{+2} levels elicit signal transduction via calcium-binding proteins, which act as cytosolic sensors of the ever-changing calcium levels (Tuteja and Mahajan, 2007). The EF hand domain (Nakayama and Kretsinger, 1994) enables proteins to chelate Ca^{+2} ions with varying degrees of affinity. Calmodulins, the most prominent calcium-binding proteins, are small adaptors which require binding to Ca^{+2} ions to release auto-inhibitory mechanisms and associate with target proteins (Hoeflich and Ikura, 2002). The binding affinity of the EF hand domains of calmodulin is often enhanced by interacting partners. Highlighting the evolutionary relevance of calcium as a signalling molecule, calmodulins have barely changed over the course of 1.5 billion years (Clapham, 2007). C2 domain-containing proteins are another group of calcium-binding agents which are commonly found in signalling cascades, with approximately 650 genes encoding C2 domain-proteins in the human genome. Binding of up to three Ca^{+2} ions promotes the translocation of C2 domain-proteins to specific regions within the membrane where their substrates are located (Clapham, 2007).

Several environmental conditions and stressors promote changes in intracellular Ca^{+2} levels, which have been termed “calcium signatures” (Tuteja and Mahajan, 2007). This short-term localised increase in the level of cytosolic calcium ion is considered a universal response to stress, and it is essential to induce the required physiological changes. Each calcium signature is unique in its subcellular localisation, duration and the magnitude of the increase in cytosolic Ca^{+2} concentration which is also dependent on the location and abundance of the Ca^{+2} channels involved (Rudd and Franklin-Tong, 2011). Subsequent “waves” of Ca^{+2} influx are generated by the opening of Ca^{+2} channels to elicit a cellular response.

1.1.2.2 Reactive oxygen species

ROS are short-lived, highly reactive by-products of metabolism which are also important second messengers in eukaryotic signalling cascades. These molecules are generated and inter-converted by spontaneous chemical reactions or enzymatic catalysis which give rise to a multitude of species. Several ROS are generated as intermediates between molecular oxygen (O_2) and water, including

superoxide anion ($O_2^{\cdot-}$), the hydroxyl radical (OH.) and hydrogen peroxide (H_2O_2) (Winterbourn, 2008). Of these, hydroxyl radical poses the greatest risk to living systems due to its high reactivity; hence the importance of scavenging of superoxide and hydrogen peroxide within eukaryotic cells to avoid the formation of hydroxyl radical via the Haber-Weiss reaction (Haber and Weiss, 1934; Hopkins, 2016). Nevertheless, the physiological importance of ROS has become increasingly clear in recent decades, replacing the earlier notion that these compounds serve no biological purpose other than damaging biomolecules (Finkel, 2011; Mullineaux et al., 2018). Among all ROS, hydrogen peroxide is considered the most suitable signalling molecule due to its increased stability, widespread accumulation and potential mobility compared to other species (Gough and Cotter, 2011). Furthermore, superoxide has been implicated in signalling in bacterial cells (Amábile-Cuevas and Demple, 1991), while singlet oxygen ($^1O_2$), yet another reactive species, is known to participate in stress-responsive signalling in plants (Mullineaux et al., 2018). Hydroxyl radical, on the contrary, is not believed to be a signalling molecule due to its high reactivity.

In plant cells, ROS are continuously generated as by-products of metabolism in several cellular compartments. The chloroplast is the major source of ROS in photosynthetic tissues, with the potential to produce superoxide, hydrogen peroxide and singlet oxygen (Takahashi and Murata, 2008). The mitochondria are the major source of ROS in non-photosynthesizing cells, although its relative contribution is minor in chloroplast-containing tissues (Navrot et al., 2007). Finally, the peroxisomes are additional production sites of hydrogen peroxide and superoxide (Foyer and Noctor, 2009). Besides the generation of ROS via the metabolic pathways taking place inside organelles, hydroxyl radical can also be produced through the Fenton and Haber-Weiss reactions in the presence of transition metals (Richards et al., 2015).

When it comes to ROS production upon signal perception, however, NADPH oxidases (NOX)/ Respiratory Burst Oxidase Homologs (RBOH) are activated to produce localised bursts of ROS during developmental and stress responses in animals and plants (Panday et al., 2015; Chapman et al., 2019). One of the most notable examples of stress-induced ROS production in plants is the oxidative burst produced by RBOHs during pathogen attack (Lamb and Dixon, 1997; Torres and Dangl, 2005). This phenomenon usually occurs in two stages: a first, transient phase which happens shortly after pathogen perception in both

resistant and susceptible hosts, followed by a second phase which is triggered hours later and only occurs in resistant plants (Yang et al., 1997; Figure 1.3). Hydrogen peroxide produced during this burst has been shown to trigger cell wall reinforcement and act as a second messenger to induce the expression of defence-related genes (Yang et al., 1997). One mechanism through which these reactive species actively participate in signal transduction is by direct interaction with transcriptional factors such as NON-EXPRESSOR OF PR GENES 1 (NPR1), a key regulator of salicylic acid (SA)-responses to pathogens (Mou et al., 2003). Under normal growth conditions, NPR1 monomers interact with each other via intermolecular disulphide bonds, forming an oligomer in the cytoplasm. Upon induction of the oxidative burst promoted by the systemic acquired resistance (SAR) response to pathogen attack, redox changes in the intracellular environment cause the reduction of the disulphide bonds within the oligomer and the release of the NPR1 monomer. Once free, NPR1 monomers move into the nucleus to regulate the expression of defence-related genes.

Besides their roles in biotic stress responses, ROS also play important roles in plant growth and development (Gapper and Dolan, 2006) and engage in a complex crosstalk with phytohormones (Xia et al., 2015). Despite the difficulties in studying ROS due to their ephemeral existence, compartmentalisation and removal by the antioxidant machinery, their role as versatile signalling molecules which promote stress adaptation and modulate cellular responses has been well established in the literature (Foyer and Noctor, 2016).

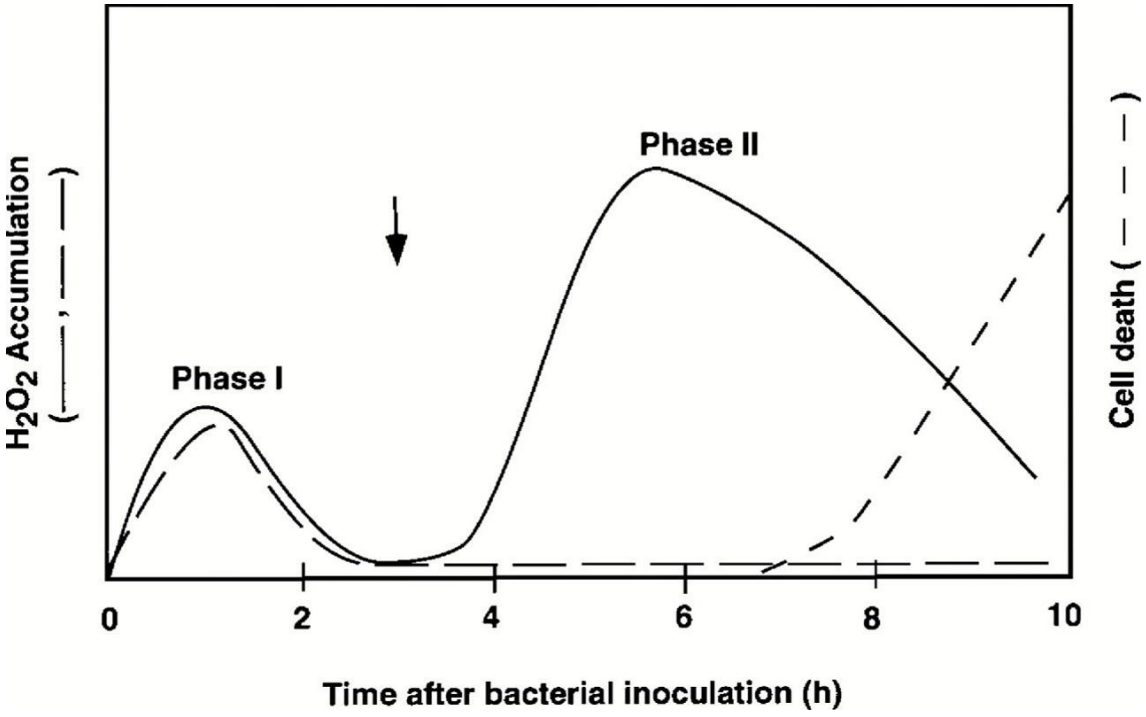

Figure 1.3 Two-phase kinetics of the accumulation of hydrogen peroxide (H_2O_2) and induction of cell death in plant cells following inoculation with avirulent and virulent pathogen.

Inoculation with virulent pathogen or nonpathogen induces a rapid single peak of H_2O_2 accumulation. Inoculation with avirulent or nonhost pathogens (solid line) induces host cell death and an oxidative burst in two stages: a first, transient and relatively weak burst (phase I), followed by a second more intense and prolonged stage of H_2O_2 production (phase II). Reproduced from Lamb and Dixon, 1997 (https://doi.org/10.1146/annurev.arplant.48.1.251); copyright notice in Appendix 1.2.

1.1.3 Mitogen-activated protein kinase cascades

Mitogen-activated protein kinase (MAPK) cascades are a conserved signalling feature in all eukaryotic organisms, from yeast through to Drosophila, mammals, and plants (Widmann et al., 1999; Morris, 2001). The general MAP kinase cascade is a signalling module where a MAP kinase kinase kinase (MAPKKK), a MAP kinase kinase (MAPKK) and a MAP kinase (MAPK) phosphorylate each other sequentially (Widmann et al., 1999; Figure 1.4). MAPKKKs are able to phosphorylate several MAPKKs, whereas MAPKK-MAPK interactions have a higher degree of specificity. The genome of Arabidopsis, for instance, contains multigene families encoding 80 MAPKKKs, 10 MAPKKs and

23 MAPKs (Jonak et al., 2002; Wang and Gou, 2020). Besides mitogens, other factors act as activators of MAPKs, including environmental cues such as osmolarity, light, heat and mechanical changes (Morris, 2001). To ensure the specificity of the signalling pathway, members of a given MAPK cascade are often held in close proximity via scaffolding proteins, forming complexes known as “signalosomes” (Whitmarsh and Davis, 1998; Chang and Karin, 2001). The activation of MAP kinases is dependent on the phosphorylation of conserved residues within their activation motifs (Payne et al., 1991; Ahn et al., 1993), and their activity is further controlled via regulation of their gene expression and dephosphorylation carried out by phosphatases (Keyse, 1998; Morris, 2001). Their participation in a wide range of biological processes has been well documented in literature, including early reports in yeast and Drosophila in the 1990s (Widmann et al., 1999). For instance, the MAPK Hog1, which is part of a cascade with the MAPKKK Ste11 and the MAPKK Pbs2, modulates the adaptation to high osmolarity conditions in yeast (Maeda et al., 1995). A signalosome comprised of Pbs2 acting as a scaffold to Ste11 and Hog1 ensures the activation of the correct signalling cascade (Posas and Saito, 1997). In Drosophila, $dMKK^{hep}$ and $dMAPK^{bsk}$ were shown to be required for dorsal closure during embryogenesis (Riesgo-Escovar et al., 1996).

In plants, MAPKs are grouped under four categories (A-D) based on their structure and the conserved TxY motif present in their activation loop. Groups A-C include the MAPKs with a TEY motif, while the TDY sequence characterises group D (Ichimura et al., 2002). Members of group A are involved in the regulation of development and responses to stress; MPK3 and MPK6, for example, activate defence responses to pathogens (Asai et al., 2002), regulate stomatal development and patterning (Wang et al., 2007) and inflorescence architecture (Meng et al., 2012). MPK4, a group B MAPK, is a regulator of systemic acquired resistance (Petersen et al., 2000), coordinates microtubule organisation and cytokinesis (Beck et al., 2010; Kosetsu et al., 2010), and mediates abiotic stress responses (Teige et al., 2004) in Arabidopsis. While the roles played by members of group C have been seldom investigated, group D MAPKs were shown to mediate ROS homeostasis (Takahashi et al., 2011), auxin signalling (Lee et al., 2009) and the function of cortical microtubules (Walia et al., 2009). Plant MAPKKs, often called MKKs, are also classified into four groups (A-D) based on sequence similarity (Ichimura et al., 2002). Members of all groups have been

shown to be multifaceted signalling molecules which participate in signal transduction during plant-pathogen interactions (Mészáros et al., 2006; Dóczi et al., 2007; Zhao et al., 2014), plant development (Xing et al., 2009; Benhamman et al., 2017) and responses to abiotic stresses (Hwa and Yang, 2007; Shen et al., 2019). Finally, MAPKKKs or MEKKs, initiate all MAP kinase signal transduction cascades and are, therefore, equally responsible for the regulation of developmental and stress-responsive processes. An example of a complete MAPK module identified in plants is the MEKK1, MKK4/MKK5 and MPK3/MPK6 cascade, which is activated during innate immune responses to confer enhanced resistance to bacterial and fungal pathogens (Asai et al., 2002). The omnipresence of MAPK cascades underlying so many aspects of plant growth and adaptation emphasizes their importance as signalling modules.

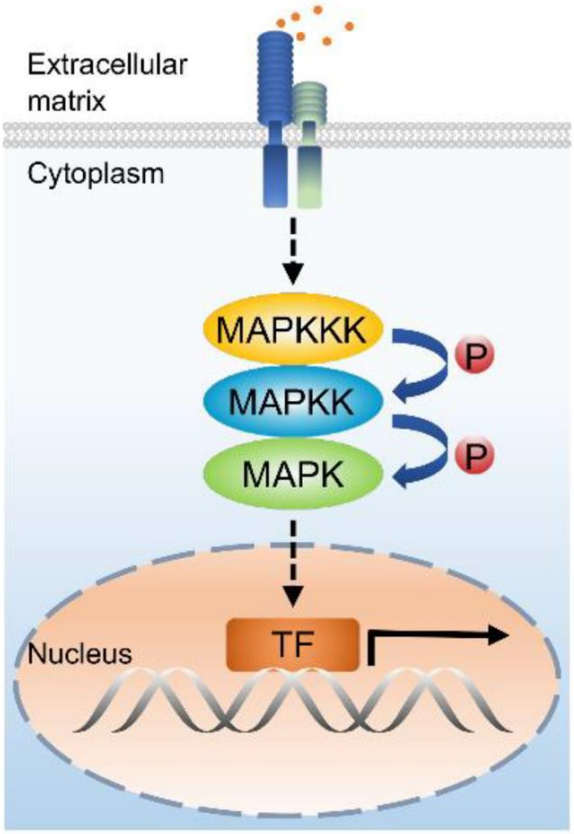

Figure 1.4 A general model of a MAPK cascade.

The model shows a typical MAPK cascade activated downstream of cell surface receptors upon ligand recognition in the extracellular environment. Following the phosphorylation of the three typical components of MAPK cascades (a MAPKKK, a MAPKK and a MAPK), the signal is transduced to downstream transcription factors in the nucleus. Orange dots represent extracellular signals recognised by

cell surface receptors. P indicates a phosphorylation event. TF, transcription factor. The black arrow indicates activation of gene expression. Reproduced from Wang and Gou, 2020 (https://doi.org/10.3390/ijms21207638) under the terms of the Creative Commons Attribution License.

1.2 Receptor-like kinases

Receptor-like kinases (RLKs) are enzyme-linked cell surface receptors localised at the plasma membrane of plant cells. Their biological relevance is reflected in the large size of the RLK superfamily in plant genomes, with over 600 and 1000 genes coding for RLKs in Arabidopsis and rice, respectively (Morris and Walker, 2003; Shiu et al., 2004). In Arabidopsis, this accounts for 60% of all kinases and 2.5% of all genes (Shiu and Bleecker, 2003). RLKs are structurally related to the animal Pelle/interleukin-1 receptor-associated kinase 1 (IRAK) kinases (Shiu and Bleecker, 2001). The highly conserved structure of RLKs is composed of an N-terminal signal peptide, an extracellular domain, a transmembrane region, and a C-terminal kinase domain (Shiu and Bleecker, 2003; Figure 1.5). This structure is reminiscent of the receptor tyrosine kinases (RTKs) and receptor serine/threonine kinases (RSKs) of the transforming growth factor β receptor (TGFβR) family of metazoans (Cock et al., 2002), although plant RLKs constitute a separate monophyletic gene family (Shiu and Bleecker, 2001). Insights from the analysis of domain organisation of RLKs in land plants suggested that domain fusion, gene duplications and whole genome rearrangements were responsible for the diversity and large size of this family of receptors in plants (Shiu and Bleecker, 2001). The diversity of the extracellular domain together with the phylogeny of the cytoplasmic kinase have been used to classify the RLK/Pelle into subfamilies (Hardie, 1999; Shiu and Bleecker, 2001; Figure 1.5).

Four main steps are recognised in the signalling events mediated by plant RLKs: (1) sensing a signal in the apoplast; (2) ligand-induced cytoplasmic kinase domain activation; (3) signal transduction via phosphorylation of downstream components of the signalling cascade; and (4) regulation of the RLK activity by interaction with inhibitory proteins, dephosphorylation or receptor internalization (Hohmann et al., 2017; Figure 1.6). The extracellular domain of RLKs are responsible for the perception of the ligand or environmental cue, the recognition of which often triggers receptor oligomerisation and activation via the

phosphorylation of serine, threonine and tyrosine residues in their kinase domains. The activation of their kinase domains via auto- and trans-phosphorylation events allows RLKs to phosphorylate intracellular targets, triggering the next steps of the signal transduction cascade (Couto and Zipfel, 2016).

One of the best-known examples of ligand-induced oligomerisation of RLKs is the association between SOMATIC EMBRYOGENESIS RECEPTOR KINASE 1 (SERK1) and BRASSINOSTEROID INSENSITIVE 1 (BRI1) in Arabidopsis, which is dependent on the presence of the ligand brassinosteroid (Santiago et al., 2013). Analysis of this complex revealed that the interaction with the co-receptor SERK1 is essential for the completion of the ligand-binding site, while the ligand itself promotes the association of receptor and co-receptor (Hohmann et al., 2017). Another example of RLK interaction with co-receptors is the heterodimer formed by BRI1 and BRI1-ASSOCIATED KINASE 1 / SOMATIC EMBRYOGENESIS RECEPTOR KINASE 3 (BAK1/SERK3; Li et al., 2002). Upon ligand-induced auto-phosphorylation, BRI1 associates with BAK1 and activates it by trans-phosphorylation of residues in the BAK1 kinase domain. The active BAK1 then phosphorylates residues in the juxtamembrane and C-terminal tail of the BRI1 kinase domain (section 1.2.2 for details of the eukaryotic kinase structure), modulating the kinase activity of BRI1 (Wang et al., 2008). BAK1 also interacts with the well-characterised LRR-LRK FLAGELLIN-SENSING 2 (FLS2) *in vivo* in a ligand-dependent manner. Analysis of the crystal structure of the heterodimer formed by the ectodomains of FLS2 and BAK1 in complex with the peptide ligand flagellin 22 (flg22) revealed that the co-receptor BAK1 also physically interacts with the FLS2-bound flg22 (Sun et al., 2013), similar to the ternary complex observed for BRI1-BAK1-brassinolide.

RLKs also interact with receptor-like proteins (RLPs), transmembrane receptors that lack a cytosolic catalytic domain (He et al., 2018). While RLKs are able to transduce the extracellular signal via phosphorylation of downstream targets in the cytoplasm, RLPs depend on the kinase activity of their interacting RLKs for signal transduction. Receptor-like cytoplasmic kinases (RLCKs), on the contrary, do not possess an extracellular domain but associate and interact with RLK complexes in the cytoplasm and play important roles in signalling via RLK-mediated trans-phosphorylation events (Lin et al., 2013).

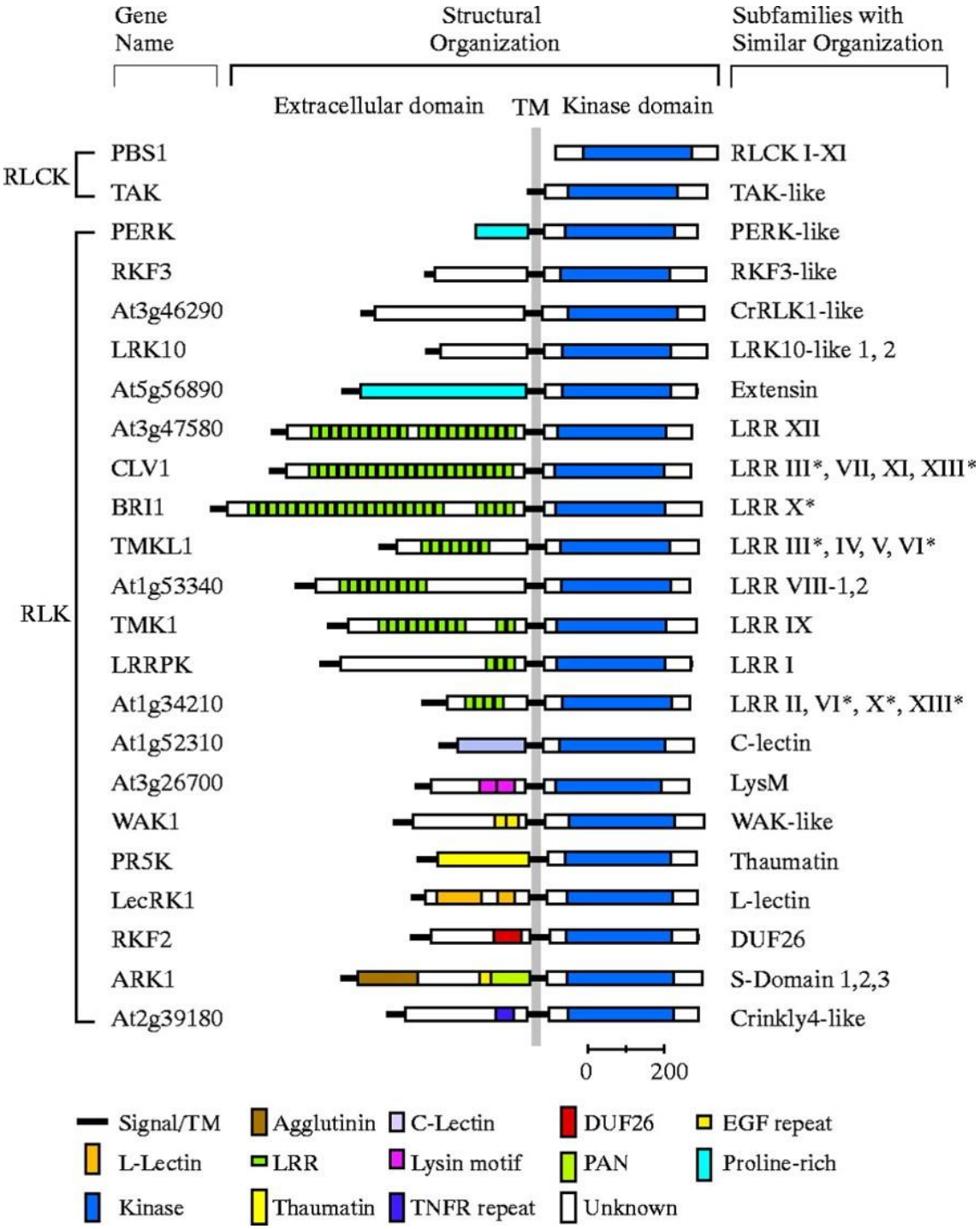

Figure 1.5 RLK subfamilies and their domain organisation.

The scheme depicts the diversity of domain organisation observed in representative members of several RLK subfamilies. The most commonly observed domain organisation among members of a given subfamily is represented in the scheme. Two RLCKs are also included. Signal peptides and transmembrane domains are represented by the solid black lines (signal peptides are not expected to be present in mature proteins but were included to indicate their presence). Domain names according to SMART and Pfam databases are

described, and subfamilies are assigned according to the kinase phylogeny. Asterisks indicate subfamilies with more than 30% of members classified under more than one major extracellular domain category. DUF, domain of unknown function; EGF, epidermal growth factor; C lectin, C-type lectin; L-lectin, legume lectin; PAN, plasminogen/apple/nematode protein domain; TM, transmembrane region; TNFR, tumor necrosis factor receptor. Reproduced from Shiu and Bleecker, 2001 (https://doi.org/10.1073/pnas.181141598); copyright notice in Appendix 1.3.

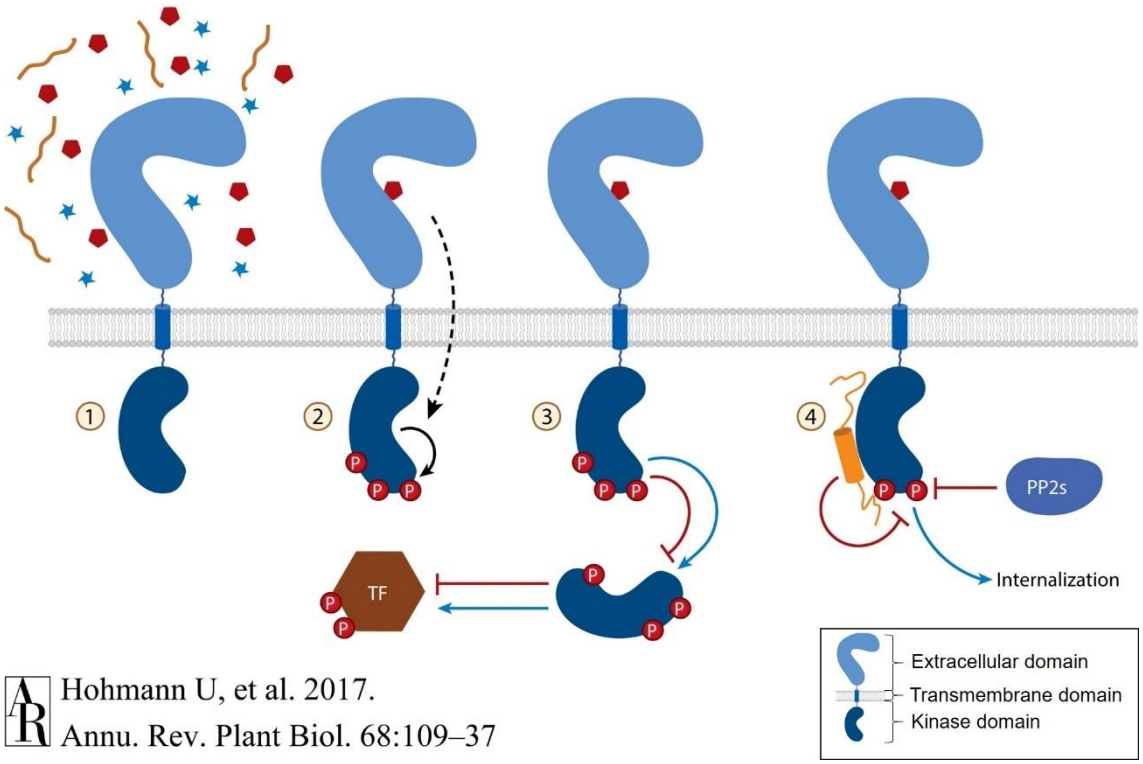

Figure 1.6 The four steps of plant receptor-like kinase signalling.

(1) The extracellular domain of plant RLKs is able to recognise specific native or exogenous ligands among the multitude of molecules present in the extracellular space. Potential ligands are shown as red pentagons, green stars, and orange sticks, and sites of protein phosphorylation are shown as red circles.

(2) Binding of a ligand to the extracellular domain of the RLK leads to the activation of the intracellular kinase domain via auto- and trans-phosphorylation with co-receptors at the plasma membrane (co-receptors are not shown in the scheme).

(3) Phosphorylation of cytoplasmic components by the kinase domain of the RLK activates (blue arrow) or inactivates (red bars) components of the cascade to transduce the signal and generate an output by ultimately modulating the activity of transcription factors (TFs).

(4) Regulation of the RLK activity to fine-tune the magnitude of cellular responses is achieved by interaction with inhibitory proteins (shown in orange), inactivation by protein phosphatases (PP2s) and endocytosis followed by recycling or degradation.

Adapted from Hohmann et al., 2017 (https://doi.org/10.1146/annurev-arplant-042916-040957) under the Creative Commons Attribution license.

1.2.1 The extracellular domain of RLKs

In contrast to the homologous nature of the kinase domain of plant RLKs, their extracellular region displays great variability with several distinct domains conferring structural and ligand-binding specificity to these receptors (Cock et al., 2002). As previously mentioned in section 1.2, the diversity of the RLK ectodomains was one of the criteria used to classify RLKs into subfamilies, with some of the best-known examples being the leucine-rich repeat (LRR)-RLKs, lysine motif (LysM) RLKs, lectin (Lec) RLKs, wall-associated kinases (WAKs) and cysteine-rich RLKs (CRKs), among several others (Tör et al., 2009).

The largest subfamily is the LRR-RLKs, with over 200 members in Arabidopsis (Shiu and Bleecker, 2001). The LRR domain is ubiquitous in all kingdoms, and several LRR-containing receptors in animals have been thoroughly investigated (Kobe and Kajava, 2001). In plants, some of the signals recognised by LRR-RLKs includes small endogenous peptides (Santiago et al., 2016), hormones (He et al., 2000) and pathogen-associated molecular patterns (PAMPs; Chinchilla et al., 2006). Units of 22-23 residues compose each LRR motif, which gets its name from its leucine-rich hydrophobic core (Hohmann et al., 2017). While stacking of LRR units gives rise to a horseshoe-like shape in animal and bacterial proteins, plant LRR domains exhibit a superhelical fold due to an additional β-strand (Kobe and Kajava, 2001). Nevertheless, the shape and size of the extracellular region of LRR-RLKs exhibits great diversity as the total number of LRR units harboured by each receptor is highly variable. For instance, the best-characterised ligand-binding LRR-RLKs to date contain 21-29 LRR units in their ectodomains, while non-ligand-binding co-receptors exhibit a much shorter extracellular region (Hohmann et al., 2017). The contrast between the ectodomains of the ligand-binding receptor FLS2 and its co-receptor BAK1/SERK3, which contain 29 and five LRR units, respectively, is one such example.

Another class of plant RLKs contains the carbohydrate-binding LysM domain in their extracellular region (Buist et al, 2008). Plant LysM are homologous to bacterial LysM proteins, an indication of their ancestral origin (Hohmann et al., 2017). Experimental evidence suggests that an individual LysM domain is responsible for recognising carbohydrates containing N-acetyl-D-glucosamine (NAG) such as chitin (Liu et al., 2012). A well-known member of this group, the LysM-RLK CERK1 was shown to undergo homodimerization *in vitro*

upon binding to chitin octamers, a mechanism which is thought to be essential for receptor activation (Liu et al., 2012).

The subfamily of wall-associated kinases (WAKs) contains sequence motifs which are similar to the mammalian epidermal growth factor (He et al., 1996). Their association with plant cell walls was determined based on a number of experimental observations, such as their apparent cross-linked status with insoluble material and their presence at both the plasma membrane and cell wall when targeted with immunocytochemistry (He et al., 1996). Growing evidence suggests that WAKs recognise pectin, oligogalacturonic acids (OGs) produced by pathogen attack and glycine-rich proteins (GRPs) in the cell wall, which is plausible given their requirement during cell expansion and responses to biotic stresses (Kohorn and Kohorn, 2012).

Another subfamily is the LecRLKs, characterised by the presence of a lectin/lectin-like domain which can bind carbohydrates (Sun et al., 2020). Several studies have described their participation in a wide range of processes, including development and responses to biotic and abiotic stresses (Vaid et al., 2013). LecRLKs are widely distributed in plant genomes, with 75 genes in Arabidopsis, 173 in rice and 231 in *Populus*, for example (Vaid et al., 2012; Yang et al., 2016). They are classified into three groups based on their extracellular lectin domain: L-, G- and C-type (Sun et al., 2020). L-type LecRLKs, first identified in Arabidopsis in 1996 by Hervé et al., possess a legume-like lectin domain folded into a β-sandwich which is responsible for the recognition of hydrophobic glycans, hormones and pathogen-derived molecules in the apoplast (Bellande et al., 2017). By contrast, G-type and C-type LecRLKs contain a mannose-binding and a calcium-dependent lectin domain, respectively (Sun et al., 2020).

The cysteine-rich RLKs (CRKs) also form large subfamilies in plant genomes, with over 40 members in Arabidopsis (Chen et al., 2004; Shiu and Bleecker, 2003). This class of RLKs was named after the cysteine-rich motif found within the Domain of Unknown Function 26 (DUF26; Gnk2 or stress-antifungal domain; PF01657) present in their ectodomains (Chen, 2001). Disulphide bridges linking cysteine residues within the conserved motif C-8X-C-2X-C were shown to be involved in the structural stabilization of a DUF26-containg protein in Arabidopsis (Vaattovaara et al., 2019). Moreover, the ability to bind mannose was demonstrated for the soluble DUF26 proteins Ginkbilobin-2 (Gnk2) from *Gingko biloba* and Anti-Fungal Protein 1 (AFP1) from maize

(Miyakawa et al., 2014; Ma et al., 2018), suggesting this domain is involved in binding of carbohydrates. As the extracellular domain of the CRKs shares around 30% of sequence identity with Gnk2 (Miyakawa et al., 2009), it is hypothesized that these RLKs bind carbohydrates in the apoplast, although this hypothesis has not been proven to date. The subfamily of CRKs is further explored in section 1.4.

1.2.2 The kinase domain of RLKs

Protein phosphorylation is a common mechanism employed by eukaryotic cells to regulate cellular processes and signalling cascades, a concept which first emerged with the work of Krebs and Fischer in the 1950s (Krebs and Fischer, 1956; Krebs et al., 1959; Cohen, 2002). A phosphorylation event can affect a protein's activity in several ways depending on the location of the phosphorylation site, resulting in its activation, inhibition or creation of an allosteric docking site for interaction with other proteins, to name a few examples (Johnson and Lewis, 2001). Protein kinases, the enzymes which catalyse the phosphorylation of substrates, form one of the largest superfamilies of proteins in eukaryotic genomes, the so-called "kinome" (Taylor et al., 2012). They have the ability to transfer a phosphoryl group from the γ-phosphate of ATP to the hydroxyl group of serine, threonine and/or tyrosine residues (Endicott et al., 2012). Despite the majority of the work to elucidate protein kinase structure and regulation having been performed in mammalian kinases (as described in this section), the high degree of homology between eukaryotic protein kinases allows us to extend these findings to the kinase domain of plant RLKs.

The determination of the protein structures of PROTEIN KINASE A (PKA) and CYCLIN DEPENDENT PROTEIN KINASE 2 (CDK2) in the early 1990s (Knighton et al., 1991; De Bondt et al; 1993) highlighted a remarkable characteristic of this protein family, which are the distinct structural conformations they adopt in their active and inactive states. Transition to the active state usually occurs in response to specific stimuli, as for instance, the binding of an extracellular ligand by plant RLKs. The core domain of eukaryotic protein kinases encompasses ~290 residues folded into two lobes, and it harbours several conserved motifs essential for catalysis and scaffolding (Endicott et al., 2012; Taylor et al., 2012). These conserved regions were classified into 12 subdomains by Hanks and Hunter according to their structure and function (Hanks and Hunter, 1995).

The smaller, N-terminal lobe of the kinase, is formed by a five-stranded β-sheet and an α-helix, while the C-terminal lobe is mainly helical (Figure 1.7). The deep cleft found between the two lobes encloses the kinase active site. The helical structure of the N-terminal lobe is referred to as the αC-helix, a crucial structure present in all eukaryotic protein kinases (Taylor et al., 2012). Two highly conserved residues within the N-lobe, a glutamate residue located in the αC-helix (Glu91; PKA numbering used here and subsequently in the text) and a lysine within the β-strand 3 (Lys72), contribute to the optimal positioning of the ATP molecule by interacting with the α- and β-phosphate groups, which tethers the conformation of this helix to nucleotide binding (Huse and Kuriyan, 2002; Endicott et al., 2012; see Figure 1.8 for a visual representation of the kinase structure described in this section). The five-stranded anti-parallel β-sheet in the N-lobe also plays an essential role in ATP-binding, as the glycine-rich loop which joins β strands 1 and 2 (known as the phosphate-binding loop / P-loop), anchors and positions the γ-phosphate for catalysis (Taylor et al., 2012). Once bound to the nucleotide binding pocket, the triphosphate group is optimally positioned to allow the transfer of the γ-phosphate to the protein substrate at the edge of the active site (Endicott et al., 2012).

The C-terminal lobe, in turn, contains the activation segment, a region of around 20-35 residues which is flanked by the conserved Asp-Phe-Gly (or DFG, in the single letter amino acid code) and Ala-Pro-Glu (APE) motifs (Huse and Kuriyan, 2002; Nolen et al., 2004). The aspartate residue of the DFG motif (Asp184) plays an important role in the active conformation of the kinase, as it contributes to the orientation of the ATP molecule by chelating a Mg^{+2} ion, an interaction which is disrupted in the inactive state. Phosphorylation of the activation segment is essential to stabilise this region in a conformation which is optimal for substrate binding (Huse and Kuriyan, 2002). Furthermore, a four-stranded β-sheet also found in the C-lobe contains the catalytic loop, a region where several key residues, such as the catalytic aspartate, are found (Taylor et al., 2012).

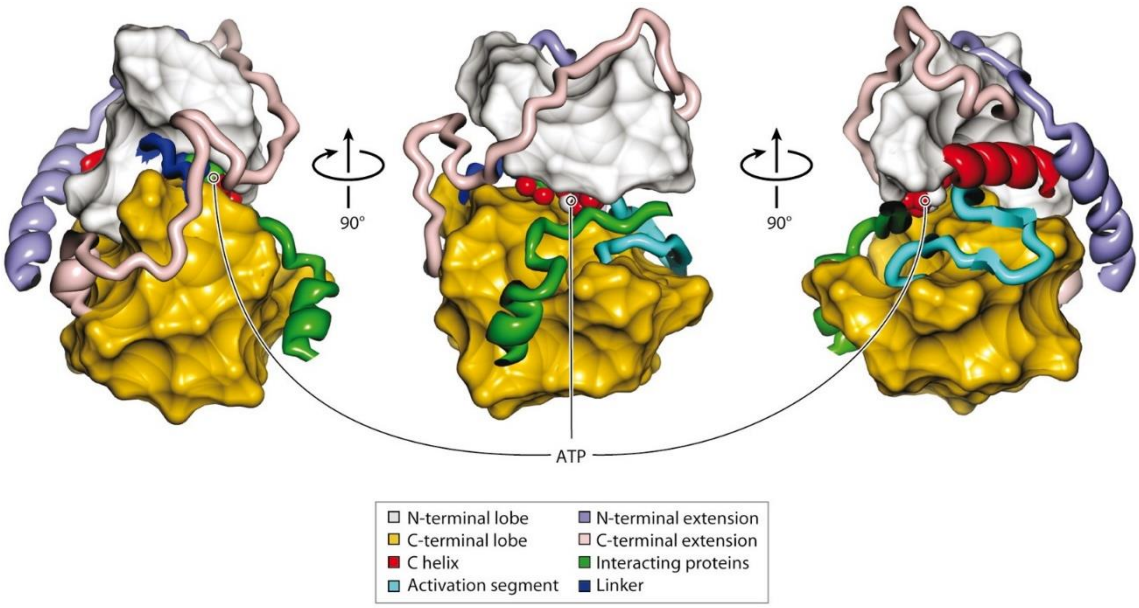

Endicott JA, et al. 2012.
Annu. Rev. Biochem. 81:587–613

Figure 1.7 Architecture of a prototypical protein kinase.

Model representation of a typical protein kinase (protein kinase A, Protein Data Bank (PDB) code 1ATP). Represented in the model are the N- and C-terminal lobes, αC-helix, activation segment, N- and C-terminal extensions and an interacting protein inhibitor. Three consecutive views are shown, each representing a rotation of 90° on vertical axis. Reproduced from Endicott et al., 2012 (https://doi.org/10.1146/annurev-biochem-052410-090317); copyright notice in Appendix 1.4.

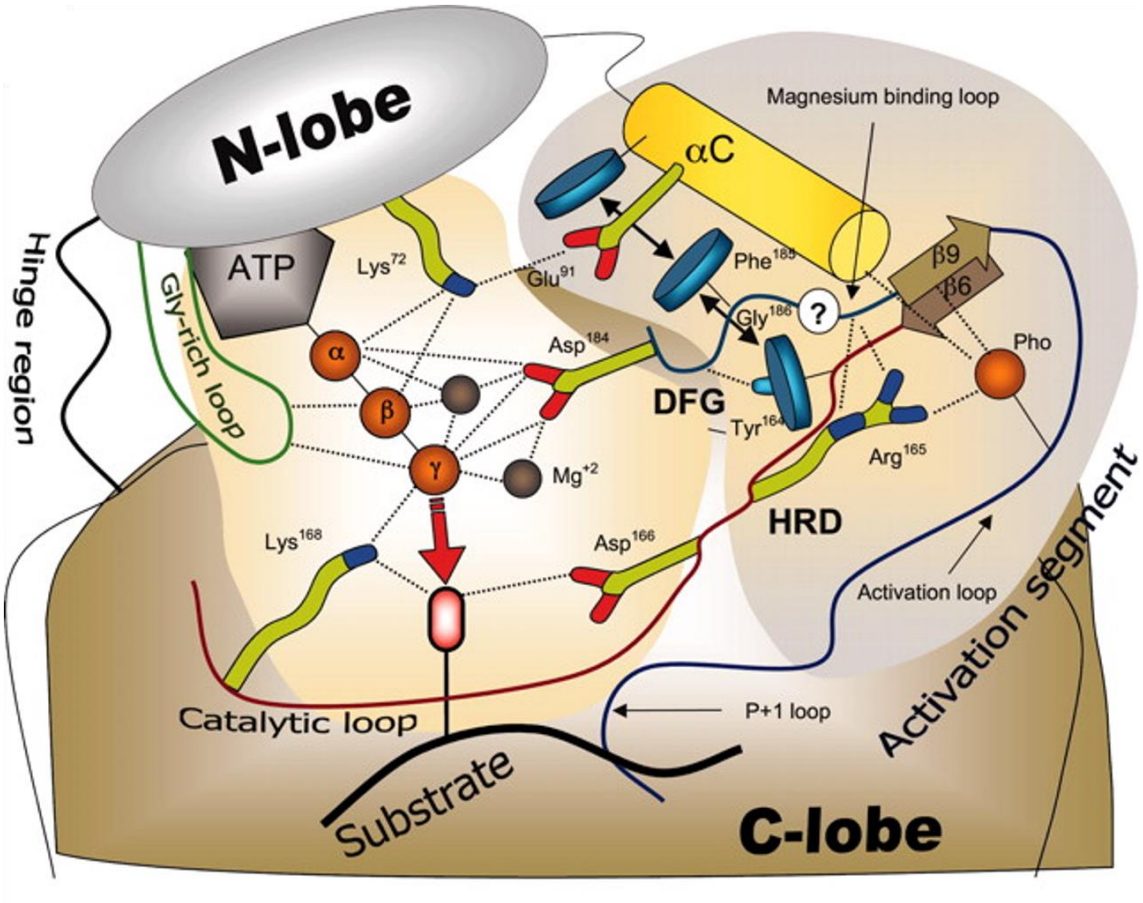

Figure 1.8 Schematic of the interactions within the catalytic core of the kinase domain.

The scheme depicts the interactions between the kinase domain, the ATP molecule and a substrate. The red arrow indicates the transfer of the γ-phosphate of ATP to the substrate. The yellow shaded area encompasses catalytically important residues which interact with the ATP molecule and/or with the substrate. The grey shaded area highlights secondary structures and residues involved with the regulation of the kinase activity. The black arrows indicate hydrophobic interactions between the HRD motif, the DFG motif and the αC helix. Dashed lines represent polar contacts. Reproduced from Kornev et al., 2006 (https://doi.org/10.1073/pnas.0607656103); copyright notice in Appendix 1.5.

Nuclear magnetic resonance analysis of PKA showed that the inactive enzyme corresponds to a state which is “uncommitted” to catalysis, whereas addition of the nucleotide molecule causes the transition to a catalytically “committed” state, where backbone motions throughout the kinase are created (Masterson et al., 2010; Masterson et al., 2011; Figure 1.9). Induction of the catalytically competent state of the activation segment is triggered by phosphorylation and involves a large conformational change between the “off” and “on” states (Johnson et al., 1996). The number and location of total phosphorylation sites varies between kinases but, generally, one phosphate occupies a central position and interacts with the catalytic loop (Huse and Kuriyan, 2002). In PKA, phosphorylation of threonine 197 leads to the formation of hydrogen bonds with the side chains of His87 within the αC-helix, Lys189 within the activation segment, and Arg165, located near the catalytic aspartate (Endicott et al., 2012). The activation segment provides a platform for the binding of the peptide substrate, which then adopts an extended conformation across the front end of the nucleotide binding pocket and exposes the hydroxyl group for catalysis (Huse and Kuriyan, 2002).

In addition to the mostly hydrophilic motifs with well-defined functions in ATP binding and catalysis, the comparison of multiple protein kinase structures using local spatial pattern (LSP) alignment unveiled the presence of a hydrophobic kinase core, composed by the αF-helix and two “spines” formed by non-adjacent residues (Kornev et al., 2006; Kornev et al., 2008; Figure 1.10). As the residues which form these spines are not contiguous, such structures would not have been identified based solely on protein sequence analysis. The first spine was found to be always intact in active kinases, but broken in the inactive state, and was therefore termed the “regulatory”, or R-spine. The formation of this spine depends on the phosphorylation of the activation segment between β-strand 9 and the αF-helix. This event flips the DFG motif and allows the phenylalanine residue to interact with a histidine from the catalytic loop and two leucine residues derived from the αC-helix and the β-strand 5; this results in the coordinated movement of both kinase lobes and the assembly of the R-spine (Kornev et al., 2006; Figure 1.9). The second spine, named the “catalytic”, or C-spine, also traverses both kinase lobes, but requires the insertion of the adenine ring of the ATP to be fully assembled. In PKA, the C-spine is comprised of two residues from the αF-felix, one residue from the αD-helix, and three residues from

β-strand 7 (Kornev et al., 2008; Figure 1.10). Although being largely immobilised due to its location within the rigid hydrophobic core of the C-terminal lobe, the αF-helix bridges several key areas for catalysis and substrate binding, including the C- and R- spines. Therefore, it constitutes an important signal-integrating element and a robust scaffold for the whole kinase molecule (Johnson et al., 2001; Kannan et al., 2005; Kornev et al., 2008).

Finally, in addition to the core kinase domain which contains the essential catalytic features, interactions with flanking regions are often required to yield optimal kinase assembly and catalytic activity. In PKA, for example, an N-terminal and a C-terminal tail are both required for kinase stability and activity. In the case of the plasma membrane-bound receptor-tyrosine kinases, the core kinase domain is flanked by a linker region (called the juxtamembrane) and a C-terminal tail, both harbouring several regulatory phosphorylation sites (Taylor et al., 2012).

Several regulatory strategies of protein kinase activation have been reported for members of different families, which allows them to function downstream of the specific signals that activates them (Huse and Kuriyan, 2002; Endicott et al., 2012). Activation via phosphorylation of residues in the activation segment is a characteristic of the so-called RD kinases, which contain an arginine residue preceding the conserved catalytic aspartic acid (Johnson et al., 1996). For many kinases, the arrangement of the activation loop and the αC-helix are coupled during kinase activation, as changes in one requires a switch in the other (Huse and Kuriyan, 2002). For example, the cell cycle kinase CDK2, relies on the allosteric interaction with a cyclin subunit to trigger the rotation of the αC-helix and the subsequent movement of the activation segment out of the catalytic site, allowing its phosphorylation (Jeffrey et al., 1995). The Src family of tyrosine kinases similarly requires a conformational change in the αC-helix for kinase activation (Sicheri et al., 1997; Xu et al., 1997). The AGC kinases, the group to which PKA belongs, require the phosphorylation of a hydrophobic motif located near the C terminus of the protein, in addition to the phosphorylation of the activation segment, for the αC-helix to change conformation (Pearce et al., 2010). Thus, the movement of the αC-helix from the so-called “out” to an “in” conformation is a well-described event during protein kinase activation (Taylor et al., 2015).

Another mechanism of kinase activation is the dimerization-dependent trans-phosphorylation of the activation segment, which is the case for receptor

tyrosine kinases. The dimerization of these receptors, which is triggered by ligand binding of their extracellular domains, allows the removal of an inhibitory sequence from the active site and the rearrangement of the activation segment, further stabilised by the phosphorylation of a conserved threonine or tyrosine (Huse and Kuriyan, 2002; Lemmon and Schlessinger, 2010). In the insulin receptor tyrosine kinase (IRK), for example, this inhibitory sequence contains three tyrosine residues originating from the activation segment, and its conformation in the inactive state precludes protein activity by blocking the binding of both the peptide substrate and the ATP molecule. Upon activation, however, these tyrosine residues are trans-phosphorylated, shifting the activation segment to the optimal conformation for substrate binding (Hubbard et al., 1994; Hubbard, 1997). A similar mechanism of activation has been described for serine/threonine protein kinases (Oliver et al., 2007).

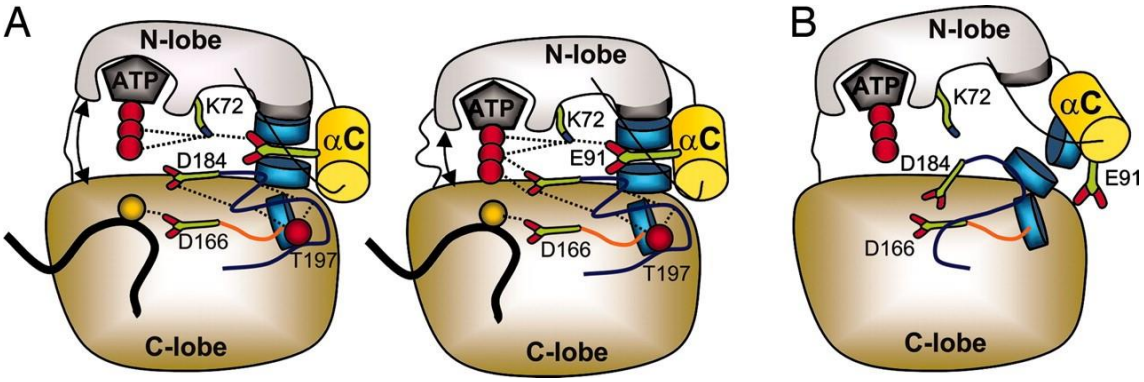

Figure 1.9 A general model of the active and inactive conformation of protein kinases.

(A) In the active conformation, phosphorylation of threonine 197 (PKA numbering used here and subsequently) arranges the Mg^{+2} binding loop and positions the aspartate and the phenylalanine residues of the DFG motif for interaction with ATP and to form the regulatory (R) spine, respectively. The movement of the αC-helix completes the formation of the spine and enables the interaction between lysine 72 and glutamate 91. Once stabilised, the kinase molecule can switch between and open (left) and closed (right) conformation.

(B) In the inactive conformation, the kinase molecule is destabilised as the Mg^{+2} binding loop and the R spine are deformed, and the N- and the C-lobe move independently.

The blue disks and the shaded portion of the N-lobe represent the residues which compose the R spine. Reproduced from Kornev et al., 2006 (https://doi.org/10.1073/pnas.0607656103); copyright notice in Appendix 1.5.

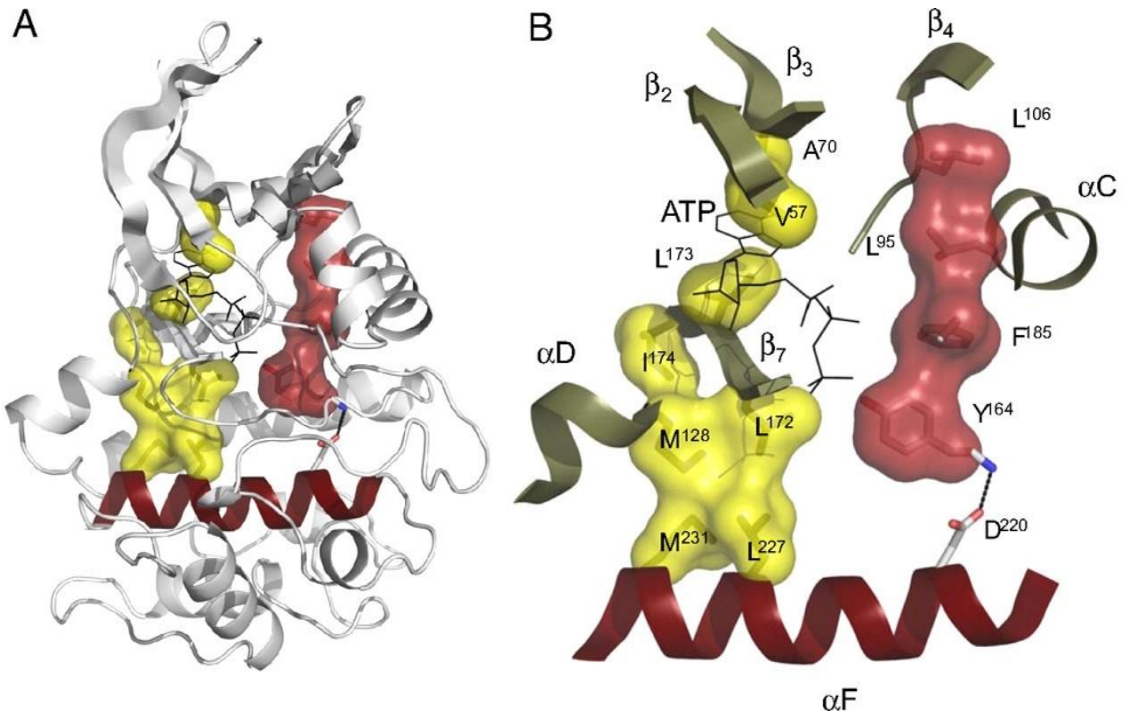

Figure 1.10 The regulatory and the catalytic spines and the αF-helix compose the hydrophobic kinase core.

(A) The hydrophobic core of the kinase domain is occupied by the R spine (red molecular surface), the C spine (yellow molecular surface) and the αF-helix (dark red ribbon). The structure of PKA is shown in the model. The red molecular surface represents the hydrophobic portion of the R spine.

(B) Model depicting the R and C spines and the αF-helix in greater detail. The residues which compose the spines are indicated by the single letter amino acid code and PKA numbering. The adenine ring of ATP which is required for the full assembly of the C spine is also shown.

Reproduced from Kornev et al., 2008 (https://doi.org/10.1073/pnas.0807988105); copyright notice in Appendix 1.6.

1.3 Biological functions of RLKs

RLKs are involved in a wide range of biological processes, including the regulation of normal growth and developmental programmes and adaptation to stress conditions. Their involvement in aspects of plant development (section 1.3.1), abiotic stresses (section 1.3.2) and plant immunity (section 1.3.3) are reviewed below.

1.3.1 RLKs in plant development

Several aspects of plant growth and development are tightly regulated by RLKs. These receptors are activated upon perception of hormones and small endogenous peptides, for example, and the downstream signalling cascades regulate numerous developmental processes (Tör et al., 2009). The LRR-RLK CLAVATA1 (CLV1) is one of the best characterised RLKs with vital roles in the regulation of developmental programmes via its interaction with CLV2 and CLV3 (De Smet et al., 2009). CLV1 is the receptor of the secreted protein CLV3, and together with the LRR-RLP CLV2, regulates stem cell population size and differentiation in shoot and floral meristems in Arabidopsis (Fletcher et al., 1999). Given the potential impacts of interfering with the signalling cascade initiated by this complex, the mild phenotypes exhibited by *clv-1* knockout mutants were puzzling (Clark et al., 1993). Later on, the discovery that the RLKs BARELY ANY MERISTEM (BAM) and CORYNE/SUPPRESSOR OF OVEREXPRESSION OF LIGAND-LIKE PROTEIN1-2 (CRN/SOL2) are redundant with CLV1 in the regulation of meristem size and differentiation clarified this observation (DeYoung et al., 2006; Müller et al., 2008). CLV3 belongs to the CLE (CLV3/ENDOSPERM SURROUNDING REGION) family, the best-studied class of small peptides in plants (De Smet et al., 2009). Other members of this family act as signals to promote root meristem maintenance and vascular development (Mitchum et al., 2008). Likewise, the LRR homologs HAESA (HAE) and HAESA-LIKE2 (HSL2) control the abscission of floral organs by potentially binding to the secreted protein INFLORESCENCE DEFICIENT IN ABSCISSION (IDA; Cho et al., 2008). Below ground, the development of the root is coordinated by several factors, including the interaction between the ROOT MERISTEM GROWTH FACTOR (RGF) peptides and the RGF receptors (RGFRs; Shinohara et al., 2016). Moreover, the RLK ARABIDOPSIS CRINKLY4 (ACR4) was shown to be the receptor of the small peptide CLE40 in Arabidopsis roots, and the signalling

cascade triggered by their interaction controls stem cell niche size via the transcription factor WOX5 (Stahl et al., 2009).

The phenomenon of self-incompatibility (SI), an important mechanism to maintain a diverse gene pool, is also controlled via RLK signalling. The stigma-localised S-locus receptor kinase (SRK) recognises the S-locus cysteine-rich protein/S-locus protein 11 (SCR/SP11) from anthers, which triggers a signalling cascade that ultimately inhibits pollen germination to avoid self-fertilization in Brassica species (Shiba et al. 2001).

When it comes to plant growth, cell elongation and division are some of the processes regulated by the binding of the hormone brassinosteroid to the LRR-RLK BRI1 (Clouse et al., 1996; He et al., 2000). Cell expansion was also shown to be regulated via the signalling cascade governed by the ligand-receptor pair phytosulfokine and PHYTOSULFOKINE RECETOR (PSKR) in carrot (Matsubayashi et al., 2002; Matsubayashi et al., 2006). The well-known LRR-RLKs ERECTA and ERECTA-like control the development and spatial patterning of stomata upon binding with the peptide hormones EPIDERMAL PATTERNING FACTORs (EPFs; Lee et al., 2012). Stomatal development is also regulated by TOO MANY MOUTHS (TMM), another LRR-RLK which governs the orientation of cell divisions that give rise to stomatal patterning, as well as the balance between stem cell niche maintenance and differentiation during stomatal and epidermal development (Geisler et al., 2000; Nadeau et al., 2002).

1.3.2 RLKs in abiotic stresses

RLKs also play pivotal roles in sensing stressors of abiotic nature and triggering cellular responses to overcome these (Ye et al., 2017). Overexpression of the RLK RECEPTOR-LIKE KINASE1 (RPK1), for example, enhances signalling pathways activated in response to drought stress and the hormone abscisic acid (ABA), a major regulator of developmental processes and responses to abiotic stresses (Osakabe et al., 2010). Another key player in ABA signalling, the RLK GUARD CELL HYDROGEN PEROXIDE-RESISTANT1 (GHR1) mediates the production of hydrogen peroxide required during stomatal movement (Hua et al., 2012).

Several members of the LecRLK family are reportedly involved with the regulation of responses to salt stress (Sun et al., 2020). For instance, SRK is transcriptionally induced by ABA, salt and drought stress in wild soybean (*Glycine*

soja) and confers increased salt tolerance to transgenic Arabidopsis plants (Sun et al., 2013). Expression of this RLK in *Medicago sativa* plants also rendered them more resistant to salt stress, as *Gs*SRK seems to modulate ROS scavenging, ion homeostasis and osmotic regulation (Sun et al., 2018). A recent study uncovered the roles of *Os*LecRLK of rice in the removal of sodium ion from the cell, which is promoted by the induction of the Na^+/K^+ channel SALT OVERLY SENSITIVE 1 (SOS1; Passricha et al., 2020). Interestingly, the FERONIA (FER) member of the *Catharanthus roseus* group of RLKs, which is mainly known for its role in male-female gametophyte interaction (Huck et al., 2003), was also reported to play roles in ABA-mediated responses to salt stress (Chen et al., 2016).

Drought is another major abiotic stress which can have detrimental effects on plant growth; thus, plants have evolved numerous strategies to endure dry growth conditions. Several studies have investigated the function of RLKs in drought responses in rice. For instance, drought resistance promoted by the overexpression of the LRR-RLK FLORAL ORGAN NUMBER 1 (FON1) was associated with the transcriptional induction of ABA- and stress-responsive genes (Feng et al., 2014). The RLK LEAF PANICLE 2 (LP2), by contrast, was shown to have the opposite effect (Wu et al., 2015). The expression of this receptor is regulated by the transcription factor DROUGHT AND SALT TOLERANCE (DST), and the protein interacts with drought-responsive aquaporins at the plasma membrane. Constitutive expression of LP2 enhanced the susceptibility of rice plants to drought, revealing this RLK is a negative regulator of drought responses. The RLKs *Os*SIK1 and *Os*SIK2 were also shown to induce enhanced tolerance to drought; while *Os*SIK1 activates the antioxidative system and reduces the number of stomata, which lessens water loss (Ouyang et al., 2010), *Os*SIK2-mediated resistance seems to rely mainly on the antioxidative machinery to dampen the effects of oxidative stress (Chen et al., 2013).

Low temperature is another environmental stressor that impairs plant growth by affecting the fluidity of membranes and enzyme activity. A calcium-regulated RLK of Arabidopsis, CRLK1, seems to be a positive regulator of plant tolerance to cold, as knockout lines were more sensitive to low temperature and showed a delay in transcriptional changes induced by cold stress (Yang and Syang, 2010).

Furthermore, RLKs also mediate the detoxification of metals, another abiotic stress which can greatly impair plant health. The wall-associated kinase WAK1 is up-regulated in Arabidopsis roots after treatment with aluminium (Al) (Sivaguru et al., 2003). Plants overexpressing WAK1 exhibited increased root growth in high-Al conditions, suggesting this RLK is an important player against metal toxicity in Arabidopsis roots.

1.3.3 RLKs in plant immunity

Phytopathogens pose a great threat to plants, and their prompt perception by plant cells is vital to elicit defence responses in a timely manner. A multitude of pathogen-derived signals is recognised by RLKs known as pattern recognition receptors (PRRs), thus activating the pattern-triggered branch of plant immunity called PTI (see section 7.1 for a more detailed description of the plant immune system). Despite being recognised by distinct PRRs, pathogen-associated molecular patterns (PAMPs) often trigger similar events at the final steps of the signalling cascade, such as the transcriptional induction of similar subsets of genes (Yang et al., 1997). Although only a few ligand-receptor pairs have been identified for PAMPs and PRRs, some examples have been thoroughly characterised (Tör et al., 2009; Greeff et al., 2012). One of these examples is the interaction between the peptide flg22, derived from the bacterial elicitor flagellin and the LRR-RLK FLS2 (Chinchilla et al., 2006). Ligand binding promotes the rapid heterodimerisation of FLS2 with the co-receptor BAK1/SERK3, and this interaction is required for the activation of flg22-triggered responses (Chinchilla et al., 2007). These observations revealed that BAK1 is not only recruited by BRI1 to regulate developmental processes (Li et al., 2002), but also associates with a PRR to elicit defence responses to pathogens. FLS2 also interacts with other members of the SERK family, although the FLS2-BAK1 dimer is the predominant form (Roux et al., 2011). The FLS2-BAK1 complex also associates and trans-phosphorylates with the receptor-like cytoplasmic kinase BOTRYTIS-INDUCED 1 (BIK1; Lu et al., 2010). Upon flg22 perception, the interaction between FLS2-BAK1 and BIK1 is diminished, which indicates the release of BIK1 from the complex (Lu et al., 2010). Moreover, a mechanism to attenuate the defence responses elicited by flg22 was uncovered in 2011 by Lu et al. Upon flg22 binding, the U-box E3 ubiquitin ligases PUB12 and PUB13 associate with the FLS2 receptor complex and are phosphorylated by BAK1. This is followed by the

ubiquitination of FLS2 by PUB12 and PUB13, which directs the receptor for degradation, thus weakening the flg22-induced signalling cascade. Besides interacting with FLS2, BAK1 also associates with the LRR-RLK EF-Tu RECEPTOR (EFR) upon binding to the bacterial-derived elongation factor (EF)-Tu peptide (Roux et al., 2011). Another well-characterised PRR is *Os*Xa21, which binds to the secreted tyrosine O-sulfonation peptide of *Xanthomonas oryzae* pv. *oryzae* (*Xoo*; Song et al., 1995). A study by Park and Ronald (2012) reported the unusual mechanism of signal transduction employed by Xa21; ligand-receptor binding promotes the cleavage of the intracellular kinase domain of Xa21 and its translocation to the nucleus, where it directly interacts with transcription factors to promote immune responses (Park and Ronald, 2012).

In addition to PAMPs, plant immune responses are also initiated via the recognition of damage-associated molecular patterns (DAMPs; Tör et al., 2009; Greeff et al., 2012). These molecules are either endogenous peptides which act as danger signals, or host-derived molecules released by pathogen-induced hydrolysis. For example, the PROPEP1 protein of Arabidopsis is the precursor of the small Pep1 peptide, which binds the LRR-RLK PEP RECEPTOR 1 (PEPR1) to amplify defence responses to pathogens (Yamaguchi et al., 2006). Other examples of RLKs which recognise DAMPs are the *Catharanthus roseus* THESEUS1 (THE1) and FER, which are thought to act as cell wall sensors (Cheung and Wu, 2011). Although no ligand has been identified to date, the activity of THE1 seems to be conditioned by perturbations in cell wall integrity, which suggests this receptor might recognise cell wall-derived fragments. Moreover, a role for FER in biotic interactions was reported by Kessler et al. (2010), indicating that this receptor's ability to sense cell wall changes during pollen tube growth are also capable of triggering defence responses to pathogens.

1.4 CYSTEINE-RICH RECEPTOR-LIKE KINASES

In the late 1990's and early 2000's, several groups reported their findings about a new class of RLKs in Arabidopsis which were transcriptionally induced by pathogen attack, ROS and the hormone SA (Czernic et al., 1999; Du and Chen, 2000; Ohtake et al., 2000). In 2001, Chen reported that members of this family contained two copies of the cysteine-rich C-X8-C-X2-C motif in their extracellular domains, distinct from the cysteine motifs of S-locus glycoproteins

and SRKs. This motif is characteristic of the DUF26 domain, and DUF26-containing RLKs were classified as CYSTEINE-RICH RECEPTOR-LIKE KINASES (CRKs). CRKs are thought to have originated from the fusion between single-domain cysteine-rich receptor-like secreted proteins (sdCRRSPs) with the transmembrane region and kinase domain of LRR_clade_3 RLKs (Zulawski et al., 2014; Vaattovaara et al., 2019). The duplication of the DUF26 domain likely occurred after the fusion event, giving rise to the double-domain extracellular region of CRKs (Vaattovaara et al., 2019; Figure 1.11). The decades that followed Chen's work in 2001 have seen numerous studies which focused on characterising the biological functions of CRKs in Arabidopsis and other plant species. Despite hypothesis based on observations of other DUF26-containing proteins (see section 1.7), no ligand has been identified for a CRK to date, and their specific mechanism of action and downstream signalling cascades remain largely elusive.

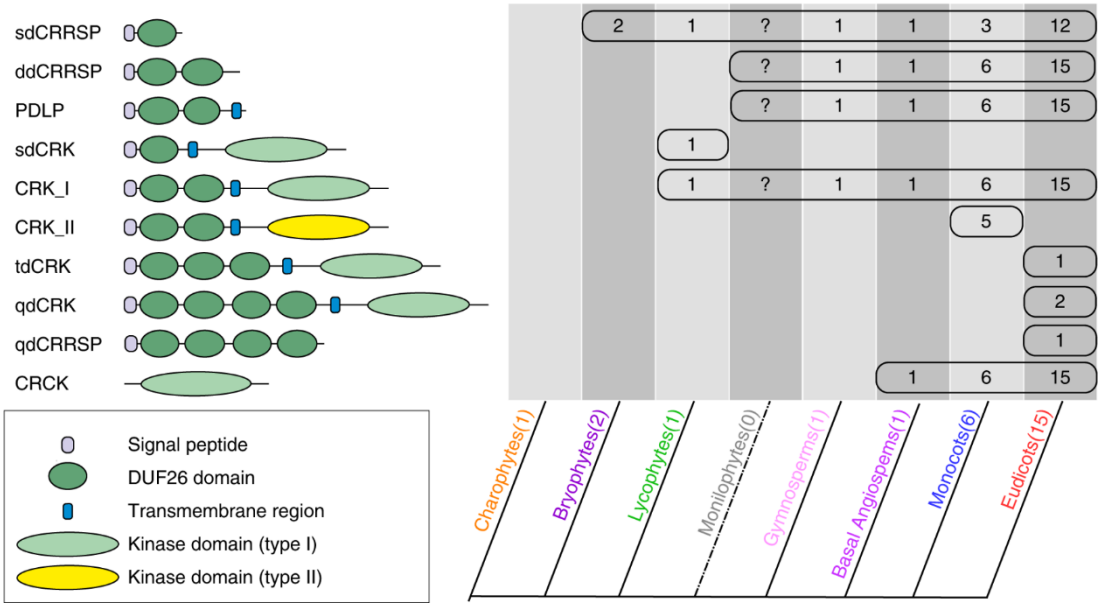

Figure 1.11 The domain organisation of DUF26-containing proteins in different plant lineages.

The schematic shows the domain organisation observed for proteins containing DUF26 domains in several plant lineages. The number in brackets next to the name of each group indicates the number of representative species analysed for that lineage. The number of species in which each domain organisation has been observed is shown in the table. Sd, single domain; dd, double domain; td, triple domain; qd, quadruple domain; CRRSP, cysteine-rich receptor-like secreted

protein; PDLP; plasmodesmata-localised protein; CRK; cysteine-rich receptor-like kinase; CRCK; cysteine-rich receptor-like cytoplasmic kinase. Reproduced from Vaattovaara et al., 2019 (https://doi.org/10.1038/s42003-019-0306-9) under the Creative Commons Attribution License.

1.4.1 CRKs in Arabidopsis

CRKs comprise one of the largest subfamilies of RLKs in Arabidopsis with over 40 homologs. Of these, 38 members are encoded by genes located on chromosome IV, 19 of which are clustered in a large tandem array (Chen, 2001; Figure 1.12). Early studies on members of the CRK family attempted to tap into their biological roles by analysing loss of function and overexpression mutants. While overexpression of *CRK6*, *CRK10* and *CRK11* did not cause any obvious phenotype in transgenic Arabidopsis plants, constitutive expression of *CRK5* at low levels led to enhanced leaf growth and increased disease resistance, whereas high levels of *CRK5* overexpression caused hypersensitive response (HR)-like cell death (Chen et al., 2003). Since then, other CRKs have also been described as players in defence responses against pathogens, as seven members of the family were transcriptionally induced by the overexpression of *LecRK-VI.2*, a positive regulator of pattern-triggered immunity (PTI; Singh et al., 2012). Overexpression of *CRK4*, *CRK13*, *CRK19* and *CRK20* also promoted HR-like lesions in plants (Chen et al., 2004; Acharya et al., 2007), and constitutive expression of *CRK4*, *CRK6* and *CRK36* increased host resistance to the biotroph *Pseudomonas syringae* pv. *tomato* (*Pst*) DC3000 (Yeh et al., 2015). Inducible overexpression of *CRK13*, an early bacterial pathogen-induced gene, also led to accumulation of SA and enhanced disease resistance to virulent and avirulent bacterial pathogens in transgenic Arabidopsis plants, whereas disruption of the *CRK13* transcript by T-DNA insertion did not affect bacterial growth during infection (Acharya et al., 2007). Both T-DNA knockout lines of *CRK20 a*nd overexpression of *CRK28* significantly increased the resistance of Arabidopsis plants to *Pst* DC3000 (Ederli et al., 2011; Yadeta et al., 2017). While plants overexpressing *CRK36* exhibited a similar resistant phenotype to *Pst* infection, they displayed increased susceptibility to the necrotrophic pathogen *Alternaria brassicicola* (Lee et al., 2017). By contrast, the knockout of *CRK36* had the opposite effects, enhancing the plant's resistance to necrotrophic infection, but rendering the plants more susceptible to the biotrophic pathogen. Furthermore,

plants overexpressing *CRK36* exhibited rapid transcriptional and physiological responses to treatment with the bacterial elicitor peptide flg22, including the upregulation of PTI genes and production of ROS and callose. Taken together, these results suggested that *CRK36* is a positive regulator of both effector-triggered immunity (ETI) and PTI processes (Lee et al., 2017).

In addition to a role in defence to pathogens, CRKs in Arabidopsis have also been associated with responses to abiotic stresses and developmental processes. As an example, the overexpression of *CRK45* (also known as *ABA- and osmotic stress-inducible receptor-like cytosolic kinase 1*; *ARCK1*) induced pathogenesis-related (PR) genes and enhanced resistance of Arabidopsis plants following inoculation with *Pst*, while also affecting plant growth, flowering time and sensitivity to ABA during seed germination (Zhang et al., 2013ab). Furthermore, *CRK45* was strongly induced by salinity and drought stresses, and the *CRK36-CRK45* complex was shown to play a negative role in ABA and osmotic stress signalling (Tanaka et al., 2012). Another example, the loss of function of *CRK5* resulted in plants with decreased biomass, reduced stomatal conductance, elevated ROS levels and accelerated senescence, while simultaneously inducing genes involved in ethylene and SA signalling (Burdiak et al., 2015). Additionally, *CRK5* overexpression caused hypersensitivity to ABA during post-germination growth arrest and stimulated drought tolerance (Lu et al., 2016). Finally, *CRK6* and *CRK7* were shown to be involved with responses to oxidative stress in the apoplast (Idänheimo et al., 2014).

Analysis of the putative promoter region of several CRKs revealed their enrichment in W-boxes, DNA sequences which are recognised by WRKY transcription factors. W-boxes in the promoter of *CRK10*, for example, are recognized by WRKY18, and this interaction is important for the inducible expression of this CRK (Du and Chen, 2000). In contrast to CRK10, WRKY18 was shown to act cooperatively with WRKY40 in binding to the *CRK5* promoter to repress its expression (Lu et al., 2016).

Subcellular localisation experiments confirmed the predicted plasma membrane localisation of CRKs, such as CRK4, CRK5, CRK6 and CRK36 (Yeh et al., 2015; Lu et al., 2016). As mentioned in section 1.2, RLKs are often found in complexes with other membrane-bound and cytoplasmic co-receptors, and this is also true for members of the CRK family. For example, experimental evidence confirmed the interaction between CRK4, CRK6 and CRK36 with the well-known

LRR-RLK FLS2 in Arabidopsis protoplasts (Yeh et al., 2015). *In vivo* interactions were also demonstrated between CRK36 with CRK45 (Tanaka et al., 2012) and the RLCK BIK1 (Lee et al., 2017), while CRK28 physically associates with the FLS2-BAK1 immune complex (Yadeta et al., 2017).

Although the function of the DUF26 domain present in the extracellular region of the CRKs remains elusive, the conserved cysteine residues were demonstrated to be essential for the biological functions of some members of the family. Mutation analysis revealed that the ability of *CRK36* to promote PTI and ETI responses is abolished in transgenic plants overexpressing mutant constructs where five and four cysteine residues of the first and second DUF26 motifs, respectively, were substituted with alanine residues (Lee et al., 2017). The substitution of a cysteine residue from each disulphide bridge with alanine was also sufficient to abolish the cell death phenotype induced by *CRK28* when transiently expressed in *Nicotiana benthamiana* (Yadeta et al., 2017).

Furthermore, the kinase activity of a few CRK members was also investigated. The recombinant GST-tagged cytoplasmic kinase domain of CRK6 and CRK7 were both shown to phosphorylate a substrate peptide *in vitro*, and CRK7 also displayed auto-phosphorylation activity (Idänheimo et al., 2014). *In vitro* assays also revealed that the GST-tagged kinase domain of CRK36 can phosphorylate CRK45, and the latter also displays auto-phosphorylation activity (Tanaka et al., 2012). A recent report from Kimura et al. (2020) revealed that CRK2 not only physically interacts with the NADPH oxidase RBOHD *in planta*, but also phosphorylates residues in the C-terminal region of the protein which promote RBOHD-dependent ROS production during immune responses (Kimura et al., 2020).

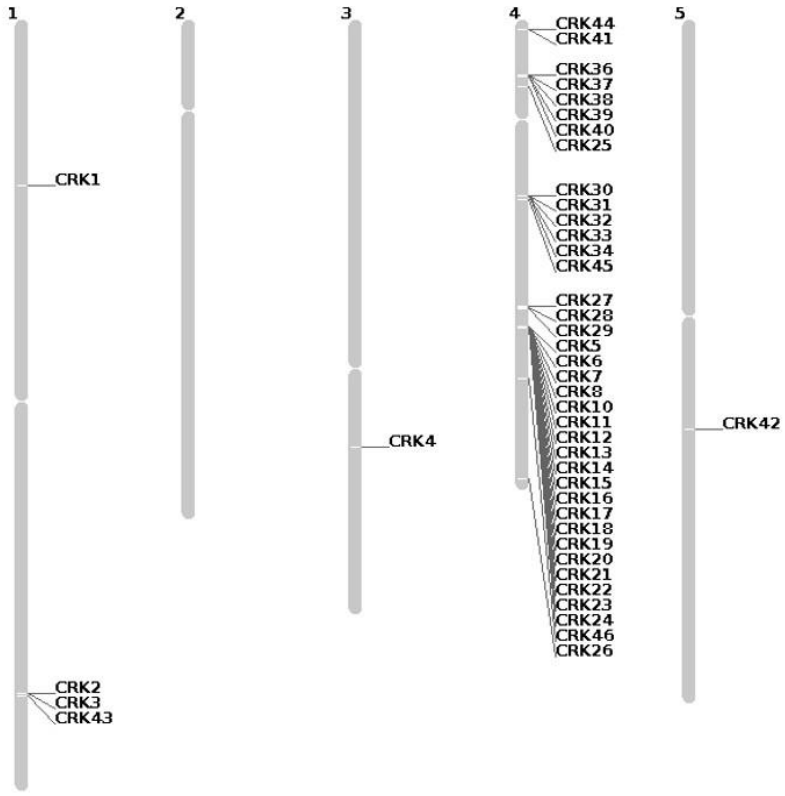

Figure 1.12 Chromosomal distribution of the CRK family in the genome of Arabidopsis.

The five chromosomes of Arabidopsis are depicted in grey and indicated by numbers 1 to 5. The location of 44 members of the CRK family are indicated. This figure was generated with the Chromosome Map Tool in The Arabidopsis Information Resource website (https://www.arabidopsis.org/index.jsp).

1.4.2 CRKs in other plant species

A growing number of reports in the literature have focused on the investigation of CRKs in plant species other than Arabidopsis, including commercially relevant crops. A comparative analysis of CRKs in plant genomes revealed that monocot- and dicot-specific genes form separate clusters, suggesting the diversification of a common set of ancient genes shared by monocots and dicots (Li et al., 2018; Figure 1.13). In rice, the CRK homologs *Os*CRK6 and *Os*CRK10 were shown to be required for the defence responses mediated by NH1, a homolog of the Arabidopsis NPR1 (Chern et al., 2016). The same study also revealed that the expression of *Os*CRK10 is induced by increased levels of NH1, and a *crk10* knockout is more susceptible to infection with *Xoo*. Another group has identified the rice lesion mimic mutant *apoptosis leaf and sheath 1* (*als1*), which harbours the single amino acid substitution of a valine

with a leucine residue in the kinase domain of the CRK ALS1 (Du et al., 2019). The name of the mutant reflects the spontaneous manifestation of lesions on the leaf and sheath of the rice plant, organs in which *ALS1* was shown to be expressed in association with vascular bundles. This mutation led to the constitutive activation of defence-related genes and accumulation of SA and jasmonic acid (JA), two hormones involved in responses to biotic stress. As a result, *als1* plants were more resistant to the leaf blast disease.

Adding to the list of CRKs identified in monocot species, *Hv*CRK1 of barley (*Hordeum vulgare*) and *Ta*CRK1 of wheat (*Triticum aestivum*) were reported. The transcript of *HvCRK1* was transiently induced in leaves of susceptible barley plants inoculated with powdery mildew *Blumeria graminis* (Rayapuram et al., 2012). Silencing of the gene in epidermal leaf cells promoted enhanced resistance to the pathogen, revealing a negative impact of *HvCRK1* on defence responses to powdery mildew. Curiously, the protein localises to the endoplasmic reticulum, in contrast to *Ta*CRK1 which displayed the usual plasma membrane localisation of CRKs (Yang et al., 2013). *TaCRK1* was isolated from a wheat cultivar resistant to *Rhizoctonia cerealis*, and its expression was induced by infection with this pathogen and the hormone ABA. Although the transcript was more abundant in resistant wheat plants compared to a susceptible variety, silencing of *TaCRK1* did not affect the outcome of infection with *R. cerealis.* Another CRK of wheat, *Ta*CRK41 reportedly regulates ABA pathways involved in germination under osmotic stress (Chen et al., 2017). Arabidopsis plants overexpressing *TaCRK41* showed reduced sensitivity to ABA and salinity, supporting a role for this CRK in ABA and abiotic stress responses. In contrast to *Hv*CRK1 and *Ta*CRK1, *Ta*CRK41 exhibited yet another subcellular localisation as the protein accumulated in the cytosol of Arabidopsis protoplasts.

Moving to eudicots, 30 *CRK* homologs were found in the genome of cotton (*Gossypium barbadense*; Li et al., 2018). Expression levels of *GbCRK18* were rapidly increased in a resistant cultivar following treatment with methyl jasmonate (MeJa) and inoculation with *Verticillium dahlia*, the causal agent of Verticillium wilt (VW). A role for *Gb*CRK18 in promoting resistance to this wilt pathogen was further confirmed by the increased susceptibility displayed by cotton plants upon silencing of this gene. In addition to modulating defence responses to pathogens, CRKs also seem to be involved in regulating plant-microbe interaction during symbiosis. SymCRK is required for the control of immune responses in symbiotic

interactions of *Medicago truncatula,* as the knockout of the gene promotes root nodule necrosis (Berrabah et al., 2014).

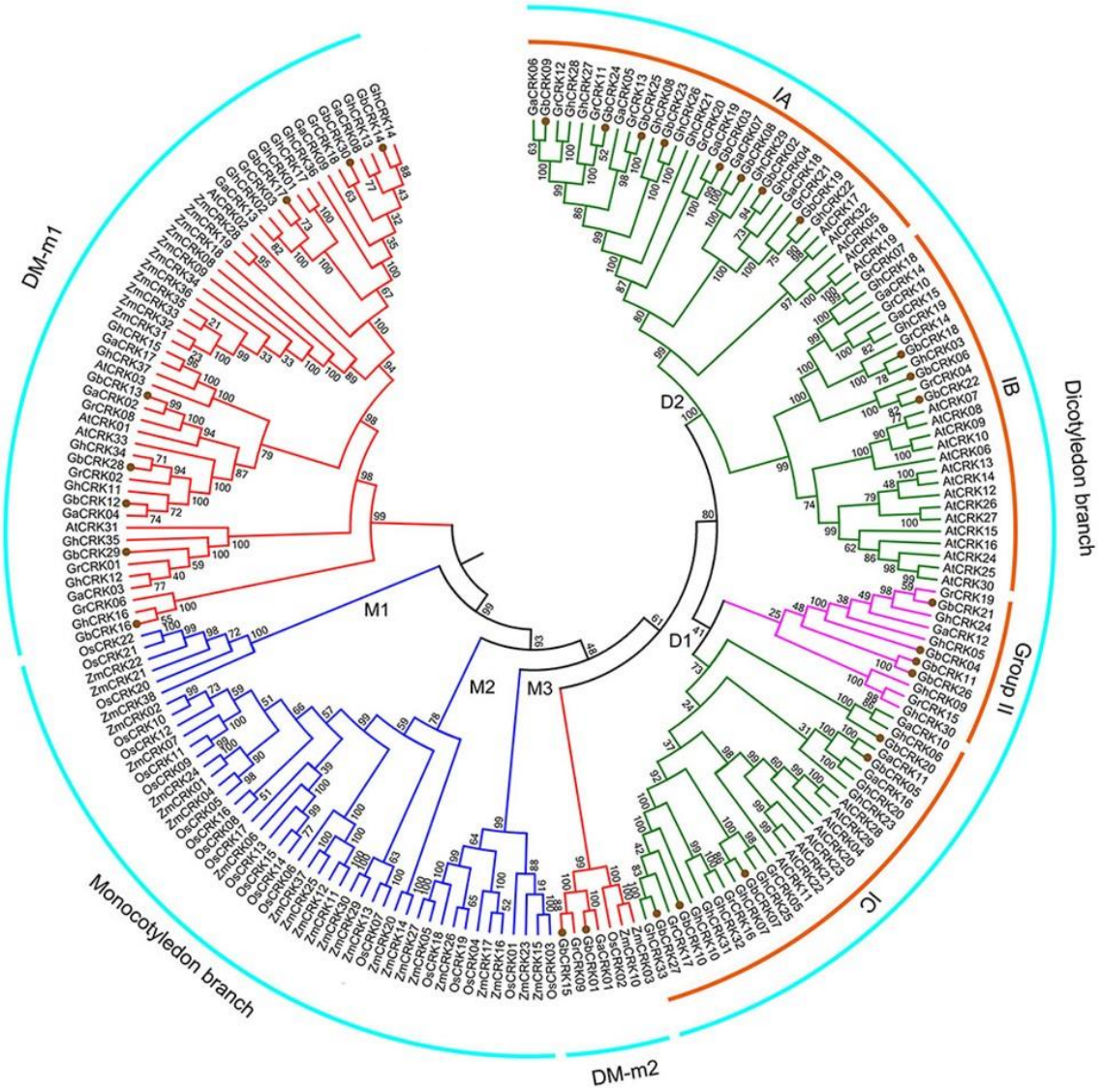

Figure 1.13 Phylogeny of members of the CRK family from seven plant species. Unrooted phylogenetic tree showing clearly distinct clusters of CRKs from the genomes of seven plant species (*G. barbadense, G. hirsutum, G. arboretum, G. raimondii, Arabidopsis thaliana, Oryza sativa*, and *Zea mays*). Reproduced from Li et al., 2018 (https://doi.org/10.3389/fpls.2018.01266) under the Creative Commons Attribution License.

1.5 Other DUF26-containing proteins

As briefly mentioned in section 1.2.1, the DUF26 domain found in the extracellular region of CRKs is also present in other classes of proteins; their classification, distribution and evolution are discussed in depth by Vaattovaara et al. (2019). One of this classes comprises the CYSTEINE-RICH RECEPTOR-LIKE SECRETED PROTEINS (CRRSPs), which are soluble proteins comprised of a signal peptide and one or more copies of the DUF26 domain interspersed with a non-conserved region. The number of copies of the DUF26 domain present in these proteins differs among plant groups; while CRRSPs with a single domain (sdCRRSPs) are found in all land plants, double domain CRRSPs (ddCRRSPs) are exclusively identified in vascular plants. The evolutionary origin of ddCRRSPs is hypothesized to come from CRKs that lost their intracellular and transmembrane domains. The other group is formed by the PLASMODESMATA-LOCALIZED PROTEINS (PDLPs); like CRKs, these proteins contain an extracellular and a transmembrane domain, but lack an intracellular kinase domain. PDLP-encoding genes are only present in spermatophytes and are the most conserved class of DUF26-containing proteins. PDLPs are believed to have evolved from CRKs via the loss of their cytoplasmic kinase domain. CRRSPs and CRKs are usually found in large clusters across plant genomes (Bourdais et al., 2015), which Vaattovaara et al. suggest is a result of both ancestral and recent events of expansion by tandem duplication.

1.5.1 CYSTEINE-RICH RECEPTOR-LIKE SECRETED PROTEINS

Phylogenetic analysis revealed that sdCRRSPs are the most likely ancestor of all DUF26-containing proteins in land plants (Vaattovaara et al., 2019). The best-characterised CRRSP, Gnk2, was identified in the endosperm of *Ginkgo biloba* seeds (Miyakawa et al., 2009), as briefly mentioned in section 1.2.1. The high level of sequence similarity of approximately 85% between Gnk2 and embryo-abundant proteins (EAP) of gymnosperms suggests these proteins might be highly conserved in the seeds of these species. The analysis of the crystal structure of Gnk2 revealed that the protein is composed of two α-helices and a five-stranded β-sheet, which fold into a single-domain architecture (Miyakawa et al., 2009). This work demonstrated for the first time the formation of three disulphide bridges involving the conserved cysteine residues of the DUF26 domain, and how these bridges affect the tertiary structure of the protein.

The most remarkable feature of Gnk2 is its antifungal property, which can inhibit the growth of fungal pathogens such as *Fusarium oxysporum* (Miyakawa et al., 2009). This antifungal activity is reportedly owed to the interaction between Gnk2 and carbohydrates from fungal cell walls, as Gnk2 was able to form a complex with the monosaccharide mannose (Miyakawa et al., 2014). Three amino acid residues (Gnk2-Asp11, Gnk2-Arg93 and Gnk2-Glu104) were shown to interact with the mannose molecule via hydrogen bonds in the crystalised Gnk2-mannose complex, and these interactions were required for the antifungal properties of Gnk2. Two ddCRRSPs from maize, AFP1 and AFP2, were identified due to their interaction with the Rsp3 effector protein of the biotrophic fungus *Ustilago maydis* (Ma et al., 2018). Comparably to Gnk2, AFP1 also binds to mannose and inhibits fungal growth. Therefore, carbohydrate-binding and antifungal activity seem to be conserved features among the CRRSPs characterised so far.

1.5.2 PLASMODESMATA-LOCALISED PROTEINS

The PDLP family in Arabidopsis is comprised of eight members with features of type I membrane receptor proteins (Thomas et al., 2008). The structure of PDLPs is comprised of a signal peptide, two DUF26 domains, a transmembrane region and a short cytoplasmic tail (Vaattovaara et al., 2019). These proteins localise at the plasma membrane lining the interior of plasmodesmata, and Amari et al. (2010) have shown they can promote the cell-to-cell movement of viral pathogens. Another study reported the co-localisation of PDLP1 of Arabidopsis with the extrahaustorial-membrane in cells infected with the downy mildew *Hyaloperonospora arabidopsidis* (*Hpa*; Caillaud et al., 2014). Interestingly, the triple knockout mutant *pdlp1,2,3* shows increased susceptibility to *Hpa* and callose depletion around haustoria, which indicates a role for these proteins in callose deposition during pathogen infection. Furthermore, PDLP1 and PDLP5 are required for cell-to-cell signalling during systemic acquired resistance (SAR; Lim et al., 2016). Similar to Gnk2, the analysis of the crystal structure of the extracellular domain of PDLP5 and PDLP8 of Arabidopsis highlighted the presence of disulphide bridges connecting six conserved cysteine residues, which are thought to be essential to maintain the three-dimensional structure of the domain (Vaattovaara et al., 2019; Figure 1.14). The superimposition of the crystal structure of the DUF26 domains of Gnk2 and

PDLP5 expose their structural homology, which is thought to be conserved in all DUF26 proteins (Vaattovaara et al., 2019; Figure 1.15). Interestingly, the residues implicated in mannose binding in Gnk2 are not conserved in PDLP5 and the protein did not bind to either mannose or other cell wall-derived carbohydrates *in vitro* (Vaattovaara et al., 2019). Nevertheless, typical lectin-dimers were detected in PDLP5 and PDLP8 crystals, which could potentially give rise to a carbohydrate-binding cleft. Furthermore, the homology of DUF26 domains with fungal lectins supports a potential role for these proteins in carbohydrate recognition.

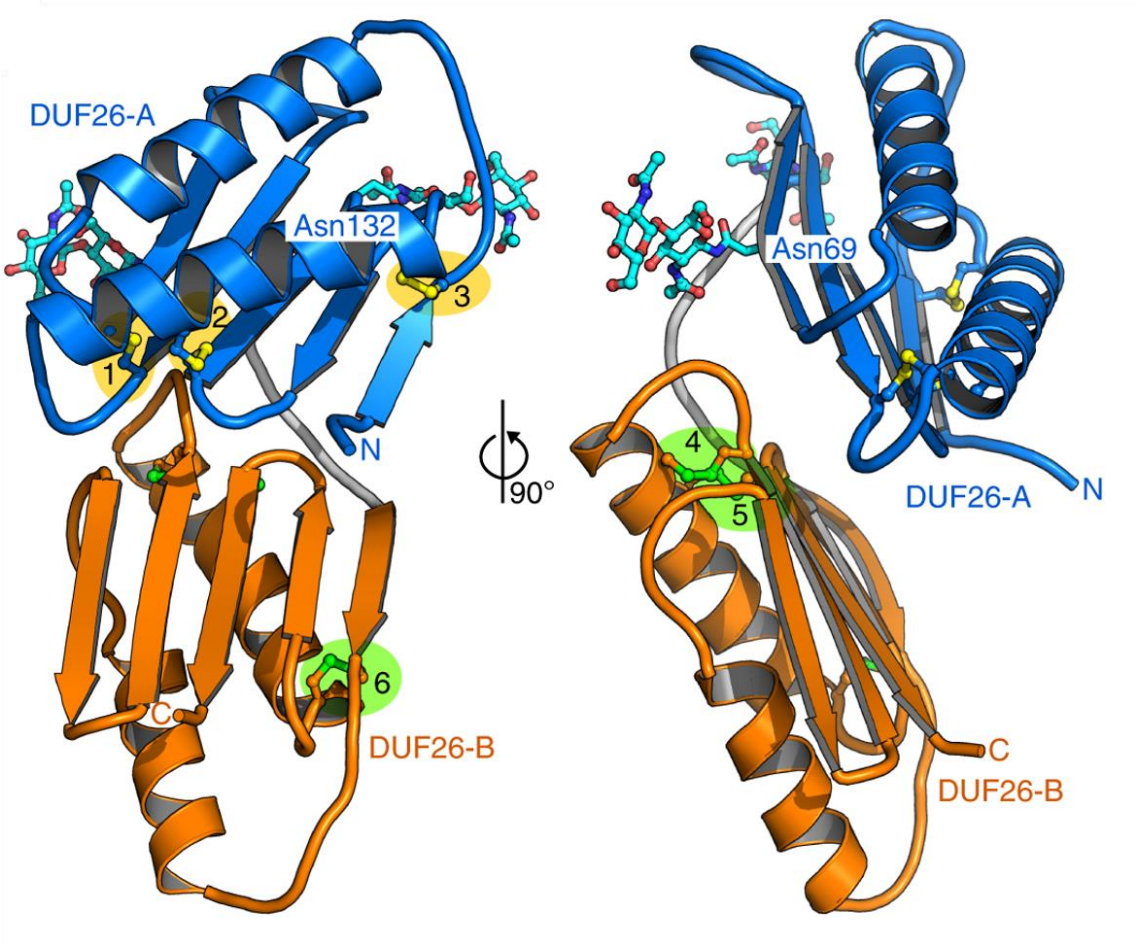

Figure 1.14 A model of the extracellular domain of PDLP5.

The two DUF26 domains in the extracellular region of PDLP5 are represented in blue (DUF26-A) and orange (DUF26-B) by ribbon diagrams. The disulphide bridges formed between the cysteine residues within each DUF26 domain are here indicated by the yellow and green shaded areas numbered 1 to 6. N-glycan groups in DUF26-A are shown in cyan in bonds representation. Reproduced from Vaattovaara et al., 2019 (https://doi.org/10.1038/s42003-019-0306-9) under the Creative Commons Attribution License.

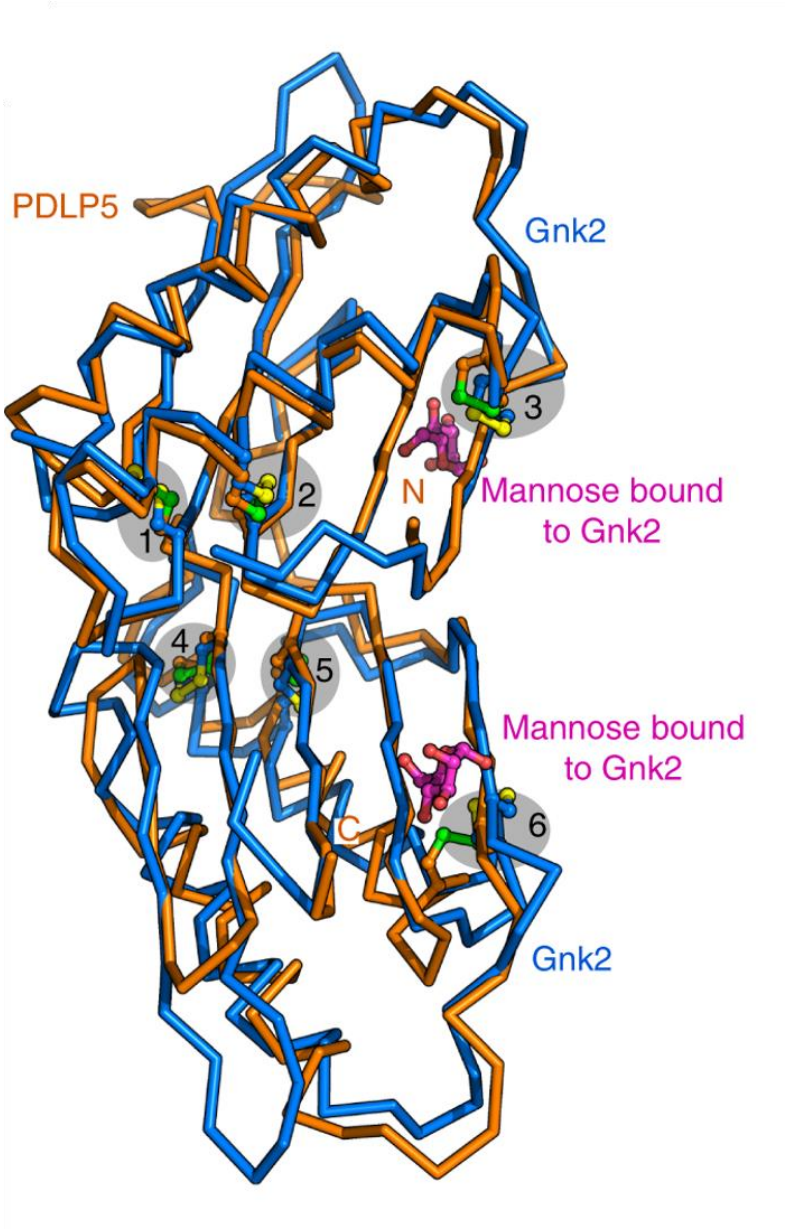

Figure 1.15 Comparison between the DUF26 domain of Gnk2 and PDLP5.
The model shows the superimposition of the Gnk2 DUF26 domain (PDB-ID 4XRE) with either DUF26-A (r.m.s.d. is ~1.4 Å comparing 100 aligned Cα atoms) and DUF26-B (r.m.s.d. is ~2.0 Å comparing 93 corresponding Cα atoms) of PDLP5. The disulphide bridges formed between the conserved cysteine residues of the DUF26 of Gnk2 (yellow) and PDLP5 (green) are shown in bonds representation in the shaded gray areas. Mannose molecules bound to Gnk2 are also shown in bonds representation (magenta). Reproduced from Vaattovaara et al., 2019 (https://doi.org/10.1038/s42003-019-0306-9) under the Creative Commons Attribution License.

1.6 The *crk10-A397T* mutant

Mutagenesis has long been used by plant scientists as a tool to generate genetic diversity and identify mutant alleles which are associated with traits of interest (Sikora et al., 2011). The chemical ethyl methanesulfonate (EMS) is one of the mutagenic compounds routinely used in plant mutagenesis screens due to its ability to generate random point mutations across the genome (Kim et al., 2006). These random mutations often generate stop codons in open reading frames (ORFs), which creates truncated transcripts and result in the loss-of-function of a gene. Alternatively, these mutations might generate a codon which results in a different amino acid residue than the one in the wild-type (WT) version of the protein, which is known as a missense mutation. These amino acid substitutions might confer a new function or enhance the activity of the protein, which is known as a gain-of-function effect. Both loss- and gain-of-function mutations have the potential to induce a phenotype in the mutant plants depending on the biological roles played by the mutated gene. Even though such mutations often induce deleterious effects, the isolation of mutants is a useful strategy to tap into the biological functions of previously uncharacterised genes, which would otherwise remain elusive.

The object of study of this PhD project is an Arabidopsis mutant isolated from an EMS mutagenesis screen. This mutant displays an obvious dwarf phenotype compared to WT plants, although the plant successfully completes its life cycle. A single point mutation in the region corresponding to the kinase domain of *CYSTEINE-RICH RECEPTOR-LIKE KINASE 10* (*CRK10*; AT4G23180) was found to be the cause of the dwarf phenotype of the mutant plants. This mutation causes the substitution of alanine 397 with a threonine residue and, therefore, the mutant allele was named *crk10-A397T*. Given that this mutation introduces a threonine in the kinase domain of a CRK, the hypothesis that this would be an additional phosphorylation site which could potentially affect the regulation and activity of CRK10 was raised. The obvious dwarf phenotype induced by this mutation in Arabidopsis plants also indicated that *crk10-A397T* causes the activation of responses and, therefore, it can be considered a gain-of-function allele. This thesis reports the morphological, molecular and biochemical characterisation of the *crk10-A397T* mutant, which provides insights into the signalling pathways regulated by this gain-of-function allele that might potentially reflect the biological roles of CRK10.

1.7 Project aims

The following objectives were pursued throughout this project:

- To characterise *crk10-A397T* mutant plants morphologically and developmentally (Chapter 3);
- To investigate the underlying cause of the dwarf phenotype of *crk10-A397T* plants (Chapter 3);
- To analyse the kinase activity of the cytoplasmic kinase domain of CRK10 (Chapter 4);
- To assess the effect of the A397T substitution in the kinase activity of the cytoplasmic kinase domain of CRK10 (Chapter 4);
- To investigate which signalling pathways are differentially regulated in the *crk10-A397T* mutant (Chapter 5);

In light of results obtained during the project, two additional aims were introduced:

- To investigate the composition and structure of the cell walls of collapsed xylem vessels in the hypocotyls of the *crk10-A397T* mutant; (Chapter 6);
- To investigate the disease susceptibility of *crk10-A397T* mutant plants to phytopathogens (Chapter 7).

In summary, the experiments described in this thesis provide a thorough characterisation of the *crk10-A397T* mutant plants, including a detailed analysis of the mutant morphology and vasculature-associated defect (see Chapter 3). The investigation of the kinase activity of CRK10 reveals that the cytoplasmic kinase domain of this RLK is an active kinase with dual specificity, and the auto-phosphorylation profile of a member of the CRK family in Arabidopsis is reported for the first time, to the best of my knowledge (see Chapter 4). Analysis of the transcriptome of the *crk10-A397T* mutant hypocotyls reveals the constitutive induction of stress-responsive pathways as well as the transcriptional reprogramming of cell wall-related genes (see Chapter 5). In agreement with the transcriptomic dataset, extensive cell wall remodelling is detected in the hypocotyls of *crk10-A397T* mutant plants, and although changes in cell wall composition are likely involved with the collapse of xylem vessels observed in this organ, further experiments will be necessary to elucidate the exact mechanism underlying this process (see Chapter 6). Finally, bioassays with a soil-borne

vascular pathogen demonstrate that the *crk10-A397T* mutant allele confers enhanced resistance to vascular wilt, which is mediated by key components of salicylic acid signalling pathways (see Chapter 7). The potential molecular mechanisms underlying the gain-of-function of CRK10 are explored, and the implications of the results here presented for our understanding of RLK regulation and activity are discussed.

Chapter 2. General Materials and Methods

2.1 Plant material and growth conditions

The plant utilised throughout this study was *Arabidopsis thaliana* (herein referred to as Arabidopsis), ecotype Columbia (Col-0). The only exception is the *mpk4* mutant line used for an experiment presented in Chapter 3, which is in the ecotype Landsberg erecta (Ler). Arabidopsis plants were grown in Levington F2+S compost (ICL Specialty Fertilizers, UK) in controlled environment Grobanks cabinets (CLF 2006, Plant Climatics, Germany) at 23 °C / 18 ºC day/night temperature and a 16 hour-light photoperiod (approximately 200 µmol m^{-2} per second of light). Seeds were sprinkled on the surface of the compost and pots were covered with a plastic lid for four to five days to create a humid environment for germination. Seedlings were individually transferred to multi-cell propagator trays (15 to 40 cells per tray) seven to ten days after germination. Plants were discarded after sample collection for each experiment was completed. Alternatively, seeds were collected upon completion of the life cycle. For this purpose, inflorescence stems were covered with glassine paper bags (Silverprint© Ltd) as soon as the majority of siliques started to dry. Once plants completed their life cycle and siliques were completely dry, the material was harvested by cutting the base of the inflorescence stems. The seeds were released from the siliques by shaking the bag a few times. The seeds were sieved to remove residual silique material debris being transferred to 1.5 mL glass vials for storage. Plants were also used for the generation of genetic crosses (described in section 7.2.6). For *in vitro* experiments, Arabidopsis seeds were surface sterilised in 1.5 mL microfuge tubes with 1 mL of 100% ethanol for one minute with inversion, followed by a wash step with 1 mL of sterile deionised water. The seeds were then sterilised in 1 mL of 10% sodium hypochlorite for ten minutes with gentle rotation on a tube roller, followed by six wash steps with deionised sterile water in a laminar flow hood. An aliquot of sterile water (100-200 µL) was added to the seeds and the tubes were covered with aluminium foil and kept at 4 °C for 48 hours. After stratification, seeds were individually transferred to ½ MS growth media (Murashige and Skoog, Duchefa Biochemie) 1% agar (Agar type E, Catalogue number A4675; Sigma-Aldrich®) plates. Plates were sealed with micropore™ medical tape (3M©, UK) before being transferred

to a growth room at 23 °C / 18 ºC day/night temperature, 16 hour-light photoperiod (approximately 200 µmol m^{-2} per second of light).

2.2. Bacterial strains

The following strains of competent *Escherichia coli* cells were used for throughout this project. JM109 cells (Catalogue number L2001; Promega) were used to propagate all constructs generated in this study (with the exception of the cases mentioned below). For transformation with plasmids following *in vitro* mutagenesis, One Shot™ MAX Efficiency™ DH5α-T1R Competent Cells (Catalogue number 12297016; Invitrogen™) were used. Library Efficiency™ DH5α Competent Cells (Catalogue number 18263012; Invitrogen™) were used for the propagation of plasmids following LR recombination reactions. The BL21 AI™ One-Shot™ Chemically Competent cells (Invitrogen™) strain was chosen for heterologous expression of recombinant proteins. *Agrobacterium tumefaciens* strain GV3101 was used for the genetic transformation of Arabidopsis plants via the floral dip method (section 2.23) and Agrobacterium-mediated transient expression of a transgene in *Nicotiana benthamiana* leaves (described in section 3.2.10).

2.3 DNA vectors

All vectors maps can be found in Appendix 2.The plasmid pJET1.2/blunt (CloneJET PCR cloning kit, Catalogue number K1231; Thermo Scientific™) was used for the cloning of blunt PCR products, vectors pJD330 and pENTR1A Dual Selection Vector (Invitrogen™) were used for intermediate cloning steps (section 2.16). The binary vectors RS_3GSeedDSRedMCS and pB2GW7 (Invitrogen™) were used for the stable expression of transgenes in Arabidopsis plants (section 2.23), and pB2GW7 was also used for the transient gene expression in *N. benthamiana* (section 3.2.10). Vector pDEST17 (Invitrogen™) was used for the heterologous expression of recombinant proteins in *E. coli* (section 4.2.5). Vector RS_3GSeedDSRedMCS is derived from pBINGlyRed3 (Nguyen et al., 2013; details in Appendix 2.7).

2.4 Genomic DNA extraction from Arabidopsis leaf tissue

Total genomic DNA was extracted from Arabidopsis leaf samples according to the alkaline lysis protocol (Klimyuk *et al*., 1993). A section of leaf

tissue (~0.5 cm^2) was removed and placed in a 0.2 mL microfuge tube. The leaf material was homogenised in 50 µL of 0.25 M sodium hydroxide (NaOH) using a plastic pestle and the samples were incubated at 96 °C for 30 seconds. A 50 µL aliquot of 0.25 M hydrochloric acid (HCl) and 25 µL of 0.5 M Tris HCl pH 8.0 / 0.25% IGEPAL CA-630 detergent was added to each tube, and the samples were incubated at 96 °C for two minutes. The tubes were briefly spun down to pellet residual leaf material before being stored at -20 °C until further processing.

2.5 RNA extraction from Arabidopsis leaf tissue

Leaf sections (~0.5 cm^2) from Arabidopsis plants were collected into 1.5 mL microfuge tubes and immediately frozen in liquid nitrogen. The leaf tissue was ground to a fine powder with a mortar and pestle using liquid nitrogen. The frozen tissue powder was transferred to a microfuge tube and a 1 mL aliquot of TRI Reagent® (Sigma Aldrich®) was added to the powder. The samples were incubated at room temperature for five minutes followed by the addition of 200 µL of chloroform to each tube. The samples were shaken vigorously for 15 seconds and incubated for another 15 minutes at room temperature before centrifugation at 12,000 x g for 15 minutes (all centrifugation steps were performed at 4 °C). The top aqueous phase of each sample was transferred to a fresh 1.5 mL microfuge tube followed by the addition of 500 µL of isopropanol. The contents of the tubes were mixed by inversion before standing at room temperature for ten minutes. The RNA pellets were collected at the bottom of the tubes by centrifugation at 12,000 x g for ten minutes. The supernatant was removed and the pellet was washed once in 1 mL of 75% ethanol by vortexing, followed by centrifugation at 7,500 x g for five minutes. The supernatant was discarded and the RNA pellets were air dried at room temperature for 15 minutes. The RNA was resuspended by pipetting in sterile deionized water and the extracts were stored at -20 ° until further processing.

2.6 Plasmid DNA extraction from bacterial cells

For the propagation of DNA plasmids, single *E. coli* colonies harbouring the construct of interest were inoculated in 5 mL of liquid 2x YT (yeast extract and tryptone) media (Catalogue number YDB0101; ForMedium™) supplemented with antibiotics (herein referred to as selective media). The cells were cultured overnight at 37 °C with agitation (220 rpm) and the resulting cultures were used

for minipreparation of plasmid DNA with the QIAprep® Spin Miniprep kit (QIAGEN; refer to manufacturer's handbook of protocol for details). Aliquots of the overnight culture were centrifuged at 4,300 x g for three minutes to pellet the bacterial cells in 1.5 mL microfuge tubes (a maximum of 3 mL of culture was used per sample). The pellets were resuspended in 250 µL of resuspension buffer (Buffer P1; supplemented with RNase A) by vortexing the tubes, followed by the lysis of the cells with the addition of 250 µL of lysis buffer (Buffer P2) and mixing by gentle inversion. A 350 µL aliquot of neutralisation buffer (Buffer N3) was added to each tube and the contents were mixed immediately by inversion. The samples were centrifuged at 11,350 x g for ten minutes, and the supernatant was transferred to a QIAprep® spin column for centrifugation at 11,350 x g for one minute (as all the following centrifugation steps). The columns were washed once with 750 µL of wash buffer (Buffer PE), and the flow through was discarded after centrifugation. To ensure the complete removal of residual wash buffer, the columns were centrifuged once more in the same collection tube. The columns were transferred to fresh 1.5 mL microfuge tubes and 50 µL of elution buffer (Buffer EB) were carefully added to the centre of the column. After standing for one minute at room temperature, the plasmid DNA was eluted from the column by centrifugation. The plasmid DNA was stored at -20 °C until further processing.

2.7 Polymerase Chain Reaction

Polymerase chain reactions (PCRs) were performed using *Taq* DNA Polymerase, recombinant (Catalogue number 10342046; Invitrogen™) for colony and genotyping PCRs. For high-fidelity amplification of PCR products, AccuPrime™ *Pfx* DNA Polymerase (Catalogue number 12344024; Invitrogen™) or Phusion® High-Fidelity DNA Polymerase (Catalogue number M0530; New England BioLabs®) were used. The reactions were prepared and performed as detailed in Tables 2.1 to 2.6 using a SimpliAmp™ thermal cycler (Applied Bioesciences™) or a PTC-200 DNA Engine thermal cycler (MJ Research, Inc). For colony PCRs, individual bacterial colonies picked from selective agar plates were used as template for amplification (1-2 µL of water per sample was added to the reaction mix to adjust the final volume). All PCR products were analysed by gel electrophoresis (section 2.8).

Table 2.1 Reaction mix for PCR reactions using *Taq* DNA Polymerase, recombinant (Invitrogen™).

Reagent	**Volume (µL)**	**Final concentration**
10x Reaction buffer	2	1x
$MgCl_2$ (50 mM)	0.6	1.5 mM
dNTPs (10 mM)	0.4	200 µM
Forward primer (10 µM)	0.75 – 2	0.375 – 1 µM
Reverse primer (10 µM)	0.75 – 2	0.375 – 1 µM
Taq DNA polymerase (5 U / µL)	0.1	0.025 U / µL
DNA template (1 – 500 ng)	1 – 2	Variable
Sterile water	Up to 20 µL	-

Table 2.2 Reaction mix for PCR reactions using AccuPrime™ *Pfx* DNA Polymerase (Invitrogen™).

Reagent	**Volume (µL)**	**Final concentration**
10x Reaction mix	5	1 x
Forward primer (10 µM)	0.75 – 2	0.375 – 1 µM
Reverse primer (10 µM)	0.75 – 2	0.375 – 1 µM
AccuPrime™ *Pfx* DNA Polymerase (2.5 U / µL)	0.5	0.025 U / µL
DNA template (10 pg to 200 ng)	1 – 2	Variable
Sterile water	Up to 50 µL	-

Table 2.3 Reaction mix for PCR reactions using Phusion® High-Fidelity DNA Polymerase (New England BioLabs®).

Reagent	**Volume (µL)**	**Final concentration**
5x Phusion HF or GC buffer	10	1x
dNTPs (10 mM)	1	200 µM
Forward primer (10 µM)	0.75 – 2	0.375 – 1 µM
Reverse primer (10 µM)	0.75 – 2	0.375 – 1 µM

Phusion® DNA Polymerase (2 U / µL)	0.5	0.02 U / µL
DNA Template (< 250 ng)	1 – 2	Variable
Sterile water	Up to 50 µL	-

Table 2.4 Programme used for PCR reactions with *Taq* DNA Polymerase, recombinant (Invitrogen™).

Step	**Temperature**	**Duration**	**Cycles**
Initial denaturation	94 °C	3 min	1
Denaturation	94 °C	45 sec	25 – 35
Annealing	55 – 72 °C	30 sec	
Extension	72 °C	90 sec / kb	
Final extension	72 °C	10 min	1

Table 2.5 Programme used for PCR reactions with AccuPrime™ *Pfx* DNA Polymerase (Invitrogen™).

Step	**Temperature**	**Duration**	**Cycles**
Initial denaturation	95 °C	2 min	1
Denaturation	95 °C	15 sec	25 – 35
Annealing	55 – 72 °C	30 sec	
Extension	68 °C	1 min / kb	

Table 2.6 Programme used for PCR reactions with Phusion® High-Fidelity DNA Polymerase (New England BioLabs®).

Step	**Temperature**	**Duration**	**Cycles**
Initial denaturation	98 °C	30 sec	1
Denaturation	98 °C	10 sec	25 – 35
Annealing	45 – 72 °C	30 sec	
Extension	72 °C	30 sec / kb	
Final extension	72 °C	10 min	1

2.8 Nucleic acid gel electrophoresis

Nucleic acid samples were resolved on 0.8 – 2% agarose gels (the concentration of the gel was dependent on the size of the molecules to be resolved). The agarose powder (Catalogue number A9539; Sigma-Aldrich®) was added to the Tris-acetate-EDTA (TAE) buffer (Catalogue number B49; Thermo Scientific™) in a conical flask, and the mixture was heated in a microwave until completely dissolved. The agarose solution was allowed to briefly cool down before the addition of ethidium bromide (Sigma-Aldrich®) to a final concentration of 0.2 µg / mL. The agarose suspension was poured onto the gel casting tray, and a comb was placed to create the wells. The same steps were followed to prepare low melting point agarose gels (MetaPhor™ Agarose, Catalogue number 50181; Lonza), which were used when a DNA fragment of interest would be excised for subsequent purification. Once polymerised, the gel was transferred to an electrophoresis tank containing 1x TAE buffer, and the comb was removed. Aliquots of the nucleic acid samples were mixed with 6x loading buffer to a 1x final concentration in PCR tubes, and the samples were individually pipetted into the wells. The GeneRuler 1 Kb DNA ladder (Thermo Scientific™) was used as molecular weight standard. Electrophoresis was performed at 80-100 V for 30 – 45 minutes, and the DNA was visualised using a GelDoc™ XR+ Molecular Imager (Bio-Rad Laboratories, Inc) or a GelDoc-It^{TS2} Imager (Analytik Jena©).

6x loading buffer:	4 g	Sucrose
	25 mg	Bromophenol blue
	10 mL	Water

2.9 DNA digestion with restriction enzymes

Restriction enzymes for the digestion of DNA molecules were obtained from New England BioLabs® (UK) and Promega (UK). A 25 – 50 µL reaction was prepared in a 1.5 mL microfuge tube for each digestion. For 1 µg of DNA, a reaction mix containing the optimum reaction buffer (as specified by the manufacturer) diluted to 1x concentration, sterile deionised water and 1 µL of the enzyme was prepared. The contents of the reaction were mixed gently by pipetting and the tubes were incubated for one hour at the optimal temperature (as specified) for digestion. For sequential restriction reactions, the enzyme with the requirement for the lowest salt concentration was used first. Upon completion

of the first reaction, the second enzyme and its respective reaction buffer were added to the tube and the samples were incubated for another hour at the optimum temperature for digestion. The digested DNA fragments were resolved by gel electrophoresis (section 2.8).

2.10 Purification of DNA fragments from agarose gels

DNA fragments were purified from low melting point agarose gels following electrophoresis for subsequent applications. The fragment of interest was excised from the agarose gel using a sterile steel blade (N° 10 Dermaplane Scalpel blade; Swann Morton Ltd) and collected into a pre-weighed 1.5 mL microfuge tube. The weight of the gel slice was determined and the DNA fragment was purified using the QIAquick® Gel Extraction Kit (QIAGEN; refer to manufacturer's handbook of protocol for details). All centrifugation steps were performed at 11,350 x g for one minute. An aliquot of binding and solubilisation buffer (Buffer QG) equivalent to three times the volume of the agarose gel was added to the tubes (considering 100 mg of gel is equivalent to approximately 100 µL). The samples were incubated at 50 °C for ten minutes or until the gel was fully dissolved in the buffer. One volume of isopropanol was added to each tube and samples were mixed by inversion. The mixture was transferred to a QIAquick spin column in 2 mL collection tubes, the samples were centrifuged and the flow through was discarded. The columns were washed once with 750 µL of wash buffer (Buffer PE) followed by centrifugation and disposal of the supernatant, and a second round of centrifugation to remove residual wash buffer. Finally, the DNA was eluted from the columns in 30 µL of elution buffer (Buffer EB). The protocol described in this section was also used for the purification of PCR products, with the only exception being the samples did not require heating at the first step of the protocol. The concentration of the eluates was determined using a NanoDrop™ (Thermo Scientific™) spectrophotometer (section 2.11).

2.11 Quantification of nucleic acid concentration with NanoDrop™ spectrophotometer

A NanoDrop™ 1000 spectrophotometer (Thermo Scientific™) was used to determine the concentration of DNA and RNA samples. The pedestal of the instrument was wiped with a paper tissue before each use and in between samples, and a first default step to ensure the cleanliness of the pedestal was

performed with 1 µL of water. The blank standard was set up with 1 µL of elution buffer or sterile deionised water, and the concentration of each sample (ng / µL) was recorded subsequently. The 260 / 280 nm and 260 / 230 nm ratios were also noted to assess sample purity.

2.12 DNase treatment of RNA samples

Aliquots of RNA extracts were treated with DNase to remove genomic DNA contamination prior to RT-PCR and qPCR reactions. The DNase I, Amplification Grade kit (Catalogue number 18068015; Invitrogen™) was used for the treatment. The reactions were prepared in 1.5 mL microfuge tubes as described in Table 2.7 and the reagents were mixed by pipetting. The samples were incubated at room temperature for 15 minutes before the addition of 1 µL of 25 mM EDTA and incubation at 65 °C for ten minutes to inactivate the enzyme. The resulting RNA samples were subsequently used for reverse transcription (section 2.13).

Table 2.7 Reaction mix for DNase treatment of RNA samples with DNase I, Amplification Grade (Invitrogen™).

Reagent	**Volume (µL)**	**Final concentration**
10x DNase I Reaction Buffer	1	1x
DNase I (1 U / µL)	1	0.1 U / µL
RNA sample (1 µg)	Variable	100 ng / µL
Sterile water	Up to 10 µL	-

2.13 Reverse transcription

DNase-treated RNA samples were used as template for first-strand cDNA synthesis using the SuperScript™ III Reverse Transcriptase kit (Catalogue number 18080093; Invitrogen™) and the Oligo(dT)$_{12\text{-}18}$ primer (Catalogue number 18418012; Invitrogen™). The reverse transcription reactions were prepared as described in Table 2.8. The reagents used in step 1 were mixed in a 1.5 mL microfuge tube and heated at 65 °C for five minutes. The tubes were transferred to ice where they were incubated for an additional minute. Step 2 reagents were added to the tubes and mixed by pipetting, and the samples were

incubated at 50 °C for one hour. The reaction was inactivated by incubation at 70 °C for 15 minutes. The cDNA samples were stored at -20 °C until use.

Table 2.8 Reaction mix for cDNA synthesis with SuperScript™ III Reverse Transcriptase kit (Invitrogen™).

Reagent	**Volume (µL)**	**Final concentration**
Step 1		
Oligo(dT)$_{12-18}$ primer (0.5 µg / µL)	1	25 ng / µL
dNTPs (10 mM)	1	0.5 mM
DNase-treated RNA (< 5 µg)	Variable	Variable
Sterile water	Up to 13 µL	-
Step 2		
5x First-strand buffer	4	1 x
0.1 M DTT	1	5 µM
SuperScript™ III RT (200 U / µL)	1	10 U / µL

2.14 Reverse Transcription – PCR (RT-PCR)

cDNA samples synthesized as described in section 2.13 were used as template for RT-PCR. The reactions were prepared and performed as described in Tables 2.1 and 2.4 using *Taq* DNA Polymerase, recombinant (Invitrogen™). The RT-PCR products were analysed by gel electrophoresis (section 2.8).

2.15 Real time quantitative PCR (qPCR)

Real time quantitative PCR (qPCR) reactions were prepared using the FastStart Essential DNA Green Master (Catalogue number 06402712001; Roche Life Science), and the reactions were performed in a LightCycler® 96 System (Roche Life Science). The reactions were prepared and performed as described in Tables 2.9 and 2.10. The reaction mix was pipetted into tube strips or 96-well plates according to the number of samples to be analysed. Technical duplicates were prepared for each sample. Information regarding the genes used as internal standards for each experiment can be found in the Materials and Methods section

of chapters 3 and 7. The qPCR results were analysed using the $2^{-\Delta\Delta Ct}$ method (Livak and Schmittgen, 2001).

Table 2.9 Reaction mix for qPCR with the FastStart Essential DNA Green Master (Roche Life Science).

Reagent	**Volume (µL)**	**Final concentration**
2x Master mix	10	1x
Forward primer (10 µM)	2	1 µM
Reverse primer (10 µM)	2	1 µM
cDNA / DNA template	1 - 2	Variable
Sterile water	Up to 20 µL	-

Table 2.10 PCR programme used with the FastStart Essential DNA Green Master (Roche Life Science).

Step	**Temperature**	**Ramp (°C / s)**	**Duration**	**Acquisition**	**Cycles**
Pre-incubation	95 °C	4.4	10 min	None	1
Denaturation	95 °C	4.4	10 sec	None	45
Annealing	55 – 72 °C	2.2	10 sec	None	
Extension	72 °C	4.4	10 sec	Single	
Melting	95 °C	4.4	10 sec	None	1
	65 °C	2.2	60 sec	None	
	97 °C	0.1	1 sec	5 / °C	

2.16 Cloning and preparation of constructs

PCR products amplified with a high-fidelity DNA polymerase (section 2.7) were subsequently cloned into the pJET1.2/blunt plasmid (CloneJET PCR cloning kit, Catalogue number K1231; Thermo Scientific™). The cloning reaction was prepared as described in Table 2.11, and the reactions were incubated at room temperature for 15 minutes. *In vitro* mutagenesis reactions were performed using the GeneArt Site-Directed Mutagenesis kit (Catalogue number A13282; Invitrogen™) and the AccuPrime™ *Pfx* DNA Polymerase (Invitrogen™). The reactions were prepared and performed as described in Tables 2.12 and 2.13. A

recombination reaction to boost the mutagenesis efficiency was performed with the PCR products as described in Table 2.14. The reagents were mixed by pipetting and the tubes were incubated at room temperature for ten minutes. The reaction was terminated with the addition of 1 µL of 0.5 M EDTA. The T4 DNA ligase kit (Catalogue number EL0011; Invitrogen™) was used to ligate linear vectors and DNA fragments with cohesive ends (sticky end ligation). The NEBioCalculator tool (https://nebiocalculator.neb.com/#!/ligation) was used to calculate the volume of linear vector and insert DNA to achieve the desired molar ratio. The ligation reactions were prepared as described in Table 2.15, and the reactions were incubated at room temperature for 15 minutes. When a vector was digested with a single enzyme creating sticky ends that are complementary to each other, the linearized plasmid was dephosphorylated with Antarctic Phosphatase (Catalogue number M0289S; New England BioLabs®) to avoid vector recircularization. The reaction was prepared as described in Table 2.16 and the tubes were incubated at 37 °C for 30 minutes before heat inactivation at 80 °C for two minutes. The Gateway™ LR Clonase™ II Enzyme Mix kit (Catalogue number 11791020; Invitrogen™) was used for the recombination of entry and destination Gateway™ vectors. The reactions were prepared as described in Table 2.17 before incubation at room temperature for one hour. The reaction was terminated with the addition of 2 µL of Proteinase K and incubation at 37 °C for ten minutes. Ligation and recombination reactions were used for the transformation of *E. coli* cells for plasmid propagation (section 2.17). Purified plasmids obtained from minipreparation (section 2.6) were sequenced to check for potential mutation/errors

Table 2.11 Reaction mix for the cloning of blunt end PCR products with the CloneJET PCR cloning kit (Thermo Scientific™).

Reagent	**Volume (µL)**	**Final concentration**
2x Reaction buffer	10	1x
Non-purified PCR product	1	-
pJET1.2/blunt plasmid (50 ng / µL)	1	2.5 ng / µL
T4 DNA ligase (5 U / µL)	1	0.25 U / µL
Sterile water	Up to 20 µL	-

Table 2.12 Reaction mix for *in vitro* mutagenesis reaction using the GeneArt Site-Directed Mutagenesis kit (Invitrogen™) and the AccuPrime™ *Pfx* DNA Polymerase (Invitrogen™).

Reagent	**Volume (µL)**	**Final concentration**
10x Reaction mix	5	1x
10x Enhancer	5	1x
Forward primer (10 µM)	1.5	0.3 µM
Reverse primer (10 µM)	1.5	0.3 µM
DNA methylase (4 U / µL)	1	0.08 U / µL
25x S-adenosyl methionine (SAM)	2	1x
AccuPrime™ *Pfx* DNA Polymerase (2.5 U / µL)	0.4	0.02 U / µL
Plasmid DNA (20 ng / µL)	1	0.4 ng / µL
Sterile water	Up to 50 µL	-

Table 2.13 PCR programme used for *in vitro* mutagenesis using the GeneArt Site-Directed Mutagenesis kit (Invitrogen™) and the AccuPrime™ *Pfx* DNA Polymerase (Invitrogen™).

Step	**Temperature**	**Duration**	**Cycles**
Methylation	37 °C	20 min	1
Initial denaturation	94 °C	2 min	1
Denaturation	94 °C	20 sec	12 – 18
Annealing	55 – 68 °C	30 sec	
Extension	68 °C	30 sec / kb	
Final extension	68 °C	5 min	1

Table 2.14 Reaction mix for the recombination reaction following *in vitro* mutagenesis using the GeneArt Site-Directed Mutagenesis kit (Invitrogen™).

Reagent	**Volume (µL)**	**Final concentration**
5x Reaction buffer	4	1x
10x Enzyme mix	2	1x
PCR product	4	-
Sterile water	10	-

Table 2.15 Reaction mix for the ligation of DNA molecules with cohesive ends using T4 DNA ligase (Invitrogen™).

Reagent	**Volume (µL)**	**Final concentration**
10x T4 DNA ligase buffer	2	1x
Linear vector (20 – 100 ng)	Variable	Variable
Insert DNA	1:1 to 5:1 molar ratio over vector	Variable
T4 DNA ligase	1	0.25 U / µL
Sterile water	Up to 20 µL	-

Table 2.16 Reaction mix for the dephosphorylation of 5'-end of DNA using Antarctic Phosphatase (New England BioLabs®).

Reagent	**Volume (µL)**	**Final concentration**
10x Reaction buffer	2	1x
Linear DNA vector	Variable	1 pmol of DNA ends
Antarctic Phosphatase (5 U / µL)	1	0.25 U / µL
Sterile water	Up to 20 µL	-

Table 2.17 Reaction mix for LR recombination reaction using the Gateway™ LR Clonase™ II Enzyme Mix (Invitrogen™).

Reagent	**Volume (µL)**	**Final concentration**
5x LR Clonase™ Reaction buffer	2	1x
Entry vector (100 – 300 ng)	Variable	Variable
Destination vector (150 ng / µL)	2	15 ng / µL
LR Clonase™ enzyme mix	2	-
Sterile water	Up to 10 µL	-

2.17 Transformation of *E. coli* cells

Microfuge tubes containing competent *E. coli* cells were transferred from the -80 °C freezer to a container with ice. Upon thawing of the cells, an appropriate amount of DNA / ligation reaction was added to the tubes (2-3 µL of ligation / recombination reactions; 5-10 ng of purified plasmid DNA). The cells were kept on ice for 30 minutes before heat shock at 42 °C for 30 seconds in a water bath. The tubes were returned to ice for two minutes before the addition of 250-450 µL of Super Optimal Broth with Catabolic Repressor (SOC; Catalogue number SOC0201; ForMedium™) media to each tube. The cells were incubated at 37 °C for one hour with agitation (220 rpm) in an orbital shaker. before an aliquot (75 – 100 µL) was plated on selective 2x YT agar plates (antibiotic concentrations can be found in Table 2.18). The plates were incubated at 37 °C overnight, and the bacterial colonies were screened by colony PCR (section 2.7).

2.18 DNA primer design

DNA primers for PCR reactions were designed using the Geneious software and the NCBI Primer-BLAST tool (https://www.ncbi.nlm.nih.gov/tools/primer-blast/). Primers were synthesized by Merck© (Germany).

2.19 DNA sequencing

Plasmid DNA and purified PCR products were sent for sequencing with the TubeSeq service provided by Eurofins Genomics (Germany). A 15 µL aliquot of plasmid DNA (50 – 100 ng / µL) or purified PCR products (1 – 10 ng / µL) were prepared in 2 mL safe-lock microfuge tubes. A DNA primer targeting the sequence of interest was mixed with the DNA sample (2 µL of 10 mM primer solution). The sequencing results were analysed using the Geneious software.

2.20 Preparation of competent *A. tumefaciens* cells

A glycerol stock of *A. tumefaciens* strain GV3101 was used to streak a plate of 2x YT agar supplemented with rifampicin and gentamycin (both antibiotics were used in all steps to select *A. tumefaciens* cells; antibiotic selection is detailed in Table 2.18). The plate was incubated at 29 °C for 48 hours and a single colony was used to inoculate 5 mL of selective liquid media. The cells were cultured overnight at 29 °C with agitation (200 rpm) on orbital shaker and a 2 mL

aliquot was used to inoculate 50 mL of fresh selective liquid media. The cells were grown as described above until an optical density (OD) of 0.5 – 1.0 measured at 600 nm was achieved (see section 2.22 for the determination of the optical density of bacterial cultures). The culture was centrifuged at 3,000 x g for five minutes at 4 °C and the supernatant was discarded. The cells were resuspended in 1 mL of pre-chilled 20 mM $CaCl_2$ solution, and 0.1 mL aliquots were transferred to 0.5 mL microfuge tubes. The cells were flash frozen in liquid nitrogen and stored at – 80 °C.

2.21 Transformation of *A. tumefaciens* cells

Competent A*. tumefaciens* cells strain GV3101 were transformed according to the freeze and thaw method (An *et al*., 1988). Microfuge tubes containing competent cells were removed from the – 80 °C freezer and 0.5 - 1 µg of DNA was immediately added to the frozen cells. The cells were incubated at 37 °C for five minutes before a 1 mL aliquot of sterile SOC. media was added to the tubes. Following an incubation period of two hours at 29 °C with agitation (200 rpm) on orbital shaker, 100 µL of cells were spread on selective 2x YT agar plates and incubated for 48 hours at 29 °C. Individual colonies were picked to inoculate the liquid cultures used for the transformation of Arabidopsis plants (section 2.23).

Table 2.18 Antibiotics used for the selection of *E. coli* and *A. tumefaciens* cells on solid and liquid growth media.

Antibiotic	**Solvent**	**Stock concentration**	**Bacterial cells**	**Final concentration**
Ampicillin	Water	50 mg / mL	*E. coli*	50 µg / mL
Kanamycin	Water	50 mg / mL	*E. coli*	50 µg / mL
			A. tumefaciens	50 µg / mL
Spectinomycin	Water	100 mg / mL	*E. coli*	100 µg / mL
			A. tumefaciens	100 µg / mL
Rifampicin	Methanol	50 mg / mL	*A. tumefaciens*	50 µg / mL
Gentamycin	Water	50 mg / mL	*A. tumefaciens*	30 µg / mL

2.22 Measuring the optical density of bacterial cultures

The optical density of bacterial cultures was measured using a 6715 UV/VIS spectrophotometer (Jenway®) at wavelength 600 nm. A plastic cuvette

containing 1 mL of fresh liquid media was used to set the blank reading in the instrument before the optical density of the bacterial cultures were measured.

2.23 Transformation of Arabidopsis plants

The floral dip method (Clough and Bent, 1998) was used to transform Arabidopsis plants. An overnight pre-culture (5 mL) of *A. tumefaciens* GV3101 cells harbouring the construct of interest was grown in selective liquid media at 29 °C with agitation (220 rpm; all bacterial growth steps were performed using the same conditions). A 2 mL aliquot of the pre-culture was used to inoculate 100 mL of fresh selective liquid media, and the cells were allowed to grow overnight. The culture was divided into two sterile 50 mL conical tubes and the cells were pelleted by centrifugation at 5000 x g for ten minutes. The supernatant was discarded and the pellets were resuspended in 250 mL of floral dip solution (5% sucrose, 0.05% Silwett L77) prior to being transferred to a beaker. Arabidopsis plants grown for seven to eight weeks in standard conditions were used for the floral dip protocol. Each pot contained eight to ten plants, and they were closely monitored in order to choose the optimal stage for transformation, when inflorescence stems contained the highest possible number of closed floral buds. Individual pots were removed from trays and carefully turned upside down to allow the inflorescence stems to be submerged in the bacterial suspension. The plants were dipped for 15 seconds with gentle agitation before being returned to the upright position on their respective trays, where they were covered with a plastic lid for 24 hours to create a humid environment. After the lids were removed, the plants were allowed to complete their life cycle in the growth cabinets until siliques were dry and seeds could be harvested.

2.24 Selection of transgenic plants

Transgenic plants harbouring the binary vector RS_3GSeedDSRedMCS, were selected based on the presence of the DS Red fluorescent protein in seeds. Seeds from the T1 population were observed under the Leica M205 stereomicroscope (Leica Microsystems©, Germany) using the DSRed filter (excitation: 545 +/-30nm; emission: 620 +/-60nm), and seeds exhibiting red fluorescence were individually picked with a toothpick. Transgenic plants harbouring the binary vector pB2GW7 were selected based on their resistance to the herbicide phosphinothricin (PPT; Catalogue number 45520; Sigma-

Aldrich™). Seeds from the T1 population were surface sterilised as described in section 2.1 and placed on MS plates supplemented with 10 µg / mL PPT. The plates were transferred to a growth room and the seeds were allowed to germinate under standard conditions (see section 2.1). Seven days after exposure to light, transgenic seedlings were readily identified on the basis of their resistance to the herbicide, as they displayed green, expanded cotyledons. Transgenic seedlings were transferred to compost and allowed to complete their life cycle. Seeds of following generations were selected following the steps outlined above until homozygous plants were identified.

2.25 Light microscopy

A ZEISS Axiophot microscope (ZEISS, Germany) equipped with a Q-Imaging Retiga EXi CCD mono digital camera with RGB filter wheel (QImaging, Canada) was used for the analysis of thick cross sections of plant material. The microscope was coupled with the Metamorph software (Molecular Devices, USA) for the acquisition of images. Details of sample preparation and imaging are provided in section 3.2.1 and 3.2.2. A Leica M205 Stereomicroscope (Leica Microsystems©, Germany) was used for the imaging of whole plant tissue specimens.

2.26 Confocal microscopy

A ZEISS 780 Confocal Laser Scanning Microscope (ZEISS, Germany) was used for the detection of fluorescent signal from cross sections of plant tissue. Fluorescence of the mCherry protein was excited at 561 nm laser and detected between 578 and 639 nm. The auto-fluorescence of lignin was excited at 405 nm and detected between 451-480 nm and 560-612 nm.

2.27 Transmission electron microscopy

Ultra-thin sections were imaged using a JEOL-2100Plus Transmission Electron Microscope (TEM; JEOL, Japan) equipped with a Gatan OneView IS Camera (Gatan, USA). The specimen cartridge containing the TEM grid was mounted onto the specimen holder which was then inserted into the TEM goniometer. The filament was switched on and slowly warmed until a beam current of 110 µA was generated. Gun alignment, condenser lens aperture alignment and eucentric height were adjusted prior to imaging. The Gatan

Microscopy Suite software (Gatan, USA) was used to acquire micrographs. Details of sample preparation, staining and imaging are provided in sections 6.2.4, 6.2.5 and 6.2.7.

2.28 Photographic documentation

The photographs presented in this thesis were acquired with a Canon PowerShot SX500 IS (Canon, UK).

2.29 Statistical analysis

Statistical tests were performed using the Genstat software (Genstat for Windows 21st Edition; VSN International, Hemel Hempstead, UK). Alternatively, student's t-test was performed using the Data Analysis tool in Excel (Microsoft Office). Student's t test was routinely used to assess statistical differences between two variants. Detailed of other statistical analysis are provided in the Materials and Methods sections of each chapter.

Chapter 3 – Characterisation of the *crk10-A397T* mutant phenotype and analysis of the pattern of expression of *CRK10* in Arabidopsis

3.1 Introduction

As mentioned in Chapter 1 (section 1.6), the object of this study is a dwarf Arabidopsis mutant which was generated by chemical mutagenesis. A single point mutation in the coding sequence of *CYSTEINE-RICH RECEPTOR-LIKE KINASE 10* (*CRK10*, AT4G23180) which causes the substitution of an alanine with a threonine residue at position 397 of the protein was found to be linked to the mutant's dwarf phenotype, and according to the guidelines for Arabidopsis nomenclature (The Arabidopsis Information Resource, TAIR; https://www.arabidopsis.org/index.jsp) the mutant allele was named *crk10-A397T*. In this chapter, the phenotypical characterisation of the *crk10-A397T* mutant plants is reported, with special attention to its most distinctive morphological feature: a dwarf growth habit.

Plant growth and development are governed by a variety of endogenous and exogenous factors, including hormonal networks, availability of resources, and stresses of a biotic and abiotic nature. Repression of growth leading to dwarfism has been extensively reported in the literature for Arabidopsis mutants which, despite sharing phenotypical similarities, can be grouped under distinct categories according to the underlying cause of their dwarf growth habit. Some of these categories include, but are not limited to, auto-immune mutants, mutants with impaired biosynthesis, perception or signalling of growth-stimulating hormones, and mutants with defective xylem vasculature, which impairs the long-distance transport of water and solutes and consequently limits plant growth. Examples of dwarf mutants belonging to these three classes are described below.

The category of auto-immune mutants harbour mutations which lead to the constitutive activation of defence responses in the absence of pathogen attack. These include loss-of-function mutations of regulators in plant immunity and gain-of-function mutations in plant immune receptors (van Wersch et al., 2016). In both cases, the activation of defence responses causes the suppression of plant growth as resources are allocated to stress-responsive pathways, in what is known as the growth-defence trade-off (Huot et al., 2014). Examples include *suppressor of salicylic acid insensitive of npr1-5-4* (*ssi4*), a gain-of-function mutant of a Toll Interleukin1 Receptor-Nucleotide Binding Site – Leu Rich repeat

(TIR-NB-LRR) protein which is a dwarf and displays spontaneous cell death, constitutive expression of pathogenesis-related (PR) genes, SA accumulation and enhanced resistance to bacterial and oomycete pathogens (Shirano et al., 2002). The dwarf phenotype of *suppressor of npr1-1, constitutive4-1D* (*snc4-1D*), a gain-of-function mutant of an atypical RLK (Bi et al., 2010), is also accompanied by the activation of defence responses. A missense mutation in an atypical TIR-NB-LRR protein also causes an auto-immune phenotype in the *chilling sensitive 3-2D* (*chs3-2D*) mutant (Bi et al., 2011). Similarly, the knockout of MAPKs, important signalling components of innate immune responses (Pedley & Martin, 2005; see section 1.1.3), often causes an auto-immune phenotype. This is the case for *mpk4*, *mkk1 mkk2* and *mekk1*, all of which exhibit dwarf phenotypes and constitutive activation of defence responses (Petersen et al., 2000; Ichimura et al., 2006; Gao et al., 2008). This cascade is guarded by the NB-LRR resistance (R) protein SUMM2, which triggers defence responses upon inactivation of the MEKK1-MKK1/MKK2-MPK4 cascade (Zhang et al., 2012). Interestingly, the dwarfism of auto-immune mutants is frequently alleviated by changes in environmental conditions such as temperature and humidity. For example, temperatures in the range of 28-30 °C partially suppress the dwarf phenotype of *mpk4*, *mkk1 mkk2* and *bir1-1* (Su et al., 2007; Gao et al., 2008; Gao et al., 2009), whereas high humidity alleviates the dwarfism of *ssi4* (Zhou et al., 2004).

Another group of dwarf mutants encompass those with impaired biosynthesis, perception or signalling of growth- and development-promoting hormones, as for instance, gibberellins (GAs), brassinosteroids (BRs) and auxin. Mutants defective in GA perception, such as *GA-insensitive* (*gai*) and *sleepy1* (*sly1*), display a range of phenotypes which resembles that of plants with reduced GA biosynthesis, including dwarfism, narrow leaf shape, reduced apical dominance, dark green colouration and delayed flowering (Koornneef et al., 1985; Steber et al., 1998; Fridborg et al., 1999). Similarly, mutants with impaired sensitivity to BR, such as *brassinosteroid insensitive1* (*bri1*), also show characteristic dark green leaves, reduced stature, delayed flowering and reduced apical dominance, as well as impaired male fertility and abnormal skotomorphogenesis in the dark (Li et al., 1996; Szekeres et al., 1996; Clouse et al., 1996). Growth-related phenotypes associated with the hormone auxin has also been reported for decades, as for example the dwarf growth of the auxin-

resistant mutant *Dwf* (Mirza and Maher, 1987) and the reduced stature of the *atpgp1-2* mutant due to impaired auxin transport (Ye et al., 2013).

Finally, a third group of dwarf mutants owe their stunted growth to vasculature-associated defects, which is of special relevance considering the results presented in this chapter. Briefly, the vascular system of plants consists of three main tissue types: xylem, phloem and the vascular meristems procambium and cambium. The xylem is mainly responsible for the transportation of water and nutrients from the root to the shoot of the plant, while the phloem transports and distributes photoassimilates from source to sink tissues. The procambium and cambium, which are pools of meristematic, pluripotent cells, give rise to the different xylem and phloem elements (Ye, 2002; Růžička et al., 2015). The xylem vasculature is comprised of three cell types: tracheary elements, which are hollow conductive cells (called vessels in angiosperms); xylem parenchyma cells, responsible for the storage of nutrient reserves, short-distance transport and lignification of neighbouring xylem vessels after vessel autolysis is complete; and xylem fibers, major providers of mechanical support to the growing plant (Ye, 2002; Ragni et al., 2011; Růžička et al., 2015).

Two distinct phases of vasculature development are observed across the lifespan of a plant: primary and secondary growth. During primary growth the vasculature develops mainly in the acropetal direction, and primary xylem and phloem differentiate from the procambium meristem. During secondary growth, the procambium gives rise to the cambium, a lateral meristem which promotes radial growth by producing secondary xylem and phloem (Ye, 2002; Růžička et al., 2015). In Arabidopsis, the architecture of vasculature development during secondary growth is organ-specific (Ye, 2002; Figure 3.1). In the inflorescence stem, vascular bundles are connected to each other via a continuous ring of interfascicular cambium, with a clear developmental gradient observed between the younger apex of the inflorescence stem and the older, mature base of the organ. In roots, however, two initial planes of symmetry observed at the root tip give rise to a full radial symmetry in the mature organ, with the development of files of xylem vessels following a radial architecture (Lehmann and Hardtke, 2016).

In Arabidopsis plants, a similar arrangement to the one observed in roots is found in the hypocotyl, also known as the embryonic stem (Figure 3.2). However, tissue elongation is uncoupled from secondary growth in this organ,

which leads to the absence of a developmental gradient (Sibout et al., 2008). For reference, elongation of the hypocotyl was empirically observed to cease four to five days after germination (DAG), immediately preceding the onset of secondary growth around five to six DAG (Sibout et al., 2008). Notably, the extensive secondary growth observed in the hypocotyl occurs in two phases (Figure 3.3). The first stage, known as the “proportional phase” or “xylem I”, is characterised by a roughly equal relative size of both phloem and xylem tissue, and the presence of xylem vessels and parenchyma cells. In the second phase, which is known as “xylem expansion” or “xylem II”, the area occupied by the xylem outgrows that of the phloem, and both xylem and phloem fibers start to differentiate as secondary growth accelerates (Chaffey et al., 2002; Lehmann and Hardtke, 2016). Interestingly, flowering has been identified as the physiological switch which triggers the onset of the xylem II phase in Arabidopsis hypocotyls (Sibout et al., 2008).

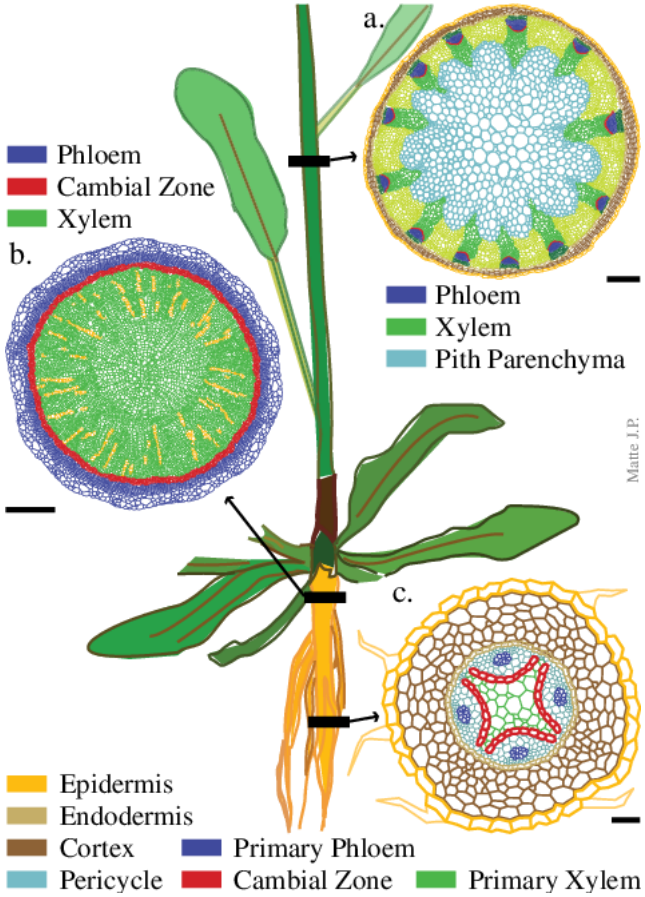

Figure 3.1 The vascular tissue in the root, hypocotyl and stem of Arabidopsis plants during secondary growth.

Schematic representations of transverse cross sections of (A) inflorescence stem, (B) hypocotyl and (C) root of Arabidopsis plants are depicted. Black bars

and arrows indicate the location of the cross sections. Bar, 200 µm. Reproduced from Risopatron et al., 2010 (https://doi.org/10.1007/s00709-010-0211-z); copyright notice in Appendix 1.7.

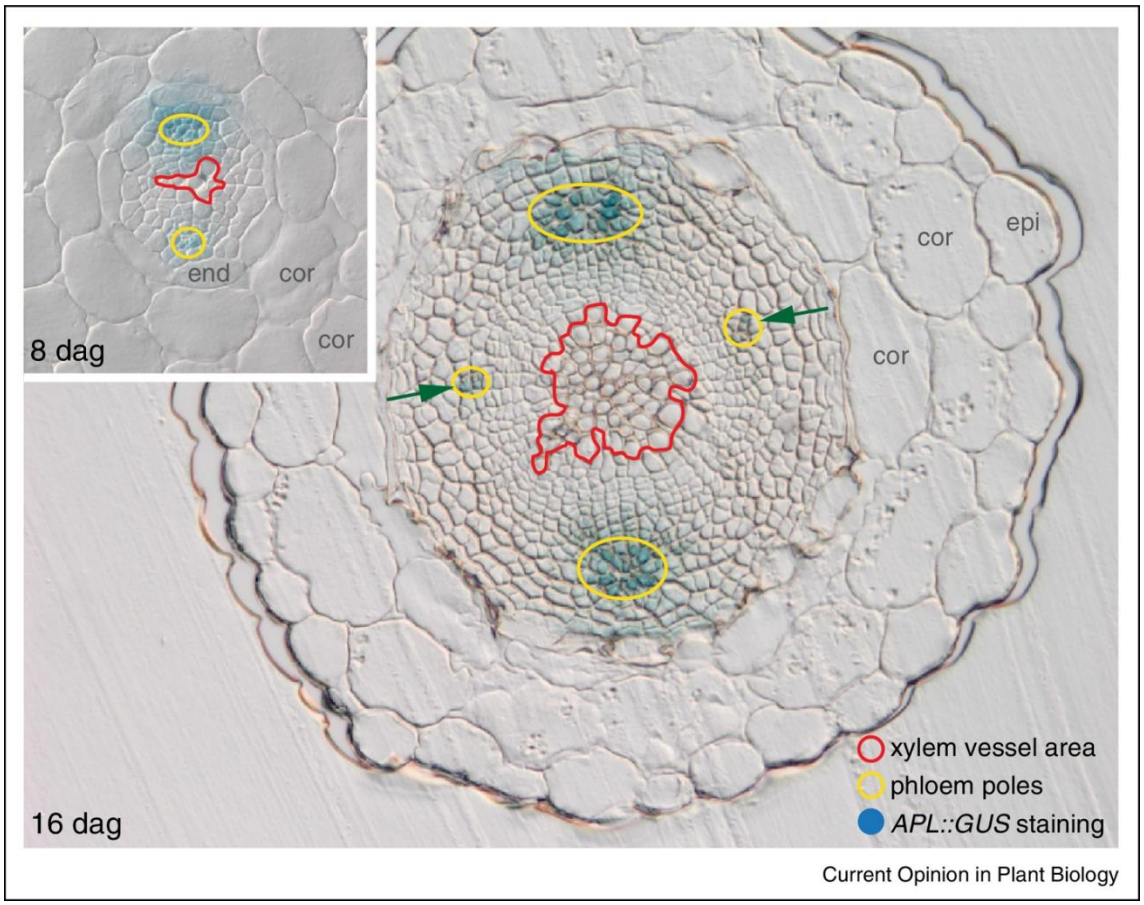

Figure 3.2 The progression of secondary growth in the hypocotyls of Arabidopsis plants.

Light micrographs showing transverse cross sections of hypocotyls of WT Col-0 plants expressing a phloem-specific promoter reporter construct (*APL::GUS*) at 8 and 16 days after germination (DAG). The location of the histochemical staining indicates the phloem poles. A two-plane symmetry can be observed in the hypocotyl at 8 dag, where a central xylem axis is flanked by two phloem poles. As secondary growth unfolds, a transition to a radial symmetry can be observed at 16 dag (green arrows indicate developing phloem poles). Epi, epidermis; cor, cortex; end, endodermis. Reproduced from Lehmann and Hardtke, 2016 (https://doi.org/10.1016/j.pbi.2015.10.011); copyright notice in Appendix 1.8.

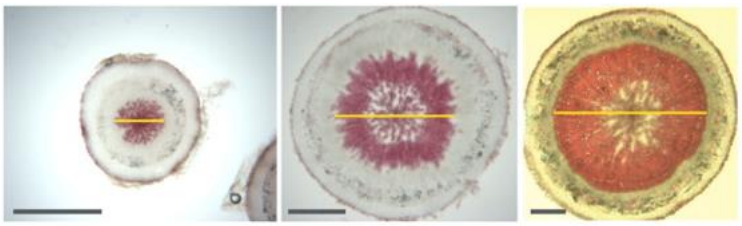

Arabidopsis thaliana	xylem area per hypocotyl area
vegetative	15.0 %
flowering *before* bolting	34.3 %
flowering *after* bolting	50.6 %

Figure 3.3 The xylem I and xylem II phases of secondary growth in the hypocotyl of Arabidopsis plants.
Light micrographs show transverse cross sections of hypocotyls of Arabidopsis plants during vegetative (xylem I) and after the onset of flowering (xylem II) stages. Phloroglucinol was used to stain the cross sections and indicate lignified xylem vessels and fibres. The yellow line indicates the diameter of the area occupied by xylem tissue, and the table displays this measurement relative to total hypocotyl area. Reproduced from Ragni et al., 2011 (https://doi.org/10.1105/tpc.111.084020) under the terms of the Creative Commons Attribution License.

Xylem vessels are the vascular cell type which are frequently defective in dwarf mutants. These cells undergo a tightly regulated developmental programme from cell differentiation to vessel maturation. Steps include cell elongation and expansion, the coordinated deposition of a secondary cell wall composed mainly of cellulose, hemicellulose and lignin, and cell autolysis by programmed cell death, which empties the cell contents to give rise to hollow conduits (Ye, 2002; Nieminen et al., 2004). The deposition of a thick secondary cell wall, a hallmark of xylem vessels, improves the mechanical strength of these elements and allows them to withstand the internal negative pressure generated by the transpiration-driven movement of water. In 1997, Turner and Somerville reported the identification of the first *irregular xylem* (*irx*) mutants of Arabidopsis, which exhibited reduced growth rate and stature due to the presence of collapsed xylem vessels in inflorescence stems. The xylem cell wall defect in mutants *irx1*, *irx2* and *irx3* was correlated with a decrease in the total amount of cellulose, which led to thinner secondary cell walls and their consequent collapse. Several other *irregular xylem* mutants have been subsequently reported in the literature and their collapsed xylem vessel phenotype was correlated to defective cell wall composition and structure (see section 6.1 for a detailed description of plant cell

walls). *irx8,* for instance, shows a significant reduction in cell wall thickness due to decreased levels of the hemicellulose glucuronoxylan and the pectic polysaccharide homogalacturonan (Persson et al., 2007). Similarly, the dwarf phenotype of the double mutants *irx10 irx10-L* and *irx14 irx14-L* and the single mutant *fragile fiber 8* (*fra8*) was correlated with reduced content of the hemicellulose xylan (Zhong et al., 2005; Wu et al., 2009; Keppler & Showalter, 2010). Additionally, the dwarf mutant *eskimo1* (*esk1*) displays a reduction in the degree of xylan acetylation, which also affects secondary cell wall thickening and the mechanical strength of the inflorescence stem (Lefebvre et al., 2011; Yuan et al., 2013).

To investigate the underlying cause behind the dwarf phenotype of the *crk10-A397T* mutant, a thorough anatomical characterisation of the mutant plants was carried out. The analysis of cross sections of roots, hypocotyl and stem samples revealed the presence of a severe *irregular xylem*-like phenotype in the roots and hypocotyls, but not in the inflorescence stem of the mutant. A correlation between the progression of the phenotype and the onset of dwarfism was possible with the analysis of a developmental time series of the hypocotyl. Moreover, reporter lines expressing the reporter gene *β-glucuronidase* (*GUS*) under the control of the putative promoter region of *CRK10* were generated to investigate the spatiotemporal expression pattern of *CRK10*, and the subcellular localisation of the protein was confirmed by transient and stable expression of a translational fusion with mCherry. To assess the contribution of aerial and below-ground organs to the dwarf phenotype, a grafting experiment was performed. Finally, knockout and overexpression lines of *CRK10* were analysed to investigate any potential phenotypes associated with changes in the abundance of the *CRK10* transcript.

3.2 Materials and Methods

The protocols used for the cloning and manipulation of DNA molecules for the generation of genetic constructs described in this section can be found in Chapter 2. Primer sequences used for the amplification of PCR products, *in vitro* mutagenesis PCR, genotyping, RT-PCR and qPCR are listed in Table 3.1, and vector maps can be found in Appendix 2 Selected constructs were sequenced after every cloning step.

3.2.1 Plant tissue fixation and resin embedding

Hypocotyls of Arabidopsis plants (approximately 2-5 mm in length) were excised with carbon steel sterile blades (N° 10 Dermaplane Scalpel blade; Swann Morton Ltd) and transferred to glass vials (Rolled Rim Vials, G100, 7mL, TAAB) containing 4-6 mL of 4% Paraformaldehyde / 2.5% Glutaraldehyde fixative solution. The hypocotyl tissue was incubated in fixative for two hours at room temperature on a tube rotator, followed by incubation at 4 °C overnight. Three washing steps of 30 minutes each were performed with 4-6 mL of 0.1 M Sorenson's phosphate buffer pH 7.2 prior to dehydration in a graded ethanol series following the steps outlined below (approximately 5 mL of ethanol was used in each step):

10 – 30% ethanol: 30 minutes each;

40 – 70% ethanol: 2 x 30 minutes each;

70% ethanol: 4 °C overnight;

80 – 90% ethanol: 2 x 30 minutes each;

100% dry ethanol: 3 x 20 minutes each.

Samples were then infiltrated with increasing concentrations of LR White resin (AGR1281 LR White Resin Medium Catalysed; Agar Scientific) at room temperature on a tube rotator, as follows:

100% ethanol : resin 4:1 ratio, one hour;

100% ethanol : resin 3:2 ratio, one hour;

100% ethanol : resin 2:3 ratio, one hour;

100% ethanol : resin 1:4 ratio, one hour;

100% resin: 1 hour.

Samples were kept overnight at 4 °C before being individually placed in embedding capsules (C094 TAAB capsule 8mm flat, polyethylene 500; TAAB) filled with fresh resin, which were incubated overnight at 60 °C to promote

polymerisation. The blocks were removed from the oven and allowed to cool down to room temperature before sectioning.

Fixative solution:	4%	Paraformaldehyde
	2.5%	Glutaraldehyde
	0.05 M	Sorenson's phosphate buffer
	pH	7.2

Sorenson's phosphate buffer:	Solution A: 0.2 M	$NaH_2PO_4.1H_2O$
	Solution B: 0.2 M	$Na_2HPO_4.7H_2O$

0.1 M Sorenson's phosphate buffer pH 7.2 was prepared by the addition of 28 mL of Solution A, 72 mL of Solution B and 100 mL of sterile deionised water.

3.2.2 Preparation and staining of thick sections for light microscopy imaging

Cross sections (section thickness: 1 – 2 µm) of embedded hypocotyl tissue were prepared using a glass knife (TAAB superglass 400mm x 25.4mm x 6.4mm, Catalogue number G067/T; TAAB Laboratories Equipment) attached to the Reichert-Jung UltraCut Microtome. Sections were collected with fine-bristle brushes and placed onto distilled water drops on microscope slides (Menzel-Glaser, Thermo Scientific™). The slides were transferred to a hot plate kept at 100 °C to allow the complete evaporation of the water drops. Sections were stained with one drop of 1% Toluidine Blue O (pH 9.2) for 30 seconds, or one drop of 4% potassium permanganate for 20 minutes. The glass slides were rinsed with distilled water and dried at 100 °C on a hot plate. The slides were mounted with DPX mounting media (Sigma Aldrich®) and glass cover slips (0.17 mm thick, AGL462250-15 Rectangular cover glasses, 22 x 50mm, 1½ thickness, Agar Scientific). Sections were observed using an upright light microscope (see section 2.25).

1% Toluidine Blue O:	1 g	Toluidine Blue O
	1 g	Sodium tetraborate
	100 mL	Distilled water
	pH	9.2

4% Potassium permanganate:	4 g	Potassium permanganate
	100 mL	Distilled water

3.2.3 Cloning of *35S:CRK10^{WT}* construct

The *35S:CRK10^{WT}* construct used to generate complementation lines of the *crk10-A397T* mutant and overexpression lines of *CRK10* in the WT Col-0 background was cloned prior to the start of this project. The cDNA sequence of *CRK10* was amplified from the cDNA clone U60398 with primers containing *Sal*I and *Sac*I restriction sites at the 5' and 3' ends, respectively. The PCR product was cloned into pJET1.2/blunt (CloneJET PCR Cloning Kit, Thermo Scientific™), and the construct was digested with *Sal*I and *Sac*I restriction enzymes. Following separation of the DNA fragments by electrophoresis on a low-melting point agarose gel, the ~2.3 kb band was excised and purified and the fragment was ligated with the pre-digested pJD330 plasmid, placing the cDNA sequence of *CRK10* under the control of the *35S* promoter. The construct *35S:CRK10^{WT}*-tNOS was then amplified with primers containing *Asc*I restriction sites, and the PCR product was cloned into pJET1.2/blunt before digestion with *Asc*I. The purified fragment was ligated with the pre-digested RS_3GSeedDSRedMCS binary vector.

3.2.4 Cloning of *CRK10$_{PRO}$:GUS* construct

Approximately 1 kb of the genomic region upstream of *CRK10* was chosen as the putative native promoter of the gene (*CRK10*$_{PRO}$; sequence in Appendix 3.1). The sequence was amplified from Arabidopsis Col-0 genomic DNA with primers containing *Sph*I and *Nco*I restriction sites at the 5' and 3' ends, respectively. The PCR product was cloned into pJET1.2/blunt and the resulting construct was digested with *Sph*I and *Nco*I restriction enzymes. Following separation of the DNA fragments by electrophoresis on a low-melting point agarose gel, the 1 kb band was excised and purified and the fragment was ligated with pre-digested pJD330 plasmid, placing the *CRK10* promoter upstream of the *β-glucuronidase* (*GUS*) coding sequence. The *CRK10*$_{PRO}$:*GUS*-tNOS construct was amplified with primers containing *Asc*I restriction sites, and the PCR product was cloned into pJET1.2/blunt before digestion with *Asc*I. The purified fragment was ligated with the pre-digested RS_3GSeedDSRedMCS binary vector to obtain

the final construct. The cloning steps outlined above are documented in Appendix 3.2.

3.2.5 Cloning of the *CRK10*$_{PRO}$:*crk10-A397T* construct

For the generation of this construct, the *CRK10*$_{PRO}$ sequence was amplified with primers containing *Sph*I and *Sal*I restriction sites. The PCR product was cloned into pJET1.2/blunt, and the resulting construct was digested with *Sph*I and *Sal*I enzymes. The pJD330 *35S:CRK10*^{WT} was also digested with *Sph*I and *Sal*I to release the *35S* promoter sequence. Following separation of the DNA fragments by electrophoresis on a low-melting point agarose gel, the fragments corresponding to *CRK10*$_{PRO}$ and pJD330 *CRK10*^{WT} were purified and ligated, generating the pJD330 *CRK10*$_{PRO}$:*CRK10*^{WT} construct. The point mutation harboured by the *crk10-A397T* allele was introduced in the cDNA sequence of *CRK10* by *in vitro* mutagenesis to obtain the *CRK10*$_{PRO}$:*crk10-A397T* construct in pJD300. Primers containing *Asc*I restriction sites were used to amplify the *CRK10*$_{PRO}$:*crk10-A397T*-tNOS sequence, and the PCR product was cloned into pJET1.2/blunt before enzymatic digestion with *Asc*I. The purified fragment was ligated with the pre-digested RS_3GSeedDSRedMCS binary vector to obtain the final construct. The cloning steps outlined above are documented in Appendix 4.1.

3.2.6 Cloning of *35S*:*CRK10-mCherry* construct

To obtain this construct, the pJD330 *CRK10*$_{PRO}$:*CRK10*^{WT} vector described in section 3.2.5 was amplified with primers containing *Asc*I restriction sites, and the PCR product was cloned in pJET1.2/blunt. The resulting construct was used as template for *in vitro* mutagenesis to replace the stop codon of *CRK10* with a *Sac*I restriction site upstream of the NOS terminator sequence, resulting in the pJET1.2 *CRK10*$_{PRO}$:*CRK10*$_{wsc/SacI}$ (wsc, without stop codon). The coding sequence of *mCherry* (in Appendix 5.1) was cloned with primers containing *Sac*I restriction sites and the digested fragment was ligated with the pre-digested pJET1.2 *CRK10*$_{PRO}$:*CRK10*$_{wsc/SacI}$ to obtain the pJET1.2 *CRK10*$_{PRO}$:*CRK10-mCherry* construct. The orientation of the insert was checked by PCR. The *CRK10-mCherry*-tNOS fragment was amplified with primers containing *Sal*I and *Not*I restriction sites at the 5' and 3' ends, respectively, and subsequently ligated with pre-digested pENTR™1A Dual Selection Vector

(Invitrogen™). pENTR™1A *CRK10-mCherry*-tNOS was used for LR recombination (Gateway™, Invitrogen™) with the binary vector pB2GW7, generating the construct *35S*:*CRK10-mCherry*-tNOS. The cloning steps outlined above are documented in Appendix 5.2.

3.2.7 Histochemical staining of *GUS* reporter lines

Whole seedlings (4-day-old to 3-week-old) or detached tissue from older plants (leaves and roots of plants older than three weeks) of *CRK10*$_{PRO}$:*GUS* reporter lines were collected and transferred to multi-well assay plates (six or eight wells; Merck™). The samples were completely submerged in 3-5 mL of X-Gluc (5-bromo-4-chloro-3-indolyl-beta-D-glucuronic acid; Melford) solution (vacuum was applied when necessary to ensure submergence of tissue sample).The closed multi-well plates were placed in a plastic container lined with wetted paper towel to ensure a humid environment. The container was wrapped with cling film and aluminium foil before being transferred to an incubator at 37 °C, where it was kept overnight. After incubation, the X-Gluc solution was removed by pipetting and the samples were rinsed with distilled water before incubation in ethanol 80% for 24 hours (to extract the chlorophyll from the plant tissues and facilitate the visualisation of the histochemical staining). Samples were washed once more with distilled water and mounted on glass microscope slides (Menzel-Glaser, Thermo Scientific™) before imaging using a stereomicroscope (section 2.25).

X-Gluc solution:	0.1 M	sodium phosphate buffer pH 7.0
	100 mM	potassium ferricyanide
	100 mM	potassium ferrocyanide
	0.01%	Triton X-100

For every 50 mL of solution, 2.5 mg of 5-bromo-4-chloro-3-indolyl-beta-D-glucuronic acid, cyclohexylammonium salt (X-Gluc) were used. The X-gluc powder was pre-dissolved in 0.25 mL of methyl cellusolve and 0.25 mL of dimethyl sulfoxide before being added to the solution, which was kept at 4 °C in the dark.

3.2.8 Micrografting of Arabidopsis seedlings

The grafting protocol was performed according to Turnbull et al., 2002. Arabidopsis seeds were surface sterilised and placed on filter paper discs on ½ MS (Murashige & Skoog, Duchefa Biochemie), 2% agar (Agar type E, Catalogue number A4675; Sigma-Aldrich®) plates. Following stratification at 4 °C for 48 hours, plates were transferred to growth room (23/18 °C, 16-hour light photoperiod; approximately 200 µmol m^{-2} per second of light) and seedlings were allowed to grow for four days. A stereomicroscope was placed in a laminar flow hood, and all surfaces were thoroughly cleaned with ethanol 70%. Using a sterile micro knife (Carbon steel tip, angled 22.5 Deg 13.5 cm, 0.15 mm thickness; Fine Science Tools, Inc) the cotyledons of seedlings were removed, and scions and rootstocks were separated by a single cut perpendicular to the hypocotyl axis. Forceps were used to move scions between plates and place them in direct contact with rootstocks, generating self-grafts and reciprocal combinations. Sterile deionised water was constantly added to the plates to keep moisture and prevent seedlings from drying. Plates were closed and sealed with micropore™ medical tape (3M©, UK) before returning to the growth room and placed at a vertical angle. Graft connections were monitored daily, and adventitious roots were removed as necessary in sterile conditions. Successful grafts (around ten per combination) were transferred to compost after seven to ten days. The experiment was repeated twice.

3.2.9 Evaluation of plant growth under different temperature conditions

WT Col-0, *mpk4* and *crk10-A397T* mutant seeds were sown in Levington F2+Sand compost. Seedlings were allowed to germinate and grow for seven days in standard growth conditions (section 2.1) before being transferred to multi-cell plastic trays. Three trays were prepared, each one containing plants of all three genotypes arranged in two contiguous rows. After a 48-hour recovery period post-repotting, one tray was transferred to a cabinet set for 18/16 °C, another tray was moved to a cabinet set at 30/28 °C, and the third tray was kept in the original cabinet under standard temperature conditions (23/18 °C; day/night temperature indicated). All cabinets were adjusted for long day conditions (16-hour light photoperiod). The plants were photographed 12 days after exposure to respective conditions.

3.2.10 *Agrobacterium*-mediated transient gene expression in *N. benthamiana* leaves

This protocol was adapted from Sparkes et al., 2006. *Nicotiana benthamiana* plants were grown for five to six weeks in greenhouse conditions. *A. tumefaciens* GV3101 cells were transformed (see section 2.21) with the pB2GW7 *35S*:*CRK10-mCherry*-tNOS construct, and a single colony was used to inoculate 5 mL of 2x YT selective media. The culture was grown overnight at 29 °C with with agitation (220 rpm) on orbital shaker. One mL of the overnight culture was transferred to a 1.5 mL microfuge tube and centrifuged for five minutes at 1075 x g. The supernatant was removed and the cells were washed once in 1 mL of freshly-made infiltration solution. Following centrifugation for five minutes at 1075 x g, the cells were resuspended in 1 mL of infiltration solution and an aliquot was diluted 10-fold for OD_{600} measurement (section 2.22). The original suspension was diluted to an OD_{600} of 0.1. For the infiltration, the tip of a 5 mL plastic syringe was firmly held against the underside of a young, healthy leaf, and the plunger was pressed down gently so that the liquid diffused throughout the mesophyll air space. The process was repeated as necessary. Plants were returned to the greenhouse for 72 hours before observation of the transient expression of fluorescent proteins with a laser-scanning confocal microscope (see section 2.26).

Infiltration solution:	50 mM	2-(N-morpholino) ethanesulfonic acid (MES)
	2 mM	trisodium orthophosphate
	0.1 mM	acetosyringone
	0.5%	D-glucose

3.2.11 Genotyping of *crk10* T-DNA lines

Arabidopsis lines with T-DNA insertions in the genomic sequence of *CRK10* were genotyped according to instructions from the Salk Institute Genomic Analysis Laboratory webpage on T-DNA primer design (http://signal.salk.edu/tdnaprimers.2.html), as explained in Figure 3.18. The results of representative genotyping PCR reactions are shown in Appendix 6.1.

3.2.12 Quantification of *CRK10* transcript abundance by RT-PCR and qPCR

For the quantification of the *CRK10* transcript in *crk10* and *CRK10* OE lines, a whole rosette leaf was collected in 1.5 mL microfuge tubes. One leaf from an individual plant was considered one biological replicate, and three biological replicates were prepared per line. For the quantification of the *CRK10* transcript in the hypocotyl and inflorescence stem of WT Col-0 plants, whole hypocotyls (2-5 mm in length) of 3-week-old plants, and a small section of the base of the inflorescence stem of 6-week-old plants (1-2 cm in length) were collected in 1.5 mL microfuge tubes. Hypocotyls and stem samples from five individual plants were pooled together per biological replicate, and three biological replicates were prepared per tissue type. The samples were immediately frozen in liquid nitrogen after being collected. The plant tissue was thoroughly ground using a mortar and pestle and the resulting powder was used for RNA extraction with the TRI Reagent® (Sigma-Aldrich®) as described in section 2.5. DNase treatment, cDNA synthesis, RT-PCR and qPCR reactions were performed as described in detail in sections 2.12 to 2.15. The gene *ACTIN2* from Arabidopsis was used as the standard control for the RT-PCR reactions, and both *ACTIN2* and *UBC21* were used as internal standards for the qPCR reactions.

3.2.13 Statistical analysis

To assess whether the pattern of segregation of the dwarf phenotype followed the expected 1:2:1 ratio, the $\chi^2 = \sum_{i=1}^{r} \frac{(Oi-Ei)^2}{Ei}$ chi-square statistic was used, where Oi is the observed count for group i and Ei is the expected count for group i. Under the null hypothesis of 1:2:1 segregation this test statistic should follow a chi-square distribution with 2 degrees of freedom.

Table 3.1. Table of primers.

Primer	Sequence (5' – 3')	Purpose
CRK10$_{PRO}$ *Sph*I For	GCATGCCCTTTGCAACTAGCTAGATGGA	Cloning of *CRK10*$_{PRO}$
CRK10$_{PRO}$ *Nco*I Rev	CCATGGAGCTTTGAGTGATATATGAA	Cloning of *CRK10*$_{PRO}$
CRK10$_{PRO}$ *Asc*I For	GGCGCGCCTTTGCAACTAGCTAGATGGA	Cloning of *CRK10*$_{PRO}$ construct
tNOS *Asc*I Rev	GGCGCGCCTATGACATGATTA	Cloning of *CRK10*$_{PRO}$ construct
CRK10$_{PRO}$ *Sal*I Rev	GTCGACAGCTTTGAGTGATATAT	Cloning of *CRK10*$_{PRO}$
CRK10 A397T For	GAGGTTGTTCTTGTTACAAAGCTACAACATAGA	*In vitro* mutagenesis
CRK10 A397T Rev	TCTATGTTGTAGCTTTGTAACAAGAACAACCTC	*In vitro* mutagenesis
CRK10 wsc *Sac*I For	GATATACATCCTCGAGAGCTCCTCGAATTGATCGTT	*In vitro* mutagenesis
CRK10 wsc *Sac*I Rev	AACGATCAATTCGAGGAGCTCTCGAGGATGTATATC	*In vitro* mutagenesis
*mCherry Sac*I For	GAGCTCATGGTGAGCAAGG	Cloning of *mCherry*
*mCherry Sac*I Rev	GAGCTCTCATTGCCAAATGTTTG	Cloning of *mCherry*
*CRK10 Sal*I For	GTCGACATGAGAAGAAACACAG	Cloning of *CRK10-mCherry* construct
tNOS *Not*I Rev	GCGGCCGCCTATGACATGATTACGAATTC	Cloning of *CRK10-mCherry* construct
LBb1.3 (SALK lines)	ATTTTGCCGATTTCGGAAC	Genotyping
LB1 (SAIL lines)	GCCTTTTCAGAAATGGATAAATAGCCTTGCTTCC	Genotyping

SALK_023945 RP	GTGACTCTGTCTGGAGCTTGG	Genotyping
SALK_023945 LP2	AGTTATTATGTTTTAAATTTTGAC	Genotyping
SALK_116653 RP	TGCCAATTTCAAGAAATCAGG	Genotyping
SALK_116653 LP2	GTTTGCCGTAGATGCGTCTCC	Genotyping
SALK_116653 LP3	TCCCGCAACGCTTCCTACTCCA	Genotyping
SAIL_427_E09 RP	TTGAAATGCAGGAAAAGATGG	Genotyping
SAIL_427_E09 LP2 / RT-PCR B Rev	AAGAAGTCTAACCAGATTTCT	Genotyping / RT-PCR
RT-PCR A For	CGACACTAATAACCACCGGT	RT-PCR
RT-PCR A Rev	CGCGGAGGAGCTGAAACTGGAGG	RT-PCR
RT-PCR B For	AATTCAAAGGTGTTAGTGATA	RT-PCR
RT-PCR C For	GGGCTTTGGAGTAACGGGCG	RT-PCR
RT-PCR C Rev	GGATGCATCGTCAACAGACC	RT-PCR
AtACT2 For	TTCCCTCAGCACATTCCAGCAGAT	qPCR
AtACT2 Rev	AACGATTCCTGGACCTGCCTCATC	qPCR
AtUBC21 For	GCTCTTATCAAAGGACCTTCGG	qPCR
AtUBC21 Rev	CGAACTTGAGGAGGTTGCAAAG	qPCR
AtCRK10 For	ACATGTCTCCCGAGTATGCAATG	qPCR
AtCRK10 Rev	CCAAAGCCCCCAAGCATATGAG	qPCR

3.3 Results

3.3.1 Isolation and identification of the *crk10-A397T* mutant

The steps outlined in this section were performed by Dr Michaela Matthes (with the exception of the generation of the *CRK10*$_{PRO}$:*crk10-A397T* lines in the *crk10-2* background, which I performed during this PhD project). The *crk10-A397T* mutant was isolated in a forward genetic screen using ethyl methanesulfonate (EMS). The mutant was backcrossed six times to the wild-type (WT) Col-0 parent in order to clean its genetic background before an in-depth characterisation was performed. The homozygous mutant displays a dwarf phenotype, but observation of the segregating F2 population of the sixth backcross revealed the semi-dominant nature of the mutation, as WT, intermediate and dwarf phenotypes segregated according to a 1:2:1 ratio with heterozygous plants being clearly discernible (Figure 3.4 A; $\chi^2_2 = 2.36$, p = 0.308). In order to determine the underlying mutation responsible for the dwarf phenotype, whole genome sequencing was performed on bulk segregants derived from the sixth backcross. This returned a list of 15 candidate genes containing point mutations in coding regions (Appendix 7.1), and among these, a single base pair substitution of a guanine with an adenine (G>A) in the 4th exon of the *CYSTEINE-RICH RECEPTOR-LIKE KINASE 10* (*CRK10*; AT4G23180) was identified (Figure 3.4 B). This point mutation leads to the substitution of alanine 397 by a threonine in the kinase domain of CRK10, which belongs to the superfamily of receptor-like kinases (RLKs). Given the important roles played by RLKs as upstream signalling molecules in several biological processes (see section 1.2) and, therefore, the potential impacts of mutating such important regulatory proteins, this mutant allele was considered the most likely candidate to cause the dwarf phenotype of the mutant. Two strategies were used to confirm this hypothesis. Firstly, a complementation line was generated to test whether the dwarf phenotype could be rescued by constitutive expression of the WT cDNA sequence of *CRK10* under the control of the constitutive promoter *CaMV 35S* promoter (herein referred to as *35S*). All T1 transformants showed a WT phenotype (Figure 3.4 C), suggesting that the correct gene had been identified. Secondly, the cDNA sequence of *CRK10* containing the G>A substitution was introduced into a *crk10* KO line (SAIL_427_E09, characterisation of KO lines to follow in section 3.3.7) under the control of the putative native promoter of *CRK10*

(1 kb genomic region upstream of the gene). A total of 25% of the recovered transformants exhibited a dwarf phenotype, establishing a direct link between the *crk10-A397T* allele and the mutant phenotype (Figure 3.4 D).

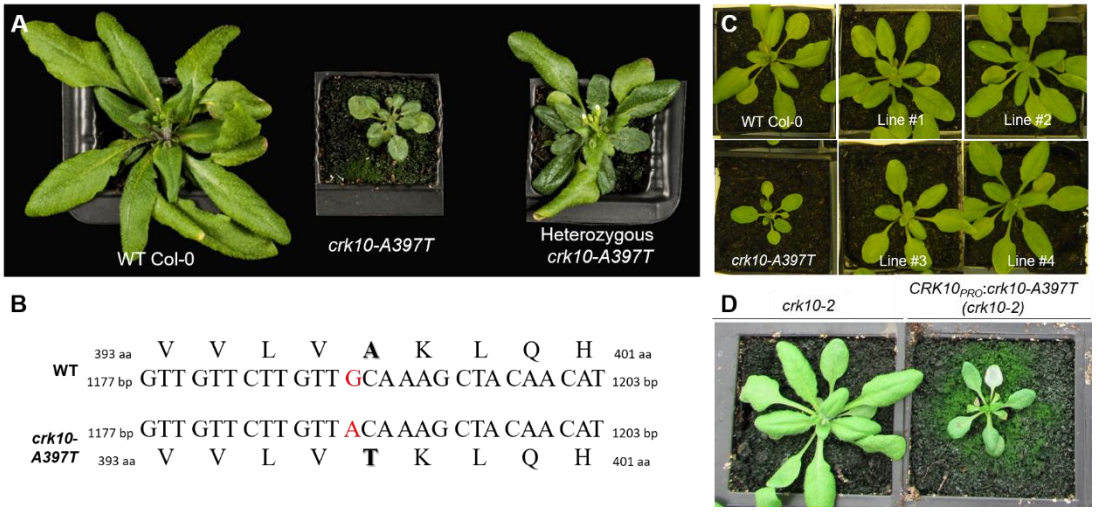

Figure 3.4 *crk10-A397T* is a semi-dominant allele of *CRK10*.

(A) Segregating phenotypes of progeny from the sixth backcross between *crk10-A397T* mutant and WT Col-0.

(B) Single point mutation harboured by the *crk10-A397T* mutant is highlighted in red (G>A on position 1189 of coding sequence of *CRK10*) and corresponding amino acid substitution is shown (alanine > threonine at position 397 of the protein sequence of CRK10).

(C) WT Col-0 and *crk10-A397T* plants next to four independent complementation lines expressing the WT sequence of *CRK10* (35S:*CRK10*) in the mutant background.

(D) A *crk10-2* plant next to a transgenic plant expressing the *crk10-A397T* allele driven by the *CRK10* native promoter (*CRK10*$_{PRO}$:*crk10-A397T*) in the *crk10-2* background.

3.3.2 Morphological characterisation of the *crk10-A397T* mutant plants

A detailed characterisation of the morphology and development of the *crk10-A397T* mutant plants compared to WT Col-0 plants was conducted. The *crk10-A397T* seeds demonstrate an accelerated germination rate compared to WT under continuous light and darkness (Figure 3.5 A-B). In the light, an average of 70% of the mutant seeds germinated after 24 hours, compared to only 10% of the WT seeds. After 48 hours, more than double the number of mutant seedlings (70%) have expanded cotyledons compared to the WT (25%) seedlings. In the dark, nearly 50% of the mutant seedlings exhibit radicle protrusion after 24 hours compared to zero of the WT seedlings. After 48 hours, 80% of the mutant seedlings show elongated hypocotyls compared to 30% for the WT seedlings. In addition to the accelerated germination rate, 4-day-old mutant seedlings also show increased size compared to the WT under continuous light (Figure 3.5 C-D).

During the first two weeks of development, no other obvious differences are observed in the growth of the *crk10-A397T* mutant plants. However, leaf development starts to be affected in the mutant between weeks two and three after sowing, when small, dark green leaves start to be produced, resulting in an obvious dwarf phenotype (Figure 3.6 A-F). Comparison between the leaf series of 4-week-old plants reveals the extent of the reduction in leaf size of the *crk10-A397T* mutant, which results in over 70% decrease in rosette size compared to WT plants (Figure 3.6 G-H). Although no differences in flowering time were observed between the mutant and WT, the main inflorescence stem of *crk10-A397T* plants remains stunted as its shoot apical meristem is frequently aborted (Figure 3.7 A-B). However, the mutant plants develop numerous lateral inflorescences at later stages, with smaller, stunted siliques filled with viable seeds, which are in general larger than those of WT plants (Figure 3.7 C-E).

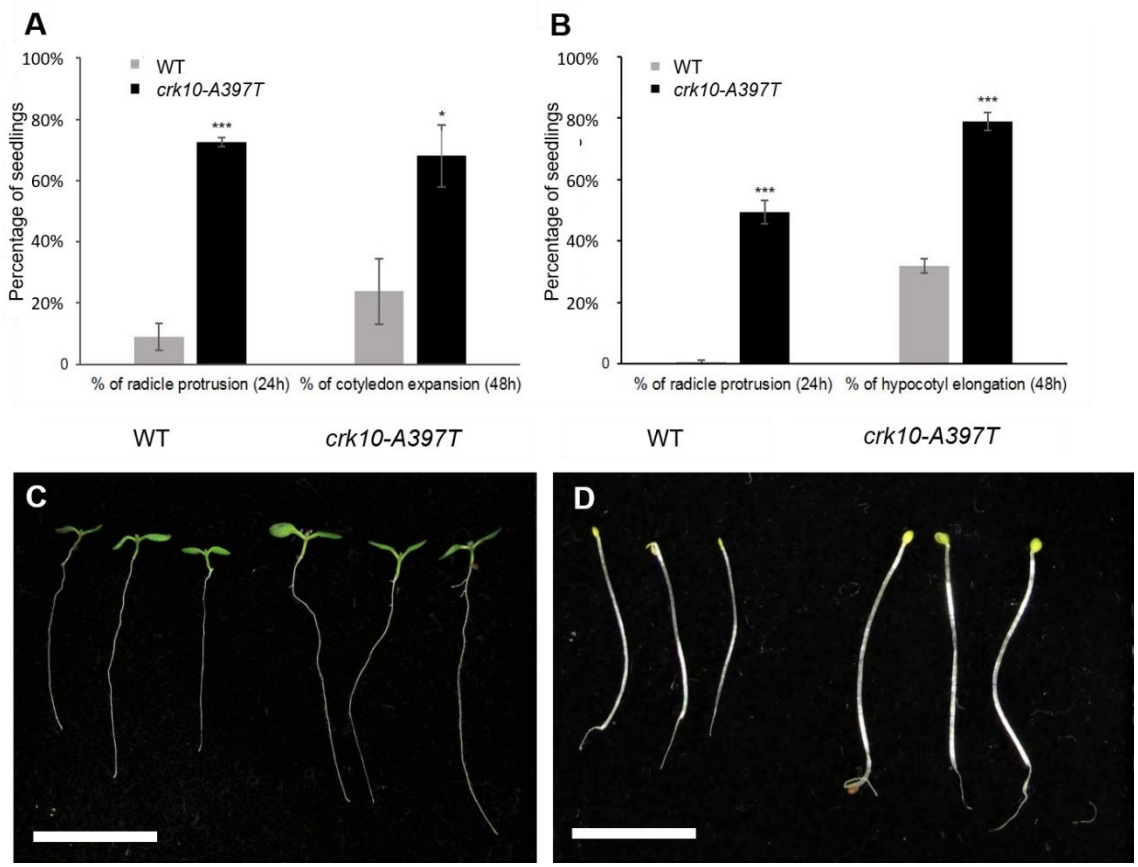

Figure 3.5 *crk10-A397T* mutant seeds germinate earlier than the WT and exhibit increased seedling size.

(A-B) Graphs show the germination rate of WT and *crk10-A397T* seeds after 24 and 48 hours of exposure to (A) continuous light or (B) darkness. Germination was assessed on MS agar plates following stratification for 48 hours. Error bars represent the standard error of three biological replicates (n=50). Asterisks indicate statistical significance (t-test): * = $p \leq 0.05$; *** = $p \leq 0.001$.

(C-D) Four-day-old seedlings grown under (C) continuous light and (D) darkness are shown. Bars, 1 cm.

Figure 3.6 *crk10-A397T* mutant plants have a dwarf phenotype.

(A-F) Rosette morphology of (A-C) WT and (D-F) *crk10-A397T* plants at (A, D) 2, (B, E) 3 and (C, F) 4 weeks after sowing. Bar, 1 cm.

(G) Leaf series of 4-week-old (top) WT and (bottom) *crk10-A397T* plants. Bar, 1 cm.

(H) Graph shows the rosette diameter of WT and *crk10-A397T* plants at 2 and 4 weeks after sowing. Error bars represent the standard error of the mean (n = 10). Asterisks indicate statistical significance (t-test): *** = $p \leq 0.001$.

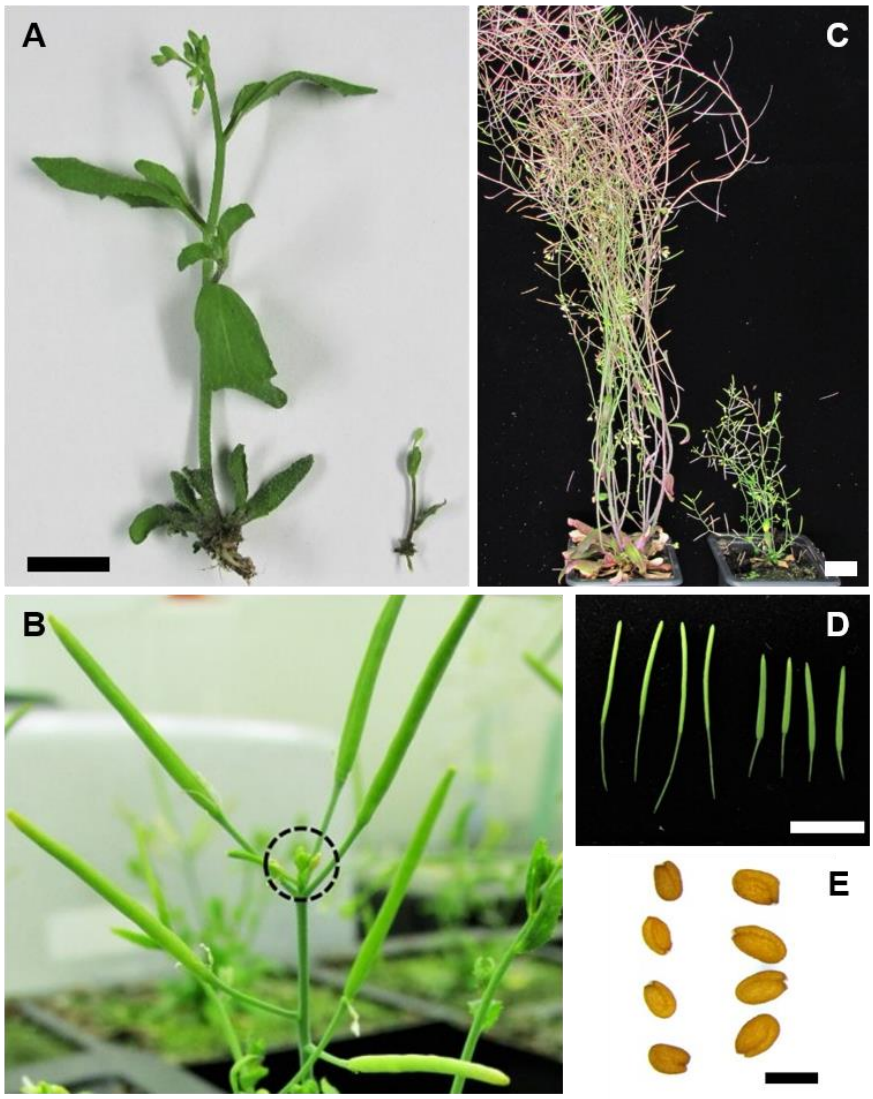

Figure 3.7 *crk10-A397T* mutant plants flower and produce viable seeds.

(A) Main inflorescence stem of 5-week-old (left) WT and (right) *crk10-A397T* plants. Bar, 1 cm.

(B) Stunted inflorescence shoot of 6-week-old *crk10-A397T* plant. Dashed circle indicates aborted shoot apical meristem.

(C) 10-week-old (left) WT and (right) *crk10-A397T* (right) plants. Bar, 1 cm.

(D) Siliques of (left) WT and (right) *crk10-A397T* plants. Bar, 1 cm.

(E) Seeds of (left) WT and (right) *crk10-A397T* plants. Bar, 500 µm.

3.3.3 Characterisation of the collapsed xylem vessel phenotype of the *crk10-A397T* mutant

An association between dwarfism and defective vascular tissue has been described in the literature for several Arabidopsis mutants (see section 3.1). To investigate potential vasculature defects associated with the dwarf phenotype of the *crk10-A397T* mutant, transverse cross sections of roots, hypocotyl and inflorescence stem of 5-week-old mutant and WT plants were analysed. The samples were chemically fixed and embedded in resin for tissue preservation, followed by the preparation of cross sections (as described in sections 3.2.1 and 3.2.2). The lignin-specific dye potassium permanganate was used to stain the cross sections, which allowed the observation of lignified xylem elements. Alternatively, the metachromatic dye Toluidine Blue O was also used, which differentially stains the components of plant cell walls (pectins exhibit a reddish-purple colour, while lignin and other phenolic compounds will show a blue / blue-green staining; Yeung, 1998). This analysis revealed the presence of severely collapsed xylem vessels in the roots and hypocotyls of 5-week-old mutant plants, whereas the vascular bundles of the inflorescence stem resemble the WT (Figure 3.8).

In order to investigate this vasculature defect throughout development and its correlation with the observed dwarf phenotype, hypocotyls of *crk10-A397T* and WT plants were collected at discrete developmental stages, spanning weeks one to five after sowing. The arrangement of xylem elements in the hypocotyl tissue of 1- and 2-week-old seedlings differs between *crk10-A397T* mutant and WT plants (Figure 3.9). The vessels in the mutant hypocotyl do not seem to display the usual radial patterning seen during secondary growth in the WT. However, no vessel deformation and/or collapse is observed at these stages. At three weeks after sowing, however, deformed lignified xylem vessels are first observed in the *crk10-A397T* mutant hypocotyl, which coincides with the stage of development at which the plants start to display a dwarf phenotype (Figure 3.10 A-B). One week later, extensive collapse of xylem vessels is evident in the hypocotyl of the *crk10-A397T* mutant plants, although older vessels present in the centre of the hypocotyl are not affected (Figure 3.10 C-F). This observation suggests that the mechanism responsible for the collapse of the vessels was initiated sometime between weeks two and three after sowing, thus only affecting vessels undergoing differentiation within that timeframe. Notably, xylem vessels in the

mutant hypocotyls consistently displayed a more intense, darker brown staining compared to the WT, indicating increased lignification of their secondary cell walls.

Between weeks four and five after sowing both the WT and *crk10-A397T* plants switch to reproductive growth as the main inflorescence stem starts to develop, a process which is known to trigger the xylem expansion phase of secondary growth in hypocotyl and roots of Arabidopsis plants (Sibout *et al*., 2008). Although both *crk10-A397T* mutant plants and WT flowered five weeks after sowing, the onset of the xylem expansion stage seems to be delayed in the mutant, as hypocotyls of 5-week-old mutant plants do not display fully differentiated, lignified xylem fibres, in contrast to WT hypocotyls (Figure 3.11). Similar to the hypocotyl, the roots of 5-week-old *crk10-A397T* mutant plants also displayed extensive collapse of xylem vessels and a delayed onset of the xylem II phase compared to WT plants (Figure 3.12).

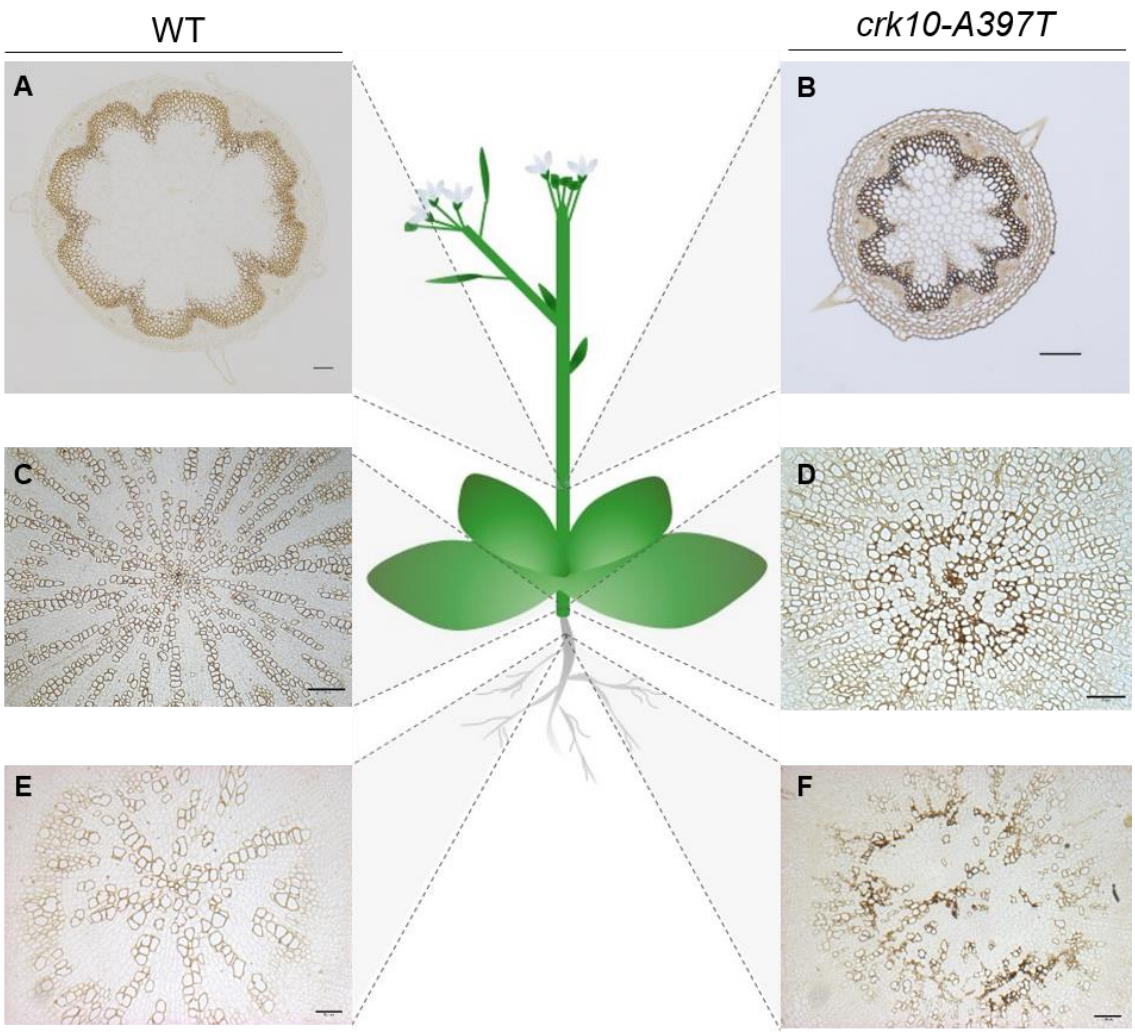

Figure 3.8 Xylem vessels collapse in the root and hypocotyl of *crk10-A397T* plants, but not in the stem.

(A-B) Light micrographs of resin embedded transverse cross sections of the base of the inflorescence stem of 5-week-old plants. Bars, 100 µm.

(C-D) Light micrographs of resin embedded transverse cross sections of hypocotyls of 5-week-old plants. Bars, (C) = 100 µm; (D) = 50 µm.

(E-F) Light micrographs of resin embedded transverse cross sections of roots of 5-week-old plants. Bars, 100 µm.

Cross sections were stained with potassium permanganate. Dashed lines and shaded grey areas indicate the location where cross sections are derived from.

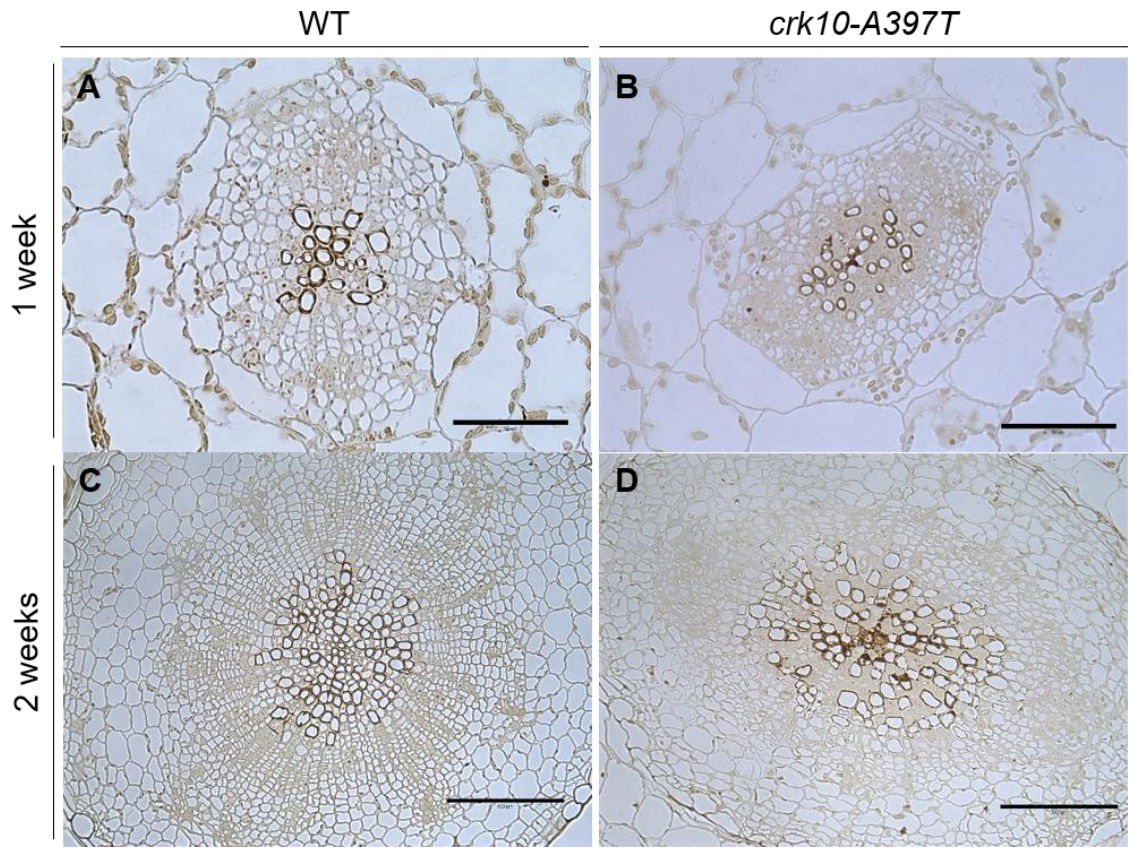

Figure 3.9 The architecture of the vasculature in the hypocotyl of young *crk10-A397T* mutant plants differs from the WT.

(A-B) Light micrographs of resin embedded transverse cross sections of hypocotyls of 1-week-old WT and *crk10-A397T* seedlings. Bars, 50 µm.

(C-D) Light micrographs of resin embedded transverse cross sections of hypocotyls of 2-week-old WT and *crk10-A397T* seedlings. Bars, 100 µm.

Cross sections were stained with potassium permanganate.

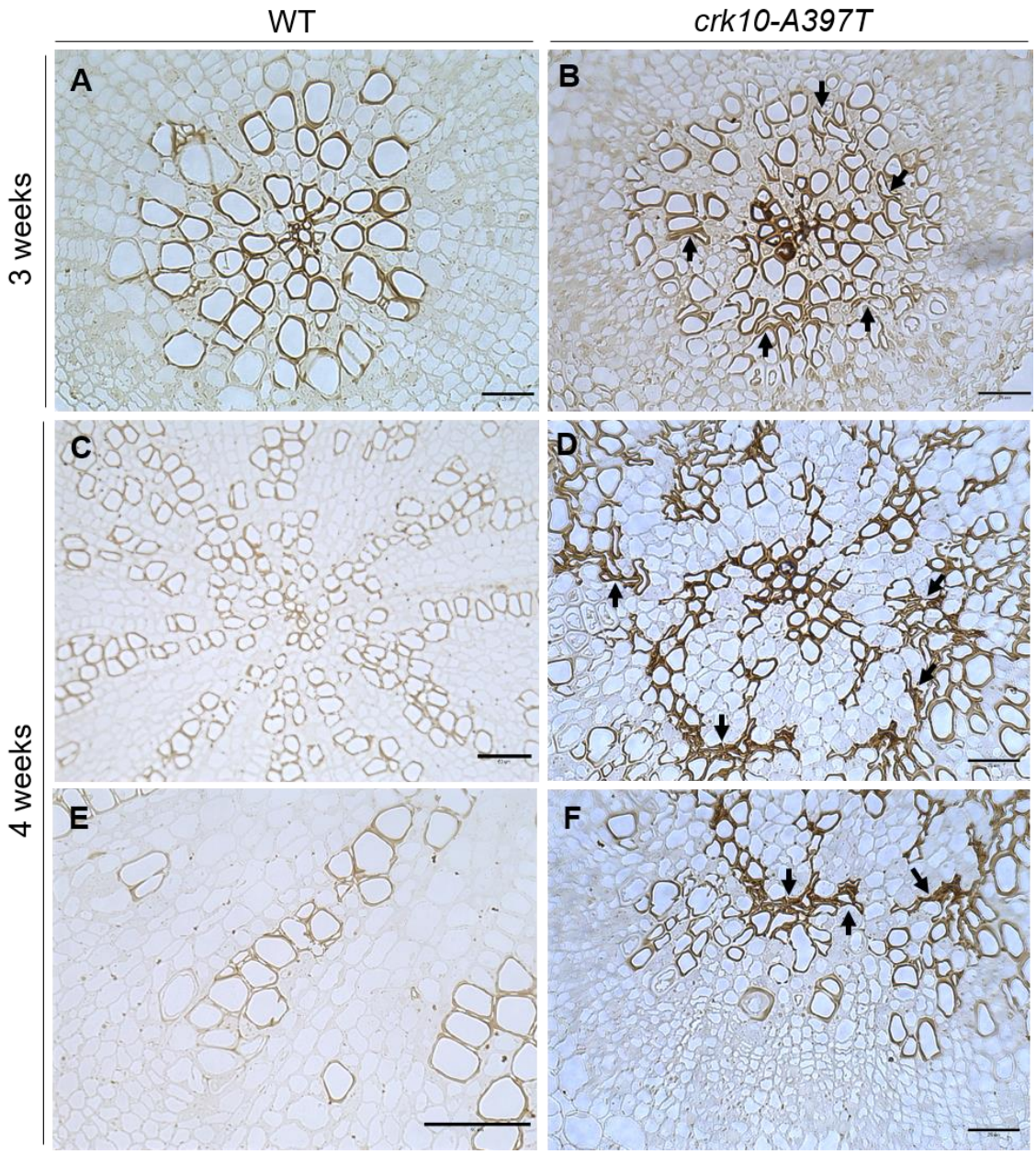

Figure 3.10 Hypocotyls of *crk10-A397T* mutant plants display extensive collapse of xylem vessels.

(A-B) Light micrographs of resin embedded transverse cross sections of hypocotyls of 3-week-old WT and *crk10-A397T* seedlings. Bars, 25 µm.

(C-F) Light micrographs of resin embedded transverse cross sections of hypocotyls of 4-week-old WT and *crk10-A397T* seedlings. Bars, (D, F) = 25 µm; (C, E) = 50 µm.

Cross sections were stained with potassium permanganate Black arrows indicate deformed and /or collapsed xylem elements.

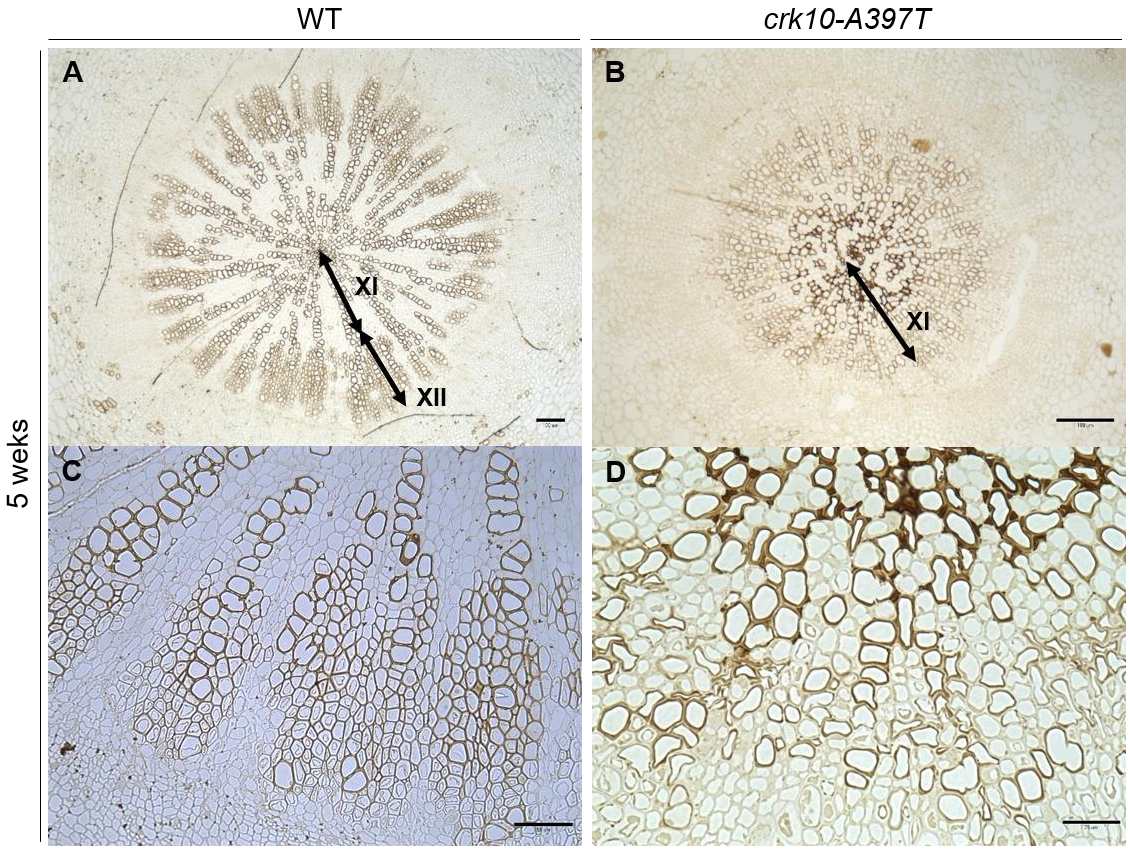

Figure 3.11 The xylem expansion phase is delayed in the hypocotyls of *crk10-A397T* mutant plants.

(A-D) Light micrographs of resin embedded transverse cross sections of hypocotyls of 5-week-old WT and *crk10-A397T* plants. (A) and (B) show an overview of xylem tissue in the hypocotyl and the xylem I (XI) and xylem II (XII) regions. (C) and (D) show detail of lignified xylem fibres in the WT and lack of thereof in the *crk10-A397T* hypocotyl.

Cross sections were stained with potassium permanganate.

Bars, (A, B) = 100 µm; (C) = 50 µm; (D) = 25 µm.

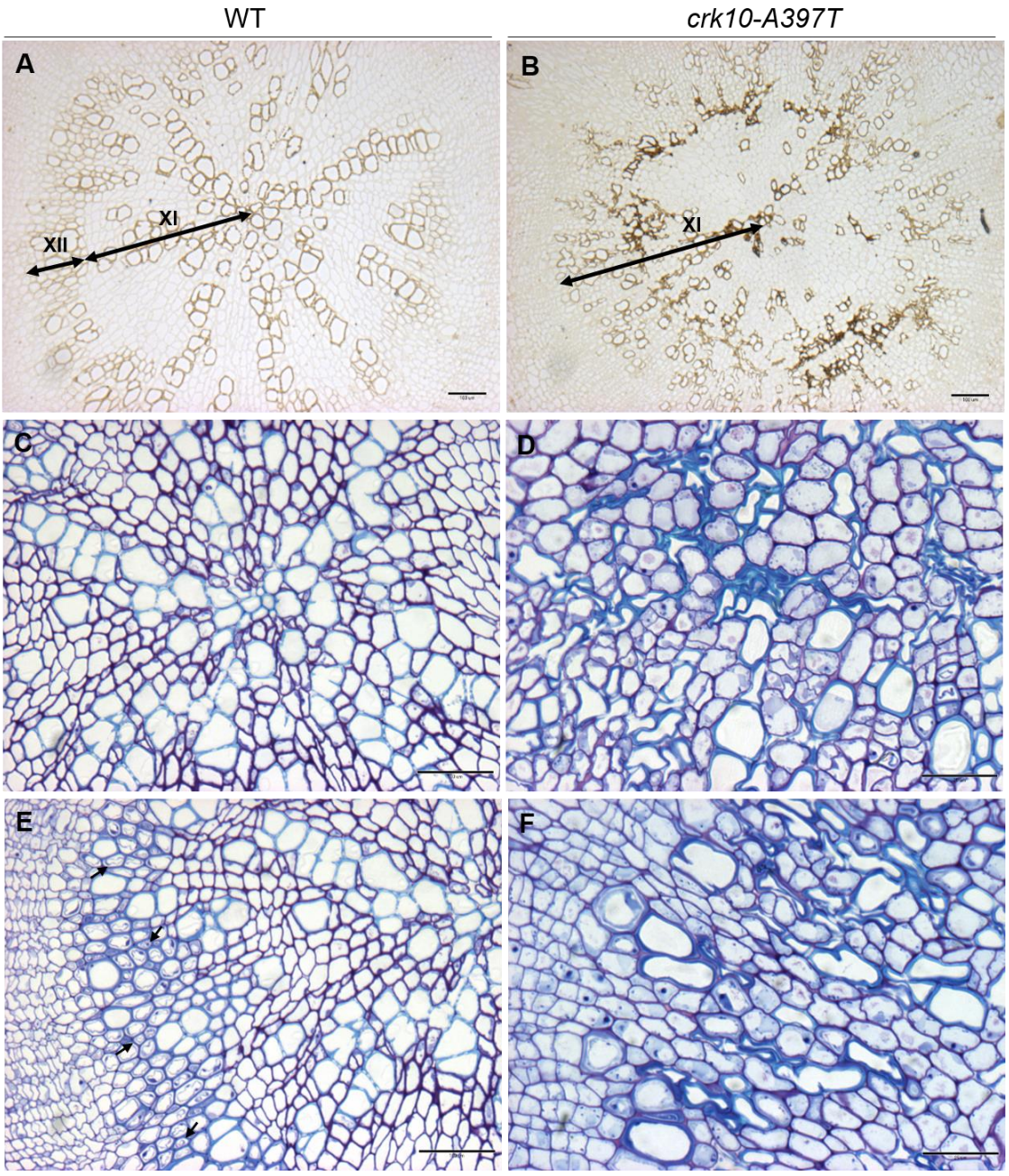

Figure 3.12 The roots of *crk10-A397T* mutant also display collapse xylem vessels and delayed onset of the xylem II developmental phase.

(A-F) Light micrographs of transverse cross sections of resin embedded roots of 5-week-old WT and *crk10-A397T* plants. (A) and (B) show an overview of xylem tissue in the root and the xylem I (XI) and xylem II (XII) areas. (C-F) show detail of fully differentiated xylem vessels in WT and *crk10-A397T* roots.

Cross sections were stained with (A-B) potassium permanganate and (C-F) toluidine blue.

Differentiating xylem fibres are indicated by black arrows in (E).

Bars: (A, B, C, E) = 100 µm; (D, F) = 25 µm.

3.3.4 Investigation of the contribution of the root and shoot systems to the dwarf phenotype of *crk10-A397T* mutant plants

The movement of signalling molecules from the root to the shoot and vice-versa is known to regulate several processes during plant growth. Therefore, to investigate if events happening in the root and hypocotyl are sufficient to promote the dwarf phenotype of the *crk10-A397T* mutant or if a potential shoot-derived signal is involved in this process, a micrografting experiment was designed. Four-day-old seedlings grown *in vitro* were used to obtain scions (upper section of hypocotyl and cotyledons) and rootstocks (lower section of hypocotyl and root), and combinations of WT and *crk10-A397T* mutant grafts were prepared. Self-grafts were used as controls. Interestingly, plants generated by a WT scion grafted on a *crk10-A397T* mutant rootstock develop a mutant-like dwarf phenotype (Figure 3.13). In contrast, when a *crk10-A397T* mutant scion was grafted on a WT rootstock, the resulting plant developed a WT-like phenotype. Therefore, these results indicate that the root and hypocotyl system of the *crk10-A397T* mutant determines the dwarf phenotype of the plant, which is likely due to the presence of collapsed xylem vessels in these organs. These results also suggest the absence of a shoot-derived signal which contributes to the development of the dwarf phenotype.

Figure 3.13 The dwarf phenotype of the *crk10-A397T* mutant is determined by its root-hypocotyl system.

Images of (A) non-grafted plants, (B) self-graft controls and (C) graft combinations of WT and *crk10-A397T mutant*. Plants were imaged three weeks after micrografting was performed. Annotation: scion / rootstock.

3.3.5 Investigation of the effect of different temperatures on the growth of the *crk10-A397T* mutant

As mentioned in Section 3.1, the dwarf phenotype of several auto-immune mutants of Arabidopsis is largely alleviated by growing the plants at temperatures between 28-30 ºC. To test the effect of different temperatures on the dwarf phenotype caused by the *crk10-A397T* mutant allele, *crk10-A397T* mutant plants were grown at 18, 23 and 30 ºC alongside WT Col-0 and *mpk4* plants, for comparison (Figure 3.14). At 23 ºC, which was the standard temperature used for the growth of Arabidopsis plants in this study, *mpk4* and *crk10-A397T* mutant plants display their usual dwarf phenotype when compared to the WT. At 18 ºC, all three genotypes showed a reduction in rosette size, consistent with a slower growth rate at lower temperatures. At 30 ºC, WT plants developed rosettes with a slightly larger diameter, and the dwarf phenotype of the *mpk4* plants was largely rescued, as previously described. Interestingly, the increased temperature not only did not alleviate the dwarfism of the *crk10-A397T* mutant, but also led to a slight reduction in rosette size compared to the standard 23 ºC conditions. Therefore, we conclude the dwarf growth habit of the *crk10-A397T* mutant plants cannot be rescued by increased temperatures such as the case of several auto-immune mutants of Arabidopsis.

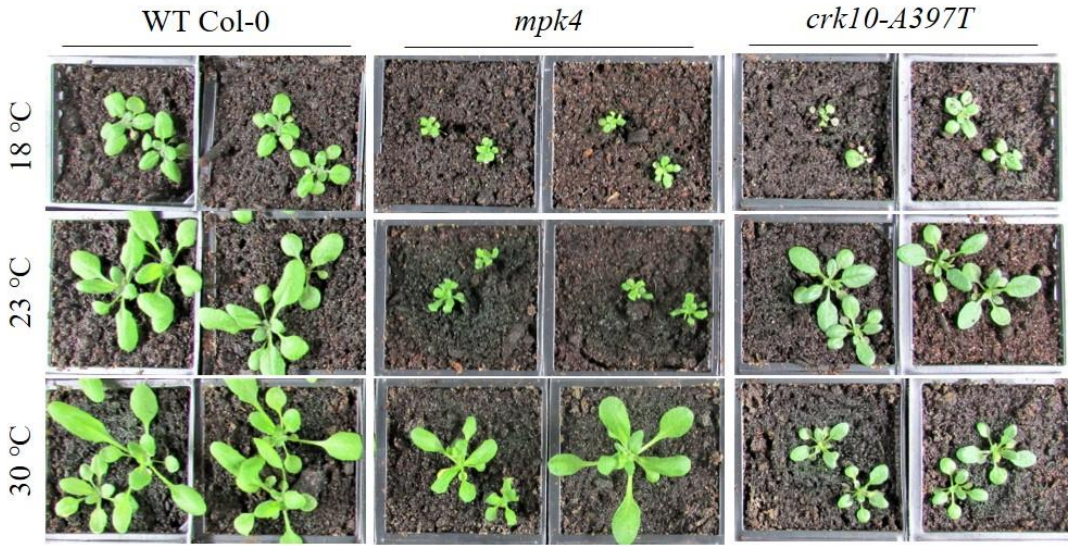

Figure 3.14 The dwarf phenotype of the *crk10-A397T* mutant is not rescued by increased temperature.

WT Col-0, *mpk4* and *crk10-A397T* mutant plants grown at 18, 23 and 30 °C are shown in the image. Plants were photographed at 12 days after exposure to the specified growth condition.

3.3.6 Analysis of the tissue specific expression of *CRK10*

In order to investigate the tissue specific expression of *CRK10*, the 1 kb genomic region upstream of the gene (*CRK10* promoter; *CRK10*$_{PRO}$) was used to direct the expression of the reporter gene *β-glucuronidase* (*GUS*). The *CRK10*$_{PRO}$:*GUS* construct was generated and introduced in WT Col-0 plants, and six independent transgenic lines were used for subsequent analyses. Histochemical staining at discrete developmental stages showed consistent expression of the reporter gene associated with vascular tissues of the root, hypocotyl, petiole, cotyledons and leaves (Figure 3.15). Staining was first observed in the internode between the hypocotyl and the cotyledons in young seedlings, as well as in the cotyledon veins, and root and hypocotyl vasculature (Figure 3.15 A-D). Staining was also observed in leaves of 3- and 4-week-old plants, initially restricted to the veins, but less specifically localised in older leaves (Figure 3.15 E-F). To investigate cell-specific promoter activity, cross sections of stained hypocotyls of 2-week-old plants were analysed, revealing reporter expression in developing xylem vessels and surrounding xylem parenchyma cells (Figure 3.16 A). Likewise, analysis of free-hand cross sections of stained inflorescence stem of GUS reporter lines also revealed promoter activity associated with vascular bundles (Figure 3.16 B).

Quantitative PCR (qPCR) was used to confirm the expression pattern suggested by the reporter gene system in the hypocotyl and inflorescence stem. Hypocotyls and inflorescence stem samples of 3- and 6-week-old WT plants, respectively, were collected for this analysis. qPCR reaction with primers targeting the *CRK10* coding sequence confirmed the presence of the *CRK10* transcript hypocotyls and inflorescence stems of Arabidopsis plants at the developmental stages analysed. (Figure 3.16 C).

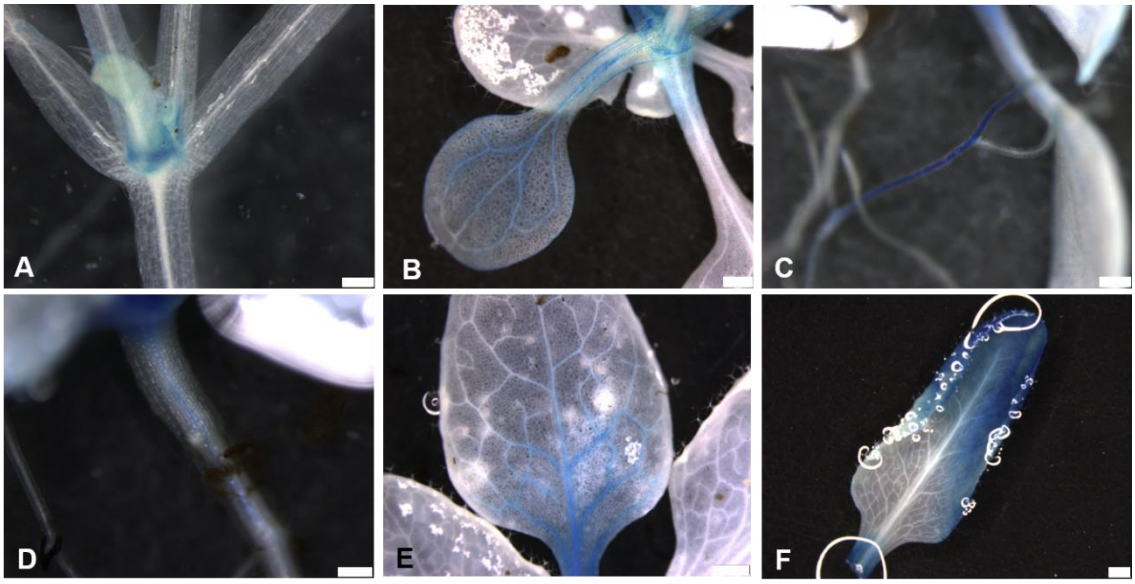

Figure 3.15 *CRK10* is primarily expressed in close association with vascular tissues.

Representative images of histochemical staining of *CRK10*$_{PRO}$:*GUS* reporter lines showing promoter activity (A) in the internodes of 10-day-old seedling, (B) petiole and cotyledon of 2-week-old seedling, (C) root of 10-day-old seedlings, (D) hypocotyl of 2-week-old seedlings and leaves of (E) 3- and (F) 4-week-old plants.

Bars, (A, C, D) = 250 µm; (B) = 500 µm; (E) = 750 µm; (F) = 1 mm.

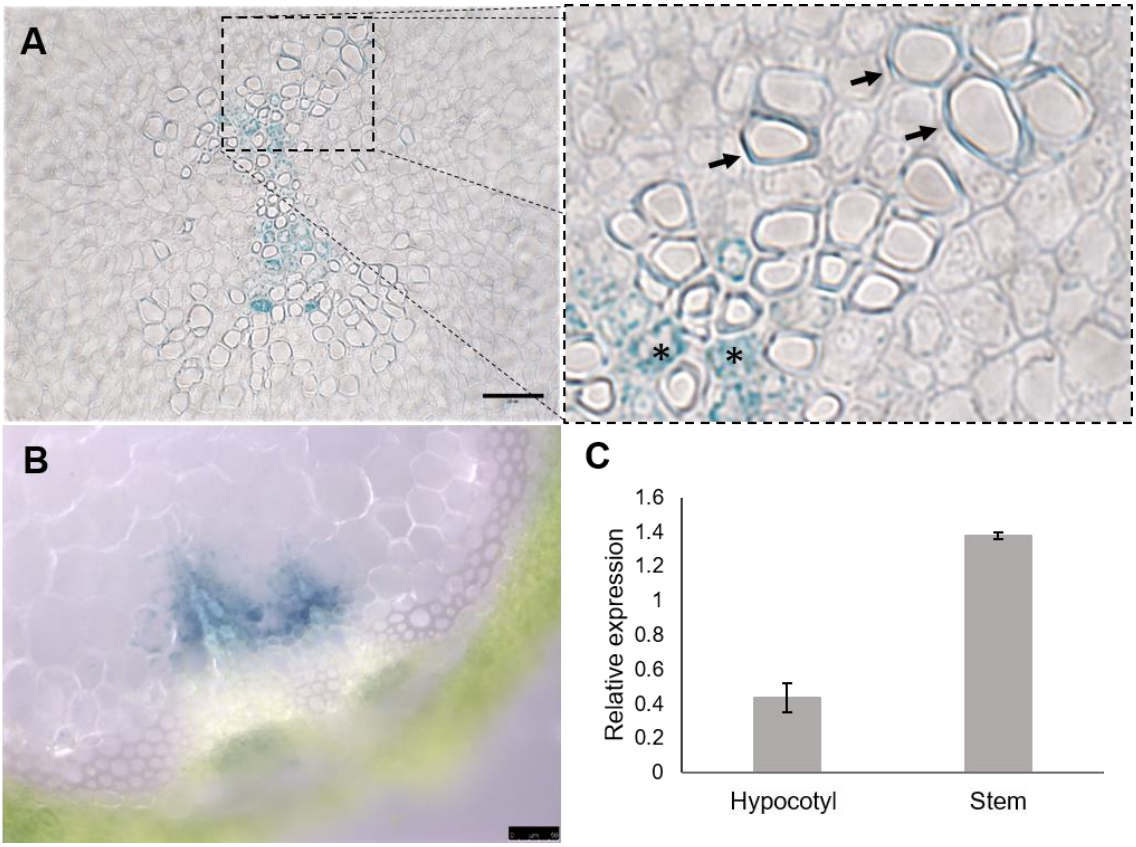

Figure 3.16 *CRK10* is expressed in the vasculature of the hypocotyl and inflorescence stem.

(A) Light micrograph of transverse cross section of 2-week-old resin embedded hypocotyl of *CRK10*$_{PRO}$:*GUS* reporter line following histochemical staining. The dashed square indicates zoomed in area of the cross section; histochemical staining in xylem parenchyma cells and differentiating xylem vessels is indicated by asterisks and arrows, respectively. Bar, 50 µm.

(B) Light micrograph of transverse free-hand cross section of 8-week-old inflorescence stem of *CRK10*$_{PRO}$:*GUS* reporter line following histochemical staining. Bar, 25 µm.

(C) Relative expression of *CRK10* in hypocotyls and stem of 3-week-old and 6-week-old WT plants, respectively. *CRK10* transcript levels were quantified by qPCR using the *ACTIN2* and *UBC21* genes from Arabidopsis as internal controls. Error bars represent standard error of 3 biological replicates.

3.3.7 Investigation of the subcellular localisation of CRK10

The presence of a single transmembrane domain (residues 286-306 according to the amino acid sequence of CRK10 in Uniprot) in the amino acid sequence of CRK10 indicates that the protein likely localises at the plasma membrane. To verify the subcellular localisation of the protein experimentally, a C-terminal translational fusion of CRK10 with the fluorescent protein mCherry was cloned under the control of the 35S promoter (*35S:CRK10-mCherry*). The construct was introduced in *N. benthamiana* leaves via infiltration with *A. tumefaciens*. The fluorescent signal of the CRK10-mCherry fusion was detected at the plasma membrane of the cells (Figure 3.17 A). To assess the subcellular localisation of the CRK10-mCherry fusion in Arabidopsis, stable transgenic lines were generated via floral dip. Epidermal cells of the hypocotyl of these transgenic lines exhibited expression of the fluorescent fusion protein in a pattern typical of plasma membrane-associated proteins (Figure 3.17 B).

To unambiguously assign the subcellular localisation of CRK10 to the plasma membrane, these hypocotyls were subjected to hypertonic conditions, which induces the plasmolysis of cells as they lose water to the surrounding environment. The plasmolysis of plant cells is readily recognised by the presence of structures called Hechtian strands, which are thin threads that connect the retracting plasma membrane to the cell wall (Oparka, 1994). Therefore, the induction of plasmolysis is a known strategy to confirm the plasma membrane localisation of a fluorescent tagged protein of interest. As expected, the fluorescent signal of the CRK10-mCherry fusion was observed in association with Hechtian strands following the induction of plasmolysis in the hypocotyl of transgenic Arabidopsis plants expressing the construct (Figure 3.17 C). Therefore, we conclude CRK10 localises to the plasma membrane of plant cells, as predicted by the presence of a transmembrane domain in its sequence.

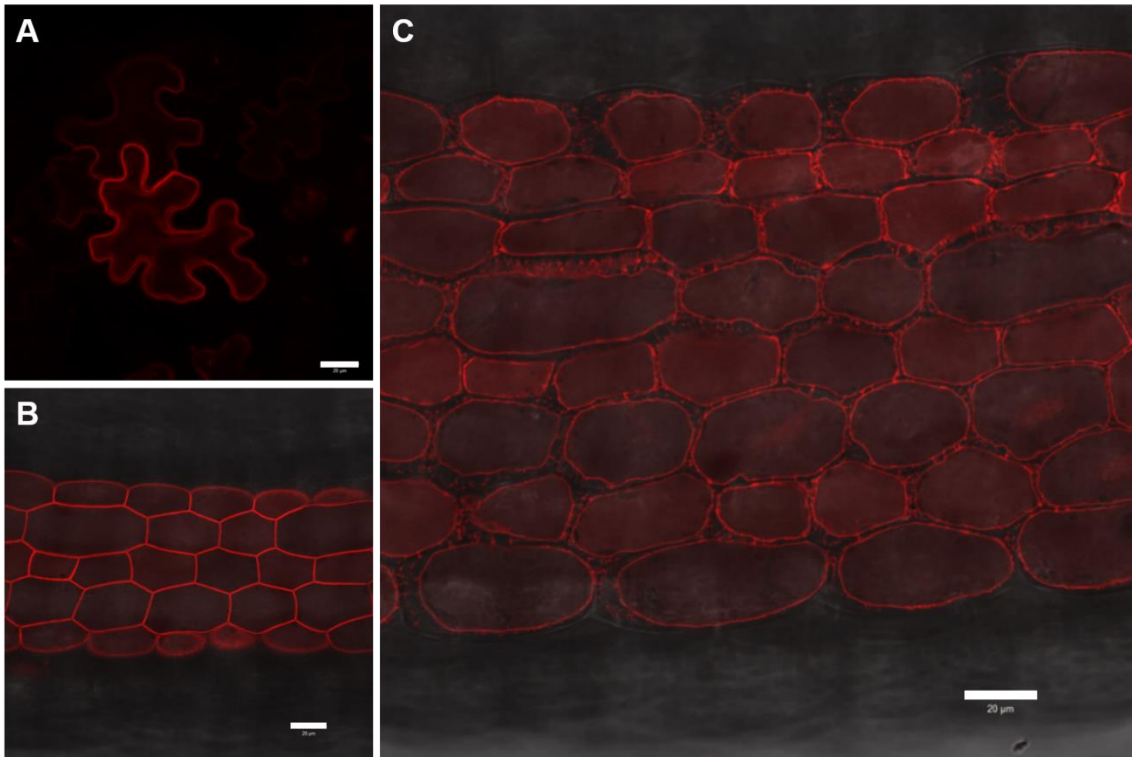

Figure 3.17 CRK10 is a plasma-membrane localised protein.

(A) *N. benthamiana* leaf cells transiently expressing 35S:CRK10-mCherry construct. Bar, 20 µm.

(B-C) Hypocotyl of 4-day-old seedling of transgenic Arabidopsis plant expressing *35S:CRK10-mCherry* (B) before and (C) after plasmolysis. Bars, 20 µm.

3.3.8 Characterisation of *crk10* knockout lines

Knockout mutants are a valuable tool to investigate the biological function of genes, as decreased levels of expression are often associated with morphological, developmental or physiological phenotypes. To investigate if the loss-of-function of *CRK10* affects the growth and development of Arabidopsis plants, three T-DNA insertion lines were identified and seeds for these were obtained from NASC (Nottingham Arabidopsis Stock Centre): SALK_023945, SALK_116653 (*crk10-4*) and SAIL_427_E09 (*crk10-2*). Individual plants of each T-DNA line were genotyped using primers targeting the T-DNA sequence and the genomic regions flanking the respective insertion site of each line, according to instructions from the Salk Institute Genomic Analysis Laboratory website (http://signal.salk.edu/tdnaprimers.2.html; Figure 3.18). Disruption of the *CRK10* transcription in homozygous plants was confirmed by RT-PCR using three pairs of primers (A, B and C) spanning different parts of the *CRK10* coding sequence (Figure 3.19).

RT-PCR using cDNA from homozygous plants for the SALK_023945 line, which contains a T-DNA insertion in the 5' UTR region of the genomic sequence of *CRK10*, exhibited PCR products for all three combinations of primers, suggestive of the presence of the full *CRK10* transcript. According to this observation, the T-DNA insertion in the 5' UTR region of CRK10 fails to disrupt gene expression, and therefore, SALK_023954 plants were not used for further analyses.

RT-PCR using cDNA from homozygous plants of the line SALK_116653, named *crk10-4,* yielded PCR products for the pairs of primers C, which targets the last exon of the gene, as well as faint PCR products for pair B, which flank the second and fourth exons. However, no amplification was detected for the pair of primers A, which targets the first exon of *CRK10* where the T-DNA is inserted in this line.

Finally, homozygous plants of the line SAIL_427_E09, or *crk10-2*, which contains the T-DNA insert in the third exon of *CRK10*, only showed RT-PCR product for the pair of primers A, but not pairs B and C. Taken together, these results suggest that lines *crk10-2* and *crk10-4* only express truncated versions of the *CRK10* transcript, which are likely non-functional, and confirms that the T-DNA insertion successfully disrupts the expression of the gene in these plants. Quantification of CRK10 expression levels in leaves of 4-week-old *crk10* plants by qPCR further confirmed that *crk10-2* and *crk10-4* are a knockout and a knockdown line for *CRK10*, respectively (Figure 3.20 A). The loss-of-function of CRK10 did not affect the growth and development of Arabidopsis plants under standard growth conditions, as 4-week-old *crk10* plants resemble the WT (Figure 3.20 B).

Knockout line *crk10-2* was used for the generation of the transgenic lines expressing the *CRK10*$_{PRO}$:*crk10-A397T* construct which was used to confirm the association between this mutant allele and the dwarf phenotype of the mutant plants (see section 3.3.1). *crk10-2* plants were also used for pathogen assays presented in Chapter 7.

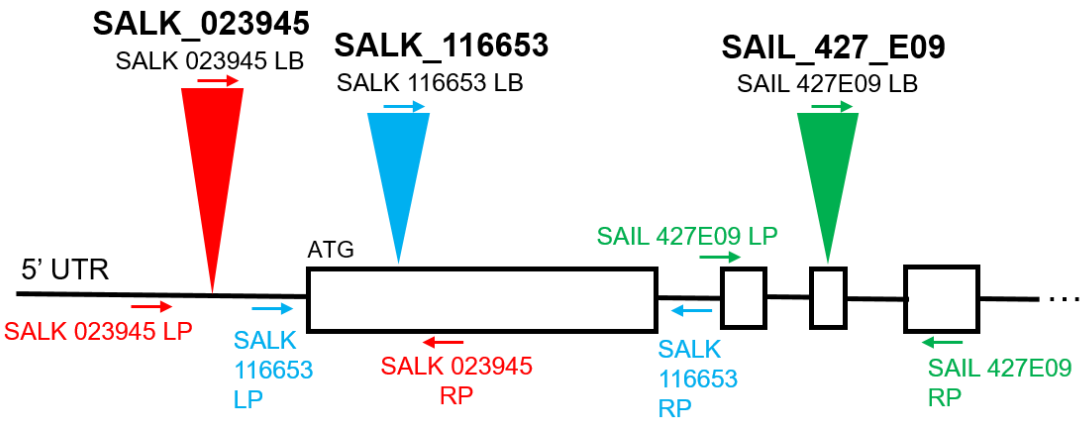

LB+RP = positive LP+RP = negative	**Homozygous** for T-DNA insertion
LB+RP = positive LP+RP = positive	**Heterozygous** for T-DNA insertion
LB+RP = negative LP+RP = positive	No T-DNA insertion

Figure 3.18 *CRK10* gene model, T-DNA insertion sites and primers used to genotype SALK and SAIL lines.

LB primers target sequences within the T-DNA, whereas LP and RP primers target regions upstream and downstream of the insertion site. By combining primers LB and LP with RP, it is possible to identify if a plant has zero, one or two copies of the T-DNA. Boxes represent exons and lines represent untranslated regions/introns. Genotyping of T-DNA lines is exemplified by representative gels in Appendix 6.1.

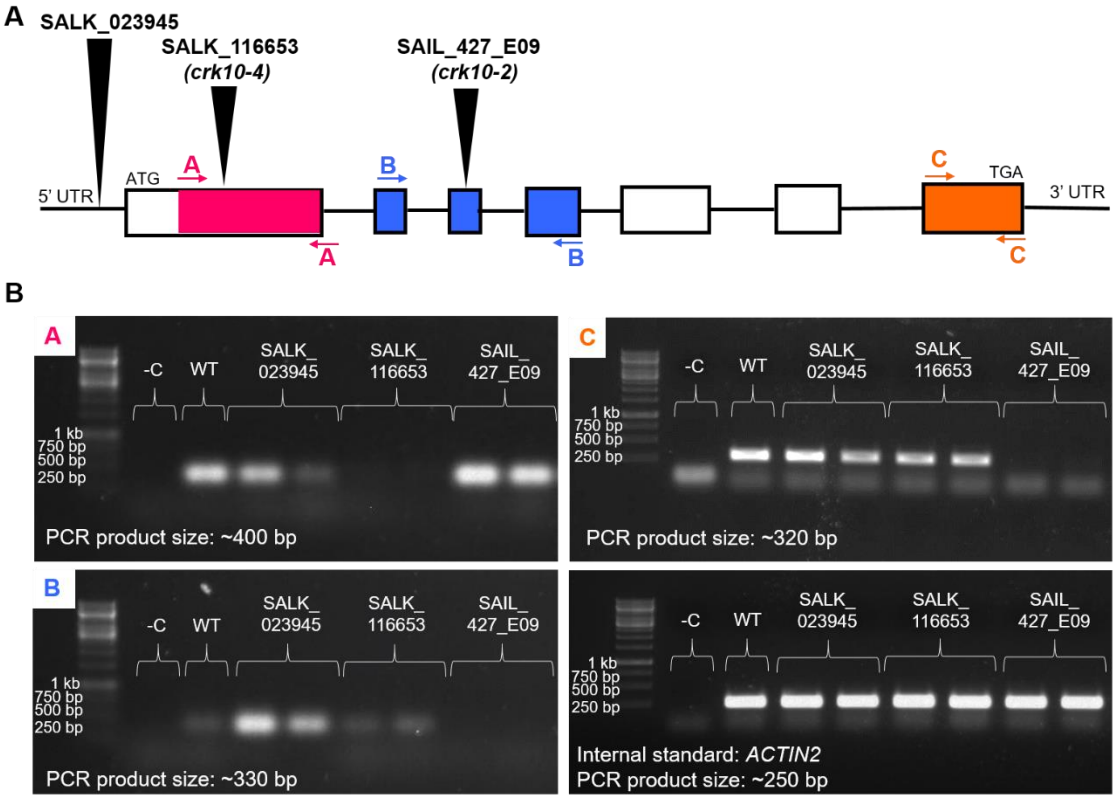

Figure 3.19 T-DNA insertion disrupts *CRK10* transcript expression.

(A) Schematic gene structure of *CRK10* showing T-DNA insertion sites and primers used to target *CRK10* transcript in SALK and SAIL lines. Boxes represent exons and lines represent untranslated regions and introns.

(B) RT-PCR gels for pairs of primers A, B and C, as well as internal control (actin). Samples included negative control (-C), positive control (WT Col-0), and homozygous individuals of SALK/SAIL lines. The expected size of the PCR product for each pair of primer is indicated in the image.

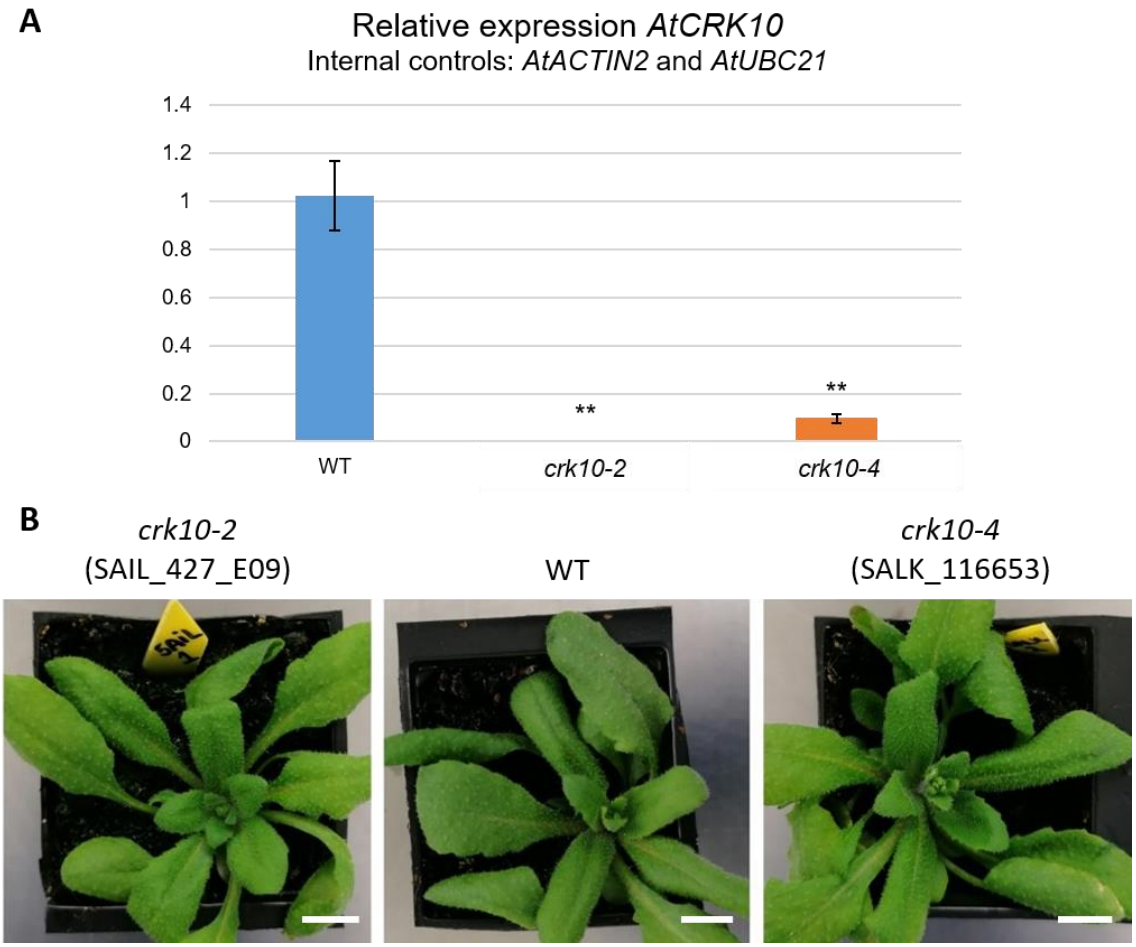

Figure 3.20 T-DNA knockout mutants of *CRK10* develop normally and resemble WT plants.

(A) Quantification of the relative expression of the *CRK10* transcript by qPCR. Template cDNA was synthesized from RNA extracted from leaves of 4-week-old plants; genes *AtACTIN2* and *AtUBC21* were used as internal controls. Error bars represent standard error of three biological replicates. Asterisks indicate statistical significance (t-test): ** = $p \leq 0.01$.

(B) Representative image of 4-week-old plants grown under standard long day conditions. Bars, 1 cm.

3.3.9 Characterisation of *CRK10* overexpression lines

To investigate the effects of the overexpression of *CRK10* in Arabidopsis plants, transgenic lines harbouring the construct 35S:*CRK10*^{WT} were generated prior to the beginning of this PhD project. Homozygous plants were identified based on the presence of the fluorescent marker DSRed in the seeds of the progeny, and the overexpression of *CRK10* in leaves of young plants was confirmed by qPCR (Figure 3.21 A). Similar to *crk10* mutant plants, the overexpression of *CRK10* did not cause any obvious phenotype in Arabidopsis, as CRK10 OE plants resemble the WT when grown in standard conditions (Figure 3.21 B). Overexpression line *CRK10* OE-1 was used for the pathogen assays presented in Chapter 7.

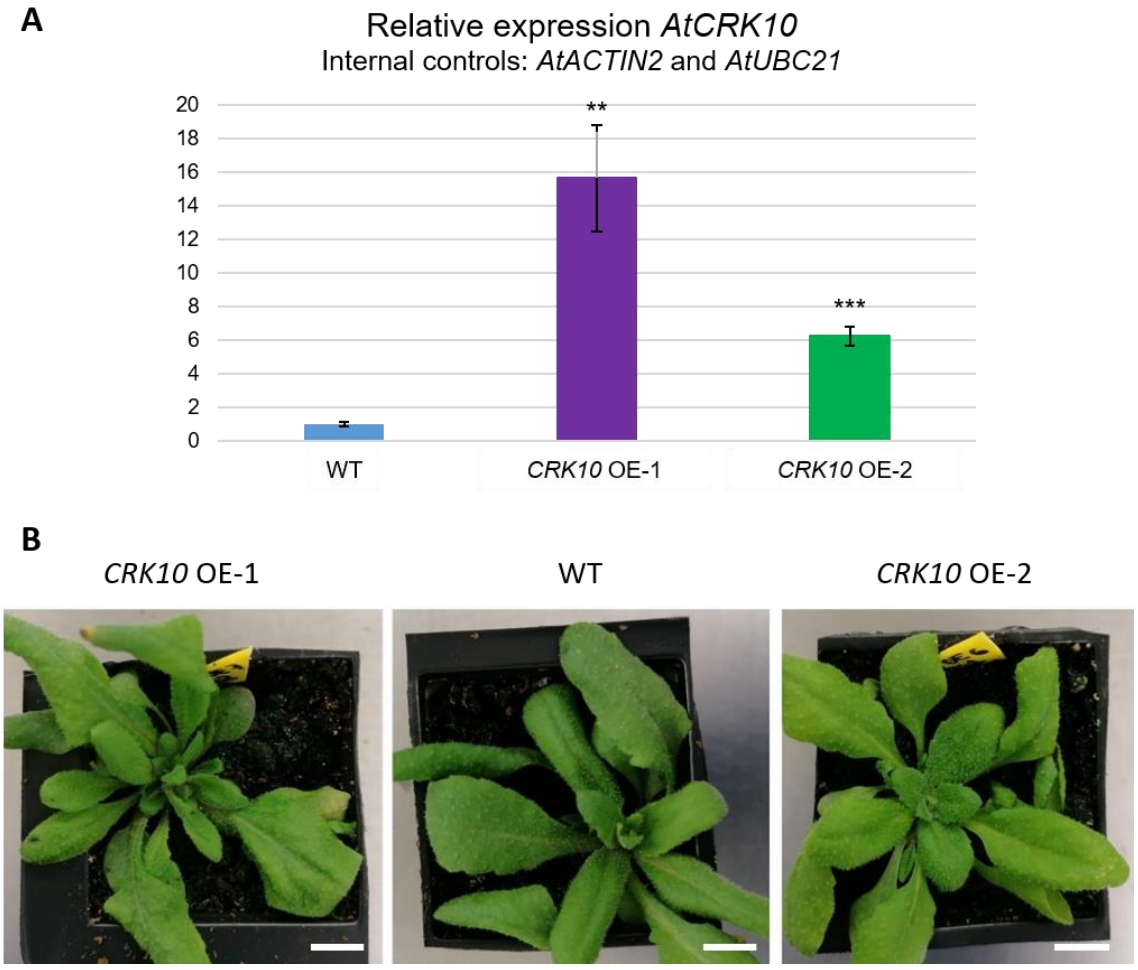

Figure 3.21 Transgenic plants overexpressing the *CRK10* transcript develop normally and resemble WT plants.

(A) Quantification of the relative expression of the *CRK10* transcript by qPCR. Template cDNA was synthesized from RNA extracted from leaves of 4-week-old plants; genes *AtACTIN2* and *AtUBC21* were used as internal controls. Error bars

represent standard error of three biological replicates. Asterisks indicate statistical significance (t-test): ** = p ≤ 0.01; *** = p ≤ 0.001.
(B) Representative image of 4-week-old plants grown under standard long day conditions. Bars, 1 cm.

3.4 Discussion

This chapter reports the phenotypical characterisation of the *crk10-A397T* mutant, which displays a dwarf growth habit when grown in standard conditions. The *crk10-A397T* mutant seeds germinate slightly earlier than the WT, and the seedlings exhibit increased size in early developmental stages. At one week after germination, though, the difference in size is no longer apparent, and the mutant seedlings resemble the WT. Interestingly, the dwarf phenotype of the mutant plants becomes apparent around three weeks after sowing, which suggests that events occurring between two and three weeks after sowing trigger this process. As vegetative growth continues, the reduced rosette size of the *crk10-A397T* mutant becomes even more apparent. Regardless of the dwarfism, the mutant flowers simultaneously to WT plants, although the main inflorescence stem is frequently aborted. However, despite never reaching the same height as WT plants, the *crk10-A397T* mutant develops numerous lateral inflorescences which produce viable siliques filled with seeds.

Despite dwarfism in plants being linked to several potential causes, such as defective hormone biosynthesis, perception and signalling or a growth-defence trade-off, analysis of cross sections of the *crk10-A397T* mutant revealed the presence of collapsed xylem vessels in the roots and hypocotyl of the plant. This phenotype is reminiscent of the *irregular xylem* mutants first described in 1997 by Turner and Somerville. The preparation of a developmental time series of the hypocotyl of WT and *crk10-A397T* plants allowed the analysis of the temporal progression of the collapse of the xylem vessels in comparison to the normal development of the vasculature in WT plants. The absence of collapsed vessels in the hypocotyls of 1- and 2-week-old mutant plants correlates with the WT-like appearance of the seedlings in the first couple of weeks of development, as the increased seedling size displayed by 4-day-old mutant seedlings is no longer obvious after two weeks of growth. The appearance of the first deformed and collapsed xylem vessels at three weeks after sowing corresponds to the first manifestation of the dwarf phenotype. This observation draws a direct parallel

between the emergence of collapsed xylem vessels in the hypocotyl and the stunted growth of the rosette of the mutant plants. As additional xylem vessels are affected at four weeks after sowing, so is the difference in rosette size between WT and mutant, which becomes more apparent at this stage. Interestingly, despite flowering simultaneously to the WT, the onset of the xylem expansion (xylem II) phase in the hypocotyl of the *crk10-A397T* mutant seems to be delayed. This is suggested by the absence of fully differentiated, lignified xylem fibers in 5-week-old mutant hypocotyls which are present in the WT at the same stage. Furthermore, it is important to note that xylem vessels in the mutant hypocotyl often displayed a more intense, darker brown staining with the lignin-specific dye potassium permanganate compared to the WT, which is suggestive of increased levels of lignification.

Although the appearance of the collapsed xylem vessels in the organs below ground correlate with the onset of the dwarf growth habit of the *crk10-A397T* mutant, it was not clear if the dwarf phenotype was the result of processes occurring exclusively in the root and hypocotyl, or if it was dependent on shoot-derived signals. Shoot-root communication is known to regulate a myriad of biological processes in plants, allowing the coordination of growth and responses to internal and external signals at a whole-plant level (Liu et al., 2009; Notaguchi and Okamoto, 2015; Ko and Helariutta, 2017). The vascular system acts as a highway for the long-distance transport of several signalling molecules, such as RNA, small peptides and phytohormones (Notaguchi and Okamoto, 2015). For instance, the induction of the cytokinin biosynthetic gene *ADENOSINE PHOSPHATE ISOPENTENYLTRANSFERASE 3* (*IPT3*) and the cytochrome P450 monooxygenase *CYP735A2* in the roots in response to high concentrations of nitrate was shown to increase the translocation of root-borne tZ-type cytokinins to the shoot (Hirose et al., 2007; Kiba et al., 2011). In corroboration, the shoot growth defects displayed by the double mutant *cyp735a1 cyp735a2*, root-expressed genes involved in the biosynthesis of tZ-type cytokinins, could be rescued by grafting onto a WT rootstock or by application of exogenous tZ (Kiba et al., 2013). On the other hand, iP-type cytokinins are transported from the shoot to the root via the phloem to signal nitrogen satiety and regulate root architecture and vascular patterning (Bishopp et al., 2011; Kiba et al., 2011). Hence, could it be possible that a shoot-derived signal induces the vasculature defects in the root and hypocotyl of the mutant and, consequently, the dwarf phenotype? Or are the

events taking place in the root and hypocotyl sufficient to induce a dwarf phenotype? To address these questions, the micrografting experiment described in section 3.2.8 was performed. Following the successful generation of self and reciprocal grafts of WT and *crk10-A397T* mutant seedlings, the observation that a mutant scion grafted onto a WT rootstock developed into a WT-like plant suggested the absence of a shoot-derived signal which is behind the *irregular xylem*-like phenotype in the mutant's root and hypocotyls. In agreement, the *crk10-A397T*-like phenotype displayed by the successful graft formed by a mutant rootstock and a WT scion demonstrates that the mutant's root and hypocotyl are required and sufficient for the development of the dwarf phenotype. Taken together, these observations support the hypothesis that no mobile signal derived from the shoot contributes to the collapse of the xylem and the dwarf phenotype of the *crk10-A397T* mutant.

Modulation of growth conditions, most notably increased growth temperatures, are known to alleviate the dwarf phenotype of certain auto-immune mutants of Arabidopsis, (van Wersch et al., 2016). This is consistent with the observation that elevated temperatures often inhibit defence responses to pathogens, which is likely associated with the temperature sensitivity of NB-LRR R and R-like genes (Zhu et al., 2010). Despite uncovering the vasculature-associated nature of the dwarf phenotype, the effect of different growth temperatures on the *crk10-A397T* mutant's development was observed to investigate whether it also displayed the temperature-dependent trait with auto-immune mutants. Interestingly, both decreased and increased temperature accentuated the dwarf phenotype of the *crk10-A397T* mutant, indicating that modulating temperature does not repress the molecular mechanisms underlying the dwarf phenotype of these plants.

The analysis of reporter lines revealed the spatiotemporal expression pattern of the native promoter of *CRK10*, which is tightly associated with the vasculature throughout the plant. The observed expression of the gene in differentiating xylem vessels in the hypocotyl of 2-week-old seedlings correlates with the fact that this is also the cell type affected by the *crk10-A397T* mutation. Additionally, we detected GUS expression in xylem parenchyma cells, which are thought to contribute to the lignification of the surrounding xylem vessels in the roots according to the "good neighbour" hypothesis (Smith et al., 2013). This phenomenon also likely occurs in hypocotyls considering the similar vasculature

developmental programmes observed in roots and hypocotyls. Therefore, *CRK10*-expressing xylem parenchyma cells could potentially contribute to the lignification of xylem vessels in the mutant's hypocotyl, although it is unclear at this stage if this process plays any role in their collapse. On the other hand, the expression of *CRK10* in the vascular bundles of the inflorescence stem is intriguing, given that the vasculature of the stem is unaffected in *crk10-A397T* mutant plants. One possible explanation could be the fact that receptor-like kinases require coreceptors with which they physically interact at the plasma membrane for successful ligand binding and signal transduction (Gou and Li, 2020). BAK1/ SERK3, for example, is known to act as a coreceptor to several RLKs involved in various biological processes, such as BRI1 in brassinosteroid signalling (Li et al., 2002; Nam and Li, 2002), and FLS2 and EFR in defence responses to pathogens (Chinchilla et al., 2007; Roux et al., 2011; see section 1.2). Therefore, we could speculate that CRK10 might interact with different co-receptors in a tissue-specific manner, and the receptor complex required to trigger the events underlying the collapse of xylem vessels in roots and hypocotyls might be absent in the inflorescence stem. Nevertheless, this hypothesis has not been experimentally tested and is purely speculative at this stage.

Finally, the lack of phenotype displayed by the knockout lines of *CRK10* was unsurprising, given the large size of the *CRK* family. With over 40 members in Arabidopsis, most of which present in a tandem array in chromosome 4, functional redundancy can be expected among the closest related homologs. Indeed, a study performed by Bourdais et al. in 2015 reported the phenotypical analysis of T-DNA knockout lines for 41 *CRK*s in Arabidopsis, with the vast majority of lines displaying a WT-like morphology. Similarly, overexpression of CRKs often does not cause any obvious phenotype as increased levels of gene expression will not result in activation of cellular responses unless the extracellular ligand required for receptor activation is present. Therefore, these traditional genetic approaches used routinely to investigate gene function are often unproductive when the gene of interest is a member of a multigene family of receptor-like kinases. In conclusion, the results reported in this chapter suggest that the point mutation harboured by the *crk10-A397T* mutant causes a dwarf phenotype in Arabidopsis plants which is associated with the collapse of xylem vessels in roots and hypocotyls.

Chapter 4 – Investigation of the kinase activity of CRK10

4.1 Introduction

Following the isolation of the *crk10-A397T* mutant from a chemical mutagenesis screen, 15 candidate genes were identified from whole genome sequencing data of bulk segregants, and the semi-dominant mutation which causes the substitution of alanine with a threonine in the kinase domain of CRK10 was subsequently confirmed to be the cause of the dwarf phenotype of the mutant (see section 3.3.1). As described in section 1.2.2, phosphorylation of serine, threonine and/or tyrosine residues are crucial for the activation and regulation of the activity of the kinase domain of RLKs. Taken together with the fact that the *crk10-A397T* is supposedly a gain-of-function allele, these observations gave rise to a hypothesis: could the introduction of Thr397 in the kinase domain of CRK10 act as an additional phosphorylation site which affects kinase regulation and activity? To address this question and speculate about the mechanisms underlying the gain-of-function effect promoted by this mutant allele, a thorough understanding of protein kinases, their structure and mechanism of action is necessary.

Eukaryotic protein kinases are regulated by a number of factors such as transcription factors, interacting partners, subcellular localisation, protein turnover, and phosphorylation itself (Endicott et al., 2012; see section 1.2.2 for a detailed description of kinase structure and regulation). The precise arrangement of conserved residues and intra-molecular interactions within the catalytic core is essential for catalysis and, therefore, a single amino acid substitution has the potential to impact kinase regulation and activity. This is exemplified by the identification of point mutations which either disrupt kinase activity or lead to a permanently “switched on” state, such as several disease-inducing mutations in mammalian organisms. For example, the substitution of an isoleucine with an asparagine residue in the catalytic loop of PTEN-INDUCED PUTATIVE KINASE 1 (PINK1) in *Homo sapiens* affects substrate and ATP binding, negatively affecting the ubiquitin kinase activity of this protein (Ando et al., 2017). A study by Ye et al. published in 2019 reported the identification of several missense mutations which abolished the catalytic activity of the human TANK BINDING KINASE 1 (TBK1), associated with amyotrophic lateral sclerosis. In contrast, the intrinsic autoinhibited state of the human EPIDERMAL GROWTH FACTOR

RECEPTOR (EGFR) is released by a mutation which replaces a leucine with an arginine residue in the activation segment, promoting intramolecular interactions that lead to spontaneous kinase activation (Zhang et al., 2006). Single residue substitutions in the kinase domain of the PROTEIN KINASE Cα (PKCα) were shown to increase kinase activity by potentially destabilising the autoinhibited conformation of the protein, promoting synaptic defects in Alzheimer's disease (Alfonso et al., 2016). Furthermore, the substitution of a tyrosine with a phenylalanine (Y2018F) in the regulatory spine of LEUCINE-RICH REPEAT KINASE 2 (LRRK2), a protein implicated in familial Parkinson's disease, causes hyperactivation of the kinase domain (Schmidt et al., 2019).

When it comes to the kinase domain of plant RLKs, a growing number of studies has focused on the identification of phosphorylation sites which are required for their activation and auto/trans-phosphorylation activity. A widely used strategy for preliminary analysis relies on the ability of the cytoplasmic kinase domain of plant RLKs to auto-phosphorylate when expressed as a recombinant protein in *E. coli* (Oh et al., 2009; Oh et al., 2012). With this approach, the auto-phosphorylation status of the recombinant kinase can be readily assessed after protein extraction and purification without the need of subsequent *in vitro* assays. Alternatively, the analysis of boiled bacterial lysates by SDS-PAGE coupled with phosphoprotein staining has been successfully used as a simplified method to assess auto-phosphorylation activity of these recombinant proteins (Taylor et al., 2013). Identification of auto-phosphorylation sites in the LRR-RLK HAESA of Arabidopsis, for example, was performed by mass spectrometry (MS) analysis of the recombinant kinase domain (Taylor et al., 2016). Nine auto-phosphorylation sites were unambiguously identified, including phosphoserine 856, which aligns to a conserved region of the activation loop normally occupied by an important activating phosphorylation site in other eukaryotic protein kinases (Huse and Kuriyan, 2002). The importance of this site for auto-phosphorylation activity was further confirmed by its substitution with an alanine residue, which caused an overall reduction in auto-phosphorylation levels (Taylor et al., 2016). Moreover, HAE-S856 aligns to threonine 450 in the kinase domain of the LRR-RLK BAK1, an important co-receptor for several ligand-binding RLKs in Arabidopsis (see section 1.2). T450 and three additional threonine residues in the activation loop of BAK1 (T446, T449 and T455) were identified as essential phosphorylation sites for the biological functions of this RLK (Wang et al., 2008). The analysis of the

crystal structure of phosphorylated BAK1 showed that the phosphate moiety of these phosphosites forms hydrogen bonds and salt bridges with residues from other regions of the kinase to stabilise the active conformation of the kinase domain (Yan et al., 2012). The phosphorylation status of the kinase domain of the LRR-RLK BRI1 has also been assessed *in vitro* and *in vivo* (Wang et al., 2005; Wang et al., 2008; Bojar et al., 2014). Residues T1039, S1042 and S1044 in the activation loop of BRI1 were found to be phosphorylated *in planta* and in the crystal structure of the activated BRI1 (Wang et al., 2005; Bojar et al., 2014). Substitution of S1044 with an alanine residue nearly abolished auto- and trans-phosphorylation activity, while an equivalent mutation of T1039 and S1042 had a greater negative impact on the phosphorylation of substrates rather than auto-phosphorylation (Wang et al., 2005). Furthermore, mutagenesis of phosphorylation sites within the juxtamembrane and C-terminal tail of the cytoplasmic domain of BRI1 did not affect auto-phosphorylation but significantly reduced the phosphorylation of a synthetic substrate *in vitro* (Wang et al., 2005). This is consistent with a model where phosphorylation of residues within the activation loop are important for general kinase activity, whereas phosphosites within the flanking regions of the kinase act as docking sites for substrates or affect the catalytic activity of the kinase for the phosphorylation of these substrates.

Although several studies have now identified phosphorylation sites which are essential for the activity of the kinase domain of plant RLKs, most efforts were concentrated on members of the LRR-RLK class in Arabidopsis, while the kinase domain of other subfamilies remains largely unexplored. Only a handful of reports have been published to date regarding the kinase activity of CRKs, for example, and none of these has looked at the phosphorylation pattern of the kinase domain (see section 1.4.1). Moreover, the majority of these studies have focused on the phosphorylation of residues within the activation loop, while phosphosites in other subdomains remain less characterised. Furthermore, considerably less mutational analyses have been performed targeting the kinase domain of plant RLKs compared to the plethora of reports which investigated the effects of disease-related mutations in mammalian kinases, with special attention paid to oncogenes (Stephens et al., 2005; Dixit et al., 2009; Dixit and Verkhivker, 2014; Kim et al., 2021). Thus, the effects of mutations in regions such as the αC-helix, which is pivotal for kinase regulation, remain largely unexplored in plants.

In this chapter, the analysis of the amino acid sequence of the kinase domain of CRK10 is presented, with the identification of highly conserved residues and motifs. Experiments assessing the auto-phosphorylation activity of the recombinant kinase domain of CRK10 are also reported, confirming that both the WT and mutated versions of the protein can auto-phosphorylate on several residues. Moreover, analysis of the recombinant kinase domain by LC-MS/MS allowed the identification of several auto-phosphorylation sites *in situ*, including threonine 397 in the mutated kinase domain. The effect of a substitution equivalent to *crk10-A397T* on the electrophoretic mobility pattern of the kinase domain of CRK homologs of Arabidopsis was also assessed. The results presented in this chapter provide insights into the auto-phosphorylation activity of the kinase domain of CRK10 *in situ*, laying the groundwork for future investigations into its regulation and function *in planta*.

4.2 Materials and Methods

The protocols used for the cloning and manipulation of DNA molecules for the generation of genetic constructs described in this section are detailed in Chapter 2. Primer sequences used for the amplification of PCR products, *in vitro* mutagenesis PCR, genotyping, RT-PCR and qPCR are listed in Table 4.5. Vector maps are described in Appendix 2. Selected constructs were sequenced after every cloning step.

4.2.1 Sequence alignments and phylogeny

All protein sequences were retrieved from Uniprot (The Uniprot Consortium, 2019; https://www.uniprot.org/). The Uniprot ID number is shown in brackets for each sequence. Sequence alignments and the phylogenetic tree were generated using the Clustal Omega (Sievers et al., 2011) alignment tool embedded in the Uniprot website. The HHalign algorithm (Söding, 2005) and its default settings are used by Clustal Omega (transition matrix, Gonnet; gap opening penalty, 6 bits; gap extension, 1 bit). The kinase domain sequences of CRK10 from Arabidopsis (Q8GYA4[348-634]) and PKA-Cα from *Homo Sapiens* (P17612[44-298]) were aligned for the identification of the twelve subdomains of the kinase domain of CRK10, as well as highly conserved residues and motifs. The amino acid sequences of the following members of the CRK family of Arabidopsis were aligned to each other to identify the residue corresponding to

CRK10-Ala397 and generate the family phylogenetic tree: CRK1 (Q9LMB9), CRK2 (Q9CAL3), CRK3 (Q9CAL2), CRK4 (Q9LZU4), CRK5 (Q9C5S8), CRK6 (Q9C5S9), CRK7 (Q8L7G3), CRK8 (O65468), CRK10 (Q8GYA4), CRK11 (Q9ZP16), CRK12 (O65472), CRK13 (Q0PW40), CRK14 (Q8H199), CRK15 (Q8W4G6), CRK16 (O65476), CRK17 (Q8L710), CRK18 (Q8RX80), CRK19 (Q8GWJ7), CRK20 (O65479), CRK21 (Q3E9X6), CRK22 (Q6NQ87), CRK23 (O65482), CRK24 (O65483), CRK25 (Q9M0X5), CRK26 (Q9T0J1), CRK27 (O49564), CRK28 (O65405), CRK29 (Q8S9L6), CRK30 (Q9LDT0), CRK31 (Q9LDM5), CRK32 (Q9LDS6), CRK33 (Q9LDN1), CRK35 (Q9LDQ3), CRK36 (Q9XEC6), CRK37 (Q9XEC7), CRK38 (Q9XEC8), CRK39 (Q9SYS7), CRK40 (Q9SYS3), CRK41 (O23081), CRK42 (Q9FNE1), CRK43 (Q9M0G5), CRK45 (Q8GY82). The activation segment of the kinase domains of CRK10 (Q8GYA4[491-520]), BRI1 (022476[1027-1056]), BAK1 (Q94F62[434-462]), RECEPTOR-LIKE PROTEIN KINASE 5 / HAESA (P47735[837-868]), ERECTA (Q42371[791-819]) and BIK1 (O48814[220-249]) of Arabidopsis were aligned for the identification of conserved phosphorylation sites.

4.2.2 Protein modelling

A structural model of the kinase domain of CRK10 of Arabidopsis was generated by homology modelling using PyMOD 3.0 (Janson et al., 2017) by Dr Richard Bayliss (University of Leeds). A BLAST search of the protein databank (PDB) with the amino acid sequence of the kinase domain of CRK10 returned the most closely related sequences. The kinase domain of BRI1 of Arabidopsis (BRI1; PDB code 5LPV) was selected as template for the homology modelling of the kinase domain of CRK10 due to its similar conformation in the region of the A397T mutation, and most likely represent an active conformation as it has a stacked configuration of the hydrophobic regulatory spine (Kornev et al., 2006). Homology modelling was carried out using the default parameters, retaining the ATP analogue (phosphoaminophosphonic acid-adenylate ester) from the AtBRI1 structure, but no other heteroatoms.

4.2.3 Cloning of His-tagged kinase domain of CRKs for expression in *E. coli*

The cDNA sequences corresponding to the cytoplasmic kinase domain (kd) of CRK2, CRK5, CRK6, CRK7, CRK10 and CRK36 were cloned as recombinant N-terminal fusion to a 6x His-tag for heterologous expression in *E. coli* (amino acid sequences are listed in Appendix 8.1). CRK5, CRK6 and CRK7 were chosen due to their phylogenetic proximity to CRK10, while CRK2 and CRK36 were chosen based on the presence of a serine and a threonine residue, respectively, at the position corresponding to CRK10-Ala397 in their kinase domain. The constructs were obtained via gene synthesis (GenScript Biotech, Netherlands) or via traditional cloning methods (section 2.16), as presented in Table 4.1. The WT and mutated versions of *CRK2kd*, *CRK6kd*, *CRK7kd* and *CRK36kd* cDNA sequences were synthesized with flanking *Sal*I (5') and *Not*I (3') restriction sites and inserted into pUC57 by GenScript Biotech. For the cloning of the *CRK5kd* constructs, the cDNA sequence of *CRK5* was originally obtained from the cDNA stock C103369 in the plasmid pUNI51. The *CRK5* cDNA sequence was excised from the plasmid by digestion with *Kpn*I and *Not*I enzymes, and the purified DNA fragment was ligated with the pre-digested pENTR™1A. The pENTR™1A *CRK5*^{WT} construct was then used as a template for *in vitro* mutagenesis reaction to introduce the A389T mutation in the cDNA sequence of CRK5, generating the pENTR™1A *CRK5*^{A389T} construct. For cloning of *CRK10kd*, the pJD330 *CRK10*$_{PRO}$*:CRK10*^{WT} and pJD330 *CRK10*$_{PRO}$*:crk10-A397T* constructs described in section 3.2.5 were used as template. The WT and mutated cDNA sequences corresponding to the kinase domain of CRK5 (*CRK5kd*^{WT}*, CRK5kd*^{A3897}) and CRK10 (*CRK10kd*^{WT}*, CRK10kd*^{A397T}) were amplified by PCR with primers containing *Sal*I (5') and *Not*I (3') restriction sites, and cloned into pJET1.2/blunt (CloneJET PCR cloning kit, Thermo Scientific™; the constructs used as template for the PCR reactions described in this section are listed in Table 4.2). After the digestion of all pUC57 and pJET1.2/blunt constructs with *Sal*I and *Not*I enzymes, the fragments of interest were purified from agarose gels and subsequently ligated into pre-digested pENTR1™A Dual Selection Vector (Invitrogen™). The pENTR™1A constructs were used as template for *in vitro* mutagenesis to generate dead kinase variants by the substitution of the catalytic aspartic acid with an asparagine residue. All constructs were used for LR recombination reaction (Gateway™ LR Clonase™

II Enzyme Mix, Invitrogen™) with pDEST™17 (Invitrogen™), where the sequences were cloned in frame with an N-terminal 6x His-tag. The cloning steps described in this section are documented in Appendix 8.2.

Table 4.1 List of constructs and respective mutations used in this chapter.

CRK homologue	**Construct**	**Cloning method**
CRK2	*His-CRK2kd^{WT}*	Gene synthesis
	His-CRK2kd^{S374A}	
	His-CRK2kd$^{WT-D450N}$	*In vitro* mutagenesis
	His-CRK2kd$^{S374A-D450N}$	
CRK5	*His-CRK5kd^{WT}*	Traditional cloning
	His-CRK5kd^{A389T}	*In vitro* mutagenesis
	His-CRK5kd$^{WT-D465N}$	
	His-CRK5kd$^{A389T-D465N}$	
CRK6	*His-CRK6kd^{WT}*	Gene synthesis
	His-CRK6kd^{A400T}	
	His-CRK6kd$^{WT-D476N}$	*In vitro* mutagenesis
	His-CRK6kd$^{A400T-D476N}$	
CRK7	*His-CRK7kd^{WT}*	Gene synthesis
	His-CRK7kd^{A385T}	
	His-CRK7kd$^{WT-D461N}$	*In vitro* mutagenesis
	His-CRK7kd$^{A385T-D461N}$	
CRK10	*His-CRK10kd^{WT}*	Traditional cloning
	His-CRK10kd^{A397T}	*In vitro* mutagenesis
	His-CRK10kd$^{WT-D473N}$	
	His-CRK10kd$^{A397T-D473N}$	
CRK36	*His-CRK36kd^{WT}*	Gene synthesis
	His-CRK36kd^{T389A}	
	His-CRK36kd$^{WT-D465N}$	*In vitro* mutagenesis
	His-CRK36kd$^{T389A-D465N}$	

Table 4.2 Constructs used as template in PCR and *in vitro* mutagenesis reactions described in section 4.2.3.

Template	**PCR / *in vitro* mutagenesis product**
pENTR™1A *CRK2kd*^{WT}	*CRK2kd*$^{WT\text{-}D450N}$
pENTR™1A *CRK2kd*^{S374A}	*CRK2kd*$^{S374A\text{-}D450N}$
pENTR™1A *CRK5*^{WT}	*CRK5kd*^{WT}
pENTR™1A *CRK5*^{A389T}	*CRK5kd*^{A389T}
pENTR™1A *CRK5kd*^{WT}	*CRK5kd*$^{WT\text{-}D465N}$
pENTR™1A *CRK5kd*^{A389T}	*CRK5kd*$^{A389T\text{-}D465N}$
pENTR™1A *CRK6kd*^{WT}	*CRK6kd*$^{WT\text{-}D476N}$
pENTR™1A *CRK6kd*^{A400T}	*CRK6kd*$^{A400T\ \text{-}D476N}$
pENTR™1A *CRK7kd*^{WT}	*CRK7kd*$^{WT\text{-}D461N}$
pENTR™1A *CRK7kd*^{A385T}	*CRK7kd*$^{A385T\text{-}D461N}$
pJD330 *CRK10*$_{PRO}$*:CRK10*^{WT}	*CRK10kd*^{WT}
pJD330 *CRK10*$_{PRO}$*:crk10-A397T*	*CRK10kd*^{A397T}
pENTR™1A *CRK10kd*^{WT}	*CRK10kd*$^{WT\text{-}D473N}$
pENTR™1A *CRK10kd*^{A397T}	*CRK10kd*$^{A397T\text{-}D473N}$

4.2.4 Transformation of *E. coli* BL21 AI™ One-Shot™ Chemically Competent cells

E. coli BL21 AI™ One-Shot™ cells (Invitrogen™) were transformed as described in section 2.17. A 50-75 µL aliquot of the transformation reaction was plated on 2x YT agar plates supplemented with 0.1% glucose (w/v; to repress basal expression of the recombinant protein) and ampicillin (50 µg/mL) as selection marker. The plates were inverted and incubated overnight at 37 °C.

4.2.5 Induction of recombinant protein expression in *E. coli*

The growth media 2x YT supplemented with ampicillin (50 µg/mL) and 0.1% glucose was used in all bacterial growth steps described in this section. Single colonies of BL21 AI™ One-Shot™ *E. coli* cells (Invitrogen™) harbouring the pDEST™17 constructs described in section 4.2.3 were picked with sterile pipette tips and inoculated into 5 mL of 2x YT growth media in glass vials (Universal glass vial, 30 mL, with fitted cap). Bacterial cultures were incubated overnight at 37 ºC with agitation at 225 rpm on orbital shaker (the same growth

conditions were used for subsequent steps). For the *His-CRK10kd* constructs, a 250 µL aliquot of the overnight culture was used to inoculate 50 mL of fresh growth media in a 500 mL glass conical flask. For all other *His-CRKkd* constructs, a 50 µL aliquot of the overnight culture was used to inoculate 5 mL of fresh growth media in 30 mL glass vials. Cells were grown until OD_{600} = 0.4-0.5 was obtained. L-arabinose was added to the cultures to a final concentration of 0.2% (w/v) to induce expression of the recombinant protein for three hours before the cells were harvested for protein extraction.

4.2.6 Extraction of total soluble protein from *E. coli*

Details of the protein extraction and purification method used for each construct can be found in Table 4.3. Following induction of the expression of His-CRK10kd recombinant protein variants, *E. coli* cells were harvested by centrifugation in 50 mL sterile conical tubes at 5,000 x g for ten minutes at room temperature. The supernatant was discarded and the cell pellet was gently resuspended in 15 mL of equilibration buffer (sodium phosphate buffer, pH 8.0) by inverting the tubes. All subsequent steps were performed on ice. The cells were lysed by sonication with eight pulses (70 kHz) of 20 seconds each. Cell lysates were centrifuged for 30 minutes at 5,000 x g at room temperature and the resulting supernatant containing the total soluble protein extract was transferred to a new sterile 50 mL sterile conical tube. Protein samples were used immediately for protein purification. For all other His-CRKkd constructs, the supernatant of boiled bacterial lysates were used for subsequent analysis (as described in Taylor et al., 2013). A 300 µL aliquot of each bacterial culture was collected into a 1.5 mL microfuge tube. The bacterial cells were pelleted at 4,300 x g for three minutes and the supernatant was discarded. The pellets were resuspended in 200 µL of 4x NuPAGE™ LDS Sample buffer (Catalogue number NP0007; Invitrogen™) diluted to 1x in sterile deionised water. The sample mixture was supplemented with 1% β-mercaptoethanol (Sigma-Aldrich®), and the samples were heated to 80 °C in a heat block for ten minutes immediately prior electrophoresis.

Equilibration buffer:	50 mM	sodium phosphate buffer
	0.3 M	NaCl
	pH	8.0

4.2.7 Purification of His-tagged recombinant protein

Protein purification for His-tagged CRK10kd constructs was performed using the His-Select® Nickel Affinity Gel (Catalogue number P6611; Sigma-Aldrich®). All mixing steps were performed on a tube roller, and all centrifugation steps were performed at 5000 x g for five minutes. Aliquots (250 µL) of the affinity gel suspension were transferred into 50 mL sterile conical tubes. The gel suspension was centrifuged and the supernatant was discarded. The gel was washed 500 µL of sterile distilled water followed by a centrifugation step and disposal of the supernatant. The wash step was performed twice. The gel was washed in 2.5 mL of equilibration buffer (sodium phosphate buffer, pH 8.0) and the supernatant was discarded after centrifugation. Total protein extracts obtained with the protocol described in section 4.2.6 were added to the pelleted affinity gel, and samples were mixed for 15 minutes. The samples were centrifuged, the supernatant was discarded and the gel was washed with 2.5 mL of wash buffer (sodium phosphate buffer, pH 8.0) for four minutes. The supernatant was discarded after centrifugation, and the washing step was performed twice. To elute purified His-tagged protein, 500 µL of elution buffer (pH 8.0) were added to the affinity gel. The samples were mixed for ten minutes followed by centrifugation. The supernatant containing the purified His-tagged protein was recovered and transferred to sterile 1.5 mL microfuge tubes pre-chilled on ice. The purified protein extracts were either immediately used for quantification or flash frozen in liquid nitrogen. Frozen samples were stored at -80 °C until further processing.

Wash buffer:	50 mM	sodium phosphate buffer
	0.3 M	NaCl
	pH	8.0

Elution buffer:	50 mM	sodium phosphate buffer
	0.3 M	NaCl
	250 mM	imidazole
	pH	8.0

4.2.8 Bradford protein assay

The concentration of the purified protein extracts was determined using the Bradford protein assay (Catalogue number 5000001; Protein Assay Dye Reagent, Bio-Rad Laboratories, Inc). Aliquots of bovine serum albumin (BSA; Promega) solutions of known concentration were used to generate a standard curve of protein concentration versus absorbance (A_{595}; Figure 4.1). A 15 µL aliquot of each solution was pipetted into a 1.5 mL plastic cuvette. After the addition of 1 mL of Bradford dye reagent to each cuvette, the samples were vortexed and incubated at room temperature for five minutes before absorbance readings were recorded. The same steps were followed to measure the absorbance of purified protein extracts. All samples were analysed in technical triplicates. The concentration of each sample was calculated using the linear regression equation of the standard curve.

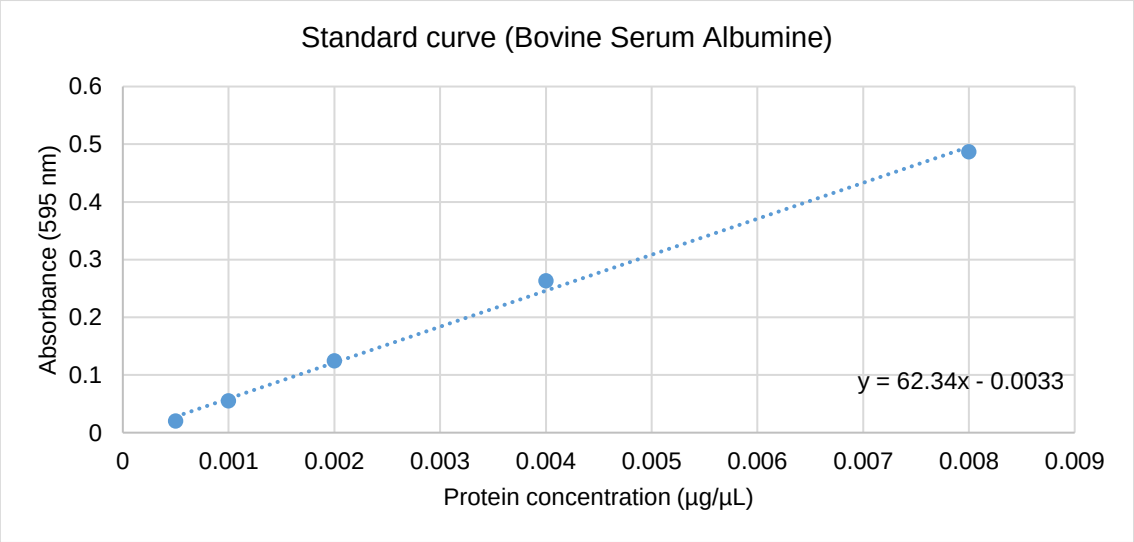

Figure 4.1 A standard curve of bovine serum albumin (BSA) used as reference for the determination of the concentration of purified protein extracts.

4.2.9 Preparation of samples for gel electrophoresis

Purified protein extracts (4 – 5 µg) were mixed with 4x NuPAGE™ LDS Sample buffer (Invitrogen™) in 1.5 mL microfuge tubes. The concentration of the buffer was adjusted to 1x in a total volume of 40 µL with sterile deionised water. The sample mixture was supplemented with β-mercaptoethanol (Sigma-Aldrich®) to a final concentration of 1%, and the tubes were heated to 80 °C in a heat block for ten minutes. All samples were centrifuged at 11,350 x g for one

minute before loading the gel. Bacterial cell lysates prepared as described in section 4.2.6 were also centrifuged and an aliquot of the uppermost phase of the supernatant was loaded on the gel.

4.2.10 Sodium dodecyl sulphate–polyacrylamide gel electrophoresis

SDS-PAGE was performed using the XCell SureLock® Mini-Cell Electrophoresis system (Catalogue number EI0001; Invitrogen™). Polyacrylamide gels (NuPAGE™ 4-12% Bis-Tris, 1.0 mm, Mini Protein Gel, 10-well; Catalogue number NP0321; Invitrogen™) were positioned into the system and the electrophoresis tank was filled with MOPS-SDS (3-(N-morpholino)propanesulfonic acid-SDS) running buffer (NuPAGE™ MOPS SDS Running buffer 20x; Catalogue number NP0001; Invitrogen™). A 35-40 µL aliquot of each sample was loaded into the gel, and 6 µL of PageRuler™ Plus Prestained Protein Ladder, 10 to 250 kDa (Catalogue number 26620; Thermo Scientific™) was used as molecular weight standard. Electrophoresis was conducted at 50 V during the stacking of the samples, followed by two to three hours at 100 V, until the loading dye reached the bottom of the gel. After electrophoresis, the gels were carefully removed from the plastic encasing and carefully transferred to a plastic container filled with 50 mL of Quick Coomassie Stain (Catalogue number NB-45-00078; Generon). Gels were incubated in the dye for 20 minutes on a rocking platform before several wash steps with deionised water. Stained gels were sealed within clear plastic sleeve prior to imaging with a computer scanner. Alternatively, unstained gels were immediately used for protein transfer to a nitrocellulose or PVDF membrane (section 4.2.11). Detection of proteins with Coomassie stain was only performed for the purified extracts of His-CRK10kd; all other constructs were detected by Western blot (see Table 4.3).

4.2.11 Anti-His tag Western blotting

Western blotting was performed for the detection of His-tagged recombinant proteins. Following gel electrophoresis, proteins were transferred from polyacrylamide gels to PVDF (iBlot™ Transfer Stack, PVDF, Catalogue number IB401002; Invitrogen™) or nitrocellulose (iBlot™ Transfer Stack, nitrocellulose, Catalogue number IB301032; Invitrogen™) membranes using the iBlot® Dry Blotting System (Invitrogen™). Programme 3 (20 V for seven minutes) was selected for the protein transfer. The PVDF membranes were carefully

transferred from the dry blot stack into a plastic container where it was incubated with 40 mL of blocking buffer A (5% milk powder diluted in 1x Tris-Buffered Saline, 0.1% Tween 20 buffer) for one hour at room temperature (all incubation steps were performed with constant agitation on a rocking platform). The blocking buffer was discarded and replaced with a freshly prepared solution of His-probe (H-3) HRP monoclonal antibody (Santa Cruz Biotechnology) diluted 1:2000 in blocking buffer A for one hour. Alternatively, nitrocellulose membranes were blocked in blocking buffer B (25 mg/mL BSA diluted in Tris-Buffered Saline-Tween (TBST) buffer) for one hour at room temperature. The blocking buffer was discarded and replaced with a freshly made solution of HisProbe™-HRP conjugate (Thermo Scientific™) diluted 1:5000 in blocking buffer B for one hour. The following steps were performed for both PVDF and nitrocellulose membranes. After incubation with the HRP antibody / probe, the membrane was washed three times for ten minutes each in TBST, and two times for ten minutes each with deionised water. The membranes were transferred to a plastic sleeve, and the whole membrane area was covered with 3 mL of Amersham™ ECL™ Western Blotting Detection Reagent (GE Healthcare©). The membrane was incubated in the dark for five minutes before the excess solution was dried with a paper towel. The plastic sleeve containing the membrane was placed inside an autoradiography cassette, and the following steps were performed in a dark room. Squares of autoradiography film (BioMax® Light Film, Kodak® or Amersham™ Hyperfilm™ ECL; GE Healthcare©) were exposed to the membrane for periods of time ranging between 30 seconds and ten minutes. The film was transferred to a tray containing Champion RG Universal Xray Developer (Silverprint Ltd) for one minute prior to rinsing in distilled water. The film was fixed by incubation in Champion RG Universal Xray Fixer (Silverprint Ltd) for another minute before a final rinsing step in distilled water. The films were imaged using a CanoScan LiDE 110 scanner (Canon, UK).

Tris-Buffered Saline (TBS) 10x stock:	200 mM	Trizma® Base (Merck)
	1.5 M	NaCl
	pH	7.6

1 x TBS 0.1 % Tween (TBST) (1 L):	100 mL	10x TBS
	1 mL	Tween 20
	899 mL	Deionised water
Blocking buffer A (50 mL):	2.5 g	Milk powder
	50 mL	TBST
Blocking buffer B (50 mL):	1.25 g	BSA
	50 mL	TBST

Table 4.3 Details of protein extraction, purification and analysis of recombinant His-tagged kinase domain constructs.

Recombinant protein	**Protein extraction method**	**Protein purification**	**Coomassie-stained gel**	**Western blot / membrane**
His-CRK2kd His-CRK5kd His-CRK6kd His-CRK7kd His-CRK36kd	Heating of bacterial lysate	No	No	Yes / nitrocellulose
His-CRK10kd	Sonication of bacterial lysates	Yes	Yes	Yes / PVDF

4.2.12 Protein phosphatase treatment

Purified protein extracts of His-CRK10kd recombinant protein were treated with Lambda Protein Phosphatase (Catalogue number P0753S; Lambda PP, New England BioLabs®). Reactions were prepared in 1.5 mL microfuge tubes as described in Table 4.4. For each sample, reactions were prepared with and without the chelating agent EDTA as negative control (EDTA inhibits phosphatase activity). Reactions were incubated for 90 minutes at 30 ºC and phosphatase-treated samples were resolved and detected by gel electrophoresis and Western blot (sections 4.2.10 and 4.2.11).

Table 4.4 Reaction mix for treatment of purified protein extracts with Lambda Protein Phosphatase (New England BioLabs®).

Reagent	**Volume (µL)**	**Final concentration**
10x NEBuffer for Protein MetalloPhosphatases	5	1x
10 mM $MnCl_2$	5	1 mM
Purified protein extract (5 µg)	Variable	100 ng / µL
Lambda PP (400 U / µL)	1	8 U / µL
500 mM EDTA (optional)	5	50 mM
Sterile water	Up to 50 µL	-

4.2.13 Liquid chromatography tandem mass spectrometry analysis

Fragments corresponding to the purified His-CRK10kd^{WT} and His-CRK10kd^{A397T} proteins were excised from Coomassie-stained polyacrylamide gel using sterile carbon steel blades (N° 10 Dermaplane Scalpel blade; Swann Morton Ltd). The excised gel fragments were placed into 1.5 mL microfuge tubes containing 50 µL of sterile deionized water, and the tubes were sealed with PARAFILM® sealing film (Heathrow Scientific). The samples were shipped to the Cambridge Centre for Proteomics (University of Cambridge) where they were further processed for liquid chromatography tandem mass spectrometry (LC-MS/MS) according to the steps herein outlined. Gel fragments were transferred into a 96-well PCR plate. Fragments were cut into 1 mm^2 pieces, destained, reduced, alkylated and subjected to enzymatic digestion with sequencing grade trypsin (Promega©) overnight at 37°C. After digestion, the supernatant was pipetted into a sample vial and loaded onto an autosampler for automated LC-MS/MS analysis. All LC-MS/MS experiments were performed using a Dionex Ultimate 3000 RSLC nanoUPLC (Thermo Scientific™) system and a QExactive Orbitrap mass spectrometer (Thermo Scientific™). Separation of peptides was performed by reverse-phase chromatography at a flow rate of 300 nL / min and a Thermo Scientific reverse-phase nano Easy-spray column (Thermo Scientific™ PepMap C18, 2 µm particle size, 100A pore size, 75 µm i.d. x 50cm length). Peptides were loaded onto a pre-column (Thermo Scientific™ PepMap 100 C18, 5 µm particle size, 100A pore size, 300 µm i.d. x 5mm length) from the Ultimate

3000 autosampler with 0.1% formic acid for three minutes at a flow rate of 10 µL / min. After this period, the column valve was switched to allow elution of peptides from the pre-column onto the analytical column. Solvent A was 0.1% formic acid in water and solvent B was 80% acetonitrile, 20% water, 0.1% formic acid. The linear gradient employed was 2-40% B in 30 minutes. Further wash and equilibration steps gave a total run time of one hour. The LC eluant was sprayed into the mass spectrometer by means of an Easy-Spray source (Thermo Scientific™). All m/z values of eluting ions were measured in an Orbitrap mass analyzer, set at a resolution of 70,000 and was scanned between m/z 380-1500. Data dependent scans (Top 20) were employed to automatically isolate and generate fragment ions by higher energy collisional dissociation (HCD, NCE:25%) in the HCD collision cell and measurement of the resulting fragment ions was performed in the Orbitrap analyser, set at a resolution of 17500. Singly charged ions and ions with unassigned charge states were excluded from being selected for MS/MS and a dynamic exclusion window of 20 seconds was employed. Individual MS/MS spectra were analysed by Dr Michael Deery (University of Cambridge) to unambiguously identify phosphorylation sites.

4.2.14 MASCOT database search

The MASCOT database search was performed by the scientific staff at the Cambridge Centre for Proteomics (University of Cambridge). Post-run, all MS/MS data were converted to mgf files which were submitted to the Mascot search algorithm (Matrix Science, London UK, version 2.6.0). The files were searched against a custom database consisting of the CRK10kd^{WT} and CRK10kd^{A397T} amino acid sequences, the UniProt *Arabidopsis thaliana* database (41552 sequences; 17578843 residues) and a common contaminant sequences containing non-specific proteins such as keratins and trypsin (125 sequences; 41129 residues). Variable modifications of oxidation (M), deamidation (NQ) and phosphorylation (STY) were applied as well as fixed modification of carbamidomethyl (C). The peptide and fragment mass tolerances were set to 20 ppm and 0.1 Da, respectively. A significance threshold value of $p < 0.05$ and a peptide cut-off score of 20 were also applied. The MS data and the MASCOT search results can be found in the PRIDE partner repository (Perez-Riverol et al., 2019) of the ProteomeXchange Consortium via the with the dataset identifier PXD023831.

Table 4.5 Table of primers.

Primer	Sequence (5' – 3')	Purpose
CRK5 KD *Sal*I For	GTCGACATGGATGACATCACAAC	Cloning of CRK5kd
CRK5 KD *Not*I Rev	GCGGCCGCTTAACGAGG	
CRK10 KD *Sal*I For	GTCGACATGGATGATATCACAAC	Cloning of CRK10kd
CRK10 KD *Not*I Rev	GCGGCCGCTTATCGAGGAT	
CRK5 A389T For	AACGAAGTTGTTGTTGTGACAAAGCTTCAGCACAGAA	*In vitro* mutagenesis
CRK5 A389T Rev	TTCTGTGCTGAAGCTTTGTCACAACAACAACTTCGTT	
CRK10 A397T For	GAGGTTGTTCTTGTTACAAAGCTACAACATAGA	*In vitro* mutagenesis
CRK10 A397T Rev	TCTATGTTGTAGCTTTGTAACAAGAACAACCTC	
CRK2 D450N For	AAAATTATTCACAGAAATATAAAAGCAAGTAAT	*In vitro* mutagenesis
CRK2 D450N Rev	ATTACTTGCTTTTATATTTCTGTGAATAATTTT	
CRK5 D465N For	ACAATCATACATCGAAATCTAAAAGCGGGTAAC	*In vitro* mutagenesis
CRK5 D465N Rev	GTTACCCGCTTTTAGATTTCGATGTATGATTGT	
CRK6 D476N For	ACAATCATACACCGTAATCTTAAAGCAAGTAAC	*In vitro* mutagenesis
CRK6 D476N Rev	GTTACTTGCTTTAAGATTACGGTGTATGATTGT	
CRK7 D461N For	ACAATCATACACCGTAATCTTAAAGCGAGTAAC	*In vitro* mutagenesis
CRK7 D461N Rev	GTTACTCGCTTTAAGATTACGGTGTATGATTGT	
CRK10 D473N For	ACAATCATACACCGTAATCTCAAAGCCAGTAAC	*In vitro* mutagenesis
CRK10 D473N Rev	GTTACTGGCTTTGAGATTACGGTGTATGATTGT	
CRK36 D465N For	AGGATTATTCACAGAAATTTGAAGGCAAGCAAT	*In vitro* mutagenesis
CRK36 D465N Rev	ATTGCTTGCCTTCAAATTTCTGTGAATAATCCT	

4.3 Results

4.3.1 Identification of the subdomains of the cytoplasmic kinase domain of CRK10

Eukaryotic protein kinases show a high degree of sequence homology, which is made evident by the presence of twelve conserved subdomains originally identified based on the consensus sequence of the eukaryotic PKA-Cα (cAMP-dependent protein kinase catalytic subunit alpha; Hanks and Hunter, 1995). Based on this classification, the subdomains of the cytoplasmic kinase domain of CRK10 were identified by alignment of its amino acid (aa) sequence with PKA-Cα from *H. sapiens* (Figure 4.2). Besides the identification of the twelve subdomains of the CRK10 kinase domain, sequence alignment also allowed the identification of highly conserved motifs such as the glycine-rich loop (aa 355-362; CRK10 aa numbering), the catalytic loop (aa 471-478) and the activation segment (aa 491-520), highlighted in Figure 4.2. The alignment also revealed that CRK10 belongs to the group of RD kinases, which contain a conserved arginine residue immediately preceding the catalytic aspartate in the catalytic loop (Asp473). The aa substitution caused by the *crk10-A397T* allele was identified at the C-terminal end of subdomain III of the kinase domain.

4.3.2 Homology modelling of the three-dimensional structure of the kinase domain of CRK10

Subdomain III corresponds to the αC-helix motif in the three-dimensional structure of eukaryotic protein kinases. In order to determine the position adopted by threonine 397 within this motif, the three-dimensional molecular structure of CRK10 was generated by homology modelling to the active kinase domain of the Arabidopsis BRI1 (PDB code 5LPV) retaining an ATP analogue (Figure 4.3). The resulting model predicts that threonine 397 is located at the C-terminal end of this helix, where its side chain is likely to be exposed on the surface of the protein.

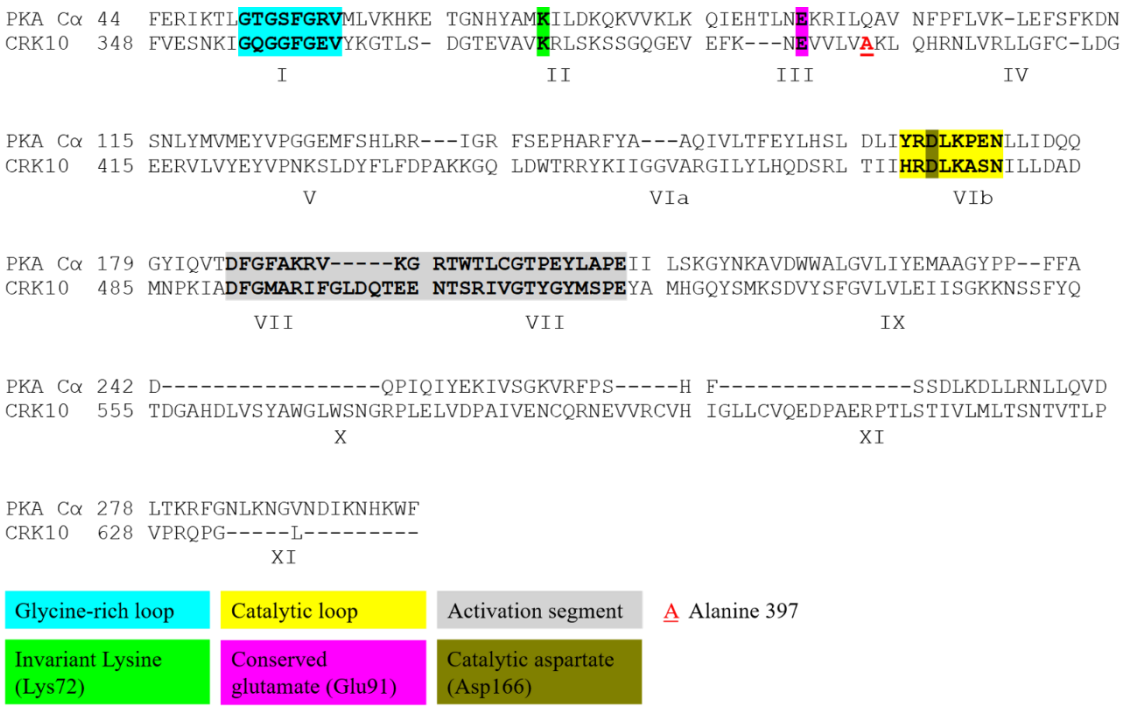

Figure 4.2 Identification of subdomains and highly conserved motifs in the cytoplasmic kinase domain of CRK10.

Alignment of the amino acid sequences of the kinase domains of the human PKA-Cα and the Arabidopsis CRK10. The twelve subdomains are indicated by roman numerals I – XI. Highly conserved motifs (glycine-rich loop, catalytic loop and activation segment) and residues (Lys72, Glu91 and Asp166 – PKA numbering) are indicated. The mutation introduced by the *crk10-A397T* allele is highlighted in red.

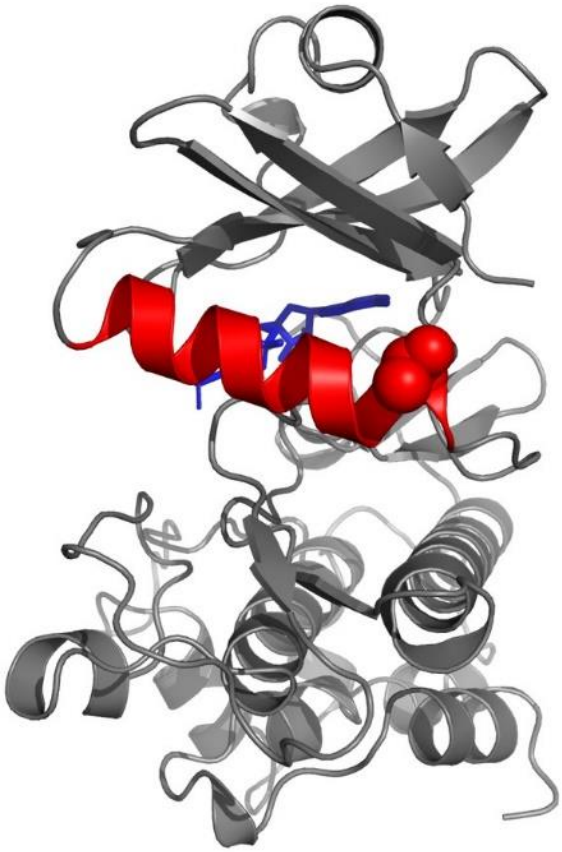

Figure 4.3 Threonine 397 lies at the C-terminal end of the αC-helix of the kinase domain of CRK10.

Structure of the CRK10 kinase domain generated by homology modelling to the active kinase domain of BRI1. The ATP analogue molecule (phosphoaminophosphonic acid-adenylate ester) occupying the kinase active site is highlighted in blue, while the αC-helix is highlighted in red. The side chain atoms of threonine 397 are depicted as red spheres.

4.3.3 Analysis of the residue corresponding to CRK10-Ala397 in other members of the CRK family of Arabidopsis

Although a high degree of sequence homology is observed among eukaryotic protein kinases, not all residues are invariably conserved. To investigate the degree of conservation of alanine 397 among members of the CRK family in Arabidopsis, the amino acid sequences of 42 members of the family were obtained from Uniprot and aligned using Clustal Omega. Interestingly, results showed that while 27 CRKs have an alanine residue at the position equivalent to Ala397 in CRK10, seven and eight members of the family have a threonine or a serine residue at that position, respectively (Figure 4.4). Analysis of the phylogenetic tree of the family revealed that CRKs containing the same residue at this position in subdomain III of their kinase domain are, in general, evolutionary closer to each other than to other members (Figure 4.5). In conclusion, this residue seems to be partially conserved among members of the family, as only alanine, threonine or serine residues occupy this position in the kinase domain of CRKs in Arabidopsis.

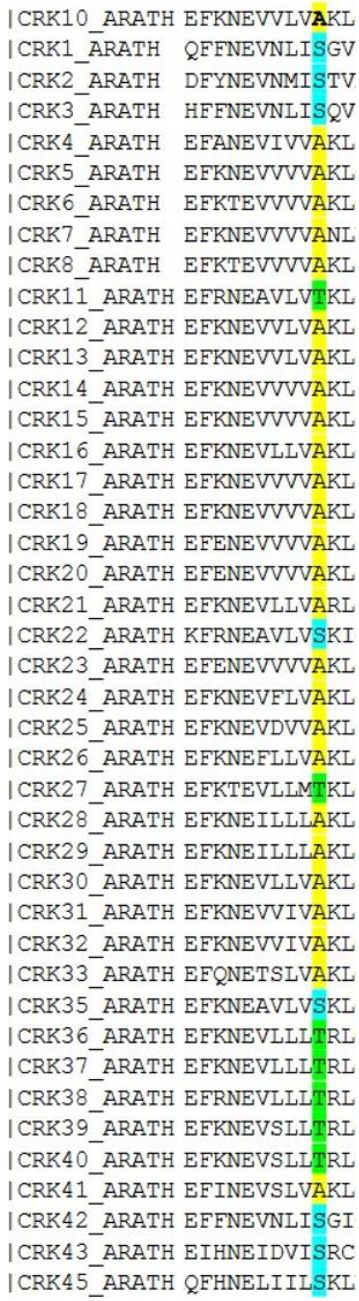

Figure 4.4 An alanine, serine or threonine residue can occupy the position corresponding to CRK10-Ala397 in the kinase domain of other members of the family in Arabidopsis.

Amino acid sequence alignment of the subdomain III of the kinase domain of 42 CRKs of Arabidopsis. Alanine, serine and threonine residues at position corresponding to Ala397 in CRK10 are highlighted in yellow, blue and green, respectively. Amino acid sequences were imported from Uniprot (Uniprot Consortium; uniprot.org) and aligned using the Clustal Omega tool embedded in the Uniprot website.

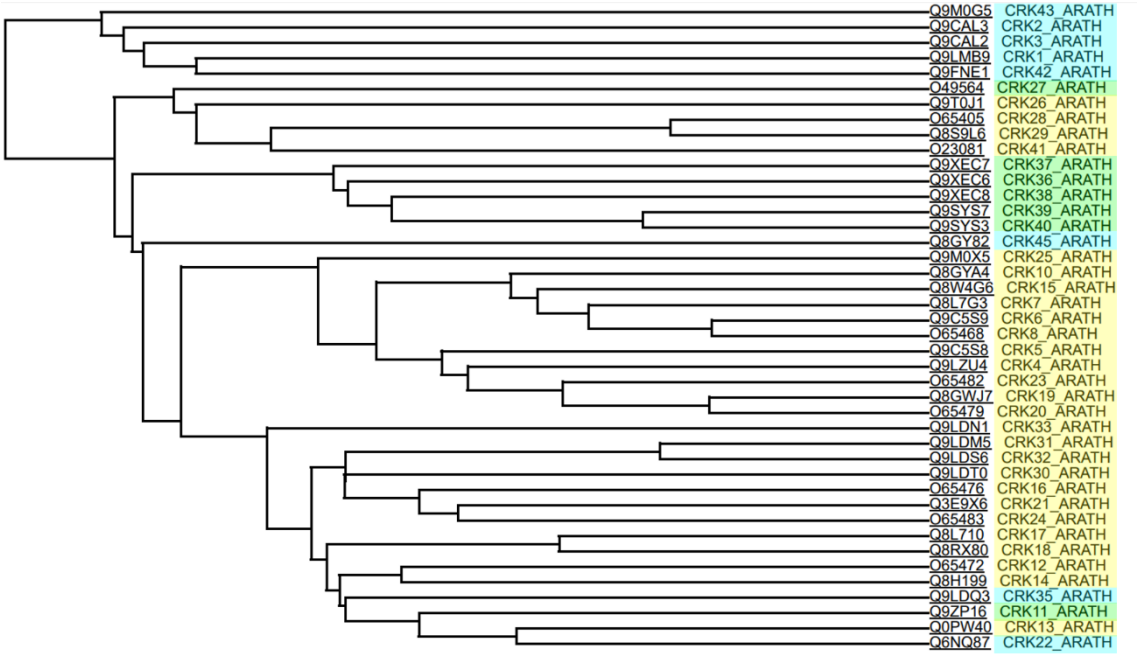

Figure 4.5 Members of the CRK family of Arabidopsis containing a conserved alanine, serine or threonine residue at the position corresponding to CRK10-Ala397 are clustered phylogenetically.

Phylogenetic tree generated based on the amino acid sequences of 42 members of the CRK family in Arabidopsis. CRKs were colour-coded according to the presence of an alanine (yellow), serine (blue) or threonine (green) in subdomain III of their kinase domains at the position corresponding to residue 397 of CRK10. Amino acid sequences were imported from Uniprot (Uniprot Consortium; uniprot.org) and the tree was generated according to the default parameters of the Clustal Omega tool embedded in the Uniprot website.

4.3.4 Determination of the auto-phosphorylation activity of CRK10 by *in situ* auto-phosphorylation assay

Plant RLKs were originally regarded as serine/threonine kinases. However, their ability to phosphorylate tyrosine residues has also been demonstrated in recent years (Oh et al., 2009; Lin et al., 2014). The observation that the kinase domain of RLKs auto-phosphorylate when expressed in *E. coli*, with virtually no background phosphorylation performed by host kinases, provided a quick, convenient method to evaluate the auto-phosphorylation activity of these protein kinases, as introduced in section 4.1 (Wu et al., 2012; Taylor et al., 2013). Thus, to investigate if CRK10 is capable of auto-phosphorylation, the WT (CRK10kd^{WT}) and mutant (CRK10kd^{A397T}) versions of its cytoplasmic kinase domain were cloned as N-terminal 6x His-tag fusion

recombinant proteins. Dead kinase variants were generated by the substitution of the invariant aspartic acid Asp473 in the active site of the kinase by an asparagine residue (CRK10kd$^{WT-D473N}$ and CRK10kd$^{A397T-D473N}$). The recombinant proteins were introduced in *E. coli* BL21 AI™ cells for heterologous expression, and purified protein extracts were resolved by SDS-PAGE and detected by staining with Coomassie blue (Figure 4.6). While the dead kinase version His-CRK10kd$^{WT-D473N}$ was detected at its predicted molecular weight (~40 kDa), the active kinase version His-CRK10kd^{WT} showed an electrophoretic mobility shift corresponding to a larger weight, a phenomenon that is often observed for proteins harbouring phosphorylated residues (Wegener and Jones, 1984). Thus, this observation indicates that the recombinant kinase domain is active and capable of auto-phosphorylation. Although both dead kinase versions His-CRK10kd$^{A397T-D473N}$ and His-CRK10kd$^{WT-D473N}$ migrated similarly on SDS-PAGE gels, His-CRK10kd^{A397T} exhibited an increased mobility shift, suggesting the presence of additional phosphorylated residues compared to His-CRK10kd^{WT}.

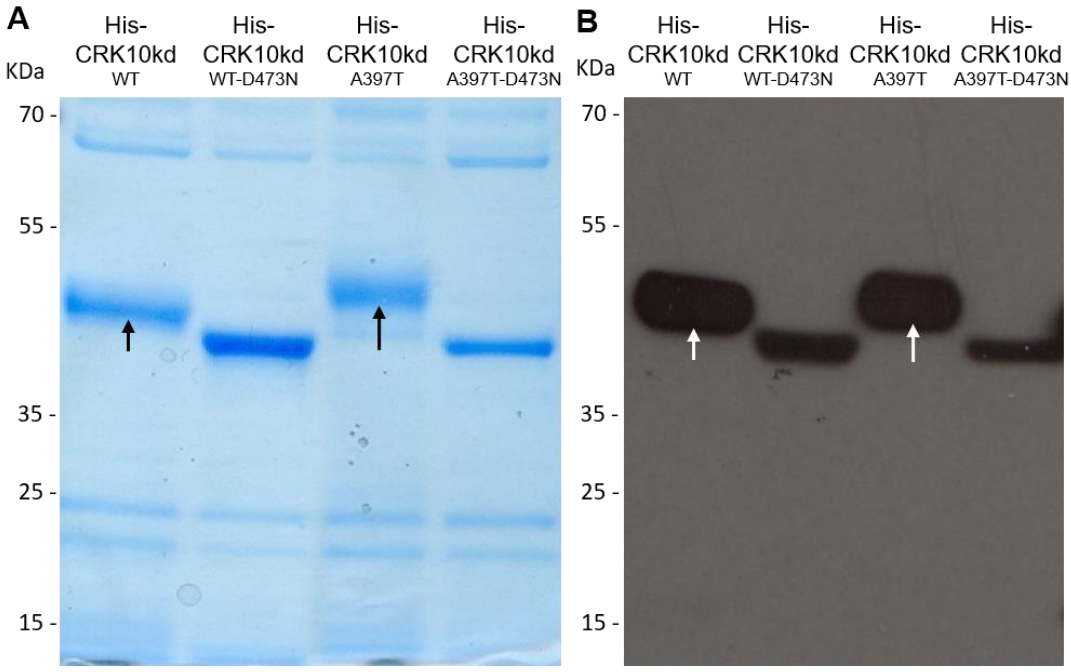

Figure 4.6 His-CRK10kd^{WT} and His-CRK10kd^{A397T} are active kinases capable of auto-phosphorylation, and His-CRK10kd^{A397T} likely has additional phosphorylation sites.

His-CRK10kd^{WT} and His-CRK10kd^{A397T} alongside respective dead kinase counterparts (His-CRK10kd$^{WT-D473N}$ and His-CRK10kd$^{A397T-D473N}$) resolved by gel

electrophoresis and detected by (A) staining with Coomassie Brilliant Blue (CBB) or (B) immunoblotting with anti-His tag antibody conjugated to Horseradish peroxidase (HRP α-His). Arrows indicate the electrophoretic mobility shift of His-CRK10kd^{WT} and His-CRK10kd^{A397T}.

4.3.5 Analysis of the recombinant kinase domain of CRK10 following phosphatase treatment

In order to confirm that the electrophoretic mobility shift observed for His-CRK10kd^{WT} and His-CRK10kd^{A397T} is due to phosphorylated residues, the purified proteins were treated with λ-phosphatase in the absence or presence of the reaction inhibitor EDTA prior to separation by SDS-PAGE electrophoresis (Figure 4.7). Irrespective of the treatments, the dead kinase versions CRK10$^{WT-D473N}$ and His-CRK10kd$^{A397T-D473N}$ migrated according to their predicted molecular weight, as confirmed by SDS-PAGE and anti-His immunoblotting. However, λ-phosphatase treatment of His-CRK10kd^{WT} and His-CRK10kd^{A397T} resulted in a clearly detectable shift, which did not occur when the reaction was inhibited by 50mM EDTA. These results suggest that phosphorylation of amino acid residues in recombinant His-CRK10kd^{WT} and His-CRK10kd^{A397T} is responsible for their electrophoretic mobility shift. Taken together, these results indicate that both His-CRK10kd^{WT} and His-CRK10kd^{A397T} are functional kinases capable of auto-phosphorylation, and His-CRK10kd^{A397T} is likely to be more heavily phosphorylated than His-CRK10kd^{WT} as it displays a greater mobility shift prior to the removal of phosphate groups.

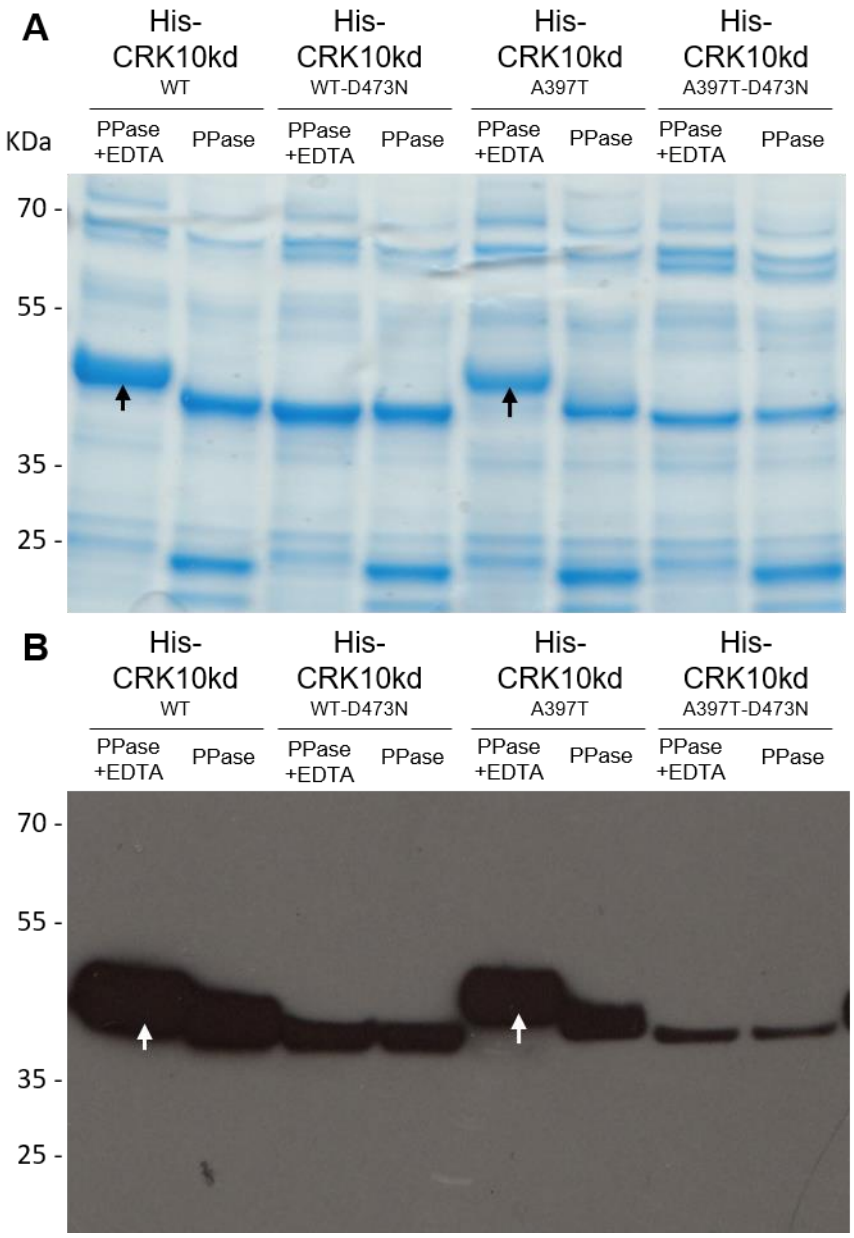

Figure 4.7 Phosphatase treatment abolishes the electrophoretic mobility shift observed for His-CRK10kd^{WT} and His-CRK10kd^{A397T}.

His-CRK10kd^{WT} and His-CRK10kd^{A397T} alongside respective dead kinase counterparts (His-CRK10kd$^{WT-D473N}$ and His-CRK10kd$^{A397T-D473N}$) resolved by gel electrophoresis and detected by (A) staining with Coomassie Brilliant Blue (CBB) or (B) immunoblotting with anti-His tag antibody conjugated to Horseradish peroxidase (HRP α-His) following treatment with λ-phosphatase (PPase). EDTA: PPase inhibitor. Arrows indicate the electrophoretic mobility shift of His-CRK10kd^{WT} and His-CRK10kd^{A397T}.

4.3.6 Post-translational modifications analysis of the recombinant kinase domain of CRK10

In order to identify the phosphorylation sites in His-CRK10kd^{WT} and His-CRK10kd^{A397T}, we subjected tryptic peptides of the recombinant proteins to LC/MS-MS. This analysis was provided as a service by the Cambridge Centre for Proteomics. The MASCOT probability-based algorithm was used to confirm the peptides match to the CRK10 kinase domain sequence (MS data and MASCOT search results have been deposited to the PRIDE repository; dataset identifier PXD023831). Individual MS/MS spectra were inspected for confirmation of phosphorylation sites, which led to the unambiguous identification of Thr340, Tyr363, Thr507, Ser508, Tyr514, Thr625, Ser662 and Thr664 as phosphosites in both His-CRK10kd^{WT} and His-CRK10kd^{A397T} proteins (Figure 4.8). Furthermore, Thr-397 itself was identified as a phosphorylation site in the His-CRK10kd^{A397T} kinase domain *in situ*, confirming our initial hypothesis that the amino acid substitution in the *crk10-A397T* mutant introduces an additional phosphorylation site in the kinase domain of the protein. Interestingly, Thr507, Ser508, and Tyr514 align to amino acid residues in the activation loop of several RLKs, phosphorylation of which is known to be essential for activation of RD kinases (Johnson et al., 1996; Figure 4.9). Phosphorylation sites were also detected in the juxtamembrane region (Thr340) as well as in the C-terminal tail of CRK10 (Thr625, Ser662, and Thr664), which are predicted to act as regulatory sites for interaction with binding partners. In addition, the identification of two phosphorylated tyrosine residues (Tyr363 and Tyr514) classifies CRK10 as a dual specificity kinase, and constitutes the first instance in which such activity has been reported for a CRK in plants to the best of our knowledge.

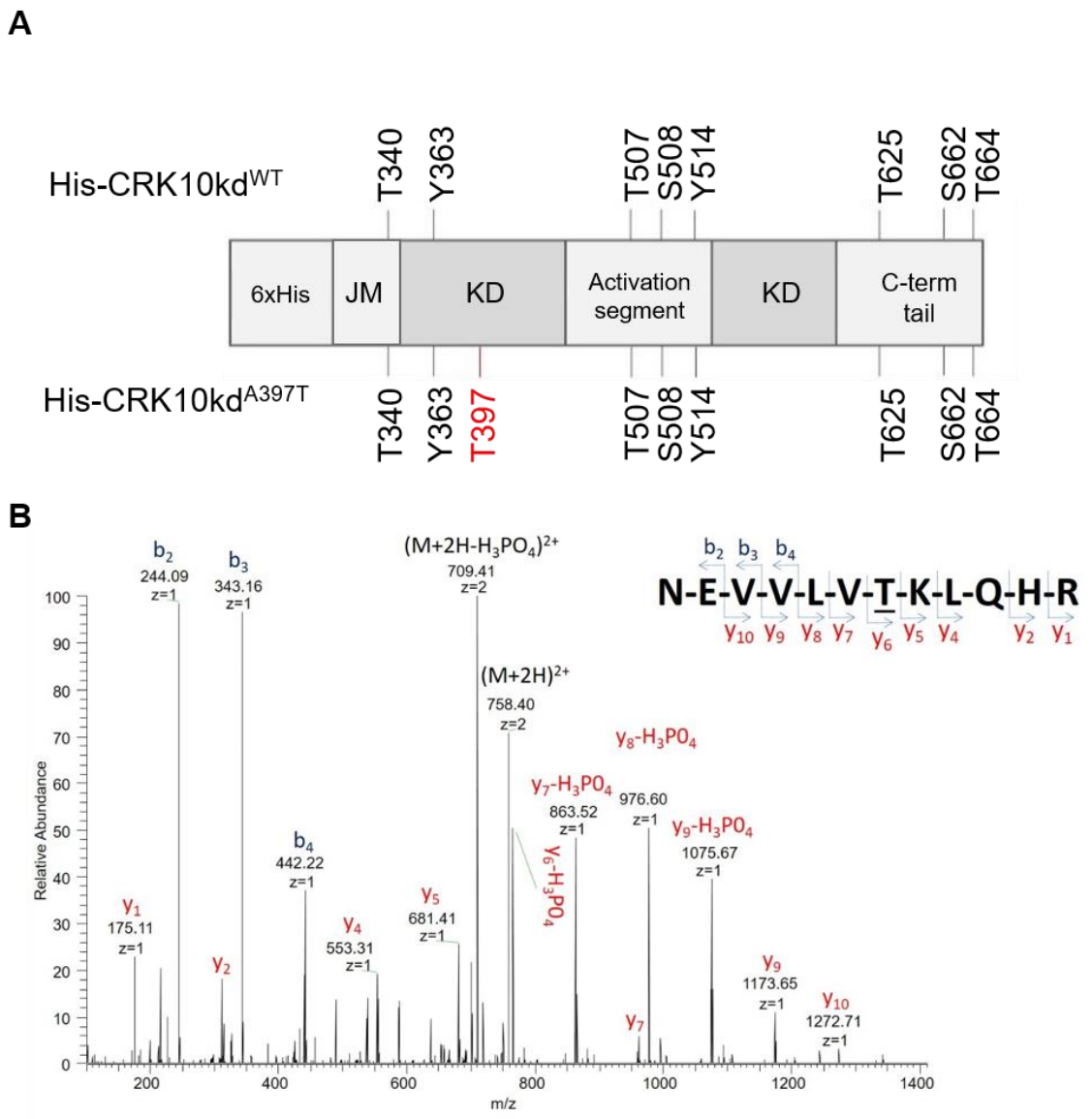

Figure 4.8 Threonine 397 is an additional auto-phosphorylation site in the kinase domain of CRK10.

(A) *In situ* auto-phosphorylation sites in His-CRK10kd^{WT} and His-CRK10kd^{A397T} identified by LC-MS/MS analysis of the recombinant protein kinase domain. Single letter code is used to indicate aa residues. Threonine 397 is highlighted in red. 6xHis: 6x His-tag; JM: juxta-membrane domain; KD: kinase domain; C-term tail: C-terminal tail.

(B) MS/MS spectrum of the doubly charged (m/z 758.4) tryptic phosphopeptide NEVVLVTKLQHR in which the threonine residue is phosphorylated. Neutral losses of phosphoric acid from both the precursor ion and the C-terminal y ions are observed.

```
CRK10       491  DFGMARIFGLDQ--TEENTSRIVGTYGYMSPE 520
BRI1        1027 DFGMARLMSAMD--THLSVSTLAGTPGYVPPE 1056
BAK1        434  DFGLAKLMDYKD--THV-TTAVRGTIGHIAPE 462
HAESA       837  DFGIAKVGQMSGSKTPEAMSGIAGSCGYIAPE 868
ERECTA      791  DFGIAKSLCVSK--SHT-STYVMGTIGYIDPE 819
BIK1        220  DFGLARDGPMGD--LSYVSTRVMGTYGYAAPE 249
                 ***:*:             : : *: *:  **
```

Figure 4.9 Phosphorylation sites in the activation loop of CRK10 align to residues which are known to be phosphorylated in other kinases.

The activation segment of the kinase domain of the RLKs CRK10, BRI1, BAK1, HAESA, ERECTA and the RLCK BIK1 from Arabidopsis were imported from Uniprot (Uniprot Consortium; uniprot.org) and aligned using the Clustal Omega tool embedded in the Uniprot website. Experimentally determined phosphorylation sites are highlighted in bold and underlined.

4.3.7 Investigation of the effect of a point mutation equivalent to *crk10-A397T* on the auto-phosphorylation activity of close homologs

The alignment of the amino acid sequence of the kinase domain of 42 members of the CRK family in Arabidopsis revealed that 27 CRKs contain an alanine residue at the position corresponding to Ala397 in CRK10 (Figure 4.4). Given the structural and functional level of conservation observed for eukaryotic protein kinases, it is reasonable to assume that a mutation equivalent to *crk10-A397T* could also affect the phosphorylation status of the kinase domain of other CRKs. To test this hypothesis, the close homologues CRK5, CRK6 and CRK7 were chosen based on their proximity to CRK10 in the family phylogenetic tree (Figure 4.5). The coding sequence of the WT kinase domain of CRK5, CRK6 and CRK7 (which belong to the alanine-containing group of CRKs) were cloned as an N-terminal fusion with a 6x-His tag (His-CRK5kd^{WT}, His-CRK6kd^{WT} and His-CRK7kd^{WT}). Mutant versions encoding the substitution of the alanine in subdomain III for a threonine residue, reproducing the mutation encoded by the *crk10-A397T* allele, were also produced (His-CRK5kd^{A389T}, His-CRK6kd^{A400T} and His-CRK7kd^{A385T}). Respective dead kinase variants were also generated to be used as negative controls (His-CRK5kd$^{WT\text{-}D465N}$, His-CRK5kd$^{A389T\text{-}D465N}$, His-CRK6kd$^{WT\text{-}D476N}$, His-CRK6kd$^{A400T\text{-}D476N}$, His-CRK7kd$^{WT\text{-}D461N}$, His-CRK7kd$^{A385T\text{-}D461N}$). All constructs were introduced in *E. coli* BL21 AI™, and boiled cell lysates were resolved by SDS-PAGE after induction of the recombinant protein

expression. The predicted molecular weight for His-CRK5kd, His-CRK6kd and His-CRK7kd recombinant protein variants was ~40 kDa. According to the initial working hypothesis, the alanine to threonine substitution should affect the auto-phosphorylation activity of these CRK homologues. Both His-CRK5kd^{WT} and His-CRK5kd^{A389T} displayed a pronounced electrophoretic shift compared to their respective dead kinase counterparts, as detected by Western blot (Figure 4.10 A). Similar to the observation with the His-CRK10kd variants, the shift displayed by His-CRK5kd^{A389T} was slightly bigger than that of His-CRK5kd^{WT}, an indication of additional phosphorylated residues in the mutant kinase domain. His-CRK6kd^{WT} and His-CRK6kd^{A400T} also displayed mobility shifts, although very small and considerably less pronounced than the ones observed for His-CRK5kd (Figure 4.10 B). However, the shift displayed by His-CRK6kd^{A400T} also appeared to be slightly increased compared to His-CRK6kd^{WT}, despite the difference not being as clear for these constructs due to the smaller shifting effect. Finally, both the WT and the mutated version of the kinase domain of CRK7 displayed a similar migration pattern to their respective dead kinase controls, which did not provide any indication regarding their auto-phosphorylation activity (Figure 4.10 C).

In contrast, some members of the CRK family in Arabidopsis harbour a serine or threonine residue in their WT sequences in position corresponding to Ala397 in CRK10. Given the deleterious effect on plant growth and development caused by the *crk10-A397T* mutation, it is puzzling that other members of the family contain a threonine or serine residue at this position in subdomain III of the kinase domain. This observation raised the question of whether these residues could also act as auto-phosphorylation sites *in situ*. If so, their substitution with an alanine residue could also promote an altered electrophoretic mobility shift due to the absence of a phosphorylation site compared to the WT kinase domain. To test this hypothesis, the coding sequence of the WT kinase domain of the serine-containing CRK2 (His-CRK2kd^{WT}) and the threonine-containing CRK36 (His-CRK36kd^{WT}) were cloned as N-terminal His-tagged proteins. Mutated versions encoding the substitution of the serine (CRK2-S374) and threonine (CRK36-T389) residues with an alanine (His-CRK2kd^{S374A} and His-CRK36kd^{T389A}) at position corresponding to CRK10-Ala397 were also generated, along with their respective dead kinase controls. The predicted molecular weight for both His-CRK2kd and His-CRK36kd recombinant proteins was ~40 kDa. After separation by gel electrophoresis and immunoblotting, electrophoretic mobility

shifts were observed for His-CRK2kd^{WT,} His-CRK2kd^{S374}, His-CRK36kd^{WT} and His-CRK36kd^{T389A} compared to the dead kinase controls (Figure 4.11). Interestingly, both WT versions of the kinase domains displayed a greater shift compared to the His-CRK2kd^{S374A} and His-CRK36kd^{T389A}, although the shift displayed by His-CRK2kd^{WT} was more pronounced than that of His-CRK36kd^{WT}. These observations suggest that the replacement of Ser374 and Thr389 with an alanine residue leads to decreased levels of auto-phosphorylation of the kinase domain of CRK2 and CRK36 *in situ*, which indicates they are auto-phosphorylation sites.

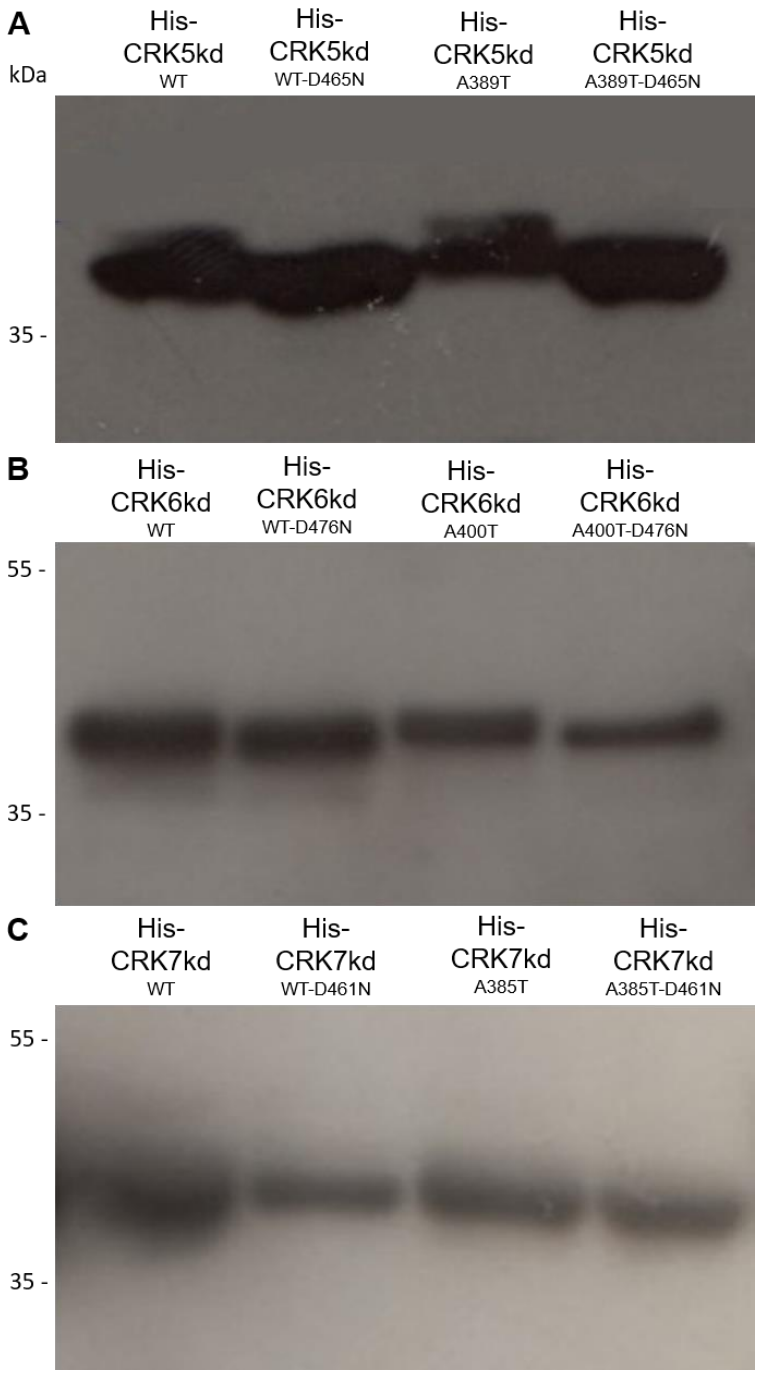

Figure 4.10 Effect of a residue substitution at position corresponding to CRK10-Ala397 on the auto-phosphorylation activity of the kinase domain of CRK5, CRK6 and CRK7 *in situ*.

The electrophoretic migration pattern of mutated versions of recombinant N-terminal His-tag fusion of the kinase domain of (A) CRK5, (B) CRK6 and (C) CRK7 was detected by Western blot (HRP-probe). Kinase domain variants harbouring a mutation equivalent to CRK10kd^{A397T} (His-CRK5kd^{A389T}, His-CRK6kd^{A400T} and His-CRK7kd^{A385T}) were compared to WT and dead kinase controls.

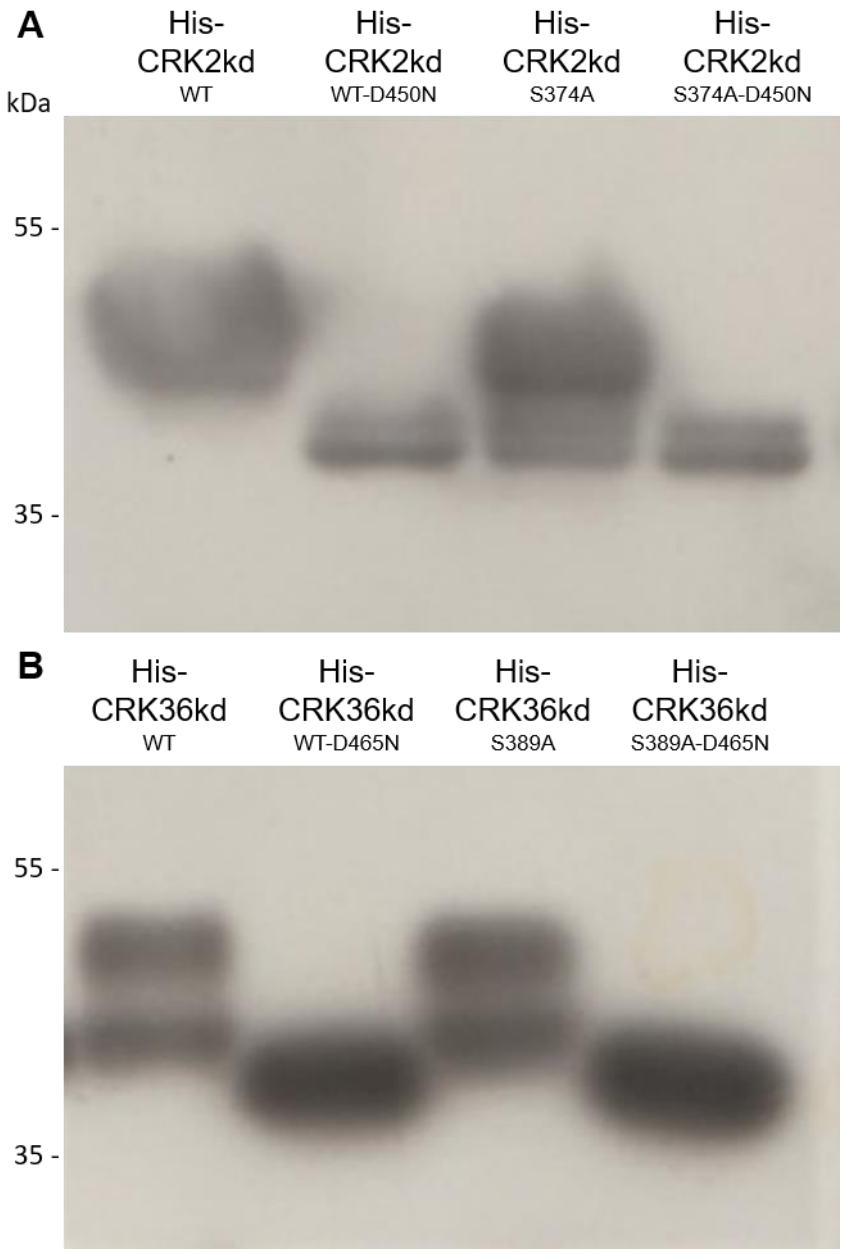

Figure 4.11 Effect of a residue substitution at position corresponding to CRK10-Ala397 on the auto-phosphorylation activity of the kinase domain of CRK2 and CRK36 *in situ*.

The electrophoretic migration pattern of mutated versions of recombinant N-terminal His-tag fusion of the kinase domain of (A) CRK2 and (B) CRK36 was detected by Western blot (HRP-probe). Kinase domain variants harbouring a mutation at position corresponding to CRK10kd^{A397T} (His-CRK2kd^{S374A} and His-CRK36kd^{A389A}) were compared to WT and dead kinase controls.

4.4 Discussion

The cytoplasmic domain of plant RLKs belongs to the class of eukaryotic protein kinases, important molecular switches in a wide range of biological processes. Auto- and trans-phosphorylation of serine, threonine and tyrosine residues in the catalytic core and flanking regions of the kinase domain are crucial for the activation and regulation of kinase activity (see section 1.2.2 for a detailed description of the activation mechanism of eukaryotic protein kinases). Several conserved phosphorylation sites which are essential for kinase activation have been identified in the kinase domain of plant RLKs, with most studies focusing on members of the LRR-RLK subfamily. Given the functional and structural importance of individual residues, mutations within the kinase domain have the potential to alter the regulation and activity of the protein and, in turn, they can have a knock-on effect on the cellular processes regulated by the kinase. The strong dwarf phenotype displayed by the *crk10-A397T* mutant (see section 3.3.1) suggests that the point mutation in the kinase domain of CRK10 somehow affects kinase activity, as it triggers cellular processes which ultimately affect plant growth and development. The experiments described in this chapter were aimed at investigating the auto-phosphorylation activity of the kinase domain of WT and mutated CRK10, with the hope that these results would provide us with hints as to how this mutation could possibly affect kinase activity *in planta*.

The amino acid sequence alignment of CRK10 with the human PKA-Cα allowed the identification of the twelve conserved subdomains in the kinase domain of CRK10. Furthermore, conserved regions such as the glycine-rich loop in subdomain I (aa 355-362; CRK10 numbering shown here and subsequently), the catalytic loop in subdomain VIb (aa 471-478), and the activation segment spanning subdomains VII and VIII (aa 491-520), were also identified. The highly conserved lysine and glutamate residues found in subdomains II and III of eukaryotic protein kinases, respectively, were found to correspond to Lys376 and Glu392 in CRK10, and the aspartate residue in position 473 aligned to the catalytic aspartic acid of PKA-Cα. An arginine residue immediately preceding Asp473 in CRK10 gives it the typical signature of RD kinases, which are known to require the phosphorylation of residues within the activation segment for kinase activation (Nolen et al., 2004).

The amino acid substitution caused by the *crk10-A397T* allele was found to be located in subdomain III of the kinase domain of CRK10. This corresponds

to the αC-helix of the N-terminal lobe of the kinase, a highly conserved signal integration motif (Johnson et al., 2001). The αC-helix has been described as a "contiguous set of wheels (or a screw) where every cog in the wheel reaches out and touches a different part of the molecule" (Taylor et al., 2015). Residues at the N-terminal end of the helix contribute to the correct positioning of the ATP molecule and directly interact with the activation segment, making it an important hub of interactions which are essential for catalysis (Huse and Kuriyan, 2002). Besides containing an R-spine residue (PKA-Leu95), the C-terminal surface of the helix is known to interact with regions outside of the conserved catalytic core which are important for kinase regulation (Taylor et al., 2015). The recent description of dynamic communities of residues within the kinase domain placed the αC-helix as the group with the greatest number of connections with other communities, highlighting its structural and regulatory relevance (McClendon et al., 2014). Thus, it is unsurprising that mutations within, or which interact with this region, have the potential to affect kinase activity and regulation. For example, a point mutation in the human cyclin-dependent kinase 2 (CDK2), which replaces a leucine with a proline residue in the αC-helix of the protein, affects its ability to interact with the cyclin subunit, although the kinase still retains activity (Child et al., 2010). On the other hand, a deletion in a region adjacent to the αC-helix in the epidermal growth factor receptor (EGFR) was shown to have an activating effect by stabilising the helix in its active conformation (Tamirat et al., 2019). Unlike the plethora of information available for the modulation of the αC-helix in mammalian kinases, studies focusing on the importance of this motif for the regulation of plant RLKs are lacking. Nevertheless, at least one other mutation in subdomain III has been reported in the literature associated with a gain-of-function effect of a plant RLK. The *snc4-1D* allele harbours a single point mutation which causes the substitution of alanine 850 for a threonine residue in the atypical RLK SUPPRESSOR OF NPR1-1 CONSTITUTIVE 4 (SNC4) in Arabidopsis (Bi et al., 2010). Given the dwarf phenotype and the activation of defence responses displayed by the mutant plants, this allele was considered to be a gain-of-function of *SNC4*. Interestingly, sequence alignment reveals that the point mutation in subdomain III of the protein encoded by *snc4-1D* aligns to a position in the vicinity of the residue corresponding to CRK10-Ala397 (Appendix 8.3). These observations support the idea that the introduction of threonine residues within the subdomain III / αC-helix of the kinase domain of plant RLKs can affect kinase

activity and promote a gain-of-function effect, although the molecular mechanism underlying this process is unclear.

In order to gather supporting evidence to demonstrate how the *crk10-A397T* mutation affects the kinase activity of CRK10, it was first necessary to assess whether the WT and mutated are active protein kinases. To do so, their cytoplasmic kinase domains were expressed as recombinant His-tagged proteins in *E. coli*, along with respective dead kinase controls. The mobility shift observed for both the His-CRK10kd^{WT} and His-CRK10kd^{A397T} was the first indication that the kinase domain of CRK10 had undergone auto-phosphorylation during expression in the bacterial cells, as it has been frequently observed for the kinase domain of other RLKs (Oh et al., 2000; Wang et al., 2005; Taylor et al., 2013; Taylor et al., 2016). Abolishment of the mobility shift following treatment with lambda phosphatase confirmed the presence of phosphorylated residues in the recombinant proteins and, therefore that CRK10 is capable of auto-phosphorylation. Mass spectrometry analysis of tryptic peptides of His-CRK10kd^{WT} and His-CRK10kd^{A397T} allowed the unambiguous identification of eight phosphorylation sites across the juxtamembrane, kinase domain and C-terminal regions of the protein. Similar analyses have never been reported for a member of the CRK family in plants to the best of my knowledge and, therefore, this study is the first to report the identification of auto-phosphorylation sites in the kinase domain of a CRK. Residues Thr507, Ser508 and Tyr514 of the activation loop were some of the auto-phosphorylation sites identified in the kinase domain of CRK10. This is consistent with the fact that CRK10 belongs to the RD class of protein kinases, which require phosphorylation of activation segment residues for kinase activation (Johnson et al., 1996). This also constitutes the first experimental observation of tyrosine phosphorylation by a member of the CRK family, revealing the dual specificity of the kinase domain of CRK10.

Alignment of the activation loop of CRK10 with receptor-like kinases BRI1, BAK1, HAESA and ERECTA, and the receptor-like cytoplasmic kinase BIK1, showed that CRK10-Thr507 and Ser508 align to BAK1-Thr449 and Thr450, phosphosites which are essential for the biological functions played by BAK1 (Wang et al., 2008; Yan et al., 2012). BAK1-Thr450 was also shown to play a pivotal role in stabilising the kinase domain of the protein, in addition to being phosphorylated in trans by BRI1. The position occupied by CRK10-Ser508 also

corresponds to BRI1-Ser1044, which when mutated to an alanine residue, nearly abolished the kinase's ability to phosphorylate itself and a peptide substrate *in vitro*, and failed to rescue the phenotype of the *bri1-5* mutant (Wang et al., 2005). The same position aligns to the auto-phosphorylation site Ser856 in HAESA (Taylor et al., 2016), to the predicted functionally important Thr807 in ERECTA (Kosentka et al., 2017), and Thr237 in BIK1, an important auto- and trans-phosphorylation site in flagelin22 (flg22)-induced signalling (Lin et al., 2014). Furthermore, the phosphotyrosine residue Tyr514 in CRK10 corresponds to BIK1-Tyr243, which was shown to be a target of auto- and trans-phosphorylation and is required during the BIK1-mediated signalling in plant immunity (Lin et al., 2014). In conclusion, the phosphorylation sites identified in the activation segment of CRK10 in this study correspond to phosphosites known to be functionally important for the activity of other RLKs in Arabidopsis, a strong indicative that they could also be biologically relevant *in vivo*.

Moreover, four out of the eight auto-phosphorylation sites in His-CRK10kd^{WT} and His-CRK10kd^{A397T} were found in the juxtamembrane and C-terminal tail regions of the protein. Despite being less conserved than the sites identified in the activation segment, phosphorylation of the areas flanking the kinase domain are known to be biologically relevant, and are in general thought to regulate the kinase's ability to trans-phosphorylate substrates and provide the formation of docking sites for interaction with other proteins. Phosphorylation of serine and threonine residues in the juxtamembrane and C-terminal regions of BRI1, for example, were shown to be required for the phosphorylation of peptide substrates (Wang et al., 2005). On the other hand, phosphorylation of BRI1-Thr872 in the juxtamembrane domain appears to be a negative regulator of peptide phosphorylation, demonstrating how different phosphorylation sites affect the kinase activity in different ways (Wang et al., 2005).

Finally, Thr397 was found to be phosphorylated in the kinase domain of His-CRK10kd^{A397T}, in agreement with the initial working hypothesis. This result corroborates the idea that this mutation can affect the phosphorylation status of the kinase *in situ*, although whether this is also true *in planta* is not currently known. Thus, the exact mechanism through which a threonine at position 397 affects the kinase activity of CRK10 *in vivo* is unclear and several questions remain unanswered. For example, is the presence of the threonine itself sufficient to unlock the gain-of-function effect of this mutation *in vivo*, or is the

phosphorylation of this residue necessary for the activation of responses? And what exactly is the mechanism through which this mutation causes the activation of downstream responses? Is it via the stabilisation of the kinase domain in a catalytically active conformation? Or could this phosphorylated residue promote novel protein-protein interactions, leading to the activation of CRK10 via a mechanism other than spontaneous self-activation? Considering the location of threonine 397 at the C-terminal end of the αC-helix, one possibility is that this mutation could disrupt interactions with non-catalytic domains of the protein which might have a regulatory function. This could, for example, disrupt an auto-inhibitory conformation which subsequently promotes constitutive kinase activation. Alternatively, this point mutation might create a novel docking site which promotes the interaction of the kinase domain of CRK10 with other proteins (Holland and Cooper, 1999). In this case, could CRK10 interact with novel partners at the plasma membrane? And could these new interactions potentially trigger the activation of CRK10? Further experiments will be necessary to address these questions moving forward, as discussed in more detail in section 8.2.

Due to the structural homology expected among the kinase domain of members of the CRK family, it was reasonable to assume that a mutation equivalent to *crk10-A397T* could also affect close homologues of CRK10. The analysis of the recombinant kinase domain of WT and mutant CRK5, CRK6 and CRK7 was performed to investigate this hypothesis. In line with the results observed for His-CRK10kd, the His-tagged WT and mutant kinase domain of CRK5 showed clear electrophoretic mobility shifts on Western blot, suggesting they were able to auto-phosphorylate in *E. coli*. Furthermore, the shift displayed by the mutated version of CRK5 was bigger than that of the WT, suggesting the threonine introduced in subdomain III of the kinase domain might also be an additional phosphorylation site, as Thr397 in CRK10. Furthermore, a very small shift was also observed for the kinase domain of CRK6, again suggesting auto-phosphorylation activity. The same migration pattern displayed by all four variants of the CRK7 kinase domain, on the other hand, hindered conclusions regarding its activity, although it is not evidence of lack thereof either, as phosphosites do not always affect protein electrophoretic mobility. Additionally, the introduction of an alanine replacing a serine/threonine in the kinase domain of CRK2 and CRK36, respectively, aimed to address if these residues were potentially

phosphorylated in the WT sequences. Curiously, the increased shifts displayed by His-CRK2kd^{WT} and His-CRK36kd^{WT} compared to their mutant counterparts suggest that the serine and threonine residue in subdomain III of their kinase domains are, indeed, auto-phosphorylation sites *in situ*. Extrapolating this observation to a scenario *in vivo*, it is puzzling that a phosphorylated threonine on this position in CRK10 leads to detrimental effects in plant growth, whereas other members of the family contain a phosphorylation site in that position, with no penalty to the plant. Taken together, these facts raise a number of questions: why have different members of the CRK family in Arabidopsis evolved to contain an alanine or a serine/threonine at this specific position within their αC-helix? And how does a threonine in the αC-helix of CRK10, phosphorylated or not, have a deleterious effect for the plant, but seemingly not incur any problems in other members of the family, such as CRK2 and CRK36? Moreover, could this be an evolutionarily important regulatory site in the kinase domain of the CRK family? And, finally, is the presence of an alanine, serine or threonine in this position correlated to the biological function played by these CRKs? In conclusion, although the strategy used in this study provided valuable preliminary information regarding the auto-phosphorylation activity of the kinase domain of these CRKs *in situ*, analysis of the purified proteins by LC-MS/MS would be required to confirm the presence of and identify phosphorylated residues, as it was performed for CRK10.

Finally, it is important to bear in mind that the identification of phosphorylation sites *in situ* / *in vitro* is not evidence of their phosphorylation *in vivo*, which is ultimately necessary for the characterisation of their biological relevance. However, assessment of phosphorylation sites *in vitro* from recombinant kinase domains expressed in bacterial cells, such as the results reported in this chapter, proved to be an excellent tool for the identification of the auto- and trans-phosphorylation sites in these kinase domains, which can subsequently be used as targets for mutagenesis studies *in vivo* (Mitra et al., 2015). The reliability of this method has also been highlighted by the observation that most phosphorylation sites identified *in vivo* were also phosphorylated by the recombinant kinase domains *in vitro*, validating this method as a preliminary tool to investigate the kinase domain of plant RLKs (Mitra et al., 2015). It is also important to remember what an invaluable resource it is to identify a mutant such as the *crk10-A397T*, given how challenging the investigation of the biological

function of RLKs is without the knowledge of their activating signal. The identification of regulatory sites within the kinase domain, such as position 397 in CRK10, opens a new avenue which can potentially be used to explore the function and regulation of other members of the family.

Although the questions raised in this chapter will require further experiments to be answered, these results confirm that threonine 397 can be auto-phosphorylated by CRK10 *in situ*, and mutations at this position also seem to affect the auto-phosphorylation status of other members of the CRK family of Arabidopsis. Although a mechanistic explanation for the gain-of-function effect promoted by this mutation cannot be concluded from the experiments presented in this chapter, the location of this mutation site within the regulatory αC-helix offers hints at how threonine 397 might affect kinase activity and regulation (see section 8.2 for further discussion).

Chapter 5 – Analysis of the transcriptome of the hypocotyl tissue of *crk10-A397T* mutant plants

5.1 Introduction

Plant RLKs are activated upon binding to an extracellular ligand, which triggers receptor oligomerisation and auto- and trans-phosphorylation of their cytoplasmic kinase domains (see section 1.2 for a detailed description of the structure and mechanism of action of RLKs). Once activated, the RLK initiates a signal transduction cascade which includes protein kinases, second messengers and transcription factors (Yang et al., 1997; Clark et al., 2001; see section 1.1 for a review on eukaryotic signalling cascades). A successful signalling cascade requires the spatial and temporal coordination of these components to relay the signal in the intracellular environment, which culminates with the transcriptional reprogramming of genes to promote cellular responses (Chrispeels et al., 1999). Pathogen-elicited signalling cascades, for example, involve the transcriptional induction of several plant protectants and defence genes, such as glutathione-S-transferases (GSTs), hydrolytic enzymes, peroxidases, pathogenesis-related (PR) proteins and phytoalexin biosynthetic enzymes (Hammond-Kosack and Jones, 1996). These changes in gene expression are achieved via the activity of transcription factors (TFs), DNA-binding proteins which recognize specific cis-elements of promoter regions in the genome and induce or repress the transcription of specific sets of genes. TFs themselves are tightly regulated at the transcriptional and post-translational levels to avoid misregulation of their targets (Zhu et al., 1996). Post-translational mechanisms such as reduction or oxidation, phosphorylation, sequestration in distinct subcellular compartments and interaction with repressor proteins are some of the strategies used to control TF activity (Moore et al., 2011).

Gain-of-function mutations which promote RLK activation and spontaneously trigger downstream responses in the absence of the extracellular ligand constitute a useful tool to investigate their biological roles. A strategy to identify the signalling cascades activated downstream of these receptors is to analyse the transcriptome of the mutant plants. Thus, an RNA-sequencing experiment was designed to compare the transcriptome of *crk10-A397T* mutant and WT Col-0 plants. Isolated hypocotyls were chosen as the tissue of interest for this experiment due to several reasons. Firstly, despite *CRK10* expression

being detected in vascular tissues of root, hypocotyl and inflorescence stem (section 3.3.5), the collapse of xylem vessels was only observed in roots and hypocotyls of the *crk10-A397T* plants (sections 3.3.2 and 3.3.3), suggesting the signalling pathways activated downstream of the *crk10-A397T* allele induce cellular responses in this organ which ultimately affect xylem vessel morphology. Secondly, considering the developmental gradient within the root, from primary growth in the young root tip to ongoing secondary growth at the mature root-hypocotyl junction, sampling of root sections undergoing different developmental stages could be a potential confounding effect for the interpretation of the transcriptomic dataset. Unlike the roots, early cessation of elongation in the hypocotyl leads to the absence of a developmental gradient and makes it a more convenient sample for this experiment.

Therefore, to provide a comprehensive scenario of the transcriptional reprogramming happening in the *crk10-A397T* mutant throughout plant development, whole hypocotyls were sampled at three time points: two, three and five weeks after sowing (WAS). These time points were selected in the hope they would provide a comprehensive snapshot of the transcriptional changes orchestrated by the putative gain-of-function of *CRK10* before (two WAS), during (three WAS) and after (five WAS) xylem vessel collapse occurs. In this chapter, the analysis of the transcriptome of *crk10-A397T* mutant plants is reported, including Gene Ontology (GO) Enrichment analysis, similarity comparisons with deposited microarray datasets, and an in-depth analysis of differentially expressed genes associated with specific biological processes / functional categories.

5.2 Materials and Methods

5.2.1 Experimental design of RNA-sequencing experiment

The experiment was designed to include three discrete developmental time points of the hypocotyl of WT and *crk10-A397T* mutant plants (two, three and five WAS), which correspond to time points analysed by light microscopy. Plants were grown in multi-cell trays (40 cells per tray) under standard growth conditions as described in section 2.1. The trays were removed from the growth cabinets and transferred to the laboratory, where sample collection was performed in a clean environment. A ceramic tile was placed on top of a container

with ice to ensure the work surface was kept cold at all times. All surfaces and materials were thoroughly wiped with 70% ethanol. For the isolation of the hypocotyls, Arabidopsis plants were carefully removed from pots and rinsed with sterile deionised water to ensure the removal of leftover compost. The hypocotyls were carefully excised using a carbon steel sterile blade (N° 10 Dermaplane Scalpel blade; Swann Morton Ltd) by performing two cuts perpendicular to the hypocotyl axis at the root-hypocotyl and rosette-hypocotyl junctions. Each hypocotyl was immediately transferred into a sterile 1.5 mL microfuge tube kept in liquid nitrogen. Pools of 50-60 hypocotyls were collected per biological replicate, and four biological replicates were sampled per genotype for each time point, accounting for 24 samples in total. Samples were stored at -80 °C until further processing.

5.2.2 RNA extraction from Arabidopsis hypocotyls

Microfuge tubes containing frozen hypocotyls were removed from the -80 °C freezer and placed in liquid nitrogen in a benchtop Dewar flask. Fresh 1.5 mL microfuge tubes and stainless-steel spatulas were kept in liquid nitrogen prior to coming in contact with the samples to avoid thawing of the tissue. A set of sterile pestle and mortar was used to grind each biological sample in liquid nitrogen until a fine powder was obtained. The powder was immediately transferred into a sterile 1.5 mL microfuge tube using a stainless-steel spatula, and the tubes were quickly returned to liquid nitrogen. Total RNA was extracted from the ground hypocotyl samples using the RNeasy® Plant Mini Kit (QIAGEN; refer to manufacturer's handbook of protocol for details). A 450 µL aliquot of lysis buffer (Buffer RLT) was added to each tube and samples were vortexed vigorously. Samples were transferred to a QIAshredder spin column and centrifuged at 11,350 x g for two minutes. The supernatant of the flow-through was carefully transferred to a new sterile 1.5 mL microfuge tube without disturbing the cell debris pellet in the collection tube. A 0.5x aliquot of 96% ethanol was added to the cleared lysate and mixed by pipetting. Samples were transferred to RNeasy® spin columns and centrifuged at 6,720 x g for 15 seconds. After discarding the flow-through, the columns were washed with 700 µL of a stringent washing buffer (Buffer RW1) and 500 µL of a mild washing buffer (Buffer RPE), consecutively. Each wash step was followed by centrifugation at 6,720 x g for 15 seconds. A third wash step with 500 µL of Buffer RPE was performed and the tubes were

centrifuged at 6,720 x g for two minutes. The columns were transferred to new, sterile 2 mL microfuge tubes and centrifuged for one minute at 11,350 x g to completely remove traces of wash buffers from the membranes and avoid carryover of the flow-through from previous steps. For the RNA elution step, the columns were transferred to fresh sterile 1.5 mL microfuge tubes, and 50 µL of sterile deionised water was pipetted directly onto the column membrane. The tubes were centrifuged for one minute at 6,720 x g and the samples were immediately transferred to a container with ice. The concentration of the RNA extracts was determined with a NanoDrop™ (Thermo Scientific™) spectrophotometer (section 2.11).

5.2.3 DNase treatment of RNA samples

RNA samples used for the RNA sequencing experiment were treated with Turbo DNA-*free*™ kit (Catalogue number AM1907; Invitrogen™) for the removal of genomic DNA. The reactions were prepared as described in Table 5.1, and the samples were incubated at 37 °C for 30 minutes. The reaction was terminated by the addition of 2 µL of DNase inactivation reagent to each sample and incubation at room temperature for five minutes. The samples were centrifuged at 11,350 x g for one minute to pellet the inactivation reagent, and the DNase-treated RNA samples were transferred to fresh 1.5 mL microfuge tubes. The concentration of the RNA samples was determined with a NanoDrop™ (Thermo Scientific™) spectrophotometer (section 2.11).

Table 5.1 Reaction mix for DNase treatment of RNA samples with Turbo DNA-*free*™ kit (Invitrogen™).

Reagent	**Volume (µL)**	**Final concentration**
10x TURBO DNase™ Buffer	5	1x
RNA (2.5 – 5 µg)	Variable	Variable
TURBO DNase™ enzyme (2 U / µL)	1	0.04 U / µL
Sterile water	Up to 50 µL	-

5.2.4 RNA quality assessment

RNA quality was assessed for each sample using an Agilent 2100 Bioanalyzer instrument (Agilent Technologies©). Chips and reagents from the RNA 6000 Nano kit (Agilent Technologies©) were used. The gel-dye mix was loaded into the chips, and 5 µL of the RNA marker was added to all sample wells. One µL of each sample (total RNA concentration ~50-100 ng/µL) and 1 µL of RNA ladder were loaded into individual wells. The chip was inserted in the instrument and the results were acquired with the 2100 Expert software. All samples displayed an RNA integrity number (RIN) equal to or above 9, which deemed them suitable for sequencing.

5.2.5 Library preparation and RNA sequencing

A total amount of 1 – 5 µg of RNA per sample were transferred to 1.5 mL microfuge tubes and the final volume was adjusted to 50 µL with sterile deionised water. The samples were shipped in dry ice to the University of Exeter (Streatham Campus, Exeter, UK) where they were used for cDNA library preparation (polyA isolation with TruSeq directional library preparation) by the Exeter Sequencing Service. Sequencing was performed with an Illumina HiSeq instrument (125 bp read length, paired-end sequencing).

5.2.6 RNA-Seq quality control and differential gene expression analysis

Sequencing results provided an average number of 10.8 million paired-end reads per sample. The processing and analysis of the sequencing results were performed in collaboration with Dr Daniel Smith (Department of Computational and Analytical Sciences, Rothamsted Research, UK). Using the Rothamsted instance of the Galaxy (https://usegalaxy.org/) bioinformatics web pipeline, the quality of the reads was assessed using MultiQC (https://multiqc.info/). The Trimmomatic tool (Bolger et al., 2014) was used to trim the reads, which were subsequently mapped to the reference *Arabidopsis thaliana* genome with HiSAT2 (Kim et al., 2015; https://daehwankimlab.github.io/hisat2/). The table of counts was acquired using the featureCounts functions in Subread (Liao et al., 2019; https://bioconductor.org/packages/release/bioc/html/Rsubread.html) on the R Bioconductor platform (https://bioconductor.org/). Genes which displayed a

number of counts equal or higher than five in less than three samples were discarded at this stage. Quality control tests were performed and differentially expressed genes were identified (using the default Wald test) using the R (v3.6.1) Bioconductor package DESeq2 (Love et al., 2014; https://bioconductor.org/packages/release/bioc/html/DESeq2.html). Differentially expressed genes below / above a threshold of $\log_2$ fold change ≥ 1 or ≤ -1 were considered for subsequent analysis.

5.2.7 Gene Ontology analyses

Gene Ontology (GO) overrepresentation analysis was performed for the set of 274 genes differentially expressed at all time points (core genes) using the Single Enrichment Tool in AgriGO v2.0 (Tian et al., 2017). The lists of up- and down-regulated core genes were analysed separately. The following settings were used:

Analysis type: Singular Enrichment Analysis

Suggested background: TAIR genome locus (TAIR10_2017)

Statistical method: Fisher

Multi-test adjustment method: Yekutieli (FDR under dependency)

Significance level: 0.05

Minimum number of mapping entries: 5

Gene Ontology type: Complete GO

5.2.8 Transcriptomic similarity analyses

Similarity comparison with deposited micro-array datasets was performed with the GENEVESTIGATOR® Signature tool (Hruz et al., 2008). The 274 core differentially expressed genes and their respective average $\log_2$ fold change of all three experimental time points were used as input. The Arabidopsis AT_AFFY_ATH1-0 gene chip was selected as reference. The top 50 perturbations which generated the most similar transcriptional signature to the *crk10-A397T* mutant were retrieved as output.

5.2.9 Quantification of hormones from hypocotyls of Arabidopsis plants

Hypocotyl samples (75 – 100 mg fresh weight) isolated from 3-week-old plants were used for the quantification of hormones as described in Camut et al.,

2019. The following protocol was performed by Dr Esther Carrera (Institute for Plant Molecular and Cell Biology, University of Valencia, Spain). A 2.6 µm Accucore RP-MS column (100 mm length x 2.1 mm i.d.; Thermo Scientific™) and a Q-Exactive mass spectrometer (Orbitrap detector; Thermo Scientific™) were used. The concentrations of hormones in the extracts were determined using embedded calibration curves and the Xcalibur 4.0 and TraceFinder 4.1 SP1 programs. Three biological replicates per genotype were analysed.

5.2.10 Gene network generation

Gene networks were generated with the *Arabidopsis thaliana* resource page in the KnetMiner website (Hassani-Pak et al., 2021; https://knetminer.com/Arabidopsis_thaliana/). Lists of genes related to biological processes of interest were searched using the "Keyword search" option, and DEGs identified in the *crk10-A397T* mutant transcriptome were selected to generate the networks.

5.2.11 Validation of RNA-Seq results with qPCR

In order to validate the transcriptional changes indicated by the RNA-Seq experiment, the transcript abundance of selected DEGs in hypocotyls of 3-week-old WT and *crk10-A397T* plants was quantified by qPCR. Sample collection and RNA extraction were performed as described in section 2.5. Ten hypocotyls were processed together per biological replicate, and three biological replicates were analysed per genotype. DNsase treatment, cDNA synthesis and qPCR reactions were performed as described in sections 2.12, 2.13 and 2.15, respectively. The *ACTIN2* and *UBC21* genes of Arabidopsis were used as internal controls in the reactions. The relative expression of target genes was calculated using the $2^{-\Delta\Delta Ct}$ method (Livak and Schmittgen, 2001). Primers sequences are listed in Table 5.2.

Table 5.2 Table of primers.

Primer	**Sequence (5' – 3')**	**Purpose**
AtACT2 For	TTCCCTCAGCACATTCCAGCAGAT	qPCR
AtACT2 Rev	AACGATTCCTGGACCTGCCTCATC	qPCR
AtUBC21 For	GCTCTTATCAAAGGACCTTCGG	qPCR
AtUBC21 Rev	CGAACTTGAGGAGGTTGCAAAG	qPCR
PR1 For	ATGAATTTTACTGGCTATTTCTCGGA	qPCR

PR1 Rev	CAAACTCCATTGCACGTGTTCGCA	qPCR
PR2 For	TCCTTCTTCAACCACACAGCTGGA	qPCR
PR2 Rev	CCCACTTGTCGGCCTCCGTT	qPCR
PR5 For	CTCGTGTTCATCACAAGCGGCA	qPCR
PR5 Rev	AGCTTGGGTCCTTGACCGGC	qPCR

5.3 Results

5.3.1 RNA sequencing results

In order to identify differentially expressed genes in the hypocotyls of *crk10-A397T* mutant plants, a transcriptome analysis of Col-0 WT and *crk10-A397T* mutant hypocotyls at two, three and five WAS was performed. The time points were chosen as to cover relevant stages of the mutant development, immediately before, during and after the collapse of xylem vessels occurs (see section 3.3.3). Library preparation and sequencing were performed by the Exeter Sequencing Service (University of Exeter), and an average of 10.8 million reads per biological replicate were returned (paired-end sequencing, 125 bp reads). Principal component analysis (PCA) of the sequencing results showed that clusters of biological replicates were clearly distinguishable from each other (Figure 5.1), a clear indication of differences between genotypes and developmental stages. The package DESeq2 (Bioconductor) was used to identify differentially expressed genes, and those with a $\log_2$ fold change greater/smaller than +1/-1 were considered for further investigation. A total of 523 (two WAS), 1836 (three WAS) and 913 (five WAS) differentially expressed genes (DEGs) were identified in the *crk10-A397T* mutant in comparison to WT hypocotyls. Subsets of DEGs were differentially expressed at more than one developmental stage, which is evidenced by the overlap between time points observed in a Venn diagram (Figure 5.2 A). A subset of 274 genes were differentially regulated all three time points, and this group was considered as the “core” set of DEGs for subsequent analyses. All three time points showed a greater proportion of up-regulated genes compared to the total number of DEGs (Figure 5.2 B).

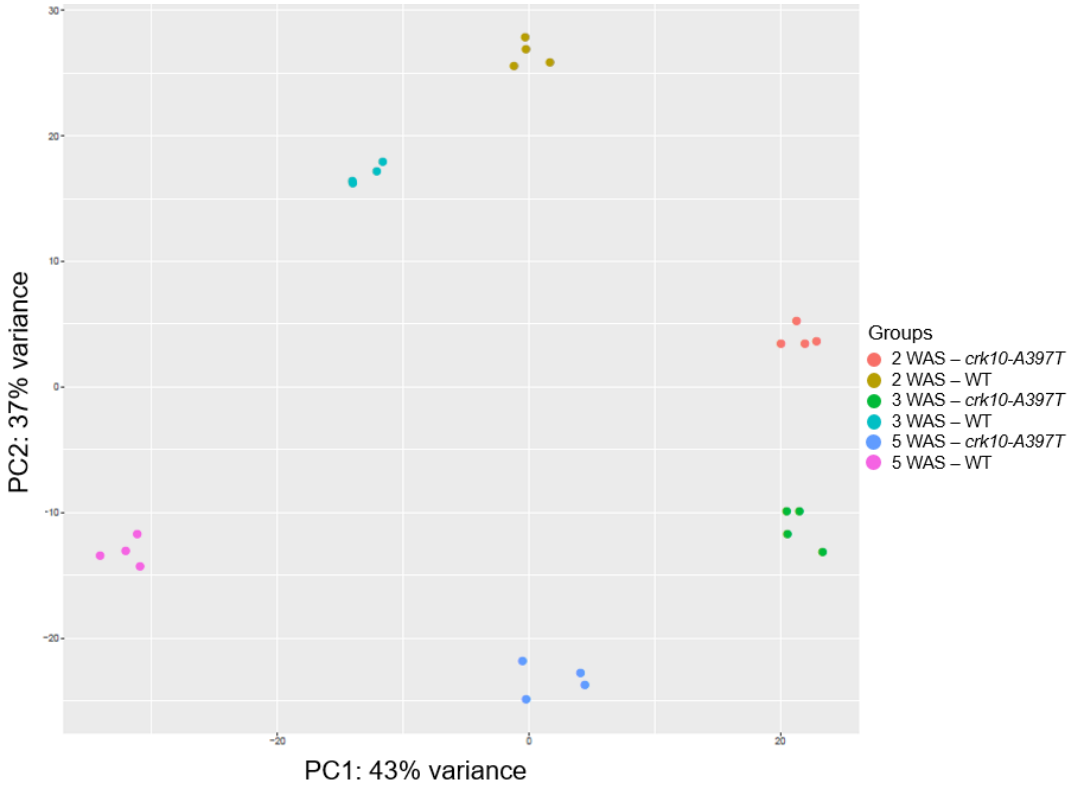

Figure 5.1 Principal component analysis (PCA) plot of RNA sequencing samples. A principal components analysis (PCA) plot was generated using the PCA plot function in the Bioconductor package DESeq2 (https://rdrr.io/bioc/DESeq2/man/rlog.html). WAS, weeks after sowing.

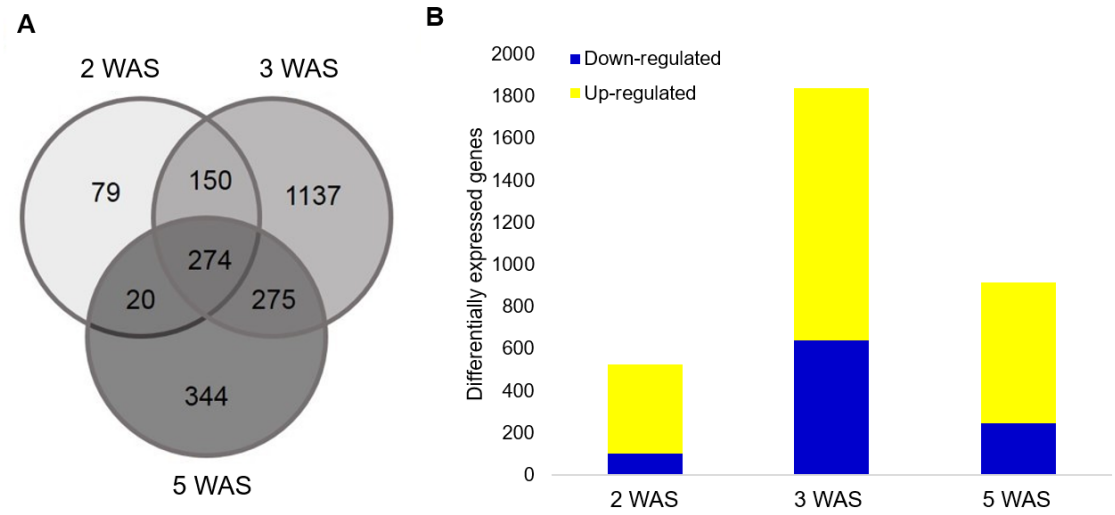

Figure 5.2 Differentially expressed genes at three developmental stages in *crk10-A397T* mutant hypocotyls.

(A) Venn diagram showing the number of differentially expressed genes (DEGs) in hypocotyls of *crk10-A397T* plants at each time point of the RNA sequencing experiment. Overlapping areas of the diagram indicate the number of genes which are differentially expressed in two or all three time points. WAS, weeks after sowing.

(B) Bar chart showing the number of up- and down-regulated genes at each individual time point of the experiment.

5.3.2 Gene Ontology Enrichment analysis of differentially expressed genes in the *crk10-A397T* mutant

To elucidate which biological processes are constitutively affected by the *crk10-A397T* mutant allele, a GO enrichment analysis was performed (AgriGO v2.0; Tian et al., 2017) using the core set of 274 DEGs as input. The analysis was carried out independently for the subsets of up- (246) and down-regulated (28) genes to allow the identification of induced and repressed pathways, respectively. Complete lists of the top 25 GO terms ranked according their False Discovery Rate (FDR) can be found in Appendix 9.1.

The GO enrichment analysis of the 246 up-regulated core genes returned terms mainly associated with responses to biotic and abiotic stresses under the Biological Process category (Figure 5.3 A). The three highest ranking terms, “Defence response” (GO:0006952), “Response to stimulus” (GO:0050896) and “Response to stress” (GO:0006950), were associated with 65, 127 and 93 genes,

respectively, disclosing the prominent induction of stress-responsive genes in the hypocotyl of the *crk10-A397T* mutant. More specifically, GO terms associated with biotic stresses were prevalent at the top of the list, such as “Response to external biotic stimulus” (GO:0043207), “Response to other organism” (GO:0051707) and “Multi-organism process” (GO:0051704). The terms “Innate immune response” (GO:0045087) and “Systemic acquired resistance” (GO:0009627) feature further down the list, and strengthen the evidence suggesting the constitutive induction of defence responses to pathogens in the hypocotyls of the mutant plants. Furthermore, the terms “Response to toxic substance “(GO:0009636) and “Toxin metabolic process” (GO:0009404) hint at the induction of detoxification processes, which is endorsed by the enrichment of genes under the “Glutathione transferase activity” (GO:0004364) category in the Molecular Function ontology table (Figure 5.3 B). This term was second only to “Catalytic activity” (GO:0003824), which was associated with over 50% of the up-regulated core genes. Overall, these results revealed the constitutive induction of genes involved with defence to stresses, especially those of biotic nature, including a large proportion of genes with catalytic activity.

In contrast, the short list of 28 core genes which were down-regulated in the hypocotyl of the *crk10-A397T* mutant reflected the repression of genes involved in RNA metabolism and DNA transcription (Figure 5.4 A). The top scoring terms included “Regulation of RNA metabolic process” (GO0051252), “RNA biosynthetic process” (GO:0032774) and “Nucleic acid-templated transcription” (GO:0097659), suggesting the repression of gene expression. Several terms related to the regulation of cellular processes also featured in the list, such as “Regulation of gene expression” (GO:0010468), “Regulation of cellular metabolic process” (GO:0031323) and “Regulation of cellular biosynthetic process” (GO:031326). In agreement with the biological processes identified by the enrichment analysis, three molecular function categories were found to be associated with the down-regulated core genes: “Transcription factor activity, sequence-specific DNA binding” (GO:0003700), “Nucleic acid binding transcription factor activity” (GO:0001071) and “DNA binding” (GO:0003677) (Figure 5.4 B). Taken together, these results indicate that the 28 genes which are constitutively repressed in the hypocotyl of the *crk10-A397T* mutant are enriched with transcription regulators.

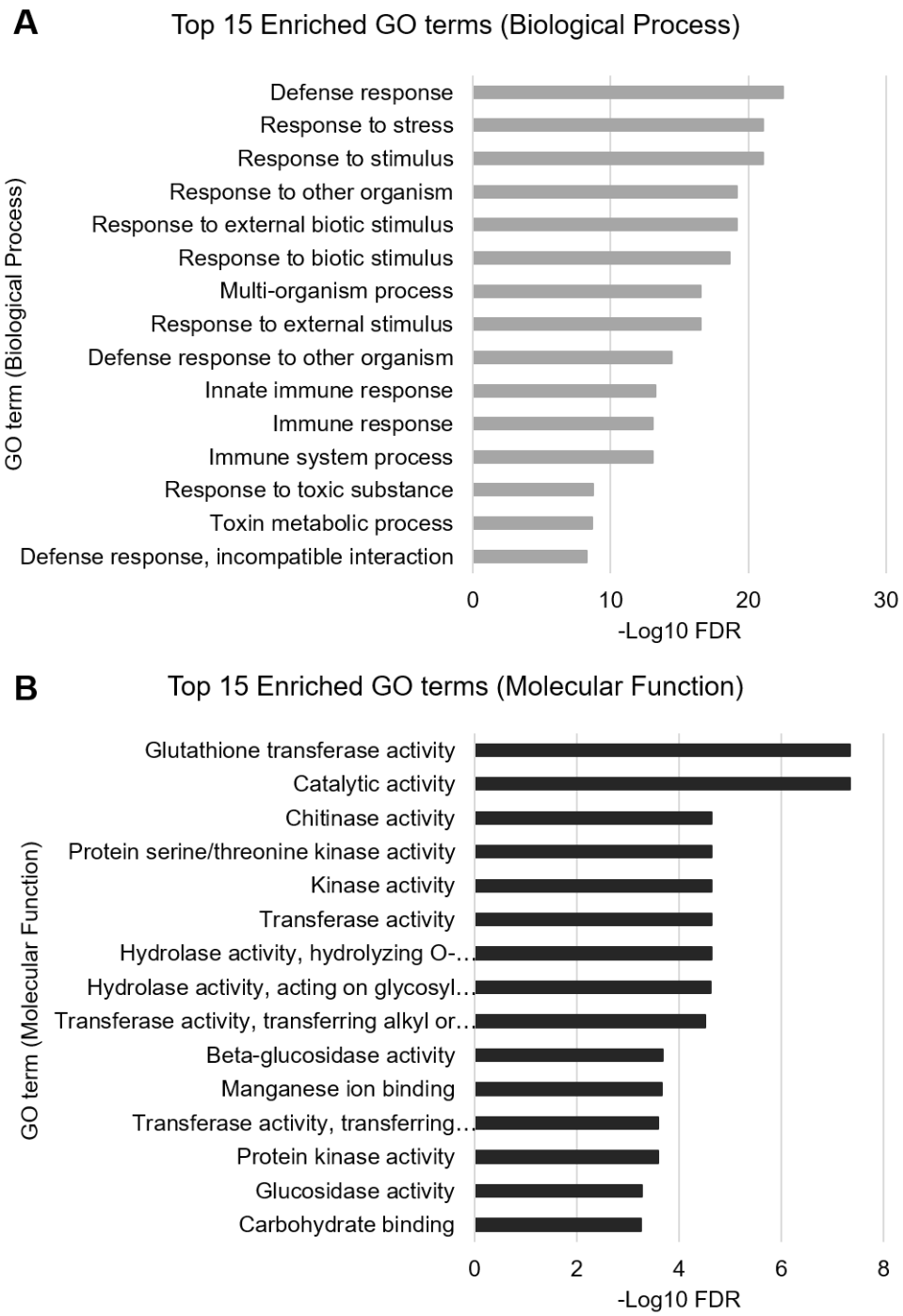

Figure 5.3 GO terms associated with defence responses to biotic and abiotic stresses, glutathione S-transferase and catalytic activity were significantly enriched among the up-regulated core DEGs of the *crk10-A397T* mutant transcriptome.

Charts show top 15 GO terms under the categories of (A) Biological Process and (B) Molecular Function which are enriched among the up-regulated core DEGs of the *crk10-A397T* transcriptome. GO terms are ranked according to the $-\text{Log}_{10}$ False Discovery Rate (FDR). The full description of abbreviated GO terms can be found in Appendix 9.1.1 and 9.1.2.

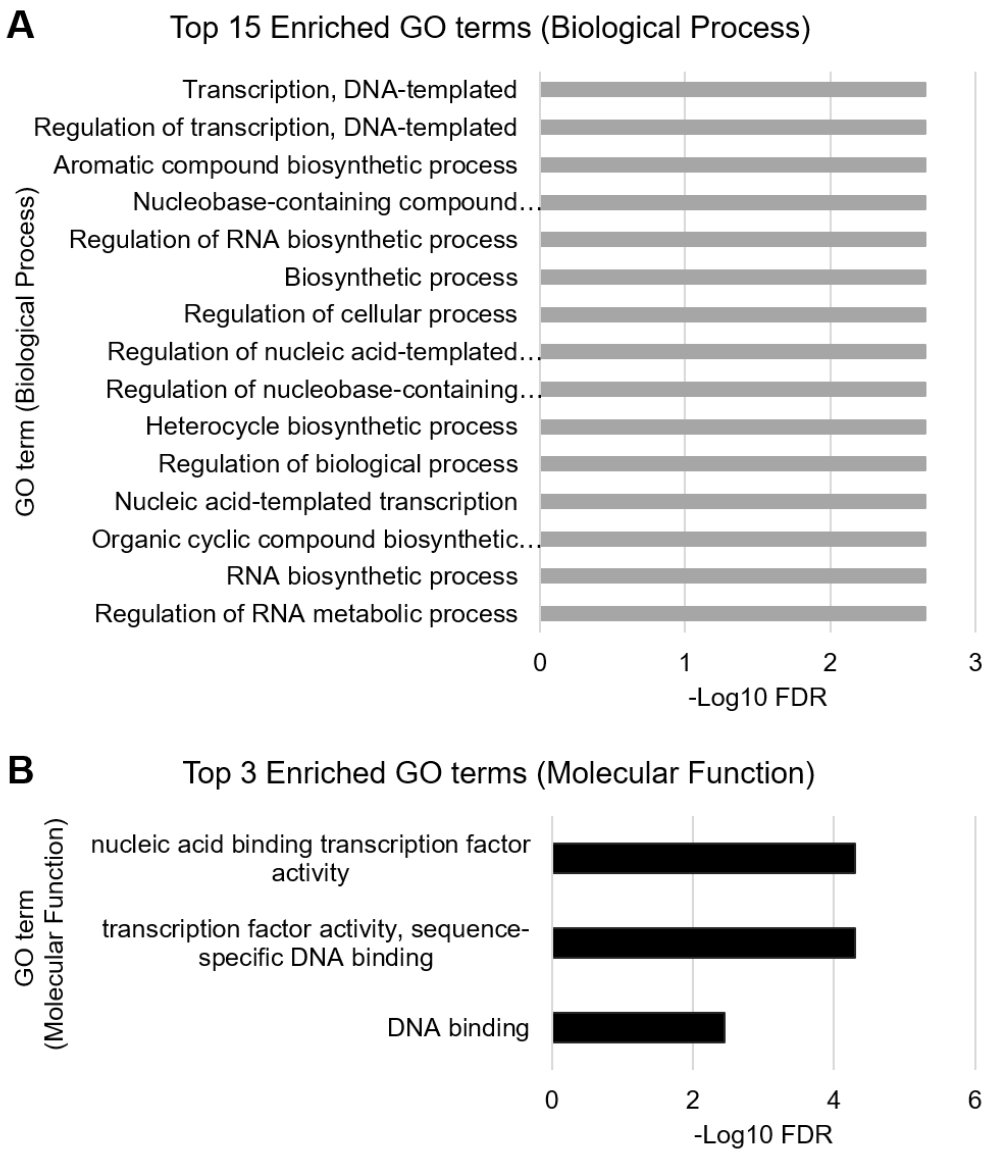

Figure 5.4 GO terms associated with gene expression and transcription factor activity were significantly enriched among the down-regulated core DEGs of the *crk10-A397T* mutant transcriptome.

Charts show top 15 GO terms under the category of (A) Biological Process and Top 3 under the category of (B) Molecular Function which are enriched among the up-regulated core DEGs of the *crk10-A397T* transcriptome. GO terms are ranked according to the $-\text{Log}_{10}$ False Discovery Rate (FDR). The full description of abbreviated GO terms can be found in Appendix 9.1.3 and 9.1.4.

5.3.3 Similarity analyses of the *crk10-A397T* mutant transcriptome using the Signature tool (GENEVESTIGATOR®)

Another useful strategy for the interpretation of transcriptomic results is to compare it with other public datasets to identify similar transcriptional signatures. This analysis is particularly useful to elucidate the transcriptome of a mutant such as the *crk10-A397T*, as the identification of factors and/or conditions which trigger similar transcriptional changes might provide hints at the biological processes regulated by the mutant allele. To perform these comparisons, the Signature tool of the GENEVESTIGATOR® programme was used. The average $\log_2$ fold change of the 274 core genes (272 of which are present in the AT_AFFY_ATH1-0 gene chip) was used as input.

The analysis revealed that pathogen attack is among the perturbations which trigger the most similar signature of transcriptional changes compared to the *crk10-A397T* mutant transcriptome (Figure 5.5). For instance, the list includes the signature of WT Col-0 plants challenged with the fungal pathogen *Alternaria brassicicola* (AT-00661), the oomycete *Phytophthora parasitica* (AT-00425) and the biotrophic bacterial pathogen *Pseudomonas syringae* pv. *maculicola* (AT-00406), with the latter being the third most similar signature to the *crk10-A397T* mutant. The transcriptional reprogramming triggered by the powdery mildew *Golovinomyces orontii* (AT-00614) in WT Col-0 plants, which involves the regulation of genes involved with cell wall modification, alkaloid metabolism and redox homeostasis, also resembles the *crk10-A397T* mutant dataset (Chandran et al., 2009). Other highly similar signatures are the ones triggered by the necrotrophic pathogen *Sclerotinia sclerotiorum* upon infection of *coi1-2* mutant and WT Col-0 plants (AT-00681). Changes in their transcriptome include the induction of genes involved in the metabolism of glucosinolates and camalexin (Guo and Stotz, 2007; Stotz et al., 2011). The transcriptome of the *agb1-1* mutant undergoing infection with another necrotrophic pathogen, *Plectosphaerella cucumerina* (AT-00648) was also fund among the highest-ranking experiments. Interestingly, the susceptibility of the *agb1-1* mutant, which is impaired in the Gβ subunit of the heterotrimeric G-protein, was shown to be independent of the SA, JA, ABA and ethylene pathways, but rather related to the misregulation of genes involved in cell wall composition (Delgado-Cerezo et al., 2011).

Adding to the evidence that the *crk10-A397T* mutation induces defence responses to pathogens in Arabidopsis, the transcriptome of auto-immune

mutants also exhibit high similarity to that of the *crk10-A397T* mutant hypocotyls. The mutants *mkk1 mkk2* (AT-00291), *mpk4 ctr1* (AT-00180) and *ssi2-1* (AT-00630), all of which accumulate salicylic acid (SA) and show activation of defence responses (Shah et al. 2001; Brodersen et al., 2006; Qiu et al., 2008), feature among the top 25 most similar signatures. The prevalence of SA-related responses in the transcriptome of the *crk10-AA397T* mutant is also reflected in the resemblance with the transcriptomic signature of WT Col-0 plants following treatment with SA (AT-00320).

Exposure to a variety of chemicals also appears in several positions along the list. The safener derivative CMP (4-chloro-6-methyl-2-phenylpyrimidine), which induces the expression of detoxifying enzymes as part of the xenobiotic response (XR) in Arabidopsis (Skipsey et al., 2011), holds the second place in the similarity ranking (AT-00459). The list goes on with the neonicotinoid imidacloprid (AT-00544), the small molecule DFPM (5-(3,4-Dichlorophenyl)Furan-2-yl]-Piperidin-1-ylMethanethione; AT-00541), and the herbicides sulfometuron methyl (AT-00533), primisulfuron and cloransulam-methyl (AT-00532). Interestingly, imidacloprid was shown to induce SA defence responses in Arabidopsis, including systemic acquired resistance and enhanced resistance to a powdery mildew (Ford et al., 2010). Arabidopsis plants treated with DFPM displayed up-regulation of genes involved with defence to pathogens, such as *EDS1* and *PR5* (Kim et al., 2012). Exposure to sulfometuron methyl was shown to induce the expression of genes involved in responses to stresses such as detoxifying enzymes, indole derivative and camalexin metabolic process and response to temperature, while on the other hand causing the repression of expansins, which are involved in cell wall modifications (Das et al., 2010).

In conclusion, this analysis undoubtedly reveals that biotic and abiotic stresses induce a similar transcriptional signature to that of *crk10-A397T* mutant hypocotyls. Taken together with the GO term enrichment analysis, these results suggest that this gain-of-function allele initiates signalling cascades involved with adaptation to stresses.

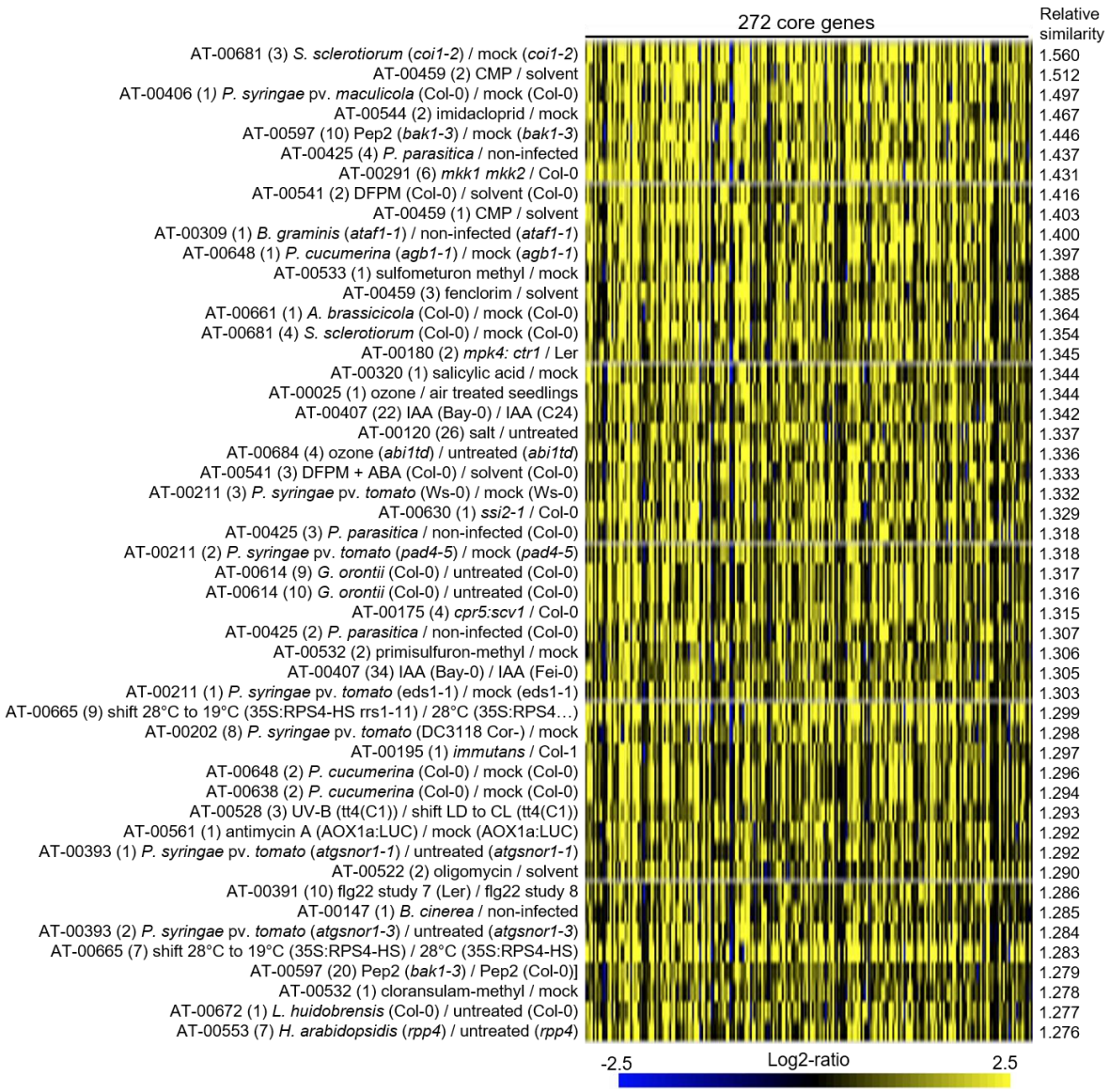

Figure 5.5 Top 50 most similar transcriptome signatures to the *crk10-A397T* mutant.

Top 50 transcriptomic signatures identified with the Signature tool (GENEVESTIGATOR®) which resemble the core transcriptome of the *crk10-A397T* mutant hypocotyls. The set of 274 genes differentially expressed at all time points of this RNA sequencing experiments (core DEGs) was entered as the input signature (272 of which are present in the AT_AFFY_ATH1-0 gene chip).

5.3.4 Analysis of the up-regulation of genes involved with defence responses to pathogens in the *crk10-A397T* mutant

GO term enrichment analysis revealed that genes associated with defence responses to biotic and abiotic stresses are prominent among the core DEGs in the *crk10-A397T* transcriptome (section 5.3.2). This notion was corroborated by the resemblance displayed between the *crk10-A397T* dataset and the transcriptomic signature of plants undergoing biotic and abiotic stresses (section 5.3.3). In order to provide a comprehensive overview of the transcriptional changes induced in the mutant hypocotyl throughout development, the next steps of the analyses were narrowed down to individual genes, including those which were differentially expressed at one or two time points only. Given the prevalence of defence responses to biotic stresses in the *crk10-A397T* mutant transcriptome, genes belonging to this category were analysed first.

Constitutive expression of pathogenesis-related (PR) genes, a hallmark of the activation of immune responses in plants, is one of the defining characteristics of the *crk10-A397T* transcriptome (Table 5.3). *PR1* (AT2G14610), *PR2* (AT3G57260) and *PR5* (AT1G75040), molecular markers for SA responses, show the greatest up-regulation among the differentially expressed PR genes in the mutant, although the induction of *PR3* (AT3G12500) and *PR4* (AT3G04720) suggests that SA-independent, JA-regulated pathways might also be up-regulated (Thomma et al., 1998; Seo et al., 2008). Constitutive induction of *CYP71A13* (AT2G30770) and *PHYTOALEXIN DEFICIENT 3* (*PAD3*, AT3G26830) indicates the production of camalexin, a major phytoalexin in Arabidopsis produced in response to pathogen attack (Zhou et al., 1999; Nafisi et al., 2007). The induction of the SA-related *ENHANCED DISEASE SUSCEPTIBILITY 1* (*EDS1*; AT3G48090) and its interacting partner *PHYTOALEXIN DEFICIENT 4* (*PAD4*; AT3G52430) further supports a role for the *crk10-A397T* allele in the activation of SA-related pathways (Feys et al., 2001; Brodersen et al., 2006). The flavin-dependent monooxygenase *FMO1* (AT1G19250), the protein *NIMIN-2* (AT3G25882) and the pipecolic acid biosynthetic enzyme *SAR-DEFICIENT 4* (*SARD4*; AT5G52810) are other critical components for the establishment of SAR which are transcriptionally up-regulated at two or more time points in the hypocotyl of the mutant plants (Weigel et al., 2001; Mishina and Zeier, 2006; Ding et al., 2016). Other highly up-regulated defence genes include the amino acid-conjugating enzyme *PBS3* (AT5G13320),

known to play a critical role in SA metabolism (Nobuta et al., 2007), and the ankyrin-repeat *BDA1* (AT5G54610), a signalling component of defence responses (Yang et al., 2012). Curiously, although SA-dependent pathways are up-regulated in *crk10-A397T* hypocotyls, the expression of *ISOCHORISMATE SYNTHASE 2* (AT1G18870), a key enzyme for SA biosynthesis normally expressed constitutively in Arabidopsis (Macaulay et al., 2017), is repressed at two and three WAS. This could be possibly caused by a negative feedback loop to fine-tune SA responses. Finally, the only member of the MAPK family which is differentially expressed in this dataset is *MITOGEN-ACTIVATED PROTEIN KINASE 11* (*MPK11*, AT1G01560), a MAPK known to be activated upon treatment with the bacterial elicitor peptide flg22 (Bethke et al., 2012).

Overall, the up-regulation of these genes indicates the concerted induction of SA- and SAR-related pathways in the *crk10-A397T* mutant hypocotyls. This is visually represented by a gene network generated with the query “salicylic acid” and “systemic acquired resistance” using the KnetMiner programme (https://knetminer.com/Arabidopsis_thaliana/), in which several of the defence-related genes induced in the *crk10-A397T* mutant hypocotyls are included (Figure 5.6).

Table 5.3 Differentially regulated genes in the *crk10-A397T* mutant transcriptome associated with defence responses to pathogens and responses to salicylic acid (SA).

UP-REGULATED GENES				
		Log_2 Fold Change		
Gene ID	**Gene name**	**2 WAS**	**3 WAS**	**5 WAS**
AT2G14610	*PATHOGENESIS-RELATED 1 (PR1)*	-	3.98	4.46
AT3G57260	*PATHOGENESIS-RELATED 2 (PR2)*	4.25	6.84	5.99
AT3G12500	*PATHOGENESIS-RELATED 3 (PR3)*	2.04	3.68	3.23
AT3G04720	*PATHOGENESIS-RELATED 4 (PR4)*	-	2.17	-
AT1G75040	*PATHOGENESIS-RELATED 5 (PR5)*	5.53	7.71	5.30
AT2G30750	*CYP71A12*	4.48	4.50	5.80
AT2G30770	*CYP71A13*	9.20	7.01	8.74
AT3G26830	*PHYTOALEXIN DEFICIENT 3 (PAD3)*	6.50	6.45	4.51
AT3G52430	*PHYTOALEXIN DEFICIENT 4 (PAD4)*	2.29	-	1.77

AT1G19250	*FLAVIN-DEPENDENT MONOOXYGENASE 1 (FMO1)*	2.63	4.75	7.48
AT3G48090	*ENHANCED DISEASE SUSCEPTIBILITY 1 (EDS1)*	1.88	1.79	2.04
AT5G54610	*ANKYRIN / BDA1*	2.68	3.43	6.8
AT5G13320	*AVRPPHB SUSCEPTIBLE 3 (PBS3)*	4.13	4.52	6.22
AT5G40990	*GDSL LIPASE 1 (GLIP1)*	6.20	6.30	2.59
AT2G31880	*SUPPRESSOR OF BIR 1 (SOBIR1)*	2.20	2.59	2.34
AT1G32960	*SUBTILASE 3.3 (SBT3.3)*	4.01	7.88	3.43
AT5G52810	*SAR DEFICIENT 4 (SARD4)*	1.96	-	2.94
AT3G25882	*NIM1-INTERACTING 2 (NIMIN-2)*	2.32	-	2.48
AT1G01560	*MITOGEN-ACTIVATED PROTEIN KINASE 11*	2.75	2.96	-
AT4G16890	*SUPPRESSOR OF NPR1-1, CONSTITUTIVE 1 (SNC1)*	-	1.61	-
DOWN-REGULATED GENES				
		Log_2 Fold Change		
Gene ID	**Gene name**	**2 WAS**	**3 WAS**	**5 WAS**
AT1G18870	*ISOCHORISMATE SYNTHASE 2 (ICS2)*	-2.12	-3.24	-

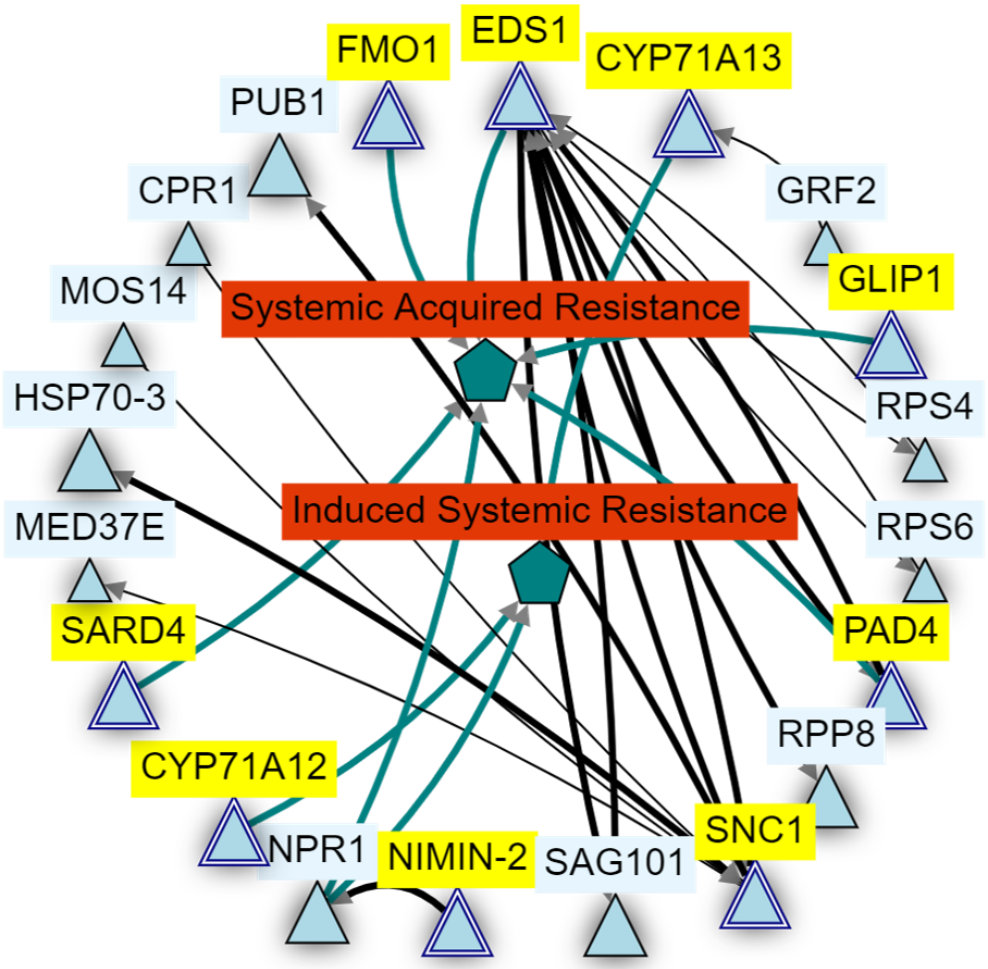

Figure 5.6 Defence-related genes which are up-regulated in the *crk10-A397T* mutant transcriptome are part of gene networks underlying disease resistance and systemic acquired resistance in Arabidopsis.

Gene network representing interactions between defence-related genes in Arabidopsis. Light blue triangles represent individual genes; those identified as differentially expressed in the *crk10-A397T* transcriptome are highlighted in yellow. The dark green pentagon represents a biological process (systemic acquired resistance / induced systemic resistance). Solid black lines indicate physical association between the proteins encoded by respective genes. Solid dark green lines indicate association between a gene and a biological process. Network created with KnetMiner (https://knetminer.com/Arabidopsis_thaliana/).

5.3.5 Analysis of the induction of genes involved with abiotic stress and detoxification processes in the *crk10-A397T* mutant

In addition to the prominent induction of genes associated with plant-pathogen interactions, the *crk10-A397T* mutant transcriptome also shows up-regulation of an extensive set of genes associated with detoxification and responses to stresses of abiotic origin (Table 5.4). This group includes detoxifying enzymes of the glutathione S-transferase (GST) family, some of which show high levels of transcriptional induction such as *GLUTATHIONE S-TRANSFERASE U11* (AT1G69930) and *GLUTATHIONE S-TRANSFERASE U12* (AT1G69920). The transcripts of *UDP-GLUCOSYL TRANSFERASE 73B4* (AT2G15490) and *PLANT CADMIUM RESISTANCE 2* (AT1G14870), which encode proteins capable of detoxifying the explosive 2,4,6-trinitrotoluene (TNT) and excess zinc, respectively (Gandia-Herrero et al., 2008; Song et al., 2010), also show significant up-regulation in the mutant hypocotyls. The production of the osmoprotectant galactinol is also induced at the transcriptional level, as galactinol synthases *GOLS2* (AT1G56600) and *GOLS4* (AT1G60470; Nishizawa et al., 2008) are up-regulated. Other constitutively induced genes, such as *AT12CYS-2 / TWIN CX9C DOMAIN PROTEIN* (AT5G09570) and *CHLOROPLASTIC ALDO-KETO REDUCTASE AKR4C9* (AT2G37770), showed an astonishing $\log_2$ fold change of over 9 and 8, respectively, at three WAS. AKR4C9 is thought to detoxify a range of stress-derived aldehydes and ketones (Simpson et al., 2009), while AT12CYS2 is induced by a variety of abiotic stresses and is responsive to genetic perturbations of the mitochondrial electron transport chain (Wang et al., 2016). Taken together, the up-regulation of these genes suggests that the *crk10-A397T* mutant allele also induces stress-responsive pathways tailored to mitigate abiotic stresses.

Table 5.4 Differentially regulated genes associated with detoxification roles in the *crk10-A397T* mutant**.**

		Log_2 Fold Change		
Gene ID	**Gene name**	**2 WAS**	**3 WAS**	**5 WAS**
AT4G02520	*GLUTATHIONE S-TRANSFERASE F2*	4.30	6.27	3.27
AT2G02930	*GLUTATHIONE S-TRANSFERASE F3*	-	6.19	-
AT1G02930	*GLUTATHIONE S-TRANSFERASE F6*	-	-	4.9
AT1G02920	*GLUTATHIONE S-TRANSFERASE F7*	3.19	4.74	4.13

AT2G29490	*GLUTATHIONE S-TRANSFERASE U1*	2.39	4.27	3.89
AT2G29480	*GLUTATHIONE S-TRANSFERASE U2*	2.68	5.1	5.61
AT2G29470	*GLUTATHIONE S-TRANSFERASE U3*	3.70	6.3	4.01
AT2G29460	*GLUTATHIONE S-TRANSFERASE U4*	-	4.66	-
AT2G29420	*GLUTATHIONE S-TRANSFERASE U7*	-	2.71	-
AT3G09270	*GLUTATHIONE S-TRANSFERASE U8*	-	1.68	-
AT5G62480	*GLUTATHIONE S-TRANSFERASE U9*	-	4.31	-
AT1G74590	*GLUTATHIONE S-TRANSFERASE U10*	3.62	4.41	2.55
AT1G69930	*GLUTATHIONE S-TRANSFERASE U11*	5.51	7.8	7.02
AT1G69920	*GLUTATHIONE S-TRANSFERASE U12*	6.11	6.82	6.77
AT1G59700	*GLUTATHIONE S-TRANSFERASE U16*	-	3.92	-
AT1G78380	*GLUTATHIONE S-TRANSFERASE U19*	-	1.96	1.51
AT1G17170	*GLUTATHIONE S-TRANSFERASE U24*	4.30	6.16	2.68
AT1G17180	*GLUTATHIONE S-TRANSFERASE U25*	-	8.14	6.45
AT3G43800	*GLUTATHIONE S-TRANSFERASE U27*	-	1.62	-
AT3G22370	*ALTERNATIVE OXIDASE 1A (AOX1A)*	2.04	5.72	2.45
AT5G09570	*AT12CYS-2 / TWIN CX9C DOMAIN PROTEIN*	5.65	9.81	7.42
AT3G13100	*ATP BINDING CASSETTE C7*	2.17	2.19	2.9
AT1G14870	*PLANT CADMIUM RESISTANCE 2*	2.57	2.96	3.52
AT1G71140	*PROTEIN DETOXIFICATION 14*	4.91	6.47	2.01
AT5G39050	*PHENOLIC GLUCOSIDE MALONYLTRANSFERASE 1 (PMAT1)*	1.93	4.2	2.72
AT2G37770	*CHLOROPLASTIC ALDO-KETO REDUCTASE AKR4C9*	4.12	8.23	3.83
AT2G40340	*DEHYDRATION-RESPONSIVE ELEMENT-BINDING PROTEIN 2C (DREB2C)*	-	3.28	-
AT1G56600	*GALACTINOL SYNTHASE 2 (GOLS2)*	2.55	4.94	-

AT1G60470	*GALACTINOL SYNTHASE 4 (GOLS4)*	3.25	5.29	4.43
AT2G15490	*UDP-GLUCOSYL TRANSFERASE 73B4*	3.04	8.08	5.2
AT2G30140	*UDP-GLYCOSYLTRANSFERASE 87A2 (UGT87A2)*	3.47	4.45	2.34

5.3.6 Analysis of abscisic acid (ABA)-related genes in the *crk10-A397T* mutant transcriptome

Despite not being present among the GO enrichment results, several genes involved with the biosynthesis, transport and signalling of the stress hormone abscisic acid (ABA) are also up-regulated in the *crk10-A397T* mutant hypocotyl tissue (Table 5.5). The regulator of ABA biosynthesis *9-CIS-EPOXYCAROTENOID DIOXYGENASE NCED5* (AT1G30100; Frey et al., 2011) and the plasma membrane ABA uptake transporter *ATP BINDING CASSETTE G40* (AT1G15520; Kang et al., 2010) are both strongly induced throughout development. Curiously, several ABA-responsive genes are exclusively induced at three WAS. One example is *ABSCISIC ACID-INSENSITIVE 5* (*ABI5*; AT2G36270), a transcription factor that plays roles in ABA signalling during germination and seedling establishment (Lopez-Molina et al., 2001). In contrast to the induction of genes involved with the biosynthesis, transport and signalling of ABA, the negative regulator of ABA signalling *ABSCISIC ACID-INSENSITIVE 2* (*ABI2*; AT5G57050) is also induced at three WAS. Taken together with the down-regulation of the ABA receptors *REGULATORY COMPONENT OF ABA RECEPTOR 1* (*RCAR1*) (AT1G01360) and *RCAR3* (AT5G53160; (Ma et al., 2009), these observations indicate a potential negative feedback loop to fine tune ABA responses in the mutant hypocotyls.

Table 5.5 Differentially regulated genes in the *crk10-A397T* mutant associated with abscisic acid (ABA) biosynthesis, transport and signalling.

UP-REGULATED GENES				
		Log_2 Fold Change		
Gene ID	**Gene name**	**2 WAS**	**3 WAS**	**5 WAS**
AT1G30100	*9-CIS-EPOXYCAROTENOID DIOXYGENASE (NCED5)*	4.26	7.26	-
AT1G66600	*ABA OVERLY SENSITIVE 3 (ABO3)*	3.73	2.30	6.26

AT1G65690	*NDR1/HIN1-LIKE PROTEIN 6 (NHL6)*	1.69	2.82	2.35
AT4G11890	*ABA- AND OSMOTIC-STRESS-INDUCIBLE RECEPTOR-LIKE CYTOSOLIC KINASE1(ARCK1) / CRK45*	2.07	3.72	3.27
AT1G15520	*ATP-BINDING CASSETTE G40 (ABCG40)*	5.68	9.64	7.75
AT1G69850	*ABA-IMPORTING TRANSPORTER 1 (AIT1)*	-	1.99	-
AT5G57050	*ABSCISIC ACID-INSENSITIVE 2 (ABI2)*	-	1.94	-
AT2G36270	*ABSCISIC ACID-INSENSITIVE 5 (ABI5)*	-	2.34	-
AT4G34220	*RECEPTOR DEAD KINASE 1*	-	1.56	-
AT5G04760	*DIVARICATA2*	-	2.25	-
AT2G26300	*G PROTEIN ALPHA SUBUNIT 1 (GP ALPHA 1)*	-	1.43	-
AT3G27250	*ABA-INDUCED TRANSCRIPTION REPRESSOR 1 (AITR1)*	5.10	5.42	-
AT5G40800	*ABA-INDUCED TRANSCRIPTION REPRESSOR 4 (AITR4)*	-	7.32	-
AT1G18100	*MOTHER OF FT AND TFL1 (MFT)*	-	5.08	-
AT5G15960	*KIN1*	2.73	-	-
AT5G59220	*HIGHLY ABA-INDUCED PP2C GENE 1 (HAI1) / SENESCENCE ASSOCIATED GENE 113 (SAG113)*	-	7.86	-
AT4G21680	*NITRATE TRANSPORTER 1.8 (NRT1.8)*	-	2.98	-
AT5G66400	*RESPONSIVE TO ABA 18 (RAB18)*	-	5.49	-
AT3G21780	*UDP-GLUCOSYL TRANSFERASE 71B6 (UGT71B6)*	-	2.99	-
DOWN-REGULATED GENES				
		Log_2 Fold Change		
Gene ID	**Gene name**	**2 WAS**	**3 WAS**	**5 WAS**
AT1G01360	*REGULATORY COMPONENT OF ABA RECEPTOR 1 (RCAR1)*	-	-1.64	-2.19

AT5G53160	*REGULATORY COMPONENT OF ABA RECEPTOR 3 (RCAR3)*	-	-1.81	-

5.3.7 Quantification of stress hormones in the hypocotyls of WT and *crk10-A397T* mutant plants

The transcriptional up-regulation of SA- and ABA-related genes suggests that increased levels of these hormones are present in the hypocotyls of *crk10-A397T* mutant plants. As briefly mentioned in previous sections, SA and ABA are both known for their roles in mediating responses to biotic and abiotic stresses (Durner et al., 1997; Tuteja, 2007; Verma et al., 2016). Jasmonic acid (JA), another key hormone in plant immunity (Vijayane t al., 1998), is known to antagonise SA responses, and the crosstalk between the signalling pathways governed by these hormones has been extensively discussed in the literature (Spoel et al., 2007; Koornneef et al., 2008; Thaler et al., 2012). Thus, to investigate whether the transcriptional reprogramming of stress responses affects the hormonal content of the *crk10-A397T* mutant, the levels of SA, ABA and JA were quantified in the hypocotyls of 3-week-old WT and *crk10-A397T* plants (Table 5.6).

In agreement with the induction of pathways regulated by SA, results showed that the free content of this hormone is three times higher in the mutant hypocotyls compared to the WT. Similarly, the level of ABA is 1.5 times increased in the mutant. Although the total content of JA is seemingly reduced in the mutant hypocotyls, the difference is not statistically significant compared to WT levels. Taken together, these results indicate that the stress responses induced by the *crk10-A397T* allele promote the accumulation of the hormones SA and ABA, but not JA, in the hypocotyls of Arabidopsis plants.

Table 5.6 Quantification of hormones in the hypocotyl of WT and *crk10-A397T* mutant plants. Average values for three biological replicates (± standard error). Asterisks indicate statistical significance (t-test): ** = p ≤ 0.01; *** = p ≤ 0.001.

	Quantification (ng / g fresh tissue)		
	ABA	**SA**	**JA**
WT	8.523 ±0.435	337.120 ±13.760	7.673 ±2.103
crk10-A397T	13.293** ±0.434	977.837*** ±65.434	4.743 ±1.713

5.3.8 Investigation of the expression levels of other members of the *CRK* family in the *crk10-A397T* mutant transcriptome

To assess if the transcriptional reprogramming triggered by the gain-of-function allele of *CRK10* affects other members of CRK family in Arabidopsis, the lists of differentially expressed genes at each time point were inspected for their presence or absence. Interestingly, 19 CRKs are transcriptionally induced in the mutant hypocotyls, while only one gene (*CRK30;* AT4G11460) was down-regulated at three WAS (Table 5.7). Of a subset of eight members which were up-regulated at all three time points, only three have been functionally characterised in Arabidopsis. *CRK6* (AT4G23140) and *CRK7* (AT4G23150) are involved with signalling in response to oxidative stress in the apoplast (Idänheimo et al., 2014), while *CRK45* (AT4G11890), also called *ABA- AND OSMOTIC STRESS-INDUCIBLE RECEPTOR-LIKE CYTOSOLIC KINASE 1* (*ARCK1*), plays a role in developmental and stress-responsive ABA signalling and disease resistance (Tanaka et al., 2012; Zhang et al., 2013). Notably, *CRK10* itself was transcriptionally induced in the mutant hypocotyl.

Table 5.7 Differentially regulated members of the CRK family in the *crk10-A397T* mutant transcriptome.

		Log_2 Fold Change		
Gene ID	**Gene name**	**2 WAS**	**3 WAS**	**5 WAS**
AT1G70520	*CRK2*	-	2.11	1.67
AT1G70530	*CRK3*	1.66	2.39	1.79
AT3G45860	*CRK4*	-	5.5	7.63
AT4G23140	*CRK6*	3.51	6.76	3.1
AT4G23150	*CRK7*	3.59	5.16	2.14

AT4G23160	*CRK8*	-	4.41	-
AT4G23170	*CRK9*	-	3.82	-
AT4G23180	*CRK10*	1.50	2.29	-
AT4G23190	*CRK11*	-	1.55	-
AT4G23220	*CRK14*	3.19	4.99	2.06
AT4G23230	*CRK15*	2.86	5.4	1.8
AT4G23250	*CRK17*	2.02	4.05	1.77
AT4G23260	*CRK18*	-	3.36	-
AT4G23280	*CRK20*	2.56	3.18	-
AT4G23310	*CRK23*	4.13	5.78	-
AT4G23320	*CRK24*	-	5.49	-
AT4G11460	*CRK30*	-	-3.84	-
AT4G11480	*CRK32*	1.66	1.74	2.16
AT4G04490	*CRK36*	-	2.12	-
AT4G11890	*CRK45*	2.07	3.72	3.27

5.3.9 Investigation of the differential regulation of transcription factors in the *crk10-A397T* mutant

Reflecting the induction of stress responsive-signalling pathways, several TFs involved with modulation of these responses were induced and/or repressed throughout development in the *crk10-A397T* mutant hypocotyls (Table 5.8). The list includes members of well-known families of transcription factors, which are explored below.

The NAC (NAM, ATAF and CUC) family is one of the largest groups of plant-specific TFs, which is characterised by the presence of the DNA-binding NAC-domain in the N-terminal portion of the protein (Olsen et al., 2005). These transcriptional regulators are implicated in the control of growth and developmental processes as well as abiotic stresses and immune responses (Zhong et al., 2010; Nakashima et al., 2012; Nuruzzaman et al., 2013; Ricachenevsky et al., 2013). Three NAC TFs are constitutively up-regulated in the *crk10-A397T* transcriptome: *NAC001* (AT1G01010), *NAC0036* (AT2G17040) and *NAC090* (AT5G22380). Although the biological functions of *NAC001* and *NAC090* are currently elusive, *NAC036* is reportedly involved with the regulation of leaf cell growth, and its overexpression causes a semi-dwarf phenotype in Arabidopsis (Kato et al., 2010). Other members of the family are differentially expressed at one or two time points only, such as *NAC002*/*ATAF1* (AT1G01720),

exclusively up-regulated at three WAS. *ATAF1* has been previously described as a negative regulator of defence responses to pathogens (Wang et al., 2009) and an upstream regulator of senescence (Garapati et al., 2015), in addition to modulating the sensitivity of Arabidopsis plants to ABA, salt and oxidative stress (Wu et al., 2009). *NAC081/ATAF2* (AT5G08790), also up-regulated in this dataset, is a known central regulator of defence to pathogens, seedling development and hormone homeostasis (Peng et al., 2015). The developmental master switch *NAC030*/*VASCULAR-RELATED NAC-DOMAIN PROTEIN 7* (*VND7*; AT1G71930), responsible for the regulation of xylem vessel formation (Yamaguchi et al., 2008) is also induced. Conversely, the TFs *NAC066/NAC SECONDARY WALL THICKENING PROMOTING FACTOR2 (NST2;* AT3G61910) and *NAC096* (AT5G46590) are both repressed in the *crk10-A397T* mutant hypocotyls. While *NST2* regulates secondary cell wall biosynthesis in xylem fibres of the inflorescence stem (Zhong and Ye, 2015), *NAC096* induces cambial cell formation at wounding sites in the stem and hypocotyl (Matsuoka et al., 2021). The multitude of biological processes regulated by some of the NAC TFs which are differentially expressed in *crk10-A397T* hypocotyls is depicted in Figure 5.7.

WRKYs comprise another family of TFs which regulate aspects of plant adaptation to stresses and secondary metabolism (Rushton et al., 2010; Phukan et al., 2016). They recognise the motif TTGACC/T present in the core of W-boxes, cis-regulatory elements found in the promoter region of WRKY-regulated genes. Several WRKYs are present among the core DEGs in the *crk10-A397T* mutant transcriptome. These include *WRKY30* (AT5G24110), which is induced by biotic and abiotic stress conditions and confers enhanced tolerance to oxidative and salinity stress during germination (Scarpeci et al., 2013). The list continues with *WRKY50* (AT5G26170) and *WRKY51* (AT5G64810), which jointly mediate the SA-dependent repression of JA-inducible defence responses in Arabidopsis (Gao et al., 2011). *WRKY6* (AT1G62300), also constitutively expressed in *crk10-A397T* hypocotyls, is involved with several aspects of plant growth and environmental adaptation, as its activity is essential for normal root growth under low-boron conditions (Kasajima et al., 2010), for the modulation of arsenate/phosphate transporter genes (Castrillo et al., 2013), and for ABA signalling during early seedling development (Huang et al., 2016). Another multifaceted member of this family found among the core DEGs is *WRKY75*

(AT5G13080), a positive regulator of immunity and leaf senescence (Encinas-Villarejo et al., 2009; Guo et al., 2017) which also modulates nutrient starvation responses and root development (Devaiah et al., 2007). A gene network representing the interactions between WRKY TFs associated with defence responses to pathogens is shown in Figure 5.8.

Next, members of the MYB class of TFs, named after the retroviral oncogene v-myb (Biedenkapp et al., 1988), were mainly identified in the *crk10-A397T* mutant transcriptome at three WAS. This family, which is ubiquitous among eukaryotic organisms, is involved with the regulation of development, responses to stresses and metabolism in plants (Dubos et al., 2010). A prominent MYB TF which is up-regulated in the *crk10-A397T* mutant is *MYB30* (AT3G28910); induced at three and five WAS, *MYB30* is an important regulatory internode of various processes, including cell death during the hypersensitive response (HR) to pathogens (Rafaelle et al., 2008), heat and oxidative stress responses (Liao et al., 2017), activation of brassinosteroid-responsive genes (Li et al., 2009) and root growth during defence (Mabuchi et al., 2018). Another member of this family which is of particular interest given the vasculature defect of the *crk10-A397T* mutant is *MYB46* (AT5G12870). This gene is induced by the developmental master switches to promote the expression of secondary cell wall biosynthetic genes (Kim et al., 2012). As opposed to these examples, a set of 10 MYB TFs is down-regulated mainly at three and five WAS. Examples include *MYB26* (AT3G13890) and *MYB58* (AT1G16490), promoters of the lignification of secondary cell walls in anthers and inflorescence stem, respectively (Yang et al., 2007; Zhou et al., 2009).

Another major family of TFs identified in the transcriptome of the *crk10-A397T* mutant was the APETALA2/ETHYLENE RESPONSE FACTOR (AP2/ERF). Members of this group are major regulators of responses to abiotic stresses, wounding and metabolic pathways (Mizoi et al., 2012; Shoji and Yuan, 2021). Two members were present in the core list of up-regulated DEGs: *ERF14* (AT1G04370) and *ERF71* (AT2G47520). *ERF14* is responsive to pathogen infection (Oñate-Sánchez et al., 2002) whereas *ERF71* responds to hypoxia and osmotic stress (Park et al., 2011). *ERF115* (AT5G07310), strongly up-regulated at three WAS, controls root quiescent centre cell division and stem cell niche longevity (Heyman et al., 2013). On the other hand, a handful of functionally uncharacterised ERFs are down-regulated in our dataset.

Finally, it is worth mentioning the constitutive down-regulation of four *RADIALIS-like* (*RAD-like*) genes: *RL2* (AT1G75250), *RL3* (AT4G36570), *RL4* (AT2G18328) and *RL6* (AT1G75250). Apart from RL2, which is involved with female gametophyte development (Pagnussat et al., 2005), this gene family is largely uncharacterised.

Taken together, the extensive list of differentially expressed TFs exposes the intricacy of the transcriptional reprogramming taking place in the hypocotyls of the *crk10-A397T* mutant, which involves important regulatory nodes of stress-responsive and developmental processes.

Table 5.8 Differentially regulated transcription factors in the *crk10-A397T* mutant transcriptome.

UP-REGULATED GENES				
		Log_2 Fold Change		
Gene ID	**Gene name**	**2 WAS**	**3 WAS**	**5 WAS**
AT1G01010	*NAC001*	2.45	2.59	2.05
AT1G01720	*NAC002 / ATAF1*	-	2.15	-
AT3G29035	*NAC003 / NAC059*	-	3.20	-
AT1G32870	*NAC013*	-	2.35	-
AT1G34180	*NAC016*	1.99	3.84	-
AT1G71930	*NAC030 / VASCULAR-RELATED NAC-DOMAIN PROTEIN 7 (VND7)*	-	2.06	3.59
AT1G77450	*NAC032*	-	2.59	-
AT2G17040	*NAC036*	1.97	3.26	1.91
AT2G43000	*NAC042*	3.53	4.60	-
AT3G04420	*NAC048*	-	2.32	-
AT3G10500	*NAC053*	-	1.86	-
AT3G44350	*NAC061*	-	4.71	-
AT4G27410	*NAC072*	-	2.34	-
AT5G08790	*NAC081 / ATAF2*	-	2.65	2.02
AT5G14490	*NAC085*	-	5.74	-
AT5G22380	*NAC090*	3.88	3.97	3.15
AT5G63790	*NAC102*	-	2.65	-
AT1G62300	*WRKY6*	2.05	3.08	3.66
AT2G23320	*WRKY15*	-	1.53	-
AT5G07100	*WRKY26*	-	2.80	-

AT5G24110	*WRKY30*	4.99	5.74	2.78
AT4G22070	*WRKY31*	-	3.78	-
AT5G22570	*WRKY38*	-	-	4.21
AT4G11070	*WRKY41*	4.90	5.34	4.75
AT3G01970	*WRKY45*	2.37	3.27	-
AT5G26170	*WRKY50*	4.53	3.77	3.29
AT5G64810	*WRKY51*	3.16	3.82	4.68
AT4G23810	*WRKY53*	1.91	2.73	-
AT2G40740	*WRKY55*	3.55	4.05	-
AT2G25000	*WRKY60*	-	3.36	1.79
AT5G01900	*WRKY62*	-	-	4.38
AT3G56400	*WRKY70*	-	-	2.04
AT5G13080	*WRKY75*	2.64	4.72	3.77
AT2G47190	*MYB2*	2.79	-	-
AT2G31180	*MYB14*	-	-	3.72
AT3G28910	*MYB30*	-	3.50	3.41
AT5G12870	*MYB46*	-	1.69	-
AT1G18710	*MYB47*	-	8.54	-
AT1G18570	*MYB51*	-	3.07	-
AT5G59780	*MYB59*	-	1.89	-
AT1G09540	*MYB61*	-	2.09	-
AT1G68320	*MYB62*	-	5.76	-
AT2G02820	*MYB88*	-	2.63	-
AT3G47600	*MYB94*	-	2.90	-
AT1G48000	*MYB112*	-	5.83	-
AT3G30210	*MYB121*	-	6.32	-
AT1G74080	*MYB122*	4.90	4.47	-
AT3G23150	*ETHYLENE RESPONSE FACTOR 2 (ERF2)*	1.84	-	-
AT1G04370	*ETHYLENE-RESPONSIVE ELEMENT BINDING FACTOR 14 (ERF14)*	5.67	4.11	6.45
AT2G47520	*ETHYLENE RESPONSE FACTOR 71 (ERF71)*	3.95	2.51	2.95
AT5G61890	*ETHYLENE RESPONSE FACTOR 114 (ERF114)*	-	-	3.27
AT5G07310	*ETHYLENE RESPONSE FACTOR 115 (ERF115)*	-	4.97	-

AT5G13330	*RELATED TO AP2 6L / ETHYLENE RESPONSE FACTOR*	-	3.63	3.07
DOWN-REGULATED GENES				
		Log_2 Fold Change		
Gene ID	**Gene name**	**2 WAS**	**3 WAS**	**5 WAS**
AT3G61910	*NAC066*	-	-	-2.26
AT4G28530	*NAC074*	-	-3.21	-
AT5G46590	*NAC096*	-	-2.60	-
AT2G21650	*RAD-LIKE 2 / MYB1*	-3.72	-6.85	-6.07
AT4G36570	*RAD-LIKE 3*	-4.15	-9.19	-5.34
AT2G18328	*RAD-LIKE 4*	-4.36	-9.33	-5.37
AT1G75250	*RAD-LIKE 6 / MYB3*	-3.11	-7.68	-3.79
AT1G30650	*WRKY14*	-	-	-2.21
AT2G37260	*WRKY44*	-	-1.99	-
AT3G12820	*MYB10*	-	-1.85	-
AT4G25560	*MYB18*	-	-3.98	-
AT3G13890	*MYB26*	-	-	-5.70
AT5G61420	*MYB28*	-	-2.67	-2.87
AT5G60890	*MYB34*	-	-2.24	-
AT5G16600	*MYB43*	-	-	-2.03
AT1G16490	*MYB58*	-	-	-2.19
AT5G49330	*MYB111*	-5.22	-	-
AT5G35550	*MYB123*	-	-	-2.95
AT1G14350	*MYB124*	-	-	-1.57
AT2G44940	*ETHYLENE RESPONSE FACTOR 34 (ERF34)*	-	-1.64	-
AT3G60490	*ETHYLENE RESPONSE FACTOR 35 (ERF35)*	-	-1.64	-
AT5G25810	*ETHYLENE RESPONSE FACTOR 40*	-	-2.24	-
AT3G23230	*ETHYLENE RESPONSE FACTOR 98*	-2.29	-4.90	-
AT4G34410	*ETHYLENE RESPONSE FACTOR 109 (ERF109)*	-3.55	-	-
AT4G36920	*APETALA2*	-	-1.82	-

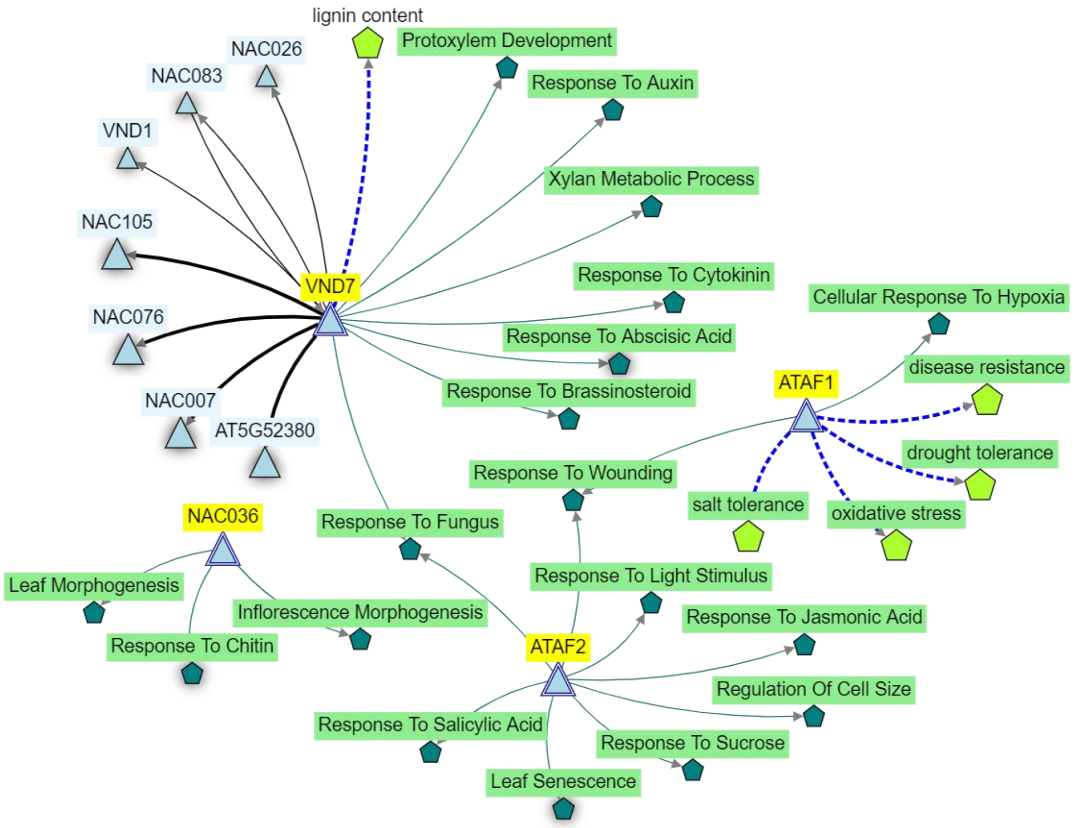

Figure 5.7 NAC transcription factors which are up-regulated in the *crk10-A397T* mutant transcriptome are associated with regulation of hormonal pathways, development and responses to stresses.

Gene network representing interactions between NAC transcription factors in Arabidopsis associated with responses to stresses, development and regulation of hormones. Light blue triangles represent individual genes; those identified as differentially expressed in the *crk10-A397T* transcriptome are highlighted in yellow. The dark green pentagons represent biological processes. Solid black lines indicate physical association between the proteins encoded by respective genes. Solid dark green lines indicate association between a gene and a biological process. Network created with KnetMiner (https://knetminer.com/Arabidopsis_thaliana/).

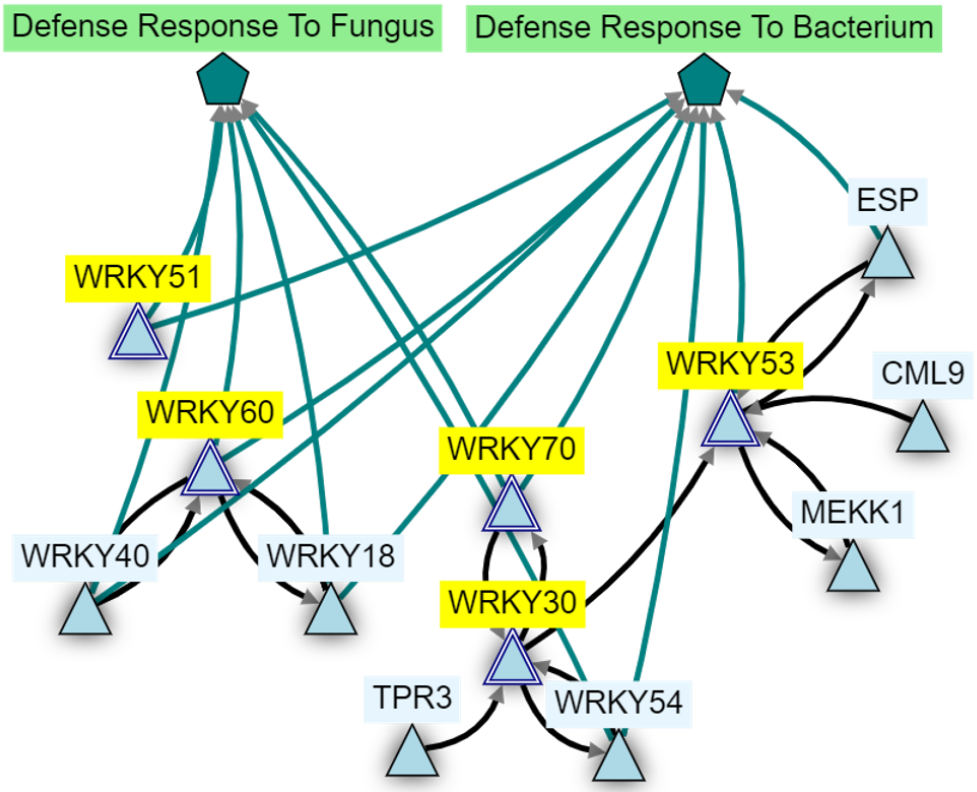

Figure 5.8 WRKY transcription factors which are up-regulated in the *crk10-A397T* mutant transcriptome are associated with defence responses to pathogens in Arabidopsis.

Gene network representing interactions between WRKY transcription factors in Arabidopsis associated with defence responses to fungal and bacterial pathogens. Light blue triangles represent individual genes; those identified as differentially expressed in the *crk10-A397T* transcriptome are highlighted in yellow. The dark green pentagons represent biological processes. Solid black lines indicate physical association between the proteins encoded by respective genes. Solid dark green lines indicate association between a gene and a biological process. Network created with KnetMiner (https://knetminer.com/Arabidopsis_thaliana/).

5.3.10 Analysis of differentially regulated genes involved with cell wall biosynthesis and modification

Although not prominent among the core set of DEGs, an extensive list of cell wall genes was differentially expressed at one or more time points in the *crk10-A397T* mutant hypocotyls (Table 5.9). Among these, several genes involved in the biosynthesis of the main components of secondary cell walls are up-regulated. Some of these genes show differential expression as early as at two WAS, when no collapsed xylem vessels are observed in transverse cross sections of hypocotyls (see section 3.3.3). These genes include *PEROXIDASE 66* (AT5G51890), involved in the biosynthesis of lignin (Tokunaga et al., 2009), as well as *IRREGULAR XYLEM 15* (*IRX15*, AT3G50220) and *GLUCURONIC ACID SUBSTITUTION OF XYLAN 1* (*GUX1*, AT3G18660), both responsible for the biosynthesis of xylan and glucuronoxylan (Brown et al., 2011; Mortimer et al., 2010). The up-regulation of *LACCASE 11* (AT5G03260) and *LACCASE 17* (AT5G60020), both involved with lignin polymerization during vascular development (Zhao et al., 2013), further implies the increased lignification of secondary cell walls in the hypocotyl of the *crk10-A397T* mutant. Notably, the major transcriptional reprogramming of cell wall genes is observed at three WAS, time point which coincides with the first observation of collapsed xylem vessels and the manifestation of the dwarf growth habit of the *crk10-A397T* mutant. This includes *IRREGULAR XYLEM 5* (*IRX5*; AT5G44030), a cellulose synthase essential for secondary cell wall cellulose biosynthesis (Taylor et al., 2002), and *IRREGULAR XYLEM 7* (*IRX7*; AT2G28110), a probable enzyme involved in the synthesis of glucuronoxylan (Zhong et al., 2005). Pectin-modifying enzymes such as *PECTIN ACETYLESTERASE 2* (AT1G57590) and *PECTIN METHYLESTERASE 35* (AT3G59010) are also up-regulated at three WAS. Interestingly, a pectin methylesterase inhibitor (*PMEI11*; AT3G47380) is consistently up-regulated at all time points, suggesting modulation of the methylesterification status of the pectic polysaccharides of primary cell walls.

Among the down-regulated cell wall genes, we find enzymes which act on several cell wall components, such as fucosidases, galactosidases and xylosidases. A rather extensive list of genes belonging to the superfamilies of pectin-lyase like and plant invertase/pectin methylesterase inhibitor are all down-regulated at three WAS, suggesting the suppression of pectin degradation and methylesterification at this time point. The list of repressed genes continues with

five members of the *TRICHOME BIREFRINGENCE-LIKE* family, which are highly homologous to the TBR family known to play roles in cell wall biology (Bischoff et al., 2010). Overall, the concerted up- and down-regulation of several classes of primary and secondary cell wall genes suggests that extensive remodelling of cell walls may be taking place in the hypocotyls of the *crk10-A397T* mutant plants, especially at three WAS.

Finally, it is worth noting the transcriptional induction of *XYLEM CYSTEINE PROTEASE 1* (AT4G35350) and *XYLEM CYSTEINE PROTEASE 2* (AT1G20850), known to participate in the xylem vessel autolysis process in roots (Avci et al., 2008). Although not involved with the deposition of the cell wall, *XCP1* and *XCP2* are essential for xylem vessel differentiation, and their transcriptional induction suggests increased levels of tracheary element formation in the hypocotyl of the *crk10-A397T* mutant.

Table 5.9 Differentially regulated genes in the *crk10-A397T* mutant transcriptome associated with cell wall biosynthesis and modification and xylem vessel formation.

UP-REGULATED GENES				
		Log2 Fold Change		
Gene ID	**Gene name**	**2 WAS**	**3 WAS**	**5 WAS**
AT5G05340	*PEROXIDASE 52 (PRX52)*	4.99	5.48	-
AT5G51890	*PEROXIDASE 66 (PRX66)*	3.91	6.52	6.79
AT4G08770	*PEROXIDASE 37 (PER37)*	3.58	-	2.79
AT5G60020	*LACCASE 17 (LAC17)*	3.16	3.97	-
AT2G29130	*LACCASE 2 (LAC2)*	4.28	2.15	-
AT5G03260	*LACCASE 11 (LAC11)*	-	2.50	2.87
AT3G50220	*IRREGULAR XYLEM 15 (IRX15)*	2.11	2.33	-
AT3G18660	*GLUCURONIC ACID SUBSTITUTION OF XYLAN 1 (GUX1)*	1.89	2.64	-
AT1G33800	*GLUCURONOXYLAN METHYLTRANSFERASE 1 (GXMT1)*	-	2.3	-
AT5G54690	*IRREGULAR XYLEM 8 (IRX8)*	-	1.59	-
AT5G44030	*CELLULOSE SYNTHASE A4 (CESA4) / IRREGULAR XYLEM 5 (IRX5)*	-	1.98	-
AT2G28110	*FRAGILE FIBER 8 (FRA8) / IRREGULAR XYLEM 7 (IRX7)*	-	1.66	-

AT3G56000	*CELLULOSE SYNTHASE LIKE A14*	-	2.77	3.65
AT1G55850	*CELLULOSE SYNTHASE LIKE E1*	-	2.64	-
AT4G24000	*CELLULOSE SYNTHASE LIKE G2*	-	6.70	-
AT1G69530	*EXPANSIN 1*	-	1.81	2.88
AT1G26770	*EXPANSIN 10*	-	4.49	-
AT1G21310	*EXTENSIN 3*	-	2.29	3.26
AT3G47380	*PECTIN METHYLESTERASE INHIBITOR 11 (PMEI11)*	4.24	4.39	5.34
AT1G57590	*PECTIN ACETYLESTERASE 2*	-	5.24	-
AT3G59010	*PECTIN METHYLESTERASE (PME35)*	-	2.34	-
AT4G12390	*PECTIN METHYLESTERASE INHIBITOR 1*	-	1.86	-
AT1G70500	Pectin lyase-like superfamily protein	1.97	2.81	2.76
AT2G43870	Pectin lyase-like superfamily protein	4.04	6.25	4.1
AT3G24130	Pectin lyase-like superfamily protein	-	4.38	-
AT3G28180	*XYLOGLUCAN GLYCOSYLTRANSFERASE 4*	-	2.95	-
AT4G25810	*XYLOGLUCAN ENDOTRANSGLUCOSYLASE 6 (XTR6)*	-	3.27	-
AT3G48580	*XYLOGLUCAN HYDROLASE 11 (XTH11)*	-	4.61	3.46
AT4G18990	*XYLOGLUCAN HYDROLASE 29 (XTH29)*	-	5.49	-
AT3G29810	*COBRA-LIKE PROTEIN 2 PRECURSOR (COBL2)*	-	3.01	
AT4G35350	*XYLEM CYSTEINE PROTEASE 1 (XCP1)*	-	1.50	2.59
AT1G20850	*XYLEM CYSTEINE PROTEASE 2 (XCP2)*	-	-	1.67
AT2G31110	*TRICHOME BIREFRINGENCE-LIKE 40*	1.68	2.42	-
AT4G08160	*ENDO-1,4-BETA-XYLANASE 3*	-	2.12	-
AT1G10050	*ENDO-1,4-BETA-XYLANASE 2*	-	1.57	-
AT5G66690	*UGT72E2*	-	4.02	2.28
AT3G24503	*ALDEHYDE DEHYDROGENASE 1A*	-	2.47	2.75

AT1G71380	*ARABIDOPSIS THALIANA GLYCOSYL HYDROLASE 9B3*	-	3.05	-
AT5G06230	*TRICHOME BIREFRINGENCE-LIKE 9*	-	2.06	-
DOWN-REGULATED GENES				
		Log2 Fold Change		
Gene ID	**Gene name**	**2 WAS**	**3 WAS**	**5 WAS**
AT2G22900	*MUCILAGE-RELATED 10*	-	-1.42	-
AT5G65810	*COTTON GOLGI RELATED 3*	-	-1.50	-
AT3G14310	*PECTIN METHYLESTERASE 3 (PME3)*	-	-2.58	-
AT5G62360	*PECTIN METHYLESTERASE INHIBITOR 13 (PMEI13)*	-	-3.55	-
AT4G23820	Pectin lyase-like superfamily protein	-	-2.68	-
AT3G62110	Pectin lyase-like superfamily protein	-	-1.56	-
AT5G48900	Pectin lyase-like superfamily protein	-1.62	-3.65	-
AT5G19730	Pectin lyase-like superfamily protein	-	-1.57	-
AT1G04680	Pectin lyase-like superfamily protein	-	-1.32	-
AT3G61490	Pectin lyase-like superfamily protein	-	-2.08	-
AT5G04310	Pectin lyase-like superfamily protein	-	-2.39	-
AT4G23500	Pectin lyase-like superfamily protein	-	-1.57	-
AT5G09760	Plant invertase/pectin methylesterase inhibitor superfamily	-	-1.41	-
AT2G26450	Plant invertase/pectin methylesterase inhibitor superfamily	-	-3.73	-
AT1G56100	Plant invertase/pectin methylesterase inhibitor superfamily protein	-	-6.23	-
AT5G20860	Plant invertase/pectin methylesterase inhibitor superfamily	-	-2.14	-
AT1G23205	Plant invertase/pectin methylesterase inhibitor superfamily protein	-	-2.95	-
AT3G62820	Plant invertase/pectin methylesterase inhibitor superfamily protein	-	-1.92	-
AT4G16980	Arabinogalactan-protein family	-	-3.54	-
AT1G71690	*GLUCURONOXYLAN 4-O-METHYLTRANSFERASE-LIKE PROTEIN (DUF579)*	-	-2.05	-
AT1G67830	*ALPHA-FUCOSIDASE 1*	-	-1.69	-

AT5G08370	*ALPHA-GALACTOSIDASE 2*	-	-1.74	-
AT5G26120	*ALPHA-L-ARABINOFURANOSIDASE 2*	-	-4.06	-
AT5G40730	*ARABINOGALACTAN PROTEIN 24*	-	-2.22	-
AT1G28290	*ARABINOGALACTAN PROTEIN 31*	-	-2.08	-
AT5G24105	*ARABINOGALACTAN PROTEIN 41*	-	-3.66	-
AT5G64570	*BETA-D-XYLOSIDASE 4*	-	-3.19	-
AT5G63810	*BETA-GALACTOSIDASE 10*	-	-2.34	-
AT3G52840	*BETA-GALACTOSIDASE 2*	-	-2.20	-
AT4G21760	*BETA-GLUCOSIDASE 47*	-1.88	-5.04	-2.07
AT1G02640	*BETA-XYLOSIDASE 2*	-	-2.53	-
AT2G13680	*CALLOSE SYNTHASE 5*	-	-2.80	-
AT1G22880	*CELLULASE 5*	-	-2.40	-
AT1G77460	*CELLULOSE SYNTHASE INTERACTIVE 3*	-	-1.51	-
AT1G24070	*CELLULOSE SYNTHASE-LIKE A10*	-	-2.58	-2.22
AT4G07960	*CELLULOSE SYNTHASE-LIKE C12*	-	-2.71	-
AT4G01630	*EXPANSIN A17*	-	-1.94	-
AT3G29030	*EXPANSIN A5*	-	-5.23	-
AT2G28950	*EXPANSIN A6*	-	-2.00	-
AT2G40610	*EXPANSIN A8*	-	-3.94	-
AT4G28250	*EXPANSIN B3*	-	-3.34	-
AT5G55730	*FASCICLIN-LIKE ARABINOGALACTAN 1*	-	-1.58	-
AT2G45470	*FASCICLIN-LIKE ARABINOGALACTAN PROTEIN 8*	-	-1.36	-
AT1G71990	*FUCOSYLTRANSFERASE 13*	-	-1.98	-
AT1G74420	*FUCOSYLTRANSFERASE 3*	-	-2.20	-
AT1G13250	*GALACTURONOSYLTRANSFERASE-LIKE 3*	-	-1.85	-
AT5G58910	*LACCASE 16*	-	-2.21	-
AT2G30210	*LACCASE 3*	-	-1.88	-
AT2G22900	*MANNAN α151 GALACTOSYL TRANSFERASE 1*	-	-1.42	-
AT5G15900	*TRICHOME BIREFRINGENCE-LIKE 19*	-	-2.72	-
AT1G60790	*TRICHOME BIREFRINGENCE-LIKE 2*	-	-1.59	-

AT2G40150	*TRICHOME BIREFRINGENCE-LIKE 28*	-	-1.80	-
AT2G30010	*TRICHOME BIREFRINGENCE-LIKE 45*	-	-2.57	-
AT3G62390	*TRICHOME BIREFRINGENCE-LIKE 6*	-	-1.74	-
AT2G36870	*XYLOGLUCAN ENDOTRANSGLUCOSYLASE / HYDROLASE 32*	-	-2.17	-
AT4G37800	*XYLOGLUCAN ENDOTRANSGLUCOSYLASE / HYDROLASE 7*	-	-1.92	-

5.3.11 Validation of RNA-Seq results with qPCR

To validate the results obtained with the RNA-Seq experiment, the transcript abundance of selected DEGs in the hypocotyls of 3-week-old WT and *crk10-A397T* plants was assessed by qPCR. The calculation of the relative expression of *PR1*, *PR2* and *PR5* confirmed that these genes are transcriptionally induced in *crk10-A397T* hypocotyls in comparison to the WT samples (Figure 5.9).

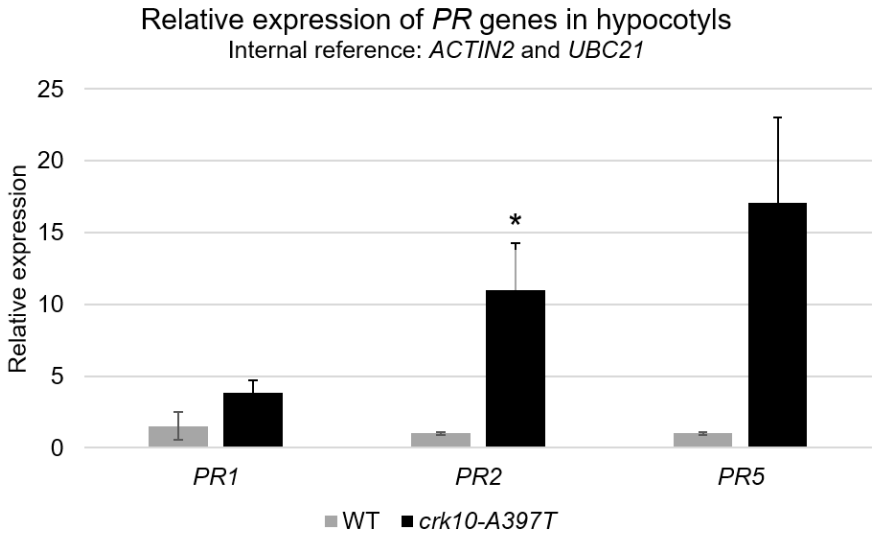

Figure 5.9 The relative expression of *PR* genes is increased in hypocotyls of *crk10-A397T* plants.

Quantification of the relative expression of the *PR1*, *PR2* and *PR5* transcripts by qPCR. Template cDNA was synthesized from RNA extracted from hypocotyls of 3-week-old plants; genes *AtACTIN2* and *AtUBC21* were used as internal

controls. Error bars represent standard error of three biological replicates. Asterisks indicate statistical significance (t-test): * = $p \leq 0.05$.

5.4. Discussion

In this chapter, the transcriptomic analysis of the hypocotyl tissue of the *crk10-A397T* mutant compared to WT plants is reported. The aim of this experiment was to identify differentially regulated signalling pathways in the hypocotyls of the mutant plants to gain insights into the biological processes regulated by this gain-of-function allele. After processing the sequencing results, 523, 1836 and 913 genes were found to be differentially regulated at two, three and five WAS, respectively.

Considering *crk10-A397T* as a gain-of-function allele which causes the activation of downstream cascades, the expression of the genes which are primary targets of these signalling pathways is expected to be differentially regulated at any given time point throughout development. Furthermore, the constitutive activation of responses also leads to the transcriptional reprogramming of genes which are not direct targets of the signalling cascades triggered by *crk10-A397T* but are indirectly regulated as part of secondary responses. In attempt to filter secondary genes and identify direct targets of the mutated CRK10, the core set of DEGs in the *crk10-A397T* mutant hypocotyls was identified and analysed. GO enrichment analysis, a common strategy to identify over-represented functional categories in a given transcriptomic dataset, was performed using the up- and down-regulated core DEGs. Given the morphological phenotypes exhibited by the *crk10-A397T* mutant plants, GO terms associated with vasculature development and cell wall metabolism were expected among the results of this analysis. Hence, the finding that the most significantly enriched GO categories among the up-regulated core genes are related with adaptation to stresses was rather surprising. The presence of several categories related with immune responses, such as “Systemic acquired resistance” (GO:0009627) and “Response to biotic stimulus” (GO:0009607), undoubtedly revealed the induction of genes involved with plant-pathogen interactions in the *crk10-A397T* mutant hypocotyl. This was further supported by the similarity analysis performed with the Signature tool of the GENEVESTIGATOR® programme, as the majority of the perturbations which induced the most similar transcriptional changes compared to the *crk10-A397T*

mutant belong to the classes of biotic or abiotic stresses. Infection with necrotrophic and biotrophic fungal, oomycete and bacterial pathogens were prominent in the list, as well as treatment with a series of herbicides, which are known to induce detoxification pathways in plants. Interestingly, several Arabidopsis mutants known to have constitutive activation of defence responses also featured among the most similar transcriptome signatures. Some of the highest-ranking mutants, such as *mkk1 mkk2*, *mpk4 ctr1* and *ssi2-1*, are also known to accumulate high levels of the hormone salicylic acid (SA), a known regulator of defence responses to biotrophic pathogens. Taken together, the GO enrichment analysis and similarity comparison revealed that the putative gain-of-function allele of *CRK10* primarily affects stress-responsive signalling pathways, especially those involved with defence to pathogens. This is in agreement with a role for CRKs in the regulation of responses to biotic stresses, as has been previously reported in the literature for several members of the family (see sections 1.4.1 and 1.4.2 for a review of studies reporting the functional characterisation of CRKs in Arabidopsis and other plant species). In Arabidopsis, the work of Du and Chen in the early 2000s reported the transcriptional induction of a group of RLKs following treatment with SA and bacterial infection, which was later followed by their identification as members of the novel family of CRKs (Du and Chen, 2000; Chen, 2001). Multiple studies showed the association between increased levels of CRK expression and enhanced resistance to pathogens, for example *CRK5* (Chen et al., 2003), *CRK13* (Acharya et al., 2007) and *CRK28* (Yadeta et al., 2017). Examples in other plant species include *CRK18* in cotton (*Gossypium barbadense*), which was shown to mediate resistance to the soil-borne fungus *Verticillium dahlia* (Li et al., 2018), and *CRK6* and *CRK10* from rice (*Oryza sativa*), which are required for *OsNPR1*-mediated defence responses (Chern et al., 2016). Despite these reports, the ligand which is recognised by the extracellular domain of CRKs and triggers the activation of the defence responses to pathogens remains unknown.

To gain a more in-depth insight into the transcriptional reprogramming elicited by the *crk10-A397T* allele, individual categories of genes were analysed. Well-known regulators of systemic acquired resistance and innate immune responses were identified, such as *EDS1* and *PAD4*. Besides triggering early defence responses, *EDS1* is required for the transcriptional induction of *PAD4,* with which it then interacts to positively regulate the accumulation of SA (Feys et

al., 2001). Furthermore, the complex *EDS1- PAD4* was shown to be essential for the successful establishment of SAR and innate immunity (Rietz et al., 2011). Camalexin and glucosinolates biosynthetic genes, hallmarks of the activation of defence responses, also showed strong levels of up-regulation across all time points, as well as the characteristic pathogenesis-related (PR) genes. Moreover, the induction of SA-related genes was reflected in increased levels of this hormone in the hypocotyls of the *crk10-A397T* mutant plants. A key regulator of plant immunity, SA is a multi-faceted molecule which is required for processes such as the hypersensitive response (HR), pathogen-induced programmed cell death and systemic and local resistance to pathogen attack (Ding and Ding, 2020). Given its biological roles, the hyper-accumulation of SA and the misregulation of its responses are known to have deleterious effects on plant growth, as is the case for several auto-immune, SA-accumulator mutants of Arabidopsis. For instance, the accumulation of SA in the knockout mutants *mekk1*, *mkk1/mkk2,* and *mpk4* leads to the constitutive induction of PR genes and a severe dwarf phenotype in Arabidopsis (Gao et al., 2008). Moreover, as discussed in Chapter 3 of this thesis (section 3.1), dwarfism as a consequence of auto-immunity is a common occurrence in plants (van Wersch, 2016). Therefore, the constitutive defence responses present in the transcriptome of the *crk10-A397T* mutant plants emerges as another facet of its dwarf phenotype, although ultimately caused by the collapse of xylem vessels. Interestingly, the dwarfism of auto-immune mutants has always been attributed to the trade-off between growth and defence, which reflects the allocation of resources to fend off a pathogen in detriment to growth-associated mechanisms. However, the observation of the vasculature-defect of the *crk10-A397T* mutant raises the question of whether this could also be the case for other dwarf auto-immune mutants, which has not been reported, perhaps simply due to the lack of investigation. The examination of root, hypocotyl and stem samples of some of these mutants with light microscopy would be a convenient approach to answer this question.

Several genes associated with responses to abiotic stresses were also induced in the *crk10-A397T* mutant hypocotyls, including a myriad of detoxifying enzymes and ABA-responsive genes. Similar to the observed increased levels in SA, ABA levels are significantly increased in the hypocotyls of the *crk10-A397T* plants, confirming the involvement of this hormone in the stress responses

regulated by this gain-of-function allele. ABA is a well-established regulator of plant growth and developmental processes, as well as an important signalling molecule during responses to abiotic stresses, such as drought and oxidative stress (Tuteja, 2007). One hypothesis to explain the induction of ABA production and signalling in the *crk10-A397T* mutant is the presence of the collapsed vessel elements in roots and hypocotyls. The deformation of xylem vessels likely hinders the transport of water within the plant, which might be perceived as drought stress and lead to the induction of ABA pathways. A similar increase in ABA levels has been observed in other cell wall mutants such as *eskimo1 (esk1)* and *irregular xylem* 1-6 (*irx1-6)* whereas *irx3*, *irx5* and *irx9* contained numerous constitutively up-regulated ABA-responsive genes (Chen et al., 2005; Hernández-Blanco et al., 2007; Lefebvre et al., 2011; Faria-Blanc et al., 2018; Xu et al., 2020). The suppression of growth observed in these mutants is thought to be the result of the response to drought signalling hormones, which might also be involved with the dwarfism of *crk10-A397T* plants. It is also worth noting that other members of the CRK family in Arabidopsis have been previously identified as regulators of ABA-mediated processes, including *CRK5* and *CRK45* (Zhang et al., 2013; Lu et al., 2016). Furthermore, the extensive reprogramming of numerous transcription factors (TFs) known to regulate developmental and stress-responsive genes exposes the complex crosstalk taking place in the mutant hypocotyls. This was expected given that modulation of TFs is usually the last step of signal transduction cascades initiated by RLKs, which allows the induction or repression of target genes to promote an appropriate cellular response.

Although not abundantly present in the list of core DEGs, a considerable number of cell wall-related genes were differentially expressed at individual time points in this dataset. Of these, genes involved with the biosynthesis of lignin, cellulose and hemicelluloses were up-regulated, which suggests the reinforcement of secondary cell walls in the mutant hypocotyl. Furthermore, several genes involved with the biosynthesis or modification of other cell wall components were also differentially expressed, especially at the second experimental time point. These observations suggest the extensive remodelling of primary and secondary cell walls in the hypocotyls of the *crk10-A397T* mutant. Although transcriptional regulation of cell wall-related genes was expected, the induction of biosynthetic genes seems to contradict the usual cell wall weakening which is seen in several mutants with collapsed xylem vessels, such as the *irx*

mutants (Turner and Somerville, 1997). On the contrary, reinforcement of the secondary cell wall of xylem vessels increases wall rigidity and, therefore, it is not expected to cause its collapse. Further investigations into the composition of the cell walls in the hypocotyls of *crk10-A397T* mutant plants in a bid to identify potential defects associated with the xylem vessel collapse are reported in Chapter 6.

Finally, considering the induction of defence responses and the cell wall remodelling in the hypocotyls of the *crk10-A397T* mutant, a question that remains unanswered is whether these processes are independent or related to each other. Cell wall reinforcement is a common feature of defence responses to pathogens aimed at halting pathogen penetration and spread (Underwood, 2012). On the other hand, defence responses are also known to be triggered upon perception of cell wall defects (Vaahtera et al., 2019). Thus, could the transcriptional reprogramming of cell wall genes be a branch of the immune responses activated downstream of *crk10-A397T*, or vice-versa? Or are the defence and cell wall-related pathways separate branches of the signalling cascade initiated by *crk10-A397T*, rather than sequential events which trigger each other? These hypotheses and experimental approaches which could be used to test them are further discussed in section 8.3.

In conclusion, the analysis of the transcriptome of the *crk10-A397T* mutant hypocotyls provided invaluable information regarding the transcriptional changes elicited downstream of the *crk10-A397T* allele. The constitutive transcriptional reprogramming of signalling pathways is consistent with the proposed gain-of-function of this allele, where the A397T mutation causes the spontaneous and constitutive activation of downstream signal transduction cascades. The prevalence of genes involved with defence responses to pathogens and general stress-responsive mechanisms in the lists of DEGs implies a role for the *crk10-A397T* mutant allele in regulating these processes.

Chapter 6 – Analysis of the composition of the cell walls of xylem vessels from the hypocotyl of the *crk10-A397T* mutant allele

6.1 Introduction

Plant cell walls are dynamic networks of carbohydrates and proteins which are far from being a rigid, immutable structure. They are a distinctive attribute of plant cells and act as a physical barrier between the protoplast and the extracellular environment. Besides acting as a protective layer, cell walls also regulate cell size and shape, confer mechanical strength to the plant tissue, determine developmental patterns, harbour cell-to-cell communication structures (plasmodesmata), and provide defence-eliciting signals during pathogen attack (Knox, 1990; Robards and Lucas, 1990; Somerville et al., 2004; Seifert and Blaukopf, 2010).

Two main types of cell walls are developed by plant cells: the primary and secondary walls. The type I primary cell walls, found in the majority of flowering plants, are composed of a cellulosic framework, hemicellulose molecules, a gelatinous pectic matrix and structural proteins (Carpita and Gibeaut, 1993). Cellulose and hemicelluloses are the major contributors to the rigidity of the primary wall, while the amorphous pectic matrix provides it with a degree of fluidity. Cellulose, the main scaffolding polymer of plant cell walls, is formed by linear, unbranched chains of (1→4)-β-D-glucose. These chains interact with each other via hydrogen bonds and van der Waals forces to form highly insoluble, crystalline cellulose microfibrils (Ochoa-Villareal et al., 2012). Directly interacting with the cellulose microfibrils are the hemicelluloses, which are heterogeneous polysaccharides with a low molecular weight (Scheller and Ulvskov, 2010). In dicotyledons, the major hemicelluloses are xyloglucans, xylans, mannans and glucomannans. Among these, xyloglucans (XGs) are the most abundant in the primary cell walls in land plants (Ochoa-Villareal et al., 2012). The linear XG chains are formed by (1→4)-β-D-glucose units, which are branched with α-D-xylose at the O-6 position (Carpita and Gibeaut, 1993). XG chains are often decorated with β-D-galactose or, less often, L-fucose-α-(1→2)-D-galactose disaccharides (Ochoa-Villareal et al., 2012). By contrast, xylan molecules are comprised of a backbone of xylose units joined by β-(1→4) links; these will be explored in detail later in this section. Mannan and glucomannans are the less abundant β-(1→4)-linked hemicelluloses; these compounds have linear

backbones formed exclusively by mannose or by alternating mannose and glucose units, as observed in glucomannans and galactoglucomannans (Scheller and Ulvskov, 2010). Finally, pectins are the most complex family of polysaccharides in nature, and they participate in biological processes such as growth, cell-to-cell adhesion, signalling and binding of ions (Mohnen, 2008). Pectins not only make up the gelatinous matrix in which cellulose and hemicelluloses are embedded, but also affect the porosity, pH, ion balance and rigidity of the cell wall (McNeil et al., 1984). The most abundant pectic polysaccharide is homogalacturonan (HG), a polymer of (1→4)-α-D-galacturonic acid (GalA) on which some carboxyl groups are partially methyl-esterified or acetyl-esterified (Ridley et al., 2000). A threshold of 50% of GalA units harbouring a methyl group at the C-6 position is used to classify a HG molecule as highly methyl-esterified (Ochoa-Villareal et al., 2012). The level of HG methyl-esterification, which directly affects the mechanical properties of the cell wall, is modulated by pectin methylesterases (PMEs) throughout development and responses to stresses (Wolf et al., 2009; Silva-Sanzana et al., 2019). Non-methyl-esterified carboxyl groups often cross-link with Ca^{+2} ions, causing anti-parallel chains to interact with each other and form the stable, rigid conformation known as “egg-box” (Jarvis, 1984). Therefore, the regulation of pectin methylesterification within tissues constitutes an important tool in modulating the rigidity of the cell wall (Levesque-Tremblay et al., 2015). The second most abundant pectic polysaccharide, rhamnogalacturonan I (RGI), is a heteropolymer of repeating (1→2)-α-L-rhamnosyl-(1→4)-α-D-GalA units. RGI is partially substituted with single glucosyl residues or polymers of α-(1→5)-L arabinans and β-(1→4)-D-galactans, arabinogalactans I and II, and galactoarabinans (Lau et al., 1985; Ochoa-Villareal et al., 2012). While RGI generally comprises 20-35% of total pectins in primary cell walls, rhamnogalacturonan II (RGII) makes up 0.5 to 8% of the plant cell walls in most plant species (Ridley et al., 2001; Ochoa-Villareal et al., 2012).

In addition to the primary cell wall, certain specialised tissue types develop a thick, lignified secondary wall, including xylem tracheary elements and fibres, the root endodermis and the endothecium of anthers (Zhong et al., 2018). The major function of the secondary wall is to provide a waterproof layer to these cells and offer mechanical support and protection to the plant. To achieve this, a secondary cell wall composed mainly of cellulose, xylan, glucomannan and lignin

is deposited (Zhong et al., 2018). Comparably to the primary cell wall, cellulose acts as the main load-bearing polymer in secondary cell walls (Zhong and Ye, 2015). Rather than XG, xylans are the major hemicelluloses in secondary cell walls of angiosperms (Timell, 1967). In Arabidopsis, the (1→4)-linked β-D-xylosyl residues which form the backbone of the xylan molecules can be substituted at O-2 with α-D-glucuronic acid or 4-O-methyl α-D-glucuronic acid (glucuronoxylan, GX), arabinose (arabinoxylan), or both (glucuronoarabinoxylan; Ebringerová and Heinze, 2000; York and O'Neill, 2008). The xylan backbone can additionally be acetylated at positions O-2 and O-3. GX is the main hemicellulose component of the secondary cell walls of dicotyledons, whereas arabinoxylan and glucuronoarabinoxylan are found in the cell walls of grasses (York and O'Neill, 2008). Finally, lignin is deposited in the secondary cell walls of vascular plants, a distinctive feature which emerged around 430 million years ago and allowed the long distance transport of water (Raven et al., 1999). Lignin is a polyphenolic compound which is synthesized *in muro* by the polymerisation of p-coumaryl, coniferyl and sinapyl alcohols, also known as monolignols (Wang et al., 2013). After their incorporation into the growing lignin polymer by laccases and peroxidases in the apoplast (Ralph et al., 2004), these monomers are called p-hydroxyphenyl (H), guaiacyl (G) and syringil (S), respectively. The proportion of H, G and S type monolignols within the lignin polymer is highly variable among plant species and tissue types (Bonawitz and Chapple, 2010). Moreover, secondary cell walls usually exhibit three distinct layers when observed with transmission electron microscopy (TEM), referred to as S1, S2 and S3. Each layer is defined by a specific arrangement of the cellulose microfibrils: crossed microfibrils in S1, parallel to the cell elongation axis in S2, and a flat helix in S3 (Timell, 1967).

In addition to the complex composition and structure of plant cell walls, studies have revealed the extensive variability in cell wall composition between different tissues, cell types, and even within a single cell (Richmond and Somerville, 2001; Somerville et al., 2004). Therefore, investigating the composition of cell walls in a given plant sample is no trivial task, given that cell-specific traits are often obscured by the multitude of cell types present in the tissue analysed. Nevertheless, several analytical techniques have helped to advance the study of plant cell walls in the last few decades, such as Fourier Transform Infrared Spectroscopy (FTIR; Alonso-Simón et al., 2011),

histochemical and immunohistochemical techniques (Soukup, 2013; Bidhendi et al., 2020; DeVree et al., 2021) and chromatography and mass spectrometry (Gunl et al., 2011; Pettolino et al., 2012).

The presence of collapsed xylem vessels in the root and hypocotyl of the *crk10-A397T* mutant was shown to be associated with its distinctive dwarf phenotype (see sections 3.3.3 and 3.3.4). This vasculature defect, reminiscent of the *irregular xylem* (*irx*) mutants of Arabidopsis (Turner and Somerville, 1997), brought into question the status of the integrity and composition of these collapsed cell walls. As briefly introduced in section 3.1, an *irx* phenotype is usually caused by the depletion of critical cell wall components, which results in the assembly of cell walls with impaired mechanical properties. For example, the *irx2* mutant contains only 30% of the total crystalline cellulose present in WT inflorescence stems (Szyjanowicz et al., 2004). In the *fragile fiber8 / irx7* mutant, a substantial reduction in xylan and cellulose was associated with the reduction in the secondary cell wall thickness of interfascicular xylem fibres (Zhong et al., 2005). Similarly, the mildly deformed xylem vessels and the uneven secondary cell wall morphology observed in the inflorescence stem of the *irx15 irx15l* double mutant were caused by a large reduction in xylose content (Brown et al., 2011). The deformed xylem vessels in the *irx8*, *irx9* and *parvus* mutants were correlated with decreased levels of glucuronoxylan, an important hemicellulose in the assembly of secondary cell walls (Lee et al., 2007; Peña et al., 2007). Lastly, lignin deficiency also causes an *irx* phenotype, as *irx4* mutant plants display a 50% reduction in lignin content, but no changes in hemicellulose or cellulose levels (Jones et al., 2001). Observation with TEM revealed that the reduced lignin content in the *irx4* mutant affected the ultrastructure of secondary cell walls, as they exhibited a diffuse and uneven appearance (Jones et al., 2001). Additionally, the lignin-deficient mutant *cinnamoyl-coenzyme reductase1-6* (*ccr1-6*) displayed the loosening of secondary cell wall layers in xylem vessels and fibres (De Meester et al., 2018). Thus, the abundance of evidence in the literature implicating the collapse of xylem vessels with defective cell wall composition steered this study in a similar direction with regard to the characterisation of the *crk10-A397T* mutant. In this chapter, a preliminary analysis of the composition of cell walls in the hypocotyls of *crk10-A397T* mutant plants is reported, shedding a light onto the biochemical and structural aspects of the collapsed xylem vessel phenotype of this mutant.

6.2 Materials and Methods

6.2.1 Fourier-transform infrared spectroscopy

Transverse cross sections of hypocotyls of 3-week-old WT and *crk10-A397T* mutant plants were prepared using a cryostat (CM1850 Cryostat, Leica Microsystems; section thickness: 20 µm). Three individual plants per genotype were sampled. The cross sections were washed with 70% ethanol in a concave watch glass before being transferred to Barium Fluoride (BaF_2) discs to air dry. The FTIR analysis and the interpretation of the resulting spectra were performed by Dr Nikolaus Wellner (Analytical Science Group, The Quadram Institute). The cross sections were analysed using a Nicolet™ iN10MX infrared microscope (Thermo Scientific™) equipped with a 15x infrared (IR) objective. FTIR maps were obtained by transmission aperture mapping with an MCT (mercury-cadmium-telluride) detector and an X-Y step size of 10 µm. To improve light throughput and spectral quality, the mapping was performed with a 20x20 μm^2 aperture. A total of 128 scans were averaged at 8 cm^{-1} for each image pixel. An empty spot on the BaF_2 disk was used as background. The maps were exported in ENVI format and processed in MATLAB (The MathWorks, Inc.). WT and *crk10-A397T* maps were combined into one data set, so that all spectra were treated together with the same analytical parameters. The spectra were truncated to 1800-700 cm^{-1}. The density map was calculated by averaging the IR absorption from 1800-800 cm^{-1}. To compare the chemical composition irrespective of their local density, the spectra in the WT and *crk10-A397T* mutant maps were area-normalised. Characteristic band intensities for the following components were mapped to visualise their distribution: 1018 cm^{-1} for pectin, 1033 cm^{-1} and 1050 cm^{-1} for hemicelluloses and cellulose, 1511 cm^{-1} for lignin, 1650 cm^{-1} for protein, and 1735 cm^{-1} for ester groups.

6.2.2 Alcohol insoluble residues preparation and hydrolysis

The protocol followed for alcohol insoluble residues (AIR) preparation was adapted from Goubet et al., 2009. Hypocotyls of 3-week-old WT and *crk10-A397T* mutant plants grown under standard conditions (see section 2.1) were sampled for this analysis. The hypocotyls were excised using a carbon steel sterile blade (N° 10 Dermaplane Scalpel blade; Swann Morton Ltd) and transferred to a 1.5 mL microfuge tubes. Thirty hypocotyls were collected per biological replicate, and

five biological replicates were analysed per genotype. All centrifugation steps were performed at 11,350 x g for one minute. One mL of 96% ethanol was added to each tube, and the hypocotyls were incubated at 65 °C for 30 minutes to inactivate endogenous enzymes. The ethanol was discarded and the hypocotyls were air dried overnight at room temperature. The dry hypocotyls were flash frozen in liquid nitrogen before being ground to a fine powder using a pestle and mortar. The material was transferred to a clean 1.5 mL microfuge tube. One mL of 100% ethanol was added to each sample, which was vigorously mixed before centrifugation to pellet the alcohol-insoluble material. The supernatant was discarded. The pellets were washed twice with 1 mL of a chloroform:methanol (2:1) mixture, followed by three consecutive washing steps with 65%, 80% and 100% ethanol. The pellet was centrifuged and the supernatant was discarded after each step. The AIR pellet was air dried overnight at room temperature. Samples were weighed and aqueous suspensions were prepared using a 10 mL glass homogenizer. A total amount of 200 - 600 µg of AIR from each sample were hydrolysed in 400 µL of 2 M trifluoroacetic acid (TFA; Sigma-Aldrich®) in screw cap 2 mL microfuge tubes at 120°C for one hour. After cooling down on ice, the samples were dried *in vacuo* at 60 °C (Concentrator Plus, Eppendorf™). The pellet was washed once with 500 µL of deionised water, followed by another step of drying *in vacuo*. The AIR samples were resuspended in 500 µL of deionised water and stored at -20°C until further processing.

6.2.3 Monosaccharide quantification by High Performance Anion-Exchange Chromatography with Pulsed Amperometric Detection

Acidic and neutral monosaccharides were quantified from AIR preparation samples by High Performance Anion-Exchange Chromatography with Pulsed Amperometric Detection (HPAEC-PAD). Acidic monosaccharides (glucuronic and galacturonic acid) were quantified using a Dionex™ ICS-3000 Ion Chromatography System (Thermo Scientific™) and CarboPac™ PA-200 columns (3x50 mm – guard column, Catalogue number 062895; and 3x250 mm – analytical column, Catalogue number 062896; Thermo Scientific™). The eluents used were (A) 0.5 M sodium hydroxide and (B) 1 M sodium acetate. A 25 µL aliquot of each sample were injected into the column. The chromatography was performed as follows: isocratic (A) 20% throughout; (B) 10%-20%, 0-5 minutes, (B) 80%, 5.5-7.5 minutes, (B) 10%, 7.6-13 minutes at 0.40 mL/minute

flow rate. For the quantification of neutral monosaccharides, a Dionex™ ICS-5000+ equipped with eluent generator (Thermo Scientific™) and CarboPac™ PA-20 columns (3x30 mm – guard column, Catalogue number 060144; and 3x150 mm – analytical column, Catalogue number 060142; Thermo Scientific™) were used. A 25 µL aliquot of each sample was injected into the column. The chromatography was performed as follows: 0.5 mL/min flow rate, isocratic 4 mM KOH, 0-14.5 minutes; 100 mM KOH, 15-18 minutes; 4 mM KOH, 18.5–23.5 minutes. Chromeleon™ analytical software (version 7.2SR5; Thermo Scientific™) was used for peak marking (as shown in Figure 6.1) and quantification. The results were exported to Excel (Microsoft Office) and the average percentage of each component relative to the total monosaccharide content was calculated.

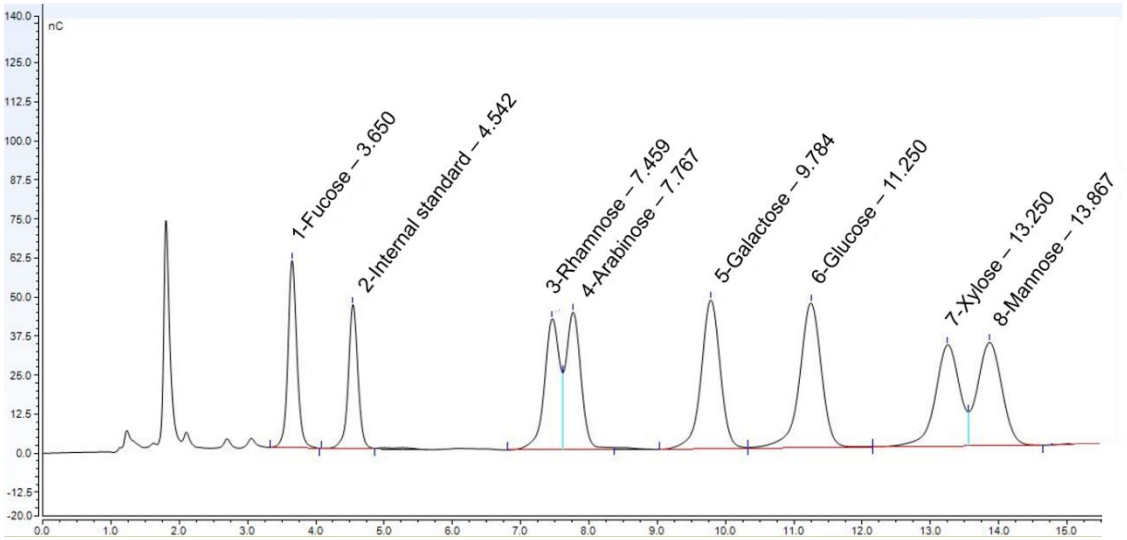

Figure 6.1 Representative monosaccharide chromatogram obtained for analysis of AIR preparation samples with HPAEC-PAD.

Respective peaks of fucose, internal standard, rhamnose, arabinose, galactose, glucose, xylose and mannose are indicated. Y-axis values indicate the detector response (nC), while x-axis represents retention time for each compound (minutes). The label of each column indicates respective monosaccharide and retention time.

6.2.4 Plant tissue sample preparation for transmission electron microscopy

Hypocotyls of 3-week-old WT and *crk10-A397T* mutant plants were excised using a carbon steel sterile blade (N° 10 Dermaplane Scalpel blade;

Swann Morton Ltd) and immediately processed by high pressure freezing (HPF) to fix the tissue. Briefly, each hypocotyl was carefully transferred to an aluminium sample carrier (6.0 x 0.5mm Type B, Catalogue number 16770127; Leica Microsystems) coated with hexadecane (Catalogue number H6703, Sigma-Aldrich®). The sample carrier was mounted onto the flat middle piece of a specimen cartridge, and the assembly was placed on the lower half cylinder of the cartridge. A drop of 0.1 M sucrose was added to the hypocotyl and another aluminium carrier was used to enclose the sample. The upper half cylinder of the cartridge was positioned to close the assembly. Each cartridge was then inserted into a EM HPM100 system (Leica Microsystems), and HPF was performed at 2100 bar pressure in under one second (time varies according to sample type and thickness). The cartridges were dispensed into a container with liquid nitrogen and each HPF sample carrier was carefully opened with fine tweezers. The hypocotyl samples were transferred to screw cap 2 mL microfuge tubes and 1 mL of 100% ethanol was added to each tube prior to freeze substitution using a Reichert AFS instrument (Leica Microsystems) according to the following programme:

Step 1: -85 °C, 26 hours;

Step 2: ramping stage, + 2 °C/hour, 12.5 hours;

Step 3: -60 °C, 8 hours;

Step 4: ramping stage, + 2 °C/hour, 15 hours;

Step 5: -30 °C, 24 hours.

The hypocotyls were transferred to glass vials (Rolled Rim Vials, G100, 7mL, TAAB) and infiltrated with LR White resin (AGR1281 LR White Resin Medium Catalysed, Agar Scientific) as described in section 3.2.1. The samples were kept overnight at 4 °C before being individually placed in embedding capsules (C094 TAAB capsule 8mm flat, polyethylene 500; TAAB) filled with fresh resin, which were incubated overnight at 60 °C to promote polymerisation. Resin blocks were removed from the oven and allowed to cool down to room temperature before sectioning.

6.2.5 Preparation and staining of ultrathin sections for transmission electron microscopy

Ultrathin sections of resin embedded hypocotyls were prepared using a UC7 Ultramicrotome (Leica Microsystems; section thickness: 90 nm) and

carefully collected onto formvar/carbon-coated copper grids (Hexagonal Pattern 200 Mesh TEM support grids, Catalogue number AGG2450C; Agar Scientific). A petri dish lined with a layer of dental wax and wrapped in aluminium foil was used as container for the staining steps. Drops of 2.5% uranyl acetate were dispensed onto the wax surface, and copper grids containing ultrathin sections were placed onto the drops for 20 minutes in the dark. The grids were individually picked with a pair of fine tweezers and rinsed by dipping in deionised water 60 times. Drops of Reynolds lead citrate (Reynolds, 1963) were dispensed onto the wax surface and the grids were once again placed in direct contact with the stain. Pellets of sodium hydroxide were scattered onto the dish to prevent the precipitation of lead by exposure to CO_2, and the petri dish was covered for three minutes. The grids were washed again by dipping in deionised water 60 times and quickly dried at 60 °C for 30 seconds. The ultrathin sections were imaged using a transmission electron microscope as described in section 2.27.

6.2.6 Immunogold labelling of resin embedded plant tissue

Ultrathin sections of resin embedded hypocotyls were prepared and collected on formvar or pioloform/carbon-coated nickel grids (Hexagonal Pattern 200 Mesh TEM support grids, Catalogue number AGG2450N; Agar Scientific). A petri dish lined with a layer of dental wax and wrapped in aluminium foil was used as container for the immunolabelling steps. The grids were placed onto drops of blocking buffer (Phosphate-buffered saline-Tween 20, 0.01% w/v BSA) and incubated for one hour at room temperature before being transferred to drops of primary antibody solution (1:10 dilution in blocking buffer). After incubation overnight at 4 °C, the grids were transferred onto drops of fresh blocking buffer for two minutes. The process was repeated three times. The grids were transferred to drops of wash buffer (PBS-T), and this step was performed twice for two minutes at a time. The grids were transferred to drops of the secondary antibody solution (1:20 dilution in blocking buffer) for one hour at room temperature followed by three wash steps of two minutes each with blocking buffer, wash buffer and distilled water, consecutively. Samples were stained with uranyl acetate and lead citrate as described in section 6.2.5. The primary monoclonal antibody LM28 (anti-glucuronoxylan, rat IgM; PlantProbes, University of Leeds) and the secondary antibody Anti-Rat IgG-gold antibody (Catalogue number G7035; Sigma-Aldrich®) were used. The experiment was performed

twice. Three biological replicates were analysed per genotype in total considering two repetitions of the experiment. Twelve randomly selected areas displaying labelling of secondary cell walls were imaged on each sample for quantification purposes. The number of gold particles per μm^2 of secondary cell wall of each image was quantified using ImageJ (Abramoff et al., 2004). The immunogold labelled ultrathin sections were imaged as described in section 2.27.

Wash buffer (PBS-T):	200 mL	Phosphate-buffered saline (PBS)
	0.1 mL	Tween 20
Blocking buffer:	10 mL	Wash buffer (PBS-T)
	0.1 g	Bovine Serum Albumin Fraction V

6.2.7 Detection of the auto-fluorescence of lignin

Transverse cross sections of resin-embedded hypocotyls of 4-week-old WT and *crk10-A397T* mutant plants were prepared (section thickness: 1 µm; see sections 3.2.1 and 3.2.2 for details of resin embedding and preparation of cross sections). The auto-fluorescence of lignin in secondary walls of xylem vessels was detected using a laser-scanning confocal microscope (see section 2.26). The lignin auto-fluorescence was excited at 405 nm and detected between 451-480 nm and 560-612 nm.

6.3 Results

6.3.1 Assessment of the cell wall composition of xylem vessels by Fourier-transform infrared spectroscopy

Previous reports in the literature have linked the collapse of xylem vessels to defects in cell wall composition, as it is the case of the *irregular xylem* (*irx*) mutants in Arabidopsis (Turner and Somerville, 1997). Therefore, potential defects in the composition of the cell walls in the hypocotyls of the *crk10-A397T* mutant were investigated. FTIR spectroscopy, a rapid technique which is routinely performed to assess the abundance and chemical properties of cell wall components in plant tissue samples (Alonso-Simón et al., 2011; Largo-Gosens et al., 2014), was used to analyse the hypocotyls of WT and *crk10-A397T* mutant plants at three weeks after sowing. This developmental stage was chosen for the

analysis as it coincides with the manifestation of the dwarf phenotype and the first observation of collapsed xylem vessels in the hypocotyl of the *crk10-A397T* mutant plants, as described in section 3.3.3.

After examination with an FTIR microscope, large variations were observed between the spectra generated from air-dried cross sections of WT and *crk10-A397T* mutant hypocotyls. The comparison between the genotypes was especially challenging as this large variation meant the spectra of individual spots were not representative of the whole cross section, while averaging across large areas could obscure regional variations. To circumvent this issue and to best represent the variability of the different samples, chemical maps were plotted to display the distribution of cell wall components across the whole hypocotyl (Figure 6.2). Maps displaying the optical density of the samples, also known as their absorbance, revealed that the *crk10-A397T* mutant hypocotyls exhibited a larger proportion of dense regions compared to the WT, although both samples display a highly dense core (Figure 6.2 A). This dense central region corresponds to the oldest, most heavily lignified xylem vessels in the hypocotyls, and it displayed high levels of polysaccharides in the WT samples (Figure 6.2 B). The *crk10-A397T* mutant hypocotyl, however, showed noticeably reduced levels of polysaccharides, besides a “fragmented” distribution compared to the WT, as regions with higher and lower content were interspersed among each other. Although the overlap between the hemicellulose and cellulose spectra precluded the quantification of these components without calibration, the ratio between the two could be calculated to provide information about their content relative to each other (1033 / 1050 cm $^{-}$1). The *crk10-A397T* mutant hypocotyls displayed a higher hemicellulose/cellulose ratio across the xylem area in comparison to the WT, in a pattern that correlates with the optical density of the sample (Figure 6.2 C). Moreover, the maps corresponding to the distribution of proteins across the hypocotyls also showed noticeable differences between the *crk10-A397T* and WT (Figure 6.2 D). Although both samples displayed low levels of proteins in their central area, a protein-rich ring surrounding the xylem in the WT samples corresponds to an area with much lower protein content in the mutant. Considering the maps generated for the characteristic 1511 cm^{-1} band of lignin, denser spots were readily identified in regions corresponding to the files of lignified xylem vessels in the WT hypocotyl (Figure 6.2 E). Although both the WT and the *crk10-A397T* mutant hypocotyls exhibit a core region containing high

levels of lignin, the outer region in the mutant showed a more fragmented pattern and a seemingly lower lignin content. We can infer that a higher ratio of lignin to polysaccharide is present in the *crk10-A397T* mutant hypocotyls considering the lower amount of total cell wall polysaccharides displayed by these samples. Finally, the maps shown in Figure 6.2 F represent the abundance of ester bonds in these hypocotyl samples. Interestingly, the area occupied by the xylem in the *crk10-A397T* mutant hypocotyl exhibited significantly reduced levels of ester bonds compared to the same region in the WT, especially across the dense xylem core.

Following the analysis of chemical maps, the spectra of individual areas containing intact xylem vessels in the WT and collapsed xylem vessels in the *crk10-A397T* mutant hypocotyl were analysed (Figure 6.3). The resulting difference spectra (*crk10-A397T* mutant – WT) revealed marked differences in the abundance of several compounds between the samples. For instance, the positive peaks at the characteristic protein amide bands (1650 and 1544 cm^{-1}) indicate increased protein levels in the mutant hypocotyls. Conversely, the smaller peaks displayed by the collapsed vessels at the characteristic 1161, 1103, 1055, and 1036 cm^{-1} bands suggest a lower content of total polysaccharides, although positive bands at 1082, 1047, 1025 and 978 cm^{-1} may indicate an increased amount of the hemicellulose xyloglucan (Kačuráková et al., 2000). The reduced height of the spectra at the ester carbonyl band at 1733 cm^{-1} possibly indicate lower levels of ester bonds within pectins and lignocellulose, and a small negative peak at 1507 cm^{-1} suggests a slightly reduced lignin content. Taken together, these negative bands suggest the potential loss of lignocellulose, although the content of lignin relative to the total amount of cell wall carbohydrates did not appear to differ significantly. Overall, the spectral differences reveal that the cell walls of the collapsed xylem vessels in the *crk10-A397T* mutant seem to have reduced levels of polysaccharides and ester crosslinks, which might impact the structure and assembly of cell walls in *crk10-A397T* hypocotyls.

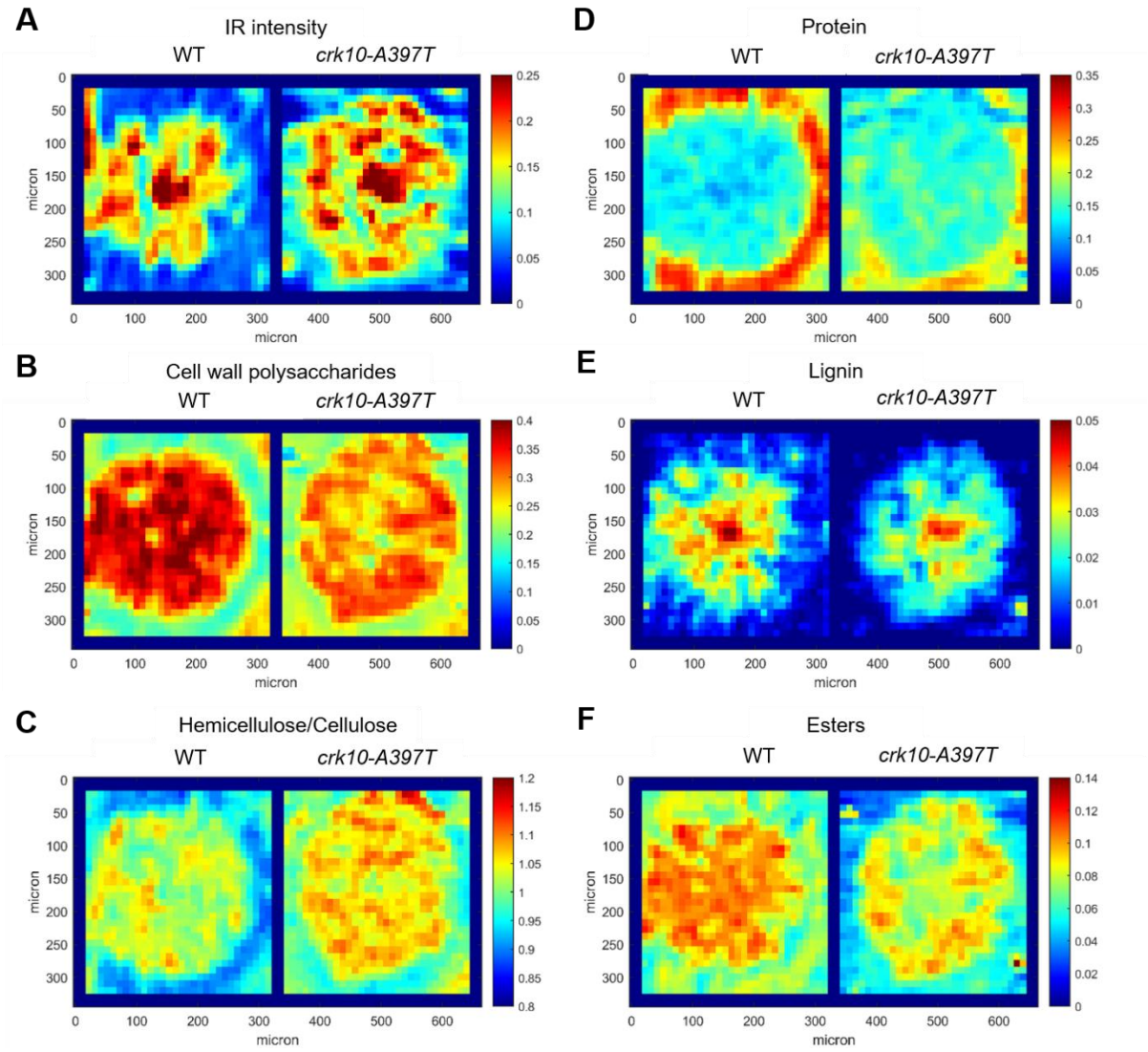

Figure 6.2 FTIR maps of the *crk10-A397T* mutant hypocotyl shows marked differences to the WT.

(A-F) Representative FTIR chemical maps of cross sections of 3-week-old WT and *crk10-A397T* mutant hypocotyls. Maps show (A) infrared (IR) intensity/spectral density, (B) the polysaccharide band maximum, (C), the hemicellulose/cellulose band ratio 1033 cm^{-1} /1050 cm^{-1}, (D) the protein amide I band (1650 cm^{-1}) intensity, (E) the lignin band (1510 cm^{-1}) intensity, and (F) the ester band (1735 cm^{-1}) intensity.

Mapping settings: XY step size = 10 µm; aperture = 20x20 $µm^2$; 128 scans were averaged at 8 cm^{-1} for each image pixel. The optical density map (A) was calculated by averaging the infrared absorption from 1800-800 cm^{-1}. Band intensities were calculated with local baselines to neighbouring minima.

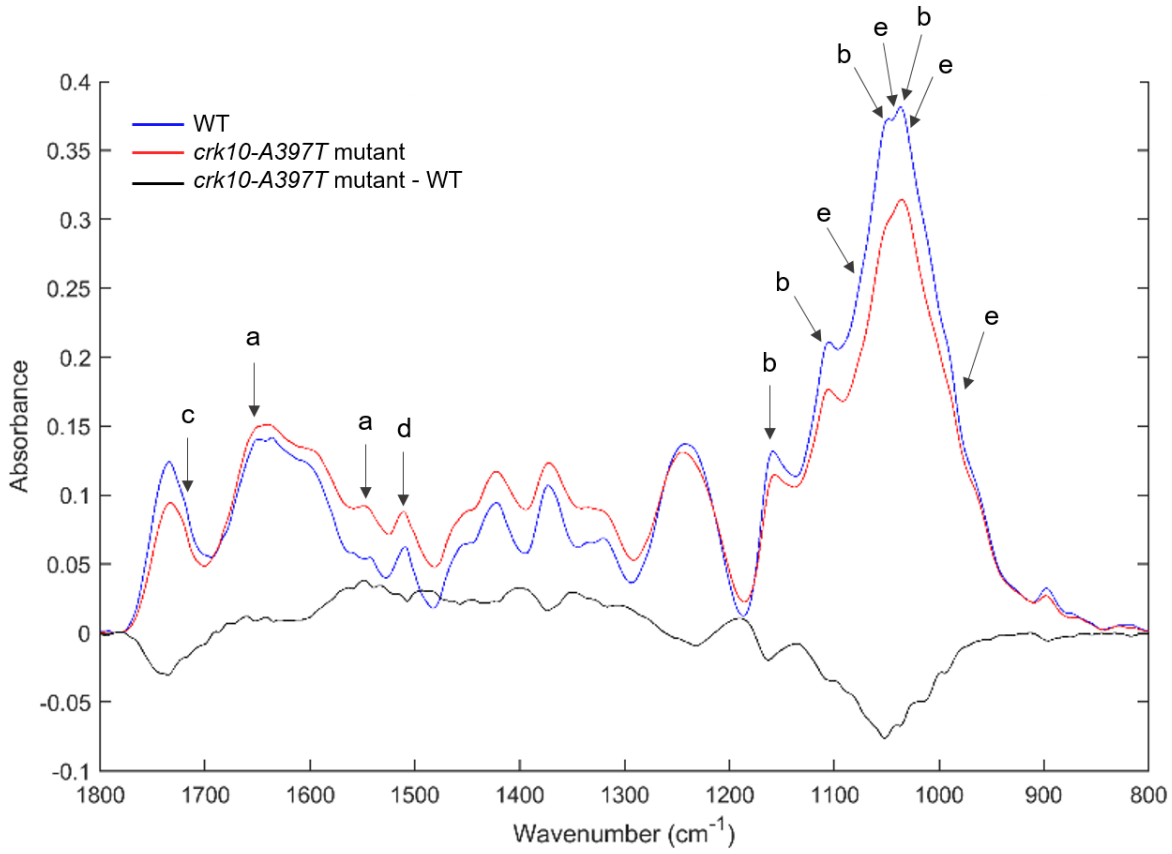

Figure 6.3 The FTIR spectra profile of collapsed xylem vessels in the *crk10-A397T* mutant hypocotyl shows marked differences to the spectra of intact vessels in the WT.

FTIR spectra of intact xylem vessels (WT), collapsed xylem vessels (*crk10-A397T* mutant), and the resulting difference spectra (*crk10-A397T* mutant – WT) are represented. Letters indicate the position of peaks corresponding to specific cell wall components: (a) protein amide (1650 and 1544 cm^{-1}); (b) polysaccharides – hemicellulose and cellulose (1161, 1103, 1055, and 1036 cm^{-1}); (c) ester carbonyl (1733 cm^{-1}); (d) lignin phenolic groups (1507 cm^{-1}); (e) xyloglucan (1082, 1047, 1025 and 978 cm^{-1}).

6.3.2 Quantification of total monosaccharides from hypocotyls of WT and *crk10-A397T* mutant plants

Monosaccharides are the building blocks of the polymers which constitute the primary and secondary cell walls of plant cells (see section 6.1). Therefore, the quantification of these molecules following hydrolysis of plant tissue sample can provide information regarding the abundance of the cell wall polymers from which they are derived. To validate and further investigate the alterations in cell wall composition suggested by the FTIR analysis of the *crk10-A397T* mutant

hypocotyls (see section 6.3.1), monosaccharides extracted from 3-week-old WT and mutant hypocotyls were quantified by HPAEC-PAD. The results were represented as the abundance of each monosaccharide relative to the total monosaccharide content, similar to the analysis performed by Brown et al. (2007; Appendix 10.1). After statistical analysis, significant differences between the content of several monosaccharides were identified between the WT and *crk10-A397T* mutant hypocotyls (Figure 6.4). Some of the most prominent differences were observed for xylose and galactose, as the *crk10-A397T* hypocotyls display a nearly 50% increase and a 30% decrease in the relative content of these monosaccharides, respectively, compared to WT samples. A more modest difference is observed for the relative content of arabinose, which is reduced by approximately 15% in the mutant hypocotyls compared to WT levels. While the levels of glucose and fucose are both increased around 26% and 24% in the *crk10-A397T* hypocotyls, respectively, the acidic monosaccharide galacturonic acid exhibits a 27% reduction compared to the WT. The content of mannose, rhamnose and glucuronic acid are not significantly different between the genotypes. These results confirm differences in the abundance of several cell wall components in the hypocotyls of the *crk10-A397T* mutant plants, as predicted by the FTIR analysis.

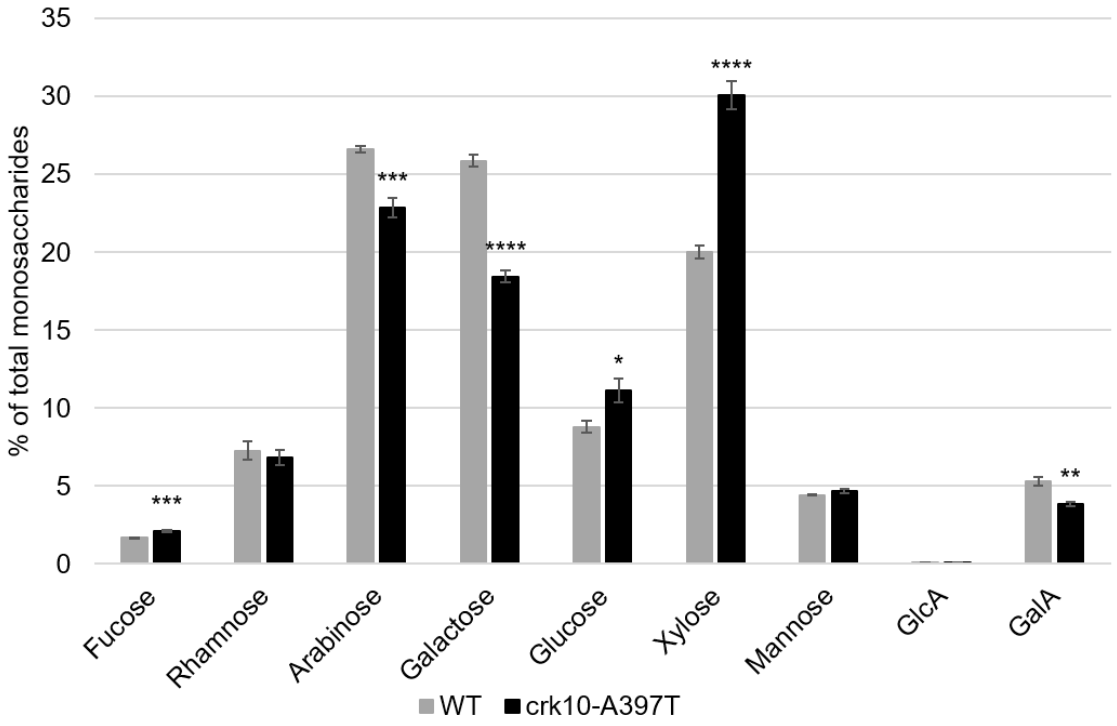

Figure 6.4 Relative quantification of neutral and acidic monosaccharides from the hypocotyls of WT and *crk10-A397T* mutant plants.

Bar chart showing the relative content of monosaccharides in the hypocotyls of 3-week-old WT and *crk10-A397T* mutant plants. Error bars represent the standard error of five biological replicates (each biological replicate was comprised of a pool of 30 hypocotyls). Asterisks indicate statistical significance (t-test): * = $p \leq 0.05$; ** = $p \leq 0.01$ *** = $p \leq 0.001$; **** = $p \leq 0.0001$.

6.3.3 Investigation of the ultrastructure of the cell wall of xylem vessels using transmission electron microscopy

Cell wall defects displayed by numerous Arabidopsis mutants have been shown to affect the ultrastructure of the secondary cell walls of xylem vessels and fibres when analysed with TEM (see section 6.1). To investigate if the secondary cell walls of collapsed xylem vessels in the *crk10-A397T* mutant hypocotyl also exhibit ultrastructural defects, resin embedded cross sections of 3-week-old hypocotyls were analysed by TEM. The secondary cell walls of intact and collapsed xylem vessels in WT and *crk10-A397T* mutant hypocotyls were closely inspected. Surprisingly, no ultrastructural defect was apparent in the cell walls of the collapsed vessels, which exhibited a similar appearance, thickness and electron density to the walls of vessels in the WT (Figure 6.5). Several xylem

vessels were imaged per biological replicate to confirm these observations were consistent, and the only outstanding characteristic observed for some, but not all, collapsed xylem vessels was the occasional presence of a layer of electron-dense material lining the inner surface of their secondary cell walls, which was also observed in some intact xylem vessels (Figure 6.6). In conclusion, unlike several cell wall mutants of Arabidopsis, ultrastructural defects do not seem to be associated with the collapse of the xylem vessels in the hypocotyls of the *crk10-A397T* mutant, as their secondary cell walls largely resemble that of xylem vessels in the WT.

Interestingly, an unexpected feature was observed in the *crk10-A397T* mutant hypocotyls during the analysis with TEM. These appear to be similar to intervessel pit membranes, which are characteristic of the xylem of angiosperms and are byproducts of the hydrolysis of non-cellulosic polysaccharides of primary cell wall and middle lamella material (Zhou et al., 2015; Kaack et al., 2019). As such, these regions are characterised by the presence of the remaining electron-lucent fine fibrils of cellulose which are not hydrolysed in the process, and can be readily identified in the hypocotyls of WT plants (Figure 6.7 A-C). Surprisingly, a prominent feature in the hypocotyls of the *crk10-A397T* mutant plants is the occurrence of pit membranes with a granulated, electron-dense appearance (Figure 6.7 D-F). A thorough literature search was unfruitful in identifying the nature of these granule-like structures, although they resemble partially hydrolysed pit membranes which also display a coarse, electron-dense appearance (Singh,1987). These structures, which were found in all biological replicates of the *crk10-A397T* mutant hypocotyls analysed in this study, were largely absent in WT hypocotyls, apart from localised instances in one of the biological samples (Figure 6.8). Unlike the *crk10-A397T* mutant hypocotyls, however, which displayed a large proportion of pit membranes with this unusual granular phenotype, the only similar observation in a WT hypocotyl consisted of a couple of intervessel regions displaying a dark staining similar to that of pit membranes in the mutant (Figure 6.8 A and C). Some of the neighbouring vessels also exhibited a thick, electron-dense lining similar to what was observed in the *crk10-A397T* mutant hypocotyl (Figure 6.8 B and D). Interestingly, these observations in the WT hypocotyl occurred in the vicinity of a xylem vessel which was occluded by round, elongated structures whose size ranged from approximately 0.3 to 1 µm (Figure 6.8 B). Following a comparison with TEM

micrographs reported in previous studies, these structures appear remarkably similar to xylem-infecting bacterial pathogens (Appendix 10.2). Taken together, these observations indicate that the granulated, electron-dense pit membranes found in the *crk10-A397T* mutant are virtually absent in WT hypocotyls, although similar features (electron-dense intervessel junction and xylem vessel lining layer) were observed in a biological replicate in the vicinity of a xylem vessel occluded with putative bacterial cells.

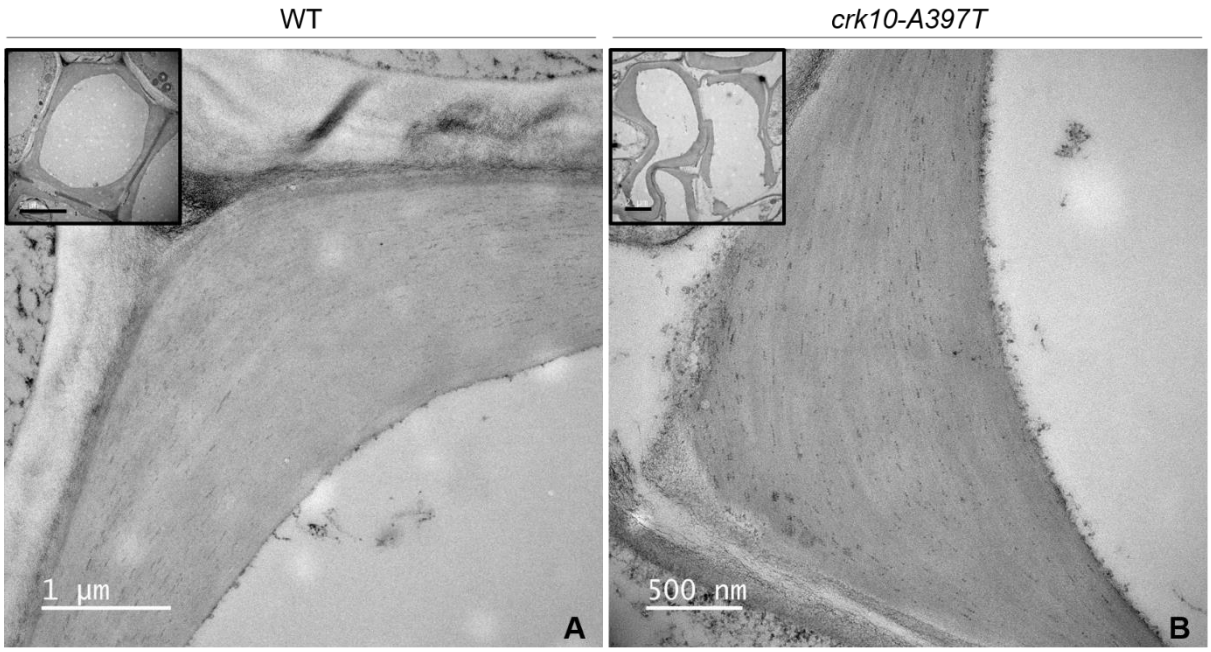

Figure 6.5 The ultrastructure of the secondary cell wall of collapsed xylem vessels resembles that of intact vessels in the WT.

TEM micrographs showing the secondary cell wall of xylem vessels from cross sections of hypocotyls of 3-week-old (A) WT and (B) *crk10-A397T* plants. Inserts at top left-hand corner show lower magnification of the imaged area. Bars, (A) 1 µm; (B) 500 nm; (insert A) 5 µm; (insert B) 2 µm.

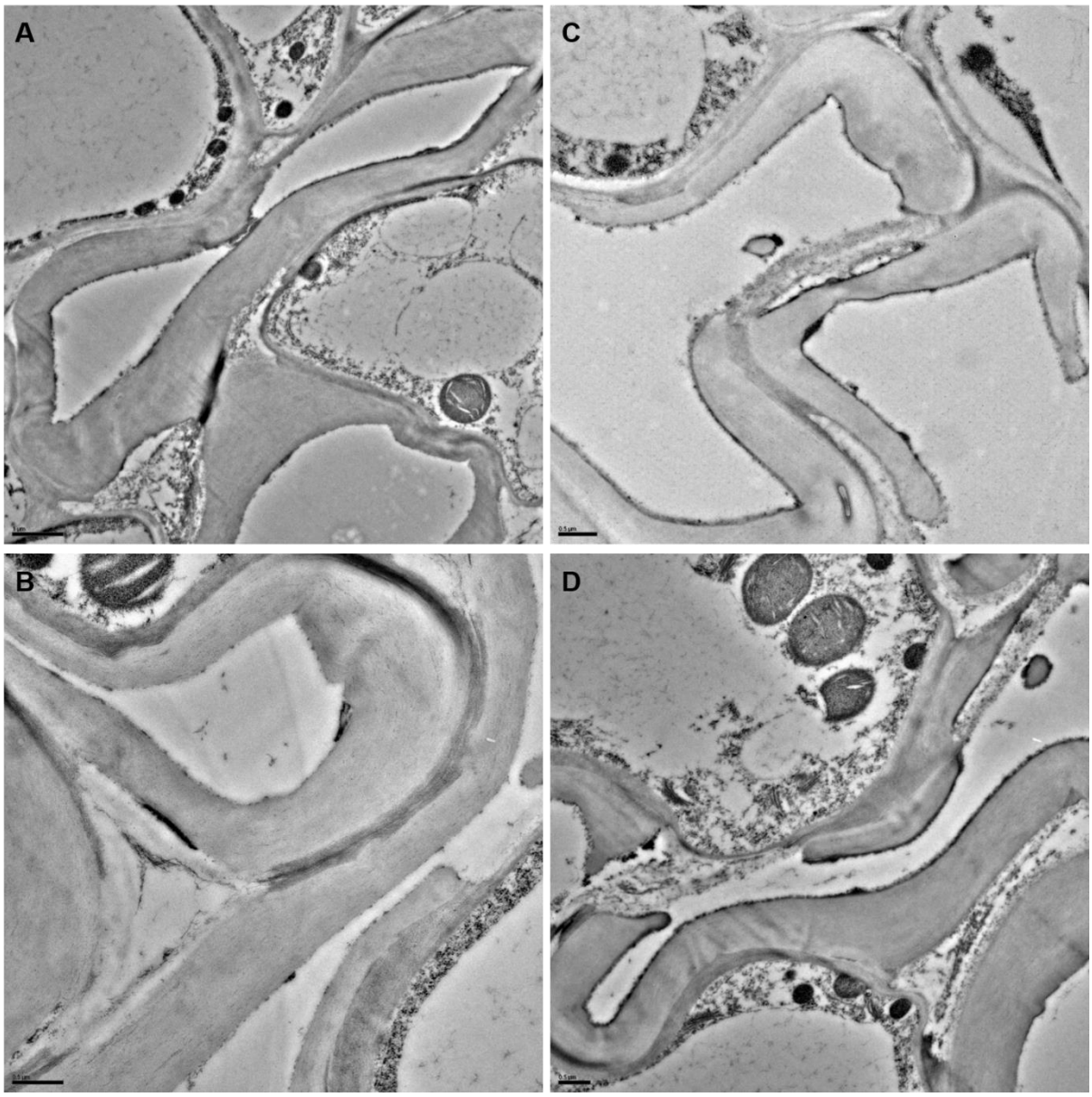

Figure 6.6 Collapsed xylem vessels in the hypocotyls of *crk10-A397T* mutant plants.

(A-D) Representative TEM micrographs showing collapsed xylem vessels in resin-embedded hypocotyls of 3-week-old plants. Hypocotyls from three individual plants were analysed, and the whole xylem area was inspected on each cross section to document the collapsed xylem vessels. Electron-dense material lining the inner surface of the secondary cell wall can be seen in (A), (C) and (D). Bars, (A) = 1 µm; (B-D) = 0.5 µm.

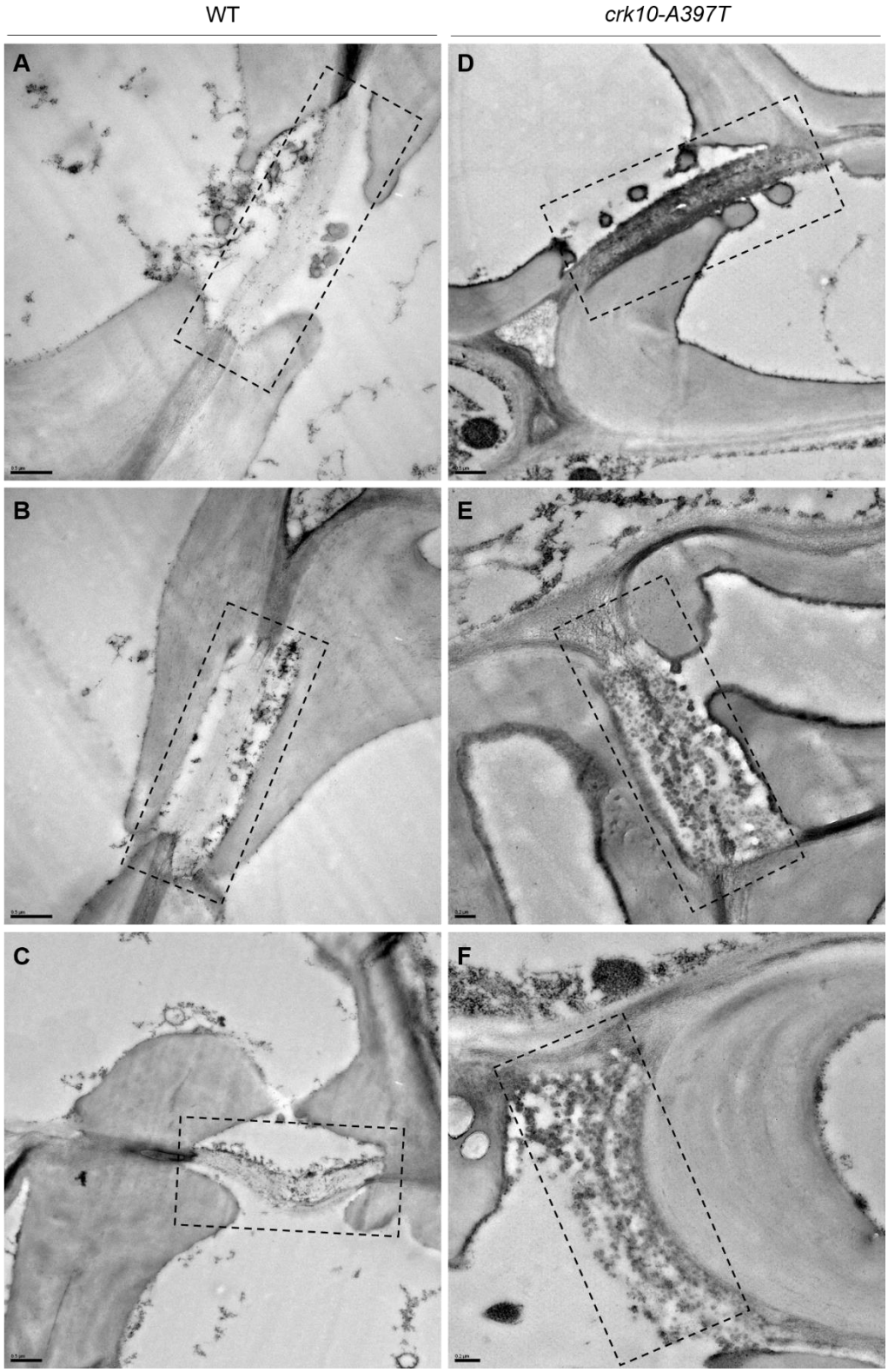

Figure 6.7 The pit membranes in the hypocotyl of the *crk10-A397T* mutant exhibit a granulated, electron-dense appearance.

TEM micrographs displaying the pit membranes of (A, B, C) WT and (D, E, F) *crk10-A397T* mutant hypocotyls from 3-week-old plants. Pit membranes are indicated by dashed rectangles. Bars, (A-D) = 0.5 µm; (E, F) = 0.2 µm.

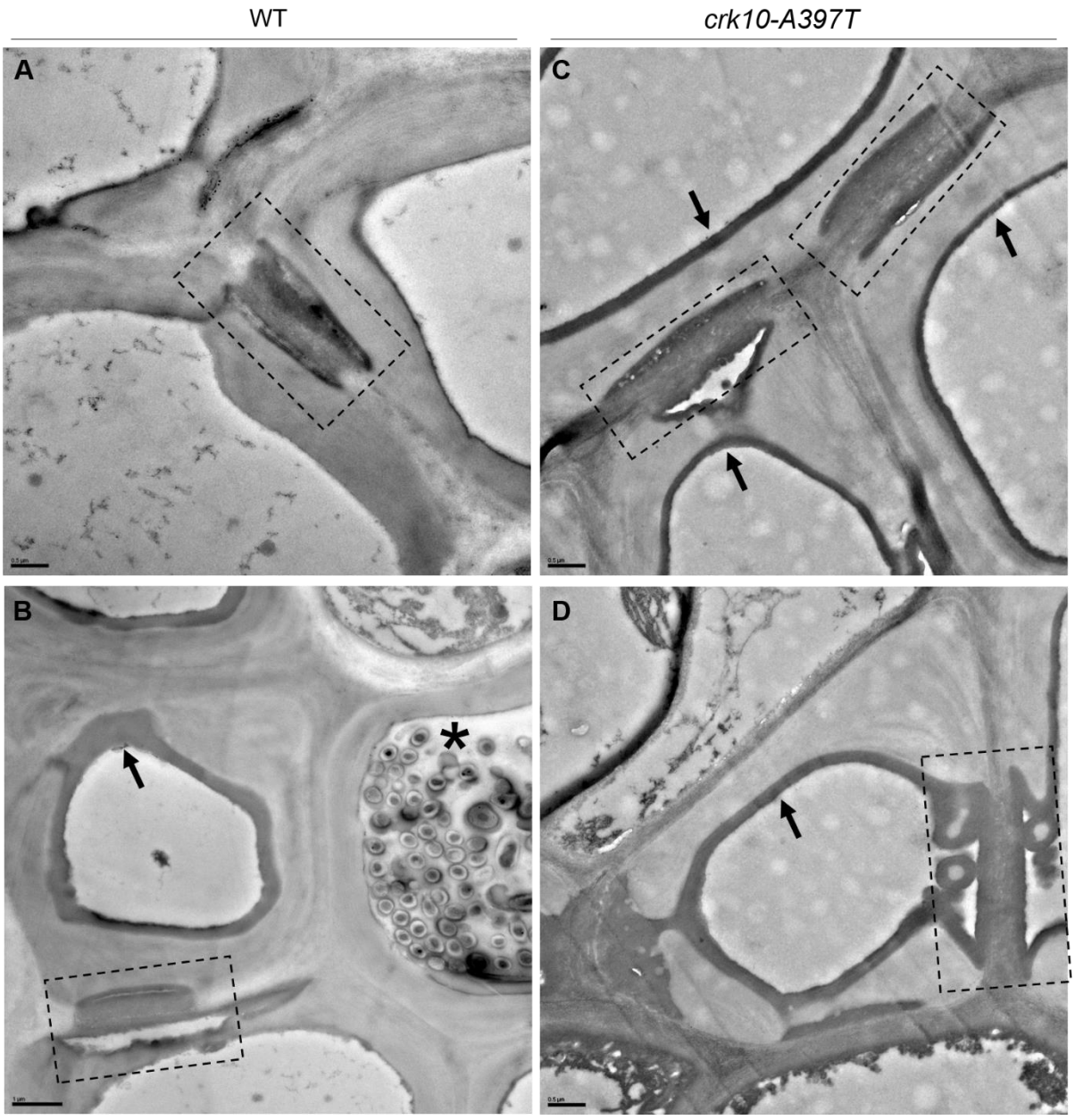

Figure 6.8 Unusual features found in pit membranes and xylem vessels in hypocotyls of the *crk10-A397T* mutant were observed in a WT hypocotyl sample. TEM micrographs showing xylem vessels and pit membranes in 3-week-old hypocotyls of (A, B) WT and (C, D) *crk10-A397T* mutant plants. Black arrows indicate electron-dense layer lining the inner surface of the secondary cell wall of xylem vessels. Dashed rectangles indicate pit membranes. Asterisk indicates occluded xylem vessel. Bars, (A, C, D) = 0.5 µm; (B) = 1 µm.

6.3.3 Detection and quantification of glucuronoxylan in the xylem vessels of WT and *crk10-A397T* mutant hypocotyls with immunogold labelling

The results of the FTIR analysis presented in section 6.3.1 suggested the presence of altered levels of cell wall polysaccharides in the hypocotyls of the *crk10-A397T* mutant plants, including a higher ratio of hemicellulose to cellulose. Additionally, the quantification of monosaccharides with HPAEC-PAD (section 6.3.2) indicated differences in the composition of cell walls in the mutant hypocotyls, including a significant increase in the relative content of xylose. This monosaccharide forms the backbone of xylan chains such as glucuronoxylan, one of the major hemicelluloses in the secondary cell walls of dicotyledons. Although the relative content of glucuronic acid in the *crk10-A397T* hypocotyls is not statistically different to the WT, the ratio between xylose and glucuronic acid is similar in both samples (Appendix 10.1). This suggests that the increased xylose content is accompanied by an increase in glucuronic acid and consequently, higher levels of glucuronoxylan. Corroborating this hypothesis, the xylan glucuronyltransferase *GLUCURONIC ACID SUBSTITUTION OF XYLAN 1* (*GUX1*), which is required for the addition of glucuronic acid and methylglucuronic acid to the xylan backbone (Mortimer et al., 2010) is transcriptionally induced in the mutant hypocotyls at three weeks after sowing (see section 5.3.10). To validate this hypothesis, resin-embedded hypocotyls of 3-week-old WT and *crk10-A397T* mutant plants were subjected to immunogold labelling.This labelling technique used in electron microscopy relies on the detection of the molecule of interest (antigen) with a specific primary antibody, which is subsequently recognised by a secondary antibody conjugated to colloidal gold particles (Pacy, 1990). When imaged using a TEM, the electron-dense gold particles appear as black dots on the labelled sample, allowing the localisation and quantification of the target antigen. The anti-glucuronoxylan antibody LM28, which binds to unmethylated and methylated glucuronosyl substitution of xylan (Cornuault et al., 2015) was used for this experiment. Three biological replicates of WT and *crk10-A397T* mutant were analysed post-labelling with LM28 (IgM) / gold-conjugated secondary antibody (IgG). Imaging of these samples by TEM confirmed that labelling was mainly associated with secondary cell walls of xylem vessels in both WT and *crk10-A397T* hypocotyls (Figure 6.9). Quantification of the number of gold particles per μm^2 of secondary cell wall revealed that intact and collapsed

xylem vessels in the *crk10-A397T* mutant hypocotyls displayed, on average, just over double the amount of labelling compared to the cell walls of WT xylem vessels (Appendix 10.3). These results confirm the presence of increased levels of the hemicellulose glucuronoxylan in the secondary cell walls of xylem vessels in the *crk10-A397T* mutant hypocotyls, as suggested by transcriptomic analysis and quantification of monosaccharides.

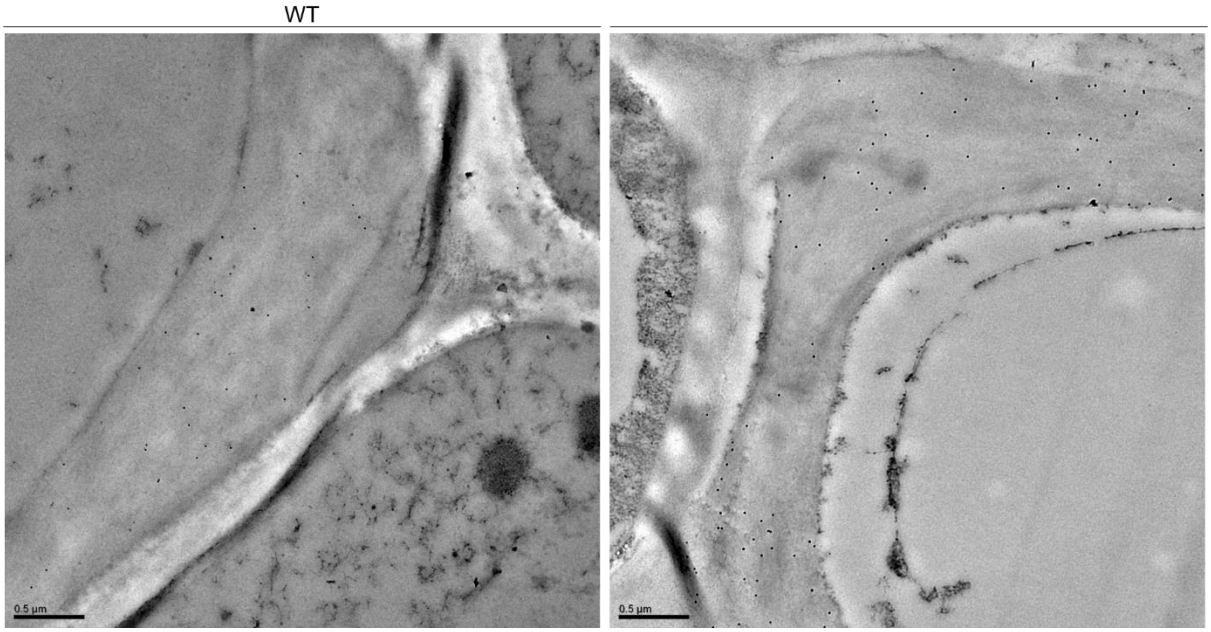

Figure 6.9 Immunogold labelling analysis confirmed that increased levels of glucuronoxylan are present in the secondary cell walls of xylem vessels in the *crk10-A397T* mutant hypocotyls.

TEM micrographs of immunogold labelled cross sections of 3-week-old hypocotyls of (A) WT and (B) *crk10-A397T* mutant plants. Gold nanoparticles are visualised as black dots. Primary antibody: LM28 (rat IgM, anti-glucuronoxylan); secondary antibody: gold-conjugated anti-rat IgG. Bars, 0.2 µm.

6.3.4 Analysis of the auto-fluorescence of lignin in hypocotyls of WT and *crk10-A397T* mutant plants

The FTIR results presented in section 6.3.1 suggest that the *crk10-A397T* mutant hypocotyls contain slightly reduced levels of lignin associated with cellulose (lignocellulose) in regions where collapsed xylem vessels are present, although the overall ratio of lignin to total cell wall polysaccharide does not seem to be greatly affected. However, light microscopy analysis revealed that collapsed xylem vessels display a more intense dark brown colouration following staining with the lignin-specific dye potassium permanganate compared to unaffected xylem vessels in the WT hypocotyl (see section 3.3.3), which suggests increased levels of lignification. Furthermore, the transcriptional induction of genes involved in the biosynthesis of lignin also indicates potential increased levels of this polymer in the hypocotyls of the *crk10-A397T* mutant plants (see section 5.3.10). Lignin is known to display auto-fluorescence when excited with ultraviolet (UV) light wavelengths, as well as having a broad emission range due to the presence of several fluorophores within the polymer (Donaldson, 2013; Donaldson, 2020). Therefore, to further investigate whether xylem vessels in WT and *crk10-A397T* mutant hypocotyls display different levels of lignification, the lignin present in resin-embedded cross sections of 4-week-old hypocotyls was visualised by auto-fluorescence using a laser scanning confocal microscope (Figure 6.10; under λ_{exc} = 405 nm; λ_{em} = 451-480 nm and 560-612 nm). Interestingly, the auto-fluorescence detected from secondary cell walls of xylem vessels in the hypocotyl of the *crk10-A397T* mutant was remarkably more intense than that of the WT xylem vessels across the whole area occupied by the xylem in the hypocotyl (Figure 6.6 A-B). The difference in the auto-fluorescence intensity is even more pronounced when clusters of xylem vessels were closely analysed under higher magnification (Figure 6.6 C-D). Therefore, the increased auto-fluorescence signal associated with the secondary cell walls of xylem vessels in the hypocotyl of the *crk10-A397T* suggests increased lignification. How to explain the contradicting results suggested by the FTIR and the detection of lignin auto-fluorescence is discussed in section 6.4.

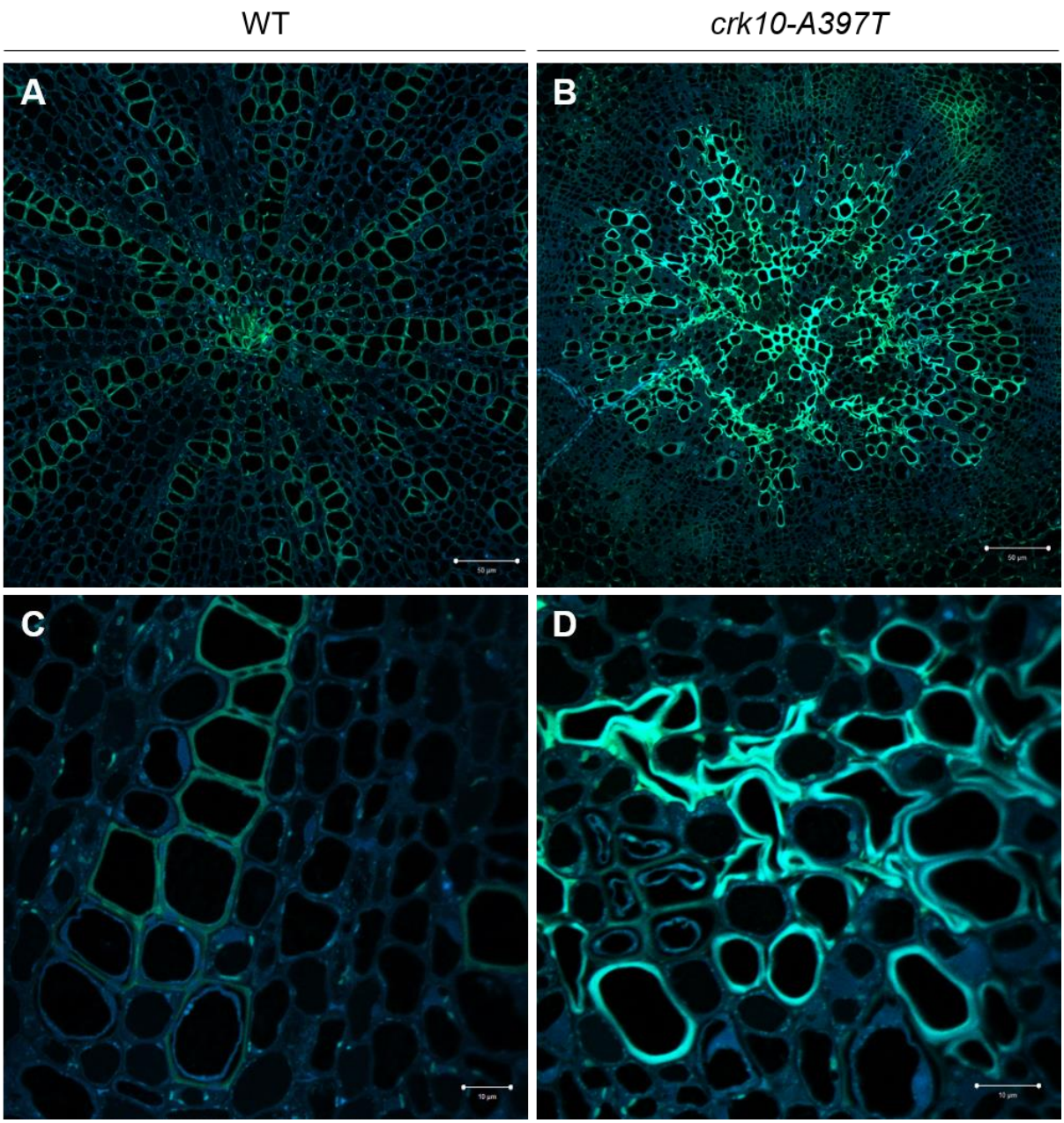

Figure 6.10 Auto fluorescence of lignin in xylem vessels of *crk10-A397T* mutant hypocotyl is more intense than in the WT.

Micrographs showing the auto-fluorescence of lignin in resin-embedded cross sections of 4-week-old (A, C) WT and (B, D) *crk10-A397T* mutant hypocotyls (excitation = 405 nm; emission = 451-480 nm / 560-612 nm). Bars, (A-B) = 50 µm; (C –D) = 10 µm.

6.4 Discussion

The severely collapsed xylem vessel phenotype observed in roots and hypocotyls of *crk10-A397T* mutant plants (see sections 3.3.3 and 3.3.4) resembles that of the *irx* mutants of Arabidopsis. This anatomical defect together with the transcriptional reprogramming of numerous cell wall-related genes (see section 5.3.10) were a strong indication that cell wall remodelling occurs in the hypocotyls of the *crk10-A397T* plants. To obtain a preliminary profile of the composition of these cells walls, cross sections of 3-week-old hypocotyls of WT and mutant plants were analysed with FTIR. This spectroscopy technique is a rapid, non-destructive method which allows the analysis of cell wall polymers and functional groups *in muro* and the visualisation of the heterogeneity of a sample when coupled with microscopy (Alonso-Simón et al., 2011). As expected, the infrared maps generated with FTIR for WT and *crk10-A397T* mutant hypocotyls revealed extensive differences in the total amount and distribution of several components. Differences in optical density indicated the presence of denser regions scattered across the mutant hypocotyl, which supposedly correlate with tight clusters of collapsed xylem vessels. A reduction in the total content of polysaccharides was also noticeable in the mutant, especially in the central area where older xylem vessels are found. The ratio of hemicelluloses to cellulose was also remarkably different between the two genotypes, with an increased ratio seen in the mutant. Although it is not feasible to distinguish the cellulose and hemicellulose peaks from each other due to their proximity in the spectrum, the ratio of these polysaccharides relative to each other was clearly altered in the xylem area of the *crk10-A397T* mutant hypocotyls. These differences were also reflected in the negative peaks observed at the characteristic polysaccharides bands (1161, 1103, 1055, and 1036 cm^{-1} bands) after spectral subtraction. The overall reduction in polysaccharide content suggested by the FTIR analysis corroborates the collapsed xylem vessel phenotype of the *crk10-A397T* mutant, as decreased levels of hemicelluloses and/or cellulose might directly impact the rigidity of cell walls.

The reduced content of ester bonds suggested by the FTIR results hints at decreased levels of pectin esterification, which is also known to affect the rigidity of the cell wall. Low methyl-esterification of pectin molecules enables them to cross-link with Ca^{+2} ions to give rise to the egg-box conformation, which is known to increase the stiffness of the cell wall. However, it is important to

remember that pectin polysaccharides primarily compose primary cell walls, which are partially hydrolysed during the xylem vessel differentiation programme (Benayoun, 1982). Therefore, it is likely that the reduction in ester bonds detected in the mutant hypocotyls also reflects reduced ester linkages in secondary cell walls of xylem vessels. The existence of α-ester, γ-ester and ferulate/diferulate esters between lignin and carbohydrates in secondary cell walls has been extensively reported in the literature (Balakshin et al., 2011; Tarasov et al., 2018; Terrett and Dupree, 2019). One of the most thoroughly investigated interactions is that of the glucuronic acid substitutions of xylan in mediating xylan:lignin cross-linking through ester bond linkages (Eriksson et al., 1980; Watanabe and Koshijima, 1988). Recent analysis using solid-state NMR have also revealed the presence of interactions between xylan and lignin in Arabidopsis, although predominantly non-covalent bonds were detected (Kang et al., 2019). Therefore, the negative peak at the carbonyl ester band in the *crk10-A397T* mutant hypocotyls might be an indication of one of two scenarios; in one instance, the number of ester linkages between lignin and carbohydrates is overall reduced, but the content of polysaccharides and lignin is unaffected. In scenario two, decreased amounts of carbohydrates and lignin in the secondary cell walls cause the apparent reduction in the number of ester bonds simply due to the lower abundance of these molecules and, consequently, the ester linkages that bind them. Taking into consideration that the FTIR analysis also suggests decreased levels of polysaccharides and slightly reduced lignin content, the second scenario is likely to at least partially explain these observations in the *crk10-A397T* mutant hypocotyl.

Another difference highlighted by the FTIR analysis is the apparent reduction in the overall lignin content in the mutant hypocotyls suggested by a small negative peak at 1507 cm^{-1}. This observation however, contradicts the results obtained with histochemical techniques. The dark brown colouration of the secondary cell walls of collapsed xylem vessels in the mutant hypocotyls when stained with potassium permanganate (section 3.3.3) was a clear indication of increased lignification. This hypothesis was reinforced by the observation of more intense lignin auto-fluorescence signal detected with confocal microscopy in the *crk10-A397T* hypocotyls. The discrepancy between the FTIR results and the histochemical analysis might be due to limitations of the spectroscopic technique. FTIR data are semi-quantitative, and the spectra generated are extremely

complex to interpret due to the overlap of numerous bands corresponding to different polymers and the complex linkages and interactions between the polysaccharides (Liu et al., 2021). The use of other analytical techniques for the quantification of lignin, such as the popular acetyl bromide method (Barnes and Anderson, 2017), would be useful to resolve the discrepancies observed in this chapter.

The quantification of neutral and acidic monosaccharides presented in section 6.3.2 is another tool to infer the abundance of cell wall polysaccharides in plant tissue samples. The preparation of alcohol insoluble residues (AIR) from plant material is an easy and quick way to obtain a cell wall enriched suspension for subsequent analysis (Pettolino et al., 2012). This method successfully removes inorganic salts, metabolites, enzymes, lipids and chlorophyll from the plant tissue extracts, although proteins, nucleic acids and polyphenols often co-precipitate with the cell wall material (Fangel et al., 2021). The method used in this study allows the quantification of monosaccharides derived mainly from hemicellulose, pectins and some amorphous cellulose, but not crystalline cellulose. This is a limitation of the chemical hydrolysis with TFA, a relatively weak acid which does not hydrolyse crystalline cellulose. The analysis of the hypocotyl-derived AIR preparation provided further insight into the differences in cell wall composition between WT and *crk10-A397T* mutant samples. The significant increase in the relative content of xylose together with a constant xylose:glucuronic acid ratio between WT and *crk10-A397T* samples were a strong indication of elevated levels of glucuronoxylan, the main hemicellulose in secondary cell walls of Arabidopsis. This result, confirmed by the immunolabelling of hypocotyl cross sections, denoted the reinforcement of secondary cell walls suggested by the up-regulation of cell wall biosynthetic genes in the *crk10-A397T* mutant transcriptome (section 5.3.10). Although not yet validated with additional analytical methods, the reduction in galactose in the *crk10-A397T* mutant hypocotyl might be an indication of reduced levels of galactose-substituted xyloglucan or depletion of arabinogalactans type I and II decorations in rhamnogalacturonan I (RGI). Likewise, the decreased content of arabinose could relate to reduced levels of the hemicellulose glucuronoarabinoxylan or arabinose-substituted RGI, and the reduction in galacturonic acid content might suggest decreased levels of pectic polysaccharides, mainly homogalacturonan. Notably, XG, RGI and HG are major components of primary rather than secondary cell

walls; thus, it is unclear how and whether reduced levels of these compounds play any role in the collapse of xylem vessels. Lastly, the increased levels of the monosaccharide glucose may be an indication of higher levels of polysaccharides with glucan-linked backbones or amorphous cellulose, but does not reflect the content of crystalline cellulose as briefly mentioned earlier in this section. To evaluate the content of crystalline cellulose-derived glucose, hydrolysis with a stronger acid as, for instance, sulphuric acid, would be required. Alternatively, a technique such as the Updegraff protocol (Updegraff, 1969; Kumar and Turner, 2015) could be performed to assess the levels of crystalline cellulose in these hypocotyls. Furthermore, other techniques could be used to complement the results here presented and provide a broader overview of the polysaccharides present in these hypocotyls, such as oligosaccharide mass profiling (OLIMP; Lerouxel et al., 2002). Labelling of hypocotyl cross sections with fluorophore-tagged antibodies (immunofluorescence) also offers the possibility to assess the abundance and localisation of cell wall components across different cell types (Verhertbruggen et al., 2017), and might be a useful strategy to validate the results suggested by FTIR and quantification of monosaccharides.

Moving on from the biochemical analysis of cell wall composition, imaging of ultrathin cross sections of plant tissue with TEM allows the visualisation of the ultrastructure of cell walls (Zhou et al., 2015). Several reports in the literature have shown the association between a defective cell wall composition and reduced secondary cell wall thickening (Zhong et al., 2005; Lee et al., 2007; Persson et al., 2007), uneven cell wall appearance and loosening of secondary cell wall layers (Jones et al., 2001; De Meester et al., 2018). Surprisingly, despite the extensive cell wall modifications suggested by the spectroscopic and biochemical analysis, the secondary cell walls of the collapsed xylem vessels in the *crk10-A397T* mutant hypocotyl display a similar appearance to the cell walls of intact vessels in the WT. Therefore, although the widespread alterations in cell wall composition are likely to play a role in the collapse of these xylem vessels, they do not cause any obvious ultrastructural defects which can be observed by TEM. Nevertheless, unexpected anatomical traits were observed in the *crk10-A397T* mutant hypocotyls thanks to the high-resolution offered by TEM. The inner surface of the secondary cell walls of intact and collapsed vessels was often coated with a layer of dark, unknown material, which was largely absent in WT vessels. The most striking feature, however, was the electron-dense, granulated

aspect of pit membranes in the mutant hypocotyls in contrast to the electron lucent fibrils of cellulose in the WT counterparts. Pit membranes lie in the centre of bordered pits, which are cavities that connect adjacent vessels and act as safety valves in the xylem (Zimmermann and Brown, 1971; Choat et al., 2007). Whilst the pit membrane allows the transport of water between xylem vessels, it must simultaneously avoid the spread of air bubbles (embolism) and vascular pathogens to ensure the proper functioning of the plant hydraulics system. The hydrolysis of primary cell wall and middle lamella material which is required for the differentiation of pit membranes involves the action of hydrolytic enzymes which remove most non-cellulosic polysaccharides, and generally results in the near transparent membrane as viewed with TEM (Kaack et al., 2019). However, pit membranes vary greatly in appearance among plant species, ranging from thick and dense to thin and highly porous (Choat et al. 2007; Zhou et al., 2015). TEM micrographs depicting pit membranes with a granulated, coarse appearance have been previously reported in the literature (Benayoun, 1983; Singh, 1987), although in these cases the granules are smaller than those observed in the *crk10-A397T* mutant. Importantly, most studies reporting TEM analysis of bordered pits were not performed in Arabidopsis, which hampers the direct comparison of anatomical features due to the variability observed among plant species. Nevertheless, the observation that one WT biological replicate contained vessel-vessel junctions which displayed similar features to these unusual pit membranes suggests this phenomenon might also occur in WT plants. The observation of a neighbouring xylem vessel occluded by structures which resemble bacterial pathogens raises the question of whether this structural modifications could be part of a response to pathogen invasion. Although purely speculative at this stage, these observations give rise to a number of questions. Could the granule-like particles observed in the mutant pit membranes be non-hydrolysed cell wall components? And could the suppression of the full hydrolysis of pit membranes be a mechanism to stop pathogen spread? Finally, are these modified pit membranes somehow contributing to the collapse of the xylem vessels, given that bordered pits are essential structures in the regulation of the hydraulics system of plants? Further experiments would be required to address these questions.

In conclusion, the results presented in this chapter reveal the profound differences in cell wall composition in the hypocotyls of WT and *crk10-A397T*

mutant plants. Although further experiments will be necessary to identify specific cell wall defects associated with the collapsed xylem vessels, these preliminary results are extremely useful to narrow down the list of potential cell wall modifications to be targeted for additional analyses. Although an obvious cause for this vasculature defect could not be unambiguously identified so far, several hypotheses can be put forward in light of these results. The reduction in both polysaccharides content and ester bonds abundance suggested by FTIR would fit well in a scenario where the secondary cell walls of these xylem vessels are weakened and, therefore, cannot withstand the internal negative pressure generated by the transport of water and ultimately collapse. However, the increased ratio of glucuronoxylan suggested by HPAEC-PAD and immunogold labelling suggests the reinforcement of secondary cell walls, in agreement with the induction of several cell wall biosynthetic genes evidenced in the mutant transcriptome. The lack of ultrastructural defects in the cell walls of the collapsed xylem vessels also deepens the mystery surrounding this phenotype, as the extensive changes in cell wall composition suggested by the results presented in this chapter do not seem to interfere with the assembly of the layers of the secondary cell wall.

The fortuitous observation of the unusual pit membranes in the *crk10-A397T* mutant hypocotyl raised yet another hypothesis to explain the mechanisms underlying the collapse of xylem vessels. As pit membranes contribute to xylem hydraulics resistance and play essential roles in limiting the spread of embolism throughout the network of xylem vessels, could the atypical pit membranes observed in the *crk10-A397T* mutant somehow contribute to collapse of xylem vessels by promoting embolism and vessel cavitation? Whatever the answer, further investigation will hopefully reveal additional details about this intriguing phenotype.

Chapter 7 – Exploring the roles of the *crk10-A397T* mutant allele in plant-pathogen interactions

7.1 Introduction

The expression of the *crk10-A397T* mutant allele is associated with the constitutive induction of genes involved in defence responses to pathogens in the hypocotyls of Arabidopsis plants (section 5.3.4). Among these genes are key players in the signalling pathways mediated by the hormone salicylic acid (SA), components of the systemic acquired resistance (SAR) machinery and several transcriptional factors which regulate defence responses (see Tables 5.3 and 5.8). However, the transcriptional reprogramming of genes is only one aspect of the multifaceted responses evolved by plants to resist pathogen attack, which also include the deployment of several "molecular weapons" aimed at evading infection and stopping pathogen spread.

Plants have evolved an elaborate innate immune system which allows the perception of pathogens and the swift activation of inducible defence responses to avoid disease. A basal layer of inducible plant immunity relies on cell surface receptor-like kinases (RLKs) and receptor-like proteins (RLPs) to recognise danger patterns in the extracellular environment, the so-called pattern recognition receptors (PRRs; see section 1.3.3 for a review on RLKs in plant immunity). The warning signals recognised by PRRs can be pathogen-derived molecules, known as pathogen-associated molecular patterns (PAMPs), or host-derived molecules released in response to or as a result of damage caused by pathogen attack, known as damage-associated molecular patterns (DAMPs; Macho and Zipfel, 2014). This first line of defence, coined as pattern-triggered immunity (PTI), is often overcome by pathogens which secrete a wide range of disease-inducing effector molecules into the intracellular environment of plant cells (Trdá et al., 2015). These effectors, however, may be recognised and targeted by the components of the effector-triggered immunity (ETI), an intracellular system that provides an extra layer of protection by accelerating and amplifying PTI responses and often causing a hypersensitive response (HR) characterised by localised host cell death (Jones and Dangl, 2006; Cui et al., 2015). ETI receptors are nucleotide binding leucine-rich repeat (NB-LRR or NLRs) proteins, molecular switches which undergo conformational changes upon effector recognition which allows the interaction with downstream signalling components (Cui et al., 2015).

The successful perception of the pathogenic threat by immune receptors is followed by downstream events such as the production of reactive oxygen species (ROS), extracellular alkalinisation, calcium signalling and cascades of mitogen-activated protein kinases (MAPKs) that promote the transcriptional reprogramming of defence-eliciting genes (Rasmussen et al., 2012; Wu et al., 2014; Tsuda et al., 2015). A “zigzag” model proposed by Jones and Dangl in 2006 represents plant immunity as a two-branched system resulting from the evolutionary arms race between host plants and pathogens: PAMP-triggered immunity mediated by PRRs is the first layer of defence (1), which is often evaded by effector-triggered susceptibility promoted by successful pathogens (2). This is, in turn, followed by the ability of resistant plants to recognise effectors and promote ETI (3), which can also be avoided by pathogens through natural selection (4). Although considered separate mechanisms in the “zigzag” model, some authors have argued in recent years that the distinction between PTI and ETI is not always clear, and therefore, plant immunity should be thought of as a continuum rather than a system comprised of subcategories (Thomma et al., 2011). In agreement with this idea, two recent studies have shown that PTI and ETI mutually potentiate each other, as PRR-mediated signalling is necessary for the activation of robust ETI responses, and NLRs are required to replenish and enhance PTI signalling components (Ngou et al., 2021; Yuan et al., 2021).

Adding to the complexity of plant immune responses, an intricate network of signalling pathways orchestrated by phytohormones, especially salicylic acid (SA), jasmonic acid (JA) and ethylene (ET), regulates plant-pathogen interactions (Pieterse et al., 2012). As a general rule, SA coordinates responses tailored specifically to pathogens which feed on living host cells (biotrophs), whereas JA/ET regulate defence to pathogens which induce host cell death and feed on the necrotic plant tissue (necrotrophs; McDowell and Dangl, 2000; Glazebrook, 2005). While ET and JA often act synergistically, SA and ET/JA pathways interact mainly via mutual repression (Schenk et al., 2000; Kunkel and Brooks, 2002). The crosstalk between the signalling pathways governed by these hormones is, however, far more complex than these simplified assumptions (De Vleesschauwer et al., 2014). SA coordinates basal immunity and the establishment of SAR, a mechanism which promotes the systemic priming of the plant to subsequent infection (Durrant and Dong, 2004). Accumulation of SA also leads to the induction of various defence-related genes, such as *EDS1* and

PAD4. These lipase-like proteins physically interact with each other and are required for basal and ETI responses downstream of NLR proteins, and together promote the accumulation of SA in a positive feedback loop (Zhou et al., 1998; Falk et al., 1999; Jirage et al., 1999; Feys et al., 2001). Additional studies have shown that *EDS1* and *PAD4* not only boost SA signalling pathways, but also act in parallel with this hormone to maintain and protect the SA-related branch of immune responses in Arabidopsis (Venugopal et al., 2009; Cui et al., 2017). The transcriptional regulator *NON-EXPRESSOR OF PR GENES* (*NPR1*), a key signalling component of responses downstream of SA, acts as a master regulator of SAR and mediates the crosstalk between SA and JA defence signalling pathways (Spoel et al., 2003; Fu and Dong, 2013). However, NPR1-independent activation of SA-induced responses has also been identified (Uquillas et al., 2004; Lu et al., 2009). JA-mediated signalling is crucial for several developmental and stress-responsive pathways, and it is tightly regulated by the jasmonate ZIM domain (JAZ) transcriptional repressors (Kazan et al., 2012). *MYC2*, a master regulator of JA signalling in response to pathogens and wounding, is one of the genes which is transcriptionally repressed by JAZ proteins in the absence of JA (Kazan and Manners, 2013; Lyons et al., 2013). Downstream of these pathways, transcription factors (TFs) act as nodes of convergence between the responses elicited by different hormones. *WRKY70*, for example, determines the balance between SA and JA responses during pathogen attack by positively regulating SA-dependent pathways while suppressing JA-related genes (Li et al., 2004; Li et al., 2006). Conversely, *WRKY33* acts as a negative regulator of SA responses, which prevents SA-dependent suppression of JA pathways during infection with the necrotrophic pathogen *Botrytis cinerea* (Birkenbihl et al., 2012).

Although a plethora of studies have investigated immune responses in the leaves of plant species, considerably less is known about the molecular and biochemical aspects of plant-pathogen interactions in roots and hypocotyls. Primarily targeted by vascular wilt pathogens, growing evidence in the literature hints at the existence of root- and hypocotyl-specific defence responses, such as patterns of transcriptional reprogramming and hormonal crosstalk which differ between leaves and roots (Berne an Javornik, 2016; Chuberre et al., 2018). These responses include physical and chemical barriers tailored to hamper the penetration of soil-borne pathogens into the network of xylem vessels, which are exploited as a route to spread to other tissues (De Coninck et al., 2015). Some

of these are preformed barriers, such as the impermeable cell walls of xylem vessels and the constitutive secretion of anti-microbial molecules at low levels (Millet et al., 2010). Despite these preformed obstacles, however, successful bacterial, fungal and oomycete invaders surpass the root cortex and breach the lignified cell walls of xylem vessels, where they thrive by acquiring nutrients from the relatively poor xylem sap, nutrient leakage from neighbouring cells and enzymatic digestion of plant cell walls (Yadeta et al., 2013). As a consequence of pathogen proliferation, infected xylem vessels are occluded and transport of water is impaired, causing plant wilting and growth arrest. In addition to obstruction due to pathogen colonisation, host-promoted deposition of pectin-rich gels and gums inside xylem vessels in a bid to restrict pathogen spread also contributes to vessel occlusion and plant wilting (Doohan, 2011; Yadeta et al., 2013). Other mechanisms triggered by the presence of vascular wilt pathogens include secondary cell wall reinforcement, vascular coating and the formation of parenchyma-derived cell protrusions known as tyloses into the xylem vessel cavity (De Coninck et al., 2015). In addition to physical barriers, the accumulation of secondary metabolites with anti-microbial activity, such as phytoalexins and phenolics, is also induced upon pathogen invasion in vascular tissues. Plants undergoing infection with vascular pathogens not only display the characteristic wilting caused by vessel occlusion, but also develop symptoms such as vein clearing, vascular browning, leaf chlorosis and necrosis (Doohan, 2011). The speed and severity at which disease progresses are also dependent on the host age and fitness, the virulence of the pathogen and local environmental conditions (Yadeta et al., 2013).

Filamentous fungi of the genus Fusarium infect a wide range of plant species around the world, including cereal crops such as wheat, barley and rice (Parry et al., 1995). These fungal pathogens cause Fusarium head blight (FHB), root rot and seedling blight among other diseases in their host species. Bioassays using Arabidopsis as a model have been increasingly employed to facilitate the study of host-pathogen interactions involving Fusarium species (Chen et al., 2006; Brown et al., 2011; Chen et al., 2014; Lyons et al., 2015; Masachis et al., 2016). FHB, mainly caused by *Fusarium graminearum*, is a serious problem for crop production worldwide, as it not only affects grain yield but also results in the accumulation of mycotoxins in the grains, deeming them unsuitable for human and animal consumption (Sutton, 1982; McMullen et al., 1997). *F. graminearum*

uses cereal florets as a point of entry in the host plants, and the production of hydrolytic enzymes aids the fungal penetration into the plant tissue (Walter et al., 2010). A coordinated biphasic response comprised of SA and ET/JA pathways was shown to be essential to promote resistance to this pathogen, given that a brief initial biotrophic phase of infection is followed by a switch to a necrotrophic lifestyle (Ding et al., 2011). *F. oxysporum,* another member of the Fusarium genus, is a vascular wilt pathogen comprising over 150 host-specific strains which is the causal agent of disease in several plant species (Gordon and Martyn, 1997; Baayen et al., 2000). This pathogen begins its infection cycle in the roots as a biotroph, but switches to a necrotrophic lifestyle once it has spread throughout the plant causing necrosis of leaf tissue and eventual plant death (Lyons et al., 2015). Studies have shown that *F. oxysporum* promotes disease by hijacking the *COI1*-mediated JA signalling pathway to induce host susceptibility and, accordingly, the *coi1* mutant of Arabidopsis is almost completely resistant to infection (Thatcher et al., 2009; Trusov et al., 2006). The knockout of other regulators of JA responses, such as the mediator complex subunit *PFT1* and the transcription factor *MYC2*, similarly conferred resistance to *F. oxysporum* (Anderson et al., 2004; Kidd et al., 2009). Comparably, overexpression of the ET- and JA-regulated *ERF1* also confer increased resistance to *F. oxysporum*, which was dependent on ET, JA and *NPR1*-dependent SA signalling pathways, but independent of *PAD4* and *EDS1* (Berrocal-Lobo and Molina, 2007). While JA mainly promotes susceptibility to vascular wilt, treatment with exogenous SA prior to pathogen inoculation led to a 50% reduction in the number of plants developing disease symptoms compared to mock-treated plants (Edgar et al., 2006). Consistent with a requirement for SA to promote resistance to Fusarium vascular wilt, impaired SA biosynthesis (*sid2*), signalling (*pad4*) and accumulation (*35S:NahG*) caused enhanced disease susceptibility in Arabidopsis mutants compared to WT plants, although *npr1* did not affect the disease outcome (Diener and Ausubel, 2005). Kidd et al. (2011) have also described the requirement of auxin for the disease progression in Arabidopsis, as auxin signalling mutants showed enhanced resistance to *F. oxysporum*.

In this chapter, experiments designed to explore the roles played by the *crk10-A397T* allele in plant immunity are reported. The transcriptional induction of defence-related genes and the vasculature-specific phenotype displayed in the roots and hypocotyls of the *crk10-A397T* mutant suggest the activation of defence

responses tailored to hamper vascular pathogen attack. To test whether these responses render the *crk10-A397T* mutant more resistant to infection with a vascular pathogen, root infection assays with *F. oxysporum* were performed. Genetic crosses were also included in the bioassays in an attempt to identify defence-related genes which are required for the defence responses mediated by the *crk10-A397T* allele. The presence of collapsed xylem vessels in the hypocotyls of these plants was also investigated to uncover a potential correlation between the vasculature defect present in the *crk10-A397T* mutant and the outcome of disease. Additionally, a detached leaf assay with *F. graminearum* was performed to test whether the defence responses elicited by the *crk10-A397T* allele could affect the outcome of foliar infection.

7.2 Materials and Methods

7.2.1 Fungal strains

The root infection assays described in section 7.2.3 were performed with *F. oxysporum* formae speciales *conglutinans 699*, kindly provided by Dr Antonio di Pietro (Department of Genetics, University of Cordoba, Spain). The detached leaf assay described in section 7.2.10 was performed using the reference WT *F. graminearum* strain PH-1, kindly provided by Dr Kim Hammond-Kosack and Dr Ana Karla Machado Wood (Department of Biointeractions and Crop Protection, Rothamsted Research, UK).

7.2.2 Determination of the concentration of fungal spore suspensions

The concentration of spore suspensions of *F. graminearum* and *F. oxysporum* was determined using a Bright-Line™ haemocytometer (Hausser Scientific™). Dilutions of the original suspension were prepared in sterile deionised water, and 10 µL aliquots were pipetted onto the haemocytometer counting chamber. After covering the chamber with a glass cover slip, the haemocytometer was placed under a Carl Zeiss binocular microscope coupled with light source (ZEISS, Germany) and the number of spores present inside the 25 central squares of the grid area were counted. The average spore count per square was used to calculate the concentration of the initial suspension using the

following equation: $\frac{Spores\ count}{4x10^{-6}}\ x\ dilution\ factor$. The suspension was diluted with sterile water to the final working concentration used for each experiment (see sections 7.2.3. and 7.2.10).

7.2.3 Root infection assay with *F. oxysporum*

The bioassay system used in this study to investigate the interaction between Arabidopsis and *F. oxysporum* was adapted from Masachis et al. (2016). Arabidopsis seeds were surface sterilised as described in section 2.1 and placed on ½ Murashige and Skoog (MS; Duchefa Biochemie) 0.8% agar (Agar type E, Catalogue number A4675; Sigma-Aldrich®) plates. The plates were sealed with micropore™ medical tape (3M©, UK) before stratification at 4 °C for two days. The plates were transferred to a growth room to allow germination and seedling growth for 12 days (16h/8h, 23/18 °C, approximately 200 µmol m^{-2} per second of light). The sealed plates were taken into a biosafety containment level 2 facility where the experiment was subsequently performed. To prepare the suspension of spores (microconidia) for inoculation, 100 mL of sterile potato dextrose broth (PDB, Catalogue number P6685; Sigma-Aldrich®) in a 500 mL conical flask was inoculated with 50 µL of a 30% glycerol stock of *F. oxysporum* f. sp*. conglutinans* 699 spores (stock concentration 5 x 10^8 per mL). The flask was incubated at 28 °C and 180 rpm in an orbital shaker for four days to allow fungal growth and production of microconidia. The fungal culture was filtered with miracloth and transferred to two 50 mL sterile conical tubes in a laminar flow hood. The samples were centrifuged at 4,500 x g for ten minutes. The supernatant was discarded and the pellet of microconidia was resuspended in 15 mL of sterile deionised water. The concentration of the microconidial suspension was determined as described in section 7.2.2, and a working suspension adjusted to a concentration of 1 x 10^6 microconidia per mL was prepared. Aliquots of the spore suspension were pipetted into the wells of a six-well cell culture plate (Merck™) and five seedlings were carefully transferred into each well ensuring the roots were fully submerged in the suspension. Mock inoculation with sterile deionised water was performed as a control. The seedlings were incubated for 20 minutes at 28 °C and 40 rpm in orbital shaker before being transferred to trays filled with Levington F2 + Sand compost plus vermiculite mixture (3:1). The seedlings were arranged according to a randomised block design, considering rows within a tray as the

block structure. Fifty to eighty plants per genotype were used in each iteration of the experiment. The trays were transferred to a growth chamber (16/8h, 28/25 ºC) and mortality was assessed daily between seven and 20 days post-inoculation (DPI). A mortality curve was plotted for each repetition of the experiment and the results were statistically analysed (see section 7.2.11).

7.2.4 DNA extraction for fungal burden quantification

Arabidopsis seedlings were grown and inoculated with *F. oxysporum* as described in section 7.2.3. At two and seven DPI, whole seedlings were carefully removed from the compost using fine tweezers and the roots were briefly rinsed with sterile water to remove residual compost. The seedlings were immediately transferred into 15 mL conical tubes kept in liquid nitrogen, and genomic DNA extraction was performed according to Yu et al., 2019. The frozen plant material was ground using a pestle and mortar, and the resulting fine powder was transferred to a 2 mL sterile microfuge tube kept in liquid nitrogen. A 500 µL aliquot of YM-CTAB buffer was added to the samples and the tubes were gently inverted several times until the mixture was homogeneous. The tubes were incubated at 65 ºC for 30 minutes with occasional mixing. A 500 µL aliquot of chloroform was added to each sample and mixed by gently inverting the tubes. The samples were kept at room temperature for one minute before being centrifuged at 12,900 x g for five minutes at 4 ºC. The top aqueous layer was transferred to a sterile 1.5 mL microfuge tube and mixed with an equal volume of isopropanol by occasional gentle inversion. Following an incubation step of 30 minutes at – 20 ºC, the tubes were centrifuged at 12,900 x g for ten minutes at 4 ºC to obtain the DNA pellet. The supernatant was discarded, and the pellet was washed twice with 1 mL of 75% ethanol with brief vortexing before air drying at room temperature for five minutes. The DNA pellet was resuspended in 100 – 500 µL of sterile deionised water and DNA concentration was assessed using a NanoDrop™ (Thermo Scientific™) instrument as described in section 2.11. The integrity of the DNA was assessed by agarose gel electrophoresis.

YM-CTAB buffer:	2.6 g	Cetrimonium bromide (CTAB)
	130 mL	1 M Tris-HCl pH 8.0
	52.65 g	NaCl
	26 mL	0.5 M EDTA
	1 L	distilled water

The buffer was autoclaved and β-mercaptoethanol was added (2-4% final concentration) immediately before use.

7.2.5 Quantification of fungal burden by qPCR

Genomic DNA extracts obtained as described in section 7.2.4 were used as template for qPCR reactions to determine relative abundance of *F. oxysporum* compared to Arabidopsis genomic DNA. The qPCR reaction and analysis were performed as described in section 2.15. The abundance of the *ACTIN1* gene of *F. oxysporum* was normalised to the *ACTIN2* gene of Arabidopsis, and fungal burden was expressed relative to the WT plants at two DPI. Eight seedlings per genotype were pooled and processed as one biological replicate per experiment. Three independent repetitions of the experiment were performed. The results were statistically analysed as described in section 7.2.11.

7.2.6 Genetic crossing of Arabidopsis plants

Seeds of Arabidopsis plants were sown on Levington F2+Sand compost and trays were kept in standard long day conditions as described in section 2.1. Seven to ten days after germination, the seedlings were transferred to individual pots and plants grown under the same conditions for six to seven weeks. Pots were removed from the cabinets and taken to a clean working station where pollination was performed. An inflorescence stem of the plant to be pollinated was gently immobilised with tape on the working surface allowing for a cluster of buds to be placed under a binocular microscope. Siliques, open flowers and open buds were removed with scissors. Sepals and petals of closed buds were carefully removed with fine tweezers. Buds in which anthers were found to have already released pollen were discarded. Buds containing immature anthers were carefully emasculated (anther removal), with special attention not to damage the stigma or style, and plants were returned to the growth chambers at this stage to allow the stigma to mature overnight. On the following day, the emasculated plants were returned to the working station and a mature anther from the pollen donor

plant was carefully picked and rubbed against the stigma of emasculated buds, ensuring some pollen was retained on the surface of the stigma. The process was repeated for several buds on consecutive days to maximise the chances of successful pollination, at the end of which the floral meristem was removed to avoid mixing cross- and self-pollinated flowers. The pollinated plants were returned to the growth room to allow for silique development. Successfully cross-pollinated siliques were collected when dry and the seeds were harvested and stored at room temperature in glass vials.

7.2.7 Genotyping of genetic crosses

The *crk10-A397T* mutant was genetically crossed to the following lines:

Table 7.1 T-DNA and transgenic lines used for genetic crosses with the *crk10-A397T* mutant.

Line	**Background**	**Type**	**Mutation / insertion**	**Reference**
eds1-2 (AT3G48090)	Col-0	Deletion	Deletion of region 905 – 1844 of genomic sequence.	Bartsch et al., 2006
pad4-1 (AT3G52430)	Col-0 (originally Ler mutant backcrossed to Col-0)	EMS mutant	Nonsense point mutation (G>A) at position 1076 of the coding sequence replacing codon 359 with a stop codon (TGG → TAG).	Jirage et al., 1999
npr1-1 (AT1G02450)	Col-0	EMS mutant	Missense point mutation (T>C) at position 1000 of the coding sequence, leading to the substitution of	Cao et al., 1997

			histidine 334 with tyrosine.	
35S:NahG	Col-0	Transgenic line	Transgenic line overexpressing the salicylate hydroxylase (*NahG*) gene from *Pseudomonas putida*.	Gaffney et al., 1993; Delaney et al., 1994
myc2 (AT1G32640)	Col-0	SALK line	SALK_017005; T-DNA insertion in exon (gene without introns).	Alonso et al., 2003
wrky33 (AT2G38470)	Col-0	GABI-Kat	GK-324B11; T-DNA insertion in first intron.	Rosso et al., 2003
wrky70 (AT3G56400)	Col-0	SALK line	SALK_025198; T-DNA insertion in first exon.	Alonso et al., 2003
cyp81d11 (AT3G28740)	Col-0	WiscDsLox line	WiscDsLOX5E07; T-DNA insertion in first intron.	Woody et al., 2007

eds1-2, *pad4-1* and *npr1-1* seeds were kindly provided by Prof Jurriaan Ton (Department of Animal and Plant Sciences, University of Sheffield, UK). *35S:NahG* seeds were kindly provided by Dr Ana Karla Machado Wood (Department of Biointeractions and Crop Protections, Rothamsted Research, UK). The *wrky33* line was obtained from the Max Planck Institute (Germany), and *myc2*, *wrky70* and *cyp81d11* seeds were ordered from NASC (Nottingham, UK). After crossing with the *crk10-A397T* mutant was performed, filial 1 (F1) hybrid seeds were sown on soil and plants were grown in cabinets under long day conditions. The hybrid status of the F1 population was easily confirmed by the observation of dark green leaves typical of the heterozygous *crk10-A397T* mutant (see section 3.3.1). Their progeny (F2) were harvested and at least 40 seeds of the F2 segregating population per genetic cross were sown. Genomic DNA

extracted from leaf samples was used for genotyping the F2 progeny (primer sequences can be found in Table 7.2). Homozygous plants for the *crk10-A397T* allele were identified based on their dwarf and/or dark green leaves phenotype and sequencing of the genomic region spanning the mutation site. Homozygous plants for T-DNA insertions were confirmed by genotyping according to instructions from the Salk Institute Genomic Analysis Laboratory webpage (http://signal.salk.edu/tdnaprimers.2.html) for SALK- and WiscDsLox-derived lines, and instructions from the GABI-Kat website (https://www.gabi-kat.de/) for GABI-Kat-derived lines. The deletion in *eds1-2* and the presence of the *NahG* transgene were detected by analysis of PCR products, and the point mutations in *pad4-1* and *npr1-1* were confirmed by sequencing of PCR products amplified from genomic DNA. Genotyping PCRs and sequencing chromatograms are documented in Appendix 11.1.

7.2.8 Sample preparation and light microscopy analysis

Arabidopsis plants were grown for four weeks under standard growth conditions as described in section 2.1. Whole hypocotyls were collected, fixed and embedded in resin as described in section 3.2.1. Transverse cross section preparation, staining and imaging was performed as detailed in section 3.2.2. Three biological replicates were analysed per genotype.

7.2.9 Micrografting of Arabidopsis plants

The micrografting of Arabidopsis plants was performed as described in section 3.2.8. Successful grafts were used for an iteration of the detached leaf assay with *F. graminearum* described in section 7.2.10.

7.2.10 Detached leaf assay with *F. graminearum*

The bioassay system used in this study to assess the interaction between Arabidopsis and *F. graminearum* was based on the protocol described by Chen et al., 2006. The bioassays were performed in biosafety containment level 2 facilities. *F. graminearum* strain PH-1 was routinely cultured on synthetic nutrient poor agar (SNA) plates at room temperature under constant light as described in Brown et al., 2011. To induce the production of fresh spores (conidiospores), 10-day-old plates were washed with TB3, and the conidial suspension was harvested in sterile water 72 hours later. The concentration of the conidial suspension was

determined as described in section 7.2.2, and a working dilution adjusted to a concentration of 4 x 10^4 spores per mL was prepared. Fully expanded rosette leaves from Arabidopsis plants grown for six weeks in short day conditions (8h/16h; 23/18 °C; 200 µmol m^{-2} s^{-1}) were excised using carbon steel sterile blades (N° 10 Dermaplane Scalpel blade; Swann Morton Ltd). A total of twelve leaves collected from individual plants were used per genotype, and each leaf was considered a biological replicate. The leaves were organised according to a block design in the first iteration of the experiment; each plate contained two rows of four leaves, with one leaf per genotype in each row. Each row within a plate was considered a block, and six plates were prepared in total. For the iteration of the experiment using grafted plants, successful grafts were kept in short day cabinets for six weeks. Nine grafted plants were sampled per genotype, and two leaves per plant were collected. All 18 leaves of each genotype were placed in the same agar plate. All leaves were placed with the abaxial side facing upwards on 1% water agar (Agar type E, Catalogue number A4675; Sigma-Aldrich®) in 10 cm^2 square sterile Petri dishes. For both experiments, two small wounds were made on each leaf by gently scratching the leaf surface with a 10 µL plastic pipette tip. A 5 µL aliquot of a suspension of *F. graminearum* spores was applied on each lesion, and mock inoculation with 5 µL of sterile distilled water was performed as a control. The plates were closed and kept in darkness for three days in growth room before being exposed to low light conditions (16h/8h; 23/18 °C; 40 µmol m^{-2} s^{-1}). The plates were photographed daily to document disease symptoms, and photographs of the plates were used for image analysis as described in Wood et al., 2021. Colour (RGB) photographs taken with a Nikon (D90) were used for the quantification of the diseased leaf area using the LemnaTec Lemna Grid software (LemnaTec GmbH, Aachen, Germany). The images were converted to grayscale and segments of leaf area were designated using a colour-based classification and thresholding. Misclassified pixels and gaps were removed with the application of filters, and a customised colour-based classification was applied to score leaf area as healthy or diseased. The results were exported to Excel (Microsoft Office) and then statistically analysed (see section 7.2.11).

Synthetic nutrient poor agar (SNA):	0.1%	KH_2PO_4
	0.1%	KNO_3
	0.1%	$MgSO_4.7H_2O$
	0.05%	KCl
	0.02%	glucose
	0.02%	sucrose
	2 %	agar
TB3:	0.3%	yeast extract
	0.3%	Bacto Peptone
	20%	sucrose

7.2.11 Statistical analyses

Statistical significance of the differences in relative diseased leaf area between genotypes were tested by analysis of variance (ANOVA); the proportion data were logit-transformed to satisfy the test requirements by using the formula $logit = \log(\frac{x+0.005}{1-(x+.005)})$, where "x" is the relative diseased leaf area obtained from the image analysis. The statistical significance of the differences between genotypes was tested, and the block structure of leaves nested within rows nested within plates was considered. The probability of survival of each genotype in the bioassay with *F. oxysporum* was assessed with a generalized linear model (Bernoulli distribution; logit link function fitted to the final mortality outcome of each plant); statistical significance of the genotypic effect was tested after removing variation associated with plant position within rows of different trays and quantified through a Chi-squared statistic of the difference in deviance. Statistical significance of the differences in fungal burden between genotypes were tested by ANOVA (expression levels were log-transformed to meet the ANOVA requirements, and each individual experiment was considered as a block).

Table 7.2 Table of primers.

Primer	Sequence (5' – 3')	Purpose
FoxACTIN1 For	ATGTCACCACCTTCAACTCCA	qPCR
FoxACTIN1 Rev	CTCTCGTCGTACTCCTGCTT	qPCR
AtACTIN2 For	TTCCCTCAGCACATTCCAGCAGAT	qPCR
AtACTIN2 Rev	AACGATTCCTGGACCTGCCTCATC	qPCR
eds1-2 Int For	AAGCCAAAGTGTCAAGCCC	Genotyping PCR
eds1-2 For	TCGGTCCAAGAGAGTGAACA	Genotyping PCR
eds1-2 Rev	TCGTATGGCTTTCCTTTGAG	Genotyping PCR
pad4-1 For	AGTGGCGTTTTAGTCAAAGAATG	PCR / sequencing
pad4-1 Rev	GCGTATCTGCTTCTCACACA	PCR / sequencing
npr1-1 For	TAGACGTAAAGAGCTTGGTTTGGAG	PCR / sequencing
npr1-1 Rev	CGAGCAGCGTCATCTTCAATTC	PCR / sequencing
NahG For	GTCGGGTCGTCCTGATCG	PCR
NahG Rev	ACCCTTGACGTAGCGCACCC	PCR
Salk_017005 (*myc2*) RP	TTTGGTACAACCGCTCGTAAC	Genotyping PCR
Salk_017005 (*myc2*) LP2	CTCCAAGTTCTAGCTCCCAGC	Genotyping PCR
GABI_324B11 (*wrky33*) For	TCACAACAATCCGGAAGAACATC	Genotyping PCR
GABI_324B11 (*wrky33)* Rev	TTGTAGTTGTAGTTGTGGTCGGAG	Genotyping PCR
GABI_KAT T-DNA	ATAATAACGCTGCGGACATCTACATTTT	Genotyping PCR
Salk_025198 (*wrky70*) RP	CAAACCACACCAAGAGGAAAG	Genotyping PCR
Salk_025198 (*wrky70*) LP2	GGCTACTTATGATTCTTGCAACC	Genotyping PCR
WiscDSLOX5E07 (cyp81d11) RP	ACGGCCGCGTAAACTAAACCT	Genotyping PCR
WiscDSLOX5E07 (cyp81d11) LP	CGGCCACCATTCTAATGATGTT	Genotyping PCR
Salk LBb1.3	ATTTTGCCGATTTCGGAAC	Genotyping PCR
WiscDSLOX p745	AACGTCCGCAATGTGTTATTAAAG	Genotyping PCR

7.3 Results

7.3.1 Exploring the role of the *crk10-A397T* mutant allele during infection with *F. oxysporum* in Arabidopsis

Vascular wilt diseases are caused by phytopathogens which exploit the network of xylem vessels to proliferate from the root to the shoot organs, obstructing the transport of water and causing plant wilting and death (Yadeta and Thomma, 2013). The reinforcement and remodelling of plant cell walls is a known defence mechanism deployed by plant cells against these pathogens, as the cell wall acts as physical barrier to halt pathogen penetration and spread (Underwood, 2012). Thus, the remodelling of cell walls (see section 5.3.9 and Chapter 6) in the hypocotyls of *crk10-A397T* plants, together with the constitutive induction of defence-related genes (see section 5.3.4) and accumulation of SA (see section 5.3.7), resemble aspects of the responses tailored to hamper invasion by vascular pathogens. Therefore, to test whether these characteristics render the *crk10-A397T* mutant more resistant to the disease induced by a vascular-infecting pathogen, a root infection assay with the soil-borne *F. oxysporum* was performed. Besides WT and *crk10-A397T* plants, a knockout (*crk10-2*; see section 3.3.7) and an overexpression (*CRK10* OE-1; see section 3.3.8) line of *CRK10* were also included in the bioassays to provide a parallel between the effects of the gain-of-function, loss-of-function and constitutive expression of *CRK10* during pathogen attack. Eighty plants per genotype were root-inoculated and transferred to trays according to a randomised block design (Figure 7.1 A-B).

Infected plants displayed the classical symptoms induced by vascular wilt pathogens, such as leaf chlorosis, vein clearing and wilting (Figure 7.1 C-F). The mortality rate of each line was recorded from seven to 20 DPI, revealing marked differences between the genotypes (Figure 7.2 A). Water-inoculated plants were also monitored as a mock control (Appendix 11.2). While WT plants reached a final death toll of over 66%, less than 19% of the *crk10-A397T* mutant plants had died by 20 DPI, a nearly three-fold reduction in mortality (Figure 7.2 A). A total of 47.5% of *CRK10* OE-1 plants did not survive the infection, whereas the mortality trend of *crk10-2* plants was remarkably similar to the WT, reaching a final death toll of 67.5%. Statistical analysis of these results using a generalised linear model (see section 7.2.11 for details of statistical analyses) confirmed the existence of

significant differences in susceptibility to *F. oxysporum*, with *crk10-A397T* mutant plants having the highest probability of survival of all four genotypes (Figure 7.2 B; deviance test, χ^2_3 = 17.50, p < 0.001). In agreement with these results, fungal burden quantification by qPCR showed increased *F. oxysporum* biomass in WT and *crk10-2* plants compared to *CRK10* OE-1 and *crk10-A397T* mutant at seven DPI (Figure 7.3; $F_{3,14}$ = 9.83; p < 0.001).

These observations confirm the hypothesis that the gain-of-function allele of *CRK10* confers enhanced resistance to the vascular pathogen *F. oxysporum*, as *crk10-A397T* plants displayed a highly increased probability of survival compared to the WT Col-0. Although the overexpression of *CRK10* also enhanced the resistance of Arabidopsis plants to infection with this pathogen, it was not as effective as the gain-of-function allele at preventing disease and mortality. Finally, the observation that the knockout of *CRK10* did not affect the outcome of disease compared to the WT is unsurprising given the functional redundancy expected between members of a large gene family such as the CRK in Arabidopsis.

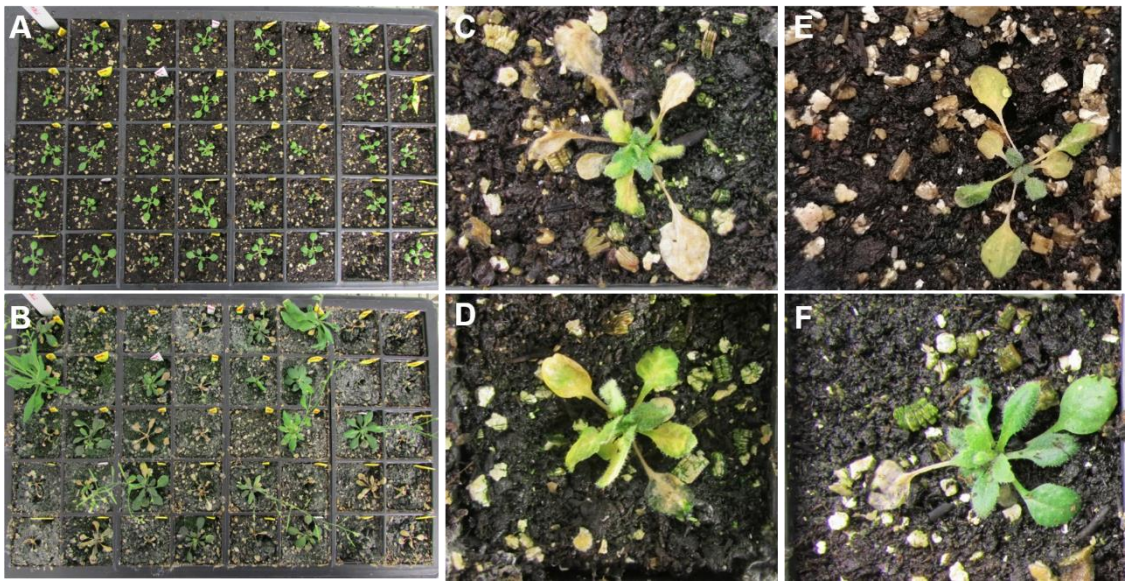

Figure 7.1 Representative plants infected with *F. oxysporum*.
(A-B) Representative photographs of a tray containing Arabidopsis plants at (A) 4 and (B) 20 DPI with *F. oxysporum*.
(C-F) Representative images of (C) WT, (D) *CRK10* OE-1, (E) *crk10-2* and (F) *crk10-A397T* mutant plants at 11 DPI with *F. oxysporum*.

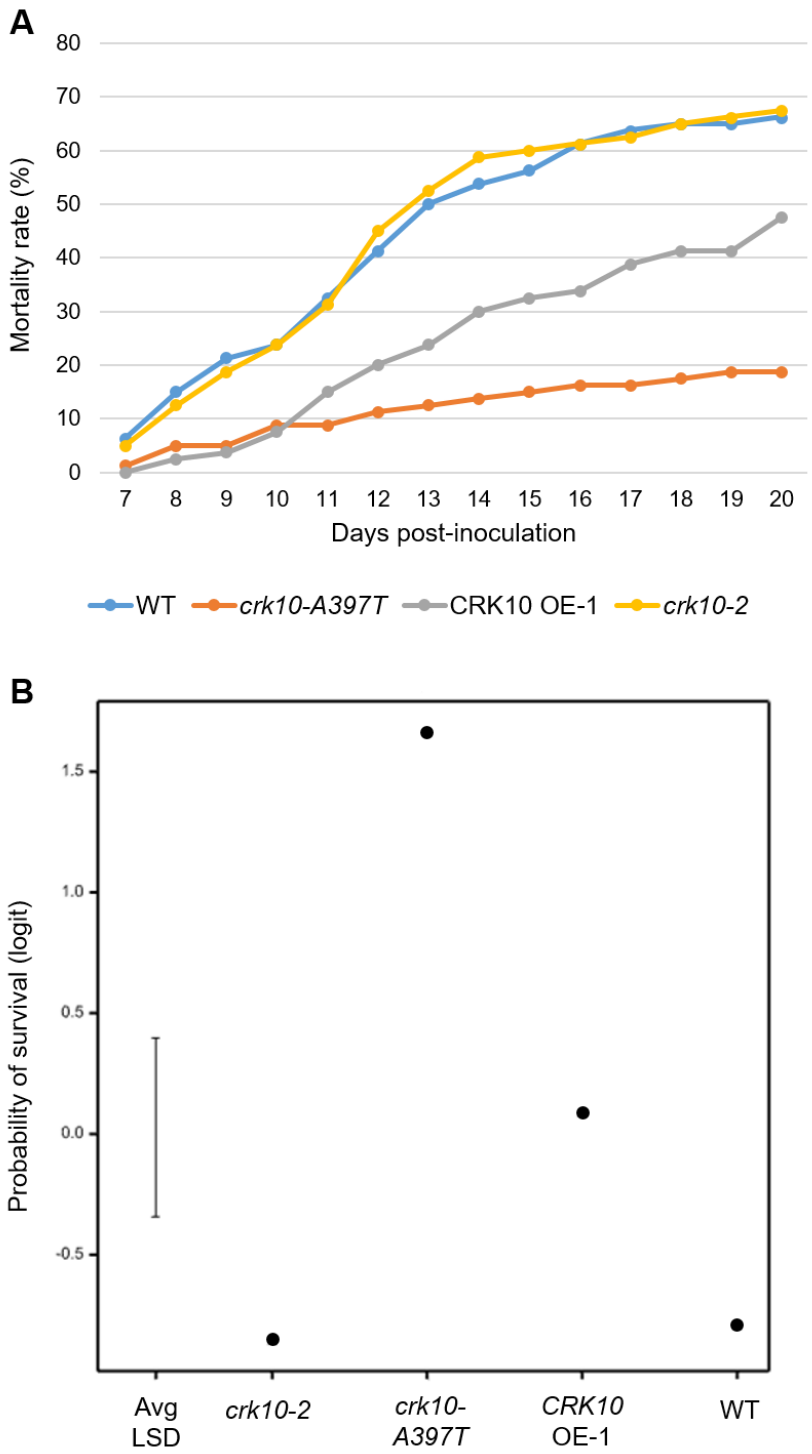

Figure 7.2 *crk10-A397T* mutant plants exhibit enhanced resistance to the vascular pathogen *F. oxysporum*.

(A) Mortality curve of Arabidopsis plants from seven to 20 days post-inoculation with *F. oxysporum*; mortality is expressed as a percentage.

(B) Chart showing the predicted probability of survival (logit scale) of each genotype calculated based on the mortality at 20 DPI with *F. oxysporum* using a generalised linear model (deviance test, χ^2_3 = 17.50, p < 0.001) Average least significant difference (Avg LSD, 5%) bar is shown.

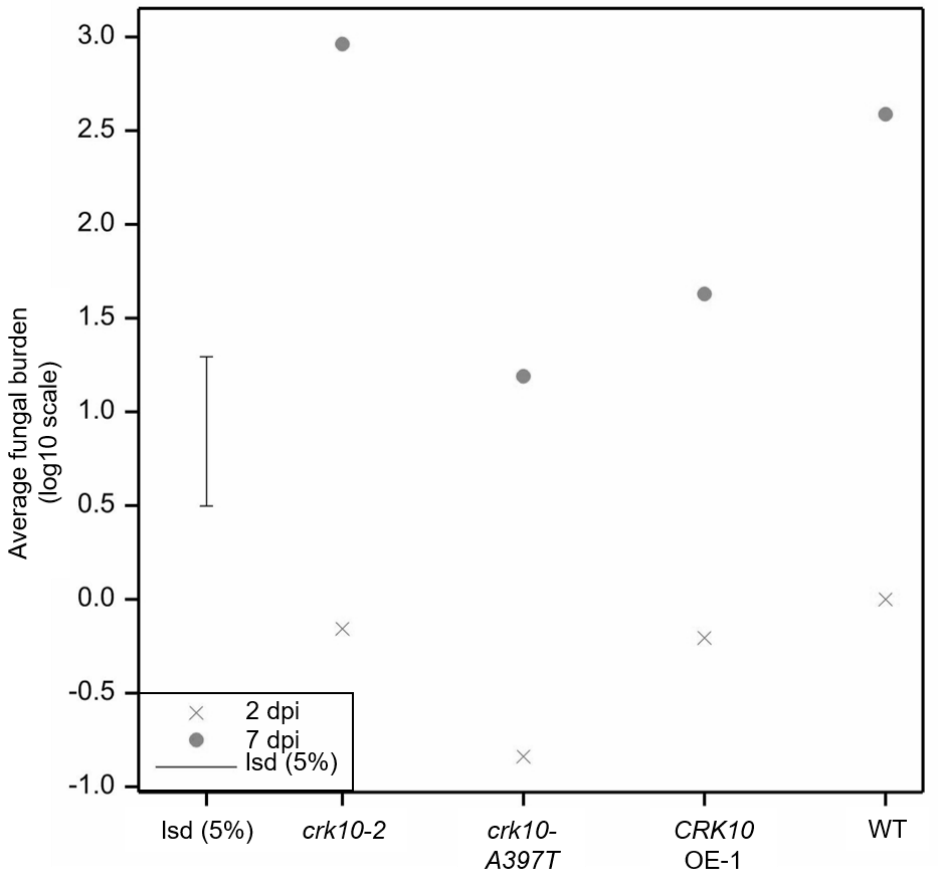

Figure 7.3 *crk10-A397T* and *CRK10* OE-1 plants display decreased fungal burden compared to WT and *crk10-2* plants following infection with *F. oxysporum.* Chart displaying average fungal burden of WT, *crk10-A397T*, *crk10-2* and *CRK10* OE-1 plants at 2 and 7 DPI determined by the relative amount of fungal (*F. oxysporum ACTIN1* gene) to plant (Arabidopsis *ACTIN2* gene) DNA. The chart shows the means of three independent experiments; least significant difference (lsd; 5%) obtained with ANOVA is shown ($F_{3,14}$ = 9.83; $p < 0.001$).

7.3.2 Identification of defence-related genes required for the dwarf phenotype of the *crk10-A397T* mutant

The morphological characterisation of *crk10-A397T* plants revealed that collapsed xylem vessels in roots and hypocotyls are associated with the dwarf growth habit of this mutant (sections 3.3.3 and 3.3.4). Interestingly, the analysis of the hypocotyl transcriptome of *crk10-A397T* plants revealed not only the transcriptional reprogramming of cell wall genes (which is likely associated with the collapse of xylem vessels), but also the constitutive induction of key signalling components of defence responses to biotic stress (see sections 5.3.4 and 5.3.10). As discussed in section 5.4, it is unclear at this stage whether the activation of plant immunity and cell wall-related processes are independent branches of the responses activated by *crk10-A397T*, or whether one event triggers the other. On the assumption that the remodelling of cell walls is activated downstream of immune signalling pathways, disruption of these cascades could potentially rescue the vasculature defect and the dwarf phenotype of the *crk10-A397T* mutant.

To test this hypothesis and identify defence-related signalling components which are required for the dwarf phenotype of *crk10-A397T* plants, this gain-of-function mutant was crossed to knockout lines of selected candidate genes. Genes involved with SA responses were of particular interest, as mutant hypocotyls accumulate increased levels of this important regulator of plant immunity (section 5.3.7). Candidate genes were chosen based on their differential expression in the *crk10-A397T* mutant transcriptome (*EDS1*, *PAD4*, *WRKY70*) or their importance in the regulation of defence responses, despite not being transcriptionally affected by the gain-of-function allele (*NPR1*, *WRKY33* and *MYC2*). In addition to these, a knockout line of *CYP81D11* was also crossed to *crk10-A397T*, as this cis-jasmone inducible gene featured among the top up-regulated genes at three weeks after sowing (log_2 fold change = 9.71). A transgenic line overexpressing the bacterial salicylate hydroxylase (*NahG*) gene, which degrades SA, was also crossed to the *crk10-A397T* mutant to investigate the effect of depleted levels of SA in the mutant background.

Double homozygous mutants of all genetic crosses were obtained and confirmed by genotyping (Appendix 11.1), and their morphology was compared to the parental lines (Figure 7.4). The knockout of *EDS1* and *PAD4* largely rescued the dwarf phenotype of the *crk10-A397T* plants, although their rosettes

still contained a few dark green leaves (Figure 7.4 A, B). Conversely, the double mutant of *crk10-A397T* with *npr1*, *myc2*, *cyp81d11*, *wrky33* and *wrky70* resembled the parental dwarf *crk10-A397T* mutant, with the exception of the light green colouration of the leaves of the *crk10-A397T wrky70* plants (Figure 7.4 C, E, F, G, H). The overexpression of the *NahG* transgene in the *crk10-A397T* mutant background resulted in a slight alleviation of the dwarf phenotype but did not fully rescue it (Figure 7.4 D). Taken together, these results indicate that the immunity regulators *EDS1* and *PAD4*, as well as the accumulation of SA, are required for the dwarf phenotype of the *crk10-A397T* mutant.

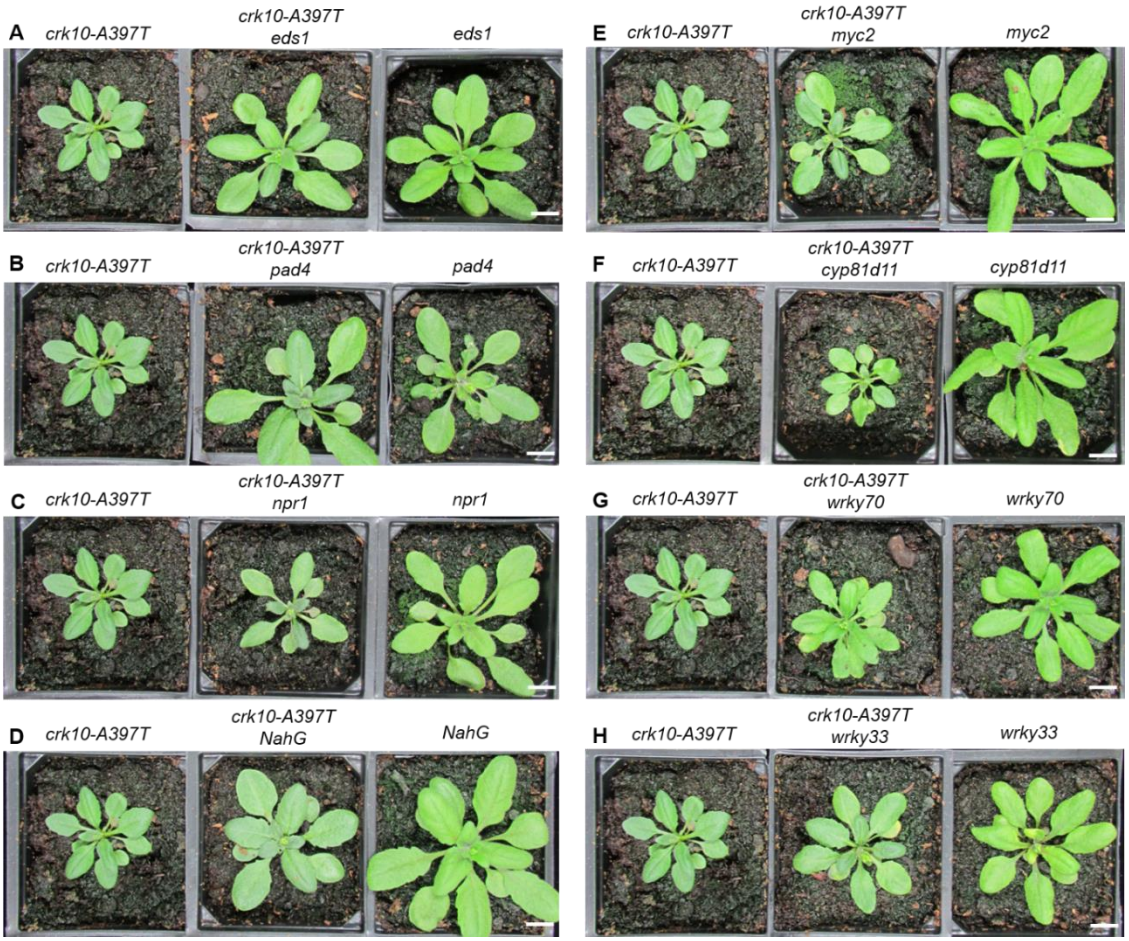

Figure 7.4 Homozygous double mutants generated by genetic crossing of the *crk10-A397T* mutant with knockout / overexpression lines of genes of interest. Photographs of parental lines and the homozygous double mutant progeny of genetic crosses. The *crk10-A397T* mutant was crossed with (A) *eds1*, (B) *pad4*, (C) *npr1*, (D) *35S:NahG*, (E) *myc2*, (F) *cyp81d11*, (G) *wrky70* and (F) *wrky33* lines. Four-week-old plants are shown. Bars, 1 cm.

7.3.3 Investigation of the possible role of defence-related genes in the disease resistance phenotype of the *crk10-A397T* mutant

The enhanced resistance of *crk10-A397T* mutant plants to infection with *F. oxysporum* is likely dependent on the transcriptional induction of immune responses and/or the accumulation of SA in hypocotyls (see section 5.3.2). In a bid to identify signalling components which are required for the increased resistance mediated by the *crk10-A397T* allele, the genetic crosses introduced in section 7.3.2 were challenged with *F. oxysporum*. Due to the large number of biological replicates used for this bioassay, the double mutants were divided into two groups, each allocated to an independent experiment.

The first experiment included *crk10-A397T eds1*, *crk10-A397T pad4*, *crk10-A397T npr1* and *crk10-A397T NahG*, as well as WT, *crk10-A397T*, *CRK10* OE-1 and *crk10-2* plants. At 20 DPI, the mortality rate of *crk10-A397T* (26.7%) was once again drastically reduced compared to WT (78.3%) and *crk10-2* (83.3%) plants, while the *CRK10* OE-1 occupied an intermediate position (63.3%) (Figure 7.5 A). Statistical analysis confirmed that the probability of survival of *crk10-A397T* plants, but not *CRK10* OE-1, was significantly increased compared to the WT in this iteration of the experiment (Figure 7.5 B; Deviance test, χ_7^2 = 11.37, $p < 0.001$). Although the loss-of-function of *NPR1* seemed to increase the susceptibility of *crk10-A397T* mutant plants to infection, this difference was not statistically significant. The expression of the *NahG* transgene more than doubled the mortality of *crk10-A397T* plants, causing the reduction in the probability of survival of the *crk10-A397T NahG* line to a level comparable to that of *CRK10* OE-1 plants. The knockout of *EDS1* and *PAD4* completely abolished the enhanced resistance of *crk10-A397T* plants to infection, as the mortality rate of *crk10-A397T eds1* and *crk10-A397T pad4* surpassed that of WT plants at 20 DPI. These results indicate that *EDS1* and *PAD4* are crucial components of the signalling pathways which promote resistance to *F. oxysporum* in *crk10-A397T* plants. Additionally, these results suggest a correlation between the alleviation of the dwarf morphology and the abolishment of the disease resistance phenotype of the *crk10-A397T* mutant, as *eds1*, *pad4* and *NahG* also rescued the dwarf habit of the mutant plants to varying degrees (section 7.3.2).

The second experiment included WT and *crk10-A397T* plants, and the double mutants *crk10-A397T wrky70*, *crk10-A397T wrky33*, *crk10-A397T cyp81d11* and *crk10-A397T myc2*. Approximately half the number of *crk10-*

A397T mutant plants (41.7%) died in comparison with the WT (81.7%), the third independent observation of the enhanced resistance phenotype promoted by this gain-of-function allele (Figure 7.6 A). The *crk10-A397T cyp81d11* mutant displayed a very similar mortality rate and, consequently, probability of survival compared to *crk10-A397T* plants (Figure 7.10 A-B; deviance test, χ^2_5 = 7.15, p < 0.001). Conversely, the knockout of *myc2* and *wrky33* increased the mortality of *crk10-A397T* plants to 56.7% and 60%, respectively, although this difference did not correspond to a statistically significant reduction in probability of survival. *crk10-A397T wrky70* plants, in contrast, reached over 70% of mortality at the end of the experiment, and the probability of survival of these plants was not significantly different to that of WT plants. In conclusion, the loss-of-function of *WRKY70* also overturned the enhanced resistance of *crk10-A397T* plants to *F. oxysporum*, unlike the knockout of *MYC2*, *WRKY33* and *CYP81D11*.

Two additional repetitions of the experiment were performed including the genetic crosses, WT, *crk10-A397T*, *CRK10* OE-1 and *crk10-2* plants to check the reproducibility of the results (Appendix 11.3). The enhanced resistance phenotype of *crk10-A397T*, *crk10-A397T cyp81d11, crk10-A397T npr1* and *crk10-A397T myc2* was consistent throughout all experiments, as well as the susceptibility levels of the *crk10-2*, *crk10-A397T eds1*, *crk10-A397T pad4* and *crk10-A397T wrky70* plants. On the contrary, the increased resistance displayed by the *CRK10* OE-1 plants in the first experiment was not reproducible across all iterations, although the source of this phenotypical variation is unclear. The *crk10-A397T NahG* plants displayed an even greater susceptibility to infection when the experiment was repeated, confirming the supposed depletion of SA in the *crk10-A397T* mutant impairs the defence mechanisms to *F. oxysporum*. Finally, the enhanced resistance of the *crk10-A397T wrky33* plants was observed in two experiments, but a similar mortality rate to the WT in a third repetition of the experiment also suggested variability.

Taken together, these results unambiguously indicate that the defence regulators *EDS1*, *PAD4* and *WRKY70* are required for the increased resistance of *crk10-A397T* plants to infection with *F. oxysporum*. Similarly, the alleged depletion of SA by the expression of the *NahG* transgene also impairs the immune responses mediated by the *crk10-A397T* allele.

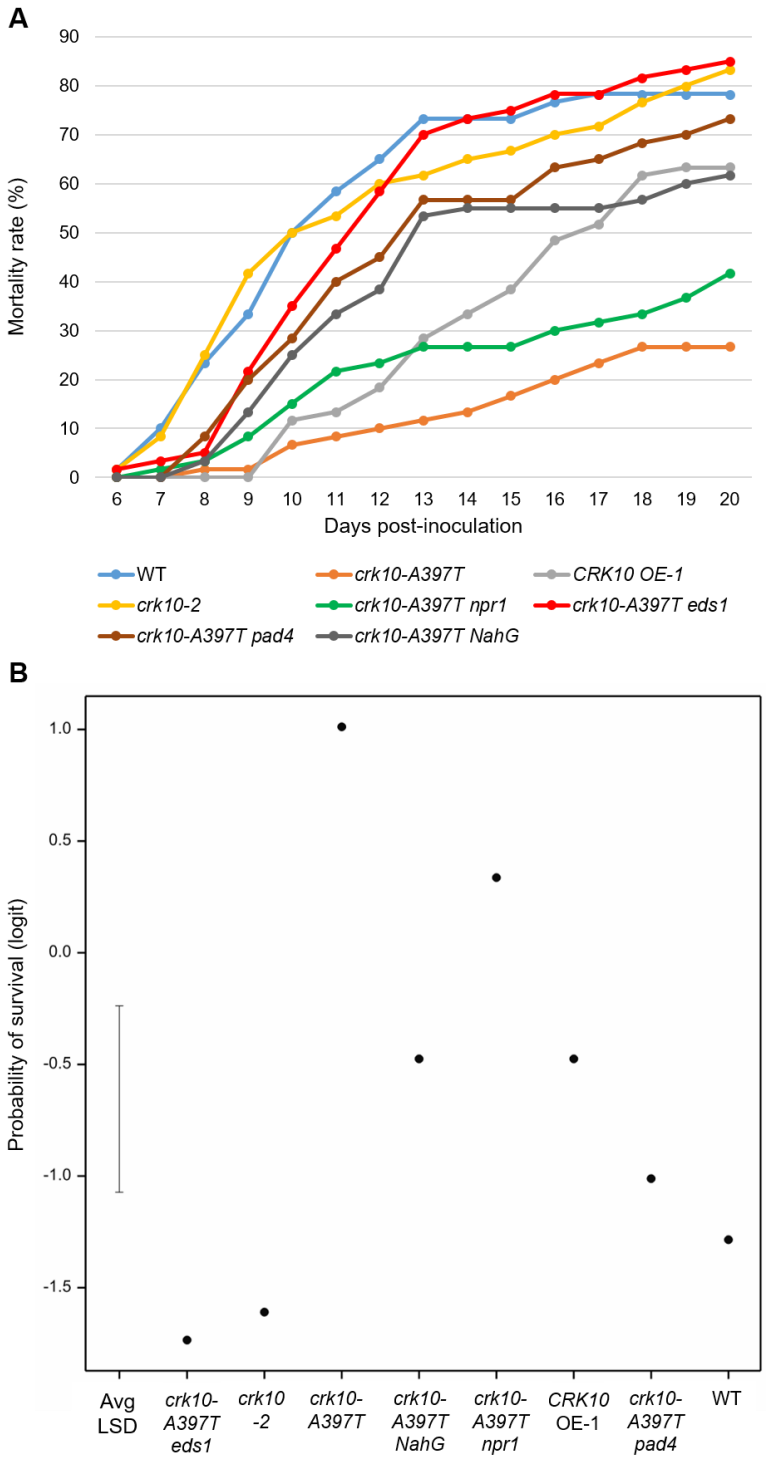

Figure 7.5 The knockout of *EDS1* and *PAD4* and the overexpression of *NahG* rescue the enhanced resistance phenotype of *crk10-A397T* plants.

(A) Mortality curve of Arabidopsis plants from 7 to 20 days post-inoculation with *F. oxysporum*.

(B) Chart showing the predicted probability of survival (logit scale) of each genotype calculated based on the mortality at 20 DPI (deviance test, χ^2_7 = 11.37, p < 0.001). Average least significant difference (Avg lsd, 5%) bar is shown.

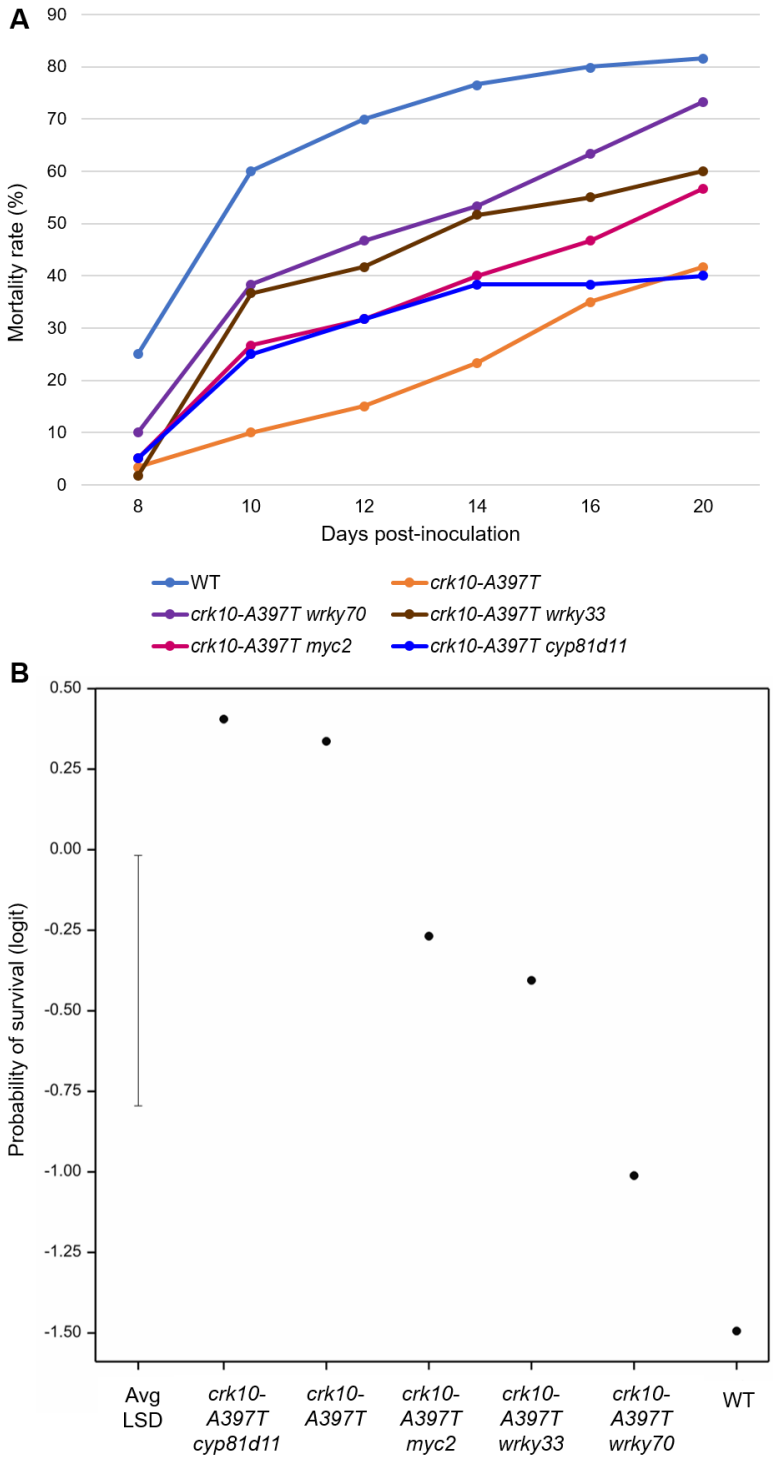

Figure 7.6 The knockout of *WRKY70* rescues the enhanced resistance phenotype of the *crk10-A397T* plants.

(A) Mortality curve of Arabidopsis plants from 7 to 20 days post-inoculation with *F. oxysporum*.

(B) Chart showing the predicted probability of survival (logit scale) of each genotype calculated based on the mortality at 20 DPI (deviance test, χ^2_5 = 7.15, p < 0.001). Average least significant difference (Avg lsd, 5%) bar is shown.

7.3.4 Investigating the presence of collapsed xylem vessels in the hypocotyls of double mutant lines

The results presented in sections 7.3.2 and 7.3.3 demonstrate that components of SA-dependent signalling pathways are required for the dwarf phenotype and the enhanced disease resistance displayed by the *crk10-A397T* mutant. As the presence of collapsed xylem vessels is known to be associated with the dwarfism of *crk10-A397T* plants, hypocotyls of the double mutant lines described in this chapter were inspected to investigate the involvement of these defence-related genes in promoting this vasculature defect. Transverse cross sections of resin embedded hypocotyls from three biological replicates were analysed per genotype. The cross sections were stained with toluidine blue O and potassium permanganate as described in section 3.3.3.

Although the anatomy of the hypocotyl of WT and *crk10-A397T* plants had already been thoroughly analysed (see section 3.3.3), these plants were regrown alongside *CRK10* OE-1, *crk10-2* and the genetic crosses to ensure all hypocotyl samples were collected from plants grown under the exact same conditions. In agreement with previous observations, WT hypocotyls display the expected radial arrangement of lignified xylem vessels (Figure 7.7), whereas extensive vessel collapse is observed in the *crk10-A397T* mutant samples (Figure 7.8). The hypocotyl vasculature of *CRK10* OE-1 and *crk10-2* both resemble that of WT (Figures 7.9 and 7.10), which is unsurprising given these plants display a WT-like rosette morphology (see sections 3.3.7 and 3.3.8). Interestingly, all double mutant lines exhibit severely collapsed xylem vessels in their hypocotyls, regardless of their rosette morphology and disease resistance phenotype (Figure 7.11 – 7.18). Moreover, unexpected features were observed in some of these lines. All three biological replicates of *crk10-A397T eds1* double mutant exhibited the ectopic formation of vascular tissue in the cortical region of the hypocotyl (Figure 7.19). These were readily identified by the presence of xylem vessels surrounded by concentric rings of cambium-like cells, which resembles the main hypocotyl stele. Moreover, dark blue- and purple-stained groups of unidentified cells were also observed in these hypocotyls, another distinctive feature compared to WT and *crk10-A397T* mutant. Both these features were also ubiquitous in the hypocotyls of *crk10-A397T pad4* plants (Figure 7.20), which is interesting considering that these lines showed the strongest alleviation of the dwarf and disease resistance phenotype of the *crk10-A397T* mutant. The

formation of ectopic stele-like bundles of cells was also observed in some, but not all, biological replicates of *crk10-A397T wrky70* and *crk10-A397T NahG,* although all hypocotyls contained the pools of dark stained cells (Figures 7.21 and 7.22).

These observations revealed that disruption of defence-related pathways does not rescue the collapsed xylem vessel phenotype in the hypocotyls of *crk10-A397T* plants, even in the double mutant lines which display an alleviation of the dwarf phenotype. This apparent contradiction is likely owed to the presence of ectopic xylem vessels in the hypocotyls of these lines, especially *crk10-A397T eds1* and *crk10-A397T pad4,* which might be a compensation mechanism in response to the presence of collapsed xylem vessels. Thus, the alleviation of the dwarf phenotype of these double mutants is likely owed to the presence of additional xylem vessels, as they increase water transport from the root to the shoot and rescue plant growth. However, additional xylem vessels in the cortical area of the hypocotyl might also facilitate the penetration and spread of *F. oxysporum*, which might be a contributing factor to the enhanced disease susceptibility observed for these lines. A similar process might also take place in the hypocotyls of *crk10-A397T wrky70* and *crk10-A397T NahG*, as ectopic xylem vessel formation was also observed in some, but not all biological replicates of these lines analysed in this study. Confirmation of this hypothesis, however, would require the analysis of the hypocotyls of the single knockout parental lines used for the genetic crosses with *crk10-A397T*, such as *eds1* and *pad4*, to rule out the presence of ectopic xylem formation in these plants. If the hypocotyl vasculature in these lines resembles the WT, it will be possible to confirm that the production of ectopic xylem vessels is a mechanism triggered in the hypocotyls of *crk10-A397T* mutant plants upon disruption of these key signalling components of SA immune responses.

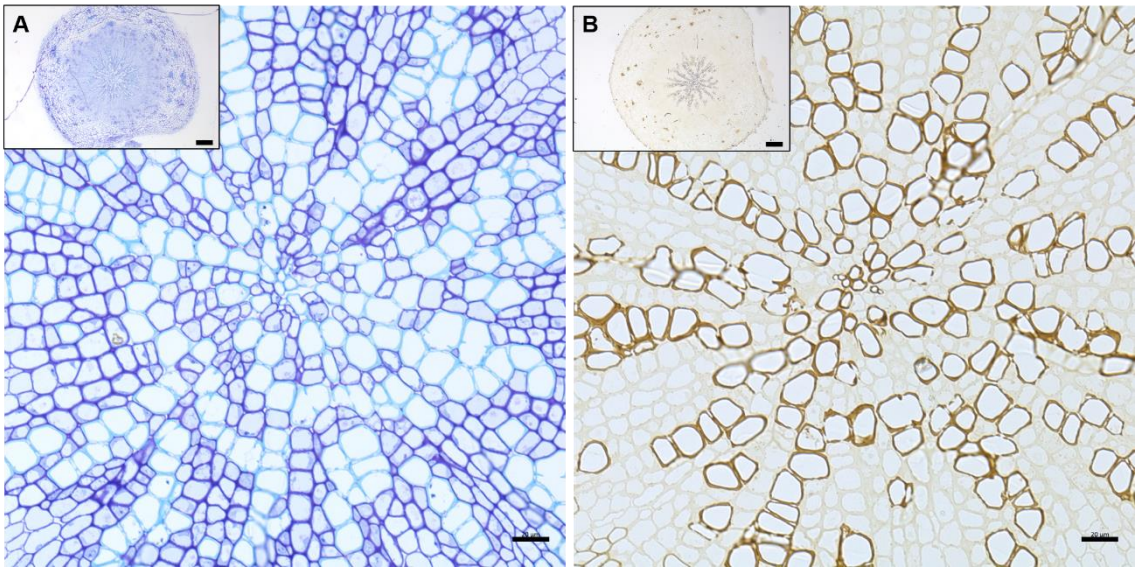

Figure 7.7 The xylem vasculature in the hypocotyls of WT plants.
(A-B) Micrographs of transverse cross sections of resin embedded hypocotyls of 4-week-old WT plants. Staining: (A) toluidine blue O and (B) potassium permanganate. (A) and (B) are cross sections of the same biological replicate. Bars, (A, B) = 20 µm; (top left corner A and B) = 200 µm.

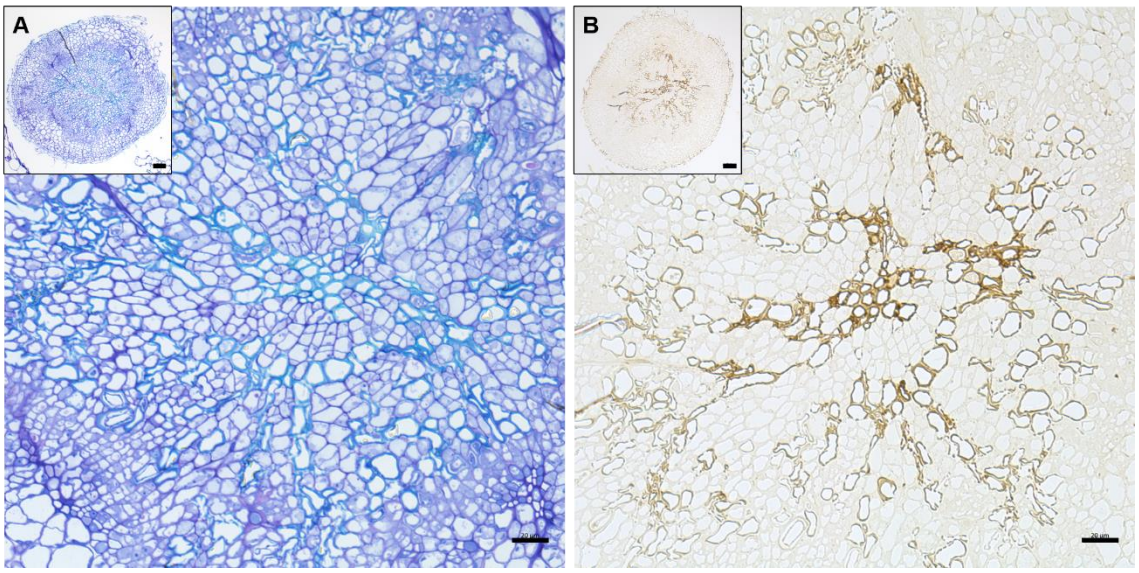

Figure 7.8 The xylem vasculature in the hypocotyls of *crk10-A397T* plants.
(A-B) Micrographs of transverse cross sections of resin embedded hypocotyls of 4-week-old *crk10-A397T* plants. Staining: (A) toluidine blue O and (B) potassium permanganate. (A) and (B) are cross sections of the same biological replicate. Bars, (A, B) = 20 µm; (top left corner A and B) = 50 µm.

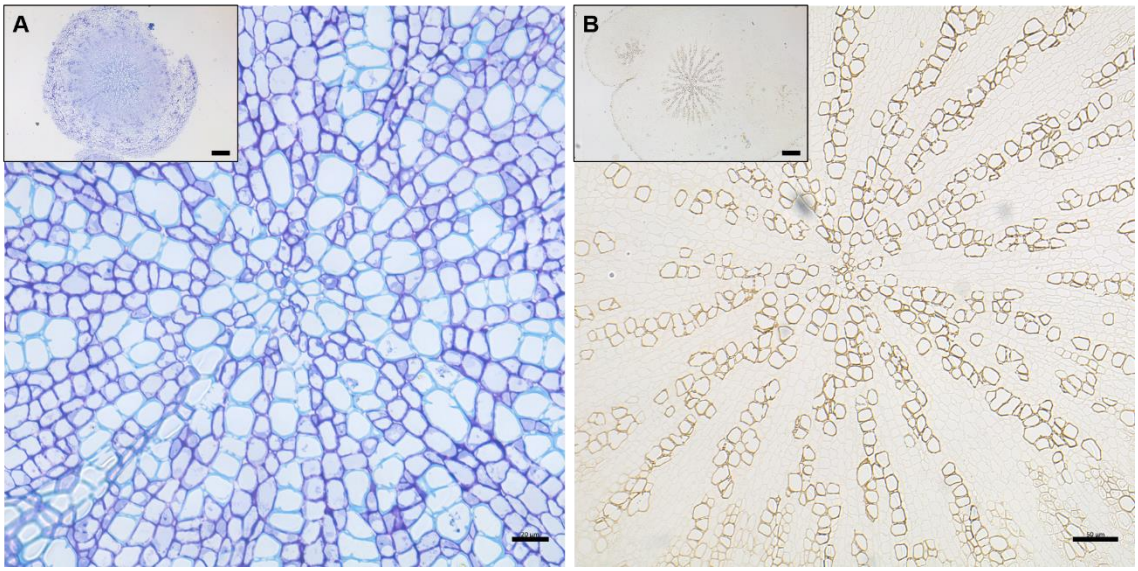

Figure 7.9 The xylem vasculature in the hypocotyls of *crk10-2* plants.
(A-B) Micrographs of transverse cross sections of resin embedded hypocotyls of 4-week-old *crk10-2* plants. Staining: (A) toluidine blue O and (B) potassium permanganate. (A) and (B) are cross sections of two independent biological replicates. Bars, (A) = 20 µm; (B) = 50 µm; (top left corner A and B) = 200 µm.

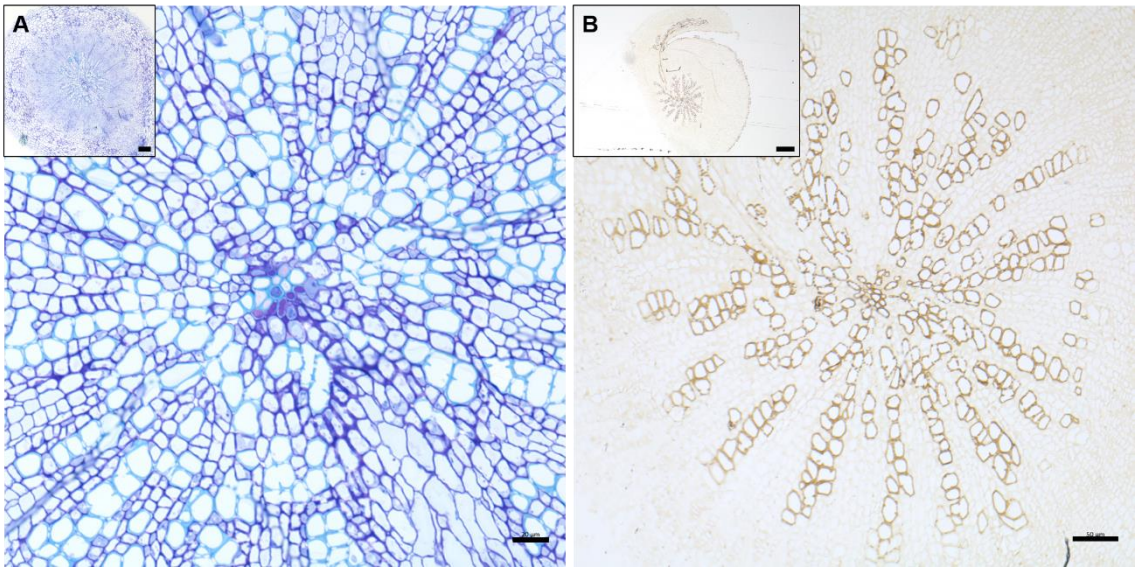

Figure 7.10 The xylem vasculature in the hypocotyls of *CRK10* OE-1 plants.
(A-B) Micrographs of transverse cross sections of resin embedded hypocotyls of 4-week-old *CRK10* OE-1 plants. Staining: (A) toluidine blue O and (B) potassium permanganate. (A) and (B) are cross sections of two independent biological replicates. Bars, (A) = 20 µm; (B) = 50 µm; (top left corner A) = 100 µm; (top left corner B) = 200 µm.

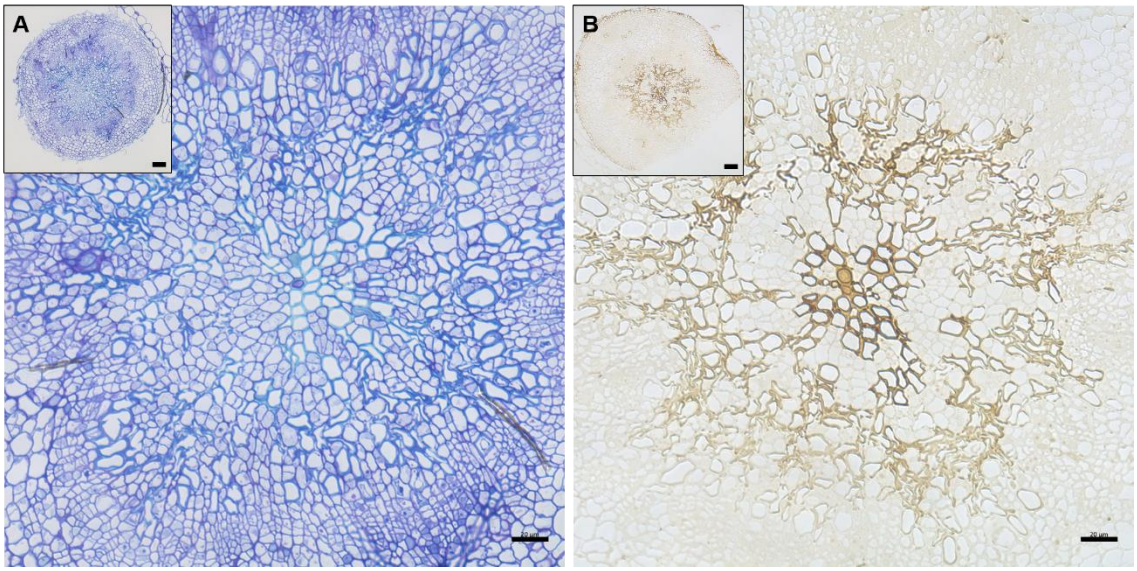

Figure 7.11 The xylem vasculature in the hypocotyls of *crk10-A397T cyp81d11* plants.

(A-B) Micrographs of transverse cross sections of resin embedded hypocotyls of 4-week-old *crk10-A397T cyp81d11* plants. Staining: (A) toluidine blue O and (B) potassium permanganate. (A) and (B) are cross sections of two independent biological replicates. Bars, (A, B) = 20 µm; (top left corner A and B) = 50 µm.

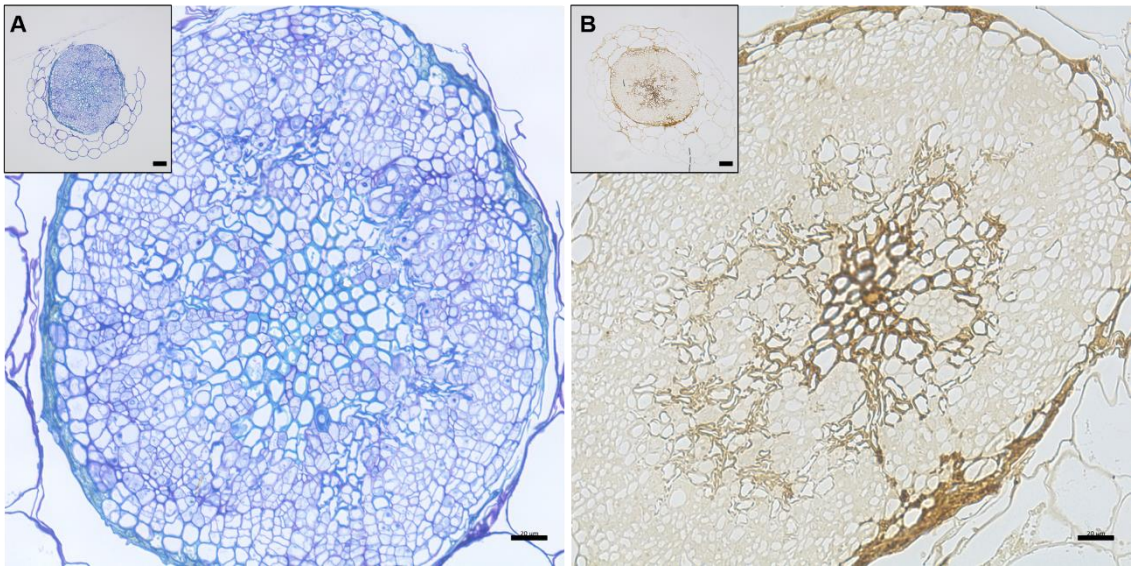

Figure 7.12 The xylem vasculature in the hypocotyls of *crk10-A397T npr1* plants.

(A-B) Micrographs of transverse cross sections of resin embedded hypocotyls of 4-week-old *crk10-A397T npr1* plants. Staining: (A) toluidine blue O and (B) potassium permanganate. (A) and (B) are cross sections of two independent biological replicates. Bars, (A, B) = 20 µm; (top left corner A and B) = 50 µm.

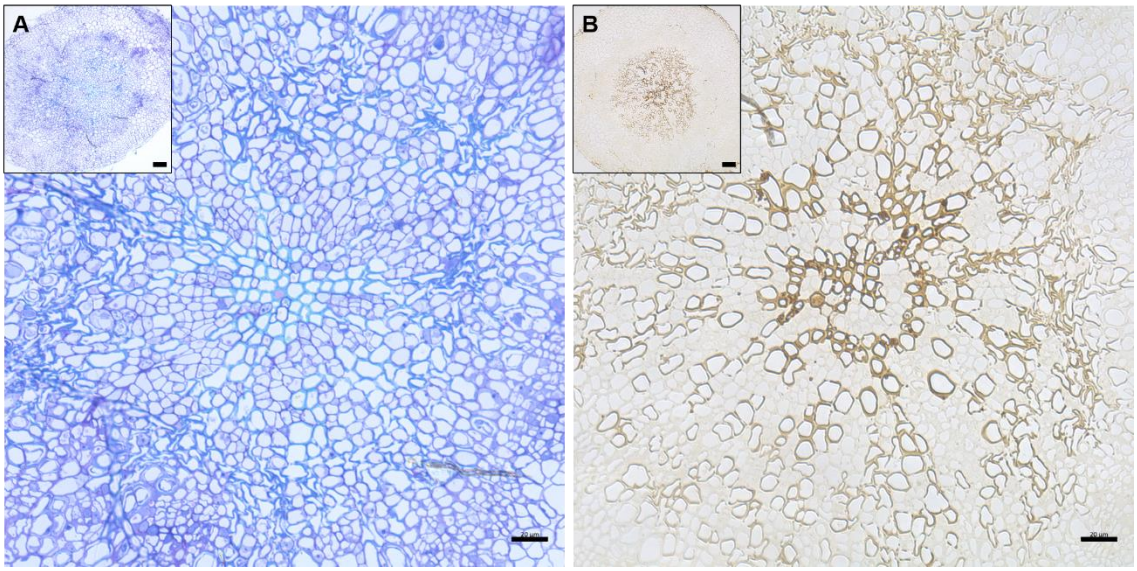

Figure 7.13 The xylem vasculature in the hypocotyls of *crk10-A397T myc2* plants.

(A-B) Micrographs of transverse cross sections of resin embedded hypocotyls of 4-week-old *crk10-A397T myc2* plants. Staining: (A) toluidine blue O and (B) potassium permanganate. (A) and (B) are cross sections of two independent biological replicates. Bars, (A, B) = 20 µm; (top left corner A and B) = 50 µm.

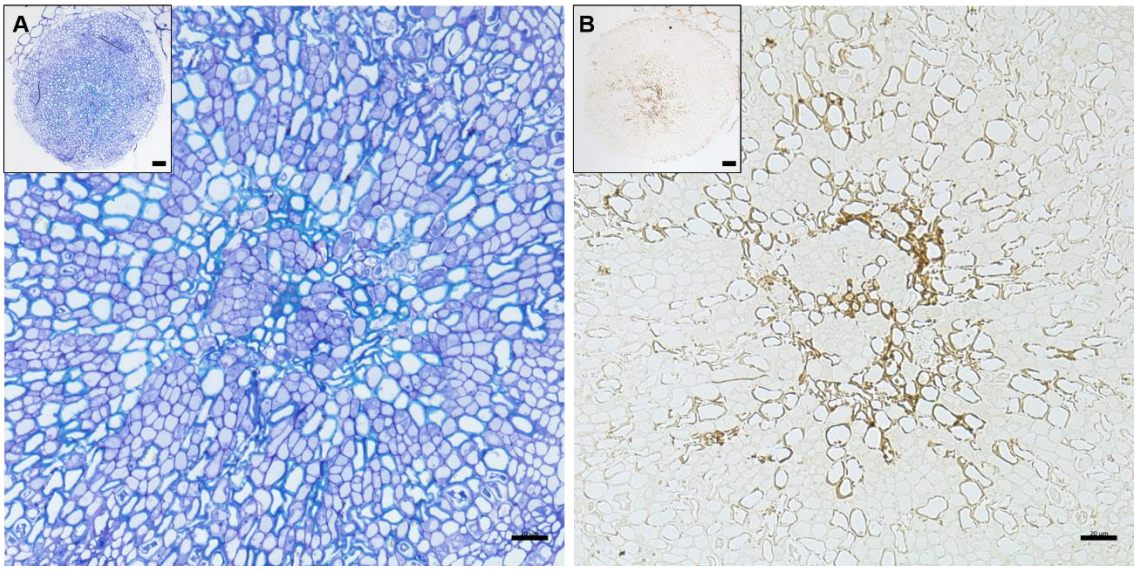

Figure 7.14 The xylem vasculature in the hypocotyls of *crk10-A397T wrky33* plants.

(A-B) Micrographs of transverse cross sections of resin embedded hypocotyls of 4-week-old *crk10-A397T wrky33* plants. Staining: (A) toluidine blue O and (B) potassium permanganate. (A) and (B) are cross sections of the same biological replicate. Bars, (A, B) = 20 µm; (top left corner A and B) = 50 µm.

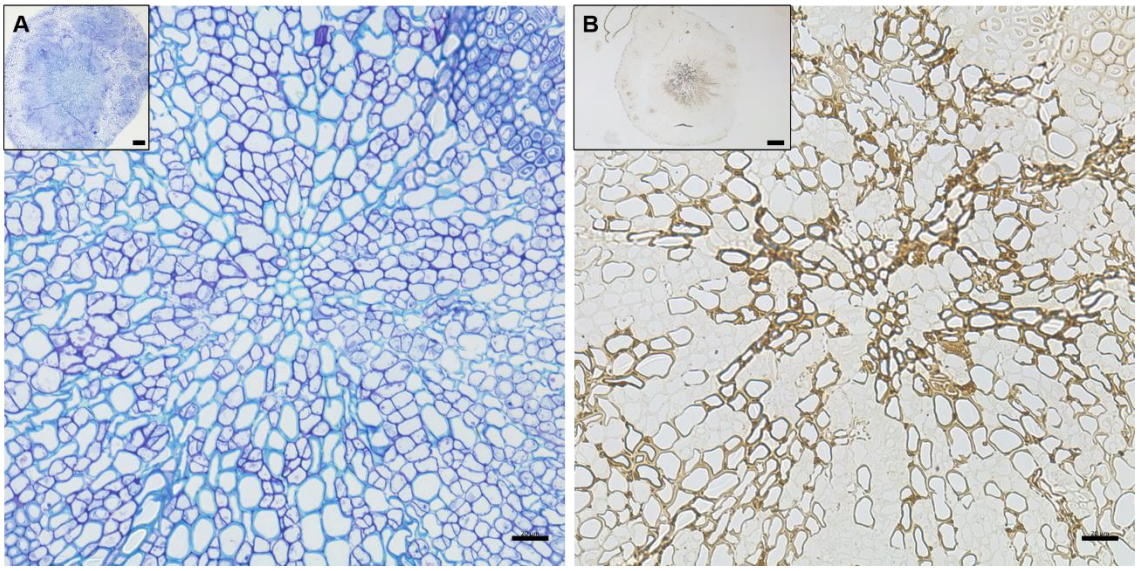

Figure 7.15 The xylem vasculature in the hypocotyls of *crk10-A397T eds1* plants. (A-B) Micrographs of transverse cross sections of resin embedded hypocotyls of 4-week-old *crk10-A397T eds1* plants. Staining: (A) toluidine blue O and (B) potassium permanganate. (A) and (B) are cross sections of two independent biological replicates. Bars, (A, B) = 20 µm; (top left corner A) = 100 µm; (top left corner B) = 200 µm.

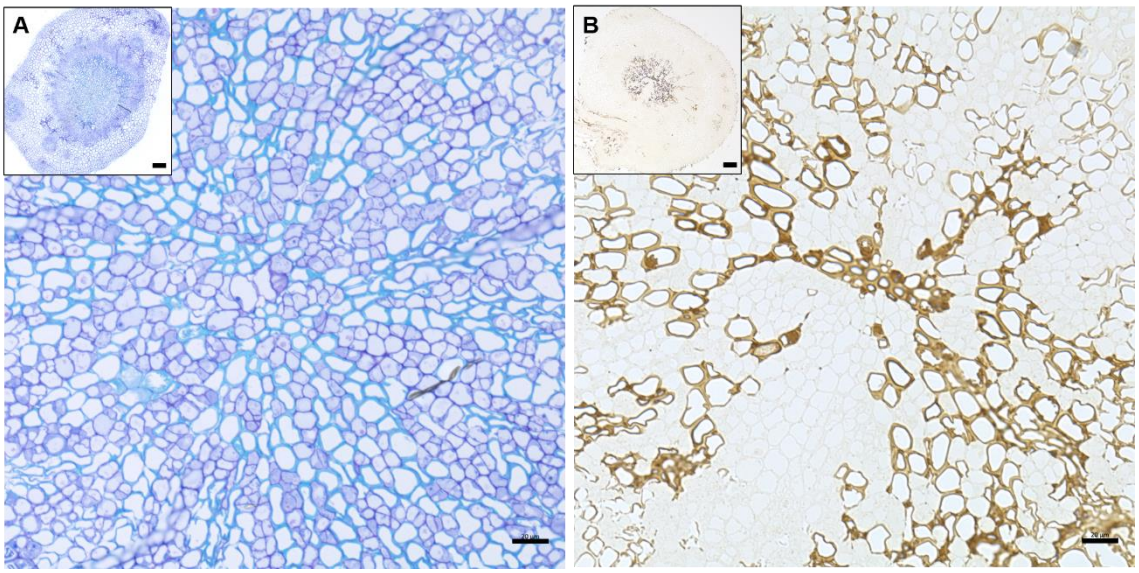

Figure 7.16 The xylem vasculature in the hypocotyls of *crk10-A397T pad4* plants. (A-B) Micrographs of transverse cross sections of resin embedded hypocotyls of 4-week-old *crk10-A397T pad4* plants. Staining: (A) toluidine blue O and (B) potassium permanganate. (A) and (B) are cross sections of two independent biological replicates. Bars, (A, B) = 20 µm; (top left corner A and B) = 100 µm.

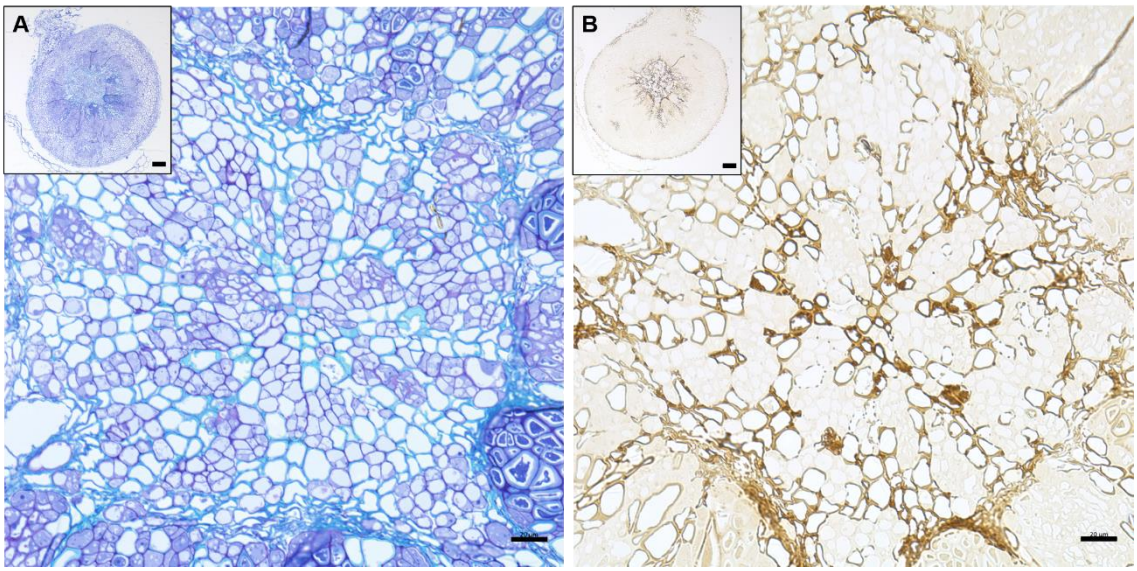

Figure 7.17 The xylem vasculature in the hypocotyls of *crk10-A397T wrky70* plants.

(A-B) Micrographs of transverse cross sections of resin embedded hypocotyls of 4-week-old *crk10-A397T wrky70* plants. Staining: (A) toluidine blue O and (B) potassium permanganate. (A) and (B) are cross sections of the same biological replicate. Bars, (A, B) = 20 µm; (top left corner A and B) = 100 µm.

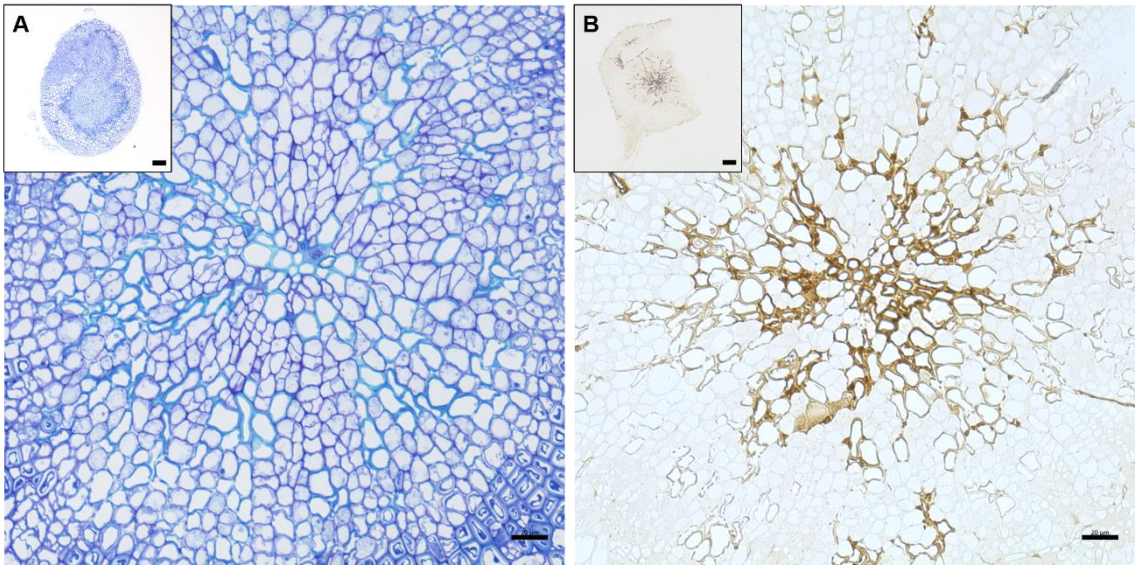

Figure 7.18 The xylem vasculature in the hypocotyls of *crk10-A397T NahG* plants.

(A-B) Micrographs of transverse cross sections of resin embedded hypocotyls of 4-week-old *crk10-A397T NahG* plants. Staining: (A) toluidine blue O and (B) potassium permanganate. (A) and (B) are cross sections of two independent biological replicates. Bars, (A, B) = 20 µm; (top left corner A and B) = 100 µm.

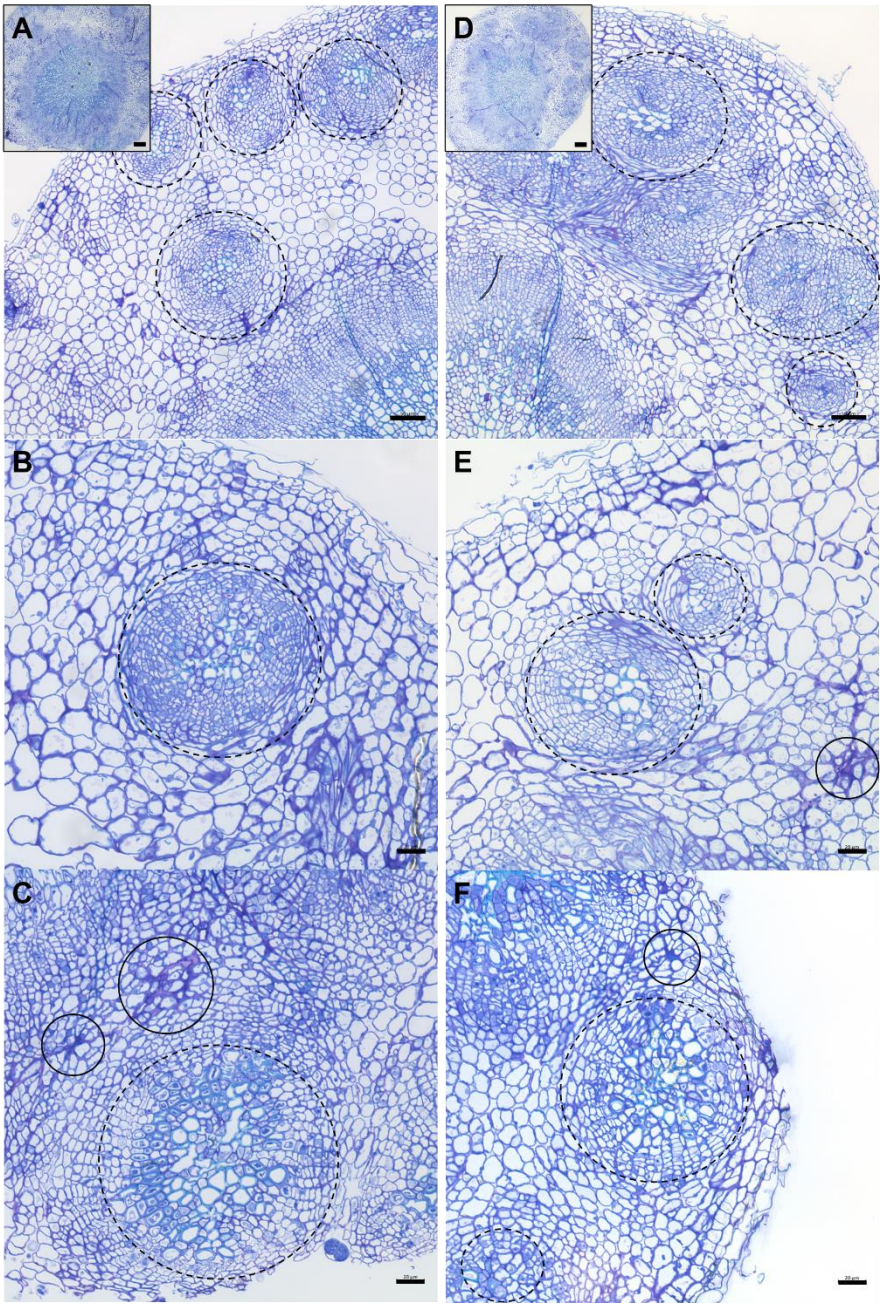

Figure 7.19 The hypocotyls of *crk10-A397T eds1* plants contain ectopic formation of xylem vessels.

(A-F) Micrographs of transverse cross sections of resin embedded hypocotyls of 4-week-old *crk10-A397T eds1* plants. Regions of ectopic formation of xylem vessels are indicated by dashed circles. Solid line circles indicate areas with clusters of dark-blue/purple-stained cells. (A-C) and (D-F) are cross sections of two independent biological replicates (shown in lower magnification in inserts A and D). All three biological replicates analysed for this line displayed these features. Micrograph in top left corner of panel D is also shown in Figure 7.15 (insert A). Staining: toluidine blue O. Bars, (A, D) = 50 µm; (B, C, E, F) = 20 µm; (top left corner A and D) = 100 µm.

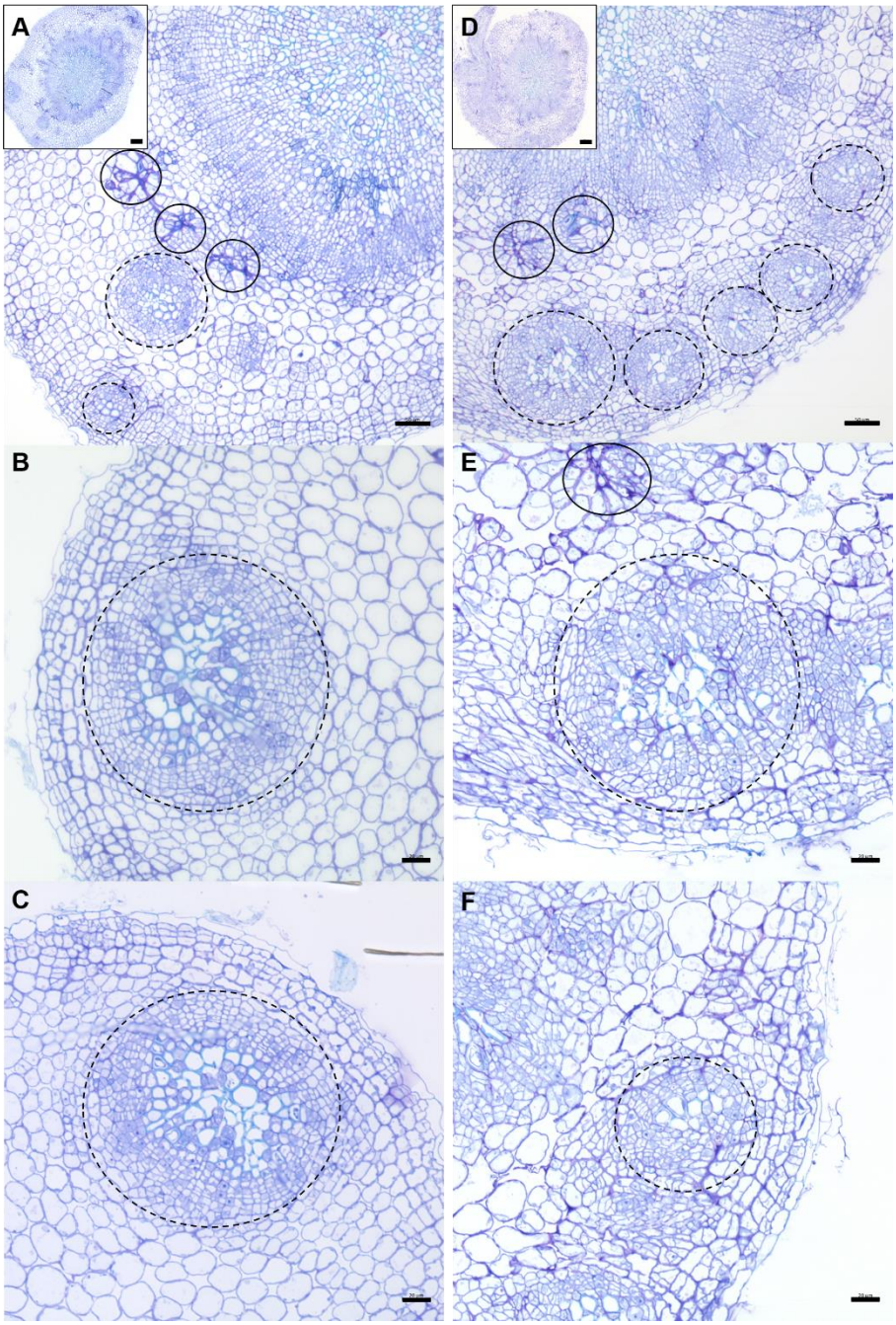

Figure 7.20 The hypocotyls of *crk10-A397T pad4* plants contain ectopic formation of xylem vessels.

(A-F) Micrographs of transverse cross sections of resin embedded hypocotyls of 4-week-old *crk10-A397T pad4* plants. Regions of ectopic formation of xylem vessels are indicated by dashed circles. Solid line circles indicate areas with dark-blue/purple-stained cells. (A-C) and (D-F) are cross sections of two independent biological replicates (shown in lower magnification in inserts A and D). All three biological replicates analysed for this line displayed these features. Micrograph in top left corner of panel A is also shown in Figure 7.16. Staining: toluidine blue O. Bars, (A, D) = 50 µm; (B, C, E, F) = 20 µm; (top left corner A and D) = 100 µm.

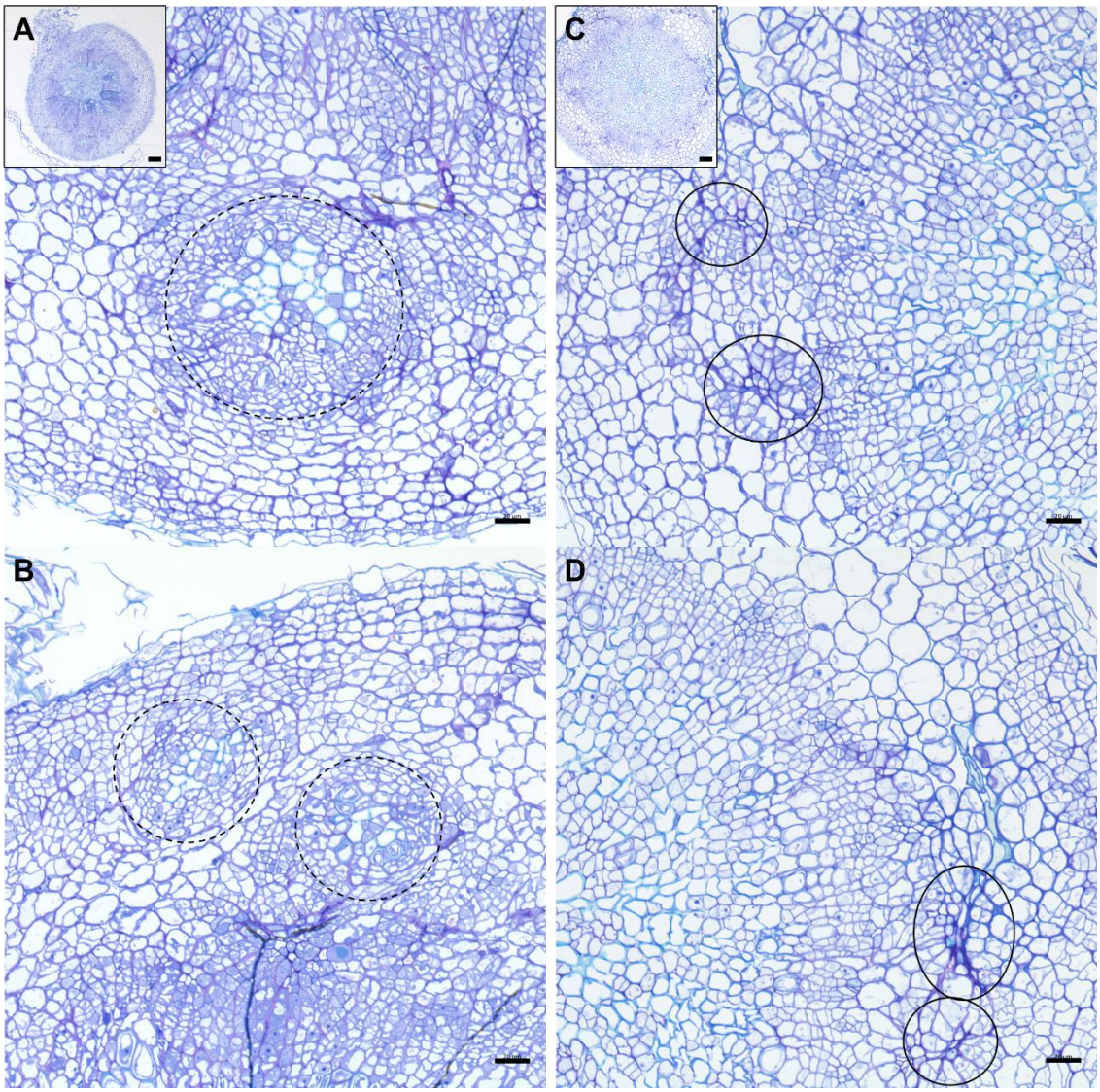

Figure 7.21 The hypocotyls of *crk10-A397T wrky70* plants contain ectopic formation of xylem vessels.

(A-D) Micrographs of transverse cross sections of resin embedded hypocotyls of 4-week-old *crk10-A397T wrky70* plants. Regions of ectopic formation of xylem vessels are indicated by dashed circles. Solid line circles indicate areas with dark-blue/purple staining. (A-B) and (C-D) are cross sections of two independent biological replicates (shown in lower magnification in inserts A and C). One biological replicate analysed for this line displayed the features seen in (A-B), and two biological replicates exhibited the features seen in (C-D). Micrograph in top left corner of panel A is also shown in Figure 7.17. Staining: toluidine blue O. Bars, (A-D) = 20 µm; (top left corner A) = 100 µm; (top left corner C) = 50 µm.

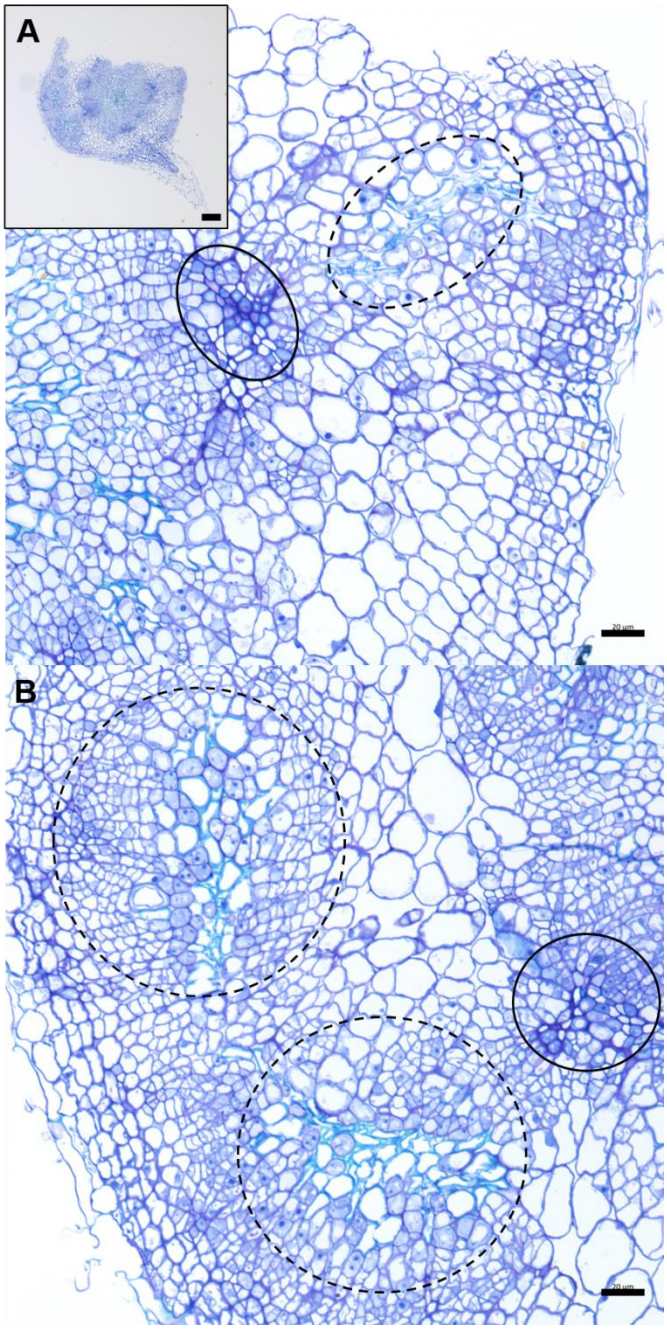

Figure 7.22 The hypocotyls of *crk10-A397T NahG* plants contain ectopic formation of xylem vessels.

(A-B) Micrographs of transverse cross sections of resin embedded hypocotyls of 4-week-old *crk10-A397T NahG* plants. Regions of ectopic formation of xylem vessels are indicated by dashed circles. Solid line circles indicate areas with dark-blue/purple staining. (A-B) are cross sections of the same biological replicate (shown in lower magnification in top left corner A). One biological replicate analysed for this line displayed the features seen in (A-B), and two biological replicates exhibited the features highlighted by the solid line circles only. Staining: toluidine blue O. Bars, (A, B) = 20 µm; (top left corner A) = 100 µm.

7.3.5 Exploring the role of the *crk10-A397T* mutant allele during infection with *F. graminearum* in Arabidopsis

Despite the fact that collapsed xylem vessels are observed in roots and hypocotyls but not in the inflorescence stem of *crk10-A397T* plants, *CRK10* expression is also detected in above-ground organs according to *CRK10*$_{PRO}$*:GUS* reporter lines (see section 3.3.5). Moreover, the transcriptional induction of genes known to promote SA-dependent systemic acquired resistance (see section 5.3.4) suggests that immune responses might be induced at a systemic rather than localised level in the *crk10-A397T* mutant. To test whether the *crk10-A397T* allele affects the outcome of infection following inoculation of above-ground organs, a detached leaf assay (Chen et al., 2006) was performed with *F. graminearum*. Leaves of WT, *crk10-A397T*, *crk10-2* and *CRK10* OE-1 plants were included in these experiments, and a randomised block design was devised.

Following wound inoculation of detached leaves with *F. graminearum* conidiospores, disease symptoms such as chlorosis and cell death were documented by photographs. At 11 DPI, differences in disease progression between the genotypes were obvious (Figure 7.23), and this time point was chosen to quantify the relative diseased area of each leaf using an image analysis software (see section 7.2.10). In agreement with the clear differences in symptom severity observed by visual inspection of the plates, the differences between the average diseased leaf area of each genotype were striking (Figure 7.24 A). Leaves of *crk10-A397T* mutant and *CRK10* OE-1 plants exhibited a pronounced increase in diseased area compared to WT and *crk10-2*, which retained a greater proportion of healthy tissue. Analysis of these results with ANOVA confirmed the enhanced disease susceptibility of both *crk10-A397T* and *CRK10* OE-1 lines compared to the WT (Figure 7.24 B; $F_{3, 33} = 12.01$; $p < 0.001$). Although the leaves of *crk10-2* plants displayed a reduction in average diseased area compared to WT leaves, that difference was not significant for this analysis. These results suggest that leaves of *crk10-A397T* mutant and *CRK10* OE-1 plants are more susceptible to infection with *F. graminearum* compared to WT and *crk10-2* plants.

Considering the diminutive size of the rosette leaves of *crk10-A397T* mutant plants, one could question if the reduced leaf area available for pathogen colonisation could result in an apparent enhanced susceptibility merely due to differences in leaf size compared to the other genotypes. To test this hypothesis, the bioassay was repeated using leaves from *crk10-A397T*/WT grafted plants,

which display a WT-like rosette morphology (see section 3.3.4). To allow the comparison between genotypes and eliminate grafting-associated confounding effects, self-grafts of WT, *crk10-2* and *CRK10* OE-1 plants were also generated and used for this experiment. Two leaves from nine individual grafted plants were collected per genotype, and four plates containing all 18 leaves of each genotype were prepared (Figure 7.25). Image analysis of individual leaves at 10 DPI revealed, once again, the increase in diseased leaf area displayed by the leaves of *crk10-A397T* mutant and *CRK10* OE-1 plants, although the differences were not as pronounced due to increased susceptibility displayed by the WT leaves (Figure 7.26 A). Nevertheless, analysis of the results using ANOVA confirmed that the difference between the WT and both the *crk10-A397T* and *CRK10* OE-1 leaves is statistically significant and, therefore, the enhanced susceptibility of the mutant plants is not a consequence of reduced leaf size (Figure 7.4 B; $F_{3, 67} = 11.60$; $p < 0.001$). Moreover, leaves of *crk10-2* plants once again displayed the lowest average diseased area of all genotypes.

Taken together, these results indicate that the gain-of-function and the overexpression of *CRK10* promote enhanced susceptibility to disease caused by *F. graminearum* in leaves of Arabidopsis, while the knockout of *CRK10* seems to be associated with increased resistance to foliar infection with this pathogen. These observations contrast with the enhanced resistance of the *crk10-A397T* mutant to *F. oxysporum,* and indicate that the defence mechanisms elicited by this gain-of-function allele are effective against a root-infecting vascular wilt, but not against foliar inoculation with *F. graminearum*.

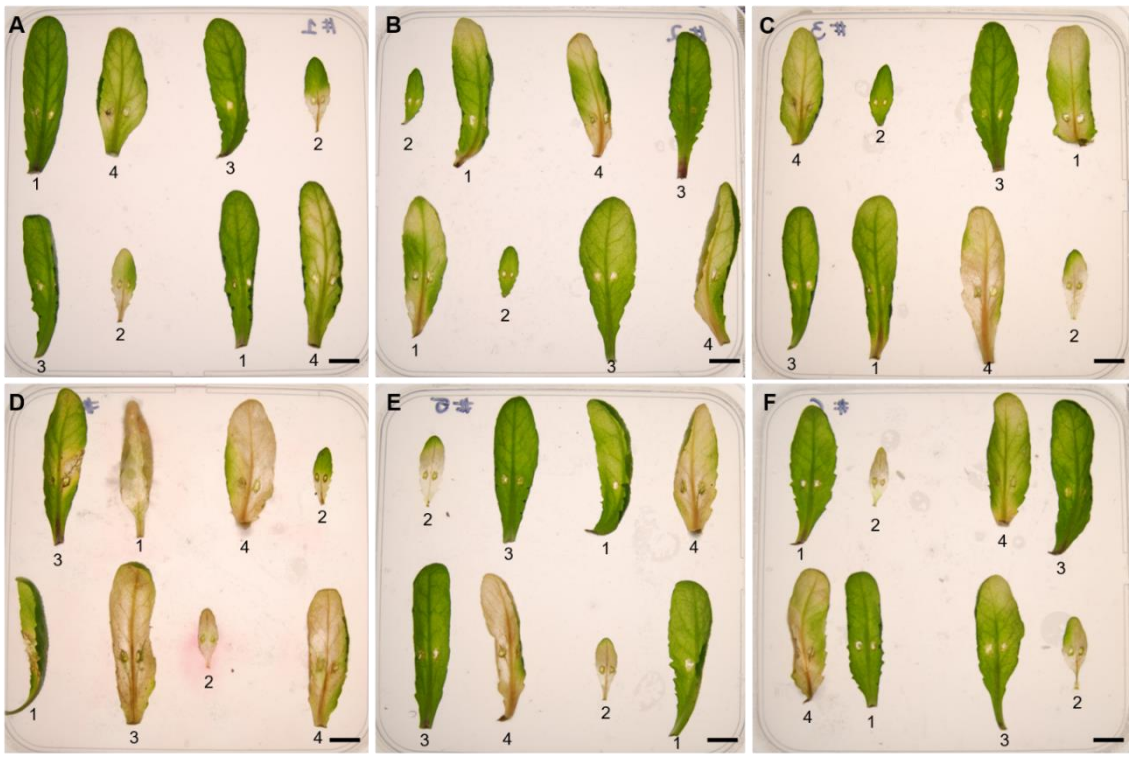

Figure 7.23 Leaves of *crk10-A397T* and *CRK10* OE-1 display increased susceptibility to *F. graminearum*.

(A-F) Photographs taken at 11 days post-inoculation with *F. graminearum* showing plates 1 to 6 (A to F, respectively) included in the experiment. The number below each leaf indicates the corresponding genotype: 1 = WT; 2 = *crk10-A397T* mutant; 3 = *crk10-2*; 4 = *CRK10* OE-1. Bars, 1 cm.

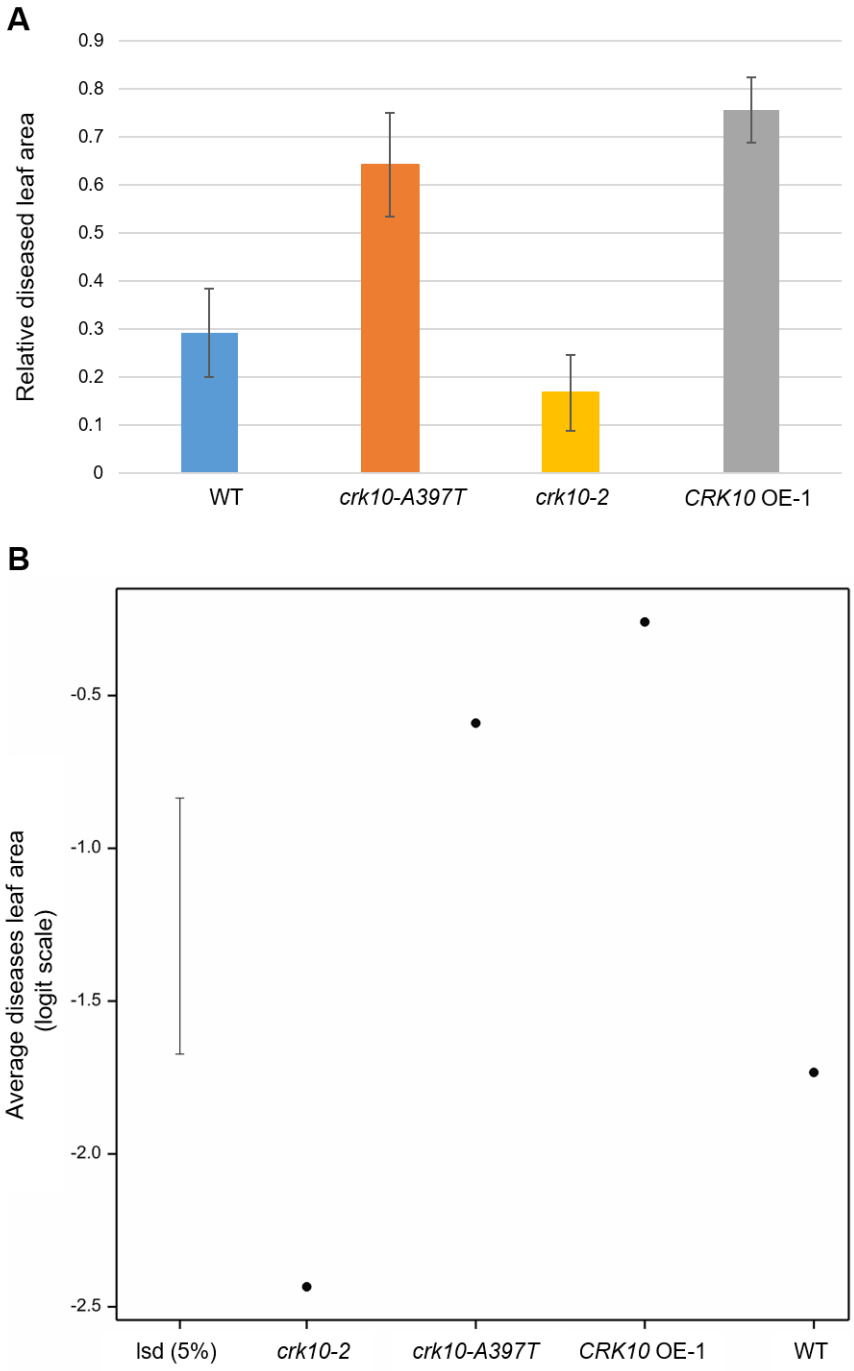

Figure 7.24 Leaves of *crk10-A397T* and *CRK10* OE-1 plants are more susceptible to infection with *F. graminearum* than WT and *crk10-2*.

(A) Average relative disease area of Arabidopsis leaves at 11 days post-inoculation with *F. graminearum*. Error bars represent the standard error of 12 biological replicates.

(B) Average diseased leaf area (logit scale) of each genotype following analysis with ANOVA ($F_{3, 33} = 12.01$; $p < 0.001$). Least significant difference (lsd 5%) bar is shown.

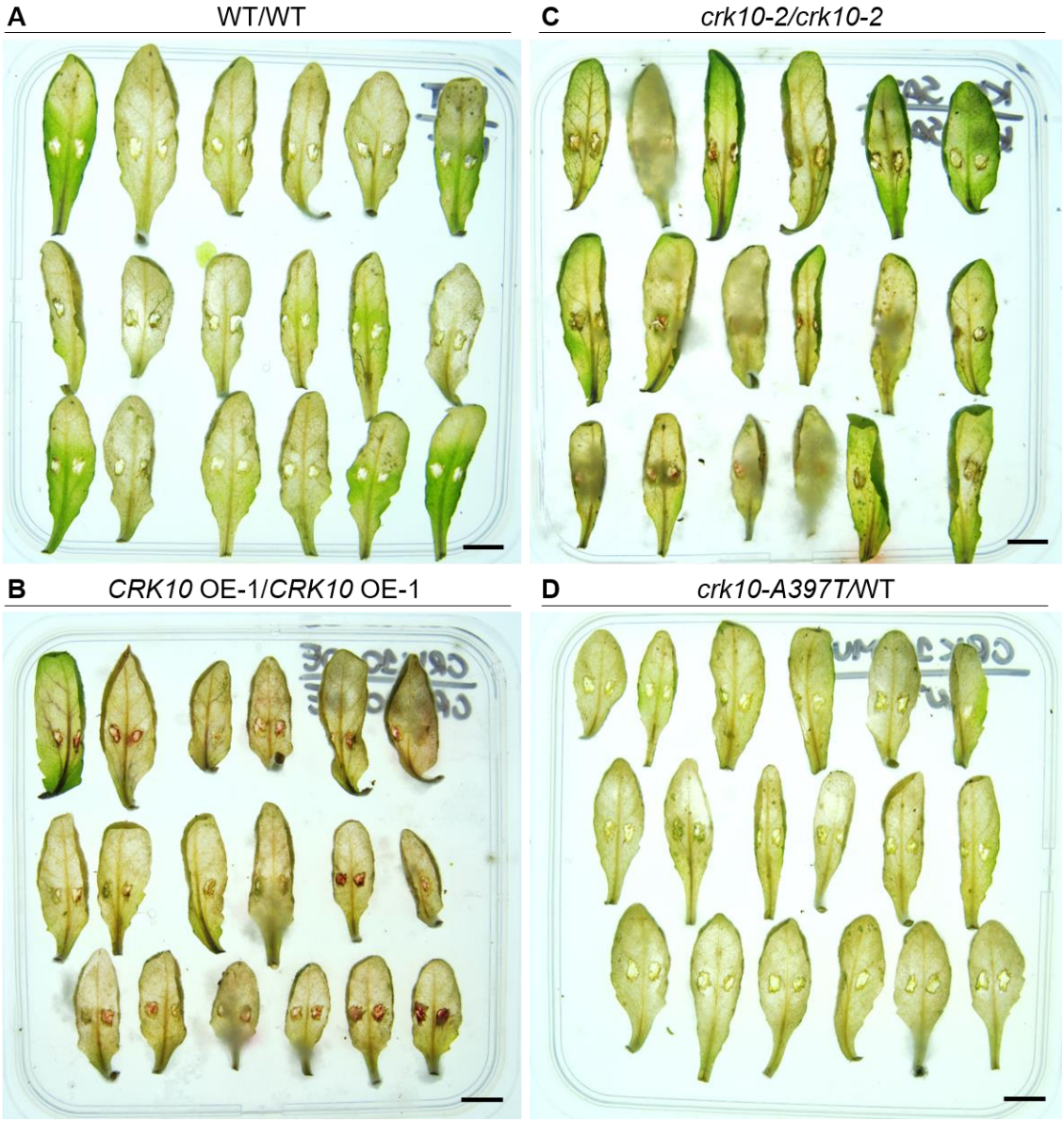

Figure 7.25 Detached leaf assay with the fungal pathogen *F. graminearum* using leaves from grafted plants.

Photographs taken at 10 DPI with *F. graminearum* showing plates with leaves of WT/WT, *crk10-2*/*crk10-2*, *CRK10* OE-1/*CRK10* OE-1 self-grafts and *crk10-A397T*/WT grafted plants. Annotation: scion/rootstock. Bars, 1 cm.

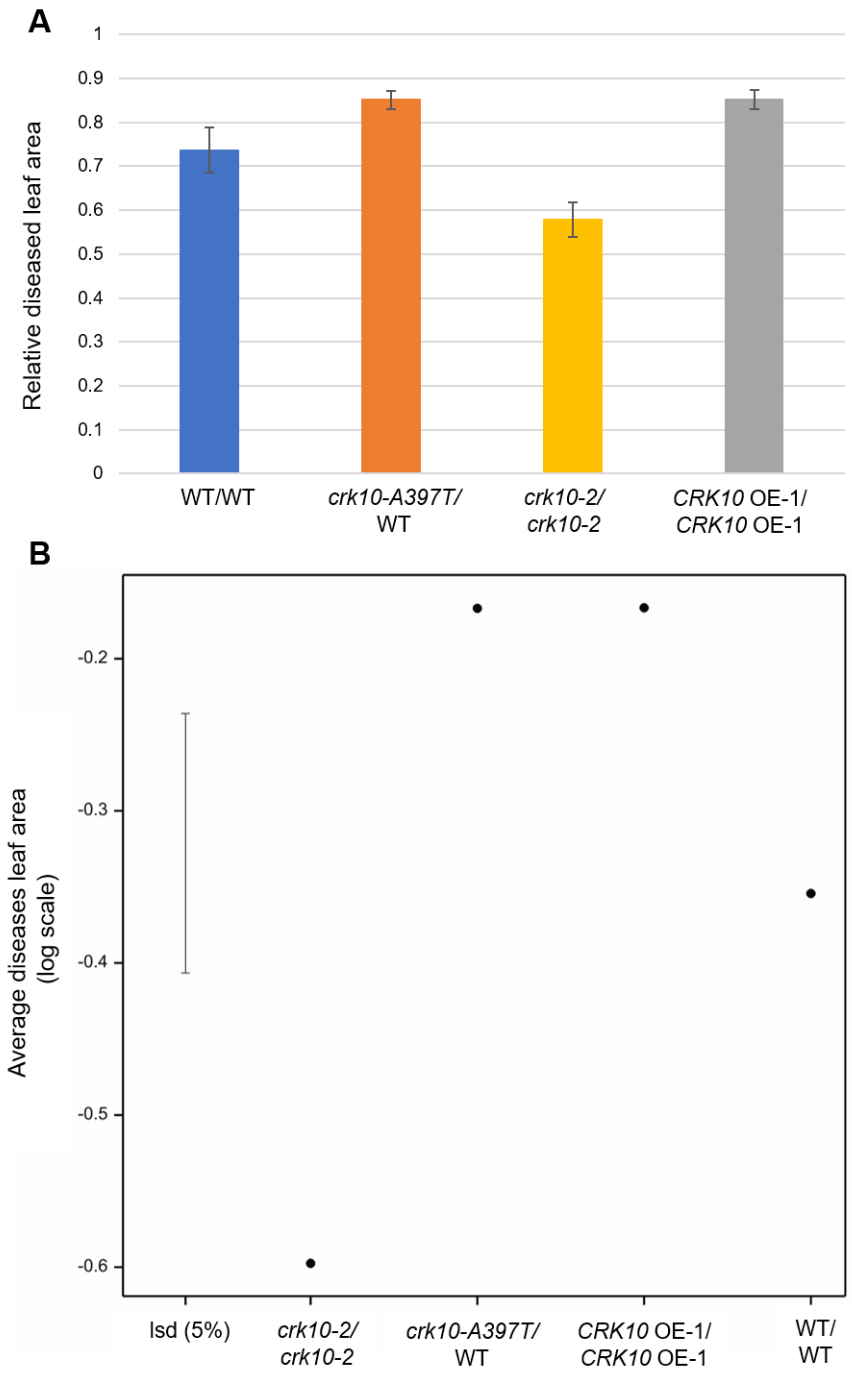

Figure 7.26 Leaves of *crk10-A397T*/WT, *CRK10* OE-1/*CRK10* OE-1 and *crk10-2/crk10-2* grafted plants show altered susceptibility to infection with *F. graminearum* compared to WT/WT leaves.

(A) Average relative diseased area of leaves from grafted plants at 10 DPI with *F. graminearum*. Error bars represent the standard error of 18 biological replicates (17 replicates for WT/WT).

(B) Average diseased leaf area (log scale) of each genotype following analysis with ANOVA ($F_{3, 67} = 11.60$; $p < 0.001$). Least significant difference (lsd 5%) bar is shown. Annotation: scion/rootstock.

7.4 Discussion

The constitutive induction of defence-related genes in the transcriptome of the *crk10-A397T* hypocotyls hints at the auto-immune phenotype triggered by this gain-of-function allele. Other auto-immune characteristics, such as accumulation of SA and stunted growth, further suggest the activation of defence responses in this mutant in the absence of pathogen attack. Auto-immunity usually causes disease resistance or susceptibility depending on the compatibility/incompatibility between the defence responses elicited in the host plant and the lifestyle of the pathogen. For example, mutants with constitutive induction of SA-dependent responses are often more resistant to biotrophic or hemi-biotrophic pathogens, whereas JA and ET pathways usually confer resistance to necrotrophs (Glazebrook, 2005). The vasculature-specific expression pattern of *CRK10* and the collapsed xylem vessel phenotype in the roots and hypocotyls was indicative of the fact that the responses activated by the *crk10-A397T* allele could be specifically tailored against vascular pathogens. Remodelling of cell walls and generation of cell wall appositions are well-known strategies used by plants to reinforce the physical barriers against pathogens (Underwood, 2012; Miedes et al., 2014). Furthermore, Yadeta and Thomma (2013) postulated that pathogen-induced cell wall modifications might cause xylem vessel collapse, which would negatively affect vascular conductivity and, consequently, pathogen movement and colonisation. Thus, could the induction of defence responses and cell wall remodelling in the *crk10-A397T* mutant confer enhanced resistance to vascular wilt disease in Arabidopsis?

To explore these questions, root infection assays with *F. oxysporum* were performed. Results of these experiments revealed the indisputable increased resistance of the *crk10-A397T* plants compared to the WT, which was consistent across five independent experiments. *CRK10* OE-1 plants also displayed enhanced resistance in some, but not all repetitions of the experiment, indicating that the overexpression of the gene is not as effective at inducing resistance as the gain-of-function. This could be due to the different speed with which these genotypes manage to deploy their defence responses. Although *CRK10* OE-1 plants constitutively express *CRK10*, the receptor is presumably only activated when exposed to an unknown signal present during the plant-pathogen interaction. The responses induced by *crk10-A397T*, however, are switched on

even before the perception of pathogen attack, which means the mutant plants are one step ahead against pathogen invasion.

Next, to identify signalling components which are required for the dwarf phenotype and the enhanced disease resistance of *crk10-A397T* plants to *F. oxysporum*, the progeny of genetic crosses between the *crk10-A397T* mutant with knockout / transgenic lines of key immune regulators were analysed. Interestingly, knockout of *EDS1* and *PAD4*, and the expression of the transgene *NahG* rescued the dwarf phenotype of the *crk10-A397T* mutant to varying levels. Interestingly, the knockout of *NPR1* affected neither the morphology nor the disease outcome of *crk10-A397T* plants. These results are in agreement with the enhanced susceptibility displayed by *35S:NahG* plants and the single mutant *pad4*, but not *npr1*, to infection with *F. oxysporum* compared to WT plants (Diener and Ausubel, 2015).These observations confirm that *EDS1/PAD4*-dependent, *NPR1*-independent branch of SA signalling is required for the disease resistance promoted by the *crk10-A397T* allele. Despite retaining the dwarf phenotype, *crk10-A397T wkry70* plants exhibited increased mortality compared to *crk10-A397T* plants, which suggests that the SA-induced repression of JA signalling pathways mediated by *WRKY70* (Li et al., 2004; Li et al., 2006) also play a role in promoting disease resistance in the *crk10-A397T* mutant plants.Conversely, components of JA signalling cascades do not seem to participate in *crk10-A397T*-mediated defence responses, as the *crk10-A397T myc2* double mutant displayed a similar probability of survival compared to the parental dwarf mutant. This was expected given the enhanced resistance to *F. oxysporum* displayed by the single mutant *myc2* (Anderson et al., 2004), and confirmed that the expression of JA-responsive genes upon knockout of the negative regulator *MYC2* does not affect the enhanced resistance of the *crk10-A397T* mutant. Completing the dataset, the knockout of *WRKY33* and *CYP81D11* also ruled out the participation of these genes in *crk10-A397T*-mediated resistance to *F. oxysporum*. One limitation of these analyses is the absence of the single mutant parental lines for comparison purposes. These lines were not included in these experiments for practical reasons, as each bioassay involved the inoculation of hundreds of plants. Given the considerable number of genotypes analysed in this chapter, including extra lines would become impracticable. Therefore, I opted to begin by screening all the genetic crosses to identify those which display an altered disease resistance phenotype. Going forward, the repetition of these experiments including the

single knockout parental lines *eds1*, *pad4*, *wrky70* and *NahG* would be ideal to generate a complete dataset for comparisons.

Defence responses might be effective at evading vascular wilt disease at several stages, such as the initial penetration of the root tissue, breaching of the xylem vessels, pathogen proliferation and movement within the xylem vasculature or reduction of pathogen-induced cell death in foliar tissue. In the case of *crk10-A397T* plants, one hypothesis may be that even if *F. oxysporum* is successful at entering the root tissue, it fails at penetrating the xylem network due to the presence of collapsed xylem vessels. Although remarkably more resistant than WT, a proportion of the *crk10-A397T* plants are severely symptomatic and die as a result of the infection with *F. oxysporum*. This means that the pathogen is capable of colonising the vasculature and causing wilting in the *crk10-A397T* mutant, although to a reduced extent at a population level compared to other genotypes. Nonetheless, the majority of *crk10-A397T* plants are either asymptomatic or develop mild symptoms, including vein clearing and leaf chlorosis, but proceed to recover and survive. At first glance, the presence of collapsed xylem vessels in the hypocotyls of all double mutants regardless of their growth and disease resistance phenotype seems to indicate they do not define the disease outcome of these plants. A thorough inspection, however, revealed the presence of ectopic xylem vessel formation in the hypocotyls of the four genotypes which rescued the disease resistance of the *crk10-A397T* mutant. *De novo* formation of xylem vessels has been previously reported in the literature in plants undergoing vascular wilt infection, such as Arabidopsis plants infected with *Verticillium longisporum* (Reusche et al., 2012). This phenomenon supposedly occurs to maintain water transport balance in response to the disease-related occlusion of xylem conduits. However, the cross sections presented in this chapter were obtained from uninfected hypocotyl samples. Nevertheless, the knockout of *eds1*, *pad4* and *wrky70* and the overexpression of *NahG* induces this process in the hypocotyls of *crk10-A397T* plants, presumably to ease the impaired water transport due to the collapsed vasculature. The prevalence and abundance of this feature in *crk10-A397T eds1* and *crk10-A397T pad4* is in agreement with their strong alleviation of the dwarf phenotype, as extra functional xylem vessels may increase water conductivity and support normal plant growth. The reason why this feature is only scarcely present among the biological replicates of *crk10-A397T wrky70* and *crk10-A397T NahG,* however, is

obscure, but it is likely associated with the milder alleviation of the growth defect of these plants. The analysis of the hypocotyls of parental *eds1*, *pad4*, *wrky70* and *35S:NahG* lines is necessary to rule out the pre-existence of these ectopic xylem vessels in the single knockout / transgenic plants, and confirm this process is exclusively triggered in the double mutant lines. Finally, the presence of extra xylem vessels might offer additional entry points for the vascular pathogen to invade the xylem network, which is possibly related to the increased mortality displayed by these double mutants compared to the parental *crk10-A397T*. Nevertheless, further experiments are necessary to elucidate the mechanisms by which these plants fail to avoid mortality, and to assess if the collapsed xylem vessels act as an additional physical barrier to pathogen invasion. One strategy would be the visualisation of the fungal pathogen within the host plant tissue by analysing root and hypocotyl cross sections of plants undergoing infection. This could be performed by the analysis of root and hypocotyl cross sections of infected plants using light microscopy, or by visualising tissue infected with a fluorophore-tagged strain of *F. oxysporum* using confocal microscopy, for example. A limitation of this approach, however, is the necessity to analyse a large number of biological replicates to account for the individual variability seen within the population of each genotype.

Finally, given the “long distance” induction of immune responses triggered by SA-dependent systemic acquired resistance, bioassays with *F. graminearum* were performed to assess whether the defence responses elicited by the *crk10-A397T* allele would also affect the outcome of infection after foliar inoculation. Despite naturally infecting floral tissues, *F. graminearum* was shown to successfully infect, induce disease and complete its life cycle on the leaves of Arabidopsis plants, which has been used elsewhere to investigate host-pathogen interactions between these species (Chen et al., 2006). Furthermore, detached leaf assays have been routinely used to investigate plant pathosystems, and it offers several advantages compared to whole plant assays, as they are quick, robust and highly reproducible. Nevertheless, an important limitation of this assay is the potential induction of wounding responses upon detaching of the leaves, which might affect the disease outcome. The assays reported in this chapter revealed that *crk10-2* plants only showed a slight reduction in disease susceptibility compared to the WT, which was not always significantly different. This is expected given the large size of the CRK family and the existence of

possible functional redundancy with other homologs. In contrast, *crk10-A397T* and *CRK10* OE-1 leaves showed increased susceptibility to infection with *F. graminearum, w*hich was statistically significant in both experiments. Considering the lifestyle of this pathogen, which undergoes an initial biotrophic stage followed by a switch to necrotrophy, a number of assumptions can be drawn to explain the outcome of infection in these genotypes. Firstly, it is important to bear in mind that the analysis of the transcriptome and quantification of hormones was performed using hypocotyls of *crk10-A397T* mutant plants, and therefore, no empirical evidence is available regarding the status of defence responses in the leaves of these plants. However, SAR, one of the processes regulated by SA, is a systemic rather than a localised process, which involves the long-distance movement of signalling molecules to trigger defence responses in healthy tissues away from the infection site (Durrant and Dong, 2004). Therefore, it is not unreasonable to assume that the accumulation of SA and the likely establishment of SAR in hypocotyls might result in the long-distance priming of leaves in *crk10-A397T* plants to fend off pathogen invasion. This strategy is highly successful at inducing resistance to biotrophic pathogens, which thrive in living plant tissues, but would actually be advantageous for a necrotroph, which could exploit the host-induced cell death to further colonise the plant (Glazebrook, 2005; Bari and Jones, 2009). Taken together, one possible explanation for the increased susceptibility of the *crk10-A397T* and *CRK10* OE-1 leaves to *F. graminearum* is that induction of SA responses ultimately favours the progression of disease following the pathogen switch to the necrotrophic phase of infection. Moreover, the observation that the overexpression of *CRK10* leads to a similar disease outcome compared to the *crk10-A397T* plants suggests that the WT and mutant allele of *CRK10* might activate similar, if not the same, defence responses to pathogens. This similarity was also observed between these genotypes in two out of three independently performed root infection assays with *F. oxysporum*, suggesting that the phenotypes induced by the *crk10-A397T* mutation may reflect the activation of the WT CRK10 protein and are, therefore, biologically relevant. Further experiments would be required, however, to confirm these hypotheses. Quantification of hormones and the analysis of the expression profile of SA- and SAR-related genes in the leaves of *crk10-A397T* mutant plants by qPCR could be used to confirm the hypothesized systemic nature of the defence responses in the mutant. Furthermore, the expression of hallmark defence-related genes

could also be monitored throughout the progression of the disease in all four genotypes, to clarify which hormonal pathways contribute to the development of susceptibility or resistance in the leaves. Additionally, performing a bioassay with biotrophic or necrotrophic pathogens would provide further insight into the nature of the defence responses orchestrated by CRK10.

Taken together, the results presented in this chapter show that the *crk10-A397T* mutant allele confers increased resistance to *F. oxysporum* which is dependent on *EDS1*, *PAD4* and *WRKY70*, and accumulation of SA signalling. Further experiments are required to clarify the molecular mechanisms underlying the increased resistance of *crk10-A397T* mutant plants to this vascular wilt, as well as to investigate whether the collapsed xylem vessels in roots and hypocotyl act as barriers to halt pathogen penetration in the xylem network.

Chapter 8. General Discussion

8.1 Main findings

This study has explored the characterisation of the novel gain-of-function mutant *crk10-A397T* of Arabidopsis. The results obtained throughout his project have shown that the *crk10-A397T* mutant allele causes a dwarf phenotype in Arabidopsis plants, which is associated with xylem vessel collapse in roots and hypocotyls (see Chapter 3). The substitution of alanine 397 with a threonine residue introduces an additional auto-phosphorylation site in the kinase domain of CRK10 as demonstrated by *in situ* auto-phosphorylation assays (see Chapter 4), although the phosphorylation status of the protein *in vivo* remains to be determined. Analysis of the transcriptome of *crk10-A397T* mutant hypocotyls has revealed the constitutive induction of stress-responsive genes, predominantly those involved with responses to biotic stress (see Chapter 5). Investigation of the composition of cell walls in the hypocotyls of *crk10-A397T* plants suggested significant alterations in comparison with WT plants, which are likely linked to the collapse of xylem vessels (see Chapter 6). Finally, this thesis reports that *crk10-A397T* mutant plants display increased resistance to a root-infecting vascular pathogen, which is dependent on salicylic acid signalling pathways (see Chapter 7). These results support the notion that *crk10-A397T* is a gain-of-function allele of *CRK10*, as it clearly activates cellular processes which affect plant development and responses to biotic and abiotic stress. This work highlights the benefits of isolating gain-of-function mutant alleles of receptor-like kinases as they might offer a glimpse into the biological processes regulated by these receptors without the requirement of discovering the ligand-receptor pair.

8.2 The gain-of-function nature of the *crk10-A397T* allele

The gain-of-function effect of the A397T point mutation in the kinase domain of CRK10 is evidenced by the extensive transcriptional reprogramming, activation of defence responses and vasculature defect observed in the hypocotyls of *crk10-A397T* mutant plants (see Chapter 3, 5 and 7). Nevertheless, the molecular mechanisms underlying the activation of responses by the mutated version of CRK10 remains elusive. Given the mode of action of plant RLKs, the simplest hypothesis is that this mutation causes the spontaneous activation of the kinase domain in the absence of a ligand and, consequently, the constitutive

initiation of downstream signalling cascades (see section 1.2 for a detailed description of the mode of action of plant RLKs). Under this assumption, two hypotheses are proposed. Firstly, considering that threonine residues can be phosphorylated by the kinase domain of plant RLKs, phosphorylation of Thr397 could act as a regulatory mechanism which triggers kinase activation. Alternatively, the presence of an unphosphorylated threonine at position 397 could be in itself sufficient to stabilise the kinase domain of CRK10 in a permanently active conformation. Although the results presented in Chapter 4 confirmed that this residue can indeed act as an auto-phosphorylation site *in situ*, the phosphorylation status of this site *in vivo* and the putative contribution to the activation of responses in the *crk10-A397T* mutant are yet to be determined. Nevertheless, the localisation of the point mutation within the αC-helix, a highly dynamic hub of regulatory motifs within the kinase domain, offers some hints at how these two putative mechanisms of activation could occur (Huse and Kuriyan, 2002; McClendon et al., 2014).

Firstly, sequence alignment of the kinase domain of CRK10 with the human PKA-Cα revealed that threonine is in close proximity to a functionally conserved residue which participates in the assembly of the R-spine, a crucial event during the activation of eukaryotic protein kinases (Kornev et al., 2006; Taylor et al., 2015; see section 4.3.1). The formation of the R-spine is accompanied by backbone motions throughout the kinase which include the repositioning of the αC-helix. For instance, the movement of the αC-helix from an "out" to an "in" conformation is essential to release the auto-inhibition of cyclin-dependent kinase 2 (CDK2) upon cyclin binding (Jeffrey et al., 1995; Jeffrey et al., 2000). Thus, could the introduction of a threonine in the vicinity of this R-spine residue promote intra-molecular interactions which spontaneously induce the active conformation of the kinase, regardless of its phosphorylation status? Or is the phosphorylation of this residue necessary to promote the "in" conformation of the αC-helix, which is conducive to R-spine formation and kinase activation?

Alternatively, the *in silico* structure of the CRK10 kinase domain generated by homology modelling predicts that threonine 397 is exposed at the surface of the C-terminal end of the αC-helix (see section 4.3.2), which is known to interact with non-catalytic regions of the kinase to regulate activity (Taylor et al., 2015). In members of the AGC family of kinases, for example, the docking of a hydrophobic motif from the C-terminal tail of the protein to a groove between the

αC-helix and β4-strand is essential to position and stabilise the αC-helix in the active conformation (Yang et al., 2002). Thus, another possible mechanistic explanation for the gain-of-function observed for the *crk10-A397T* allele is the creation of a new motif which promotes the interaction between the αC-helix and non-catalytic regions of the kinase. This intra-molecular interaction could potentially result in the coordinated movement of the kinase and the adoption of a permanently active state, similar to what is observed for activated AGC kinases.

Finally, a third scenario in which the constitutive activation of the kinase domain of CRK10 is not the outcome of the A397T substitution must also be considered. Given that threonine 397 is supposedly exposed at the surface of the protein, this mutation could potentially create a novel protein-protein interaction motif or docking site at the outer surface of the αC-helix, which might promote novel interactions between CRK10 and co-receptors within receptor complexes at the plasma membrane. If this assumption is true, the mutated version of CRK10 could assume a new function by interacting with different partners, which would not reflect the biological functions of the WT protein. Therefore, the notion that the *crk10-A397T* gain-of-function allele is a constitutively active version of CRK10 cannot be confirmed until this hypothesis is experimentally refuted.

Although the scenarios mentioned above are purely speculative at this stage, a number of experiments could be performed to elucidate some of the outstanding questions regarding the gain-of-function mode of *crk10-A397T*. As presented in Chapter 1, the expression of the *crk10-A397T* mutant allele under the control of the native promoter of *CRK10* (*CRK10*$_{PRO}$:*crk10-A397T*) is capable of inducing a dwarf phenotype in a knockout line of *CRK10* (see section 3.3.1). Thus, to test whether an active CRK10 is necessary for the induction of the dwarf phenotype, a dead kinase variant of the *crk10-A397T* allele could be introduced in the same background. If the activation of the kinase domain is necessary to trigger the responses downstream of the mutant allele, the kinase dead version of the *crk10-A397T* allele will fail to promote a dwarf phenotype in transgenic plants. Furthermore, to investigate if the phosphorylation of threonine 397 is required for the responses triggered by the mutant allele, the generation of phosphomimetic versions of the *crk10-A397T* allele could be useful. This approach consists of replacing a putative phosphorylation site with a negatively charged aspartate or glutamate residue to mimic the presence of phosphate groups (Pearlman et al., 2011). In this case, phosphomimetic alleles encoding a

glutamate (*crk10-A397E*) or and aspartate (*crk10-A397D*) residue at position 397 would also be introduced in the *CRK10* knockout background; if plants harbouring the phosphomimetic alleles display a dwarf phenotype, we can conclude that the phosphorylation of threonine 397 *in vivo* is required to trigger the responses downstream of the *crk10-A397T* allele. Moreover, mutant alleles encoding phosphomimetic residues within the activation loop of CRK10 could be used in an attempt to trigger constitutive activation. If successful at inducing a dwarf phenotype of *crk10-2* plants, these transgenic lines would be an indication that the *crk10-A397T* allele promotes the constitutive activation of CRK10. A drawback of this approach, however, is that only a small proportion of transgenic plants harbouring the *CRK10*$_{PRO}$:*crk10-A397T* construct displays the dwarf phenotype in the first place. This is likely due to the absence of cis-regulatory elements which are important for the expression of CRK10 but are absent in the 1 kb promoter region used in this study, possibly in combination with a position effect considering the genome area where the construct is inserted in each independent transgenic line. These factors might preclude the expression of the transgene at similar levels to the endogenous *CRK10* gene, thus failing to induce the dwarf phenotype. Nevertheless, this limitation can be overcome by analysing a large number of independent transgenic lines. Additionally, to test whether the A397T mutation promotes the interaction of CRK10 with different partners *in vivo*, a co-immunoprecipitation experiment could be performed. The identification of different interacting partners for the WT and mutated CRK10 following immunoprecipitation from plant tissue could be an indication that threonine 397 interferes with protein-protein interactions. The analysis of the crystal structure of phosphorylated and unphosphorylated CRK10kd^{WT} and CRK10kd^{A397T} could provide further insights into the impact of the A397T mutation on the folding of the protein and its potential role in stabilising the kinase domain in an active conformation or creating a docking site for intra- or inter-molecular interactions.

8.3 The relationship between defence responses and vasculature defect in the *crk10-A397T* mutant

Distinctive features of the *crk10-A397T* mutant are the presence of collapsed xylem vessels in roots and hypocotyls (see section 3.3.3) and the constitutive induction of defence responses (see section 5.3.2). Despite the predominance of defence-related genes in the transcriptome of *crk10-A397T*

mutant hypocotyls, transcriptional reprogramming of numerous cell wall biosynthesis and remodelling genes are also noteworthy across development (see section 5.3.10). Cell walls are important physical barriers encountered by pathogens attempting host colonisation and perception of pathogen elicitor molecules often triggers localised cell wall reinforcement and the production of appositions to halt pathogen penetration and spread (Underwood, 2012). Equally, cell wall-derived fragments known as damage-associated molecular patterns (DAMPs) are often released during pathogen-induced hydrolysis of plant cell walls, and are recognised by cell surface receptors to trigger immune responses (Engelsdorf and Hamann, 2014; Malinovsky et al., 2014). Furthermore, cell wall integrity (CWI) surveillance receptors play an essential role in the activation of defence responses and cell wall repair mechanisms in response to cell wall perturbations caused by developmental defects or pathogen attack (Vaahtera et al., 2019). Notably, a recent study by Molina et al. (2021) has shown that out of a panel of 34 Arabidopsis mutants with cell wall defects, over 80% displayed increased disease resistance.

Thus, both the perception of pathogen elicitors and host cell wall perturbation can trigger defence responses and cell wall remodelling mechanisms in plants. In light of the phenotypes displayed by the *crk10-A397T* mutant, a question arises: are the defence-related signalling pathways and the cell wall remodelling mechanisms independently activated by the *crk10-A397T* allele, or is one of these processes triggered in response to the other? From the perspective of the transcriptomic analysis, the induction of immune responses seems to precede the activation of cell wall remodelling as defence-related genes are prominent at the earliest time point analysed in the RNA sequencing experiment in comparison to cell wall genes (see Chapter 5). At a later time point, however, a myriad of cell wall-related genes are differentially expressed and the collapse of xylem vessels takes place, suggesting that cell wall remodelling may occur after the activation of defence responses. However, the observation that the knockout of key signalling members of SA responses (*EDS1*, *PAD4* and *WRKY70*) impairs the increased resistance of the *crk10-A397T* plants to *F. oxysporum,* but not the collapsed xylem vessel phenotype, suggests otherwise (see sections 7.3.3 and 7.3.4). If the vasculature defect was triggered by SA-responses which seemingly mediate the resistance of the *crk10-A397T* plants to *F. oxysporum*, the disruption of these signalling pathways and the depletion of

this hormone would not only affect the disease outcome, but also abolish or at least partially alleviate the collapse of xylem vessels. As this is not observed in the genetic crosses examined in this study, we can infer that SA-mediated responses are not upstream of the vasculature defect observed in the *crk10-A397T* mutant hypocotyls, but are rather downstream or independent events to the processes which promote xylem collapse. Quantification of SA levels and the analysis of the transcript abundance of hallmark SA-induced genes in the genetic crosses of *crk10-A397T* with *eds1*, *pad4*, *wrky70* and *35S:NahG* would be necessary to confirm the disruption of defence responses in these plants. Furthermore, the generation of transgenic lines expressing the *crk10-A397T* allele under the control of an inducible promoter could also be a useful tool to confirm the order of transcriptional events taking place upon expression of the mutant allele. These observations provide the basis for the discussion of the putative roles of CRK10 explored in section 8.4.

8.4 The putative roles of CRK10

Assuming that the A397T mutation promotes the constitutive activation of CRK10, the phenotype induced by this gain-of-function mutant allele would reflect the biological processes triggered by the activation of the WT CRK10 receptor (as discussed in section 8.2). Therefore, if further experiments confirm this hypothesis is correct, it would be possible to infer that the signalling cascades initiated by CRK10 induce defence responses to pathogens and cell wall remodelling mechanisms in Arabidopsis. But what could be the ligand recognised by the extracellular domain of CRK10?

As introduced in section 1.5, studies have demonstrated that certain DUF26-containing proteins have antifungal properties and are able to bind mannose, a component of the polysaccharide mannan of fungal cell walls (Miyakawa et al., 2014; Ma et al., 2018). Given the structural homology between the ectodomain of CRKs, PDLPs and secreted DUF26 proteins such as Gnk2, Vaattovaara et al. (2019) suggested that the carbohydrate-binding ability might be a conserved feature across all DUF26-containing proteins. This hypothesis would be in accordance with a role for CRK10 as a sensor for pathogen- or host-derived cell wall fragments, as perception of molecules belonging to either of these classes are known to induce defence responses to pathogens and cell wall remodelling mechanisms (as discussed in section 8.3). Under this assumption,

CRK10 could function either as an immune receptor which recognises pathogen attack, or a member of the CWI surveillance system which senses host cell wall perturbations.

Among several strategies that could be used to test this hypothesis, the investigation of the carbohydrate-binding ability of the extracellular domain of CRK10 *in vitro* would be a logical first step. Overexpression and knockout lines of *CRK10* could also be useful in this pursuit by subjecting them to treatment with putative ligand molecules and evaluating the activation of downstream responses. For instance, transcriptional induction of defence-related marker genes, production of second messengers such as ROS, and activation of MAPK cascades are some of the aspects which can be monitored to evaluate the activation of responses upon treatment with putative ligands. This strategy has been extensively used to monitor the responses elicited by the bacterial-derived flg22 peptide, chitin oligomers and plant cell wall-derived oligosaccharides (Denoux et al., 2008; Takai et al., 2008; Cao et al., 2014; Shinya et al., 2014; Jiménez-Góngora et al., 2015; Davidsson et al., 2017). If CRK10 signals via receptor complexes which recognise these putative ligands, downstream responses should be increased in *CRK10* overexpression lines compared to WT and *crk10* knockout lines.

8.5 The importance of characterising mutant alleles such as *crk10-A397T* for the wider research community

Despite collaborative efforts from the research community, the precise biological roles and mechanism of action of CRKs have not yet been determined. Since this class of RLKs was first identified in Arabidopsis around two decades ago, several studies have described their association with developmental and stress-responsive processes, although details such as their activating ligand, co-receptors and downstream targets remain largely unknown. Most reports have relied on traditional approaches such as the analysis of knockout and overexpression lines of members of the family. Although this strategy can provide insights by comparing the performance of these lines to WT plants under stress-inducing conditions, for example, it is often inefficient for the study of gene families such as the CRKs for a number of reasons. Firstly, the large size of the family means that functional redundancy is expected among homologues, which can mask potential effects of the knockout of a single CRK. Furthermore, the

occurrence of several CRKs in large tandem arrays across plant genomes precludes the generation of higher order mutants which could be used to simultaneously knockout functionally redundant homologues. Additionally, the overexpression of CRKs often does not cause any phenotype due to the absence of the activating ligand, which could be an environmental cue or endogenous molecule which is only present during specific stress conditions.

Therefore, the fortuitous isolation of gain-of-function mutants such as *crk10-A397T* is an invaluable tool to study the roles of CRKs *in planta*, as the phenotypes displayed by these mutants might provide hints about the functions, regulation and specificity of these receptors. In addition to providing clues about the gene harbouring the mutation, gain-of-function lines might also offer insights about general aspects of the regulation of this class of proteins. The A397T mutation in CRK10, for example, highlights the importance of the αC-helix in mediating the regulation and/or protein-protein interactions of the kinase domain of CRKs (depending on which hypothesis discussed in section 8.2 proves to be correct). Results presented in Chapter 4 also suggest that an equivalent mutation in the kinase domain of other CRK homologs affects their auto-phosphorylation status *in situ*, which is an indication that it could possibly affect their phosphorylation status *in planta* as well. The observation that the position corresponding to Ala397 in CRK10 is always occupied by an alanine, serine or threonine residue in all members of the family in Arabidopsis is rather intriguing, and further investigation about the role of this residue in regulating kinase activity would be interesting. Moreover, even though previous studies have demonstrated the auto/trans-phosphorylation ability of the kinase domain of CRKs (see section 1.4), the results presented in this thesis constitute the first report of the identification of auto-phosphorylation sites for a member of this family to the best of my knowledge.

Furthermore, the high degree of structural and functional homology shared by the kinase domain of plant RLKs means that characteristics of kinase regulation and activity might be conserved among members of different subfamilies. As mentioned in Chapter 4, the substitution of an alanine with a threonine residue in subdomain III / αC-helix of the kinase domain of an atypical RLK also causes a gain-of-function effect in Arabidopsis plants (Bi et al., 2010), suggesting that mutations within the αC-helix have the potential to affect kinase activity and/or regulation in other members of the RLK superfamily. Furthermore,

the structural and functional similarities observed between the kinase domain of LysM-containing receptor-like kinase 3 (LYK3) of *Medicago truncatula* and the human Interleukin-1 receptor-associated kinase/Pelle-soluble kinase 4 (IRAK4) exemplify the homology existent across the plant and animal kingdom (Klaus-Heisen et al., 2011). Thus, the identification of regulatory sites in the kinase domain of a plant RLK, such as CRK10, not only contributes to expand the current knowledge about kinase regulation and activity in plant species, but also holds the potential to uncover previously uncharacterised mechanisms which are conserved among the superfamily of eukaryotic kinases.

8.6 The potential implications of this work for crops sciences

Fundamental research using the model species Arabidopsis has been instrumental for some of the most important discoveries in plant sciences to date, allowing scientists to uncover the molecular basis of numerous biological processes (Provart et al., 2015). Among these, the identification of genes which mediate responses to stresses such as drought, flooding and pathogen attack is increasingly coveted, especially in light of the daunting prospects of climate change (Raza et al., 2019). Given the importance of RLKs in the regulation of several aspects of plant growth, development and adaptation to stresses, they constitute promising targets for the improvement of commercially relevant crops which will likely be affected by the changing environment. For instance, Marshall et al. (2012) have discussed the potential of exploring RLKs to enhance crop resistance to drought stress, one of the biggest issues caused by increasing global temperatures. This work especially highlights the fact that orthologous peptide ligands and their respective cognate RLKs display homologous functions in Arabidopsis and in crop species such as maize and rice, an indication that research on RLKs using model species can often be translated into commercially relevant crops (Marshall et al., 2012). Therefore, the characterisation of mutant alleles which confer enhanced resistance to stresses or improve crop performance can contribute not only to our understanding of the molecular basis of these processes, but also to identify novel targets for crop improvement. In the case of the *crk10-A397T* mutant allele, however, the activation of defence responses is accompanied by a fitness penalty, which makes it less appealing for direct transfer into a crop. Nevertheless, the discovery that CRK10 is an RLK potentially involved with plant pathogen interactions in Arabidopsis can be used

as a guide by plant breeders to identify CRK10 orthologues in non-cultivated varieties of crop species, for example, which could then be targeted for introduction into commercial cultivars by traditional breeding. Additionally, CRKs are large multigene families across plant genomes, with 30 members in cotton (Li et al., 2018), 45 in rice (Chern et al., 2016) and 46 in the common bean (Quezada et al., 2019), for instance, which might allow the identification of homologues which confer desirable traits without incurring fitness penalties. As an example, a CRK allele in wheat which is nearly absent in cultivated varieties was recently found to confer resistance to *Septoria tritici* blotch, a devastating pathogen of wheat (Saintenac et al., 2021). This work highlights the importance of exploiting the genetic diversity of modern and ancient crop germplasm to identify alleles with the potential to enhance crop performance, a process which can be sped up via the functional characterisation of genes of interest in model species to identify the best candidates for plant breeding. Furthermore, the identification of mutations which promote a desirable trait without inflicting a deleterious effect on plant fitness could be potentially introduced into crop species via a gene editing approach (Zhang et al., 2018; Nasti and Voytas, 2021). In conclusion, the characterisation of mutants such as the *crk10-A397T* are not only an invaluable tool to explore the regulation, mode of action and biological functions of previously uncharacterised genes in a model species, but also holds the potential to provide novel information which could be applied for the generation of more resilient crops in the field.

Appendix 1

Appendix 1.1: Republished with permission from Elsevier Ltd from Anaesthesia and Intensive Care Medicine, Vol 21, Issue 1, Cameron J. Weir, “Ion channels, receptors, agonists and antagonists”. Copyright © (2020) Elsevier Ltd. Permission conveyed through Copyright Clearance Center, Inc.

Appendix 1.2: Republished with permission from Annual Reviews Inc from Annual Review of Plant Physiology and Plant Molecular Biology, Vol 48, Chris Lamb and Richard A. Dixon, “The oxidative burst in plant disease resistance”. Copyright © (2002) Annual Reviews, Inc. Permission conveyed through Copyright Clearance Center, Inc.

Appendix 1.3: Republished with permission from National Academy of Sciences from Proceedings of the National Academy of Sciences of the United States of America, Vol 98, Issue 19, Shin-Han Shiu and Anthony B. Bleecker, “Receptor-like kinases from Arabidopsis form a monophyletic gene family related to animal receptor kinases”. Copyright © (2001) National Academy of Sciences, USA.

Appendix 1.4: Republished with permission Annual Reviews Inc from Annual Review of Biochemistry, Vol 81, Jane A. Endicott, Martin E.M. Noble, and Louise N. Johnson, “The Structural Basis for Control of Eukaryotic Protein Kinases”. Copyright © (2012) Annual Reviews, Inc. Permission conveyed through Copyright Clearance Center, Inc.

Appendix 1.5: Republished with permission from National Academy of Sciences Proceedings of the National Academy of Sciences of the United States of America, Vol 103, Issue 47, Alexandr P. Kornev, Nina M. Haste, Susan S. Taylor, and Lynn F. Ten Eyck, “Surface comparison of active and inactive protein kinases identifies a conserved activation mechanism”. Copyright © (2006) National Academy of Sciences, USA.

Appendix 1.6: Republished with permission from National Academy of Sciences from Proceedings of the National Academy of Sciences of the United States of America, Vol 105, Issue 38, Alexandr P. Kornev, Susan S. Taylor, and Lynn F.

Ten Eyck, “A helix scaffold for the assembly of active protein kinases”. Copyright © (2008) National Academy of Sciences, USA.

Appendix 1.7: Republished with permission from Springer-Verlag from Protoplasma, Vol 247, Juan Pablo Matte Risopatron, Yuqiang Sun & Brian Joseph Jone, “The vascular cambium: molecular control of cellular structure”. Copyright © (2010) Springer-Verlag. Permission conveyed through Copyright Clearance Center, Inc.

Appendix 1.8: Republished with permission from Elsevier Ltd from Current Opinion in Plant Biology, Vol 29, Fabio Lehmann and Christian S Hardtke, “Secondary growth of the Arabidopsis hypocotyl — vascular development in 4 dimensions”. Copyright © (2010) Elsevier Ltd. Permission conveyed through Copyright Clearance Center, Inc.

Appendix 1.9: Republished by permission from Springer Nature Customer Service Centre GmbH: Springer; Plant Cell, Tissue and Organ Culture, Junji Miyazaki, Beng H. Tan & Steve G. Errington, “Eradication of endophytic bacteria via treatment for axillary buds of *Petunia hybrida* using Plant Preservative Mixture (PPM^{TM})”. Copyright © (2010).

Appendix 1.10: Republished with permission from Elsevier Ltd from Physiological and Molecular Plant Pathology, Vol 34, Karin E. Bretschneider, Michael P. Gonella, David J. Robeson, “A comparative light and electron microscopical study of compatible and incompatible interactions between *Xanthomonas campestris* pv. *campestris* and cabbage (*Brassica oleracea*)”, Pg 287-297. Copyright © (1989).

Appendix 2

Appendix 2.1: Vector map of pJET1.2/blunt (Thermo Scientific™).

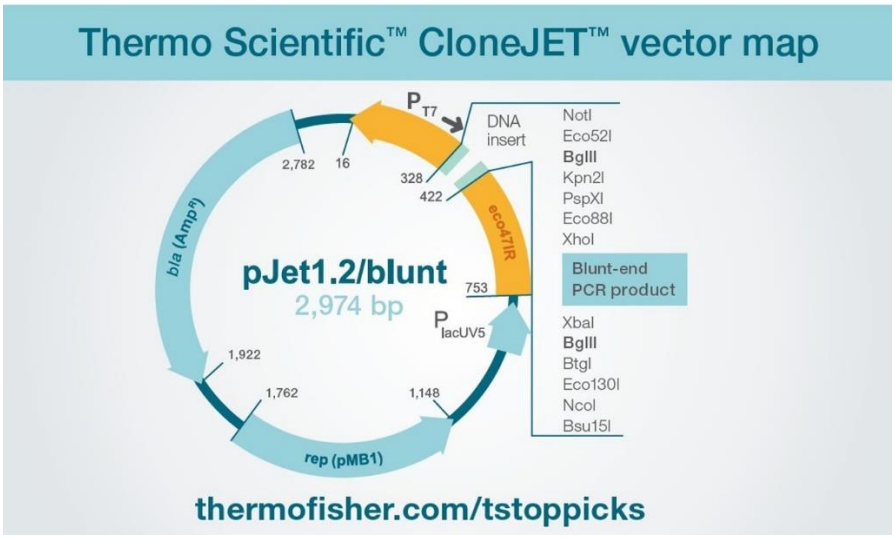

Appendix 2.2: Vector map of pJD330.

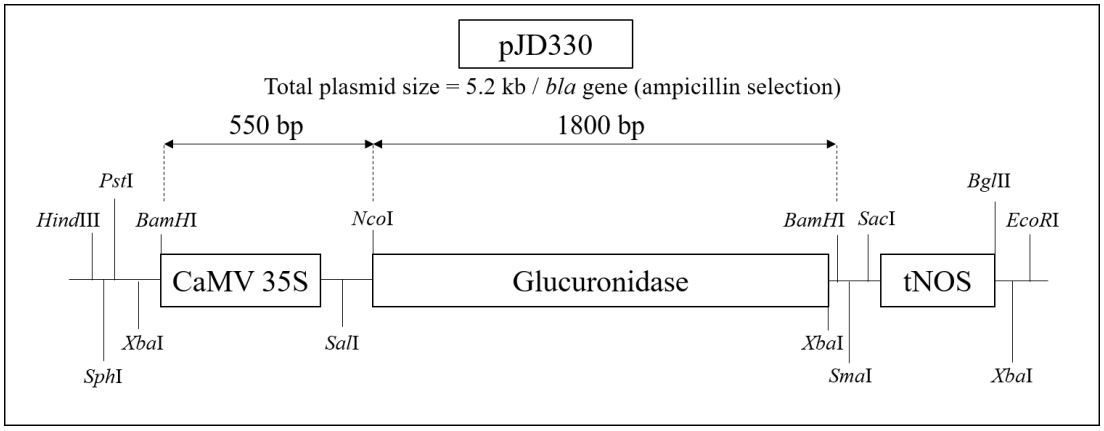

Appendix 2.3: Vector map of pENTR™1A Dual Selection Vector (Invitrogen™).

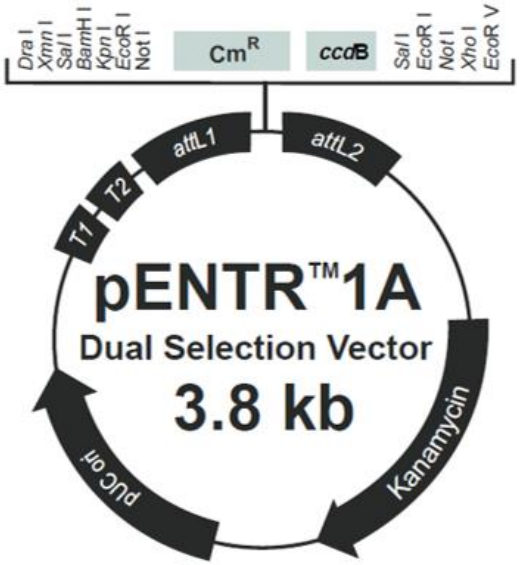

Appendix 2.4: Vector map of pUNI51.

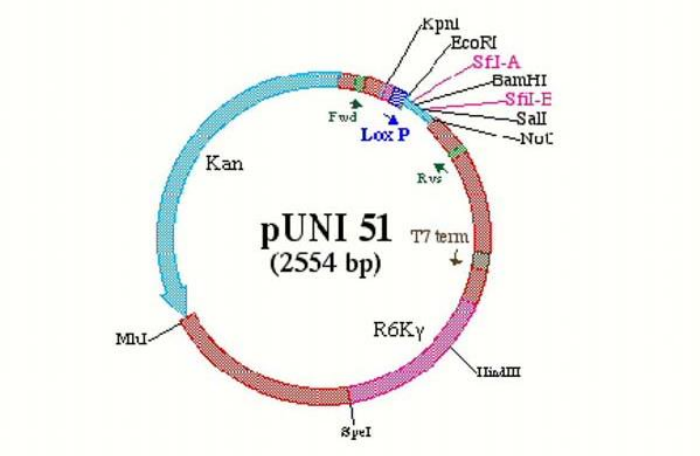

Appendix 2.5: Vector map of pUC57 (obtained from the GenScript website).

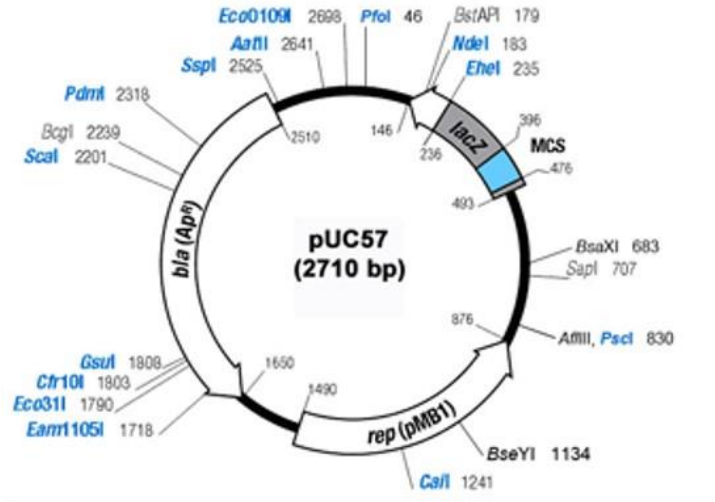

Appendix 2.6: Vector map of pDEST™17 (Invitrogen™).

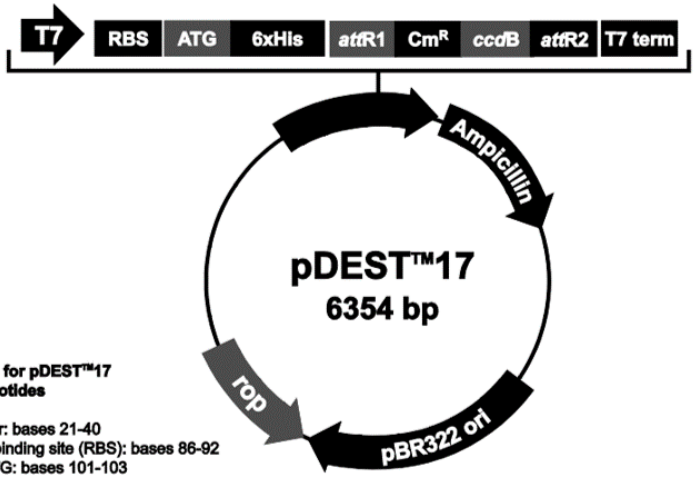

Comments for pDEST™17
6354 nucleotides

T7 promoter: bases 21-40
Ribosome binding site (RBS): bases 86-92
Initiation ATG: bases 101-103
6xHis tag: bases 113-130
attR1: bases 140-264
Chloramphenicol resistance gene (Cm^R): bases 373-1032
ccdB gene: bases 1374-1679
attR2: bases 1720-1844
T7 transcription termination region: bases 1855-1983
bla promoter: bases 2471-2569
Ampicillin (*bla*) resistance gene: bases 2570-3430
pBR322 origin: bases 3575-4248
ROP ORF: bases 4619-4810 (C)

C=complementary strand

Appendix 2.7: Vector map of RS_3GSeedDSredMCS. The plasmid contains two additional base pairs compared to pBINGlyRed3 (*Pst*I restriction site 5' CTGCAG 3' (9,312 – 9,317 bp) mutagenised to 5' CCTGCCAG 3'.

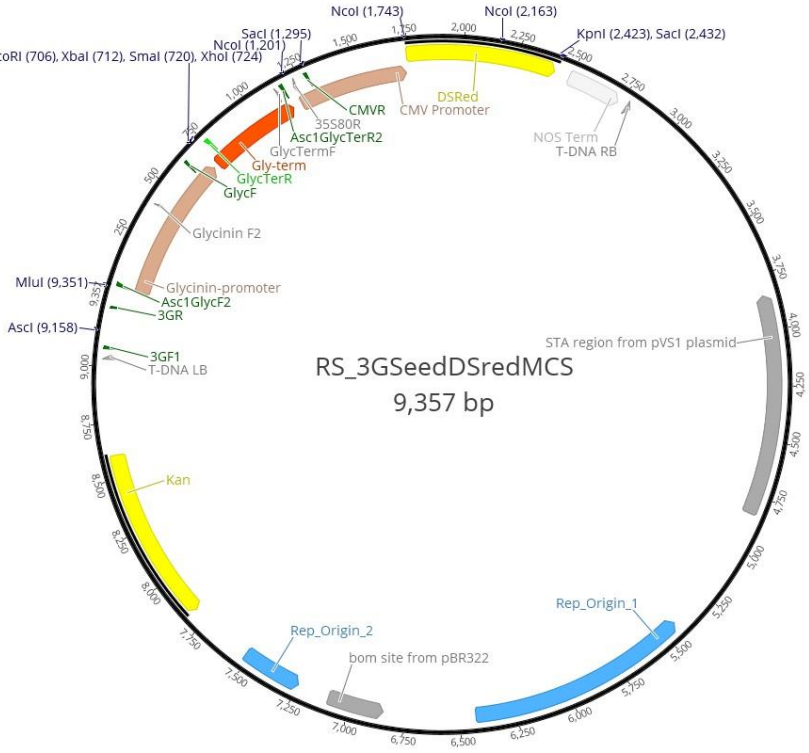

Appendix 2.8: Vector map of pB2GW7.

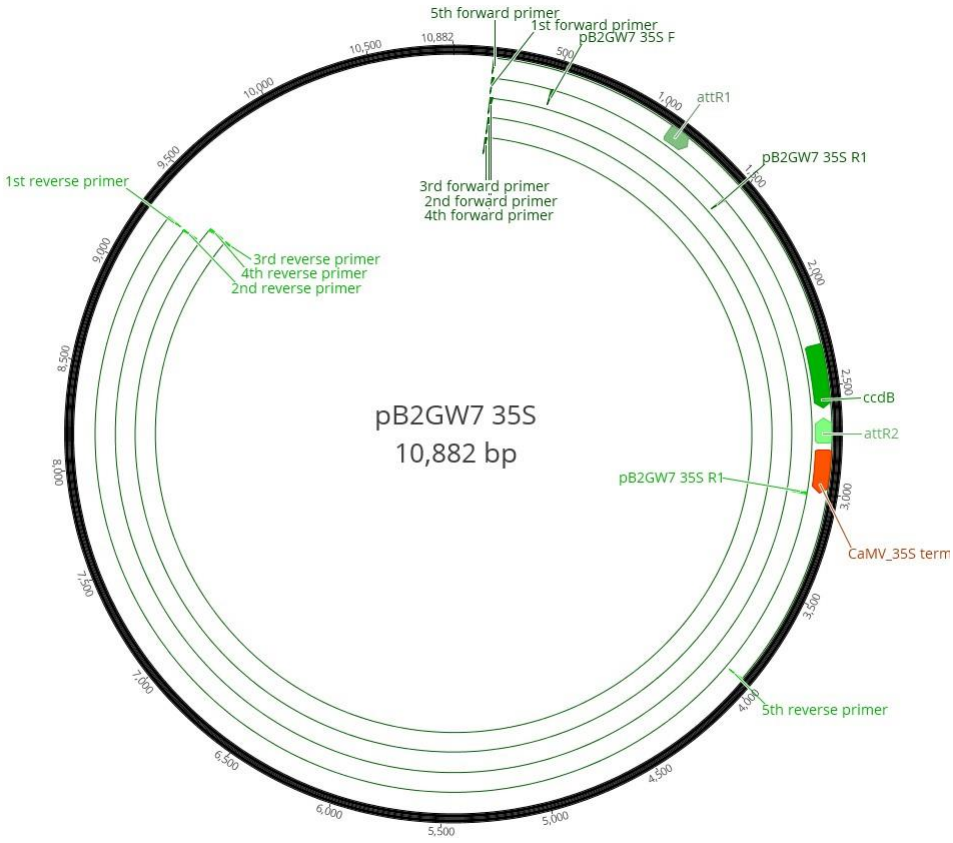

Appendix 3

Appendix 3.1: Genomic sequence of the putative native promoter of *CRK10* (~1 kb genomic region upstream of start codon; 5' – 3').

CCTTTGCAACTAGCTAGATGGAGCTTATGGATGCAAAATTCGTTTTAAAACACATTGTATTC
GGATGATGTCAAAATATTTCACATTCATATAGCAAATTCATGTTTATATATTCCGATATTAAC
TTTAAATATTAAAACTTATATGCTGTAGATTCATATCCGGGTGAAAACACGAAAGGACTTAT
GATGGAACCATTATATGGAACGACGTCATGTGGAATATCAAGTTATTTAACTTCTCGCGAGT
AAGACTATAAAAAGTAATAGAATAATTAGTAACTAACAATATCAGATAACGATAGGCAGAT
GATTTGGTAATACTATTTTAGTATCACTACATCACAATAACCATACTAGCATATACGATATAC
AAATTAATAAATTATCGTGCTTAAAACAAAAACCTATTATCAACCAATAATTTCTTCGCATC
AGTGGCGACAATTTTTTCAGCCCCAGAATGATTCTTTGAAGAATAGTCAACAAAGATTCCTA
ATTTCAACAATTCTGTTCAAGGAAAAGTACGAAACAAATTCTACTGCTAGCTAGTTTCTCTC
ATGTATATCTAAATTCTATTACTAGTAATTAAGATCTTTGAAATCATGCCAACTGCTACATTT
ATTTTCTCTTGAAAATCCCAACTACCTTTTTTTTGATCAAAAAAAAAAAAAGACTTTAGAGTTC
AAAGCTTGAATTTAGAGTTATTATGTTTTAAATTTTGACAGTTTTGATAATTTTCTTCATTTTA
AAATGATTTTATATTTTCCGTAATTTTTTTCTATATTTCATATATTAAAAAAATAAGTAATGG
ATTAGTAGCTAAACACAAGAAGTTGGACAAGACCCGACAATTTAATACGAGACGCGTTGAC
CTTGACCTTGACTTTTCGTCAGCACAAAACGTTATCTACGGTAGTCACTGAGAGAGAACAAA
CAATCAAATTTGTTTCATATATCACTCAAAGCTTGATGA

Appendix 3.2: Representative cloning steps to obtain the *CRK10$_{PRO}$:GUS* construct in RS_3GSeedDSredMCS binary vector. Steps are outlined in section 3.2.4.

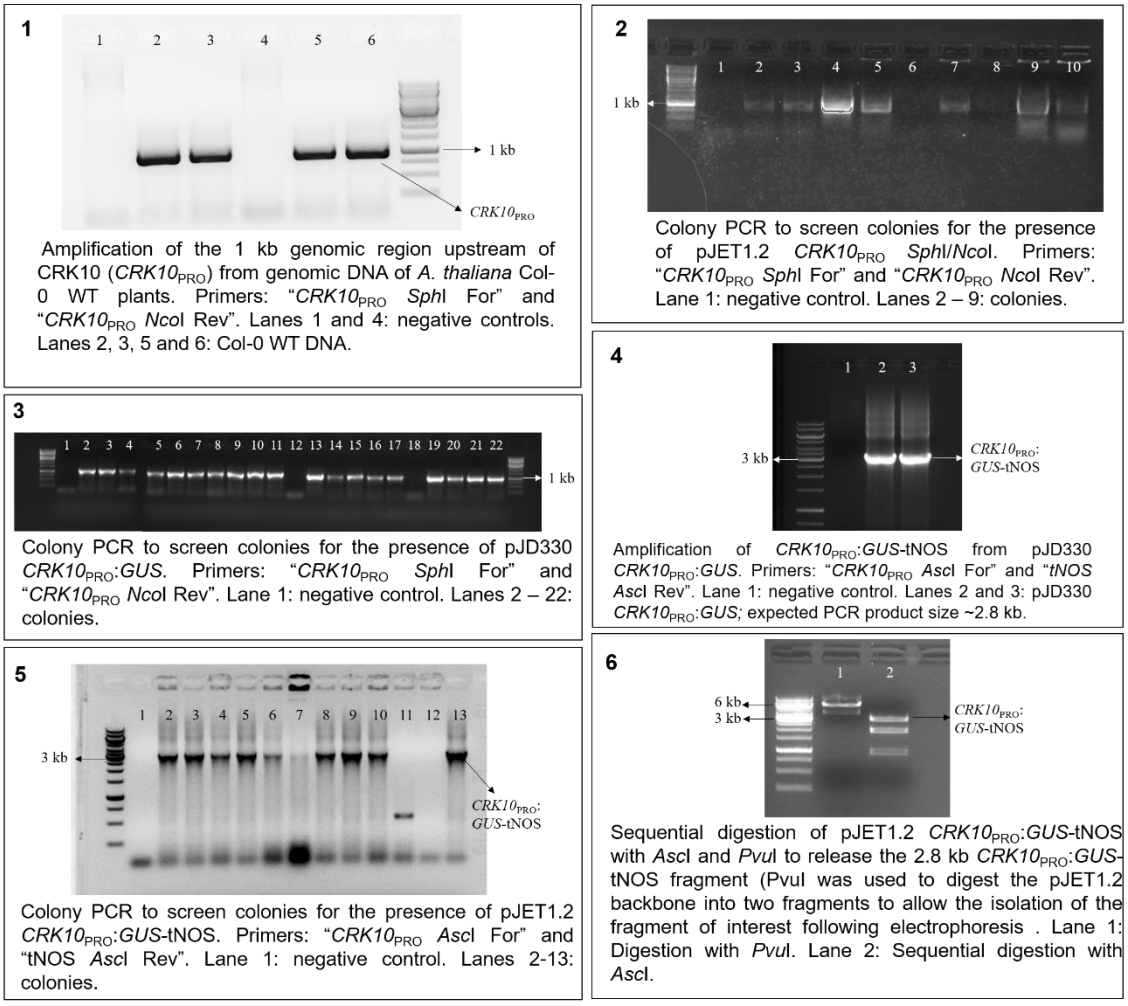

Appendix 4

Appendix 4.1: Representative cloning steps to obtain the *CRK10*$_{PRO}$:*crk10-A397T* construct RS_3GSeedDSredMCS binary vector. Steps are outlined in section 3.2.5.

1

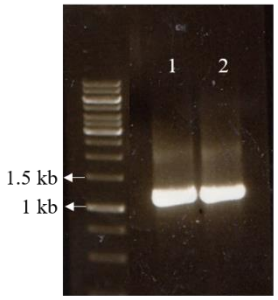

Amplification of the ~1 kb *CRK10*$_{PRO}$ (*Sph*I/*Sal*I) from pJET1.2 *CRK10*$_{PRO}$ (*Sph*I/*Nco*I). Primers: "*CRK10 Sph*I For" and "*CRK10*$_{PRO}$ *Sal*I Rev". Lanes 1 and 2: pJET1.2 *CRK10*$_{PRO}$ (*Sph*I/*Nco*I).

2

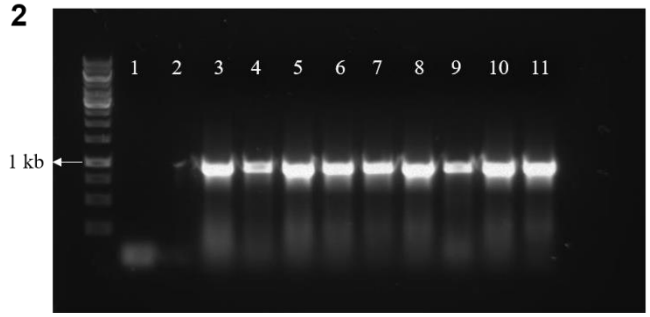

Colony PCR to screen colonies for the presence of pJET1.2 *CRK10*$_{PRO}$ (*Sph*I/*Sal*I). Primers: "*CRK10*$_{PRO}$ *Sph*I For" and "*CRK10*$_{PRO}$ *Sal*I Rev". Lane 1: negative control. Lanes 2-11: colonies; expected PCR product size ~1 kb.

3

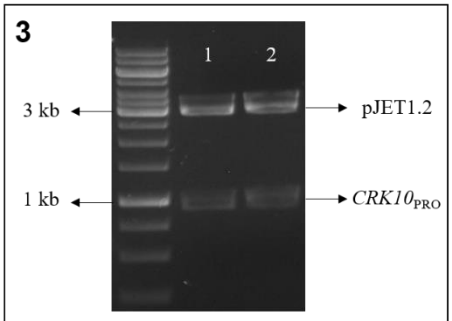

Double digestion of pJET1.2 *CRK10*$_{PRO}$ (*Sph*I/*Sal*I) with *Sph*I and *Sal*I. Lanes 1 and 2: minipreps #1 and #2; expected fragment sizes ~1 kb (*CRK10*$_{PRO}$) and ~3 kb (vector backbone).

4

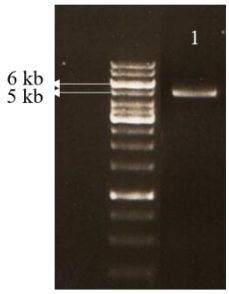

Double digestion of pJD330 *35S:CRK10*^{WT} with *Sph*I and *Sal*I. Lane 1: digested vector; expected fragment sizes ~5.5 kb (pJD330 *CRK10*^{WT}) and ~550 bp (35S promoter, too faint to be detected here). The double digestion was repeated with increased amount of initial plasmid DNA and the fragment corresponding to pJD330 *CRK10*^{WT} was purified from the gel.

5

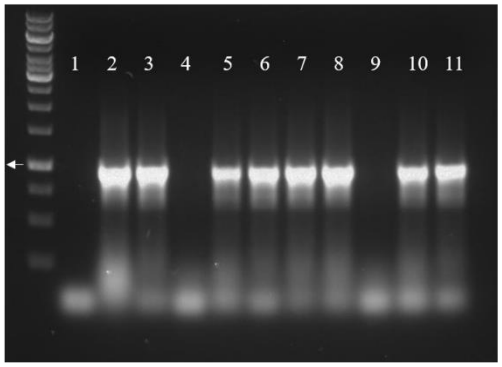

Colony PCR to screen colonies for the presence of the pJD330 *CRK10*$_{PRO}$:*CRK10*^{WT} construct. Primers: "*CRK10*$_{PRO}$ *Sph*I For" and "*CRK10*$_{PRO}$ *Sal*I Rev". Lane 1: negative control. Lanes 2-11: colonies. Expected PCR product size ~1 kb.

6

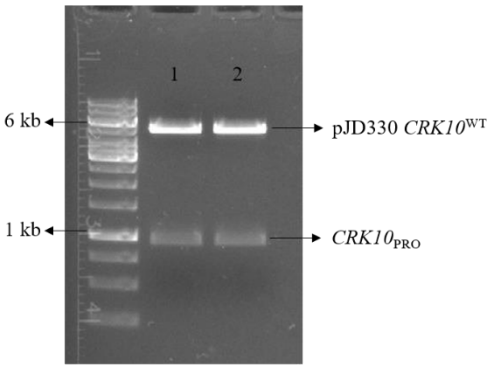

Double digestion of pJD330 *CRK10*$_{PRO}$:*CRK10*^{WT} with *Sph*I and *Sal*I to check construct. Lanes 1 and 2: digested vector; expected fragment sizes of ~1 kb (*CRK10*$_{PRO}$) and ~6 kb (pJD330 *CRK10*^{WT}).

7

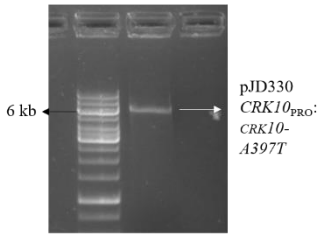

In vitro mutagenesis PCR to introduce *crk10-A397T* mutation in pJD330 *CRK10*$_{PRO}$:*CRK10*^{WT}. Primers: *CRK10* A397T For and *CRK10* A397T Rev. Lane 1: mutagenised pJD330 *CRK10*$_{PRO}$:*CRK10*^{WT}*;* expected PCR product size ~7 kb.

8

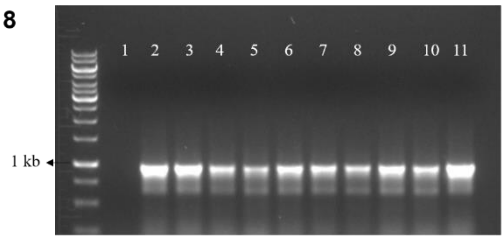

Colony PCR to screen colonies for the presence of pJD330 *CRK10*$_{PRO}$:*crk10-A397T*. Primers: "*CRK10*$_{PRO}$ *Sph*I For" and "*CRK10*$_{PRO}$ *Sal*I Rev". Lane 1: negative control. Lanes 2-11: colonies.

9

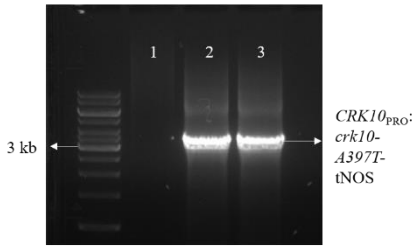

Amplification of the approximately 3 kb construct *CRK10*$_{PRO}$:*crk10-A397T*-tNOS from pJD330 *CRK10*$_{PRO}$:*crk10-A397T*. Primers: "*CRK10*$_{PRO}$ *Asc*I For" and "tNOS *Asc*I Rev". Lane 1: negative control. Lanes 2 and 3: pJD330 *CRK10*$_{PRO}$:*crk10-A397T*-tNOS.

10

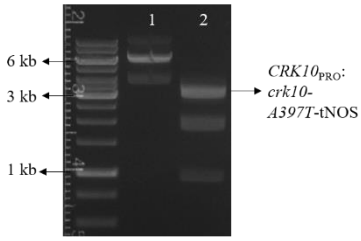

Digestion of pJET1.2 *CRK10*$_{PRO}$:*crk10-A397T* construct with *Pvu*I and *Asc*I to release construct for ligation with binary vector. Lane 1: Digestion with *Pvu*I. Lane 2: Sequential digestion with *Asc*I. Fragment of interest *CRK10*$_{PRO}$:*crk10-A397T*-tNOS

11

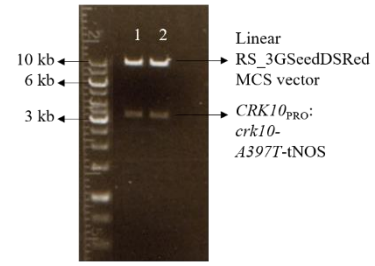

Digestion of pJET1.2 *CRK10*$_{PRO}$:*crk10-A397T* construct with *Asc*I to check construct. Lanes 1 and 2: digested vector; expected fragment sizes of ~3 kb (*CRK10*$_{PRO}$:*crk10-A397T*-tNOS) and ~9.4 kb (vector backbone).

Appendix 5

Appendix 5.1: Coding sequence of the fluorescent protein mCherry

ATGGTGAGCAAGGGCGAGGAGGATAACATGGCCATCATCAAGGAGTTCATGCGTTTCAAGG
TGCACATGGAGGGCTCCGTGAACGGCCACGAGTTCGAGATCGAGGGCGAGGGCGAGGGCCG
CCCCTACGAGGGCACCCAGACCGCCAAGCTGAAGGTGACCAAGGGTGGCCCCCTGCCCTTC
GCCTGGGACATCCTGTCCCCTCAGTTCATGTACGGCTCCAAGGCCTACGTGAAGCACCCCGC
CGACATCCCCGACTACTTGAAGCTGTCCTTCCCCGAGGGCTTCAAGTGGGAGCGCGTGATGA
ACTTCGAGGACGGCGGCGTGGTGACCGTGACCCAGGACTCCTCCCTGCAGGACGGCGAGTT
CATCTACAAGGTGAAGCTGCGCGGCACCAACTTCCCCTCCGACGGCCCCGTAATGCAGAAG
AAGACCATGGGCTGGGAGGCCTCCTCCGAGCGGATGTACCCCGAGGACGGCGCCCTGAAGG
GCGAGATCAAGCAGAGGCTGAAGCTGAAGGACGGCGGCCACTACGACGCTGAGGTCAAGA
CCACCTACAAGGCCAAGAAGCCCGTGCAGCTGCCCGGCGCCTACAACGTCAACATCAAGTT
GGACATCACCTCCCACAACGAGGACTACACCATCGTGGAACAGTACGAACGCGCCGAGGGC
CGCCACTCCACCGGCGGCATGGACGAGCTGTACAAGTAAACGCGTGATGGGCGAGCTCGAA
TTGATCGTTCAAACATTTGGCAA

Appendix 5.2: Representative cloning steps to obtain the *35S:CRK10-mCherry* construct in pB2GW7 binary vector. Steps are outlined in section 3.2.6.

1

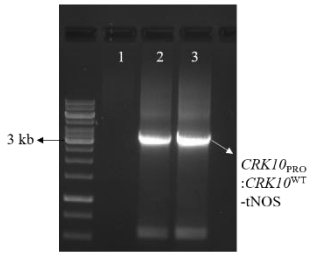

Amplification of the ~3 kb construct *CRK10*$_{PRO}$:*CRK10*^{WT}-tNOS from pJD330 *CRK10*$_{PRO}$:*CRK10*^{WT}. Primers: "*CRK10*$_{PRO}$ *Asc*I For" and "tNOS *Asc*I Rev". Lane 1: negative control. Lanes 2 and 3: pJD330 *CRK10*$_{PRO}$:*CRK10*^{WT}.

2

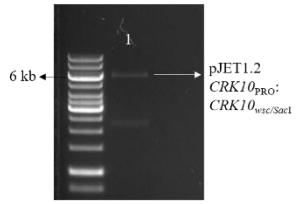

In vitro mutagenesis PCR to amplify the *CRK10* cDNA sequence without stop codon (wsc) from pJET1.2 *CRK10*$_{PRO}$:*CRK10*^{WT}. Primers: "*CRK10* wsc *Sac*I For" and "*CRK10* wsc *Sac*I Rev". Lane 1: pJET *CRK10*$_{PRO}$:*CRK10*^{WT}; expected PCR product size ~6 kb.

3

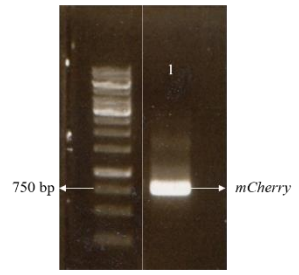

Amplification of the coding sequence of the fluorescent protein mCherry from a stock plasmid kindly provided by Dr Michaela Matthes. Primers: "*mCherry Sac*I For" and "*mCherry Sac*I Rev". Lane 1: mCherry stock; expected PCR product size ~750 bp.

4

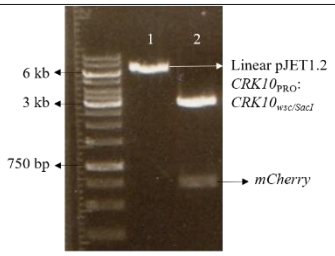

Digestion of pJET1.2 *CRK10*$_{PRO}$:*CRK10*$_{wsc/SacI}$ and pJET1.2 *mCherry* with *Sac*I. Lane 1: digested pJET1.2 *CRK10*$_{PRO}$:*CRK10*$_{wsc/SacI}$; linearised vector ~6.3 kb. Lane 2: digested pJET1.2 *mCherry;* expected fragments ~3 kb (vector backbone) and ~750 bp (*mCherry*).

5

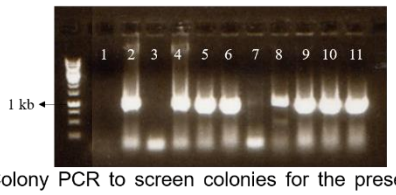

Colony PCR to screen colonies for the presence of pJET1.2 *CRK10*$_{PRO}$:*CRK10-mCherry*. Primers: "*mCherry Sac*I For" and "tNOS *Asc*I Rev". Lane 1: negative control. Lanes 2-11: colonies. Expected PCR product size ~1 kb.

6

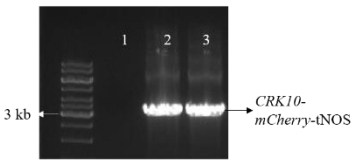

Amplification of *CRK10-mCherry*-tNOS from pJET1.2 *CRK10*$_{PRO}$:*CRK10-mCherry*-tNOS. Primers: "*CRK10 Sal*I For" and "tNOS *Not*I Rev". Lane 1: negative control. Lanes 2 and 3: pJET1.2 *CRK10*$_{PRO}$:*CRK10-mCherry-tNOS;* expected PCR product size ~2.8 kb

7

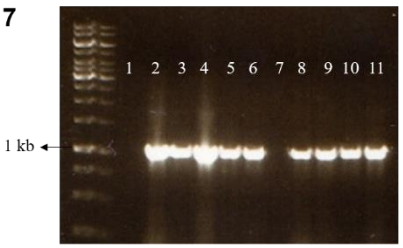

Colony PCR to screen colonies for the presence of *mCherry*-tNOS in the correct orientation in pJET1.2 *CRK10-mCherry*-tNOS. Primers: "*mCherry Sac*I For" and "tNOS *Asc*I Rev". Lane 1: negative control. Lanes 2-11: colonies. Expected PCR product size ~1 kb.

8

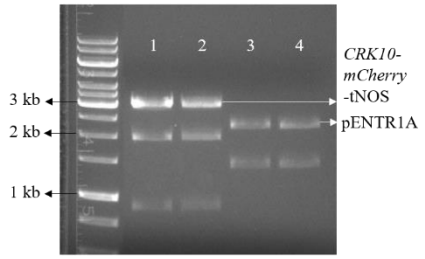

Sequential digestions of pJET *CRK10-mCherry*-tNOS and pENTR1A. Lanes 1 and 2: Double digestion of pJET *CRK10-mCherry*-tNOS with *Not*I and *Pvu*I (1) followed by sequential digestion with *Sal*I (2). Lanes 3 and 4: Sequential digestion of pENTR1A with *Not*I (3) and *Sal*I (4). 3 kb fragment in lane 2 (*CRK10-mCherry*-tNOS) and 2.3 kb fragment in lane 4 (pENTR1A) were excised and purified from agarose gel.

9

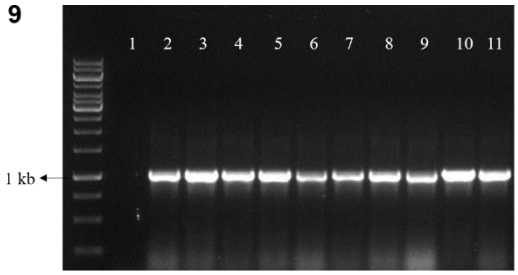

Colony PCR to screen colonies for the presence of pENTR1A *CRK10-mCherry-tNOS*. Primers: "*mCherry Sac*I For" and "*NOS Not*I Rev". Lane 1: negative control. Lanes 2-11: colonies.

10

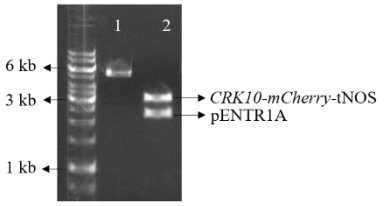

Sequential digestion of pENTR1A harbouring the *CRK10-mCherry*-tNOS construct. Lane 1: digestion with *Not*I; linearized plasmid ~5.3 kb. Lane 2: sequential digestion with *Sal*I; expected fragment sizes ~3 kb and ~2.3 kb.

11

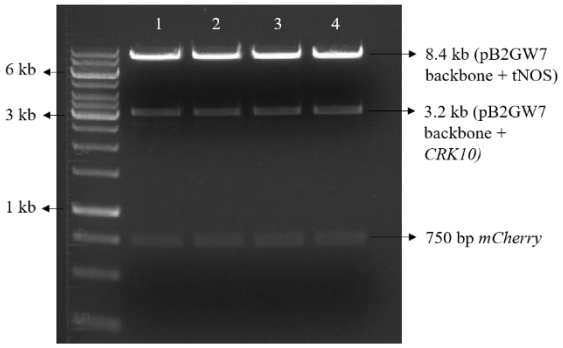

Digestion of pB2GW7 harbouring *CRK10-mCherry-tNOS* to confirm construct. Lanes 1 - 4: minipreps #1 to #4 digested with *Sac*I. Expected fragment sizes ~8.4 kb, ~3.2 kband ~750 bp (mCherry).

Appendix 6

Appendix 6.1 Representative genotyping PCR of T-DNA line (SALK_116653).

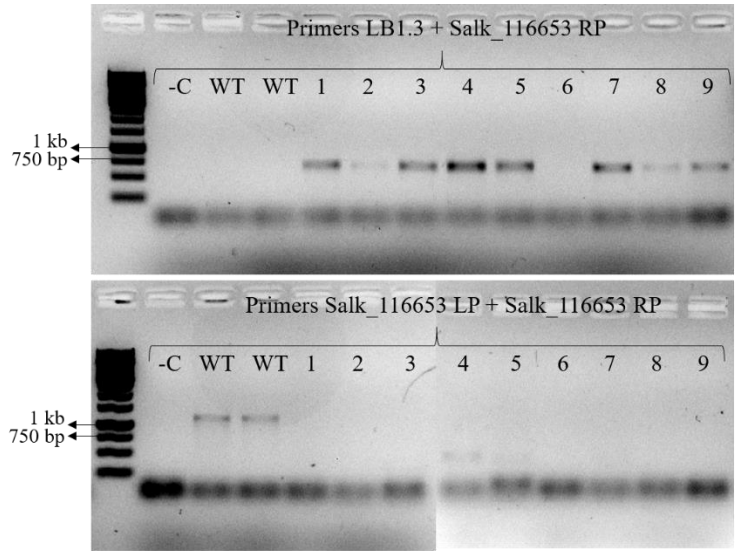

Genotyping PCR to identify plants of line Salk_116653 homozygous for T-DNA insertion.
Lane -C: negative control. Lanes WT: Col-0 WT genomic DNA. Lanes 1-9: Salk_116653 genomic DNA.
Result: all plants but #6 were homozygous for T-DNA insertion.

Appendix 7

Appendix 7.1: List of candidate mutations identified by whole genome sequencing of bulk segregants of the sixth backcross between the *crk10-A397T* mutant and WT Col-0.

Chromosome	Position	Ref base	Alt base	Gene	Description	Position in gene	AA change
4	10040156	G	A	AT4G18120	RNA binding proteins	exon	arginine --> lysine
4	10325224	G	A	AT4G18810	NAD(P)-binding Rossmann-fold superfamily protein	exon	threonine--> isoleucine
4	10637738	G	A	AT4G19510	Disease resistance protein (TIR-NBS-LRR class); ATP Binding	exon	Arginine--> Glutamine
4	10669042	A	G	AT4G19580	DNAJ heat shock N-terminal domain-containing protein;	exon	Asparagine--> Aspartic Acid
4	10951982	C	G	AT4G20270	Encodes a CLAVATA1-related receptor kinase-like protein required for both shoot and flower meristem function	exon	Arginine--> Glycine
4	10951983	G	C	AT4G20270	Encodes a CLAVATA1-related receptor kinase-like protein required for both shoot and flower meristem function	exon	Arginine--> Proline
4	10960624	G	C	AT4G20310	Peptidase M50 family protein;	990bp upstream	n/a
4	11499352	G	A	AT4G21640	Subtilase family protein;	exon	n/a
4	11825071	G	A	AT4G22415	transposable element gene	unknown	n/a
4	12087341	G	A	AT4G23060	Q-domain 22 (IQD22);	exon	Glycine--> Aspartic Acid
4	12139655	G	A	AT4G23180	CRK10, Encodes a receptor-like protein kinase	exon	Alanine--> Threonine
4	12741613	G	A	AT4G24690	Encodes NBR1 a selective autophagy substrate	exon	Arginine --> lysine
4	13352393	C	G	AT4G26420	A member of the Arabidopsis SABATH methyltransferase gene family. Encodes GAMT1	exon	Arginine--> Proline
4	13352394	G	C	AT4G26420	A member of the Arabidopsis SABATH methyltransferase gene family. Encodes GAMT1	exon	Arginine --> Glycine
4	13369938	G	C	AT4G26460	S-adenosyl-L-methionine-dependent methyltransferases superfamily protein	exon	Glycine--> Alanine

Appendix 8

Appendix 8.1: Sequence of the cytoplasmic kinase domain of CRKs which was expressed as recombinant protein in *E. coli*. First methionine residue is not part of the WT sequence and was introduced by PCR / gene synthesis to allow expression of the recombinant protein.

Residue highlighted in yellow: position corresponding to Ala397 in CRK10.
Residue highlighted in pink: conserved catalytic aspartic acid.

CRK2:

MAKTLKDSSLNFKYSTLEKATGSFDNANKLGQGGFGTVYKGVLPDGRDIAVKRLFFNNRHRATDFYNEVN
MISTVEHKNLVRLLGCSCSGPESLLVYEYLQNKSLDRFIFDVNRGKTLDWQRRYTIIVGTAEGLVYLHEQSS
VKIIHRDIKASNILLDSKLQAKIADFGLARSFQDDKSHISTAIAGTLGYMAPEYLAHGQLTEMVDVYSFGVLVL
EIVTGKQNTKSKMSDYSDSLITEAWKHFQSGELEKIYDPNLDWKSQYDSHIIKKEIARVVQIGLLCTQEIPSL
RPPMSKLLHMLKNKEEVLPLPSNPPFMDERVMELRDGSDGDSAGCASLATVSQSSFYGR

CRK5:

MDDITTAGSLQFDFKVIEAATDKFSMCNKLGQGGFGQVYKGTLPNGVQVAVKRLSKTSGQGEKEFKNEV
VVVAKLQHRNLVKLLGFCLEREEKILVYEFVSNKSLDYFLFDSRMQSQLDWTTRYKIIGGIARGILYLHQDS
RLTIIHRDLKAGNILLDADMNPKVADFGMARIFEIDQTEAHTRRVVGTYGYMSPEYAMYGQFSMKSDVYSF
GVLVLEIISGRKNSSLYQMDASFGNLVTYTWRLWSDGSPLDLVDSSFRDSYQRNEIIRCIHIALLCVQEDTE
NRPTMSAIVQMLTTSSIALAVPQPPGFFFRSNHEQAGPSMDKSSLCSIDAASITILAPR

CRK6:

MDDMATADSLQLDYRTIQTATNDFAESNKIGRGGFGEVYKGTFSNGKEVAVKRLSKNSRQGEAEFKTEVV
VVAKLQHRNLVRLLGFSLQGEERILVYEYMPNKSLDCLLFDPTKQIQLDWMQRYNIIGGIARGILYLHQDSR
LTIIHRDLKASNILLDADINPKIADFGMARIFGLDQTQDNTSRIVGTYGYMAPEYAMHGQFSMKSDVYSFGV
LVLEIISGRKNSSFGESDGAQDLLTHAWRLWTNKKALDLVDPLIAENCQNSEVVRCIHIGLLCVQEDPAKRP
AISTVFMMLTSNTVTLPVPRQPGFFIQCRAVKDPLDSDQSTTTKSFPASIDDESITDLYPR

CRK7:

MDDKTTIESLQLDYRAIQAATNDFSENNKIGRGGFGDVYKGTFSNGTEVAVKRLSKTSEQGDTEFKNEVV
VVANLRHKNLVRILGFSIEREERILVYEYVENKSLDNFLFDPAKKGQLYWTQRYHIIGGIARGILYLHQDSRL
TIIHRDLKASNILLDADMNPKIADFGMARIFGMDQTQQNTSRIVGTYGYMSPEYAMRGQFSMKSDVYSFGV
LVLEIISGRKNNSFIETDDAQDLVTHAWRLWRNGTALDLVDPFIADSCRKSEVVRCTHIGLLCVQEDPVKRP
AMSTISVMLTSNTMALPAPQQPGFFVRSRPGTNRLDSDQSTTNKSVTVSIDDKSMSDLDPR

CRK10:

MDDITTADSLQLDYRTIQTATDDFVESNKIGQGGFGEVYKGTLSDGTEVAVKRLSKSSGQGEVEFKNEVVL
VAKLQHRNLVRLLGFCLDGEERVLVYEYVPNKSLDYFLFDPAKKGQLDWTRRYKIIGGVARGILYLHQDSR
LTIIHRDLKASNILLDADMNPKIADFGMARIFGLDQTEENTSRIVGTYGYMSPEYAMHGQYSMKSDVYSFGV
LVLEIISGKKNSSFYQTDGAHDLVSYAWGLWSNGRPLELVDPAIVENCQRNEVVRCVHIGLLCVQEDPAER
PTLSTIVLMLTSNTVTLPVPRQPGLFFQSRIGKDPLDTDTTSKSLLGSVDDASITDIHPR

CRK36:

MSDSDGQATLRFDLGMILIATNEFSLENKLGQGGFGSVYKGILPSGQEIAVKRLAGGSGQGELEFKNEVLL
LTRLQHRNLVKLLGFCNEGNEEILVYEHVPNSSLDHFIFDEDKRWLLTWDVRYRIIEGVARGLLYLHEDSQL
RIIHRDLKASNILLDAEMNPKVADFGMARLFNMDETRGETSRVVGTYGYMAPEYVRHGQFSAKSDVYSFG
VMLLEMISGEKNKNFETEGLPAFAWKRWIEGELESIIDPYLNENPRNEIIKLIQIGLLCVQENAAKRPTMNSVI
TWLARDGTFTIPKPTEAAFVTLPLSVKPENRSMSERKDKDPFSVDEVSITVLYPR

Appendix 8.2: Representative cloning steps to obtain pDEST™17 *CRKkd* constructs. Steps are outlined in section 4.2.3.

1

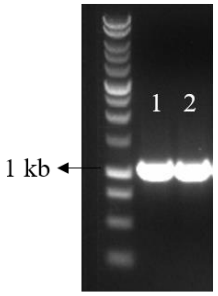

Amplification of CRK10kd sequence. Primers: "CRK10 KD *Sal*I For" and "CRK10 KD *Not*I Rev". Lanes 1 and 2: CRK10kd^{WT} and CRK10kd^{A397T}. Expected PCR product size ~1 kb.

2

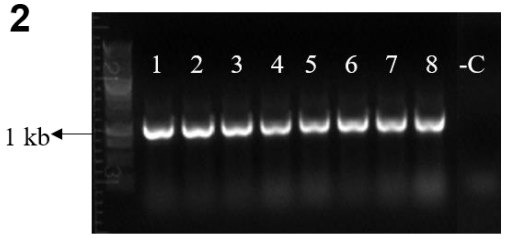

Colony PCR to screen colonies for the presence of pJET1.2 CRK10kd^{WT}. Primers: "CRK10 KD *Sal*I For" and "CRK10 KD *Not*I Rev". Lanes 1-8: colonies; -C: negative control. Expected PCR product size ~ 1kb.

3

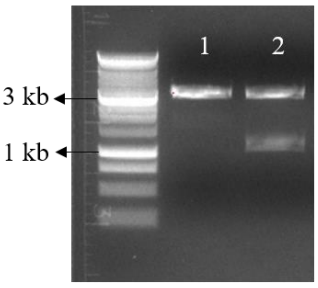

Sequential digestion of pJET CRK10kd^{A397T} with SalI and NotI. Lane 1: digestion with NotI; lane 2: sequential digestion with SalI. Expected fragment sizes ~1 kb (CRK10kd^{A397T}) and ~3 kb (vector backbone).

4

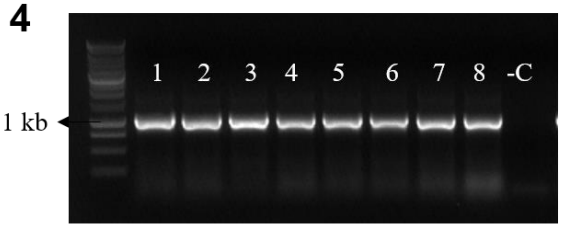

Colony PCR to screen colonies for the presence of pENTR1A CRK10kd^{WT}. Primers: "CRK10 KD *Sal*I For" and "CRK10 KD *Not*I Rev". Lanes 1-8: colonies; -C: negative control. Expected PCR product size ~ 1kb.

5

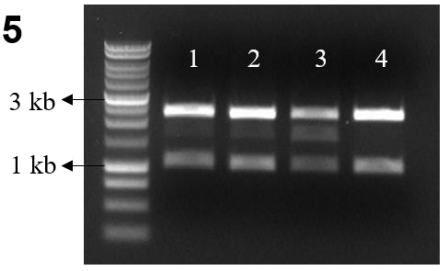

Digestion of pENTR1A CRK10kd constructs with SalI and NotI to check construct. Lanes 1 – 4: digested pENTR1A CRK10kd constructs; expected fragment sizes ~2.8 kb (vector backbone) and ~1 kb (CRK10kd). Faint band in lanes 1, 2 and 3 is likely supercoiled, non-digested vector.

6

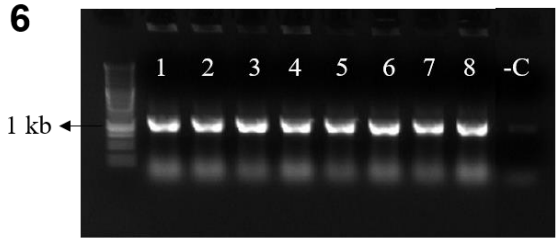

Colony PCR to screen colonies for the presence of pDESDT17 CRK10kd^{WT}. Primers: "CRK10 KD *Sal*I For" and "CRK10 KD *Not*I Rev". Lanes 1-8: colonies; -C: negative control. Expected PCR product size ~ 1kb.

Appendix 8.3: Alignment of the subdomain III of the kinase domain of CRK10 and SNC4 of Arabidopsis. SNC4-Ala850 and CRK10-Ala397 are highlighted in bold and underlined.

SNC4_ARATH 844 DFINEV**A**TMSRT 855
CRK10_ARATH 388 EFKNEVVLV**A**KL 399

Appendix 9

Appendix 9.1: GO term enrichment results (AgriGOv.20).

Appendix 9.1.1 Significantly enriched Gene Ontology – Biological Process terms for 246 up-regulated core genes.

	GO term	Description	Input genes	Ref genes	FDR
1	GO:0006952	Defence response	65	1566	3.10E-23
2	GO:0050896	Response to stimulus	127	6250	9.00E-22
3	GO:0006950	Response to stress	93	3506	9.00E-22
4	GO:0043207	Response to external biotic stimulus	53	1212	6.60E-20
5	GO:0051707	Response to other organism	53	1210	6.60E-20
6	GO:0009607	Response to biotic stimulus	53	1253	2.30E-19
7	GO:0051704	Multi-organism process	57	1631	2.70E-17
8	GO:0009605	Response to external stimulus	56	1582	3.00E-17
9	GO:0098542	Defence response to other organism	41	936	3.70E-15
10	GO:0045087	Innate immune response	25	323	5.50E-14
11	GO:0002376	Immune system process	26	369	9.40E-14
12	GO:0006955	Immune response	25	333	9.40E-14
13	GO:0009636	Response to toxic substance	13	102	2.00E-09
14	GO:0009404	Toxin metabolic process	11	60	2.10E-09
15	GO:0009814	Defence response, incompatible interaction	15	170	5.90E-09

16	GO:0009620	Response to fungus	25	573	5.90E-09
17	GO:0042221	Response to chemical	58	2853	3.90E-08
18	GO:0009617	Response to bacterium	21	441	4.20E-08
19	GO:0090487	Secondary metabolite catabolic process	9	46	5.80E-08
20	GO:0009407	Toxin catabolic process	9	46	5.80E-08
21	GO:0006979	Response to oxidative stress	21	453	5.80E-08
22	GO:0009627	Systemic acquired resistance	10	67	6.60E-08
23	GO:0050832	Defence response to fungus	20	504	1.60E-06
24	GO:0019748	Secondary metabolic process	19	492	5.20E-06
25	GO:0042742	Defence response to bacterium	16	354	7.20E-06

Appendix 9.1.2 Significantly enriched Gene Ontology – Molecular Function terms for 246 up-regulated core genes.

	GO term	**Description**	**Input genes**	**Ref genes**	**FDR**
1	GO:0003824	Catalytic activity	126	9101	4.50E-08
2	GO:0004364	Glutathione transferase activity	10	55	4.50E-08
3	GO:0004553	Hydrolase activity, hydrolyzing O-glycosyl compounds	17	405	2.30E-05
4	GO:0016740	Transferase activity	62	3791	2.30E-05
5	GO:0016301	Kinase activity	33	1436	2.30E-05
6	GO:0004674	Protein serine/threonine kinase activity	23	767	2.30E-05
7	GO:0004568	Chitinase activity	6	25	2.30E-05
8	GO:0016798	Hydrolase activity, acting on glycosyl bonds	17	438	2.40E-05
9	GO:0016765	Transferase activity, transferring alkyl or	10	138	3.10E-05

		aryl (other than methyl) groups			
10	GO:0008422	Beta-glucosidase activity	7	71	0.00021
11	GO:0030145	Manganese ion binding	6	46	0.00022
12	GO:0004672	Protein kinase activity	23	925	0.00026
13	GO:0016772	Transferase activity, transferring phosphorus-containing groups	33	1657	0.00026
14	GO:0015926	Glucosidase activity	7	87	0.00053
15	GO:0030246	Carbohydrate binding	12	303	0.00056
16	GO:0045735	Nutrient reservoir activity	6	68	0.0012
17	GO:0016773	Phosphotransferase activity, alcohol group as acceptor	23	1072	0.0018
18	GO:0016491	Oxidoreductase activity	29	1547	0.002
19	GO:0005509	Calcium ion binding	10	266	0.0033
20	GO:0030247	Polysaccharide binding	5	58	0.0044
21	GO:0001871	Pattern binding	5	58	0.0044
22	GO:0015238	Drug transmembrane transporter activity	5	73	0.011
23	GO:0090484	Drug transporter activity	5	77	0.014
24	GO:0030554	Adenyl nucleotide binding	34	2366	0.042
25	GO:0032559	Adenyl ribonucleotide binding	34	2364	0.042

Appendix 9.1.3 Significantly enriched Gene Ontology – Biological Process terms for 28 down-regulated core genes.

	GO term	**Description**	**Number in input list**	**Number in Ref**	**FDR**
1	GO:0051252	Regulation of RNA metabolic process	10	2474	0.0022
2	GO:0032774	RNA biosynthetic process	10	2566	0.0022

3	GO:1901362	Organic cyclic compound biosynthetic process	12	3174	0.0022
4	GO:0097659	Nucleic acid-templated transcription	10	2561	0.0022
5	GO:0050789	Regulation of biological process	15	5306	0.0022
6	GO:0018130	Heterocycle biosynthetic process	11	2957	0.0022
7	GO:0019219	Regulation of nucleobase-containing compound metabolic process	10	2529	0.0022
8	GO:1903506	Regulation of nucleic acid-templated transcription	10	2445	0.0022
9	GO:0050794	Regulation of cellular process	14	4857	0.0022
10	GO:0009058	Biosynthetic process	16	6255	0.0022
11	GO:2001141	Regulation of RNA biosynthetic process	10	2445	0.0022
12	GO:0034654	Nucleobase-containing compound biosynthetic process	11	2781	0.0022
13	GO:0019438	Aromatic compound biosynthetic process	11	3058	0.0022
14	GO:0006355	Regulation of transcription, DNA-templated	10	2443	0.0022
15	GO:0006351	Transcription, DNA-templated	10	2559	0.0022
16	GO:0044249	Cellular biosynthetic process	15	5870	0.0025
17	GO:2000112	Regulation of cellular macromolecule biosynthetic process	10	2657	0.0025
18	GO:0010556	Regulation of macromolecule biosynthetic process	10	2666	0.0025
19	GO:0031326	Regulation of cellular biosynthetic process	10	2734	0.0027
20	GO:0065007	Biological regulation	15	6062	0.0027
21	GO:0009889	Regulation of biosynthetic process	10	2752	0.0027

22	GO:0051171	Regulation of nitrogen compound metabolic process	10	2739	0.0027
23	GO:0010468	Regulation of gene expression	10	2814	0.0031
24	GO:0080090	Regulation of primary metabolic process	10	2889	0.0037
25	GO:0031323	Regulation of cellular metabolic process	10	2980	0.0046

Appendix 9.1.4 Significantly enriched Gene Ontology – Molecular Function terms for 28 down-regulated core genes.

	GO term	**Description**	**Number in input list**	**Number in Ref**	**FDR**
1	GO:0003700	transcription factor activity, sequence-specific DNA binding	10	1729	5.00E-05
2	GO:0001071	nucleic acid binding transcription factor activity	10	1730	5.00E-05
3	GO:0003677	DNA binding	9	2417	0.0036

Appendix 10

Appendix 10.1: Quantification of monosaccharides from hypocotyls of 3-week-old WT and *crk10-A397T* mutant plants. Values presented in the table are average of five biological replicates.

	% of total monosaccharide content								
	Fucose	Rhamnose	Arabinose	Galactose	Glucose	Xylose	Mannose	GlcA	GalA
WT	1.683	7.26	26.622	25.857	8.805	20.023	4.423	0.052	5.28
crk10-A397T	2.098	6.807	22.862	18.44	11.114	30.077	4.674	0.086	3.846

Appendix 10.2:

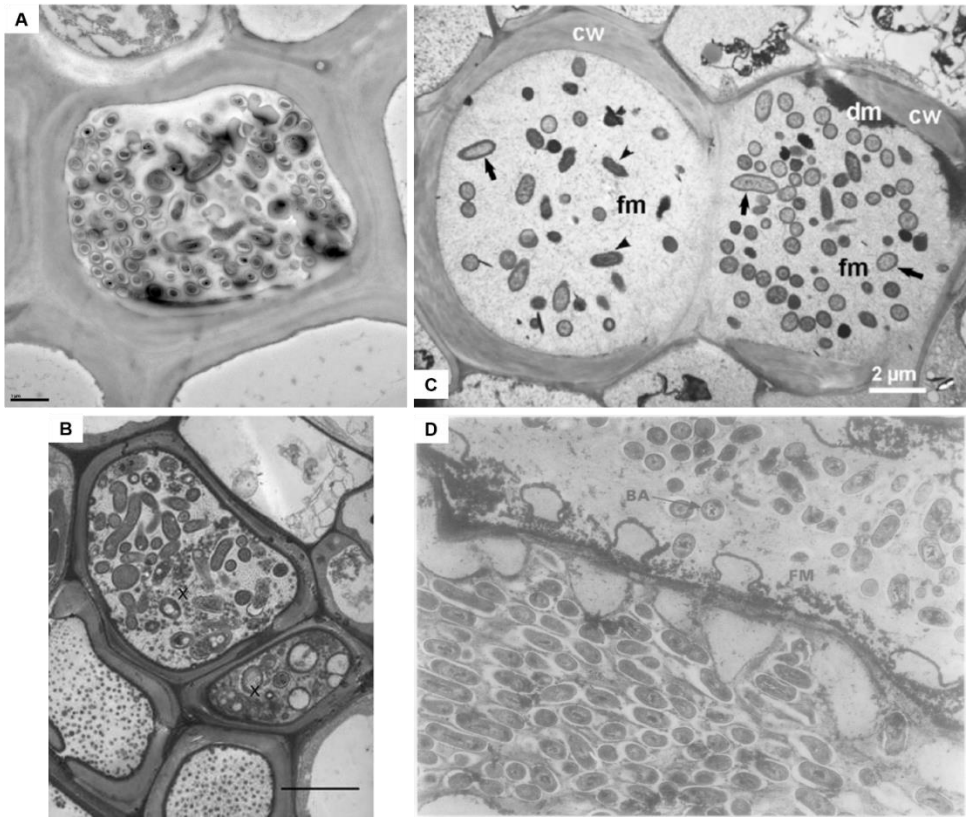

Structures occluding xylem vessel in the hypocotyl of WT plant resemble bacterial pathogens imaged with TEM in previous studies.

(A) Micrograph of xylem vessel in the hypocotyl of 3-week-old WT plant occluded with bacterial-like structures; bar, 1 µm. (B) Bacterial cells (*Sphingomonas paucimobilis)* in stem xylem vessels (X) of *Petunia hybrida*; bar, 2 µm; reproduced from Miyazaki et al., 2010 (https://doi.org/10.1007/s11240-010-9741-5); copyright notice in Appendix 1.9. (C) Bacterial cells (*Pantoea stewartii*; arrows) in xylem vessels of infected maize leaf; bar, 2 µm; reproduced from Ammar et al., 2014 (https://doi.org/10.1016/j.jmau.2014.01.001) under the terms of the Creative Commons Attribution License. (D) Bacterial cells (BA) (*Xanthomonas campestris* pv. *campestris*) surrounded by a dark staining fibrillary material (FM) in the xylem conductive elements of Early Fuji cultivar cabbage (Brassica oleracea) plants; 8700 x; reproduced from Bretschneider et al., 1988 (https://doi.org/10.1016/0885-5765(89)90026-X); copyright notice in Appendix 1.10.

Appendix 10.3: Quantification of immunogold labelling with antibody LM28 (anti-glucuronoxylan; Plant Probes, University of Leeds) in the hypocotyls of 3-week-old WT and *crk10-A397T* plants.

Experimental replicate 1:

***crk10-A397T* #1**	Area (μm^2)	Counts	Counts/ μm^2	**WT #1**	Area (μm^2)	Counts	Counts/ μm^2
1	8.842	117	13.23	1	2.553	24	9.40
2	3.816	72	18.87	2	1.528	17	11.13
3	4.331	53	12.24	3	4.061	37	9.11
4	5.287	80	15.13	4	5.113	33	6.45
5	2.873	28	9.75	5	5.389	61	11.32
6	4.083	73	17.88	6	5.183	35	6.75
7	3.023	46	15.22	7	4.205	27	6.42
8	4.387	70	15.96	8	6.999	57	8.14
9	5.579	94	16.85	9	3.865	18	4.66
10	4.21	72	17.10	10	4.229	26	6.15
11	6.167	127	20.59	11	6.509	27	4.15
12	4.641	77	16.59	12	2.503	16	6.40
		Average	**15.78**			**Average**	**7.51**
Ratio *crk10-A397T* / WT							**2.10**
***crk10-A397T* #2**	Area (µm2)	Counts	Counts/µm2	**WT #2**	Area (µm2)	Counts	Counts/µm2
1	4.732	95	20.08	1	5.14	68	13.23
2	3.773	63	16.70	2	4.3	55	12.79
3	6.231	136	21.83	3	6.712	92	13.71
4	2.715	60	22.10	4	6.311	74	11.73
5	4.225	58	13.73	5	4.254	28	6.58
6	1.474	33	22.39	6	4.516	38	8.41
7	3.677	56	15.23	7	6.93	82	11.83
8	3.218	76	23.62	8	3.682	22	5.97
9	4.433	88	19.85	9	6.874	59	8.58
10	4.094	65	15.88	10	4.792	45	9.39
11	3.656	70	19.15	11	4.421	39	8.82
12	2.639	46	17.43	12	4.72	33	6.99
		Average	**18.99**			**Average**	**9.84**
Ratio *crk10-A397T* / WT							**1.93**

Experimental replicate 2:

crk10-A397T #3	Area (μm^2)	Counts	Counts/ μm^2	**WT #3**	Area (μm^2)	Counts	Counts/ μm^2
1	5.371	294	54.74	1	3.619	69	19.07
2	2.971	149	50.15	2	10.868	185	17.02
3	2.18	65	29.82	3	4.425	108	24.41
4	3.686	150	40.69	4	3.358	86	25.61

5	2.828	172	60.82	5	0.93	16	17.20
6	2.301	141	61.28	6	5.52	90	16.30
7	11.891	402	33.81	7	4.112	58	14.10
8	2.606	117	44.90	8	2.565	42	16.37
9	3.142	171	54.42	9	2.852	55	19.28
10	2.758	133	48.22	10	1.378	35	25.40
11	3.411	128	37.52	11	4.873	50	10.26
12	1.823	88	48.27	12	2.052	60	29.24
		Average	**47.05**			**Average**	**19.52**
			Ratio *crk10-A397T* / WT				**2.41**

Average ratio of *crk10-A397T* / WT among three biological replicates = 2.15

Appendix 11

Appendix 11.1: Genotyping of genetic crosses; details in section 7.2.7.

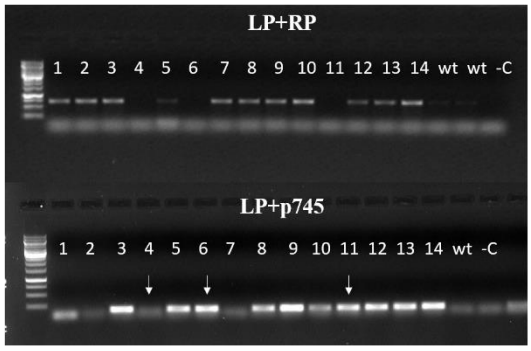

PCR to genotype F2 progeny of *crk10-A397T cyp81d11* genetic cross. Primers: WiscDSLOX5E07 (*cyp81d11*) RP + WiscDSLOX5E07 (*cyp81d11*) LP and WiscDSLOX5E07 (*cyp81d11*) LP + WiscDSLOX p745. Lanes 1-14: individual plants of segregating population. –C = negative control. Arrows indicate individuals which are homozygous for T-DNA insertion.

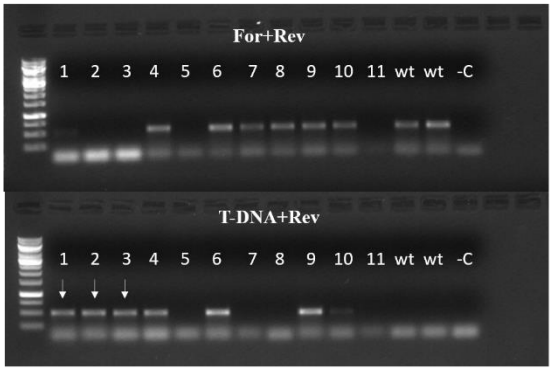

PCR to genotype F2 progeny of *crk10-A397T wrky33* genetic cross. Primers: GABI_324B11 (*wrky33*) For + GABI_324B11 (*wrky33*) Rev and GABI_KAT T-DNA + GABI_324B11 (*wrky33*) Rev. Lanes 1-16: individual plants of segregating population. –C = negative control. Arrows indicate individuals which are homozygous for T-DNA insertion.

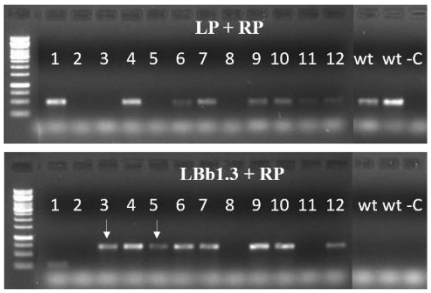

PCR to genotype F2 progeny of *crk10-A397T myc2* genetic cross. Primers: Salk_017005 (*myc2*) RP + Salk_017005 (*myc2*) LP2 and Salk_017005 (*myc2*) RP + Salk LBb1.3. Lanes 1-12: individual plants of segregating population. –C = negative control. Arrows indicate individuals which are homozygous for T-DNA insertion.

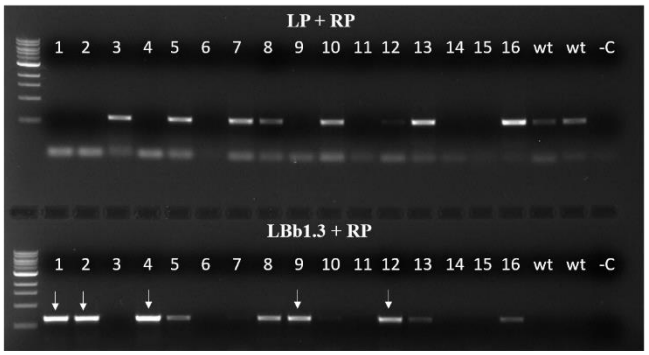

PCR to genotype F2 progeny of *crk10-A397T wrky70* genetic cross. Primers: Salk_025198 (*wrky70*) RP + Salk_025198 (*wrky70*) LP2 and Salk LBb1.3 + Salk_025198 (*wrky70*) RP. Lanes 1-16: individual plants of segregating population. –C = negative control. Arrows indicate individuals which are homozygous for T-DNA insertion.

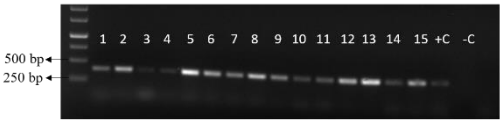

Genotyping PCR to identify homozygous *crk10-A397T 35S:NahG* line. Primers: "*NahG* For" and "*NahG* Rev". Lanes 1-15: progeny of putative homozygous plant. +C: positive control (DNA of known positive plant for the *NahG* transgene). –C: negative control. Expected PCR product size ~350 bp. As all plants were positive, we can confirm the parental plant is homozygous for transgene.

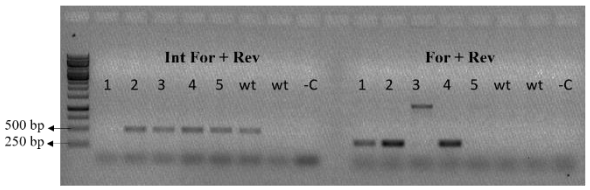

Genotyping PCR to identify homozygous *crk10-A397T eds1-2*. Primers: "*eds1-2* Int For", "*eds1-2* For" and "*eds1-2* Rev." Lanes 1-5: *crk10-A397T eds1-2*. –C: negative control. Expected PCR product size ~500 bp. Plant #1 is homozygous for eds1-2 deletion.

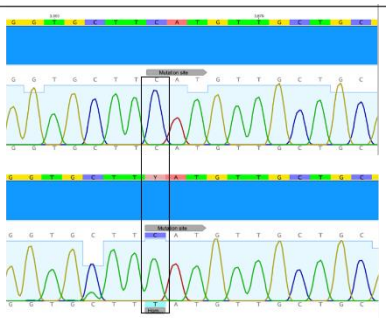

Sequencing to identify point mutation in *crk10-A397T npr1-1* plants. Sequencing of WT (top) and homozygous *npr1-1* plant (bottom). Mutation site is indicated by black rectangle.

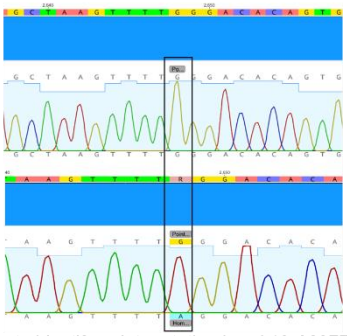

Sequencing to identify point mutation in *crk10-A397T pad4-1* plants. Sequencing of WT (top) and homozygous *pad4-1* plant (bottom). Mutation site is indicated by black rectangle.

Appendix 11.2: Mock control (water inoculation) of bioassays with (A) *F. oxysporum* and (B) *F. graminearum*.

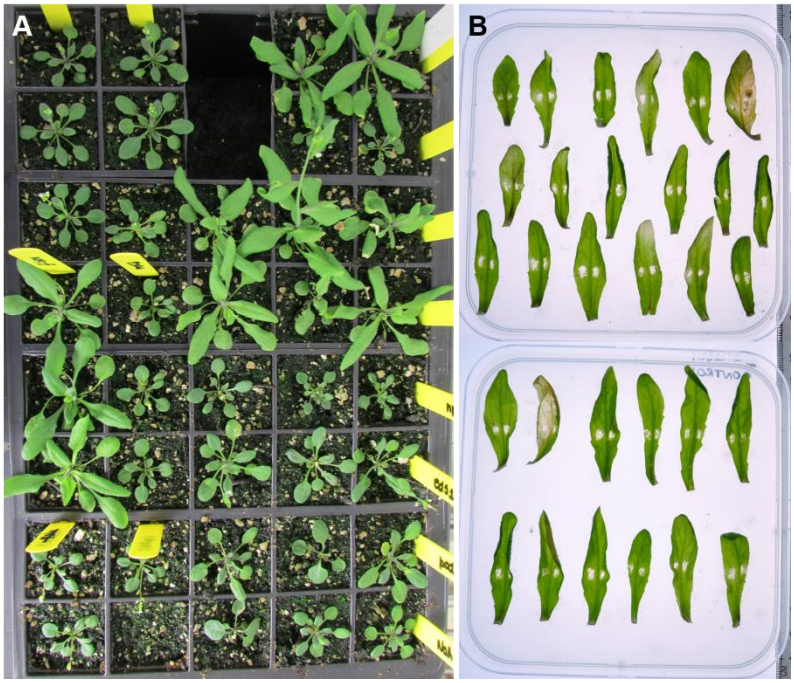

Appendix 11.3: Extra repetitions of the bioassay with *F. oxysporum* mentioned in section 7.3.3.

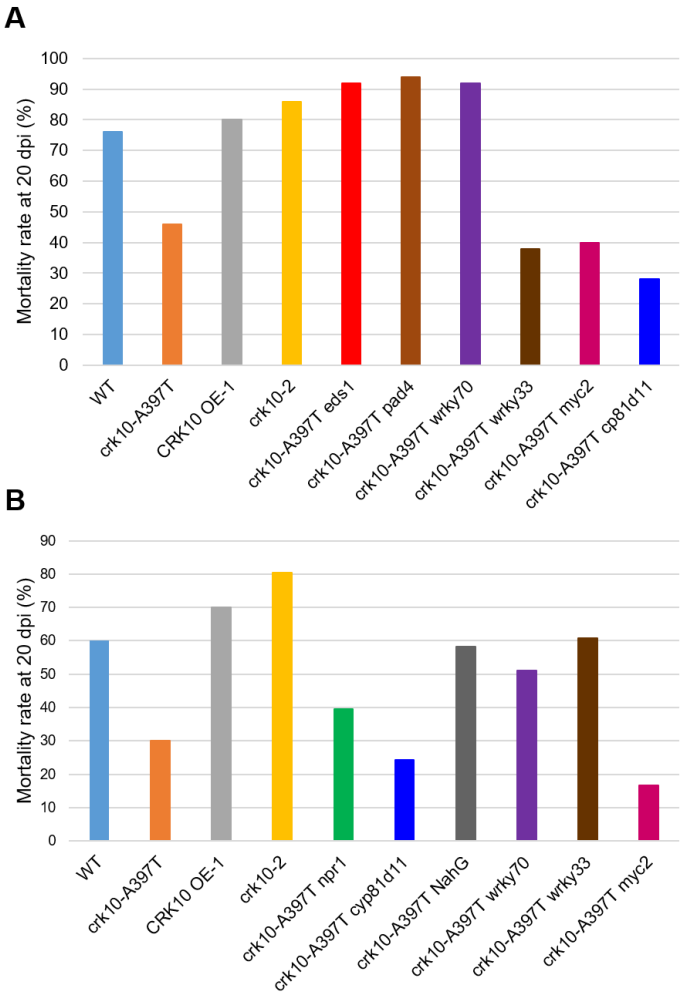

Bibliography

ACHARYA, B. R., RAINA, S., MAQBOOL, S. B., JAGADEESWARAN, G., MOSHER, S. L., APPEL, H. M., SCHULTZ, J. C., KLESSIG, D. F. & RAINA, R. 2007. Overexpression of CRK13, an Arabidopsis cysteine-rich receptor-like kinase, results in enhanced resistance to Pseudomonas syringae. The Plant Journal, 50.

AHN, N. G., CAMPBELL, J. S., SEGER, R., JENSEN, A. L., GRAVES, L. M. & KREBS, E. G. 1993. Metabolic labeling of mitogen-activated protein kinase kinase in A431 cells demonstrates phosphorylation on serine and threonine residues. Proceedings of the National Academy of Sciences, 90.

ALBERTS, B., JOHNSON, A., LEWIS, J., RAFF, M., ROBERTS, K. & WALTER, P. 2002. Molecular Biology of the Cell, 4th edition, New York.

ALFONSO, S. I., CALLENDER, J. A., HOOLI, B., ANTAL, C. E., MULLIN, K., SHERMAN, M. A., LESNÉ, S. E., LEITGES, M., NEWTON, A. C., TANZI, R. E. & MALINOW, R. 2016. Gain-of-function mutations in protein kinase Cα (PKCα) may promote synaptic defects in Alzheimer's disease. Science Signaling, 9, ra47-ra47.

ALONSO-SIMÓN, A., GARCÍA-ANGULO, P., MÉLIDA, H., ENCINA, A., ÁLVAREZ, J. M. & ACEBES, J. L. 2011. The use of FTIR spectroscopy to monitor modifications in plant cell wall architecture caused by cellulose biosynthesis inhibitors. Plant Signaling & Behavior, 6.

AMÁBILE-CUEVAS, C. F. & DEMPLE, B. 1991. Molecular characterization of the soxRS genes of Escherichia coli: two genes control a superoxide stress regulon. Nucleic Acids Research, 19.

AMARI, K., BOUTANT, E., HOFMANN, C., SCHMITT-KEICHINGER, C., FERNANDEZ-CALVINO, L., DIDIER, P., LERICH, A., MUTTERER, J., THOMAS, C. L., HEINLEIN, M., MÉLY, Y., MAULE, A. J. & RITZENTHALER, C. 2010. A Family of Plasmodesmal Proteins with Receptor-Like Properties for Plant Viral Movement Proteins. PLoS Pathogens, 6, e1001119-e1001119.

AMMAR, E.-D., CORREA, V., HOGENHOUT, S. & REDINBAUGH, M. 2014. Immunofluorescence localization and ultrastructure of Stewart's wilt disease bacterium Pantoea stewartii in maize leaves and in its flea beetle vector Chaetocnema pulicaria (Coleoptera: Chrysomelidae). Journal of Microscopy and Ultrastructure, 2.

AN, G., EBERT, P. R., MITRA, A. & HA, S. B. 1988. Binary vectors. In: GELVIN, S. B. & SCHILPEROOT, R. A. (eds.) Plant Molecular Biology Manual. Kluwer.

ANDERSON, J. P., BADRUZSAUFARI, E., SCHENK, P. M., MANNERS, J. M., DESMOND, O. J., EHLERT, C., MACLEAN, D. J., EBERT, P. R. & KAZAN, K. 2004. Antagonistic Interaction between Abscisic Acid and Jasmonate-Ethylene Signaling Pathways Modulates Defense Gene Expression and Disease Resistance in Arabidopsis. The Plant Cell, 16, 3460-3479.

ANDO, M., FIESEL, F. C., HUDEC, R., CAULFIELD, T. R., OGAKI, K., GÓRKA-SKOCZYLAS, P., KOZIOROWSKI, D., FRIEDMAN, A., CHEN, L., DAWSON, V. L., DAWSON, T. M., BU, G., ROSS, O. A., WSZOLEK, Z. K. & SPRINGER, W. 2017. The PINK1 p.I368N mutation affects protein stability and ubiquitin kinase activity. Molecular Neurodegeneration, 12, 32-32.

ASAI, T., TENA, G., PLOTNIKOVA, J., WILLMANN, M. R., CHIU, W.-L., GOMEZ-GOMEZ, L., BOLLER, T., AUSUBEL, F. M. & SHEEN, J. 2002. MAP kinase signalling cascade in Arabidopsis innate immunity. Nature, 415, 977-983.

ASHCROFT, F. M. 2006. From molecule to malady. Nature, 440.

ASHIKARI, M., WU, J., YANO, M., SASAKI, T. & YOSHIMURA, A. 1999. Rice gibberellin-insensitive dwarf mutant gene Dwarf 1 encodes the alpha -subunit of GTP-binding protein. Proceedings of the National Academy of Sciences, 96.

AVCI, U., EARL PETZOLD, H., ISMAIL, I. O., BEERS, E. P. & HAIGLER, C. H. 2008. Cysteine proteases XCP1 and XCP2 aid micro-autolysis within the intact central vacuole during xylogenesis in Arabidopsis roots. The Plant Journal, 56.

AXELSEN, K. B. & PALMGREN, M. G. 2001. Inventory of the Superfamily of P-Type Ion Pumps in Arabidopsis. Plant Physiology, 126.

BAAYEN, R. P., O'DONNELL, K., BONANTS, P. J. M., CIGELNIK, E., KROON, L. P. N. M., ROEBROECK, E. J. A. & WAALWIJK, C. 2000. Gene Genealogies and AFLP Analyses in the Fusarium oxysporum Complex Identify Monophyletic and Nonmonophyletic Formae Speciales Causing Wilt and Rot Disease. Phytopathology®, 90.

BALAKSHIN, M., CAPANEMA, E., GRACZ, H., CHANG, H.-M. & JAMEEL, H. 2011. Quantification of lignin–carbohydrate linkages with high-resolution NMR spectroscopy. Planta, 233.

BARI, R. & JONES, J. D. G. 2009. Role of plant hormones in plant defence responses. Plant Molecular Biology, 69.

BARNES, W. & ANDERSON, C. 2017. Acetyl Bromide Soluble Lignin (ABSL) Assay for Total Lignin Quantification from Plant Biomass. BIO-PROTOCOL, 7.

BECK, M., KOMIS, G., MÜLLER, J., MENZEL, D. & ŠAMAJ, J. 2010. Arabidopsis Homologs of Nucleus- and Phragmoplast-Localized Kinase 2 and 3 and Mitogen-Activated Protein Kinase 4 Are Essential for Microtubule Organization. The Plant Cell, 22.

BELLANDE, K., BONO, J.-J., SAVELLI, B., JAMET, E. & CANUT, H. 2017. Plant Lectins and Lectin Receptor-Like Kinases: How Do They Sense the Outside? International Journal of Molecular Sciences, 18.

BENAYOUN, J. 1983. A Cytochemical Study of Cell Wall Hydrolysis in the Secondary Xylem of Poplar (Populus italica Moench). Annals of Botany, 52.

BENHAMMAN, R., BAI, F., DRORY, S. B., LOUBERT-HUDON, A., ELLIS, B. & MATTON, D. P. 2017. The Arabidopsis Mitogen-Activated Protein Kinase Kinase Kinase 20 (MKKK20) Acts Upstream of MKK3 and MPK18 in Two Separate Signaling Pathways Involved in Root Microtubule Functions. Frontiers in Plant Science, 8.

BERGEY, D. R., HOWE, G. A. & RYAN, C. A. 1996. Polypeptide signaling for plant defensive genes exhibits analogies to defense signaling in animals. Proceedings of the National Academy of Sciences, 93.

BERNE, S. & JAVORNIK, B. 2016. Signalling Crosstalk of Plant Defence Responses to Xyleminvading Pathogens. Abiotic and Biotic Stress in Plants - Recent Advances and Future Perspectives. InTech.

BERRABAH, F., BOURCY, M., ESCHSTRUTH, A., CAYREL, A., GUEFRACHI, I., MERGAERT, P., WEN, J., JEAN, V., MYSORE, K. S., GOURION, B. & RATET, P. 2014. A non RD receptor-like kinase prevents nodule early senescence and defense-like reactions during symbiosis. New Phytologist, 203.

BERROCAL-LOBO, M. & MOLINA, A. 2007. Ethylene Response Factor 1 Mediates Arabidopsis Resistance to the Soilborne Fungus Fusarium oxysporum. Molecular Plant-Microbe Interactions®, 17, 763-770.

BETHKE, G., PECHER, P., ESCHEN-LIPPOLD, L., TSUDA, K., KATAGIRI, F., GLAZEBROOK, J., SCHEEL, D. & LEE, J. 2012. Activation of the Arabidopsis thaliana Mitogen-Activated Protein Kinase MPK11 by the Flagellin-Derived Elicitor Peptide, flg22. Molecular Plant-Microbe Interactions®, 25.

BI, D., CHENG, Y. T., LI, X. & ZHANG, Y. 2010. Activation of Plant Immune Responses by a Gain-of-Function Mutation in an Atypical Receptor-Like Kinase Plant Physiology, 153, 1771-1779.

BI, D., JOHNSON, K. C. M., ZHU, Z., HUANG, Y., CHEN, F., ZHANG, Y. & LI, X. 2011. Mutations in an Atypical TIR-NB-LRR-LIM Resistance Protein Confer Autoimmunity. Frontiers in Plant Science, 2.

BIDHENDI, A. J., CHEBLI, Y. & GEITMANN, A. 2020. Fluorescence visualization of cellulose and pectin in the primary plant cell wall. Journal of Microscopy, 278.

BIEDENKAPP, H., BORGMEYER, U., SIPPEL, A. E. & KLEMPNAUER, K.-H. 1988. Viral myb oncogene encodes a sequence-specific DNA-binding activity. Nature, 335.

BIRKENBIHL, R. P., DIEZEL, C. & SOMSSICH, I. E. 2012. Arabidopsis WRKY33 Is a Key Transcriptional Regulator of Hormonal and Metabolic Responses toward Botrytis cinerea Infection Plant Physiology, 159.

BISCHOFF, V., SELBIG, J. & SCHEIBLE, W.-R. 2010. Involvement of TBL/DUF231 proteins into cell wall biology. Plant Signaling & Behavior, 5.

BISHOPP, A., LEHESRANTA, S., VATÉN, A., HELP, H., EL-SHOWK, S., SCHERES, B., HELARIUTTA, K., MÄHÖNEN, ARI P., SAKAKIBARA, H. & HELARIUTTA, Y. 2011. Phloem-Transported Cytokinin Regulates Polar Auxin Transport and Maintains Vascular Pattern in the Root Meristem. Current Biology, 21.

BOJAR, D., MARTINEZ, J., SANTIAGO, J., RYBIN, V., BAYLISS, R. & HOTHORN, M. 2014. Crystal structures of the phosphorylated BRI1 kinase domain and implications for brassinosteroid signal initiation. The Plant Journal, 78, 31-43.

BOLGER, A. M., LOHSE, M. & USADEL, B. 2014. Trimmomatic: a flexible trimmer for Illumina sequence data. Bioinformatics, 30.

BONAWITZ, N. D. & CHAPPLE, C. 2010. The Genetics of Lignin Biosynthesis: Connecting Genotype to Phenotype. Annual Review of Genetics, 44.

BOURDAIS, G., BURDIAK, P., GAUTHIER, A., NITSCH, L., SALOJÄRVI, J., RAYAPURAM, C., IDÄNHEIMO, N., HUNTER, K., KIMURA, S., MERILO, E., VAATTOVAARA, A., ORACZ, K., KAUFHOLDT, D., PALLON, A., ANGGORO, D. T., GLÓW, D., LOWE, J., ZHOU, J., MOHAMMADI, O., PUUKKO, T., ALBERT, A., LANG, H., ERNST, D., KOLLIST, H., BROSCHÉ, M., DURNER, J., BORST, J. W., COLLINGE, D. B., KARPIŃSKI, S., LYNGKJÆR, M. F., ROBATZEK, S., WRZACZEK, M. & KANGASJÄRVI, J. 2015. Large-Scale Phenomics Identifies Primary and Fine-Tuning Roles for CRKs in Responses Related to Oxidative Stress. PLOS Genetics, 11, e1005373-e1005373.

BRETSCHNEIDER, K. E., GONELLA, M. P. & ROBESON, D. J. 1989. A comparative light and electron microscopical study of compatible and incompatible interactions between Xanthomonas campestris pv. campestris and cabbage (Brassica oleracea). Physiological and Molecular Plant Pathology, 34.

BRODERSEN, P., PETERSEN, M., BJØRN NIELSEN, H., ZHU, S., NEWMAN, M.-A., SHOKAT, K. M., RIETZ, S., PARKER, J. & MUNDY, J. 2006. Arabidopsis MAP kinase 4 regulates salicylic acid- and jasmonic acid/ethylene-dependent responses via EDS1 and PAD4. The Plant Journal, 47.

BROWN, D., WIGHTMAN, R., ZHANG, Z., GOMEZ, L. D., ATANASSOV, I., BUKOWSKI, J.-P., TRYFONA, T., MCQUEEN-MASON, S. J., DUPREE, P. & TURNER, S. 2011a. Arabidopsis genes IRREGULAR XYLEM (IRX15) and IRX15L encode DUF579-containing proteins that are essential for normal xylan deposition in the secondary cell wall. The Plant Journal, 66.

BROWN, D. M., GOUBET, F., WONG, V. W., GOODACRE, R., STEPHENS, E., DUPREE, P. & TURNER, S. R. 2007. Comparison of five xylan synthesis mutants reveals new insight into the mechanisms of xylan synthesis. The Plant Journal, 52.

BROWN, N. A., BASS, C., BALDWIN, T. K., CHEN, H., MASSOT, F., CARION, P. W. C., URBAN, M., VAN DE MEENE, A. M. L. & HAMMOND-KOSACK, K. E. 2011b. Characterisation of the Fusarium graminearum-Wheat Floral Interaction. Journal of Pathogens, 2011.

BUIST, G., STEEN, A., KOK, J. & KUIPERS, O. P. 2008. LysM, a widely distributed protein motif for binding to (peptido)glycans. Molecular Microbiology, 68.

BURDIAK, P., RUSACZONEK, A., WITOŃ, D., GŁÓW, D. & KARPIŃSKI, S. 2015. Cysteine-rich receptor-like kinase CRK5 as a regulator of growth, development, and ultraviolet radiation responses in Arabidopsis thaliana. Journal of Experimental Botany, 66.

CAILLAUD, M.-C., WIRTHMUELLER, L., SKLENAR, J., FINDLAY, K., PIQUEREZ, S. J. M., JONES, A. M. E., ROBATZEK, S., JONES, J. D. G. & FAULKNER, C. 2014. The Plasmodesmal Protein PDLP1 Localises to Haustoria-Associated Membranes during Downy Mildew Infection and Regulates Callose Deposition. PLoS Pathogens, 10.

CAMUT, L., REGNAULT, T., SIRLIN-JOSSERAND, M., SAKVARELIDZE-ACHARD, L., CARRERA, E., ZUMSTEG, J., HEINTZ, D., LEONHARDT, N., LANGE, M. J. P., LANGE, T., DAVIÈRE, J.-M. & ACHARD, P. 2019. Root-derived GA12 contributes to temperature-induced shoot growth in Arabidopsis. Nature Plants, 5.

CAO, Y., LIANG, Y., TANAKA, K., NGUYEN, C. T., JEDRZEJCZAK, R. P., JOACHIMIAK, A. & STACEY, G. 2014. The kinase LYK5 is a major chitin receptor in Arabidopsis and forms a chitin-induced complex with related kinase CERK1. eLife, 3.

CARPITA, N. C. & GIBEAUT, D. M. 1993. Structural models of primary cell walls in flowering plants: consistency of molecular structure with the physical properties of the walls during growth. The Plant Journal, 3.

CASTRILLO, G., SÁNCHEZ-BERMEJO, E., DE LORENZO, L., CREVILLÉN, P., FRAILE-ESCANCIANO, A., TC, M., MOURIZ, A., CATARECHA, P., SOBRINO-PLATA, J., OLSSON, S., LEO DEL PUERTO, Y., MATEOS, I., ROJO, E., HERNÁNDEZ, L. E., JARILLO, J. A., PIÑEIRO, M., PAZ-ARES, J. & LEYVA, A. 2013. WRKY6 Transcription Factor Restricts Arsenate Uptake and Transposon Activation in Arabidopsis. The Plant Cell, 25.

CHAFFEY, N., CHOLEWA, E., REGAN, S. & SUNDBERG, B. 2002. Secondary xylem development in Arabidopsis : a model for wood formation. Physiologia Plantarum, 114.

CHANDRAN, D., TAI, Y. C., HATHER, G., DEWDNEY, J., DENOUX, C., BURGESS, D. G., AUSUBEL, F. M., SPEED, T. P. & WILDERMUTH, M. C. 2009. Temporal Global Expression Data Reveal Known and Novel Salicylate-Impacted Processes and Regulators Mediating Powdery Mildew Growth and Reproduction on Arabidopsis Plant Physiology, 149.

CHANG, L. & KARIN, M. 2001. Mammalian MAP kinase signalling cascades. Nature, 410.

CHEN, D., WU, J., ZHAO, M., MA, X., ZHANG, W., XIA, G. & WANG, M. 2017. A novel wheat cysteine-rich receptor-like kinase gene CRK41 is involved in the regulation of seed germination under osmotic stress in Arabidopsis thaliana. Journal of Plant Biology, 60, 571-581.

CHEN, J., YU, F., LIU, Y., DU, C., LI, X., ZHU, S., WANG, X., LAN, W., RODRIGUEZ, P. L., LIU, X., LI, D., CHEN, L. & LUAN, S. 2016. FERONIA interacts with ABI2-type phosphatases to facilitate signaling cross-talk between abscisic acid and RALF peptide in Arabidopsis. Proceedings of the National Academy of Sciences, 113.

CHEN, J. G. 2003. A Seven-Transmembrane RGS Protein That Modulates Plant Cell Proliferation. Science, 301.

CHEN, K., DU, L. & CHEN, Z. 2003. Sensitization of defense responses and activation of programmed cell death by a pathogen-induced receptor-like protein kinase in Arabidopsis. Plant Molecular Biology, 53.

CHEN, K., FAN, B., DU, L. & CHEN, Z. 2004. Activation of hypersensitive cell death by pathogen-induced receptor-like protein kinases from Arabidopsis. Plant Molecular Biology, 56, 271-283.

CHEN, L.-J., WURIYANGHAN, H., ZHANG, Y.-Q., DUAN, K.-X., CHEN, H.-W., LI, Q.-T., LU, X., HE, S.-J., MA, B., ZHANG, W.-K., LIN, Q., CHEN, S.-Y. & ZHANG, J.-S. 2013. An S-Domain Receptor-Like Kinase, OsSIK2, Confers Abiotic Stress Tolerance and Delays Dark-Induced Leaf Senescence in Rice Plant Physiology, 163.

CHEN, X., STEED, A., HARDEN, C. & NICHOLSON, P. 2006. Characterization of Arabidopsis thaliana-Fusarium graminearum interactions and identification of variation in resistance among ecotypes. Molecular Plant Pathology, 7, 391-403.

CHEN, Y. C., WONG, C. L., MUZZI, F., VLAARDINGERBROEK, I., KIDD, B. N. & SCHENK, P. M. 2015. Root defense analysis against Fusarium oxysporum reveals new regulators to confer resistance. Scientific Reports, 4, 5584-5584.

CHEN, Z. 2001. A Superfamily of Proteins with Novel Cysteine-Rich Repeats. Plant Physiology, 126, 473-476.

CHERN, M., XU, Q., BART, R. S., BAI, W., RUAN, D., SZE-TO, W. H., CANLAS, P. E., JAIN, R., CHEN, X. & RONALD, P. C. 2016. A Genetic Screen Identifies a Requirement for Cysteine-Rich–Receptor-Like Kinases in Rice NH1 (OsNPR1)-Mediated Immunity. PLOS Genetics, 12, e1006049-e1006049.

CHEUNG, A. Y. & WU, H.-M. 2011. THESEUS 1, FERONIA and relatives: a family of cell wall-sensing receptor kinases? Current Opinion in Plant Biology, 14, 632-641.

CHILD, E. S., HENDRYCHOVÁ, T., MCCAGUE, K., FUTREAL, A., OTYEPKA, M. & MANN, D. J. 2010. A cancer-derived mutation in the PSTAIRE helix of cyclin-dependent kinase 2 alters the stability of cyclin binding. Biochimica et Biophysica Acta (BBA) - Molecular Cell Research, 1803.

CHINCHILLA, D., BAUER, Z., REGENASS, M., BOLLER, T. & FELIX, G. 2006. The Arabidopsis Receptor Kinase FLS2 Binds flg22 and Determines the Specificity of Flagellin Perception. The Plant Cell, 18.

CHINCHILLA, D., ZIPFEL, C., ROBATZEK, S., KEMMERLING, B., NÜRNBERGER, T., JONES, J. D. G., FELIX, G. & BOLLER, T. 2007. A flagellin-induced complex of the receptor FLS2 and BAK1 initiates plant defence. Nature, 448.

CHO, S. K., LARUE, C. T., CHEVALIER, D., WANG, H., JINN, T.-L., ZHANG, S. & WALKER, J. C. 2008. Regulation of floral organ abscission in Arabidopsis thaliana. Proceedings of the National Academy of Sciences, 105.

CHOAT, B., COBB, A. R. & JANSEN, S. 2008. Structure and function of bordered pits: new discoveries and impacts on whole-plant hydraulic function. New Phytologist, 177.

CHRISPEELS, M. J., HOLUIGUE, L., LATORRE, R., LUAN, S., ORELLANA, A., PEÑA-CORTES, H., RAIKHEL, N. V., RONALD, P. C. & TREWAVAS, A. 1999. Signal transduction networks and the biology of plant cells. Biological Research, 32, 35-60.

CHUBERRE, C., PLANCOT, B., DRIOUICH, A., MOORE, J. P., BARDOR, M., GÜGI, B. & VICRÉ, M. 2018. Plant Immunity Is Compartmentalized and Specialized in Roots. Frontiers in Plant Science, 9.

CLAPHAM, D. E. 2007. Calcium Signaling. Cell, 131, 1047-1058.

CLARK, G. B., THOMPSON, G. & ROUX, S. J. 2001. Signal transduction mechanisms in plants: An overview. Current Science, 80, 170-177.

CLARK, S. E., RUNNING, M. P. & MEYEROWITZ, E. M. 1993. CLAVATA1, a regulator of meristem and flower development in Arabidopsis. Development, 119.

CLOUGH, S. J. & BENT, A. F. 1998. Floral dip: a simplified method forAgrobacterium-mediated transformation ofArabidopsis thaliana. The Plant Journal, 16.

CLOUSE, S. D., LANGFORD, M. & MCMORRIS, T. C. 1996. A Brassinosteroid-Insensitive Mutant in Arabidopsis thaliana Exhibits Multiple Defects in Growth and Development. Plant Physiology, 111.

COCK, J. M., VANOOSTHUYSE, V. & GAUDE, T. 2002. Receptor kinase signalling in plants and animals: distinct molecular systems with mechanistic similarities. Current Opinion in Cell Biology, 14, 230-236.

COHEN, P. 2002. The origins of protein phosphorylation. Nature Cell Biology, 4.

CORNUAULT, V., BUFFETTO, F., RYDAHL, M. G., MARCUS, S. E., TORODE, T. A., XUE, J., CRÉPEAU, M.-J., FARIA-BLANC, N., WILLATS, W. G. T., DUPREE, P., RALET, M.-C. & KNOX, J. P. 2015. Monoclonal antibodies indicate low-abundance links between heteroxylan and other glycans of plant cell walls. Planta, 242.

COUTO, D. & ZIPFEL, C. 2016. Regulation of pattern recognition receptor signalling in plants. Nature Reviews Immunology, 16.

CUI, H., GOBBATO, E., KRACHER, B., QIU, J., BAUTOR, J. & PARKER, J. E. 2017. A core function of EDS1 with PAD4 is to protect the salicylic acid defense sector in Arabidopsis immunity. New Phytologist, 213.

CUI, H., TSUDA, K. & PARKER, J. E. 2015. Effector-Triggered Immunity: From Pathogen Perception to Robust Defense. Annual Review of Plant Biology, 66, 487-511.

CZERNIC, P., VISSER, B., SUN, W., SAVOURÉ, A., DESLANDES, L., MARCO, Y., VAN MONTAGU, M. & VERBRUGGEN, N. 1999. Characterization of an Arabidopsis thaliana receptor-like protein kinase gene activated by oxidative stress and pathogen attack. The Plant Journal, 18.

DAS, M., REICHMAN, J. R., HABERER, G., WELZL, G., ACEITUNO, F. F., MADER, M. T., WATRUD, L. S., PFLEEGER, T. G., GUTIÉRREZ, R. A., SCHÄFFNER, A. R. & OLSZYK, D. M. 2010. A composite transcriptional signature differentiates responses towards closely related herbicides in Arabidopsis thaliana and Brassica napus. Plant Molecular Biology, 72.

DAVIDSSON, P., BROBERG, M., KARIOLA, T., SIPARI, N., PIRHONEN, M. & PALVA, E. T. 2017. Short oligogalacturonides induce pathogen resistance-associated gene expression in Arabidopsis thaliana. BMC Plant Biology, 17.

DE BONDT, H. L., ROSENBLATT, J., JANCARIK, J., JONES, H. D., MORGANT, D. O. & KIM, S.-H. 1993. Crystal structure of cyclin-dependent kinase 2. Nature, 363.

DE CONINCK, B., TIMMERMANS, P., VOS, C., CAMMUE, B. P. A. & KAZAN, K. 2015. What lies beneath: belowground defense strategies in plants. Trends in Plant Science, 20.

DE MEESTER, B., DE VRIES, L., ÖZPARPUCU, M., GIERLINGER, N., CORNEILLIE, S., PALLIDIS, A., GOEMINNE, G., MORREEL, K., DE BRUYNE, M., DE RYCKE, R., VANHOLME, R. & BOERJAN, W. 2018. Vessel-Specific Reintroduction of CINNAMOYL-COA REDUCTASE1 (CCR1) in Dwarfed ccr1 Mutants Restores Vessel and Xylary Fiber Integrity and Increases Biomass. Plant Physiology, 176.

DE SMET, I., VOß, U., JÜRGENS, G. & BEECKMAN, T. 2009. Receptor-like kinases shape the plant. Nature Cell Biology, 11, 1166-1173.

DE VLEESSCHAUWER, D., XU, J. & HÖFTE, M. 2014. Making sense of hormone-mediated defense networking: from rice to Arabidopsis. Frontiers in Plant Science, 5.

DELGADO-CEREZO, M., SÁNCHEZ-RODRÍGUEZ, C., ESCUDERO, V., MIEDES, E., FERNÁNDEZ, P. V., JORDÁ, L., HERNÁNDEZ-BLANCO, C., SÁNCHEZ-VALLET, A., BEDNAREK, P., SCHULZE-LEFERT, P., SOMERVILLE, S., ESTEVEZ, J. M., PERSSON, S. & MOLINA, A. 2012. Arabidopsis Heterotrimeric G-protein Regulates Cell Wall Defense and Resistance to Necrotrophic Fungi. Molecular Plant, 5.

DENOUX, C., GALLETTI, R., MAMMARELLA, N., GOPALAN, S., WERCK, D., DE LORENZO, G., FERRARI, S., AUSUBEL, F. M. & DEWDNEY, J. 2008. Activation of Defense Response Pathways by OGs and Flg22 Elicitors in Arabidopsis Seedlings. Molecular Plant, 1.

DESPRÉS, C., DELONG, C., GLAZE, S., LIU, E. & FOBERT, P. R. 2000. The Arabidopsis NPR1/NIM1 protein enhances the DNA binding activity of a subgroup of the TGA family of bZIP transcription factors. Plant Cell, 12, 279-290.

DEVAIAH, B. N., KARTHIKEYAN, A. S. & RAGHOTHAMA, K. G. 2007. WRKY75 Transcription Factor Is a Modulator of Phosphate Acquisition and Root Development in Arabidopsis. Plant Physiology, 143.

DEVREE, B. T., STEINER, L. M., GŁAZOWSKA, S., RUHNOW, F., HERBURGER, K., PERSSON, S. & MRAVEC, J. 2021. Current and future advances in fluorescence-based visualization of plant cell wall components and cell wall biosynthetic machineries. Biotechnology for Biofuels, 14.

DEYOUNG, B. J., BICKLE, K. L., SCHRAGE, K. J., MUSKETT, P., PATEL, K. & CLARK, S. E. 2006. The CLAVATA1-related BAM1, BAM2 and BAM3 receptor kinase-like proteins are required for meristem function in Arabidopsis. The Plant Journal, 45.

DIENER, A. C. & AUSUBEL, F. M. 2005. RESISTANCE TO FUSARIUM OXYSPORUM 1, a Dominant Arabidopsis Disease-Resistance Gene, Is Not Race Specific. Genetics, 171, 305-321.

DIETRICH, P., ANSCHÜTZ, U., KUGLER, A. & BECKER, D. 2010. Physiology and biophysics of plant ligand-gated ion channels. Plant Biology, 12, 80-93.

DING, L., XU, H., YI, H., YANG, L., KONG, Z., ZHANG, L., XUE, S., JIA, H. & MA, Z. 2011. Resistance to Hemi-Biotrophic F. graminearum Infection Is Associated with Coordinated and Ordered Expression of Diverse Defense Signaling Pathways. PLoS ONE, 6.

DING, P. & DING, Y. 2020. Stories of Salicylic Acid: A Plant Defense Hormone. Trends in Plant Science, 25.

DING, P., REKHTER, D., DING, Y., FEUSSNER, K., BUSTA, L., HAROTH, S., XU, S., LI, X., JETTER, R., FEUSSNER, I. & ZHANG, Y. 2016. Characterization of a Pipecolic Acid Biosynthesis Pathway Required for Systemic Acquired Resistance. The Plant Cell, 28.

DIXIT, A. & VERKHIVKER, G. M. 2014. Structure-Functional Prediction and Analysis of Cancer Mutation Effects in Protein Kinases. Computational and Mathematical Methods in Medicine, 2014.

DIXIT, A., YI, L., GOWTHAMAN, R., TORKAMANI, A., SCHORK, N. J. & VERKHIVKER, G. M. 2009. Sequence and Structure Signatures of Cancer Mutation Hotspots in Protein Kinases. PLoS ONE, 4.

DÓCZI, R., BRADER, G., PETTKÓ-SZANDTNER, A., RAJH, I., DJAMEI, A., PITZSCHKE, A., TEIGE, M. & HIRT, H. 2007. The Arabidopsis Mitogen-Activated Protein Kinase Kinase MKK3 Is Upstream of Group C Mitogen-Activated Protein Kinases and Participates in Pathogen Signaling. The Plant Cell, 19.

DONALDSON, L. 2013. Softwood and Hardwood Lignin Fluorescence Spectra of Wood Cell Walls in Different Mounting Media. IAWA Journal, 34.

DONALDSON, L. 2020. Autofluorescence in Plants. Molecules, 25.

DOOHAN, F. & ZHOU, B. 2017. Fungal Pathogens of Plants. Fungi. Hoboken, NJ, USA: John Wiley & Sons, Inc.

DOOLITTLE, R. F., FENG, D. F., TSANG, S., CHO, G. & LITTLE, E. 1996. Determining Divergence Times of the Major Kingdoms of Living Organisms with a Protein Clock. Science, 271.

DU, D., LIU, M., XING, Y., CHEN, X., ZHANG, Y., ZHU, M., LU, X., ZHANG, Q., LING, Y., SANG, X., LI, Y., ZHANG, C. & HE, G. 2019. Semi-dominant mutation in the cysteine-rich receptor-like kinase gene, <scp>ALS</scp> 1 , conducts constitutive defence response in rice. Plant Biology, 21.

DU, L. & CHEN, Z. 2000. Identification of genes encoding receptor-like protein kinases as possible targets of pathogen- and salicylic acid-induced WRKY DNA-binding proteins in Arabidopsis. The Plant Journal, 24, 837-847.

DUBOS, C., STRACKE, R., GROTEWOLD, E., WEISSHAAR, B., MARTIN, C. & LEPINIEC, L. 2010. MYB transcription factors in Arabidopsis. Trends in Plant Science, 15.

DURNER, J., GOW, A. J., STAMLER, J. S. & GLAZEBROOK, J. 1999. Ancient origins of nitric oxide signaling in biological systems. Proceedings of the National Academy of Sciences, 96.

DURNER, J., SHAH, J. & KLESSIG, D. F. 1997. Salicylic acid and disease resistance in plants. Trends in Plant Science, 2.

DURRANT, W. E. & DONG, X. 2004. SYSTEMIC ACQUIRED RESISTANCE. Annual Review of Phytopathology, 42.

EBRINGEROVÁ, A. & HEINZE, T. 2000. Xylan and xylan derivatives - biopolymers with valuable properties, 1. Naturally occurring xylans structures, isolation procedures and properties. Macromolecular Rapid Communications, 21.

EDERLI, L., MADEO, L., CALDERINI, O., GEHRING, C., MORETTI, C., BUONAURIO, R., PAOLOCCI, F. & PASQUALINI, S. 2011. The Arabidopsis thaliana cysteine-rich receptor-like kinase CRK20 modulates host responses to Pseudomonas syringae pv. tomato DC3000 infection. Journal of Plant Physiology, 168, 1784-1794.

EDGAR, C. I., MCGRATH, K. C., DOMBRECHT, B., MANNERS, J. M., MACLEAN, D. C., SCHENK, P. M. & KAZAN, K. 2006. Salicylic acid mediates resistance to the vascular wilt pathogen Fusarium oxysporum in the model host Arabidopsis thaliana. Australasian Plant Pathology, 35.

ELLIS, M., EGELUND, J., SCHULTZ, C. J. & BACIC, A. 2010. Arabinogalactan-Proteins: Key Regulators at the Cell Surface? Plant Physiology, 153.

ENCINAS-VILLAREJO, S., MALDONADO, A. M., AMIL-RUIZ, F., DE LOS SANTOS, B., ROMERO, F., PLIEGO-ALFARO, F., MUÑOZ-BLANCO, J. & CABALLERO, J. L. 2009. Evidence for a positive regulatory role of strawberry (Fragaria×ananassa) Fa WRKY1 and Arabidopsis At WRKY75 proteins in resistance. Journal of Experimental Botany, 60.

ENDICOTT, J. A., NOBLE, M. E. M. & JOHNSON, L. N. 2012. The Structural Basis for Control of Eukaryotic Protein Kinases. Annual Review of Biochemistry, 81, 587-613.

ENGELSDORF, T. & HAMANN, T. 2014. An update on receptor-like kinase involvement in the maintenance of plant cell wall integrity. Annals of Botany, 114.

ERIKSSON, Ö., GORING, D. A. I. & LINDGREN, B. O. 1980. Structural studies on the chemical bonds between lignins and carbohydrates in spruce wood. Wood Science and Technology, 14, 267-279.

FALK, A., FEYS, B. J., FROST, L. N., JONES, J. D. G., DANIELS, M. J. & PARKER, J. E. 1999. EDS1, an essential component of R gene-mediated disease resistance in Arabidopsis has homology to eukaryotic lipases. Proceedings of the National Academy of Sciences, 96.

FANGEL, J. U., JONES, C. Y., ULVSKOV, P., HARHOLT, J. & WILLATS, W. G. T. 2021. Analytical implications of different methods for preparing plant cell wall material. Carbohydrate Polymers, 261.

FARIA-BLANC, N., MORTIMER, J. C. & DUPREE, P. 2018. A Transcriptomic Analysis of Xylan Mutants Does Not Support the Existence of a Secondary Cell Wall Integrity System in Arabidopsis. Frontiers in Plant Science, 9.

FENG, L., GAO, Z., XIAO, G., HUANG, R. & ZHANG, H. 2014. Leucine-Rich Repeat Receptor-Like Kinase FON1 Regulates Drought Stress and Seed Germination by Activating the Expression of ABA-Responsive Genes in Rice. Plant Molecular Biology Reporter, 32.

FEYS, B. J. 2001. Direct interaction between the Arabidopsis disease resistance signaling proteins, EDS1 and PAD4. The EMBO Journal, 20.

FINKEL, T. 2011. Signal transduction by reactive oxygen species. Journal of Cell Biology, 194, 7-15.

FLETCHER, J. C. 1999. Signaling of Cell Fate Decisions by CLAVATA3 in Arabidopsis Shoot Meristems. Science, 283.

FORD, K. A., CASIDA, J. E., CHANDRAN, D., GULEVICH, A. G., OKRENT, R. A., DURKIN, K. A., SARPONG, R., BUNNELLE, E. M. & WILDERMUTH, M. C. 2010. Neonicotinoid insecticides induce salicylate-associated plant defense responses. Proceedings of the National Academy of Sciences, 107.

FOYER, C. H. & NOCTOR, G. 2009. Redox Regulation in Photosynthetic Organisms: Signaling, Acclimation, and Practical Implications. Antioxidants & Redox Signaling, 11.

FOYER, C. H. & NOCTOR, G. 2016. Stress-triggered redox signalling: what's in pROSpect? Plant, Cell & Environment, 39, 951-964.

FREY, A., EFFROY, D., LEFEBVRE, V., SEO, M., PERREAU, F., BERGER, A., SECHET, J., TO, A., NORTH, H. M. & MARION-POLL, A. 2011. Epoxycarotenoid cleavage by NCED5 fine-tunes ABA accumulation and affects seed dormancy and drought tolerance with other NCED family members. The Plant Journal, 70, 501-512.

FRIDBORG, I., KUUSK, S., MORITZ, T. & SUNDBERG, E. 1999. The Arabidopsis Dwarf Mutant shi Exhibits Reduced Gibberellin Responses Conferred by Overexpression of a New Putative Zinc Finger Protein. The Plant Cell, 11.

FU, Z. Q. & DONG, X. 2013. Systemic Acquired Resistance: Turning Local Infection into Global Defense. Annual Review of Plant Biology, 64.

FURDUI, C. M., LEW, E. D., SCHLESSINGER, J. & ANDERSON, K. S. 2006. Autophosphorylation of FGFR1 Kinase Is Mediated by a Sequential and Precisely Ordered Reaction. Molecular Cell, 21.

GAMBALE, F. & UOZUMI, N. 2006. Properties of Shaker-type Potassium Channels in Higher Plants. Journal of Membrane Biology, 210.

GANDIA-HERRERO, F., LORENZ, A., LARSON, T., GRAHAM, I. A., BOWLES, D. J., RYLOTT, E. L. & BRUCE, N. C. 2008. Detoxification of the explosive 2,4,6-trinitrotoluene in Arabidopsis: discovery of bifunctional O - and C -glucosyltransferases. The Plant Journal, 56.

GAO, M., LIU, J., BI, D., ZHANG, Z., CHENG, F., CHEN, S. & ZHANG, Y. 2008. MEKK1, MKK1/MKK2 and MPK4 function together in a mitogen-activated protein kinase cascade to regulate innate immunity in plants. Cell Research, 18.

GAO, M., WANG, X., WANG, D., XU, F., DING, X., ZHANG, Z., BI, D., CHENG, Y. T., CHEN, S., LI, X. & ZHANG, Y. 2009. Regulation of Cell Death and Innate Immunity by Two Receptor-like Kinases in Arabidopsis. Cell Host & Microbe, 6.

GAO, Q.-M., VENUGOPAL, S., NAVARRE, D. & KACHROO, A. 2011. Low Oleic Acid-Derived Repression of Jasmonic Acid-Inducible Defense Responses Requires the WRKY50 and WRKY51 Proteins Plant Physiology, 155.

GAPPER, C. & DOLAN, L. 2006. Control of Plant Development by Reactive Oxygen Species. Plant Physiology, 141.

GARAPATI, P., XUE, G.-P., MUNNÉ-BOSCH, S. & BALAZADEH, S. 2015. Transcription Factor ATAF1 in Arabidopsis Promotes Senescence by Direct Regulation of Key Chloroplast Maintenance and Senescence Transcriptional Cascades. Plant Physiology, 168.

GEISLER, M., NADEAU, J. & SACK, F. D. 2000. Oriented Asymmetric Divisions That Generate the Stomatal Spacing Pattern in Arabidopsis Are Disrupted by the too many mouths Mutation. The Plant Cell, 12.

GILMAN, A. G. 1987. G Proteins: Transducers of Receptor-Generated Signals. Annual Review of Biochemistry, 56.

GILMAN, A. G. 1995. G proteins and regulation of adenylyl cyclase1. Bioscience Reports, 15.

GLAZEBROOK, J. 2005. Contrasting Mechanisms of Defense Against Biotrophic and Necrotrophic Pathogens. Annual Review of Phytopathology, 43.

GOLDSTEIN, J. L., ANDERSON, R. G. W. & BROWN, M. S. 1979. Coated pits, coated vesicles, and receptor-mediated endocytosis. Nature, 279.

GORDON, T. R. & MARTYN, R. D. 1997. THE EVOLUTIONARY BIOLOGY OF FUSARIUM OXYSPORUM. Annual Review of Phytopathology, 35.

GOU, X. & LI, J. 2020. Paired Receptor and Coreceptor Kinases Perceive Extracellular Signals to Control Plant Development. Plant Physiology, 182.

GOUBET, F., BARTON, C. J., MORTIMER, J. C., YU, X., ZHANG, Z., MILES, G. P., RICHENS, J., LIEPMAN, A. H., SEFFEN, K. & DUPREE, P. 2009. Cell wall glucomannan in Arabidopsis is synthesised by CSLA glycosyltransferases, and influences the progression of embryogenesis. The Plant Journal, 60.

GOUGH, D. R. & COTTER, T. G. 2011. Hydrogen peroxide: a Jekyll and Hyde signalling molecule. Cell Death & Disease, 2.

GREEFF, C., ROUX, M., MUNDY, J. & PETERSEN, M. 2012. Receptor-like kinase complexes in plant innate immunity. Frontiers in Plant Science, 3.

GÜNL, M., KRAEMER, F. & PAULY, M. 2011. Oligosaccharide Mass Profiling (OLIMP) of Cell Wall Polysaccharides by MALDI-TOF/MS.

GUO, P., LI, Z., HUANG, P., LI, B., FANG, S., CHU, J. & GUO, H. 2017. A Tripartite Amplification Loop Involving the Transcription Factor WRKY75, Salicylic Acid, and Reactive Oxygen Species Accelerates Leaf Senescence. The Plant Cell, 29.

GUO, X. & STOTZ, H. U. 2007. Defense Against Sclerotinia sclerotiorum in Arabidopsis Is Dependent on Jasmonic Acid, Salicylic Acid, and Ethylene Signaling. Molecular Plant-Microbe Interactions®, 20, 1384-1395.

HABER, F. & WEISS, J. 1934. The catalytic decomposition of hydrogen peroxide by iron salts. Proceedings of the Royal Society of London. Series A - Mathematical and Physical Sciences, 147.

HAMMOND-KOSACK, K. E. & JONES, J. D. 1996. Resistance gene-dependent plant defense responses. The Plant Cell, 8.

HANKS, S. K. & HUNTER, T. 1995. The eukaryotic protein kinase superfamily: kinase (catalytic) domain structure and classification ¹. The FASEB Journal, 9, 576-596.

HARDIE, D. G. 1999. PLANT PROTEIN SERINE/THREONINE KINASES: Classification and Functions. Annual Review of Plant Physiology and Plant Molecular Biology, 50.

HASSANI-PAK, K., SINGH, A., BRANDIZI, M., HEARNSHAW, J., PARSONS, J. D., AMBERKAR, S., PHILLIPS, A. L., DOONAN, J. H. & RAWLINGS, C. 2021. KnetMiner: a comprehensive approach for supporting evidence-based gene discovery and complex trait analysis across species. Plant Biotechnology Journal, 19.

HE, Y., ZHOU, J., SHAN, L. & MENG, X. 2018. Plant cell surface receptor-mediated signaling – a common theme amid diversity. Journal of Cell Science, 131.

HE, Z.-H., FUJIKI, M. & KOHORN, B. D. 1996. A Cell Wall-associated, Receptor-like Protein Kinase. Journal of Biological Chemistry, 271, 19789-19793.

HE, Z. 2000. Perception of Brassinosteroids by the Extracellular Domain of the Receptor Kinase BRI1. Science, 288, 2360-2363.

HERNÁNDEZ-BLANCO, C., FENG, D. X., HU, J., SÁNCHEZ-VALLET, A., DESLANDES, L., LLORENTE, F., BERROCAL-LOBO, M., KELLER, H., BARLET, X., SÁNCHEZ-RODRÍGUEZ, C., ANDERSON, L. K., SOMERVILLE, S., MARCO, Y. & MOLINA, A. 2007. Impairment of Cellulose Synthases Required for Arabidopsis Secondary Cell Wall Formation Enhances Disease Resistance. The Plant Cell, 19.

HERVÉ, C., DABOS, P., GALAUD, J. P., ROUGÉ, P. & LESCURE, B. 1996. Characterization of anArabidopsis thalianaGene that Defines a New Class of Putative Plant Receptor Kinases with an Extracellular Lectin-like Domain. Journal of Molecular Biology, 258, 778-788.

HEYMAN, J., CANHER, B., BISHT, A., CHRISTIAENS, F. & DE VEYLDER, L. 2018. Emerging role of the plant ERF transcription factors in coordinating wound defense responses and repair. Journal of Cell Science.

HEYMAN, J., COOLS, T., VANDENBUSSCHE, F., HEYNDRICKX, K. S., VAN LEENE, J., VERCAUTEREN, I., VANDERAUWERA, S., VANDEPOELE, K., DE JAEGER, G., VAN DER STRAETEN, D. & DE VEYLDER, L. 2013. ERF115 Controls Root Quiescent Center Cell Division and Stem Cell Replenishment. Science, 342.

HIROSE, N., TAKEI, K., KUROHA, T., KAMADA-NOBUSADA, T., HAYASHI, H. & SAKAKIBARA, H. 2007. Regulation of cytokinin biosynthesis, compartmentalization and translocation. Journal of Experimental Botany, 59.

HIRSCHI, K. 2001. Vacuolar H+/Ca2+ transport: who's directing the traffic? Trends in Plant Science, 6.

HOEFLICH, K. P. & IKURA, M. 2002. Calmodulin in Action. Cell, 108.

HOHMANN, U., LAU, K. & HOTHORN, M. 2017. The Structural Basis of Ligand Perception and Signal Activation by Receptor Kinases. Annual Review of Plant Biology, 68, 109-137.

HOHMANN, U., SANTIAGO, J., NICOLET, J., OLSSON, V., SPIGA, F. M., HOTHORN, L. A., BUTENKO, M. A. & HOTHORN, M. 2018. Mechanistic basis for the activation of plant membrane receptor kinases by SERK-family coreceptors. Proceedings of the National Academy of Sciences, 115.

HOPKINS, R. 2016. Superoxide in Biology and Medicine: An Overview. Reactive Oxygen Species.

HRUZ, T., LAULE, O., SZABO, G., WESSENDORP, F., BLEULER, S., OERTLE, L., WIDMAYER, P., GRUISSEM, W. & ZIMMERMANN, P. 2008. Genevestigator V3: A

Reference Expression Database for the Meta-Analysis of Transcriptomes. Advances in Bioinformatics, 2008.

HUA, D., WANG, C., HE, J., LIAO, H., DUAN, Y., ZHU, Z., GUO, Y., CHEN, Z. & GONG, Z. 2012. A Plasma Membrane Receptor Kinase, GHR1, Mediates Abscisic Acid- and Hydrogen Peroxide-Regulated Stomatal Movement in Arabidopsis. The Plant Cell, 24.

HUANG, Y., FENG, C.-Z., YE, Q., WU, W.-H. & CHEN, Y.-F. 2016. Arabidopsis WRKY6 Transcription Factor Acts as a Positive Regulator of Abscisic Acid Signaling during Seed Germination and Early Seedling Development. PLOS Genetics, 12.

HUBBARD, S. R. 1997. Crystal structure of the activated insulin receptor tyrosine kinase in complex with peptide substrate and ATP analog. The EMBO Journal, 16.

HUBBARD, S. R., WEI, L. & HENDRICKSON, W. A. 1994. Crystal structure of the tyrosine kinase domain of the human insulin receptor. Nature, 372.

HUCK, N., MOORE, J. M., FEDERER, M. & GROSSNIKLAUS, U. 2003. The Arabidopsis mutant feronia disrupts the female gametophytic control of pollen tube reception. Development, 130.

HUOT, B., YAO, J., MONTGOMERY, B. L. & HE, S. Y. 2014. Growth–Defense Tradeoffs in Plants: A Balancing Act to Optimize Fitness. Molecular Plant, 7.

HUSE, M. & KURIYAN, J. 2002. The Conformational Plasticity of Protein Kinases. Cell, 109, 275-282.

HWA, C.-M. & YANG, X.-C. 2008. The AtMKK3 pathway mediates ABA and salt signaling in Arabidopsis. Acta Physiologiae Plantarum, 30.

ICHIMURA, K., CASAIS, C., PECK, S. C., SHINOZAKI, K. & SHIRASU, K. 2006. MEKK1 Is Required for MPK4 Activation and Regulates Tissue-specific and Temperature-dependent Cell Death in Arabidopsis. Journal of Biological Chemistry, 281.

ICHIMURA, K., SHINOZAKI, K., TENA, G., SHEEN, J., HENRY, Y., CHAMPION, A., KREIS, M., ZHANG, S., HIRT, H., WILSON, C., HEBERLE-BORS, E., ELLIS, B. E., MORRIS, P. C., INNES, R. W., ECKER, J. R., SCHEEL, D., KLESSIG, D. F., MACHIDA, Y., MUNDY, J., OHASHI, Y. & WALKER, J. C. 2002. Mitogen-activated protein kinase cascades in plants: a new nomenclature. Trends in Plant Science, 7, 301-308.

IDÄNHEIMO, N., GAUTHIER, A., SALOJÄRVI, J., SILIGATO, R., BROSCHÉ, M., KOLLIST, H., MÄHÖNEN, A. P., KANGASJÄRVI, J. & WRZACZEK, M. 2014. The Arabidopsis thaliana cysteine-rich receptor-like kinases CRK6 and CRK7 protect against apoplastic oxidative stress. Biochemical and Biophysical Research Communications, 445, 457-462.

JANSON, G., ZHANG, C., PRADO, M. G. & PAIARDINI, A. 2016. PyMod 2.0: improvements in protein sequence-structure analysis and homology modeling within PyMOL. Bioinformatics.

JARVIS, M. C. 1984. Structure and properties of pectin gels in plant cell walls. Plant, Cell and Environment, 7.

JEFFREY, P. D. 2000. Structural basis of inhibition of CDK-cyclin complexes by INK4 inhibitors. Genes & Development, 14.

JEFFREY, P. D., RUSSO, A. A., POLYAK, K., GIBBS, E., HURWITZ, J., MASSAGUÉ, J. & PAVLETICH, N. P. 1995. Mechanism of CDK activation revealed by the structure of a cyclinA-CDK2 complex. Nature, 376, 313-320.

JIANG, G. & HUNTER, T. 1999. Receptor signaling: When dimerization is not enough. Current Biology, 9.

JIMÉNEZ-GÓNGORA, T., KIM, S.-K., LOZANO-DURÁN, R. & ZIPFEL, C. 2015. Flg22-Triggered Immunity Negatively Regulates Key BR Biosynthetic Genes. Frontiers in Plant Science, 6.

JIRAGE, D., TOOTLE, T. L., REUBER, T. L., FROST, L. N., FEYS, B. J., PARKER, J. E., AUSUBEL, F. M. & GLAZEBROOK, J. 1999. Arabidopsis thaliana PAD4 encodes a lipase-like gene that is important for salicylic acid signaling. Proceedings of the National Academy of Sciences, 96.

JOHNSON, L. N. & LEWIS, R. J. 2001. Structural Basis for Control by Phosphorylation. Chemical Reviews, 101, 2209-2242.

JOHNSON, L. N., NOBLE, M. E. M. & OWEN, D. J. 1996. Active and Inactive Protein Kinases: Structural Basis for Regulation. Cell, 85.

JOHNSTON, C. A., TAYLOR, J. P., GAO, Y., KIMPLE, A. J., GRIGSTON, J. C., CHEN, J. G., SIDEROVSKI, D. P., JONES, A. M. & WILLARD, F. S. 2007. GTPase acceleration as the rate-limiting step in Arabidopsis G protein-coupled sugar signaling. Proceedings of the National Academy of Sciences, 104.

JONAK, C. 2002. Complexity, Cross Talk and Integration of Plant MAP Kinase Signalling. Current Opinion in Plant Biology, 5.

JONES, J. D. G. & DANGL, J. L. 2006. The plant immune system. Nature, 444.

JONES, L., ENNOS, A. R. & TURNER, S. R. 2001. Cloning and characterization of irregular xylem4 (irx4): a severely lignin-deficient mutant of Arabidopsis. The Plant Journal, 26.

KAACK, L., ALTANER, C. M., CARMESIN, C., DIAZ, A., HOLLER, M., KRANZ, C., NEUSSER, G., ODSTRCIL, M., JOCHEN SCHENK, H., SCHMIDT, V., WEBER, M., ZHANG, Y. & JANSEN, S. 2019. Function and three-dimensional structure of intervessel pit membranes in angiosperms: a review. IAWA Journal, 40.

KACURÁKOVÁ, M. 2000. FT-IR study of plant cell wall model compounds: pectic polysaccharides and hemicelluloses. Carbohydrate Polymers, 43.

KANG, J., HWANG, J.-U., LEE, M., KIM, Y.-Y., ASSMANN, S. M., MARTINOIA, E. & LEE, Y. 2010. PDR-type ABC transporter mediates cellular uptake of the phytohormone abscisic acid. Proceedings of the National Academy of Sciences, 107.

KANG, X., KIRUI, A., DICKWELLA WIDANAGE, M. C., MENTINK-VIGIER, F., COSGROVE, D. J. & WANG, T. 2019. Lignin-polysaccharide interactions in plant secondary cell walls revealed by solid-state NMR. Nature Communications, 10.

KANNAN, N. & NEUWALD, A. F. 2005. Did Protein Kinase Regulatory Mechanisms Evolve Through Elaboration of a Simple Structural Component? Journal of Molecular Biology, 351.

KAPLAN, B., SHERMAN, T. & FROMM, H. 2007. Cyclic nucleotide-gated channels in plants. FEBS Letters, 581.

KASAJIMA, I., IDE, Y., YOKOTA HIRAI, M. & FUJIWARA, T. 2010. WRKY6 is involved in the response to boron deficiency in Arabidopsis thaliana. Physiologia Plantarum, 139.

KATO, H., MOTOMURA, T., KOMEDA, Y., SAITO, T. & KATO, A. 2010. Overexpression of the NAC transcription factor family gene ANAC036 results in a dwarf phenotype in Arabidopsis thaliana. Journal of Plant Physiology, 167.

KAZAN, K. & MANNERS, J. M. 2012. JAZ repressors and the orchestration of phytohormone crosstalk. Trends in Plant Science, 17.

KAZAN, K. & MANNERS, J. M. 2013. MYC2: The Master in Action. Molecular Plant, 6.

KEPPLER, B. D. & SHOWALTER, A. M. 2010. IRX14 and IRX14-LIKE, Two Glycosyl Transferases Involved in Glucuronoxylan Biosynthesis and Drought Tolerance in Arabidopsis. Molecular Plant, 3.

KESSLER, S. A., SHIMOSATO-ASANO, H., KEINATH, N. F., WUEST, S. E., INGRAM, G., PANSTRUGA, R. & GROSSNIKLAUS, U. 2010. Conserved Molecular Components for Pollen Tube Reception and Fungal Invasion. Science, 330.

KEYSE, S. M. 1998. Protein phosphatases and the regulation of MAP kinase activity. Seminars in Cell & Developmental Biology, 9.

KIBA, T., KUDO, T., KOJIMA, M. & SAKAKIBARA, H. 2011. Hormonal control of nitrogen acquisition: roles of auxin, abscisic acid, and cytokinin. Journal of Experimental Botany, 62.

KIBA, T., TAKEI, K., KOJIMA, M. & SAKAKIBARA, H. 2013. Side-Chain Modification of Cytokinins Controls Shoot Growth in Arabidopsis. Developmental Cell, 27.

KIDD, B. N., EDGAR, C. I., KUMAR, K. K., AITKEN, E. A., SCHENK, P. M., MANNERS, J. M. & KAZAN, K. 2009. The Mediator Complex Subunit PFT1 Is a Key Regulator of Jasmonate-Dependent Defense in Arabidopsis The Plant Cell, 21.

KIDD, B. N., KADOO, N. Y., DOMBRECHT, B., TEKEOGLU, M., GARDINER, D. M., THATCHER, L. F., AITKEN, E. A. B., SCHENK, P. M., MANNERS, J. M. & KAZAN, K. 2011. Auxin Signaling and Transport Promote Susceptibility to the Root-Infecting Fungal Pathogen Fusarium oxysporum in Arabidopsis. Molecular Plant-Microbe Interactions®, 24.

KIM, D., LANGMEAD, B. & SALZBERG, S. L. 2015. HISAT: a fast spliced aligner with low memory requirements. Nature Methods, 12.

KIM, P., LI, H., WANG, J. & ZHAO, Z. 2021. Landscape of drug-resistance mutations in kinase regulatory hotspots. Briefings in Bioinformatics, 22.

KIM, T.-H., HAUSER, F., HA, T., XUE, S., BÖHMER, M., NISHIMURA, N., MUNEMASA, S., HUBBARD, K., PEINE, N., LEE, B.-H., LEE, S., ROBERT, N., PARKER, JANE E. & SCHROEDER, JULIAN I. 2011. Chemical Genetics Reveals Negative Regulation of Abscisic Acid Signaling by a Plant Immune Response Pathway. Current Biology, 21, 990-997.

KIM, W.-C., KO, J.-H., KIM, J.-Y., KIM, J., BAE, H.-J. & HAN, K.-H. 2012. MYB46 directly regulates the gene expression of secondary wall-associated cellulose synthases in Arabidopsis. The Plant Journal, 73, 26-36.

KIM, Y., SCHUMAKER, K. S. & ZHU, J.-K. EMS Mutagenesis of Arabidopsis. Arabidopsis Protocols. New Jersey: Humana Press.

KIMURA, S., HUNTER, K., VAAHTERA, L., TRAN, H. C., CITTERICO, M., VAATTOVAARA, A., ROKKA, A., STOLZE, S. C., HARZEN, A., MEIßNER, L., WILKENS, M. M. T., HAMANN, T., TOYOTA, M., NAKAGAMI, H. & WRZACZEK, M. 2020. CRK2 and C-terminal Phosphorylation of NADPH Oxidase RBOHD Regulate Reactive Oxygen Species Production in Arabidopsis. The Plant Cell, 32, 1063-1080.

KLAUS-HEISEN, D., NURISSO, A., PIETRASZEWSKA-BOGIEL, A., MBENGUE, M., CAMUT, S., TIMMERS, T., PICHEREAUX, C., ROSSIGNOL, M., GADELLA, T. W. J., IMBERTY, A., LEFEBVRE, B. & CULLIMORE, J. V. 2011. Structure-Function Similarities between a Plant Receptor-like Kinase and the Human Interleukin-1 Receptor-associated Kinase-4. Journal of Biological Chemistry, 286.

KLIMYUK, V. I., CARROLL, B. J., THOMAS, C. M. & JONES, J. D. G. 1993. Alkali treatment for rapid preparation of plant material for reliable PCR analysis. The Plant Journal, 3.

KNIGHTON, D., ZHENG, J., TEN EYCK, L., ASHFORD, V., XUONG, N., TAYLOR, S. & SOWADSKI, J. 1991. Crystal structure of the catalytic subunit of cyclic adenosine monophosphate-dependent protein kinase. Science, 253.

KNOCH, E., DILOKPIMOL, A. & GESHI, N. 2014. Arabinogalactan proteins: focus on carbohydrate active enzymes. Frontiers in Plant Science, 5.

KO, D. & HELARIUTTA, Y. 2017. Shoot–Root Communication in Flowering Plants. Current Biology, 27.

KOBE, B. 2001. The leucine-rich repeat as a protein recognition motif. Current Opinion in Structural Biology, 11.

KOHORN, B. D. & KOHORN, S. L. 2012. The cell wall-associated kinases, WAKs, as pectin receptors. Frontiers in Plant Science, 3.

KOORNEEF, M., ELGERSMA, A., HANHART, C. J., LOENEN-MARTINET, E. P., RIJN, L. & ZEEVAART, J. A. D. 1985. A gibberellin insensitive mutant of Arabidopsis thaliana. Physiologia Plantarum, 65.

KOORNNEEF, A., LEON-REYES, A., RITSEMA, T., VERHAGE, A., DEN OTTER, F. C., VAN LOON, L. C. & PIETERSE, C. M. J. 2008. Kinetics of Salicylate-Mediated Suppression of Jasmonate Signaling Reveal a Role for Redox Modulation. Plant Physiology, 147.

KORNEV, A. P., HASTE, N. M., TAYLOR, S. S. & TEN EYCK, L. F. 2006. Surface comparison of active and inactive protein kinases identifies a conserved activation mechanism. Proceedings of the National Academy of Sciences, 103, 17783-17788.

KORNEV, A. P., TAYLOR, S. S. & TEN EYCK, L. F. 2008. A helix scaffold for the assembly of active protein kinases. Proceedings of the National Academy of Sciences, 105, 14377-14382.

KOSENTKA, P. Z., ZHANG, L., SIMON, Y. A., SATPATHY, B., MARADIAGA, R., MITOUBSI, O. & SHPAK, E. D. 2017. Identification of critical functional residues of receptor-like kinase ERECTA. Journal of Experimental Botany, 68.

KOSETSU, K., MATSUNAGA, S., NAKAGAMI, H., COLCOMBET, J., SASABE, M., SOYANO, T., TAKAHASHI, Y., HIRT, H. & MACHIDA, Y. 2010. The MAP Kinase MPK4 Is Required for Cytokinesis in Arabidopsis thaliana The Plant Cell, 22.

KREBS, E. G. & FISCHER, E. H. 1956. The phosphorylase b to a converting enzyme of rabbit skeletal muscle. Biochimica et Biophysica Acta, 20.

KREBS, E. G., GRAVES, D. J. & FISCHER, E. H. 1959. Factors Affecting the Activity of Muscle Phosphorylase b Kinase. Journal of Biological Chemistry, 234.

KUMAR, M. & TURNER, S. 2015. Protocol: a medium-throughput method for determination of cellulose content from single stem pieces of Arabidopsis thaliana. Plant Methods, 11.

KUNKEL, B. N. & BROOKS, D. M. 2002. Cross talk between signaling pathways in pathogen defense. Current Opinion in Plant Biology, 5.

LAMB, C. & DIXON, R. A. 1997. THE OXIDATIVE BURST IN PLANT DISEASE RESISTANCE. Annual Review of Plant Physiology and Plant Molecular Biology, 48, 251-275.

LARGO-GOSENS, A., HERNÃ¡NDEZ-ALTAMIRANO, M., GARCÃ-A-CALVO, L., ALONSO-SIMÃ³N, A., Ã• LVAREZ, J. S. & ACEBES, J. L. 2014. Fourier transform mid infrared spectroscopy applications for monitoring the structural plasticity of plant cell walls. Frontiers in Plant Science, 5.

LATORRE, R., MUÑOZ, F., GONZÁLEZ, C. & COSMELLI, D. 2003. Structure and function of potassium channels in plants: some inferences about the molecular origin of inward rectification in KAT1 channels (Review). Molecular Membrane Biology, 20.

LAU, J. M., MCNEIL, M., DARVILL, A. G. & ALBERSHEIM, P. 1985. STRUCTURE OF THE BACKBONE OF RHAMNOGALACTURONAN I, A PECTIC POLYSACCHARIDE IN THE PRIMARY CELL WALLS OF PLANTS. Carbohydrate Research, 137, 111-125.

LEASE, K. A., WEN, J., LI, J., DOKE, J. T., LISCUM, E. & WALKER, J. C. 2001. A Mutant Arabidopsis Heterotrimeric G-Protein b Subunit Affects Leaf, Flower, and Fruit Development. The Plant Cell, 13.

LEE, C., ZHONG, R., RICHARDSON, E. A., HIMMELSBACH, D. S., MCPHAIL, B. T. & YE, Z.-H. 2007. The PARVUS Gene is Expressed in Cells Undergoing Secondary Wall Thickening and is Essential for Glucuronoxylan Biosynthesis. Plant and Cell Physiology, 48.

LEE, D. S., KIM, Y. C., KWON, S. J., RYU, C.-M. & PARK, O. K. 2017. The Arabidopsis Cysteine-Rich Receptor-Like Kinase CRK36 Regulates Immunity through Interaction with the Cytoplasmic Kinase BIK1. Frontiers in Plant Science, 8.

LEE, J. S., KUROHA, T., HNILOVA, M., KHATAYEVICH, D., KANAOKA, M. M., MCABEE, J. M., SARIKAYA, M., TAMERLER, C. & TORII, K. U. 2012. Direct interaction of ligand-receptor pairs specifying stomatal patterning. Genes & Development, 26.

LEE, J. S., WANG, S., SRITUBTIM, S., CHEN, J.-G. & ELLIS, B. E. 2009. Arabidopsis mitogen-activated protein kinase MPK12 interacts with the MAPK phosphatase IBR5 and regulates auxin signaling. The Plant Journal, 57.

LEFEBVRE, V., FORTABAT, M.-N., DUCAMP, A., NORTH, H. M., MAIA-GRONDARD, A., TROUVERIE, J., BOURSIAC, Y., MOUILLE, G. & DURAND-TARDIF, M. 2011. ESKIMO1 Disruption in Arabidopsis Alters Vascular Tissue and Impairs Water Transport. PLoS ONE, 6.

LEFKOWITZ, R. J. & MICHEL, T. 1983. Plasma membrane receptors. Journal of Clinical Investigation, 72, 1185-1189.

LEHMANN, F. & HARDTKE, C. S. 2016. Secondary growth of the Arabidopsis hypocotyl — vascular development in dimensions. Current Opinion in Plant Biology, 29, 9-15.

LEMMON, M. A. & SCHLESSINGER, J. 2010. Cell Signaling by Receptor Tyrosine Kinases. Cell, 141.

LEROUXEL, O., CHOO, T. S., SÉVENO, M., USADEL, B. R., FAYE, L. C., LEROUGE, P. & PAULY, M. 2002. Rapid Structural Phenotyping of Plant Cell Wall Mutants by Enzymatic Oligosaccharide Fingerprinting. Plant Physiology, 130.

LEVESQUE-TREMBLAY, G., PELLOUX, J., BRAYBROOK, S. A. & MÜLLER, K. 2015. Tuning of pectin methylesterification: consequences for cell wall biomechanics and development. Planta, 242.

LI, J., BRADER, G., KARIOLA, T. & TAPIO PALVA, E. 2006. WRKY70 modulates the selection of signaling pathways in plant defense. The Plant Journal, 46.

LI, J., BRADER, G. N. & PALVA, E. T. 2004. The WRKY70 Transcription Factor: A Node of Convergence for Jasmonate-Mediated and Salicylate-Mediated Signals in Plant Defense[W]. The Plant Cell, 16.

LI, J., WEN, J., LEASE, K. A., DOKE, J. T., TAX, F. E. & WALKER, J. C. 2002. BAK1, an Arabidopsis LRR Receptor-like Protein Kinase, Interacts with BRI1 and Modulates Brassinosteroid Signaling. Cell, 110.

LI, L., YU, X., THOMPSON, A., GUO, M., YOSHIDA, S., ASAMI, T., CHORY, J. & YIN, Y. 2009. Arabidopsis MYB30 is a direct target of BES1 and cooperates with BES1 to regulate brassinosteroid-induced gene expression. The Plant Journal, 58.

LI, S., WONG, A. H. C. & LIU, F. 2014. Ligand-gated ion channel interacting proteins and their role in neuroprotection. Frontiers in Cellular Neuroscience, 8.

LI, T.-G., ZHANG, D.-D., ZHOU, L., KONG, Z.-Q., HUSSAINI, A. S., WANG, D., LI, J.-J., SHORT, D. P. G., DHAR, N., KLOSTERMAN, S. J., WANG, B.-L., YIN, C.-M., SUBBARAO, K. V., CHEN, J.-Y. & DAI, X.-F. 2018. Genome-Wide Identification and Functional Analyses of the CRK Gene Family in Cotton Reveals GbCRK18 Confers Verticillium Wilt Resistance in Gossypium barbadense. Frontiers in Plant Science, 9.

LIAO, C., ZHENG, Y. & GUO, Y. 2017. MYB30 transcription factor regulates oxidative and heat stress responses through ANNEXIN-mediated cytosolic calcium signaling in Arabidopsis. New Phytologist, 216.

LIAO, Y., SMYTH, G. K. & SHI, W. 2019. The R package Rsubread is easier, faster, cheaper and better for alignment and quantification of RNA sequencing reads. Nucleic Acids Research, 47.

LIN, W., LI, B., LU, D., CHEN, S., ZHU, N., HE, P. & SHAN, L. 2014. Tyrosine phosphorylation of protein kinase complex BAK1/BIK1 mediates Arabidopsis innate immunity. Proceedings of the National Academy of Sciences, 111.

LIU, T.-Y., CHANG, C.-Y. & CHIOU, T.-J. 2009. The long-distance signaling of mineral macronutrients. Current Opinion in Plant Biology, 12.

LIU, T., LIU, Z., SONG, C., HU, Y., HAN, Z., SHE, J., FAN, F., WANG, J., JIN, C., CHANG, J., ZHOU, J. M. & CHAI, J. 2012. Chitin-Induced Dimerization Activates a Plant Immune Receptor. Science, 336.

LIU, X., RENARD, C. M. G. C., BUREAU, S. & LE BOURVELLEC, C. 2021. Revisiting the contribution of ATR-FTIR spectroscopy to characterize plant cell wall polysaccharides. Carbohydrate Polymers, 262.

LOPEZ-MOLINA, L., MONGRAND, S. & CHUA, N. H. 2001. A postgermination developmental arrest checkpoint is mediated by abscisic acid and requires the ABI5 transcription factor in Arabidopsis. Proceedings of the National Academy of Sciences, 98.

LOVE, M. I., HUBER, W. & ANDERS, S. 2014. Moderated estimation of fold change and dispersion for RNA-seq data with DESeq2. Genome Biology, 15.

LU, D., LIN, W., GAO, X., WU, S., CHENG, C., AVILA, J., HEESE, A., DEVARENNE, T. P., HE, P. & SHAN, L. 2011. Direct Ubiquitination of Pattern Recognition Receptor FLS2 Attenuates Plant Innate Immunity. Science, 332.

LU, D., WU, S., GAO, X., ZHANG, Y., SHAN, L. & HE, P. 2010. A receptor-like cytoplasmic kinase, BIK1, associates with a flagellin receptor complex to initiate plant innate immunity. Proceedings of the National Academy of Sciences, 107, 496-501.

LU, K., LIANG, S., WU, Z., BI, C., YU, Y.-T., WANG, X.-F. & ZHANG, D.-P. 2016. Overexpression of an Arabidopsis cysteine-rich receptor-like protein kinase, CRK5, enhances abscisic acid sensitivity and confers drought tolerance. Journal of Experimental Botany, 67.

LYONS, R., MANNERS, J. M. & KAZAN, K. 2013. Jasmonate biosynthesis and signaling in monocots: a comparative overview. Plant Cell Reports, 32.

LYONS, R., STILLER, J., POWELL, J., RUSU, A., MANNERS, J. M. & KAZAN, K. 2015. Fusarium oxysporum Triggers Tissue-Specific Transcriptional Reprogramming in Arabidopsis thaliana. PLOS ONE, 10.

MA, L.-S., WANG, L., TRIPPEL, C., MENDOZA-MENDOZA, A., ULLMANN, S., MORETTI, M., CARSTEN, A., KAHNT, J., REISSMANN, S., ZECHMANN, B., BANGE, G. & KAHMANN, R. 2018. The Ustilago maydis repetitive effector Rsp3 blocks the antifungal activity of mannose-binding maize proteins. Nature Communications, 9, 1711-1711.

MA, Y., SZOSTKIEWICZ, I., KORTE, A., MOES, D., YANG, Y., CHRISTMANN, A. & GRILL, E. 2009. Regulators of PP2C Phosphatase Activity Function as Abscisic Acid Sensors. Science.

MABUCHI, K., MAKI, H., ITAYA, T., SUZUKI, T., NOMOTO, M., SAKAOKA, S., MORIKAMI, A., HIGASHIYAMA, T., TADA, Y., BUSCH, W. & TSUKAGOSHI, H. 2018. MYB30 links ROS signaling, root cell elongation, and plant immune responses. Proceedings of the National Academy of Sciences, 115.

MACAULAY, K. M., HEATH, G. A., CIULLI, A., MURPHY, A. M., ABELL, C., CARR, J. P. & SMITH, A. G. 2017. The biochemical properties of the two Arabidopsis thaliana isochorismate synthases. Biochemical Journal, 474.

MACHO, ALBERTO P. & ZIPFEL, C. 2014. Plant PRRs and the Activation of Innate Immune Signaling. Molecular Cell, 54.

MAEDA, T., TAKEKAWA, M. & SAITO, H. 1995. Activation of yeast PBS2 MAPKK by MAPKKKs or by binding of an SH3-containing osmosensor. Science, 269.

MALINOVSKY, F. G., FANGEL, J. U. & WILLATS, W. G. T. 2014. The role of the cell wall in plant immunity. Frontiers in Plant Science, 5.

MARSHALL, A., AALEN, R. B., AUDENAERT, D., BEECKMAN, T., BROADLEY, M. R., BUTENKO, M. A., CAÑO-DELGADO, A. I., DE VRIES, S., DRESSELHAUS, T., FELIX, G., GRAHAM, N. S., FOULKES, J., GRANIER, C., GREB, T., GROSSNIKLAUS, U., HAMMOND, J. P., HEIDSTRA, R., HODGMAN, C., HOTHORN, M., INZÉ, D., ØSTERGAARD, L., RUSSINOVA, E., SIMON, R., SKIRYCZ, A., STAHL, Y., ZIPFEL, C. & DE SMET, I. 2012. Tackling Drought Stress: RECEPTOR-LIKE KINASES Present New Approaches. The Plant Cell, 24, 2262-2278.

MASACHIS, S., SEGORBE, D., TURRÀ, D., LEON-RUIZ, M., FÜRST, U., EL GHALID, M., LEONARD, G., LÓPEZ-BERGES, M. S., RICHARDS, T. A., FELIX, G. & DI PIETRO, A. 2016. A fungal pathogen secretes plant alkalinizing peptides to increase infection. Nature Microbiology, 1.

MASTERSON, L. R., CHENG, C., YU, T., TONELLI, M., KORNEV, A., TAYLOR, S. S. & VEGLIA, G. 2010. Dynamics connect substrate recognition to catalysis in protein kinase A. Nature Chemical Biology, 6, 821-828.

MASTERSON, L. R., SHI, L., METCALFE, E., GAO, J., TAYLOR, S. S. & VEGLIA, G. 2011. Dynamically committed, uncommitted, and quenched states encoded in protein kinase A revealed by NMR spectroscopy. Proceedings of the National Academy of Sciences, 108, 6969-6974.

MATSUBAYASHI, Y. 2002. An LRR Receptor Kinase Involved in Perception of a Peptide Plant Hormone, Phytosulfokine. Science, 296.

MATSUBAYASHI, Y., OGAWA, M., KIHARA, H., NIWA, M. & SAKAGAMI, Y. 2006. Disruption and Overexpression of Arabidopsis Phytosulfokine Receptor Gene Affects Cellular Longevity and Potential for Growth. Plant Physiology, 142.

MATSUOKA, K., SATO, R., MATSUKURA, Y., KAWAJIRI, Y., IINO, H., NOZAWA, N., SHIBATA, K., KONDO, Y., SATOH, S. & ASAHINA, M. 2021. Wound-inducible ANAC071 and ANAC096 transcription factors promote cambial cell formation in incised Arabidopsis flowering stems. Communications Biology, 4.

MATTE RISOPATRON, J. P., SUN, Y. & JONES, B. J. 2010. The vascular cambium: molecular control of cellular structure. Protoplasma, 247.

MCCARTY, D. R. & CHORY, J. 2000. Conservation and Innovation in Plant Signaling Pathways. Cell, 103, 201-209.

MCCLENDON, C. L., KORNEV, A. P., GILSON, M. K. & TAYLOR, S. S. 2014. Dynamic architecture of a protein kinase. Proceedings of the National Academy of Sciences, 111, E4623-E4631.

MCDOWELL, J. M. & DANGL, J. L. 2000. Signal transduction in the plant immune response. Trends in Biochemical Sciences, 25.

MCMULLEN, M., JONES, R. & GALLENBERG, D. 1997. Scab of Wheat and Barley: A Re-emerging Disease of Devastating Impact. Plant Disease, 81.

MCNEIL, M., DARVILL, A. G., FRY, S. C. & ALBERSHEIM, P. 1984. Structure and Function of the Primary Cell Walls of Plants. Annual Review of Biochemistry, 53.

MENG, X., WANG, H., HE, Y., LIU, Y., WALKER, J. C., TORII, K. U. & ZHANG, S. 2013. A MAPK Cascade Downstream of ERECTA Receptor-Like Protein Kinase Regulates Arabidopsis Inflorescence Architecture by Promoting Localized Cell Proliferation The Plant Cell, 24.

MÉSZÁROS, T., HELFER, A., HATZIMASOURA, E., MAGYAR, Z., SERAZETDINOVA, L., RIOS, G., BARDÓCZY, V., TEIGE, M., KONCZ, C., PECK, S. & BÖGRE, L. 2006. The Arabidopsis MAP kinase kinase MKK1 participates in defence responses to the bacterial elicitor flagellin. The Plant Journal, 48.

MIEDES, E., VANHOLME, R., BOERJAN, W. & MOLINA, A. 2014. The role of the secondary cell wall in plant resistance to pathogens. Frontiers in Plant Science, 5.

MILLER, W. T. 2012. Tyrosine kinase signaling and the emergence of multicellularity. Biochimica et Biophysica Acta (BBA) - Molecular Cell Research, 1823, 1053-1057.

MILLET, Y. A., DANNA, C. H., CLAY, N. K., SONGNUAN, W., SIMON, M. D., WERCK-REICHHART, D. & AUSUBEL, F. M. 2010. Innate Immune Responses Activated in Arabidopsis Roots by Microbe-Associated Molecular Patterns The Plant Cell, 22.

MIRZA, J. I. & MAHER, E. P. 1987. Physiological characteristics of two auxin-resistant mutants of Arabidopsis thaliana, aux-2 and Dwf. Plant Growth Regulation, 5.

MISHINA, T. E. & ZEIER, J. R. 2006. The Arabidopsis Flavin-Dependent Monooxygenase FMO1 Is an Essential Component of Biologically Induced Systemic Acquired Resistance Plant Physiology, 141.

MITCHUM, M. G., WANG, X. & DAVIS, E. L. 2008. Diverse and conserved roles of CLE peptides. Current Opinion in Plant Biology, 11.

MITRA, S. K., CHEN, R., DHANDAYDHAM, M., WANG, X., BLACKBURN, R. K., KOTA, U., GOSHE, M. B., SCHWARTZ, D., HUBER, S. C. & CLOUSE, S. D. 2015. An autophosphorylation site database for leucine-rich repeat receptor-like kinases in <scp>A</scp> rabidopsis thaliana . The Plant Journal, 82, 1042-1060.

MIYAKAWA, T., HATANO, K.-I., MIYAUCHI, Y., SUWA, Y.-I., SAWANO, Y. & TANOKURA, M. 2014. A Secreted Protein with Plant-Specific Cysteine-Rich Motif Functions as a Mannose-Binding Lectin That Exhibits Antifungal Activity Plant Physiology, 166, 766-778.

MIYAKAWA, T., MIYAZONO, K.-I., SAWANO, Y., HATANO, K.-I. & TANOKURA, M. 2009. Crystal structure of ginkbilobin-2 with homology to the extracellular domain of plant cysteine-rich receptor-like kinases. Proteins: Structure, Function, and Bioinformatics, 77, 247-251.

MIYAZAKI, J., TAN, B. H. & ERRINGTON, S. G. 2010. Eradication of endophytic bacteria via treatment for axillary buds of Petunia hybrida using Plant Preservative Mixture (PPMTM). Plant Cell, Tissue and Organ Culture (PCTOC), 102.

MIZOI, J., SHINOZAKI, K. & YAMAGUCHI-SHINOZAKI, K. 2012. AP2/ERF family transcription factors in plant abiotic stress responses. Biochimica et Biophysica Acta (BBA) - Gene Regulatory Mechanisms, 1819.

MOHNEN, D. 2008. Pectin structure and biosynthesis. Current Opinion in Plant Biology, 11.

MOLINA, A., MIEDES, E., BACETE, L., RODRÍGUEZ, T., MÉLIDA, H., DENANCÉ, N., SÁNCHEZ-VALLET, A., RIVIÈRE, M.-P., LÓPEZ, G., FREYDIER, A., BARLET, X., PATTATHIL, S., HAHN, M. & GOFFNER, D. 2021. Arabidopsis cell wall composition determines disease resistance specificity and fitness. Proceedings of the National Academy of Sciences, 118.

MOORE, J. W., LOAKE, G. J. & SPOEL, S. H. 2011. Transcription Dynamics in Plant Immunity. The Plant Cell, 23.

MORRIS, E. R. & WALKER, J. C. 2003. Receptor-like protein kinases: the keys to response. Current Opinion in Plant Biology, 6.

MORRIS, P. C. 2001. MAP kinase signal transduction pathways in plants. New Phytologist, 151, 67-89.

MORTIMER, J. C., MILES, G. P., BROWN, D. M., ZHANG, Z., SEGURA, M. P., WEIMAR, T., YU, X., SEFFEN, K. A., STEPHENS, E., TURNER, S. R. & DUPREE, P. 2010. Absence of branches from xylan in Arabidopsis gux mutants reveals potential for simplification of lignocellulosic biomass. Proceedings of the National Academy of Sciences, 107.

MOU, Z., FAN, W. & DONG, X. 2003. Inducers of Plant Systemic Acquired Resistance Regulate NPR1 Function through Redox Changes. Cell, 113, 935-944.

MÜLLER, R., BLECKMANN, A. & SIMON, R. D. 2008. The Receptor Kinase CORYNE of Arabidopsis Transmits the Stem Cell–Limiting Signal CLAVATA3 Independently of CLAVATA1. The Plant Cell, 20.

MULLINEAUX, P. M., EXPOSITO-RODRIGUEZ, M., LAISSUE, P. P. & SMIRNOFF, N. 2018. ROS-dependent signalling pathways in plants and algae exposed to high light: Comparisons with other eukaryotes. Free Radical Biology and Medicine, 122, 52-64.

NADEAU, J. A. 2002. Control of Stomatal Distribution on the Arabidopsis Leaf Surface. Science, 296.

NAFISI, M., GOREGAOKER, S., BOTANGA, C. J., GLAWISCHNIG, E., OLSEN, C. E., HALKIER, B. A. & GLAZEBROOK, J. 2007. Arabidopsis Cytochrome P450 Monooxygenase 71A13 Catalyzes the Conversion of Indole-3-Acetaldoxime in Camalexin Synthesis. The Plant Cell, 19.

NAKASHIMA, K., TAKASAKI, H., MIZOI, J., SHINOZAKI, K. & YAMAGUCHI-SHINOZAKI, K. 2012. NAC transcription factors in plant abiotic stress responses. Biochimica et Biophysica Acta (BBA) - Gene Regulatory Mechanisms, 1819.

NAKAYAMA, S. & KRETSINGER, R. H. 1994. Evolution of the EF-Hand Family of Proteins. Annual Review of Biophysics and Biomolecular Structure, 23, 473-507.

NAM, K. H. & LI, J. 2002. BRI1/BAK1, a Receptor Kinase Pair Mediating Brassinosteroid Signaling. Cell, 110.

NASTI, R. A. & VOYTAS, D. F. 2021. Attaining the promise of plant gene editing at scale. Proceedings of the National Academy of Sciences, 118.

NAVROT, N., ROUHIER, N., GELHAYE, E. & JACQUOT, J.-P. 2007. Reactive oxygen species generation and antioxidant systems in plant mitochondria. Physiologia Plantarum, 129, 185-195.

NEWTON, A. C., BOOTMAN, M. D. & SCOTT, J. D. 2016. Second Messengers. Cold Spring Harbor Perspectives in Biology, 8.

NGOU, B. P. M., AHN, H.-K., DING, P. & JONES, J. D. G. 2021. Mutual potentiation of plant immunity by cell-surface and intracellular receptors. Nature.

NGUYEN, H. T., SILVA, J. E., PODICHETI, R., MACRANDER, J., YANG, W., NAZARENUS, T. J., NAM, J.-W., JAWORSKI, J. G., LU, C., SCHEFFLER, B. E.,

MOCKAITIS, K. & CAHOON, E. B. 2013. Camelina seed transcriptome: a tool for meal and oil improvement and translational research. Plant Biotechnology Journal, 11.

NIEMINEN, K. M., KAUPPINEN, L. & HELARIUTTA, Y. 2004. A Weed for Wood? Arabidopsis as a Genetic Model for Xylem Development. Plant Physiology, 135.

NISHIZAWA, A., YABUTA, Y. & SHIGEOKA, S. 2008. Galactinol and Raffinose Constitute a Novel Function to Protect Plants from Oxidative Damage Plant Physiology, 147.

NOBUTA, K., OKRENT, R. A., STOUTEMYER, M., RODIBAUGH, N., KEMPEMA, L., WILDERMUTH, M. C. & INNES, R. W. 2007. The GH3 Acyl Adenylase Family Member PBS3 Regulates Salicylic Acid-Dependent Defense Responses in Arabidopsis. Plant Physiology, 144.

NOLEN, B., TAYLOR, S. & GHOSH, G. 2004. Regulation of Protein Kinases. Molecular Cell, 15, 661-675.

NOTAGUCHI, M. & OKAMOTO, S. 2015. Dynamics of long-distance signaling via plant vascular tissues. Frontiers in Plant Science, 6.

NURUZZAMAN, M., SHARONI, A. M. & KIKUCHI, S. 2013. Roles of NAC transcription factors in the regulation of biotic and abiotic stress responses in plants. Frontiers in Microbiology, 4.

OCHOA-VILLARREAL, M., AISPURO-HERNNDEZ, E., VARGAS-ARISPURO, I. & NGEL, M. 2012. Plant Cell Wall Polymers: Function, Structure and Biological Activity of Their Derivatives. Polymerization. InTech.

OEHLENSCHLÆGER, C. B., GERSBY, L. B. A., AHSAN, N., PEDERSEN, J. T., KRISTENSEN, A., SOLAKOVA, T. V., THELEN, J. J. & FUGLSANG, A. T. 2017. Activation of the LRR Receptor-Like Kinase PSY1R Requires Transphosphorylation of Residues in the Activation Loop. Frontiers in Plant Science, 8.

OH, M.-H., CLOUSE, S. D. & HUBER, S. C. 2009. Tyrosine phosphorylation in brassinosteroid signaling. Plant Signaling & Behavior, 4.

OH, M.-H., RAY, W. K., HUBER, S. C., ASARA, J. M., GAGE, D. A. & CLOUSE, S. D. 2000. Recombinant Brassinosteroid Insensitive 1 Receptor-Like Kinase Autophosphorylates on Serine and Threonine Residues and Phosphorylates a Conserved Peptide Motif in Vitro. Plant Physiology, 124.

OHTAKE, Y., TAKAHASHI, T. & KOMEDA, Y. 2000. Salicylic Acid Induces the Expression of a Number of Receptor-Like Kinase Genes in Arabidopsis thaliana. Plant and Cell Physiology, 41.

OLIVER, A. W., KNAPP, S. & PEARL, L. H. 2007. Activation segment exchange: a common mechanism of kinase autophosphorylation? Trends in Biochemical Sciences, 32.

OLSEN, A. N., ERNST, H. A., LEGGIO, L. L. & SKRIVER, K. 2005. NAC transcription factors: structurally distinct, functionally diverse. Trends in Plant Science, 10.

OÑATE-SÁNCHEZ, L. & SINGH, K. B. 2002. Identification of Arabidopsis Ethylene-Responsive Element Binding Factors with Distinct Induction Kinetics after Pathogen Infection. Plant Physiology, 128.

OPARKA, K. J. 1994. Plasmolysis: new insights into an old process. New Phytologist, 126.

OSAKABE, Y., MIZUNO, S., TANAKA, H., MARUYAMA, K., OSAKABE, K., TODAKA, D., FUJITA, Y., KOBAYASHI, M., SHINOZAKI, K. & YAMAGUCHI-SHINOZAKI, K. 2010. Overproduction of the Membrane-bound Receptor-like Protein Kinase 1, RPK1, Enhances Abiotic Stress Tolerance in Arabidopsis. Journal of Biological Chemistry, 285.

OUYANG, S.-Q., LIU, Y.-F., LIU, P., LEI, G., HE, S.-J., MA, B., ZHANG, W.-K., ZHANG, J.-S. & CHEN, S.-Y. 2010. Receptor-like kinase OsSIK1 improves drought and salt stress tolerance in rice (Oryza sativa) plants. The Plant Journal, 62.

PACY, J. Immunogold Labeling for Electron Microscopy. Animal Cell Culture. New Jersey: Humana Press.

PAGNUSSAT, G. C., YU, H.-J., NGO, Q. A., RAJANI, S., MAYALAGU, S., JOHNSON, C. S., CAPRON, A., XIE, L.-F., YE, D. & SUNDARESAN, V. 2005. Genetic and molecular identification of genes required for female gametophyte development and function in Arabidopsis. Development, 132.

PANDAY, A., SAHOO, M. K., OSORIO, D. & BATRA, S. 2015. NADPH oxidases: an overview from structure to innate immunity-associated pathologies. Cellular & Molecular Immunology, 12.

PARK, C.-J. & RONALD, P. C. 2012. Cleavage and nuclear localization of the rice XA21 immune receptor. Nature Communications, 3.

PARK, H.-Y., SEOK, H.-Y., WOO, D.-H., LEE, S.-Y., TARTE, V. N., LEE, E.-H., LEE, C.-H. & MOON, Y.-H. 2011. AtERF71/HRE2 transcription factor mediates osmotic stress response as well as hypoxia response in Arabidopsis. Biochemical and Biophysical Research Communications, 414.

PARRY, D. W., JENKINSON, P. & MCLEOD, L. 1995. Fusarium ear blight (scab) in small grain cereals?a review. Plant Pathology, 44.

PASSRICHA, N., SAIFI, S. K., KHARB, P. & TUTEJA, N. 2020. Rice lectin receptor-like kinase provides salinity tolerance by ion homeostasis. Biotechnology and Bioengineering, 117.

PAUL, K. 1990. Emerging patterns of organization at the plant cell surface. Journal of Cell Science, 96.

PAYNE, D. M., ROSSOMANDO, A. J., MARTINO, P., ERICKSON, A. K., HER, J. H., SHABANOWITZ, J., HUNT, D. F., WEBER, M. J. & STURGILL, T. W. 1991. Identification of the regulatory phosphorylation sites in pp42/mitogen-activated protein kinase (MAP kinase). The EMBO Journal, 10.

PEARCE, L. R., KOMANDER, D. & ALESSI, D. R. 2010. The nuts and bolts of AGC protein kinases. Nature Reviews Molecular Cell Biology, 11.

PEARLMAN, SAMUEL M., SERBER, Z. & FERRELL, JAMES E. 2011. A Mechanism for the Evolution of Phosphorylation Sites. Cell, 147.

PEDLEY, K. F. & MARTIN, G. B. 2005. Role of mitogen-activated protein kinases in plant immunity. Current Opinion in Plant Biology, 8.

PEÑA, M. J., ZHONG, R., ZHOU, G.-K., RICHARDSON, E. A., O'NEILL, M. A., DARVILL, A. G., YORK, W. S. & YE, Z.-H. 2007. Arabidopsis irregular xylem8 and irregular xylem9: Implications for the Complexity of Glucuronoxylan Biosynthesis. The Plant Cell, 19.

PENG, H., ZHAO, J. & NEFF, M. M. 2015. ATAF2 integrates Arabidopsis brassinosteroid inactivation and seedling photomorphogenesis. Development.

PEREZ-RIVEROL, Y., CSORDAS, A., BAI, J., BERNAL-LLINARES, M., HEWAPATHIRANA, S., KUNDU, D. J., INUGANTI, A., GRISS, J., MAYER, G., EISENACHER, M., PÉREZ, E., USZKOREIT, J., PFEUFFER, J., SACHSENBERG, T., YılMAZ, Ş., TIWARY, S., COX, J., AUDAIN, E., WALZER, M., JARNUCZAK, A. F., TERNENT, T., BRAZMA, A. & VIZCAÍNO, J. A. 2019. The PRIDE database and related tools and resources in 2019: improving support for quantification data. Nucleic Acids Research, 47.

PERSSON, S., CAFFALL, K. H., FRESHOUR, G., HILLEY, M. T., BAUER, S., POINDEXTER, P., HAHN, M. G., MOHNEN, D. & SOMERVILLE, C. 2007. The Arabidopsis irregular xylem8 Mutant Is Deficient in Glucuronoxylan and Homogalacturonan, Which Are Essential for Secondary Cell Wall Integrity. The Plant Cell, 19.

PETERSEN, M., BRODERSEN, P., NAESTED, H., ANDREASSON, E., LINDHART, U., JOHANSEN, B., NIELSEN, H. B., LACY, M., AUSTIN, M. J., PARKER, J. E., SHARMA, S. B., KLESSIG, D. F., MARTIENSSEN, R., MATTSSON, O., JENSEN, A. B. & MUNDY, J. 2000. Arabidopsis MAP Kinase 4 Negatively Regulates Systemic Acquired Resistance. Cell, 103.

PETTOLINO, F. A., WALSH, C., FINCHER, G. B. & BACIC, A. 2012. Determining the polysaccharide composition of plant cell walls. Nature Protocols, 7.

PHUKAN, U. J., JEENA, G. S. & SHUKLA, R. K. 2016. WRKY Transcription Factors: Molecular Regulation and Stress Responses in Plants. Frontiers in Plant Science, 7.

PIETERSE, C. M. J., VAN DER DOES, D., ZAMIOUDIS, C., LEON-REYES, A. & VAN WEES, S. C. M. 2012. Hormonal Modulation of Plant Immunity. Annual Review of Cell and Developmental Biology, 28.

POSAS, F. 1997. Osmotic Activation of the HOG MAPK Pathway via Ste11p MAPKKK: Scaffold Role of Pbs2p MAPKK. Science, 276, 1702-1705.

PROVART, N. J., ALONSO, J., ASSMANN, S. M., BERGMANN, D., BRADY, S. M., BRKLJACIC, J., BROWSE, J., CHAPPLE, C., COLOT, V., CUTLER, S., DANGL, J., EHRHARDT, D., FRIESNER, J. D., FROMMER, W. B., GROTEWOLD, E., MEYEROWITZ, E., NEMHAUSER, J., NORDBORG, M., PIKAARD, C., SHANKLIN, J., SOMERVILLE, C., STITT, M., TORII, K. U., WAESE, J., WAGNER, D. & MCCOURT, P. 2016. 50 years of Arabidopsis research: highlights and future directions. New Phytologist, 209.

QIU, J.-L., ZHOU, L., YUN, B.-W., NIELSEN, H. B., FIIL, B. K., PETERSEN, K., MACKINLAY, J., LOAKE, G. J., MUNDY, J. & MORRIS, P. C. 2008. Arabidopsis Mitogen-Activated Protein Kinase Kinases MKK1 and MKK2 Have Overlapping Functions in Defense Signaling Mediated by MEKK1, MPK4, and MKS1. Plant Physiology, 148.

QUEZADA, E.-H., GARCÍA, G.-X., ARTHIKALA, M.-K., MELAPPA, G., LARA, M. & NANJAREDDY, K. 2019. Cysteine-Rich Receptor-Like Kinase Gene Family Identification in the Phaseolus Genome and Comparative Analysis of Their Expression Profiles Specific to Mycorrhizal and Rhizobial Symbiosis. Genes, 10.

RAFFAELE, S., VAILLEAU, F., LÉGER, A., JOUBÈS, J. R. M., MIERSCH, O., HUARD, C., BLÉE, E., MONGRAND, S. B., DOMERGUE, F. D. R. & ROBY, D. 2008. A MYB Transcription Factor Regulates Very-Long-Chain Fatty Acid Biosynthesis for Activation of the Hypersensitive Cell Death Response in Arabidopsis The Plant Cell, 20.

RAGNI, L., NIEMINEN, K., PACHECO-VILLALOBOS, D., SIBOUT, R., SCHWECHHEIMER, C. & HARDTKE, C. S. 2011. Mobile Gibberellin Directly Stimulates Arabidopsis Hypocotyl Xylem Expansion. The Plant Cell, 23, 1322-1336.

RALPH, J., BUNZEL, M., MARITA, J. M., HATFIELD, R. D., LU, F., KIM, H., SCHATZ, P. F., GRABBER, J. H. & STEINHART, H. 2004. Peroxidase-dependent cross-linking reactions of p-hydroxycinnamates in plant cell walls. Phytochemistry Reviews, 3.

RASMUSSEN, M. W., ROUX, M., PETERSEN, M. & MUNDY, J. 2012. MAP Kinase Cascades in Arabidopsis Innate Immunity. Frontiers in Plant Science, 3.

RAVEN, P. H., EVERT, R. F. & EICHHORN, S. E. 1999. Biology of plants, New York, Freemand and Company.

RAYAPURAM, C., JENSEN, M. K., MAISER, F., SHANIR, J. V., HORNSHØJ, H., RUNG, J. H., GREGERSEN, P. L., SCHWEIZER, P., COLLINGE, D. B. & LYNGKJAER, M. F. 2012. Regulation of basal resistance by a powdery mildew-induced cysteine-rich receptor-like protein kinase in barley. Molecular Plant Pathology, 13, 135-147.

RAZA, A., RAZZAQ, A., MEHMOOD, S., ZOU, X., ZHANG, X., LV, Y. & XU, J. 2019. Impact of Climate Change on Crops Adaptation and Strategies to Tackle Its Outcome: A Review. Plants, 8.

REUSCHE, M., THOLE, K., JANZ, D., TRUSKINA, J., RINDFLEISCH, S., DRÜBERT, C., POLLE, A., LIPKA, V. & TEICHMANN, T. 2012. Verticillium Infection Triggers VASCULAR-RELATED NAC DOMAIN7–Dependent de Novo Xylem Formation and Enhances Drought Tolerance in Arabidopsis. The Plant Cell, 24.

REYNOLDS, E. S. 1963. THE USE OF LEAD CITRATE AT HIGH pH AS AN ELECTRON-OPAQUE STAIN IN ELECTRON MICROSCOPY. Journal of Cell Biology, 17.

RICACHENEVSKY, F. K., MENGUER, P. K. & SPEROTTO, R. A. 2013. kNACking on heaven's door: how important are NAC transcription factors for leaf senescence and Fe/Zn remobilization to seeds? Frontiers in Plant Science, 4.

RICHARDS, S. L., WILKINS, K. A., SWARBRECK, S. M., ANDERSON, A. A., HABIB, N., SMITH, A. G., MCAINSH, M. & DAVIES, J. M. 2015. The hydroxyl radical in plants: from seed to seed. Journal of Experimental Botany, 66.

RICHMOND, T. A. & SOMERVILLE, C. R. 2001. Integrative approaches to determining Csl function. Plant Cell Walls. Dordrecht: Springer Netherlands.

RIDLEY, B. L., O'NEILL, M. A. & MOHNEN, D. 2001. Pectins: structure, biosynthesis, and oligogalacturonide-related signaling. Phytochemistry, 57.

RIESGO-ESCOVAR, J. R., JENNI, M., FRITZ, A. & HAFEN, E. 1996. The Drosophila Jun-N-terminal kinase is required for cell morphogenesis but not for DJun-dependent cell fate specification in the eye. Genes & Development, 10.

RIETZ, S., STAMM, A., MALONEK, S., WAGNER, S., BECKER, D., MEDINA-ESCOBAR, N., CORINA VLOT, A., FEYS, B. J., NIEFIND, K. & PARKER, J. E. 2011. Different roles of Enhanced Disease Susceptibility1 (EDS1) bound to and dissociated from Phytoalexin Deficient4 (PAD4) in Arabidopsis immunity. New Phytologist, 191.

ROBARDS, A. W. & LUCAS, W. J. 1990. Plasmodesmata. Annual Review of Plant Physiology and Plant Molecular Biology, 41.

RODBELL, M. 1995. Signal transduction: Evolution of an idea. Bioscience Reports, 15, 117-133.

ROUX, M., SCHWESSINGER, B., ALBRECHT, C., CHINCHILLA, D., JONES, A., HOLTON, N., MALINOVSKY, F. G., TÖR, M., DE VRIES, S. & ZIPFEL, C. 2011. The Arabidopsis Leucine-Rich Repeat Receptor–Like Kinases BAK1/SERK3 and BKK1/SERK4 Are Required for Innate Immunity to Hemibiotrophic and Biotrophic Pathogens. The Plant Cell, 23.

RUDD, J. J. & FRANKLIN-TONG, V. E. 2001. Unravelling response-specificity in Ca ²⁺ signalling pathways in plant cells. New Phytologist, 151, 7-33.

RUSHTON, P. J., SOMSSICH, I. E., RINGLER, P. & SHEN, Q. J. 2010. WRKY transcription factors. Trends in Plant Science, 15.

RŮŽIČKA, K., URSACHE, R., HEJÁTKO, J. & HELARIUTTA, Y. 2015. Xylem development – from the cradle to the grave. New Phytologist, 207.

SAINTENAC, C., CAMBON, F., AOUINI, L., VERSTAPPEN, E., GHAFFARY, S. M. T., POUCET, T., MARANDE, W., BERGES, H., XU, S., JAOUANNET, M., FAVERY, B., ALASSIMONE, J., SÁNCHEZ-VALLET, A., FARIS, J., KEMA, G., ROBERT, O. &

LANGIN, T. 2021. A wheat cysteine-rich receptor-like kinase confers broad-spectrum resistance against Septoria tritici blotch. Nature Communications, 12, 433-433.

SANDERS, D., PELLOUX, J., BROWNLEE, C. & HARPER, J. F. 2002. Calcium at the Crossroads of Signaling. The Plant Cell, 14, S401-S417.

SANTIAGO, J., BRANDT, B., WILDHAGEN, M., HOHMANN, U., HOTHORN, L. A., BUTENKO, M. A. & HOTHORN, M. 2016. Mechanistic insight into a peptide hormone signaling complex mediating floral organ abscission. eLife, 5.

SANTIAGO, J., HENZLER, C. & HOTHORN, M. 2013. Molecular Mechanism for Plant Steroid Receptor Activation by Somatic Embryogenesis Co-Receptor Kinases. Science, 341.

SCARPECI, T. E., ZANOR, M. I., MUELLER-ROEBER, B. & VALLE, E. M. 2013. Overexpression of AtWRKY30 enhances abiotic stress tolerance during early growth stages in Arabidopsis thaliana. Plant Molecular Biology, 83, 265-277.

SCHELLER, H. V. & ULVSKOV, P. 2010. Hemicelluloses. Annual Review of Plant Biology, 61.

SCHENK, P. M., KAZAN, K., WILSON, I., ANDERSON, J. P., RICHMOND, T., SOMERVILLE, S. C. & MANNERS, J. M. 2000. Coordinated plant defense responses in Arabidopsis revealed by microarray analysis. Proceedings of the National Academy of Sciences, 97.

SCHLESSINGER, J. 1988. Signal transduction by allosteric receptor oligomerization. Trends in Biochemical Sciences, 13.

SCHLESSINGER, J. 2000. Cell Signaling by Receptor Tyrosine Kinases. Cell, 103, 211-225.

SCHMIDT, S. H., KNAPE, M. J., BOASSA, D., MUMDEY, N., KORNEV, A. P., ELLISMAN, M. H., TAYLOR, S. S. & HERBERG, F. W. 2019. The dynamic switch mechanism that leads to activation of LRRK2 is embedded in the DFGψ motif in the kinase domain. Proceedings of the National Academy of Sciences, 116.

SEIFERT, G. J. & BLAUKOPF, C. 2010. Irritable Walls: The Plant Extracellular Matrix and Signaling. Plant Physiology, 153.

SEO, P. J., LEE, A. K., XIANG, F. & PARK, C. M. 2008. Molecular and Functional Profiling of Arabidopsis Pathogenesis-Related Genes: Insights into Their Roles in Salt Response of Seed Germination. Plant and Cell Physiology, 49.

SHAH, J., KACHROO, P., NANDI, A. & KLESSIG, D. F. 2001. A recessive mutation in the Arabidopsis SSI2 gene confers SA- and NPR1-independent expression of PR genes and resistance against bacterial and oomycete pathogens. The Plant Journal, 25.

SHEN, L., ZHUANG, B., WU, Q., ZHANG, H., NIE, J., JING, W., YANG, L. & ZHANG, W. 2019. Phosphatidic acid promotes the activation and plasma membrane localization of MKK7 and MKK9 in response to salt stress. Plant Science, 287.

SHIBA, H., TAKAYAMA, S., IWANO, M., SHIMOSATO, H., FUNATO, M., NAKAGAWA, T., CHE, F.-S., SUZUKI, G., WATANABE, M., HINATA, K. & ISOGAI, A. 2001. A Pollen Coat Protein, SP11/SCR, Determines the Pollen S -Specificity in the Self-Incompatibility of Brassica Species. Plant Physiology, 125.

SHINOHARA, H., MORI, A., YASUE, N., SUMIDA, K. & MATSUBAYASHI, Y. 2016. Identification of three LRR-RKs involved in perception of root meristem growth factor in Arabidopsis. Proceedings of the National Academy of Sciences, 113.

SHINYA, T., YAMAGUCHI, K., DESAKI, Y., YAMADA, K., NARISAWA, T., KOBAYASHI, Y., MAEDA, K., SUZUKI, M., TANIMOTO, T., TAKEDA, J., NAKASHIMA, M., FUNAMA, R., NARUSAKA, M., NARUSAKA, Y., KAKU, H., KAWASAKI, T. & SHIBUYA, N. 2014.

Selective regulation of the chitin-induced defense response by the Arabidopsis receptor-like cytoplasmic kinase PBL27. The Plant Journal, 79.

SHIRANO, Y., KACHROO, P., SHAH, J. & KLESSIG, D. F. 2002. A Gain-of-Function Mutation in an Arabidopsis Toll Interleukin1 Receptor–Nucleotide Binding Site–Leucine-Rich Repeat Type R Gene Triggers Defense Responses and Results in Enhanced Disease Resistance. The Plant Cell, 14.

SHIU, S.-H. & BLEECKER, A. B. 2003. Expansion of the Receptor-Like Kinase/Pelle Gene Family and Receptor-Like Proteins in Arabidopsis. Plant Physiology, 132, 530-543.

SHIU, S.-H., KARLOWSKI, W. M., PAN, R., TZENG, Y.-H., MAYER, K. F. X. & LI, W.-H. 2004. Comparative Analysis of the Receptor-Like Kinase Family in Arabidopsis and Rice[W]. The Plant Cell, 16.

SHIU, S. H. & BLEECKER, A. B. 2001. Receptor-like kinases from Arabidopsis form a monophyletic gene family related to animal receptor kinases. Proceedings of the National Academy of Sciences, 98, 10763-10768.

SHOJI, T. & YUAN, L. 2021. ERF Gene Clusters: Working Together to Regulate Metabolism. Trends in Plant Science, 26.

SIBOUT, R., PLANTEGENET, S. & HARDTKE, C. S. 2008. Flowering as a Condition for Xylem Expansion in Arabidopsis Hypocotyl and Root. Current Biology, 18, 458-463.

SICHERI, F., MOAREFI, I. & KURIYAN, J. 1997. Crystal structure of the Src family tyrosine kinase Hck. Nature, 385.

SIEVERS, F., WILM, A., DINEEN, D., GIBSON, T. J., KARPLUS, K., LI, W., LOPEZ, R., MCWILLIAM, H., REMMERT, M., SÖDING, J., THOMPSON, J. D. & HIGGINS, D. G. 2011. Fast, scalable generation of high-quality protein multiple sequence alignments using Clustal Omega. Molecular Systems Biology, 7.

SIKORA, P., CHAWADE, A., LARSSON, M., OLSSON, J. & OLSSON, O. 2011. Mutagenesis as a Tool in Plant Genetics, Functional Genomics, and Breeding. International Journal of Plant Genomics, 2011.

SILVA-SANZANA, C., CELIZ-BALBOA, J., GARZO, E., MARCUS, S. E., PARRA-ROJAS, J. P., ROJAS, B., OLMEDO, P., RUBILAR, M. A., RIOS, I., CHORBADJIAN, R. A., FERERES, A., KNOX, P., SAEZ-AGUAYO, S. & BLANCO-HERRERA, F. 2019. Pectin Methylesterases Modulate Plant Homogalacturonan Status in Defenses against the Aphid Myzus persicae. The Plant Cell, 31.

SIMPSON, P. J., TANTITADAPITAK, C., REED, A. M., MATHER, O. C., BUNCE, C. M., WHITE, S. A. & RIDE, J. P. 2009. Characterization of Two Novel Aldo–Keto Reductases from Arabidopsis: Expression Patterns, Broad Substrate Specificity, and an Open Active-Site Structure Suggest a Role in Toxicant Metabolism Following Stress. Journal of Molecular Biology, 392.

SINGH, A. P. 1987. Fine Structure of Hydrolysed Primary Walls in Tracheary Elements of Petiolar Xylem in Eucalyptus delegatensis. Annals of Botany, 60.

SINGH, P., KUO, Y.-C., MISHRA, S., TSAI, C.-H., CHIEN, C.-C., CHEN, C.-W., DESCLOS-THEVENIAU, M., CHU, P.-W., SCHULZE, B., CHINCHILLA, D., BOLLER, T. & ZIMMERLI, L. 2012. The Lectin Receptor Kinase-VI.2 Is Required for Priming and Positively Regulates Arabidopsis Pattern-Triggered Immunity. The Plant Cell, 24.

SIVAGURU, M., EZAKI, B., HE, Z.-H., TONG, H., OSAWA, H., BALUŠKA, F. E., VOLKMANN, D. & MATSUMOTO, H. 2003. Aluminum-Induced Gene Expression and Protein Localization of a Cell Wall-Associated Receptor Kinase in Arabidopsis. Plant Physiology, 132.

SKIPSEY, M., KNIGHT, K. M., BRAZIER-HICKS, M., DIXON, D. P., STEEL, P. G. & EDWARDS, R. 2011. Xenobiotic Responsiveness of Arabidopsis thaliana to a Chemical Series Derived from a Herbicide Safener. Journal of Biological Chemistry, 286.

SMITH, R. A., SCHUETZ, M., ROACH, M., MANSFIELD, S. D., ELLIS, B. & SAMUELS, L. 2013. Neighboring Parenchyma Cells Contribute to Arabidopsis Xylem Lignification, while Lignification of Interfascicular Fibers Is Cell Autonomous. The Plant Cell, 25.

SODING, J. 2005. Protein homology detection by HMM-HMM comparison. Bioinformatics, 21.

SOMERVILLE, C. 2004. Toward a Systems Approach to Understanding Plant Cell Walls. Science, 306.

SONG, W.-Y., CHOI, K. S., KIM, D. Y., GEISLER, M., PARK, J., VINCENZETTI, V., SCHELLENBERG, M., KIM, S. H., LIM, Y. P., NOH, E. W., LEE, Y. & MARTINOIA, E. 2010. Arabidopsis PCR2 Is a Zinc Exporter Involved in Both Zinc Extrusion and Long-Distance Zinc Transport. The Plant Cell, 22.

SONG, W. Y., WANG, G. L., CHEN, L. L., KIM, H. S., PI, L. Y., HOLSTEN, T., GARDNER, J., WANG, B., ZHAI, W. X., ZHU, L. H., FAUQUET, C. & RONALD, P. 1995. A Receptor Kinase-Like Protein Encoded by the Rice Disease Resistance Gene, Xa21. Science, 270.

SOUKUP, A. 2014. Selected Simple Methods of Plant Cell Wall Histochemistry and Staining for Light Microscopy.

SPARKES, I. A., RUNIONS, J., KEARNS, A. & HAWES, C. 2006. Rapid, transient expression of fluorescent fusion proteins in tobacco plants and generation of stably transformed plants. Nature Protocols, 1.

SPOEL, S. H., JOHNSON, J. S. & DONG, X. 2007. Regulation of tradeoffs between plant defenses against pathogens with different lifestyles. Proceedings of the National Academy of Sciences, 104.

SPOEL, S. H., KOORNNEEF, A., CLAESSENS, S. M. C., KORZELIUS, J. P., VAN PELT, J. A., MUELLER, M. J., BUCHALA, A. J., MÉTRAUX, J.-P., BROWN, R., KAZAN, K., VAN LOON, L. C., DONG, X. & PIETERSE, C. M. J. 2003. NPR1 Modulates Cross-Talk between Salicylate- and Jasmonate-Dependent Defense Pathways through a Novel Function in the Cytosol. The Plant Cell, 15.

STAHL, Y., WINK, R. H., INGRAM, G. C. & SIMON, R. 2009. A Signaling Module Controlling the Stem Cell Niche in Arabidopsis Root Meristems. Current Biology, 19.

STEBER, C. M., COONEY, S. E. & MCCOURT, P. 1998. Isolation of the GA-response mutant sly1 as a suppressor of ABI1-1 in Arabidopsis thaliana. Genetics, 509-521.

STEPHENS, P., EDKINS, S., DAVIES, H., GREENMAN, C., COX, C., HUNTER, C., BIGNELL, G., TEAGUE, J., SMITH, R., STEVENS, C., O'MEARA, S., PARKER, A., TARPEY, P., AVIS, T., BARTHORPE, A., BRACKENBURY, L., BUCK, G., BUTLER, A., CLEMENTS, J., COLE, J., DICKS, E., EDWARDS, K., FORBES, S., GORTON, M., GRAY, K., HALLIDAY, K., HARRISON, R., HILLS, K., HINTON, J., JONES, D., KOSMIDOU, V., LAMAN, R., LUGG, R., MENZIES, A., PERRY, J., PETTY, R., RAINE, K., SHEPHERD, R., SMALL, A., SOLOMON, H., STEPHENS, Y., TOFTS, C., VARIAN, J., WEBB, A., WEST, S., WIDAA, S., YATES, A., BRASSEUR, F., COOPER, C. S., FLANAGAN, A. M., GREEN, A., KNOWLES, M., LEUNG, S. Y., LOOIJENGA, L. H. J., MALKOWICZ, B., PIEROTTI, M. A., TEH, B., YUEN, S. T., NICHOLSON, A. G., LAKHANI, S., EASTON, D. F., WEBER, B. L., STRATTON, M. R., FUTREAL, P. A. & WOOSTER, R. 2005. A screen of the complete protein kinase gene family identifies diverse patterns of somatic mutations in human breast cancer. Nature Genetics, 37.

STOTZ, H. U., SAWADA, Y., SHIMADA, Y., HIRAI, M. Y., SASAKI, E., KRISCHKE, M., BROWN, P. D., SAITO, K. & KAMIYA, Y. 2011. Role of camalexin, indole glucosinolates, and side chain modification of glucosinolate-derived isothiocyanates in defense of Arabidopsis against Sclerotinia sclerotiorum. The Plant Journal, 67, 81-93.

STREHLER, E. & TREIMAN, M. 2004. Calcium Pumps of Plasma Membrane and Cell Interior. Current Molecular Medicine, 4, 323-335.

SU, S.-H., SUAREZ-RODRIGUEZ, M. C. & KRYSAN, P. 2007. Genetic interaction and phenotypic analysis of the Arabidopsis MAP kinase pathway mutations mekk1 and mpk4 suggests signaling pathway complexity. FEBS Letters, 581.

SUHARSONO, U., FUJISAWA, Y., KAWASAKI, T., IWASAKI, Y., SATOH, H. & SHIMAMOTO, K. 2002. The heterotrimeric G protein subunit acts upstream of the small GTPase Rac in disease resistance of rice. Proceedings of the National Academy of Sciences, 99.

SUN, M., QIAN, X., CHEN, C., CHENG, S., JIA, B., ZHU, Y. & SUN, X. 2018. Ectopic Expression of GsSRK in Medicago sativa Reveals Its Involvement in Plant Architecture and Salt Stress Responses. Frontiers in Plant Science, 9.

SUN, X.-L., YU, Q.-Y., TANG, L.-L., JI, W., BAI, X., CAI, H., LIU, X.-F., DING, X.-D. & ZHU, Y.-M. 2013a. GsSRK, a G-type lectin S-receptor-like serine/threonine protein kinase, is a positive regulator of plant tolerance to salt stress. Journal of Plant Physiology, 170, 505-515.

SUN, Y., LI, L., MACHO, A. P., HAN, Z., HU, Z., ZIPFEL, C., ZHOU, J. M. & CHAI, J. 2013b. Structural Basis for flg22-Induced Activation of the Arabidopsis FLS2-BAK1 Immune Complex. Science, 342.

SUN, Y., QIAO, Z., MUCHERO, W. & CHEN, J.-G. 2020. Lectin Receptor-Like Kinases: The Sensor and Mediator at the Plant Cell Surface. Frontiers in Plant Science, 11.

SUTTON, J. C. 1982. Epidemiology of wheat head blight and maize ear rot caused by Fusarium graminearum. Canadian Journal of Plant Pathology, 4.

SZEKERES, M., NÉMETH, K., KONCZ-KÁLMÁN, Z., MATHUR, J., KAUSCHMANN, A., ALTMANN, T., RÉDEI, G. P., NAGY, F., SCHELL, J. & KONCZ, C. 1996. Brassinosteroids Rescue the Deficiency of CYP90, a Cytochrome P450, Controlling Cell Elongation and De-etiolation in Arabidopsis. Cell, 85.

SZYJANOWICZ, P. M. J., MCKINNON, I., TAYLOR, N. G., GARDINER, J., JARVIS, M. C. & TURNER, S. R. 2004. The irregular xylem 2 mutant is an allele of korrigan that affects the secondary cell wall of Arabidopsis thaliana. The Plant Journal, 37.

TAKAHASHI, F., MIZOGUCHI, T., YOSHIDA, R., ICHIMURA, K. & SHINOZAKI, K. 2011. Calmodulin-Dependent Activation of MAP Kinase for ROS Homeostasis in Arabidopsis. Molecular Cell, 41.

TAKAHASHI, S. & MURATA, N. 2008. How do environmental stresses accelerate photoinhibition? Trends in Plant Science, 13.

TAKAI, R., ISOGAI, A., TAKAYAMA, S. & CHE, F.-S. 2008. Analysis of Flagellin Perception Mediated by flg22 Receptor OsFLS2 in Rice. Molecular Plant-Microbe Interactions®, 21.

TAMIRAT, M. Z., KOIVU, M., ELENIUS, K. & JOHNSON, M. S. 2019. Structural characterization of EGFR exon 19 deletion mutation using molecular dynamics simulation. PLOS ONE, 14.

TANAKA, H., OSAKABE, Y., KATSURA, S., MIZUNO, S., MARUYAMA, K., KUSAKABE, K., MIZOI, J., SHINOZAKI, K. & YAMAGUCHI-SHINOZAKI, K. 2012. Abiotic stress-inducible receptor-like kinases negatively control ABA signaling in Arabidopsis. The Plant Journal, 70, 599-613.

TARASOV, D., LEITCH, M. & FATEHI, P. 2018. Lignin–carbohydrate complexes: properties, applications, analyses, and methods of extraction: a review. Biotechnology for Biofuels, 11.

TAYLOR, I., SEITZ, K., BENNEWITZ, S. & WALKER, J. C. 2013. A simple in vitro method to measure autophosphorylation of protein kinases. Plant Methods, 9, 22-22.

TAYLOR, I., WANG, Y., SEITZ, K., BAER, J., BENNEWITZ, S., MOONEY, B. P. & WALKER, J. C. 2016. Analysis of Phosphorylation of the Receptor-Like Protein Kinase HAESA during Arabidopsis Floral Abscission. PLOS ONE, 11.

TAYLOR, N. G., HOWELLS, R. M., HUTTLY, A. K., VICKERS, K. & TURNER, S. R. 2003. Interactions among three distinct CesA proteins essential for cellulose synthesis. Proceedings of the National Academy of Sciences, 100, 1450-1455.

TAYLOR, S. S., KESHWANI, M. M., STEICHEN, J. M. & KORNEV, A. P. 2012. Evolution of the eukaryotic protein kinases as dynamic molecular switches. Philosophical Transactions of the Royal Society B: Biological Sciences, 367.

TAYLOR, S. S., SHAW, A. S., KANNAN, N. & KORNEV, A. P. 2015. Integration of signaling in the kinome: Architecture and regulation of the αC Helix. Biochimica et Biophysica Acta (BBA) - Proteins and Proteomics, 1854, 1567-1574.

TEIGE, M., SCHEIKL, E., EULGEM, T., DÓCZI, R., ICHIMURA, K., SHINOZAKI, K., DANGL, J. L. & HIRT, H. 2004. The MKK2 Pathway Mediates Cold and Salt Stress Signaling in Arabidopsis. Molecular Cell, 15.

TERRETT, O. M. & DUPREE, P. 2019. Covalent interactions between lignin and hemicelluloses in plant secondary cell walls. Current Opinion in Biotechnology, 56.

THALER, J. S., HUMPHREY, P. T. & WHITEMAN, N. K. 2012. Evolution of jasmonate and salicylate signal crosstalk. Trends in Plant Science, 17.

THATCHER, L. F., MANNERS, J. M. & KAZAN, K. 2009. Fusarium oxysporum hijacks COI1-mediated jasmonate signaling to promote disease development in Arabidopsis. The Plant Journal, 58, 927-939.

THOMAS, C. L., BAYER, E. M., RITZENTHALER, C., FERNANDEZ-CALVINO, L. & MAULE, A. J. 2008. Specific Targeting of a Plasmodesmal Protein Affecting Cell-to-Cell Communication. PLoS Biology, 6.

THOMMA, B. P. H. J., EGGERMONT, K., PENNINCKX, I. A. M. A., MAUCH-MANI, B., VOGELSANG, R., CAMMUE, B. P. A. & BROEKAERT, W. F. 1998. Separate jasmonate-dependent and salicylate-dependent defense-response pathways in Arabidopsis are essential for resistance to distinct microbial pathogens. Proceedings of the National Academy of Sciences, 95.

THOMMA, B. P. H. J., NÜRNBERGER, T. & JOOSTEN, M. H. A. J. 2011. Of PAMPs and Effectors: The Blurred PTI-ETI Dichotomy. The Plant Cell, 23.

TIAN, T., LIU, Y., YAN, H., YOU, Q., YI, X., DU, Z., XU, W. & SU, Z. 2017. agriGO v2.0: a GO analysis toolkit for the agricultural community, 2017 update. Nucleic Acids Research, 45.

TIMELL, T. E. 1967. Recent progress in the chemistry of wood hemicelluloses. Wood Science and Technology, 1.

TOKUNAGA, N., KANETA, T., SATO, S. & SATO, Y. 2009. Analysis of expression profiles of three peroxidase genes associated with lignification in Arabidopsis thaliana. Physiologia Plantarum, 136.

TOR, M., LOTZE, M. T. & HOLTON, N. 2009. Receptor-mediated signalling in plants: molecular patterns and programmes. Journal of Experimental Botany, 60, 3645-3654.

TORRES, M. A. & DANGL, J. L. 2005. Functions of the respiratory burst oxidase in biotic interactions, abiotic stress and development. Current Opinion in Plant Biology, 8.

TRDÁ, L., BOUTROT, F., CLAVERIE, J., BRULÉ, D., DOREY, S. & POINSSOT, B. 2015. Perception of pathogenic or beneficial bacteria and their evasion of host immunity: pattern recognition receptors in the frontline. Frontiers in Plant Science, 6.

TRUSOV, Y., ROOKES, J. E., CHAKRAVORTY, D., ARMOUR, D., SCHENK, P. M. & BOTELLA, J. R. N. 2006. Heterotrimeric G Proteins Facilitate Arabidopsis Resistance to Necrotrophic Pathogens and Are Involved in Jasmonate Signaling. Plant Physiology, 140, 210-220.

TSUDA, K. & SOMSSICH, I. E. 2015. Transcriptional networks in plant immunity. New Phytologist, 206.

TURNBULL, C. G. N., BOOKER, J. P. & LEYSER, H. M. O. 2002. Micrografting techniques for testing long-distance signalling in Arabidopsis. The Plant Journal, 32.

TURNER, S. R. & SOMERVILLE, C. R. 1997. Collapsed xylem phenotype of Arabidopsis identifies mutants deficient in cellulose deposition in the secondary cell wall. The Plant Cell, 9.

TUTEJA, N. 2007. Abscisic Acid and Abiotic Stress Signaling. Plant Signaling & Behavior, 2.

TUTEJA, N. 2009. Signaling through G protein coupled receptors. Plant Signaling & Behavior, 4, 942-947.

TUTEJA, N. & MAHAJAN, S. 2007. Calcium Signaling Network in Plants. Plant Signaling & Behavior, 2, 79-85.

ULLAH, H., CHEN, J.-G., WANG, S. & JONES, A. M. 2002. Role of a Heterotrimeric G Protein in Regulation of Arabidopsis Seed Germination. Plant Physiology, 129.

UNDERWOOD, W. 2012. The Plant Cell Wall: A Dynamic Barrier Against Pathogen Invasion. Frontiers in Plant Science, 3.

UPDEGRAFF, D. M. 1969. Semimicro determination of cellulose inbiological materials. Analytical Biochemistry, 32.

URANO, D., CHEN, J.-G., BOTELLA, J. R. & JONES, A. M. 2013. Heterotrimeric G protein signalling in the plant kingdom. Open Biology, 3, 120186-120186.

URANO, D. & JONES, A. M. 2014. Heterotrimeric G Protein–Coupled Signaling in Plants. Annual Review of Plant Biology, 65.

VAAHTERA, L., SCHULZ, J. & HAMANN, T. 2019. Cell wall integrity maintenance during plant development and interaction with the environment. Nature Plants, 5, 924-932.

VAATTOVAARA, A., BRANDT, B., RAJARAMAN, S., SAFRONOV, O., VEIDENBERG, A., LUKLOVÁ, M., KANGASJÄRVI, J., LÖYTYNOJA, A., HOTHORN, M., SALOJÄRVI, J. & WRZACZEK, M. 2019. Mechanistic insights into the evolution of DUF26-containing proteins in land plants. Communications Biology, 2, 56-56.

VAID, N., MACOVEI, A. & TUTEJA, N. 2013. Knights in Action: Lectin Receptor-Like Kinases in Plant Development and Stress Responses. Molecular Plant, 6.

VAID, N., PANDEY, P. K. & TUTEJA, N. 2012. Genome-wide analysis of lectin receptor-like kinase family from Arabidopsis and rice. Plant Molecular Biology, 80.

VAN WERSCH, R., LI, X. & ZHANG, Y. 2016. Mighty Dwarfs: Arabidopsis Autoimmune Mutants and Their Usages in Genetic Dissection of Plant Immunity. Frontiers in Plant Science, 7.

VENUGOPAL, S. C., JEONG, R.-D., MANDAL, M. K., ZHU, S., CHANDRA-SHEKARA, A. C., XIA, Y., HERSH, M., STROMBERG, A. J., NAVARRE, D., KACHROO, A. & KACHROO, P. 2009. Enhanced Disease Susceptibility 1 and Salicylic Acid Act Redundantly to Regulate Resistance Gene-Mediated Signaling. PLoS Genetics, 5.

VERHERTBRUGGEN, Y., WALKER, J. L., GUILLON, F. & SCHELLER, H. V. 2017. A Comparative Study of Sample Preparation for Staining and Immunodetection of Plant Cell Walls by Light Microscopy. Frontiers in Plant Science, 8.

VERMA, V., RAVINDRAN, P. & KUMAR, P. P. 2016. Plant hormone-mediated regulation of stress responses. BMC Plant Biology, 16.

VIJAYAN, P., SHOCKEY, J., LEVESQUE, C. A., COOK, R. J. & BROWSE, J. 1998. A role for jasmonate in pathogen defense of Arabidopsis. Proceedings of the National Academy of Sciences, 95.

WALIA, A., LEE, J. S., WASTENEYS, G. & ELLIS, B. 2009. Arabidopsis mitogen-activated protein kinase MPK18 mediates cortical microtubule functions in plant cells. The Plant Journal, 59.

WALTER, S., NICHOLSON, P. & DOOHAN, F. M. 2010. Action and reaction of host and pathogen during Fusarium head blight disease. New Phytologist, 185.

WANG, H., NGWENYAMA, N., LIU, Y., WALKER, J. C. & ZHANG, S. 2007. Stomatal Development and Patterning Are Regulated by Environmentally Responsive Mitogen-Activated Protein Kinases in Arabidopsis. The Plant Cell, 19.

WANG, X., GOSHE, M. B., SODERBLOM, E. J., PHINNEY, B. S., KUCHAR, J. A., LI, J., ASAMI, T., YOSHIDA, S., HUBER, S. C. & CLOUSE, S. D. 2005. Identification and Functional Analysis of in Vivo Phosphorylation Sites of the Arabidopsis BRASSINOSTEROID-INSENSITIVE1 Receptor Kinase. The Plant Cell, 17, 1685-1703.

WANG, X., KOTA, U., HE, K., BLACKBURN, K., LI, J., GOSHE, M. B., HUBER, S. C. & CLOUSE, S. D. 2008. Sequential Transphosphorylation of the BRI1/BAK1 Receptor Kinase Complex Impacts Early Events in Brassinosteroid Signaling. Developmental Cell, 15, 220-235.

WANG, X. E., BASNAYAKE, B. M. V. S., ZHANG, H., LI, G., LI, W., VIRK, N., MENGISTE, T. & SONG, F. 2009. The Arabidopsis ATAF1, a NAC Transcription Factor, Is a Negative Regulator of Defense Responses Against Necrotrophic Fungal and Bacterial Pathogens. Molecular Plant-Microbe Interactions®, 22.

WANG, Y., CHANTREAU, M., SIBOUT, R. & HAWKINS, S. 2013. Plant cell wall lignification and monolignol metabolism. Frontiers in Plant Science, 4.

WANG, Z. & GOU, X. 2020. Receptor-Like Protein Kinases Function Upstream of MAPKs in Regulating Plant Development. International Journal of Molecular Sciences, 21, 7638-7638.

WATANABE, T. & KOSHIJIMA, T. 1988. Evidence for an Ester Linkage between Lignin and Glucuronic Acid in Lignin–Carbohydrate Complexes by DDQ-Oxidation. Agricultural and Biological Chemistry, 52.

WEGENER, A. D. & JONES, L. R. 1984. Phosphorylation-induced mobility shift in phospholamban in sodium dodecyl sulfate-polyacrylamide gels. Evidence for a protein structure consisting of multiple identical phosphorylatable subunits. Journal of Biological Chemistry, 259.

WEIGEL, R. R., BÄUSCHER, C., PFITZNER, A. J. P. & PFITZNER, U. M. 2001. NIMIN-1, NIMIN-2 and NIMIN-3, members of a novel family of proteins from Arabidopsis that interact with NPR1/NIM1, a key regulator of systemic acquired resistance in plants. Plant Molecular Biology, 46.

WEIR, C. J. 2020. Ion channels, receptors, agonists and antagonists. Anaesthesia & Intensive Care Medicine, 21, 62-68.

WHITMARSH, A. J. & DAVIS, R. J. 1998. Structural organization of MAP-kinase signaling modules by scaffold proteins in yeast and mammals. Trends in Biochemical Sciences, 23.

WIDMANN, C., GIBSON, S., JARPE, M. B. & JOHNSON, G. L. 1999. Mitogen-Activated Protein Kinase: Conservation of a Three-Kinase Module From Yeast to Human. Physiological Reviews, 79.

WINTERBOURN, C. C. 2008. Reconciling the chemistry and biology of reactive oxygen species. Nature Chemical Biology, 4.

WOLF, S., MOUILLE, G. & PELLOUX, J. 2009. Homogalacturonan Methyl-Esterification and Plant Development. Molecular Plant, 2.

WU, A.-M., RIHOUEY, C., SEVENO, M., HÖRNBLAD, E., SINGH, S. K., MATSUNAGA, T., ISHII, T., LEROUGE, P. & MARCHANT, A. 2009a. The Arabidopsis IRX10 and IRX10-LIKE glycosyltransferases are critical for glucuronoxylan biosynthesis during secondary cell wall formation. The Plant Journal, 57.

WU, F., SHENG, P., TAN, J., CHEN, X., LU, G., MA, W., HENG, Y., LIN, Q., ZHU, S., WANG, J., WANG, J., GUO, X., ZHANG, X., LEI, C. & WAN, J. 2015. Plasma membrane receptor-like kinase leaf panicle 2 acts downstream of the DROUGHT AND SALT TOLERANCE transcription factor to regulate drought sensitivity in rice. Journal of Experimental Botany, 66.

WU, S., SHAN, L. & HE, P. 2014. Microbial signature-triggered plant defense responses and early signaling mechanisms. Plant Science, 228.

WU, X., OH, M.-H., KIM, H. S., SCHWARTZ, D., IMAI, B. S., YAU, P. M., CLOUSE, S. D. & HUBER, S. C. 2012. Transphosphorylation of E. coli Proteins during Production of Recombinant Protein Kinases Provides a Robust System to Characterize Kinase Specificity. Frontiers in Plant Science, 3.

WU, Y., DENG, Z., LAI, J., ZHANG, Y., YANG, C., YIN, B., ZHAO, Q., ZHANG, L., LI, Y., YANG, C. & XIE, Q. 2009b. Dual function of Arabidopsis ATAF1 in abiotic and biotic stress responses. Cell Research, 19.

XIA, X.-J., ZHOU, Y.-H., SHI, K., ZHOU, J., FOYER, C. H. & YU, J.-Q. 2015. Interplay between reactive oxygen species and hormones in the control of plant development and stress tolerance. Journal of Experimental Botany, 66, 2839-2856.

XING, Y., JIA, W. & ZHANG, J. 2009. AtMKK1 and AtMPK6 are involved in abscisic acid and sugar signaling in Arabidopsis seed germination. Plant Molecular Biology, 70.

XU, D., DHIMAN, R., GARIBAY, A., MOCK, H. P., LEISTER, D. & KLEINE, T. 2020. Cellulose defects in the Arabidopsis secondary cell wall promote early chloroplast development. The Plant Journal, 101.

XU, W., HARRISON, S. C. & ECK, M. J. 1997. Three-dimensional structure of the tyrosine kinase c-Src. Nature, 385.

YADETA, K. A., ELMORE, J. M., CREER, A. Y., FENG, B., FRANCO, J. Y., RUFIAN, J. S., HE, P., PHINNEY, B. & COAKER, G. 2017. A Cysteine-Rich Protein Kinase Associates with a Membrane Immune Complex and the Cysteine Residues Are Required for Cell Death. Plant Physiology, 173, 771-787.

YADETA, K. A. & J. THOMMA, B. P. H. 2013. The xylem as battleground for plant hosts and vascular wilt pathogens. Frontiers in Plant Science, 4.

YAMAGUCHI, M., KUBO, M., FUKUDA, H. & DEMURA, T. 2008. VASCULAR-RELATED NAC-DOMAIN7 is involved in the differentiation of all types of xylem vessels in Arabidopsis roots and shoots. The Plant Journal, 55.

YAMAGUCHI, Y., PEARCE, G. & RYAN, C. A. 2006. The cell surface leucine-rich repeat receptor for AtPep1, an endogenous peptide elicitor in Arabidopsis, is functional in transgenic tobacco cells. Proceedings of the National Academy of Sciences, 103.

YAN, L., MA, Y., LIU, D., WEI, X., SUN, Y., CHEN, X., ZHAO, H., ZHOU, J., WANG, Z., SHUI, W. & LOU, Z. 2012. Structural basis for the impact of phosphorylation on the activation of plant receptor-like kinase BAK1. Cell Research, 22.

YANG, C., XU, Z., SONG, J., CONNER, K., VIZCAY BARRENA, G. & WILSON, Z. A. 2007. Arabidopsis MYB26/MALE STERILE35 Regulates Secondary Thickening in the Endothecium and Is Essential for Anther Dehiscence. The Plant Cell, 19.

YANG, J., CRON, P., THOMPSON, V., GOOD, V. M., HESS, D., HEMMINGS, B. A. & BARFORD, D. 2002. Molecular Mechanism for the Regulation of Protein Kinase B/Akt by Hydrophobic Motif Phosphorylation. Molecular Cell, 9.

YANG, K., RONG, W., QI, L., LI, J., WEI, X. & ZHANG, Z. 2013. Isolation and characterization of a novel wheat cysteine-rich receptor-like kinase gene induced by Rhizoctonia cerealis. Scientific Reports, 3, 3021-3021.

YANG, T., CHAUDHURI, S., YANG, L., DU, L. & POOVAIAH, B. W. 2010. A Calcium/Calmodulin-regulated Member of the Receptor-like Kinase Family Confers Cold Tolerance in Plants. Journal of Biological Chemistry, 285.

YANG, Y., LABBÉ, J., MUCHERO, W., YANG, X., JAWDY, S. S., KENNEDY, M., JOHNSON, J., SREEDASYAM, A., SCHMUTZ, J., TUSKAN, G. A. & CHEN, J.-G. 2016. Genome-wide analysis of lectin receptor-like kinases in Populus. BMC Genomics, 17.

YANG, Y., SHAH, J. & KLESSIG, D. F. 1997. Signal perception and transduction in plant defense responses. Genes & Development, 11, 1621-1639.

YANG, Y., ZHANG, Y., DING, P., JOHNSON, K., LI, X. & ZHANG, Y. 2012. The Ankyrin-Repeat Transmembrane Protein BDA1 Functions Downstream of the Receptor-Like Protein SNC2 to Regulate Plant Immunity. Plant Physiology, 159.

YAYON, A., KLAGSBRUN, M., ESKO, J. D., LEDER, P. & ORNITZ, D. M. 1991. Cell surface, heparin-like molecules are required for binding of basic fibroblast growth factor to its high affinity receptor. Cell, 64.

YE, L., LIU, L., XING, A. & KANG, D. 2013. Characterization of a dwarf mutant allele of Arabidopsis MDR-like ABC transporter AtPGP1 gene. Biochemical and Biophysical Research Communications, 441.

YE, Y., DING, Y., JIANG, Q., WANG, F., SUN, J. & ZHU, C. 2017. The role of receptor-like protein kinases (RLKs) in abiotic stress response in plants. Plant Cell Reports, 36, 235-242.

YE, Z.-H. 2002. VASCULAR TISSUE DIFFERENTIATION AND PATTERN FORMATION IN PLANTS. Annual Review of Plant Biology, 53.

YEH, Y.-H., CHANG, Y.-H., HUANG, P.-Y., HUANG, J.-B. & ZIMMERLI, L. 2015. Enhanced Arabidopsis pattern-triggered immunity by overexpression of cysteine-rich receptor-like kinases. Frontiers in Plant Science, 6.

YEUNG, E. C. 1998. A Beginner's Guide to the Study of Plant Structure. In: KARCHER, S. J. (ed.) Tested studies for laboratory teaching.

YORK, W. & ONEILL, M. 2008. Biochemical control of xylan biosynthesis — which end is up? Current Opinion in Plant Biology, 11.

YU, D., ZHANG, J., TAN, G., YU, N., WANG, Q., DUAN, Q., QI, X., CHENG, M., YAN, C., WEI, Z., YU, Z., HUANG, W. & LI, C. 2019. An easily-performed high-throughput method for plant genomic DNA extraction. Analytical Biochemistry, 569.

YUAN, M., JIANG, Z., BI, G., NOMURA, K., LIU, M., WANG, Y., CAI, B., ZHOU, J.-M., HE, S. Y. & XIN, X.-F. 2021. Pattern-recognition receptors are required for NLR-mediated plant immunity. Nature.

YUAN, Y., TENG, Q., ZHONG, R. & YE, Z.-H. 2013. The Arabidopsis DUF231 Domain-Containing Protein ESK1 Mediates 2-O- and 3-O-Acetylation of Xylosyl Residues in Xylan. Plant and Cell Physiology, 54.

ZHANG, X., GUREASKO, J., SHEN, K., COLE, P. A. & KURIYAN, J. 2006. An Allosteric Mechanism for Activation of the Kinase Domain of Epidermal Growth Factor Receptor. Cell, 125, 1137-1149.

ZHANG, X., HAN, X., SHI, R., YANG, G., QI, L., WANG, R. & LI, G. 2013a. Arabidopsis cysteine-rich receptor-like kinase 45 positively regulates disease resistance to Pseudomonas syringae. Plant Physiology and Biochemistry, 73, 383-391.

ZHANG, X., YANG, G., SHI, R., HAN, X., QI, L., WANG, R., XIONG, L. & LI, G. 2013b. Arabidopsis cysteine-rich receptor-like kinase 45 functions in the responses to abscisic acid and abiotic stresses. Plant Physiology and Biochemistry, 67.

ZHANG, Y., FAN, W., KINKEMA, M., LI, X. & DONG, X. 1999. Interaction of NPR1 with basic leucine zipper protein transcription factors that bind sequences required for salicylic acid induction of the PR-1 gene. Proceedings of the National Academy of Sciences, 96.

ZHANG, Y., MASSEL, K., GODWIN, I. D. & GAO, C. 2018. Applications and potential of genome editing in crop improvement. Genome Biology, 19.

ZHANG, Z., WU, Y., GAO, M., ZHANG, J., KONG, Q., LIU, Y., BA, H., ZHOU, J. & ZHANG, Y. 2012. Disruption of PAMP-Induced MAP Kinase Cascade by a Pseudomonas syringae Effector Activates Plant Immunity Mediated by the NB-LRR Protein SUMM2. Cell Host & Microbe, 11.

ZHAO, C., NIE, H., SHEN, Q., ZHANG, S., LUKOWITZ, W. & TANG, D. 2014. EDR1 Physically Interacts with MKK4/MKK5 and Negatively Regulates a MAP Kinase Cascade to Modulate Plant Innate Immunity. PLoS Genetics, 10.

ZHAO, Q., NAKASHIMA, J., CHEN, F., YIN, Y., FU, C., YUN, J., SHAO, H., WANG, X., WANG, Z.-Y. & DIXON, R. A. 2013. LACCASE Is Necessary and Nonredundant with PEROXIDASE for Lignin Polymerization during Vascular Development in Arabidopsis. The Plant Cell, 25.

ZHONG, R., CUI, D. & YE, Z. H. 2018. Secondary cell wall biosynthesis. New Phytologist, 221, 1703-1723.

ZHONG, R., LEE, C. & YE, Z.-H. 2010. Evolutionary conservation of the transcriptional network regulating secondary cell wall biosynthesis. Trends in Plant Science, 15.

ZHONG, R., PEÑA, M. J., ZHOU, G.-K., NAIRN, C. J., WOOD-JONES, A., RICHARDSON, E. A., MORRISON, W. H., DARVILL, A. G., YORK, W. S. & YE, Z.-H. 2005. Arabidopsis Fragile Fiber8, Which Encodes a Putative Glucuronyltransferase, Is Essential for Normal Secondary Wall Synthesis. The Plant Cell, 17.

ZHONG, R. & YE, Z.-H. 2015a. The Arabidopsis NAC transcription factor NST2 functions together with SND1 and NST1 to regulate secondary wall biosynthesis in fibers of inflorescence stems. Plant Signaling & Behavior, 10.

ZHONG, R. & YE, Z.-H. 2015b. Secondary Cell Walls: Biosynthesis, Patterned Deposition and Transcriptional Regulation. Plant and Cell Physiology, 56, 195-214.

ZHOU, F., MENKE, F. L. H., YOSHIOKA, K., MODER, W., SHIRANO, Y. & KLESSIG, D. F. 2004. High humidity suppresses ssi4 -mediated cell death and disease resistance upstream of MAP kinase activation, H ₂ O ₂ production and defense gene expression. The Plant Journal, 39.

ZHOU, J., LEE, C., ZHONG, R. & YE, Z.-H. 2009. MYB58 and MYB63 Are Transcriptional Activators of the Lignin Biosynthetic Pathway during Secondary Cell Wall Formation in Arabidopsis The Plant Cell, 21.

ZHOU, N., TOOTLE, T. L. & GLAZEBROOK, J. 1999. Arabidopsis PAD3, a Gene Required for Camalexin Biosynthesis, Encodes a Putative Cytochrome P450 Monooxygenase. The Plant Cell, 11.

ZHOU, N., TOOTLE, T. L., TSUI, F., KLESSIG, D. F. & GLAZEBROOK, J. 1998. PAD4 Functions Upstream from Salicylic Acid to Control Defense Responses in Arabidopsis. The Plant Cell, 10.

ZHOU, X., DING, D., MA, J., JI, Z., ZHANG, X. & XU, F. 2015. Ultrastructure and Topochemistry of Plant Cell Wall by Transmission Electron Microscopy. The Transmission Electron Microscope - Theory and Applications. InTech.

ZHU, Q., DRÖGE-LASER, W., DIXON, R. A. & LAMB, C. 1996. Transcriptional activation of plant defense genes. Current Opinion in Genetics & Development, 6.

ZHU, Y., QIAN, W. & HUA, J. 2010. Temperature Modulates Plant Defense Responses through NB-LRR Proteins. PLoS Pathogens, 6.

ZIMMERMANN, M. H. & BROWN, C. L. 1971. Trees: structure and function, Springer-Verlag Berlin Heidelberg.

ZULAWSKI, M., SCHULZE, G., BRAGINETS, R., HARTMANN, S. & SCHULZE, W. X. 2014. The Arabidopsis Kinome: phylogeny and evolutionary insights into functional diversification. BMC Genomics, 15.